DEEP CARBON SCIENCE

EDITED BY: Isabelle Daniel, Sabin Zahirovic, Dan J. Bower, Artur Ionescu, Mattia Pistone, Sami Mikhail and Dawn Cardace

PUBLISHED IN: Frontiers in Earth Science, Frontiers in Microbiology and Frontiers in Astronomy and Space Sciences

frontiers Research Topics

ISSN 1664-8714
ISBN 978-2-88966-328-6
DOI 10.3389/978-2-88966-328-6

About Frontiers

Frontiers is more than just an open-access publisher of scholarly articles: it is a pioneering approach to the world of academia, radically improving the way scholarly research is managed. The grand vision of Frontiers is a world where all people have an equal opportunity to seek, share and generate knowledge. Frontiers provides immediate and permanent online open access to all its publications, but this alone is not enough to realize our grand goals.

Frontiers Journal Series

The Frontiers Journal Series is a multi-tier and interdisciplinary set of open-access, online journals, promising a paradigm shift from the current review, selection and dissemination processes in academic publishing. All Frontiers journals are driven by researchers for researchers; therefore, they constitute a service to the scholarly community. At the same time, the Frontiers Journal Series operates on a revolutionary invention, the tiered publishing system, initially addressing specific communities of scholars, and gradually climbing up to broader public understanding, thus serving the interests of the lay society, too.

Dedication to Quality

Each Frontiers article is a landmark of the highest quality, thanks to genuinely collaborative interactions between authors and review editors, who include some of the world's best academicians. Research must be certified by peers before entering a stream of knowledge that may eventually reach the public - and shape society; therefore, Frontiers only applies the most rigorous and unbiased reviews.
Frontiers revolutionizes research publishing by freely delivering the most outstanding research, evaluated with no bias from both the academic and social point of view. By applying the most advanced information technologies, Frontiers is catapulting scholarly publishing into a new generation.

What are Frontiers Research Topics?

Frontiers Research Topics are very popular trademarks of the Frontiers Journals Series: they are collections of at least ten articles, all centered on a particular subject. With their unique mix of varied contributions from Original Research to Review Articles, Frontiers Research Topics unify the most influential researchers, the latest key findings and historical advances in a hot research area! Find out more on how to host your own Frontiers Research Topic or contribute to one as an author by contacting the Frontiers Editorial Office: researchtopics@frontiersin.org

DEEP CARBON SCIENCE

Topic Editors:
Isabelle Daniel, Université Claude Bernard Lyon 1, France
Sabin Zahirovic, The University of Sydney, Australia
Dan J. Bower, University of Bern, Switzerland
Artur Ionescu, Babeș-Bolyai University, Romania
Mattia Pistone, University of Georgia, United States
Sami Mikhail, University of St Andrews, United Kingdom
Dawn Cardace, University of Rhode Island, United States

Citation: Daniel, I., Zahirovic, S., Bower, D. J., Ionescu, A., Pistone, M., Mikhail, S., Cardace, D., eds. (2021). Deep Carbon Science. Lausanne: Frontiers Media SA. doi: 10.3389/978-2-88966-328-6

Table of Contents

frontiers in Earth Science

EDITORIAL
published: 12 November 2020
doi: 10.3389/feart.2020.611295

Editorial: Deep Carbon Science

Dawn Cardace[1], Dan J. Bower[2], Isabelle Daniel[3], Artur Ionescu[4,5], Sami Mikhail[6], Mattia Pistone[7] and Sabin Zahirovic[8]*

[1]Department of Geosciences, University of Rhode Island, Kingston, RI, United States, [2]Center for Space and Habitability (CSH), University of Bern, Bern, Switzerland, [3]Univ Lyon, Univ Lyon 1, ENSL, CNRS, LGL-TPE, Villeurbanne, France, [4]Faculty of Environmental Science and Engineering, Babes-Bolyai University, Cluj-Napoca, Romania, [5]Department of Physics and Geology, University of Perugia, Perugia, Italy, [6]School of Earth and Environmental Sciences, University of St Andrews, St Andrews, United Kingdom, [7]Department of Earth Sciences, Franklin College of Arts and Sciences, University of Georgia, Athens, GA, United States, [8]Earth Byte Group, School of Geosciences, The University of Sydney, Darlington, NSW, Australia

Keywords: carbon, geology, tectonics, biosphere, volcanism, geodynamics, volatiles, carbon cycle

Editorial on the Research Topic

Deep Carbon Science

Our understanding of the slow, deep carbon cycle, key to Earth's habitability is examined here. Because the carbon cycle links Earth's reservoirs on nano- to mega-scales, we must integrate geological, physical, chemical, biological, and mathematical methods to understand objects and processes so small and yet so vast. Here, we profile current research in the physical chemistry of carbon in natural and model systems, processes ongoing in the deepest portions of planets, and observations of carbon utilization by the deep biosphere. The relationships between the carbon cycle and planetary habitability are undeniable, forming a conceptual anchor to all work in deep carbon science.

Carbon minerals respond to changing pressures, temperatures, and geochemical conditions. The geologic record preserves evidence of transitional periods at the submicroscopic to regional landscape scales, and demonstrates interplay between carbon-bearing phases and the biosphere. In a new review, Morrison et al. (2020) cast a retrospective look through deep time and call for emerging approaches to clarify the coevolution of the biosphere and geosphere.

Critical to transformations of Earth's carbon inventory over time are indomitable tectonics – which influence Earth's surface environment, weathering, metamorphism, magmatism, and volcanism. The slow, deep (endogenous) carbon cycle refines and re-distributes carbon within Earth. In fact, over the 200-million-year-long time scale, important tectonic controls on carbon cycling emerge (Wong et al., 2019). Wong et al. (2019) document the spatiotemporal evolution of fluxes inferred from plate tectonic reconstructions, and highlight CO_2 fluxes from continental rift settings post-Pangea. The volcanic flux of CO_2 has been successfully reconstructed by direct study of CO_2 flux through lakes and adjacent soils (Hughes et al., 2019), an important and often overlooked CO_2 valve linking lithosphere, atmosphere, and hydrosphere. From perspectives rooted deeper in the tectonic system, the important roles that serpentinites play in the carbon cycle are evaluated in two senses: 1) serpentinite as a carbon vector to the deep mantle (Merdith et al., 2019), and 2) serpentine mud volcanoes as sites of carbon mobilization through organic acid release (Eickenbusch et al., 2019), in a Mariana Trench case study.

The physical properties of carbonaceous melt extraction and chemical exchange are experimentally examined as reduced metallic Fe-C melts (Dong et al., 2019) and oxidized carbonate melts (Sanloup et al., 2019b—note corrigendum). Regarding carbon-bearing metallic melts in the mid-mantle, Dong et al. (2019) apply experimental data to predict immobility of metallic carbon, meaning deep Fe-C melts will remain isolated in a silicate rock. Sanloup et al. (2019a) experimentally determine the density, structure and glass-forming ability of Fe-carbonate melt ($FeCO_3$) in the mid- to lower-mantle, and find that carbon becomes fully four-fold coordinated and the melt highly viscous, hence largely unreactive in the deep lower mantle. Both studies show deep carbon to be immobile and unreactive, under the conditions of their experimental designs.

Edited and reviewed by:
Carmen Sanchez-Valle, University of Münster, Germany

****Correspondence:***
Dawn Cardace
cardace@mail.uri.edu

Specialty section:
This article was submitted to Earth and Planetary Materials, a section of the journal Frontiers in Earth Science

Received: *28 September 2020*
Accepted: *23 October 2020*
Published: *12 November 2020*

Citation:
Cardace D, Bower DJ, Daniel I, Ionescu A, Mikhail S, Pistone M and Zahirovic S (2020) Editorial: Deep Carbon Science. Front. Earth Sci. 8:611295. doi: 10.3389/feart.2020.611295

Linking geological and biological aspects of carbon cycling reveal emerging challenges. The drawdown of atmospheric carbon into rock reservoirs is examined through the lens of Urey reactions and the efficiency of carbon deposition in the continental crust reservoir (Kellogg et al., 2019); the authors argue that carbon stored in Earth's continental crust could have been extracted either from the early atmosphere or from the mantle (over a longer period of time) or both. Kellogg et al. (2019) challenge the community to prioritize better constraints on the concentration of carbon in the atmosphere and continental crust over geologic time. Their work also addresses the recovery (relaxation time) of Earth's climate to volcanically-forced climate change, using the Paleocene-Eocene thermal maximum as a case study; the calculated relaxation time is ~50,000 years. This timeframe is certainly of modern concern, given anthropogenic injections of carbon into the atmosphere.

Shales are known to be large carbon sinks in low pressure settings. Basu et al. (2019) ask whether shales can retain significant carbon during low pressure-temperature and high pressure-temperature processes during the subduction of Earth's crust. In a custom-built high vacuum line, they incrementally heat shale samples from 200 to 1,400°C in the presence of O_2 gas and record the carbon and nitrogen abundances, $\delta^{13}C$ values, and the atomic C/N ratios for the gas at each stage of heating. Basu et al. (2019) propose that carbon silicate minerals, biomineralized and/or occluded, can be efficiently retained as a refractory phase and transferred into Earth's mantle through subduction.

The important role of serpentinization is emphasized in this context also: Barbier et al. (2020) offer a detailed review of hydrogen, methane, and hydrocarbon formation through experimental serpentinization, informed by network analysis. The relevance of the frequently invoked Fischer-Tropsch-type (FTT) reactions to produce methane from the abiotic reduction of oxidized carbon by H_2 is questioned. Barbier et al. (2020) follow the forms and movement of carbon through the near ubiquitous, extensive serpentinization process, operating beneath most past and present seabeds.

Carbon cycling mediated by the deep biosphere is tracked also, in terms of function, detection, and novel findings. The deep mine microbial observatory in south Dakota, United States, described by Osburn et al. (2019), is a stable portal to the continental deep subsurface, with a rich, initial database on which future studies can pivot. In the marine realm, Cario et al. (2019) offer a perspective on the state of the science exploring the deep biosphere beneath the seabed. Aspects of the growth and resilience of subseafloor crustal biofilms are documented (Ramirez et al., 2019), and methods enabling new discernment of virus abundance in the subseafloor sedimentary blanket are shared (Pan et al., 2019). A new serpentinite-influenced organism, *Petrocella atlantisensis*, cultured from Atlantis Massif oceanic core complex rocks sampled during IODP Expedition 357 is described, observed at controlled hydrostatic pressure (Quemeneur et al., 2019).

The findings reported in deep carbon science underscore the need for multidisciplinary commitment to open questions related to Earth's carbon cycle. It is clear that the processes driven by, and driving, plate tectonics buffer the carbon fluxes on which life has been dependent for billions of years (e.g., fluctuations in atmosphere-ocean geochemistry). Important work includes methodical application of current techniques, but much work requires new ways of thinking: multifaceted investigations that connect the deep and shallow biospheres, and/or describe links between the whole biosphere and points of contact with geosphere have the potential to transform our thinking. The breadth of disciplines and scientific approaches collated in deep carbon science provides exciting insight into a future where the traditional boundaries of classic disciplines become blurred. This, we argue, is the only way to reveal the true nature and extent of carbon cycle phenomena that are both vast and diminutive, slow yet fast, known but inaccessible, and everywhere all at once.

AUTHOR CONTRIBUTIONS

DC drafted a first version of this editorial. All authors contributed to and approved the final version.

FUNDING

SZ was supported by Australian Research Council grant IH130200012, a University of Sydney Robinson Fellowship, and Alfred P. Sloan grants G-2017-9997 and G-2018-11296.

ACKNOWLEDGMENTS

This research topic developed under the auspices of the Deep Carbon Observatory, whose continuous support led to profound changes in our understanding of the connections between fast and slow, shallow and deep, modern and ancient processes undergone by carbon in its various forms. DB acknowledges Swiss National Science Foundation (SNSF) Ambizione Grant 173992. DC acknowledges the support of the NASA Astrobiology Institute (Cooperative Agreement NNA15BB02A). MP acknowledges the support of the Swiss National Science Foundation (Ambizione Fellowship PZ00P2_168166) and the UGA Presidential Funds.

REFERENCES

Barbier, S., Huang, F., Andreani, M., Tao, R., Hao, J., Eliesh, A., et al. (2020). A review of H2, CH4, and hydrocarbon formation in experimental serpentinization using network analysis. *Front. Earth Sci.* 8, 209. doi:10.3389/feart.2020.00209

Basu, S., Verchovsky, A. B., Bogush, A., Jones, A. P., and Jourdan, A.-L. (2019). Stability of organic carbon components in shale: implications for carbon cycle. *Front. Earth Sci.* 7, 297. doi:10.3389/feart.2019.00297

Cario, A., Oliver, G. C., and Rogers, K. L. (2019). Exploring the deep marine biosphere: challenges, innovations, and opportunities. *Front. Earth Sci.* 7, 225. doi:10.3389/feart.2019.00225

Dong, J., Li, J., and Zhu, F. (2019). Wetting behavior of iron–carbon melt in silicates at mid-mantle pressures with implications for Earth's deep carbon cycle. *Front. Earth Sci.* 7, 268. doi:10.3389/feart.2019.00268

Eickenbusch, P., Takai, K., Sissman, O., Suzuki, S., Menzies, C., Sakai, S., et al. (2019). Origin of short-chain organic acids in serpentinite mud volcanoes of the Mariana convergent margin. *Front. Microbiol.* 10, 1729. doi:10.3389/fmicb.2019.01729

Hughes, E. C., Mazot, A., Kilgour, G., Asher, C., Michelini, M., Britten, K., et al. (2019). Understanding degassing pathways along the 1886 tarawera (New Zealand) volcanic fissure by combining soil and lake CO2 fluxes. *Front. Earth Sci.* 7, 264. doi:10.3389/feart.2019.00264

Kellogg, L. H., Turcotte, D. L., and Lokavarapu, H. (2019). On the role of the Urey reaction in extracting carbon from the earth's atmosphere and adding it to the continental crust. *Front. Astron. Space Sci.* 6, 62. doi:10.3389/fspas.2019.00062

Merdith, A. S., Atkins, S. E., and Tetley, M. G. (2019). Tectonic controls on carbon and serpentinite storage in subducted upper oceanic lithosphere for the past 320 ma. *Front. Earth Sci.* 7, 332. doi:10.3389/feart.2019.00332

Morrison, S. M., Buongiorno, J., Downs, R. T., Eleish, A., Fox, P., Giovannelli, D., et al. (2020). Exploring carbon mineral systems: recent advances in C mineral evolution, mineral ecology, and network analysis. *Front. Earth Sci.* 8, 208. doi:10.3389/feart.2020.00208

Osburn, M. R., Kruger, B., Masterson, A. L., Casar, C. P., and Amend, J. P. (2019). Establishment of the deep mine microbial observatory (DeMMO), South Dakota, USA, a geochemically stable portal into the deep subsurface. *Front. Earth Sci.* 7, 196. doi:10.3389/feart.2019.00196

Pan, D., Morono, Y., Inagaki, F., and Takai, K. (2019). An improved method for extracting viruses from sediment: detection of far more viruses in the subseafloor than previously reported. *Front. Microbiol.* 10, 878. doi:10.3389/fmicb.2019.00878

Quéméneur, M., Erauso, G., Frouin, E., Zeghal, E., Vandecasteele, C., Ollivier, B., et al. (2019). Hydrostatic pressure helps to cultivate an original anaerobic bacterium from the Atlantis Massif subseafloor (IODP expedition 357): Petrocella atlantisensis gen. Nov. sp. nov. *Front. Microbiol.* 10, 1497. doi:10.3389/fmicb.2019.01497

Ramírez, G. A., Garber, A. I., Lecoeuvre, A., D'Angelo, T., Wheat, C. G., and Orcutt, B. N. (2019). Ecology of subseafloor crustal biofilms. *Front. Microbiol.* 10, 1983. doi:10.3389/fmicb.2019.01983

Sanloup, C., Hudspeth, J. M., Afonina, V., Cochain, B., Konôpková, Z., Lelong, G., et al. (2019a). Polymerized 4-fold coordinated carbonate melts in the deep mantle. *Front. Earth Sci.* 7, 72. doi:10.3389/feart.2019.00155

Sanloup, C., Hudspeth, J. M., Afonina, V., Cochain, B., Konôpková, Z., Lelong, G., et al. (2019b). Corrigendum: polymerized 4-fold coordinated carbonate melts in the deep mantle. *Front. Earth Sci.* 7, 155. doi:10.3389/feart.2019.00155

Wong, K., Mason, E., Brune, S., East, M., Edmonds, M., and Zahirovic, S. (2019). Deep carbon cycling over the past 200 million years: a review of fluxes in different tectonic settings. *Front. Earth Sci.* 7, 263. doi:10.3389/feart.2019.00263

Conflict of Interest: The authors declare that the research was conducted in the absence of any commercial or financial relationship that could be construed as a potential conflict of interest.

frontiers in Earth Science

ORIGINAL RESEARCH
published: 10 April 2019
doi: 10.3389/feart.2019.00072

Polymerized 4-Fold Coordinated Carbonate Melts in the Deep Mantle

Chrystèle Sanloup[1], Jessica M. Hudspeth[2], Veronika Afonina[3], Benjamin Cochain[2], Zuzana Konôpková[4], Gérald Lelong[1], Laurent Cormier[1] and Chiara Cavallari[5]*

[1] Muséum National d'Histoire Naturelle, UMR CNRS 7590, IRD, Institut de Minéralogie, de Physique des Matériaux et de Cosmochimie, IMPMC, Sorbonne Université, Paris, France, [2] Institut des Sciences de la Terre de Paris, Sorbonne Université, CNRS, Paris, France, [3] SUPA, Centre for Science at Extreme Conditions and School of Physics and Astronomy, University of Edinburgh, Edinburgh, United Kingdom, [4] DESY Photon Science, Hamburg, Germany, [5] European Synchrotron Radiation Facility, ESRF, Grenoble, France

Our understanding of the deep carbon cycle has witnessed amazing advances in the last decade, including the discovery of tetrahedrally coordinated high pressure (*P*) carbonate phases. However, little is known about the physical properties of their molten counterpart at moderate depths, while their properties at lower mantle conditions remain unexplored. Here, we report the structure and density of $FeCO_3$ melts and glasses from 44 to 110 GPa by means of *in situ* x-ray synchrotron diffraction, and *ex situ* Raman and x-ray Raman spectroscopies. Carbon is fully transformed to 4-fold coordination, a bond change recoverable at ambient *P*. While low *P* melts react with silica, resulting in the formation of silico-carbonate glasses, high *P* melts are not contaminated but still quench as glasses. Carbonate melts are therefore polymerized, highly viscous and poorly reacting with silicates in the lower mantle, in stark opposition with their low *P* properties.

Keywords: carbonate melts, high pressure, x-ray diffraction, Raman, x-ray Raman, polymerization, deep mantle

OPEN ACCESS

Edited by:
Dan J. Bower, University of Bern, Switzerland

Reviewed by:
Zhicheng Jing, Southern University of Science and Technology, China
Alexander F. Goncharov, Carnegie Institution for Science (CIS), United States

****Correspondence:***
Chrystèle Sanloup
chrystele.sanloup@sorbonne-universite.fr

Specialty section:
This article was submitted to Earth and Planetary Materials, a section of the journal Frontiers in Earth Science

Received: *15 January 2019*
Accepted: *19 March 2019*
Published: *10 April 2019*

Citation:
Sanloup C, Hudspeth JM, Afonina V, Cochain B, Konôpková Z, Lelong G, Cormier L and Cavallari C (2019) Polymerized 4-Fold Coordinated Carbonate Melts in the Deep Mantle. Front. Earth Sci. 7:72. doi: 10.3389/feart.2019.00072

1. INTRODUCTION

Although the lower mantle is mostly a reducing environment with the presence of reduced Fe (Frost et al., 2004; Smith et al., 2016), significant amount of subducted carbonates are estimated to be preserved (Litasov and Shatskiy, 2018). Transition to 4-fold carbon was first predicted for crystalline $CaCO_3$ (Oganov et al., 2006; Arapan et al., 2007). This transition strongly depends on the carbonate composition, occurring for $CaCO_3$ above 105 GPa (Lobanov et al., 2017), 80 GPa for $MgCO_3$ (Oganov et al., 2008; Boulard et al., 2011), and 50 GPa for $FeCO_3$ (Liu et al., 2015), while intermediate $CaCO_3$-$MgCO_3$-$FeCO_3$ compositions form a single tetrahedral carbonate phase (Merlini et al., 2017) unlike silicates. This transition induces polymerization such as sheets or 3-membered rings for $MgCO_3$ (Oganov et al., 2008), and chains for $CaCO_3$ (Oganov et al., 2006). In contrast, our knowledge of carbonate melts structure at depth is scarce and limited to upper mantle pressures. The melting curves of $CaCO_3$, Na_2CO_3, and $FeCO_3$ have been measured over most of the upper mantle regime (Kang et al., 2015; Li et al., 2017), and viscosity measurements up to 6 GPa span several compositions [$K_2Ca(CO_3)_2$ and $K_2Mg(CO_3)_2$ by (Dobson et al., 1996), $CaCO_3$ and natural dolomite by (Kono et al., 2014), Na_2CO_3 by (Stagno, 2018)]. Structural data instead have only been collected on molten $CaCO_3$ below 10 GPa (Hudspeth et al., 2018) while theoretical investigations of the properties of carbonate melts cover a larger *P*-range but are also limited to the carbon 3-fold stability field (Vuilleumier et al., 2014; Zhang and Liu , 2015; Du et al., 2018; Desmaele et al., 2019). One main question is therefore how this 3 to 4-fold transition translates in the molten state, and what are the consequences on the physical and chemical properties of carbonate melts? Of particular interest is the mobility and reactivity of carbonate melts in the lower

mantle, knowing that these properties underpin the key role played by carbonate melts in mantle geodynamics through lubrication of plate tectonics, cratonic roots (Foley, 2008) and ascending plumes (Litasov et al., 2013).

The role of Fe in the deep carbon cycle is emphasized by the predominance of Fe-rich ferropericlase in diamond inclusions from the lower mantle (Kaminsky, 2012). The lowest transition *P* from 3 to 4-fold C in $FeCO_3$ amongst carbonates justifies its choice as the first composition to investigate. Not only this transition occurs at less challenging experimental conditions, but it might be driven by Fe high spin to low spin transition at 40.4 GPa (Weis et al., 2017), a consequence of which being the large enrichment in Fe of (Mg,Fe)-carbonates coexisting with bridgmanite to almost pure $FeCO_3$ (Lobanov et al., 2015). Besides, high Fe concentration stabilizes $(Ca,Mg,Fe)^{IV}CO_3$ with respect to single cation 3-fold carbonates at mid mantle conditions (30–50 GPa) (Solomatova and Asimow, 2018). Formation of Fe-carbonates in the lower mantle might also result from carbonation of Fe-oxides [(Mg,Fe)O, FeOOH] with CO_2 (Boulard et al., 2018, 2012). Last but not least, $FeCO_3$ is a technical choice as it can be laser heated, which is required to reach lower mantle conditions without the need for additional laser coupler.

2. MATERIALS AND METHODS

2.1. Materials and Chemical Analyses

The starting natural crystalline siderite sample (mineralogical collection at Sorbonne Université) was loaded in the sample chamber laser-drilled in a rhenium gasket as 20 μm-thick platelet between two equally thick platelets of compressed SiO_2 powder. The SiO_2 platelets act as thermal insulators and *P*-transmitting medium. Only one sample was used per *P* point (**Figure 1**) to avoid repeated laser-heatings, and preserve the chemical integrity of the sample. Six samples could be recovered after the experiments, embedded in epoxy and polished for analysis. Samples 8, 9, and 15 were carbon-coated for SEM imaging (**Figure 2**), samples 8 and 15 were then repolished and gold-coated along with samples 13, 14, and 20 for electron microprobe analysis using a CAMECA SX-FIVE analyzer (EMPA) at the Camparis center of Sorbonne Université (**Table 1**), using the following operating conditions: 15 keV, 10 nA. We used a defocused beam size of 10 μm to get an average composition at the laser-heated spot.

2.2. *P-T* Conditions

We used diamond-anvil cells and a double-sided infra-red laser focussed down to 20 μm to generate high *T* and *P*. For each *P* point, targeted power was increased in 2 W increments from 20 to 50 W of power on each laser depending on *P* until complete melting of the sample. Melting was identified by disappearance of diffraction peaks apart from SiO_2 peaks, and by the appearance of diffuse scattering. As we used the off-axis heating system to avoid using carbon mirrors that would add to the x-ray background signal and compromise processing of the scattered signal, *T* could not be measured by pyrometric techniques. $FeCO_3$ melting curve has only been measured up to 20 GPa (Kang et al., 2015), where it reaches 1,865 K. The stishovite to $CaCl_2$ SiO_2 transition has been investigated up to 90 GPa (Fischer et al., 2018), this constrains *T* to a maximum of 2,300 K at 79 GPa and 2,500 K at 83 GPa as $CaCl_2$ is the observed SiO_2 structure for the three highest *P* runs, while stishovite is observed below. We therefore consider that x-ray diffraction patterns were collected on molten $FeCO_3$ within the 2,000 K–2,500 K interval except for the highest *P* point that is only constrained to below 3,500 K from extrapolation of the stishovite-$CaCl_2$ Clapeyron slope (Fischer et al., 2018). *P* is measured at room *T* using fluorescence of a ruby sphere added in the sample chamber (Mao et al., 1986) and SiO_2 equations of state (Andrault et al., 1998; Nishihara et al., 2005) for quenched samples, and using only SiO_2 equations of state for molten samples with error bars on *P* including the effect of a 2,000 K–2,500 K *T*-range, and up to 3,500 K for the 110 GPa data point.

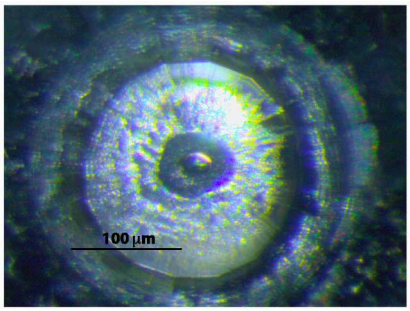

FIGURE 1 | Microphotograph of the sample after laser heating at 110 GPa. Single shot laser heating resulted in the formation of a quasi-spherical pure carbonate glass that was removed from the gasket for EPMA and/or SEM analyses.

2.3. X-ray Diffraction Methods

We collected *in situ* high *P-T* x-ray diffraction data in laser-heated diamond anvil cells at the extreme conditions beamline P02.2 at the PETRAIII synchrotron. We used symmetric diamond-anvil cells equipped with 70° opening Boehler-Almax seats in order to access a wider *q*-range up to 10 $Å^{-1}$, and reduce the diamond Compton contribution as Boehler-Almax anvils are only 1.5 mm thick. The x-ray monochromatic beam (42.7 keV) was focussed down to a size of 4 × 6 $μm^2$, allowing high spatial resolution in direct space. To limit iron migration away from the laser heating spot due to Soret effect, the laser shutters were opened only once the targeted power was reached, and held open for 10 s during which 10 x-ray diffraction patterns of 1 s acquisition time were recorded on a Perkin-Elmer 2-D detector. 2-D patterns were integrated using the Fit2D software (Hammersley et al., 1996). In order to isolate the scattered intensity from the molten $FeCO_3$ only, each sample was removed from the gasket, and the gasket put back in place to collect x-ray data on the empty cell. Obtained patterns were then scaled vertically to match the baseline of x-ray patterns collected on the starting crystalline sample under *P* (Sanloup and de Grouchy, 2018). This last step ensures that any *P* effect on the background is corrected for. Amongst eight successful runs (**Table 1**) for

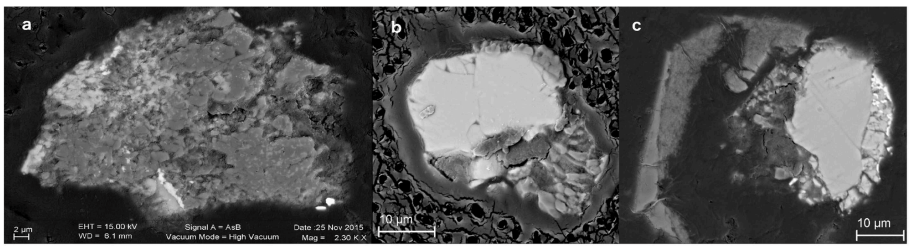

FIGURE 2 | SEM images of recovered samples. Low *P* sample 8 **(a)** shows pervasive contamination of carbonate sample with SiO_2 *P*-transmitting medium. High *P* samples 9 **(b)** and 15 **(c)** show that chemical integrity of carbonate melt (homogeneous light gray zone) was preserved.

TABLE 1 | Run conditions, quenched products and their chemical composition in wt% obtained from EMPA. One standard deviations are given in parentheses. Starting natural siderite sample also contained <0.1 wt% CaO and MnO.

#	*P* melt/ glass (GPa)	CO_2	FeO	MgO	SiO_2	Total
6	11.6/ –	Not recovered, reaction confirmed by XRD (**Figure 4**)				
8	15/14	25.7(9.2)	42.2(5.8)	0.1(0.1)	24.2(6.7)	92.2
15	51/44	40.6(0.5)	58.9(9.3)	0.3(0.1)	0.3(0.2)	100.0
13	55/–	41.2(2.6)	54.4(1.3)	0.3(0.2)	2.0(1.9)	98.0
20	63/57	36.6(6.8)	57.7(1.3)	0.4(0.4)	0.7(0.8)	95.4
9	79/72	Not analyzed, C-coated for SEM (**Figure 2**)				
12	83/77	Not recovered				
14	110/108	37.8(8.7)	58.5(1.1)	0.2(0.1)	0.7(0.8)	97.3
Sample for x-ray Raman	59	Not analyzed, only glass sphere preserved				

which full melting was observed, intensity from molten $FeCO_3$ could only be processed for the highest *P* run for which the sample vs. SiO_2 platelets thickness ratio was slightly higher, the scattered intensity being too weak for the lower *P* points. All glass patterns could be processed. The x-ray diffracted intensity data are converted into the structure factor, $S(q)$ (**Figures 3A**, **4**), using the Ashcroft-Langreth formalism. The radial distribution function $g(r)$ (**Figure 3B**), that describes ion-ion contributions in real space, is obtained by Fourier transforming of $S(q)$,

$$g(r) = \frac{1}{2\pi^2 rn}\int_0^\infty qS(q)\sin(qr)\,dq \tag{1}$$

where $n = \frac{\rho \mathcal{N}_A}{M}$, $\mathcal{N}_A$ is the Avogadro number, M the mean atomic molar mass, and ρ the density.

2.4. Density Measurements

The method to derive density from x-ray diffraction data on melts compressed in diamond-anvil cell experiments (Eggert et al., 2002; Sanloup et al., 2013) consists in minimizing the oscillations in $g(r)$ where there should not be any signal, i.e., below the minimum interatomic distance ($r < 0.95$ Å here). This method requires that the background, essentially the Compton signal from the diamond anvils that dominates the total diffracted intensity, is perfectly subtracted.

As the C-O contribution is distinct on $g(r)$ of quenched glasses up to 83 GPa, we also ran consistency checks by fixing the C-O coordination number to 4 as indicated by x-ray Raman spectra (*cf* Results section), and simulating the C-O contribution using the obtained density values against a gaussian with the following equation:

$$g(r) = \frac{c_C c_O K_C K_O}{Z_{tot}^2 n S_\infty}\frac{A}{\sigma\sqrt{2\pi}}exp\left(-\frac{(r-d)^2}{2\sigma^2}\right) \tag{2}$$

where c_C and c_O are the atomic proportions of carbon and oxygen, K_C and K_O are defined as the average effective atomic number over the experimental q-range (Eggert et al., 2002) and calculated using form factors from Hajdu (1972).

$$S_\infty = \frac{\Sigma_p K_p^2}{Z_{tot}^2} \tag{3}$$

and

$$A = \frac{CN}{\int \frac{4\pi r^2}{\sigma\sqrt{2\pi}}exp\left(\frac{-(r-d)^2}{2\sigma^2}\right)dr} \tag{4}$$

with K_p, the effective atomic number (Eggert et al., 2002), Z_{tot} the total atomic number of the compositional unit (e.g., $FeCO_3$), CN the C-O coordination number fixed to 4, d the C-O inter-atomic distance, and σ a parameter depending on structural disorder, $\sigma = k\sqrt{d}$ where k is an adjustable parameter (Hosemann and Bagchi, 1962) with a value of 0.11 here. The C-O contribution to $g(r)$ thus calculated adequately fits the experimental ion-ion contribution (dashed lines on **Figure 2b**), hence comforting the obtained density values.

2.5. X-ray Raman and Raman Methods

Raman and x-ray Raman spectra were collected at ambient conditions on glassy $FeCO_3$ recovered from x-ray diffraction experiments and from additional laser-heated diamond anvil cell synthesis, respectively.

X-ray Raman data were collected at an incident energy of 9.7 keV at the C K-edge on beamline ID20 of the European Synchrotron Radiation Facility (ESRF), beamsize was 15 ×

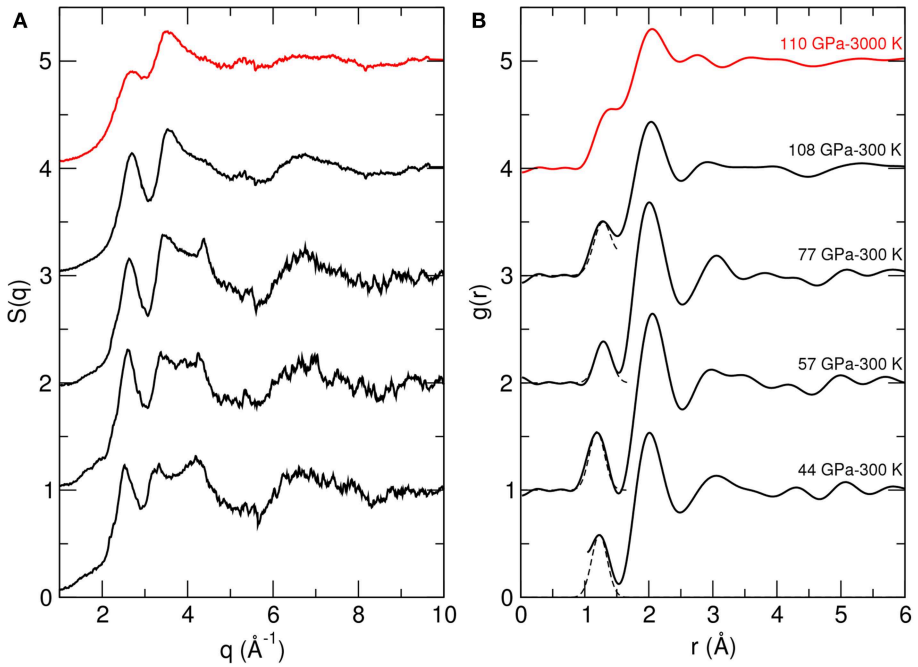

FIGURE 3 | Structure of non-crystalline $FeCO_3$ at high pressures. **(A)** Structure factor, *S*(*q*), for all quenched glasses (black) and the highest *P* melt (red). **(B)** Corresponding radial distribution functions, *g*(*r*). Dashed lines are fits to the C-O contribution at 1.2-1.3 Å where there is no overlap with farther contributions.

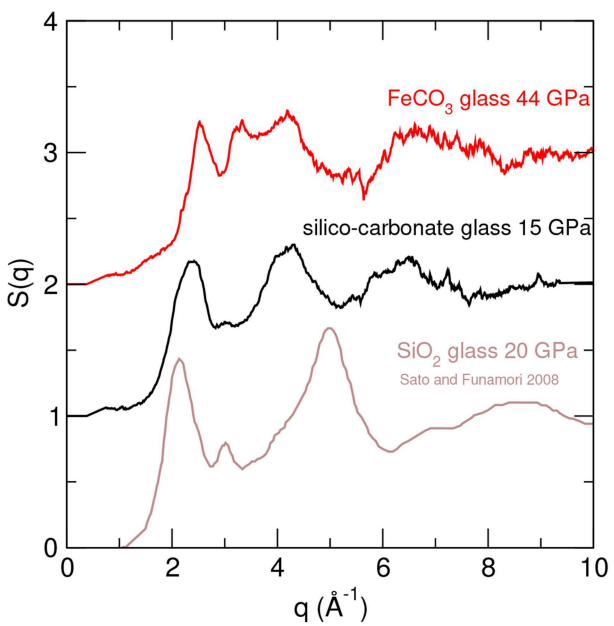

FIGURE 4 | Structure factor, *S*(*q*), for low *P* reacted $FeCO_3$+SiO_2 glass (black), compared to SiO_2 glass at 20 GPa (Sato and Funamori, 2008) (brown) and $FeCO_3$ glass at 44 GPa (red). Low *P* sample 8 (15 GPa) shows intermediate structure between SiO_2 glass and high *P* $FeCO_3$ glasses.

15 μm^2. The large-solid-angle x-ray scattering spectrometer (Huotari et al., 2017) was set up with 24 Si(660) analyzer crystals for an average momentum transfer of 7.3 ± 0.2 Å^{-1} and an overall energy resolution of 0.7 eV. All experimental data were analyzed using the XRStools software package (Sahle et al., 2015). The integrated intensity of each spectrum was normalized over a 35 eV energy range. Glassy $FeCO_3$ spheres had been previously synthesized at 59 GPa using the same P02.2 laser heating system in PetraIII as for x-ray diffraction experiments. LiF was used instead of SiO_2 as a *P*-transmitting medium to avoid any contamination of the x-ray Raman signal by oxygen from SiO_2 as measurements at the O K-edge were initially planned but signal was to weak for data to be processed. Despite its higher melting curve than siderite (Boehler et al., 1997), LiF salt could not be used for the x-ray diffraction experiments due to its continuous powder diffracted signal that prevents a qualitative analysis of the diffuse scattering signal from molten $FeCO_3$.

Raman spectra were collected on glassy $FeCO_3$ recovered from x-ray diffraction experiments using 633 nm wavelength in order to preserve the samples, using more energetic lower wavelengths resulted in dissociation of the sample and detection of hematite signal.

3. RESULTS

All samples are systematically quenched as a glass. Chemical integrity of $FeCO_3$ molten spheres is observed for runs conducted above 40 GPa, apart from a marginal fraction at the glass-SiO_2 interface in one sample showing enrichment of the *P*-transmitting medium in Fe and C. Instead, the lowest *P* samples, i.e., 11 and 15 GPa, have reacted with the SiO_2 *P*-transmitting medium. This is shown by SEM imaging (**Figure 2**) and EMPA analysis on sample 8 (**Table 1**). High *P* carbonate melts are thus

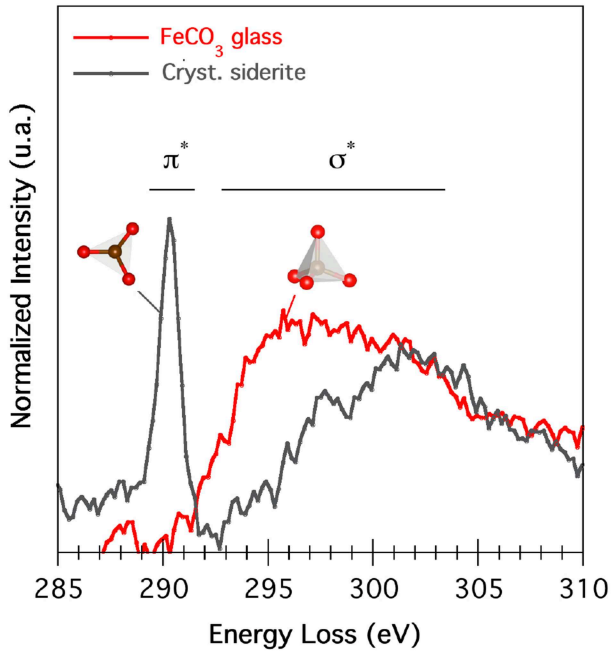

FIGURE 5 | X-ray Raman spectra collected at the carbon K-edge on crystalline siderite and high *P*-quenched $FeCO_3$ glasses at ambient conditions. The disappearance of the π^* feature, which is solely related to the three-fold coordinated carbon, is a spectroscopic evidence of a full four-fold coordination state in the glassy structure of $FeCO_3$.

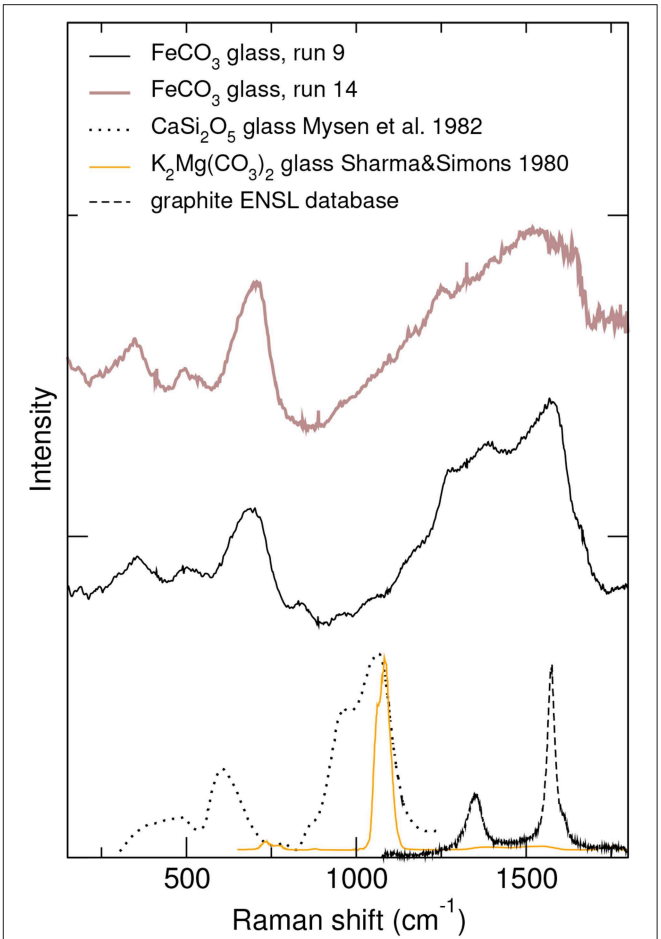

FIGURE 6 | Raman spectra collected on high *P*-quenched $FeCO_3$ glasses (runs 9 and 14) at ambient conditions.

much less reactive than low *P* melts. This might not contradict the observed reactivity of high *P* crystalline $MgCO_3$ with SiO_2 (Seto et al., 2008; Maeda et al., 2017) due to the much longer heating durations (20–240 min against 10 s heating duration in this work); alternatively, Fe stabilizing effect on high *P* carbonates could be at stake. We observe no disproportionation of Fe as was reported in the crystalline state in some studies (Boulard et al., 2011; Cerantola et al., 2017) but not in others (Liu et al., 2015). This might be due to different *P*-*T* paths followed, i.e., flash heating here instead of continuous *T* increase (Boulard et al., 2011; Cerantola et al., 2017).

A striking characteristic of glassy $FeCO_3$ is its strong first sharp diffraction peak (FSDP) that persists in the structure factor up to the highest *P* investigated (**Figure 3A**), indicative of a strong medium-range order. This is in stark contrast to silicate glasses that lose their medium-range order with increased *P* (Sato and Funamori, 2008), but consistent with *ab initio* calculations on carbon-bearing silicate melts reporting *P*-induced polymerization of carbonate species into dimers and with the silicate network (Ghosh et al., 2017; Solomatova and Asimow, 2019). A second noticeable feature is the decrease of the contribution at 4 $Å^{-1}$ attributed in molten carbonates to the O-O bond (Wilding et al., 2016). On radial distribution functions, $g(r)$ (**Figure 3B**), the C-O contribution is clearly visible at 1.2-1.3 Å with none or little overlap with the second contribution (Fe-O and O-O) at ∼2 Å in the glass, and with some overlap in the melt. No significant structural changes are observed between molten and quenched glassy state at 110 GPa, apart from a generally lower intensity in the melt due to the high *T* and consequent higher degree of disorder. For $g(r)$, this weaker intensity translates into broader C-O and Fe-O/O-O contributions in the molten state. For glasses quenched at 11 GPa and 15 GPa, the x-ray structure factor, $S(q)$, is intermediate between that of pure SiO_2 glass (Sato and Funamori, 2008) and high-*P* $FeCO_3$ glasses (**Figure 4**). SEM image of sample 8 (15 GPa, **Figure 2**) shows heterogeneities in the quenched glass, which indicates that the x-ray structure factor likely averages at least two types of glass structure and therefore data cannot be interpreted quantitatively.

The x-ray Raman C K-edge spectrum of quenched $FeCO_3$ glass shows no presence of sp2 3-fold carbon characterized by an intense π^* peak at 290 eV (**Figure 5**, π^* peak). Only the σ^* peak of tetrahedrally coordinated carbon (Shieh et al., 2013) is visible (**Figure 5**, σ^* peak). The totally missing π^* peak is indicative of a fully sp3 state of carbon atoms in the siderite glass. *P*-induced coordination changes of major cations in silicate melts (e.g., Si, Al) were first reported from the study of glasses quenched from high *P* (Yarger et al., 1995; Meade, Hemley and Mao,

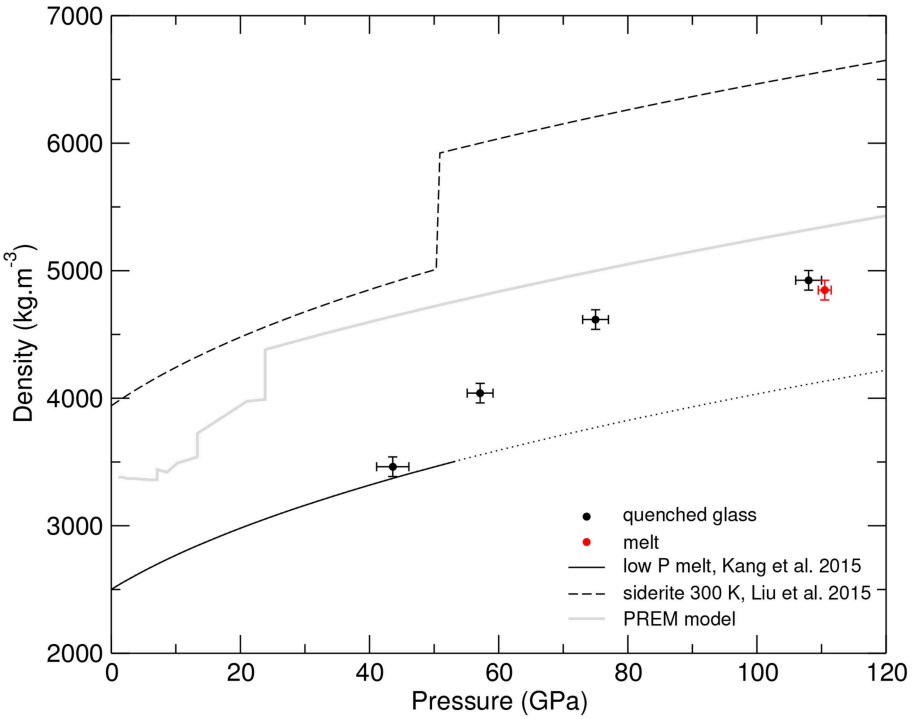

FIGURE 7 | Density evolution of glassy, molten, and cristalline siderite with pressure. Molten low *P* siderite (plain curve), high *P* data on glass (black points) and the highest *P* melt (red point), crystalline equation of state (dashed curve) includes the transition from high spin siderite I to low spin siderite II at 50 GPa (Liu et al., 2015).

1992), and later confirmed by *in situ* studies in the molten phase (Sanloup et al., 2013; Drewitt, 2015). However, the opposite, i.e., coordination change occurring only in the quenched glass, not in the high *P* melt, have not been reported nor been theoretically predicted. The 3 to 4-fold transition therefore occurs in molten Fe-carbonates at *P* less or equal to 51 GPa. This transition is preserved upon quenching to the glassy state, and is recoverable at ambient conditions, opening the way to the synthesis of a new class of glassy materials. Two broad bands are observed in the Raman spectra (**Figure 6**), very different from those of the only two carbonate systems that quench as glasses at room P, $MgCO_3$-K_2CO_3 and $La(OH)_3$-$Ca(OH)_2$-$CaCO_3$-CaF_2BaSO_4 (Sharma and Simons, 1979), that are essential dominated by the strong CO_3^{2-} stretching mode at ∼1,080 cm^{-1}. Instead, present Raman spectra are reminiscent of those reported for calcium silicate glasses (**Figure 6**) (Mysen et al., 1982) albeit at higher Raman shift values for the broadest band (1,200–1,600 cm^{-1} for glassy $FeCO_3$ vs. 850–1,100 cm^{-1} for calcium silicate glasses).

Density values are reported in **Figure 7** along with predictions for lower *P* melt properties (Kang et al., 2015), *P*-evolution of crystalline siderite, and with the Earth's seismological PREM model (Dziewonski and Anderson, 1981). Density profile below 40 GPa is calculated using $K_{T,0}$ value of 80.23 GPa (Kang et al., 2015), consistent with that reported for molten calcite (Hudspeth et al., 2018), and density at room *P* of 2,500 $kg{\cdot}m^{-3}$ by assuming a similar density jump upon melting as for other carbonates for which room *P* density is known. Comparison with PREM model shows that Fe-carbonate melts are buoyant at all depths. Density contrast between the high *P* polymerized melt or glass and extrapolated equation of state for low *P* melt is 15%, i.e., similar to volume collapse reported upon transition from crystalline high spin siderite I to low spin siderite II (Liu et al., 2015). The volume collapse is smoothed out over a ∼ 30 GPa range in the molten state with, as a direct consequence, a steepening of the melting curve from 55 GPa on (Cerantola et al., 2017).

4. DISCUSSION

The 3 to 4-fold transition occurs in molten Fe-carbonates at *P* less or equal to 51 GPa, compared to 50 GPa for crystalline $FeCO_3$ (Liu et al., 2015), 80 GPa for $MgCO_3$ (Oganov et al., 2008; Boulard et al., 2011), and 130 GPa for $CaCO_3$ (Oganov et al., 2006; Arapan et al., 2007). A consequence of the effect of Fe on the 3-fold C to 4-fold C transition *P* is that crystalline Fe-poor $(Ca,Mg,Fe)^{III}CO_3$ and Fe-enriched $(Ca,Mg,Fe)^{IV}CO_3$ melts could co-exist at depth. In the case of Si isotopes, fractionation between ^{VI}Si bridgmanite and ^{IV}Si olivine structures is theoretically estimated to ∼ −1 ‰ ^{28}Si at 2000 K (Huang et al., 2014). If this effect can be scaled to C simply using mass difference considerations, then a few ‰ ^{13}C fractionation is expected, and could potentially explain isotopic differences between calcite inclusions from super-deep diamonds (Kaminsky et al., 2016). This effect might be sufficient to confer a mantle-like signature to deep diamonds grown from slab-derived carbonate melts while co-existing tetrahedral crystalline carbonate are expected to get lighter.

Density of non-crystalline $FeCO_3$ remains considerably lower than that of its crystalline counter parts, even at the highest investigated *P*, by 15%. The situation is thus very different from

that of molten and crystalline silicates which density converge at deep mantle conditions (Petitgirard et al., 2015; Sanloup, 2016), and such difference could be attributed to the very strong medium-range order preserved in tetrahedral high *P* carbonate melts while it is mostly collapsed by 5 GPa in silicate melts. That high *P* $FeCO_3$ melts quench as glasses contrasts with the behavior observed at lower *P*, and suggests an important increase of carbonate melt viscosity consistent with the observation of a very strong medium-range order. It is also opposite to the behavior of molten basalt that systematically quenches as crystalline phases above 11 GPa (Sanloup et al., 2013) and as a glass below. The strongly reduced chemical reactivity of high *P* $FeCO_3$ melts with silica along with their glass-forming ability suggest that unlike at lower *P*, tetrahedral carbonate melts are not pervasive, which could contribute to the longevity of carbonates in the deep mantle where allowed by oxidizing conditions or slow reduction kinetics (Litasov and Shatskiy, 2018).

AUTHOR CONTRIBUTIONS

JH and CS: devised the project; CS: processed x-ray diffraction data and wrote the paper with input from GL and LC; JH, CS, BC, VA, and ZK: participated in x-ray diffraction data acquisition; JH, GL, LC, CS, and CC: participated in x-ray Raman data acquisition; JH: collected Raman data.

FUNDING

The research leading to these results has received funding from the European Community's Seventh Framework Programme (FP7/2007-2013) under grant agreements no. 312284 and 259649 (European Research Council starting grant to CS). Portions of this research were carried out at the light source PETRAIII at DESY, a member of the Helmholtz Association (HGF). The laser heating system on beamline P02.2 is funded by the German BMBF (project number 05K10RFA).

ACKNOWLEDGMENTS

We acknowledge E. Boulard for providing the starting siderite sample, K. Glazyrin for his help with *ex situ* diamond-anvil cell laser-heating synthesis in PETRAIII, L. Rémusat at Museum National d'Histoire Naturelle (Paris, France) for gold coating of the recovered samples, the ESRF (Grenoble, France) and PETRAIII (Hamburg, Germany) for provision of synchrotron radiation facilities.

REFERENCES

Andrault, D., Fiquet, G., Guyot, F., and Hanfland, M. (1998). Pressure-induced landau-type transition in stishovite. *Science* 282, 720–724. doi: 10.1126/science.282.5389.720

Arapan, S., De Almeida, J. S., and Ahuja, R. (2007). Formation of sp(3) hybridized bonds and stability of $CaCO_3$ at very high pressure. *Phys. Rev. Lett.* 98:268501. doi: 10.1103/PhysRevLett.98.268501

Boehler, R., Ross, M., and Boercker D. B. (1997). Melting of LiF and NaCl to 1 Mbar: systematics of ionic solids at extreme conditions *Phys. Rev. Lett.* 78, 4589–4592. doi: 10.1103/PhysRevLett.78.4589

Boulard, E., Gloter, A., Corgne, A., Antonangeli, D., Auzende, A.-L., Perrillat, J.-P., et al. (2011). New host for carbon in the deep Earth. *Proc. Natl Acad. Sci. U.S.A.* 108, 5184–5187. doi: 10.1073/pnas.1016934108

Boulard, E., Guyot, F., and Fiquet, G. (2012). The influence on Fe content on Raman spectra and unit cell parameters of magnesite-siderite solid solutions. *Phys. Chem. Miner.* 39, 239–246. doi: 10.1007/s00269-011-0479-3

Boulard, E., Guyot, F., Menguy, N., Corgne, A., Auzende, A.-L., Perrillat, J.-P., et al. (2018). CO_2-induced destabilization of pyrite-structured FeO_2H_x in the lower mantle. *Natl. Sci. Rev.* 5, 870–877. doi: 10.1093/nsr/nwy032

Cerantola, V., Bykova, E., Kupenko, I., Merlini, M., Ismailova, L., McCammon, C., et al. (2017). Stability of iron-bearing carbonates in the deep Earth's interior. *Nat. Commun.* 8:15960. doi: 10.1038/ncomms15960

C. Meade and R. J. Hemley and H. K. Mao (1992). High-pressure x-ray diffraction of SiO_2 glass. *Phys. Rev. Lett.* 69, 1387–1390.

Desmaele, E., Sator, N., Vuilleumier, R. and Guillot, B. (2019). Atomistic simulations of molten carbonates: thermodynamic and transport properties of the Li_2CO_3-Na_2CO_3-K_2CO_3 system. *J. Chem. Phys.* 150:094504. doi: 10.1063/1.5082731

Dobson, D. P., Jones, A. P., Rabe, R., Sekine, T., Kurita, K., Taniguchi, T., et al. (1996). In-situ measurement of viscosity and density of carbonate melts at high pressure. *Earth Planet. Sci. Lett.* 143, 207–215. doi: 10.1016/0012-821X(96)00139-2

Drewitt, J. W. E., Jahn, S., Sanloup, C., de Grouchy, C., Garbarino, G. and Hennet L. (2015). Development of chemical and topological structure in aluminosilicate liquids and glasses at high pressure. *J. Phys.: Cond. Matt.* 27:105103. doi: 10.1088/0953-8984/27/10/105103

Du, X., Wu, M., Tse, J. S., and Pan, Y. (2018). Structures and transport properties of CaCO3 melts under Earth's mantle conditions *ACS Earth Space Chem* 2, 1–8. doi: 10.1021/acsearthspacechem.7b00100

Dziewonski, A. M. and Anderson, D. L. (1981). Preliminary reference Earth model. *Phys. Earth Planet. Int.* 25, 297–356.

Eggert, J. H., Weck, G., Loubeyre, P., and Mezouar, M. (2002). Quantitative structure factor and density measurements of high-pressure in diamond anvil cells by x-ray diffraction: Argon and water. *Phys. Rev. B* 65:174105. doi: 10.1103/PhysRevB.65.174105

Fischer, R. A., Campbell, A. J., Chidester, B. A., Reaman, D. M., Thompson, E. C., Pigott, J. S., et al. (2018). Equations of state and phase boundary for stishovite and $CaCl_2$-type SiO_2. *Am. Mineral.* 103, 792–802. doi: 10.2138/am-2018-6267

Foley, S. F. (2008). Rejuvenation and erosion of the cratonic lithosphere. *Nature Geosci.* 1, 503–510. doi: 10.1038/ngeo261

Frost, D., Liebske, C., Langenhorst, F., McCammon, C., Tronnes, R., and Rubie, D. (2004). Experimental evidence for the existence of iron-rich metal in the Earth's lower mantle. *Nature* 428, 409–412. doi: 10.1038/nature02413

Ghosh, D. B., Bajgain, S. K., Mookherjee, M., and Karki, B. B. (2017). Carbon-bearing silicate melt at deep mantle conditions. *Sci. Rep.* 7:848. doi: 10.1038/s41598-017-00918-x

Hajdu F. (1972). Revised parameters of the analytic fits for coherent and incoherent scattered X-ray intensities of the first 36 atoms. *Acta Cryst. A* 28, 250–252.

Hammersley, A. P., Svensson, S. O., Hanfland, M., Fitch, A. N., and Hausermann, D. (1996). Two-dimensional detector software: From real detector to idealised image or two-theta scan. *High Press. Res.* 14, 235–248. doi: 10.1080/08957959608201408

Hosemann, R. and Bagchi, S. N. (1962). *Direct Analysis of Diffraction by Matter*. Amsterdam: North-Holland.

Huang, F., Wu, Z., Huang, S., and Wu, F. (2014). First-principles calculations of equilibrium silicon isotope fractionation among mantle minerals. *Geochim. Cosmochim. Acta* 140, 509–520. doi: 10.1016/j.gca.2014.05.035

Hudspeth, J., Sanloup, C., and Kono, Y. (2018). Properties of molten $CaCO_3$ at high pressure. *Geochem. Persp. Let.* 7, 27–31. doi: 10.7185/geochemlet.1813

Huotari, S., Sahle, C. J., Henriquet, C., Al-Zein, A., Martel, K., Simonelli, L., et al. (2017). A large-solid-angle X-ray Raman scattering spectrometer at ID20 of the European Synchrotron Radiation Facility. *J. Sync. Rad.* 24, 521–530. doi: 10.1107/S1600577516020579

Kaminsky, F. (2012). Mineralogy of the lower mantle: a review of 'super-deep' mineral inclusions in diamond. *Earth Sci. Rev.* 110, 127–147. doi: 10.1016/j.earscirev.2011.10.005

Kaminsky, F., Matzel, J., Jacobsen, B., Hutcheon, I., and Wirth, R. (2016). Isotopic fractionation of oxygen and carbon in decomposed lower-mantle inclusions in diamond. *Mineral. Petrol.* 110, 379–385. doi: 10.1007/s00710-015-0401-7

Kang, N., Schmidt, M. W., Poli, S., Franzolin, E., and Connolly, A. D. (2015). Melting of siderite to 20 GPa and thermodynamic properties of $FeCO_3$-melt. *Chem. Geol.* 400, 34–43. doi: 10.1016/j.chemgeo.2015.02.005

Kono, Y. , Kenney-Benson C., Hummer, D., Ohfuji H. , Park, C., Shen, G., et al. (2014). Ultralow viscosity of carbonate melts at high pressures. *Nat. Comm.* 5:5091. doi: 10.1038/ncomms6091

Li, Z., Li, J.., Lange, R., Liu, J., and Militzer, B. (2017). Determination of calcium carbonate and sodium carbonate melting curves up to Earth's transition zone pressures with implications for the deep carbon cycle. *Earth Planet. Sci. Lett.* 457, 395–402. doi: 10.1016/j.epsl.2016.10.027

Litasov, K. D. and Shatskiy, A. (2018). *Chap. 2: Carbon-Bearing Magmas in the Earth's Deep Interior*. Amsterdam: Elsevier.

Litasov, K. D., Shatskiy, A., Ohtani, E., and Yaxley, G. M. (2013). Solidus of alkaline carbonatite in the deep mantle. *Geology* 41, 79–82. doi: 10.1130/G33488.1

Liu, J., Lin, J.-F., and Prakapenka, V. B. (2015). High-pressure orthorhombic ferromagnesite as a potential deep-mantle carbon Carrier. *Sci. Rep.* 5:7640. doi: 10.1038/srep07640

Lobanov, S. S., Goncharov, A. F., and Litasov, K. D. (2015). Optical properties of siderite ($FeCO_3$) across the spin transition: Crossover to iron-rich carbonates in the lower mantle. *Am. Mineral.* 100, 1059–1064. doi: 10.2138/am-2015-5053

Lobanov, S. S., Stevanovic, V., Gavryushkin, P. N., Litasov, K. D., Greenberg, E., Prakapenka, V. B., Oganov, A. R. and Goncharov, Al. F. (2017). Raman spectroscopy and x-ray diffraction of sp(3) $CaCO_3$ at lower mantle pressures. *Phys. Rev. B* 96:104101. doi: 10.1103/PhysRevB.96.104101

Maeda, F., Ohtani, E., Kamada, S., Sakamaki, T., Hirao, N., and Ohishi, Y. (2017). Diamond formation in the deep lower mantle: a high-pressure reaction of $MgCO_3$ and SiO_2. *Sci. Rep.* 7:40602. doi: 10.1038/srep40602

Mao, H. K., Xu, J., and Bell, P. M. (1986). Calibration of the ruby pressure gauge to 800 kbar under quasi-hydrostatic conditions. *J. Geophys. Res.* 91, 4673–4676.

Merlini, M., Cerantola, V., Gatta, G. D., Gemmi, M., Hanfland, M., Kupenko, I., et al. (2017). Dolomite-IV: candidate structure for a carbonate in the Earth's lower mantle. *Am. Mineral.* 102, 1763–1766. doi: 10.2138/am-2017-6161

Mysen, B. O., Finger, L. W., Virgo, D., and Seifert, F. A. (1982). Curve-fitting of Raman spectra of silicate glasses. *Am. Mineral.* 67, 686–695.

Nishihara, Y., Nakayama, K., Takahashi, E., Iguchi, T., and i. Funakoshi, K. (2005). P-V-T equation of state of stishovite to the mantle transition zone conditions. *Phys. Chem. Min.* 31, 660–670. doi: 10.1007/s00269-004-0426-7

Oganov, A., Glass, C., and Ono, S. (2006). High-pressure phases of $CaCO_3$: crystal structure prediction and experiment. *Earth Planet. Sci. Lett.* 241, 95–103. doi: 10.1016/j.epsl.2005.10.014

Oganov, A. R., Ono, S., Ma, Y., Glass, C. W., and Garcia, A. (2008). Novel high-pressure structures of $MgCO_3$, $CaCO_3$ and CO_2 and their role in Earth's lower mantle. *Earth Planet. Sci. Lett.* 273, 38–47. doi: 10.1016/j.epsl.2008.06.005

Petitgirard, S., Malfait, W. J., Sinmyo, R., Kupenko, I., Hennet, L., Harries, D., et al. (2015). Fate of $MgSiO_3$ melts at core-mantle boundary conditions. *P. Natl. Acad. Sci. U.S.A.* 112, 14186–14190. doi: 10.1073/pnas.1512386112

Sahle, C. J., Mirone, A., Niskanen, J., Inkinen, J., Krisch, M., and Huotari, S. (2015). Planning, performing and analyzing X-ray Raman scattering experiments. *J. Sync. Rad.* 22, 400–409. doi: 10.1107/S1600577514027581

Sanloup, C. (2016). Density of magmas at depth. *Chem. Geol.* 429, 51–59. doi: 10.1016/j.chemgeo.2016.03.002

Sanloup, C. and de Grouchy, C. J. L. (2018). *Chap. 5: X-ray Diffraction Structure Measurements*. Amsterdam: Elsevier.

Sanloup, C., Drewitt, J. W. E., Konôpková, Z., Dalladay-Simpson, P., Morton, D. M., Rai, N., et al. (2013). Structural change in molten basalt at deep mantle conditions. *Nature* 503, 104–107. doi: 10.1038/nature12668

Sato, T. and Funamori, N. (2008). Sixfold-coordinated amorphous polymorph of SiO_2 under high pressure. *Phys. Rev. Lett.* 101:255502. doi: 10.1103/PhysRevLett.101.255502

Seto, Y., Hamane, D., Nagai, T., and Fujino, K. (2008). Fate of carbonates within oceanic plates subducted to the lower mantle, and a possible mechanism of diamond formation. *Phys. Chem. Miner.* 35, 223–229. doi: 10.1007/s00269-008-0215-9

Sharma, S. and Simons, B. (1979). *Raman Study of K_2CO_3-$MgCO_3$ Glasses*, Vol. 79. Washington, DC: Carnegie Institute, 322–326.

Shieh, S. R., Jarrige, I., Wu, M., Hiraoka, N., Tse, J. S., Mi, Z., et al. (2013). Electronic structure of carbon dioxide under pressure and insights into the molecular-to-nonmolecular transition. *Proc. Natl. Acad. Sci. U. S. A.* 110, 18402–18406. doi: 10.1073/pnas.1305116110

Smith, E. M., Shirey, S. B., Nestola, F., Bullock, E. S., Wang, J., Richardson, S. H., et al. (2016). Large gem diamonds from metallic liquid in earth's deep mantle. *Science* 354, 1403–1405. doi: 10.1126/science.aal1303

Solomatova, N. V. and Asimow, P. D. (2018). First-principles calculations of high-pressure iron-bearing monoclinic dolomite and single-cation carbonates with internally consistent Hubbard U. *Phys. Chem. Miner.* 45, 293–302. doi: 10.1007/s00269-017-0918-x

Solomatova, N. V., Caracas, R., and Manning, C. E. (2019). Carbon sequestration during core formation implied by complex carbon polymerization. *Nat. Comm.* 10:789. doi: 10.1038/s41467-019-08742-9

Stagno, V., Stopponi, V., Kono, Y., Manning, C. E. and Tetsuo, I. (2018). Experimental determination of the viscosity of Na_2CO_3 melt between 1.7 and 4.6 GPa at 1200-1700 degrees C: implications for the rheology of carbonatite magmas in the Earth's upper mantle. *Chem. Geol.* 501,19–25. doi: 10.1016/j.chemgeo.2018.09.036

Vuilleumier, R., Seitsonen, A., Sator, N., and Guillot, B. (2014). Structure, equation of state and transport properties of molten calcium carbonate ($CaCO_3$) by atomistic simulations. *Geochim. Cosmchim. Acta* 141, 547–566. doi: 10.1016/j.gca.2014.06.037

Weis, C., Sternemann, C., Cerantola, V., Sahle, C. J., Spiekermann, G., Harder, M., et al. (2017). Pressure driven spin transition in siderite and magnesiosiderite single crystals. *Sci. Rep.* 7:16526. doi: 10.1038/s41598-017-16733-3

Wilding, M. C., Wilson, M., Alderman, O. L. G., Benmore, C., Weber, J. K. R., Parise, J. B., et al. (2016). Low-dimensional network formation in molten sodium carbonate. *Sci. Reports* 6:24415. doi: 10.1038/srep24415

Yarger, J. L., Smith, K. H., Nieman, R. A., Diefenbacher, J., Wolf, G. H., Poe, B. T., McMillan, P. F. (1995). Al coordination changes in high-pressure aluminosilicate liquids. *Science* 270, 1964–1967.

Zhang, Z., and Liu, Z. (2015). High pressure equation of state for molten $CaCO_3$ from first principles simulations. *Chin. J. Geochem.* 34, 13–20. doi: 10.1007/s11631-015-0036-8

Conflict of Interest Statement: The authors declare that the research was conducted in the absence of any commercial or financial relationships that could be construed as a potential conflict of interest.

frontiers in Earth Science

CORRECTION
published: 25 June 2019
doi: 10.3389/feart.2019.00155

Corrigendum: Polymerized 4-Fold Coordinated Carbonate Melts in the Deep Mantle

Chrystèle Sanloup[1], Jessica M. Hudspeth[2], Veronika Afonina[3], Benjamin Cochain[2], Zuzana Konôpková[4], Gérald Lelong[1], Laurent Cormier[1] and Chiara Cavallari[5]*

[1] Muséum National d'Histoire Naturelle, UMR CNRS 7590, IRD, Institut de Minéralogie, de Physique des Matériaux et de Cosmochimie, IMPMC, Sorbonne Université, Paris, France, [2] Institut des Sciences de la Terre de Paris, Sorbonne Université, CNRS, Paris, France, [3] SUPA, Centre for Science at Extreme Conditions and School of Physics and Astronomy, University of Edinburgh, Edinburgh, United Kingdom, [4] DESY Photon Science, Hamburg, Germany, [5] European Synchrotron Radiation Facility, ESRF, Grenoble, France

Keywords: carbonate melts, high pressure, x-ray diffraction, Raman, x-ray Raman, polymerization, deep mantle

A Corrigendum on

Polymerized 4-Fold Coordinated Carbonate Melts in the Deep Mantle
by Sanloup, C., Hudspeth, J. M., Afonina, V., Cochain, B., Konôpková, Z., Lelong, G., et al. (2019). Front. Earth Sci. 7:72. doi: 10.3389/feart.2019.00072

OPEN ACCESS

Edited and reviewed by:
Dan J. Bower,
University of Bern, Switzerland

****Correspondence:***
Chrystèle Sanloup
chrystele.sanloup@sorbonne-universite.fr

Specialty section:
This article was submitted to Earth and Planetary Materials, a section of the journal Frontiers in Earth Science

Received: *20 May 2019*
Accepted: *03 June 2019*
Published: *25 June 2019*

Citation:
Sanloup C, Hudspeth JM, Afonina V, Cochain B, Konôpková Z, Lelong G, Cormier L and Cavallari C (2019) Corrigendum: Polymerized 4-Fold Coordinated Carbonate Melts in the Deep Mantle. Front. Earth Sci. 7:155. doi: 10.3389/feart.2019.00155

In the original article, there was a mistype in Equation (2) used to simulate the experimental C-O contribution on $g(r)$ (Figure 3B).

A correction has been made to Section 2, Density Measurements, equation 2:

$$g(r) = \frac{c_C c_O K_C K_O}{Z_{tot}^2 n S_\infty} \frac{A}{\sigma\sqrt{2\pi}} exp\left(-\frac{(r-d)^2}{2\sigma^2}\right) \quad (2)$$

where c_C and c_O are the atomic proportions of carbon and oxygen, K_C and K_O are defined as the average effective atomic number over the experimental q-range (Eggert et al., 2002) and calculated using form factors from Hajdu (1972). Other parameters are as defined in the article.

The authors apologize for this error and state that this does not change the scientific conclusions of the article in any way. The original article has been updated.

REFERENCES

Eggert, J. H., Weck, G., Loubeyre, P., and Mezouar, M. (2002). Quantitative structure factor and density measurements of high-pressure in diamond anvil cells by x-ray diffraction: Argon and water. *Phys. Rev. B* 65:174105. doi: 10.1103/PhysRevB.65.174105

Hajdu F. (1972). Revised parameters of the analytic fits for coherent and incoherent scattered X-ray intensities of the first 36 atoms. *Acta Cryst. A* 28, 250–252.

frontiers in Microbiology

METHODS
published: 29 April 2019
doi: 10.3389/fmicb.2019.00878

An Improved Method for Extracting Viruses From Sediment: Detection of Far More Viruses in the Subseafloor Than Previously Reported

Donald Pan[1†], Yuki Morono[2,3†], Fumio Inagaki[2,3,4†] and Ken Takai[1,3,5†]*

[1] Department of Subsurface Geobiological Analysis and Research, Japan Agency for Marine-Earth Science and Technology, Yokosuka, Japan, [2] Geomicrobiology Group, Kochi Institute for Core Sample Research, Japan Agency for Marine-Earth Science and Technology, Nankoku, Japan, [3] Research and Development Center for Submarine Resources, Japan Agency for Marine-Earth Science and Technology, Yokosuka, Japan, [4] Research and Development Center for Ocean Drilling Science, Japan Agency for Marine-Earth Science and Technology, Yokohama, Japan, [5] Earth-Life Science Institute, Tokyo Institute of Technology, Tokyo, Japan

OPEN ACCESS

Edited by:
Dawn Cardace,
The University of Rhode Island,
United States

Reviewed by:
Kenneth Stedman,
Portland State University,
United States
Rui Zhang,
Xiamen University, China

***Correspondence:**
Donald Pan
donald.pan@jamstec.go.jp

†Present address:
Donald Pan, Yuki Morono, and Ken Takai,
X-STAR, Japan Agency for Marine-Earth Science and Technology (JAMSTEC), Yokosuka, Japan;
Fumio Inagaki,
Mantle Drilling Promotion Office (MDP), Institute for Marine-Earth Exploration and Engineering (MarE3), Japan Agency for Marine-Earth Science and Technology (JAMSTEC), Yokohama, Japan

Specialty section:
This article was submitted to Extreme Microbiology, a section of the journal Frontiers in Microbiology

Received: 25 January 2019
Accepted: 05 April 2019
Published: 29 April 2019

Citation:
Pan D, Morono Y, Inagaki F and Takai K (2019) An Improved Method for Extracting Viruses From Sediment: Detection of Far More Viruses in the Subseafloor Than Previously Reported. Front. Microbiol. 10:878. doi: 10.3389/fmicb.2019.00878

Viruses are the most abundant biological entities on Earth and perform essential ecological functions in aquatic environments by mediating biogeochemical cycling and lateral gene transfer. Cellular life as well as viruses have been found in deep subseafloor sediment. However, the study of deep sediment viruses has been hampered by the complexities involved in efficiently extracting viruses from a sediment matrix. Here, we developed a new method for the extraction of viruses from sediment based on density separation using a Nycodenz density step gradient. The density separation method resulted in up to 2 orders of magnitude greater recovery of viruses from diverse subseafloor sediments compared to conventional methods. The density separation method also showed more consistent performance between samples of different sediment lithology, whereas conventional virus extraction methods were highly inconsistent. Using this new method, we show that previously published virus counts have underestimated viral abundances by up to 2 orders of magnitude. These improvements suggest that the carbon contained within viral biomass in the subseafloor environment may potentially be revised upward to 0.8–3.7 Gt from current estimates of 0.2 Gt. The vastly improved recovery of viruses indicate that viruses represent a far larger pool of organic carbon in subseafloor environments than previously estimated.

Keywords: virus, phage, subseafloor, sediment, subsurface, carbon, virus extraction, virus quantification

INTRODUCTION

Marine sediments are a major biome on Earth, covering ¾ of the Earth's surface and containing approximately 10^{29} cells (Kallmeyer et al., 2012). Viruses are highly abundant within shallow marine sediments and have been observed in deep subsurface sediments as well (Bird et al., 2001; Middelboe et al., 2011; Engelhardt et al., 2014; Yanagawa et al., 2014). Viruses are the most abundant biological entities on Earth and play important biogeochemical and ecological roles in the ocean such as cell mortality and horizontal gene transfer (Suttle, 2005; Rohwer and Thurber, 2009). However, many questions remain regarding the roles of viruses in deep sediment. The progress of research on viruses in subseafloor sediment lags far behind that of subseafloor cellular life.

The major challenge in the study of subseafloor viral ecology is the technical problem of separating viruses from the surrounding sediment matrix. Methods exist for the separation and enumeration of viruses from sediments (Danovaro et al., 2001; Danovaro and Middelboe, 2010), however, the separation of viruses from sediment is complicated by interactions between viruses and particulate matter (Weinbauer et al., 2009). The efficiency of virus separation may vary with the composition of the sediment (Helton et al., 2006). Sediment properties such as mineralogy, organic content (Fuhs et al., 1985; Powelson et al., 1991), pH (Kinoshita et al., 1993; Loveland et al., 1996; Guan et al., 2003), as well as the isoelectric point of viruses (Dowd et al., 1998) can all influence the strength of virus-sediment adsorption. Clays (Lipson and Stotzky, 1983; Helton et al., 2006) and iron oxyhydroxide minerals are especially strong sorbents of viruses (Moore et al., 1981; Ryan et al., 2002; You et al., 2005; Zhu et al., 2005; Bradley et al., 2011; John et al., 2011).

Accurate virus quantification in sediment depends on techniques for the separation of viruses from sediment particles. Conventional virus extraction methods involve suspending the sediment in a buffer such as virus-free seawater (Danovaro and Middelboe, 2010), SM buffer (Yanagawa et al., 2014), or beef extract (Farkas et al., 2018), along with amendments like pyrophosphate (Danovaro et al., 2001), potassium citrate (Williamson et al., 2003), or EDTA (Helton et al., 2006) to aid in desorption. Conventional procedures typically include a shaking or sonication step to physically dissociate the viruses from sediment particles. The final step removes the sediment particles. In most conventional procedures, this involves pelleting the sediment by centrifugation in order to collect the viruses in the supernatant. Insufficient separation of viruses from sediment particles can result in underestimation of viral numbers or co-extraction of non-viral particles which obscures viruses and decreases their fluorescence (Montanié et al., 2015). Virus extraction efficiencies vary greatly between methods, and recovery can be as low as 0.09 to 0% in coastal and estuarine sediments (Miura et al., 2009; Hassard et al., 2016). The efficiency of conventional virus extraction techniques has not been assessed on a variety of sediment types, so comparisons of viral counts from different sediment lithologies may be problematic. Studies of cell extraction from subseafloor sediment show that cell recovery is also influenced by the sediment matrix, but improvements in cell separation methodology can improve recovery from across a variety of subseafloor sediment types (Morono et al., 2013). Improving the efficiency of separation from subsurface sediment may also make it possible to extract more viral DNA from less sediment, opening the doors to a wide spectrum of viral metagenomic studies in subseafloor sediments.

To this end, we developed a buoyant density based separation method modified from similar cell separation methods used for deep subseafloor sediments (Morono et al., 2013). The modified method utilizes a Nycodenz step gradient to separate sediment particles from virus extract. Using a variety of diverse subseafloor sediments, we compared the density separation method to conventional methods used for deep subseafloor virus enumeration (Engelhardt et al., 2014; Yanagawa et al., 2014).

MATERIALS AND METHODS

Definitions

In this study, we infer SYBR-stained fluorescent particles that pass through some size cutoff, generally 0.2 μm, to be viruses. This operational definition will exclude prophage, giant viruses, and may exclude viruses that do not stain efficiently such as ssDNA and RNA viruses. It will also encompass membrane vesicles, gene transfer agents and very small cells. However, recent studies have suggested that membrane vesicles are only a minor portion of SYBR-stained particles compared to viruses (Biller et al., 2017). The majority of studies employing fluorescent staining techniques use this general criterion when determining values for "viral abundance" and "virus counts." The term "virus-like particle" (VLP) has also been used to describe these particles, however, this can cause confusion because the term is also used in immunology to refer to virus-derived particles that lack nucleic acids. Even within the same study, the terms "VLP" and "virus" are often used interchangeably. Therefore, for the sake of consistency, we use only the term "virus," inferred by SYBR-stained particles that pass through 0.2 μm filtration, throughout this paper.

Some studies of sedimentary viruses include a nuclease treatment step in order to reduce background fluorescence or to degrade extracellular DNA which may appear as fluorescing particles (Fischer et al., 2005; Helton et al., 2006; Danovaro and Middelboe, 2010). Because viral nucleic acids are protected by a capsid shell, nuclease treatment would not affect viruses. For the sake of comparison with previous subsurface virus studies (Engelhardt et al., 2014; Yanagawa et al., 2014), we have elected to not include a DNase I treatment step here because previous studies did not include this step. To test whether this was an acceptable omission, we conducted DNase I treatment on several samples and confirmed that DNase treatment did not make a substantial difference (**Supplementary Figure S1**), consistent with previous studies that have used DNase (Fischer et al., 2005; Danovaro and Middelboe, 2010).

Density Based Virus-Sediment Separation

The density gradient separation method (**Figure 1A**) is adapted from previously published methods for virus separation (Danovaro and Middelboe, 2010) and cell separation from sediments (Morono et al., 2013).

All reagents were filtered through 0.02 μm Anotop syringe filters (GE Healthcare, 6809-2102) to remove viruses.

(1) Add a solution of 2.5% NaCl–5 mM sodium tetrapyrophosphate to 0.1–0.33 cm^3 of sediment for a total volume of 6 mL. The volume of sediment that can be extracted will vary depending on the sediment characteristics. Some adjustments of volume may be necessary. See Section "Methodological Considerations."

(2) Shake and vortex the mixture until solid clumps are broken apart and the sediment is dispersed into an even slurry. Then sonicate on ice for 1 min. We used a probe sonicator (15 W, UH-50 Ultrasonic Homogenizer SMT, Tokyo).

(3) Layer the sonicated sample onto a step gradient of 30 and 50% Nycodenz prepared in a 15 mL Falcon tube (**Figure 1B**). In this study, we used a volume of 1 mL for both Nycodenz layers. Centrifuge for 30 min at 2900 × *g* in a swinging bucket rotor. Low-speed centrifugation causes cells and sediment particles to migrate to denser layers while viruses should remain mostly unaffected. The majority of viruses should remain in the top layer, while a fraction of viruses will cross into the 30% layer, carried by the movement of larger particles. Theoretically, higher speed centrifugation may potentially be used, however, it was not tested due to limitations of the swinging bucket rotor used to develop this method.

(4) Using a syringe and needle, collect the liquid layers down to the 50% Nycodenz layer which may appear as a different color (**Figure 1B**). Care should be taken to avoid collecting the 50% layer because particles in this layer may obscure epifluorescence images. Filter the collected liquid through a 0.2 μm pore size PES (polyethersulfone) syringe filter (Merck Millipore SLGP033RS) in order to remove any remaining cells and large particulates. This step may also remove some large viruses.

(5) Further rounds of extraction can be performed in order to improve extraction efficiency. The number of times that a sample can be re-extracted may depend on the characteristics of the sediment. Add the NaCl-tetrapyrophosphate solution to the remaining material in the tube to a final volume of 6 mL and resuspend. Repeat the sonication and layer the suspension onto a fresh Nycodenz step gradient tube. After centrifugation, collect the liquid down to the 50% layer. Filter through a 0.2 μm pore size PES syringe filter.

(6) Pool the filtered extract from each round.

Sediment Sample Collection and Description

Samples were selected to encompass a range of subseafloor sediment types. Nankai Trough samples representing clay rich sediments were collected during IODP Expedition 370 at Site C0023 Hole A located in the protothrust zone off of Cape Muroto, Japan (Heuer et al., 2017). Sediment cores were processed onboard and subsequently transported by helicopter to the Kochi Core Center (KCC) where subsamples were taken under cleanroom conditions and stored at −80°C (Heuer et al., 2017). Samples from offshore Shimokita, Japan, representing organic-rich hemipelagic sediments were collected from frozen cores collected during the *Chikyu* Shakedown Cruise CK06-06 at Site C9001 Hole C (Aoike, 2007). South Pacific Gyre samples representing organic poor, oligotrophic sediments were taken from frozen cores collected during IODP Expedition 329 at Sites U1366, U1367, and U1368 (D'Hondt et al., 2011, 2013, 2015). Iron mat sediment samples were collected from Tarama Knoll in the Okinawa Trough during cruise YK17-17 (Makita, 2017). Iron oxyhydroxide rich coastal sediment was collected from Nagahama Bay in Satsuma Iwo-Jima, Japan (Hoshino et al., 2015). These iron-rich samples were stored at 4°C.

Comparison of Methods

Re-analysis of Previously Published Virus Counts From Subseafloor Sediment

Using subseafloor sediment samples for which virus counts had been previously published, virus enumeration was repeated using the density separation method. Enumeration was repeated on samples from the South Pacific Gyre [International Ocean Drilling Program (IODP) Exp. 329] (Engelhardt et al., 2014) and offshore Shimokita Peninsula (Chikyu Cruise CK06-06) (Yanagawa et al., 2014), representing oligotrophic sediments and organic-rich hemipelagic sediments, respectively. Viruses were enumerated from two rounds of extraction, however, only one round of extraction was possible for the Shimokita samples due to clogging of Anodisc filters. In order to calculate the virus-to-cell ratio (VCR), cell counts were obtained from previously published data for the same core samples/depths

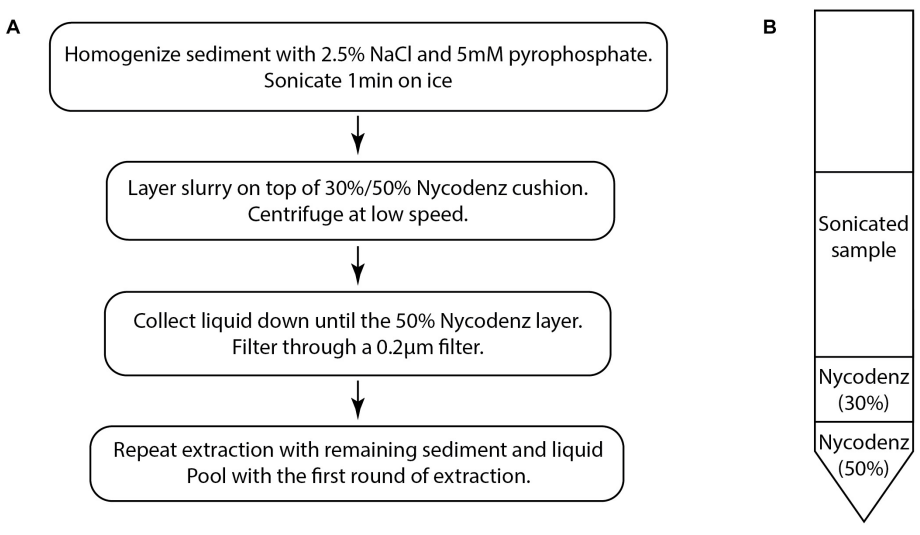

FIGURE 1 | (A) The basic flow chart of the virus extraction protocol based on density separation. **(B)** Diagram of the density separation tube prior to centrifugation.

(Engelhardt et al., 2014; Yanagawa et al., 2014; D'Hondt et al., 2015). Values obtained using the density separation method were compared to the previously published values. For two samples, published virus counts did not exist, so viruses were re-extracted and enumerated following the methods used in the original publications.

Method Comparison for Iron-Rich Sediment Samples

Samples of iron mat from Tarama Knoll, Okinawa Trough, Japan (Makita, 2017) and iron-rich sediment from Nagahama Bay, Satsuma, Japan (Hoshino et al., 2015) were also used to demonstrate the effectiveness of the density separation technique for extracting viruses from sediment containing high concentrations of iron oxyhydroxides. Viruses were enumerated from two rounds of extraction. Results were compared to virus counts obtained by the conventional virus separation method used by Engelhardt et al. (2014).

Evaluation of Recovery Efficiency

The recovery efficiency of the density separation method was evaluated using sediments from various depths from the Nankai Trough (Site C0023 Hole A), representing several sedimentary units and lithologies from 257 to 829 m below the seafloor (mbsf) (Heuer et al., 2017). A known concentration of viruses collected from seawater via filtration (0.2 μm) was amended to 0.33 cm^3 of sediment and allowed to adsorb for 15 min. We verified (using the density separation method) that the abundance of indigenous viruses in the sediment was insignificant (less than 1 per field of view at 1000× magnification) compared to the number of viruses applied. The viruses were then extracted (two rounds) using the density separation protocol described above. The extraction was also performed using conventional protocols used for virus counts of subseafloor sediment cores (Engelhardt et al., 2014; Yanagawa et al., 2014). To summarize briefly, in the protocol employed by Engelhardt et al. (2014), 1 cm^3 of sediment is added to 3.5 mL ddH_2O and 1 mL sodium pyrophosphate (55 mM) and turned into a slurry. The slurry is mixed for 15 min and sonicated. The sediment is then pelleted. The supernatant is retained, and Tris-EDTA buffer is used to wash the pellet in order to retrieve more viruses. In the protocol employed by Yanagawa et al. (2014), 3 cm^3 of sediment is added to 10 mL of SM buffer containing 2% formaldehyde. After mixing the slurry, the sediment is sonicated. The sediment is then pelleted, and the supernatant is retained. In order to make a comparison of the methods, we adjusted all volumes for 0.33 cm^3 of sediment and used the same filtration and staining steps as the density separation method.

To determine the number of rounds of extraction necessary to maximize the recovery of viruses from a single sample, repeated extractions were performed. A known concentration of viruses collected from seawater via filtration (0.2 μm) was spiked to 0.33 cm^3 sediment samples from the Nankai Trough (Heuer et al., 2017) and South Pacific Gyre (Engelhardt et al., 2014) and allowed to adsorb for 15 min. Viruses were extracted for five iterations and enumerated after each round.

Enumeration of Viruses

Viruses were enumerated by epifluoresence microscopy based on standard methods (Suttle and Fuhrman, 2010). In brief, separated viruses were filtered onto 0.02 μm Anodisc filters (GE Healthcare, 6809-6002) and stained by SYBR Green I (Invitrogen, S7567) for 15 min in the dark according to standard procedures. Excess stain was removed by vacuum filtration. Filters were mounted onto slides with VECTASHIELD antifade mounting medium (Vector Laboratories, H-1000) and enumerated under epifluorescence at 1000× magnification (Olympus BX53 microscope with 130 W U-HGLGPS fluorescence light source, Olympus U-FGFP filter cube). Fluorescent beads (Fluoresbrite BB Carboxylate Microspheres 0.5 μm, Polysciences, 18339-10) were applied to filters when it was necessary to help with focusing. Images of random fields were captured by camera connected to a computer and enumerated to determine the original concentration of viruses.

RESULTS AND DISCUSSION

Deep Subseafloor Sediments

Previously published studies of deep subseafloor sediment viruses (Engelhardt et al., 2014; Yanagawa et al., 2014) were re-evaluated using the new density separation method. The density separation method resulted in dramatically greater numbers of extractable viruses. Using the new method, 2–10 times more viruses were extracted from South Pacific Gyre samples compared to the originally published results, whereas 87–350 times more viruses were extracted from Shimokita sediments (**Figure 2**). Accordingly, the VCR of these Shimokita samples, originally reported as less than 0.01, now have a range of 0.17–2.7, altering how such data would be interpreted. While the VCR of South Pacific Gyre samples should also increase along with the virus counts, the VCR decreased due to higher cell abundances in revised cell counts (D'Hondt et al., 2015). Despite this, the updated VCR we calculated were in basic agreement with the trends and interpretations of the original publication (Engelhardt et al., 2014).

Sediment organic matter may cause high background fluorescence that obscures the epifluorescence imaging of viruses. South Pacific Gyre sediments are characterized as metalliferous and organic-poor (0.25% TOC to below detection) (Aoike, 2007; D'Hondt et al., 2015), whereas samples from offshore Shimokita are high in organic matter (avg. 1.35%) (Kobayashi et al., 2008). During the analysis of viruses extracted from Shimokita samples, we encountered high background noise which obscured the imaging of viruses, so we found it necessary to lower the volume of sediment (0.1 cm^3) that we could extract and also to limit the extraction to a single round. We experienced clogged Anodisc filters or poor visibility when working with higher sediment volumes (0.2 cm^3) or multiple rounds of extraction. Because of this, the high amounts of sediment organic matter in the Shimokita sediment may have caused previous attempts to enumerate viruses to result in 2

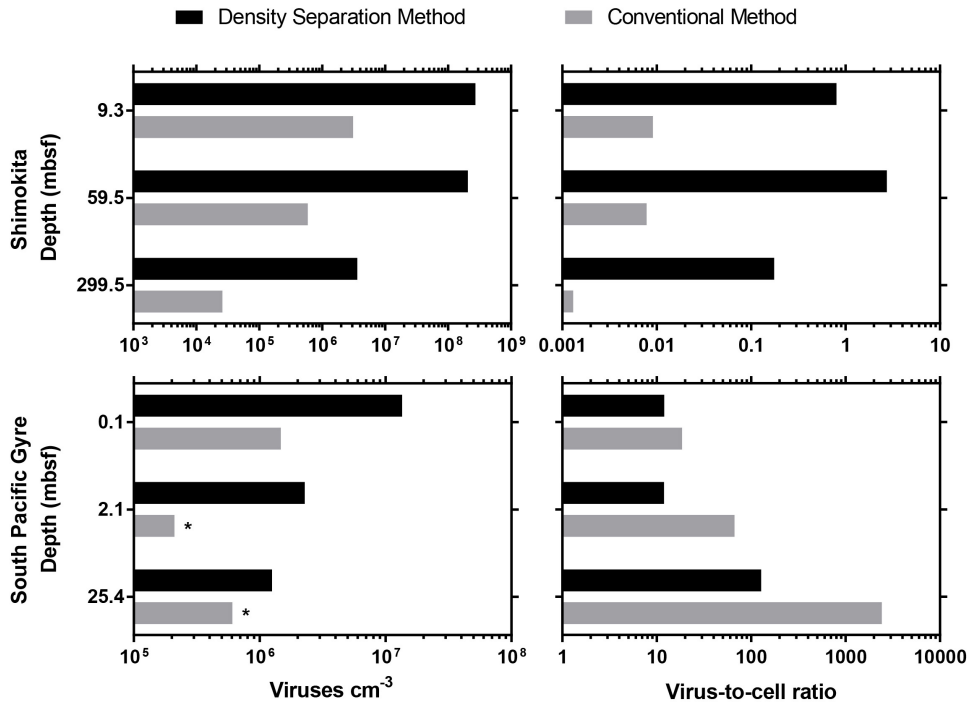

FIGURE 2 | Comparison between the density separation method and conventional methods used in previously published viral enumeration studies from IODP subseafloor sediment cores. *indicates a sample that did not have a previously published result, so the sample was re-enumerated according to the original published method. For Shimokita samples, only a single round of extraction was possible.

orders of magnitude fewer viruses than what we found by the density separation method.

Iron-Rich Sediments

Iron oxyhydroxide minerals are strong sorbents of viruses (Moore et al., 1981; Ryan et al., 2002; Bradley et al., 2011). The strong affinity between iron oxyhydroxide minerals and viruses has been utilized in industrial applications to remove viruses from wastewater (You et al., 2005; Zhu et al., 2005) as well as scavenge and concentrate viruses from large volumes of water (John et al., 2011). Because the presence of iron oxyhydroxide minerals within sediments may pose a problem for virus separation, we compared the effectiveness of the density separation method to the conventional method using iron rich sediment from Nagahama Bay (Hoshino et al., 2015) and an iron mat sample from Tarama Knoll, Okinawa Trough, Japan (Makita, 2017). In both samples tested, the density separation method resulted in higher viral abundances by 1–2 orders of magnitude. The density separation method increased viral abundance by 200-fold in the Nagahama Bay sample, from 1.81×10^6 viruses/cm^3 to 3.61×10^8 viruses/cm^3 (**Figure 3B**). In the iron mat sample, viral abundance was increased 13-fold to 1.08×10^8 viruses/cm^3. The ratio of the fluorescence signal of the viruses to background noise was greatly improved compared to the conventional method due to a better separation of high-density abiotic particles by the density separation method (**Figure 3A**). This was observed as significantly less particle accumulation on the Anodisc filters (**Supplementary Figure S2**). The use of density layers may also help to improve virus extraction efficiency by acting as a barrier between the separated viruses and iron oxyhydroxide particles, preventing re-adsorption. Conventional methods do not have any barrier between viruses and the pelleted sediment particles, so there is a greater opportunity for viruses to re-adsorb to the highly adsorptive iron minerals.

Virus Recovery Efficiency

Within a single sediment core, sediment lithology may vary dramatically. Previous studies have shown that sediment physical and chemical properties can influence the extractability of viruses from sediment (Helton et al., 2006), so we tested virus recovery efficiency on a single sediment core covering several sedimentary units with varying lithological features, porosity, and clay content. The efficiency of virus recovery was tested by spiking a known concentration of seawater viruses to sediment samples collected at various depths from the Nankai Trough Site C0023 (257–829 mbsf). The sediments chosen for this test represent various different sedimentary units with a range of porosities and clay content, while organic carbon ranged from 0.2 to 0.5% TOC (Heuer et al., 2017). The density separation method was able to consistently recover between 23.5 and 27.9% of the spiked viruses whereas the conventional methods varied greatly between samples (**Figure 4A**). Using the conventional method employed by Yanagawa et al. (2014), virus recovery varied from 17.3% at the Axial Trench-Wedge (sand, silt, and mud, 257 mbsf) to 1.2% at the Lower Shikoku basin (hemipelagic mudstone, 829 mbsf). The recovery efficiency of the method

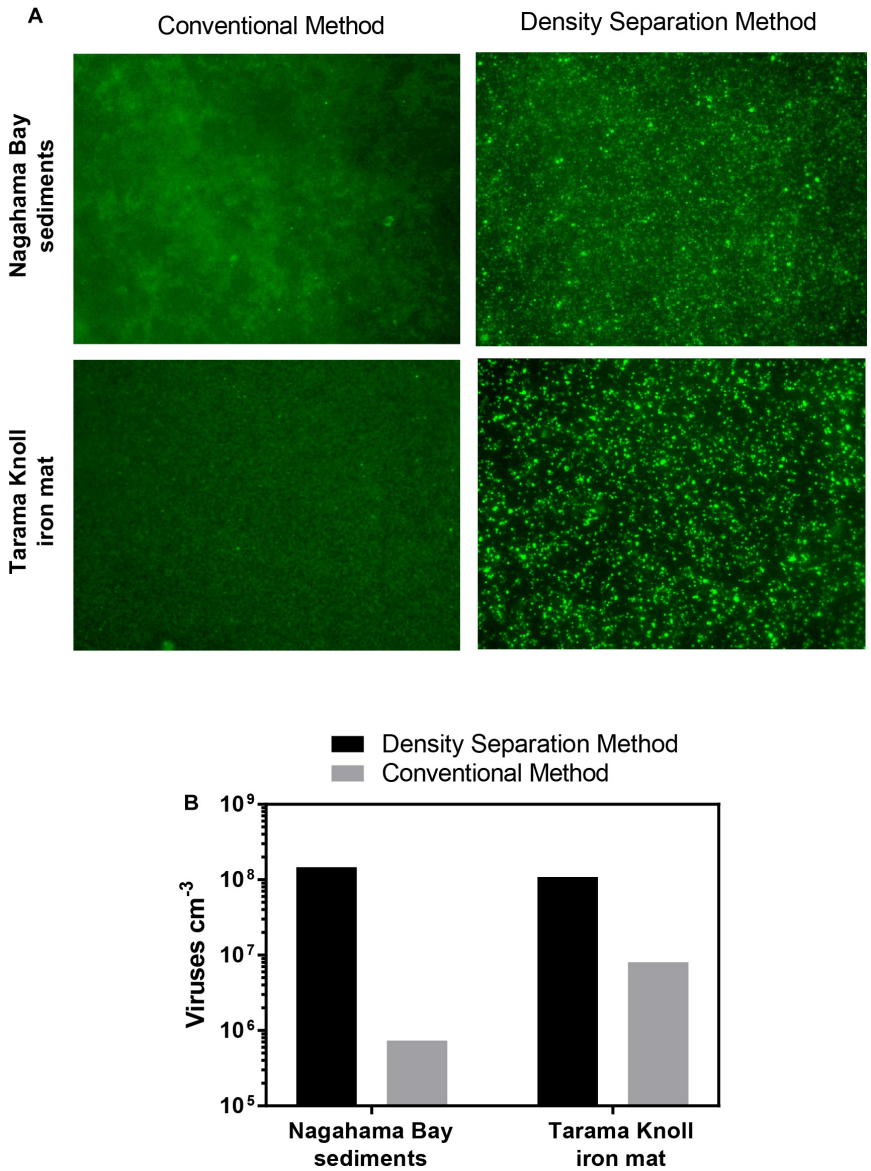

FIGURE 3 | (A) Fluorescence images of SYBR Green I stained viruses extracted using the density separation method and conventional method. The density separation method dramatically improves the separation and fluorescence of viruses from iron rich sediment. Iron oxyhydroxide floc from Nagahama bay, Satsuma and an iron mat sample from Tarama Knoll, Okinawa Trough was used. **(B)** Comparison of the virus counts resulting from the density separation method and conventional method. Viral abundance for the density separation method may be underestimated due to the presence of some overlapping fluorescent particles in the micrographs.

used by Engelhardt et al. (2014) varied from as high as 20.7% in the Upper Shikoku Basin (562 mbsf) to as low as 0.88% for sediment between the Trench-to-Basin and Upper Shikoku Basin units (499 mbsf) (**Figure 4B**). This large variability in virus extraction efficiency when using conventional methods can explain the large variabilities in viral abundance observed in previously published sediment core depth profiles (Yanagawa et al., 2014; Peduzzi, 2016) and other sediment samples (Pinto et al., 2013). These data show that conventional methods do not have the consistency necessary for confident comparisons of viral abundances within depth and lithological profiles. This suggests that the high variability in sediment virus abundances observed in previous publications may be more reflective of the efficiency of virus extraction rather than actual abundances. Even between the two conventional methods, the recovery efficiency differed greatly. The reason may be due to the use of different buffers, differences in the proportion of sediment to buffer as well as sonication times and the number of rounds of extraction. Using conventional virus extraction methods, the large variability in extraction efficiency makes it challenging to make meaningful comparisons between datasets from different studies or even different sites/depths within the same study (Pinto et al., 2013).

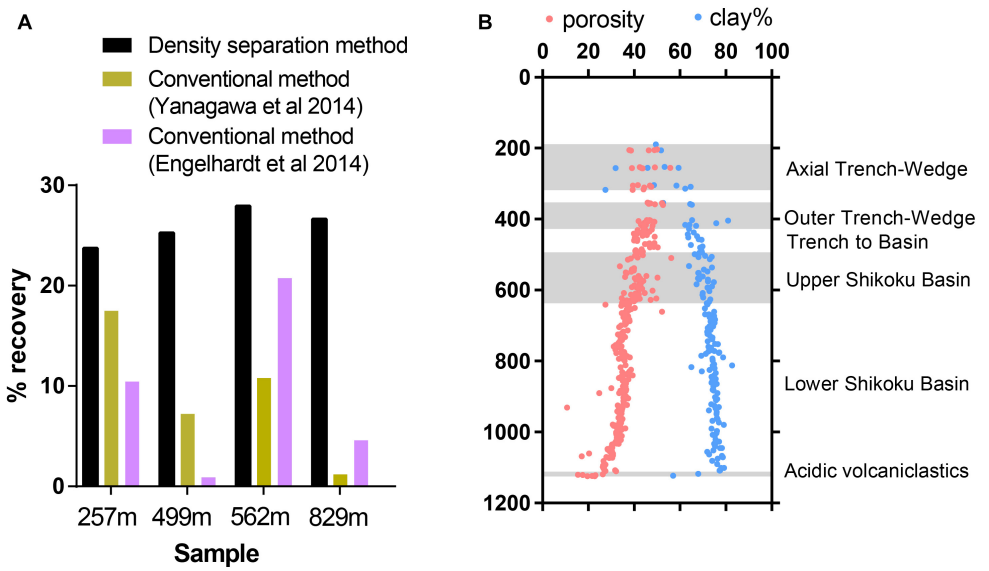

FIGURE 4 | (A) Efficiency of extraction of spiked viruses from sediment from Nankai Trough, Japan. **(B)** Sediments represent various sedimentary units with a range of porosities and clay content. Shadowed areas highlight the locations of alternating sedimentary units. Porosity and clay data reproduced from IODP Expedition 370 Report Summary (Heuer et al., 2017).

Nankai Trough sediments consist of high proportions of clay minerals, which can cause inefficient virus extraction due to the high adsorptivity of viruses onto clays (Sobsey et al., 1980; Chattopadhyay and Puls, 1999; Helton et al., 2006). The strength of adsorption between viruses and clays is positively correlated to the cation exchange capacity of clay minerals (Lipson and Stotzky, 1983). The primary clay mineral is smectite, with illite becoming the primary clay in the deeper portion of the profile. Even though smectite has a higher cation exchange capacity than illite, the consistency of the density separation method is maintained through the smectite-illite clay mineral transition in the profile (Moore et al., 2005; Heuer et al., 2017).

Furthermore, when using the conventional virus separation approach, as many as 30–50 repeated extractions may be needed to obtain the maximal number of viruses (Siem-Jørgensen et al., 2008). With the low extraction efficiency of conventional extraction approaches, each extraction may result in the removal of only a small fraction of viruses such that a large number of extractions would be required to approach the maximal number. Because conducting 30–50 serial extractions is impractical, extraction procedures are often limited to 1–3 extractions. With the density separation method, only 2 rounds of extractions are sufficient to extract close to the total number of viruses that would be extracted by further rounds (**Figure 5**).

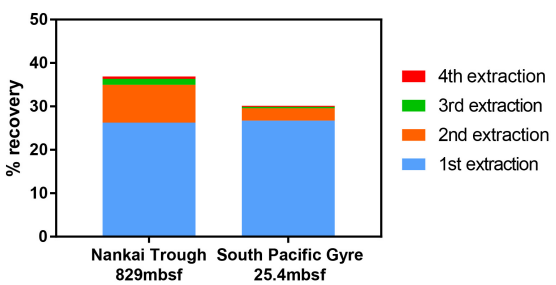

FIGURE 5 | Recovery of spiked viruses from sediment with sequential extractions. Two extractions were sufficient to recover nearly all of the viruses that could be extracted. A fifth extraction was performed, but the contribution to the total virus count was negligible.

Methodological Considerations

Extraction of spiked viruses from the sediments shows that only 20–40% of viruses were able to be recovered despite multiple extractions. It is possible that a fraction of the spiked viruses may be destroyed upon contact with certain minerals in the sediment (Ryan et al., 2002; Harvey and Ryan, 2004; Pecson et al., 2012). This may mean that a 100% recovery of all spiked viruses may not be possible. If this is not the primary reason for the relatively low recovery, the remaining unextractable viruses may be irreversibly bound to the sediment or lost during the extraction process. It may be possible to push the recovery closer toward 100% with improved methods. For now, the density separation method is the most effective method for virus extraction from subseafloor sediments (**Supplementary Figure S3**).

Oversonication may also destroy viruses, so optimization of the sonication procedure may help to improve recovery (Danovaro et al., 2001). The optimal strength and length of sonication will depend on the sonicator model and tip diameter as well as the sediment characteristics. Sonication has sometimes been found to be problematic enough to warrant omission from some virus extraction methods (Montanié et al., 2015). Experimenters are

encouraged to find the optimal settings for their own sonication system.

The volume of sediment that can be extracted in a single extraction should be adjusted according to the sediment characteristics. In the case of organic rich sediments, the amount of extract that can be filtered through a single Anodisc filter may be limited, likely due to incomplete separation of viruses from other low-density organic particles in the 20–200 nm size range. Organic-rich sediments such as the Shimokita samples had to be limited to 0.1 cm^3. Attempts at filtering extracts from larger volumes (0.2 cm^3) of Shimokita sediment through Anodisc filters resulted in clogged and unusable filters. For low organic sediments from the South Pacific Gyre and Nankai Trough, we did not encounter clogging of Anodisc filters. Pooling multiple extracts from high organic Shimokita sediments also ran into the same problem. In such cases, it would be necessary to use separate Anodisc filters for each round of extraction, which may be cost prohibitive. Samples high in organic matter [e.g., terrestrial soils (Williamson et al., 2013; Trubl et al., 2016)] may require some method optimization in order to further separate viruses from other organic particles.

In our virus extraction method, a final step of filtration (0.2 μm) is used to separate cells and large particulates from viruses. Due to this cutoff, giant viruses will be excluded. Some small fraction of viruses that are smaller than 0.2 μm in diameter may potentially also be caught onto the filter as well. It may be possible to use larger size cutoffs or even forego final filtration. However, forgoing filtration may come with the risk of introducing some cells or large organic particulates into the extraction. If the presence of small cells is a major concern, a 0.1 μm final cutoff may be used instead, however, virus abundances may potentially decrease. In any case, the experimenter should determine what works best for their research goals.

Viruses extracted using the density separation technique may potentially retain their infectivity, allowing for isolation and culture-based applications. Viruses that are extracted from sediment minerals may still retain their infectivity (Schaub and Sagik, 1975). Clay minerals such as montmorillonite, attapulgite, vermiculite, and kaolinite have been demonstrated to protect viruses from decay or inactivation (Bitton and Mitchell, 1974; Babich and Stotzky, 1980). Because Nycodenz has been successfully applied to the isolation of viable cells from other materials (Hevia et al., 2015), it is plausible that the viruses extracted by the density separation method may also be viable, however, this has not been verified yet. If the use of Nycodenz as the compound to generate the density layers does not yield viable viruses, other compounds may potentially be used. Other compounds such as polytungstate have been successfully used to separate cells from sediment (Morono et al., 2013).

Implications

There is estimated to be on the order of 10^{31} viruses on Earth, the overwhelming majority of which inhabit soil and sediments, with estimates ranging from 79% (Bar-On et al., 2018) to 97% (Cobián Güemes et al., 2016). By some estimates, viruses in marine subseafloor sediments are estimated to comprise approximately half of the viruses on Earth (4.8×10^{30}) (Bar-On et al., 2018). The density separation method has demonstrated that conventional methods underestimate sediment viral abundance and that viruses may in fact be far more numerous than previous studies have indicated. Although the total abundance of marine sediment viruses is not yet well constrained, we can attempt to estimate the new method's potential for revising current estimates of the pool of viral carbon in subseafloor sediments. We evaluate the potential based on the factor increase we observed when employing the density separation method and applying the factor increases to current estimates of subseafloor viral biomass (Bar-On et al., 2018). Oligotrophic, open ocean sediments such as those from the South Pacific Gyre cover 42% of the ocean while containing 10% of the cells (Kallmeyer et al., 2012). Within the South Pacific Gyre sediments, we observed an increase of a factor of 2–10 when we applied the density separation method. Coastal sediments such as those from Shimokita cover 7% of the ocean but carry 33% of the cells in subseafloor sediment. Using Shimokita sediments to represent coastal sediment, we observed an increase of a factor of 80–350 when we use the density separation method. For the remaining portion of the ocean, we will use a conservative factor of 1–10 for the possible increase in virus abundance that may possibly be expected. Using these correction factors, the total abundance of subseafloor viruses may potentially be revised upward to $3.3–16.2 \times 10^{31}$ viruses. This would result in revised estimates of 0.8–3.7 Gt of viral carbon in the deep subsurface compared to the current estimate of 0.2 Gt (Bar-On et al., 2018). The improved recovery over conventional methods indicates that a large portion of viruses have heretofore been undetected in subsurface sediment, suggesting that the global subsurface biomass of viruses may be far larger than previously estimated. Revising viral abundance numbers for subseafloor sediments may significantly alter the subseafloor carbon budget, especially if the viral pool of carbon approaches the same order of magnitude as the prokaryotic pool (approximately 10 Gt C) (Bar-On et al., 2018). Revised estimates of viral biomass indicate that viruses may actually an important pool of subsurface organic matter, especially organic phosphorus (Jover et al., 2014), for supporting subseafloor microbial populations (Dell'Anno et al., 2015).

Ratios of viruses to cells have been used to interpret microbial ecology (Wigington et al., 2016; Parikka et al., 2017), however, previously published VCR values measured by conventional methods from sediment must be reconsidered in light our findings. For example, VCR observed in environments such as seafloor chimney structures [as low as 0.002 (Yoshida-Takashima et al., 2012)] may need reinterpretation if the density separation method dramatically increases viral extraction efficiency. We have shown that conventional methods can vary greatly in extraction efficiency between samples of different lithology, even within a single sediment core (**Figure 4A**). We suggest that VCR measured by conventional sediment extraction methods should not be the basis of comparison between different sedimentary environments unless if there is reason to believe that the extraction efficiencies would be expected to be similar, such as two samples very close in proximity and composition.

It is especially not recommended to compare VCR between solid-associated and aquatic samples due to methodological differences. Researchers must also consider differences between virus extraction efficiency and cell extraction efficiency when interpreting results, especially if the methodology used for the extraction of microbial cells and viruses differs substantially (Parikka et al., 2017). Because the density separation method is methodologically based on a similar density-based cell extraction method (Morono et al., 2013), it is ideal to pair these two methods for calculation of VCR in sediment.

While recent advances in cell-sediment separation techniques have allowed cells to be quantified at extremely low biomass (<10 cells/cm^3) (Morono et al., 2013, 2017; Inagaki et al., 2015; Morono and Inagaki, 2016), virus-sediment separation techniques have not made similar advances. The detection limits of conventional sediment virus separation and enumeration techniques have already been reached for some sites such as the South Pacific Gyre (Engelhardt et al., 2014). As IODP and ICDP expeditions begin to investigate subsurface life in sediments with conditions approaching life's limits, the development of the density separation method makes it possible to study viruses in deeper, lower biomass environments than ever before.

AUTHOR CONTRIBUTIONS

DP conceived, designed and conducted all experiments, and analyzed the data. YM contributed to method development. DP wrote the manuscript with contribution from YM, FI, and KT.

FUNDING

The authors are grateful to IODP for their support for the opportunities for core sampling. This work was supported in part by the Japan Society for the Promotion of Science (JSPS) Grant-in Aid for Research Activity Start-up (Grant No. 16H07489 to DP) and JAMSTEC International Postdoctoral Fellowship fund (to DP). Additional support was provided by the Center for Deep-Earth Exploration (CDEX) for embarkation on the Chikyu for IODP Expedition 370.

ACKNOWLEDGMENTS

We thank all crews, drilling team members, lab technicians, and scientists for their supporting core sampling and onboard measurements during Chikyu shakedown cruise CK06-06, IODP Expeditions 329, 370, Yokosuka cruise YK17-17. We also thank H. Kashima, H. Makita, T. Terada, T. Nunoura, and K. Yanagawa for providing access to samples; B. Engelen and T. Engelhardt for providing access to data; and K. Yang for helpful discussion about clays. This is a contribution to the Deep Carbon Observatory.

SUPPLEMENTARY MATERIAL

The Supplementary Material for this article can be found online at: https://www.frontiersin.org/articles/10.3389/fmicb.2019.00878/full#supplementary-material

REFERENCES

Aoike, K. (2007). *CDEX Laboratory Operation Report: CK06-06 D/V Chikyu Shakedown Cruise Offshore Shimokita*. Minato: Yokohama.

Babich, H., and Stotzky, G. (1980). Reductions in inactivation rates of bacteriophages by clay minerals in lake water. *Water Res.* 14, 185–187. doi: 10.1016/0043-1354(80)90236-5

Bar-On, Y. M., Phillips, R., and Milo, R. (2018). The biomass distribution on Earth. *Proc. Natl. Acad. Sci. U.S.A.* 115, 6506–6511. doi: 10.1073/pnas.1711842115

Biller, S. J., Mcdaniel, L. D., Breitbart, M., Rogers, E., Paul, J. H., and Chisholm, S. W. (2017). Membrane vesicles in sea water: heterogeneous DNA content and implications for viral abundance estimates. *ISME J.* 11, 394–404. doi: 10.1038/ismej.2016.134

Bird, D., Juniper, S., Ricciardi-Rigault, M., Martineu, P., Prairie, Y., and Calvert, S. (2001). Subsurface viruses and bacteria in Holocene/Late Pleistocene sediments of Saanich Inlet, BC: ODP holes 1033b and 1034b, Leg 169s. *Mar. Geol.* 174, 227–239. doi: 10.1016/S0025-3227(00)00152-3

Bitton, G., and Mitchell, R. (1974). Effect of colloids on the survival of bacteriophages in seawater. *Water Res.* 8, 227–229. doi: 10.1016/0043-1354(74)90159-6

Bradley, I., Straub, A., Maraccini, P., Markazi, S., and Nguyen, T. H. (2011). Iron oxide amended biosand filters for virus removal. *Water Res.* 45, 4501–4510. doi: 10.1016/j.watres.2011.05.045

Chattopadhyay, S., and Puls, R. W. (1999). Adsorption of bacteriophages on clay minerals. *Environ. Sci. Technol.* 33, 3609–3614. doi: 10.1021/es9811492

Cobián Güemes, A. G., Youle, M., Cantú, V. A., Felts, B., Nulton, J., and Rohwer, F. (2016). Viruses as winners in the game of life. *Annu. Rev. Virol.* 3, 197–214. doi: 10.1146/annurev-virology-100114-054952

Danovaro, R., Dell'anno, A., Trucco, A., Serresi, M., and Vanucci, S. (2001). Determination of virus abundance in marine sediments. *Appl. Environ. Microbiol.* 67, 1384–1387. doi: 10.1128/AEM.67.3.1384-1387.2001

Danovaro, R., and Middelboe, M. (2010). "Separation of free virus particles from sediments in aquatic systems," in *Manual of Aquatic Viral Ecology*, eds S. W. Wilhelm, M. G. Weinbauer, and C. A. Suttle (Washington, DC: ASLO), 74–81.

Dell'Anno, A., Corinaldesi, C., and Danovaro, R. (2015). Virus decomposition provides an important contribution to benthic deep-sea ecosystem functioning. *Proc. Natl. Acad. Sci. U.S.A.* 112, E2014–E2019. doi: 10.1073/pnas.1422234112

D'Hondt, S., Inagaki, F., Alvarez Zarikian, C., and The, I. E. S. P. (2013). IODP expedition 329: life and habitability beneath the seafloor of the south pacific gyre. *Sci. Dril.* 15, 4–10. doi: 10.5194/sd-15-4-2013

D'Hondt, S., Inagaki, F., Zarikian, C. A., Abrams, L. J., Dubois, N., Engelhardt, T., et al. (2015). Presence of oxygen and aerobic communities from sea floor to basement in deep-sea sediments. *Nat. Geosci.* 8:299. doi: 10.1038/ngeo2387

D'Hondt, S., Inagaki, F., Zarikian, C. A., and Scientists, T. E. (2011). *South Pacific Gyre Subseafloor Life*. College Station TX: Integrated Ocean Drilling Program Management International, Inc., for the Integrated Ocean Drilling Program.

Dowd, S. E., Pillai, S. D., Wang, S., and Corapcioglu, M. Y. (1998). Delineating the specific influence of virus isoelectric point and size on virus adsorption and transport through sandy soils. *Appl. Environ. Microbiol.* 64, 405–410.

Engelhardt, T., Kallmeyer, J., Cypionka, H., and Engelen, B. (2014). High virus-to-cell ratios indicate ongoing production of viruses in deep subsurface sediments. *ISME J.* 8, 1503–1509. doi: 10.1038/ismej.2013.245

Farkas, K., Cooper, D. M., Mcdonald, J. E., Malham, S. K., De Rougemont, A., and Jones, D. L. (2018). Seasonal and spatial dynamics of enteric viruses in wastewater and in riverine and estuarine receiving waters. *Sci. Total Environ.* 634, 1174–1183. doi: 10.1016/j.scitotenv.2018.04.038

Fischer, U. R., Kirschner, A. K., and Velimirov, B. (2005). Optimization of extraction and estimation of viruses in silty freshwater sediments. *Aquat. Microb. Ecol.* 40, 207–216. doi: 10.3354/ame040207

Fuhs, G. W., Chen, M., Sturman, L. S., and Moore, R. S. (1985). Virus adsorption to mineral surfaces is reduced by microbial overgrowth and organic coatings. *Microb. Ecol.* 11, 25–39. doi: 10.1007/BF02015106

Guan, H., Schulze-Makuch, D., Schaffer, S., and Pillai, S. D. (2003). The effect of critical pH on virus fate and transport in saturated porous medium. *Groundwater* 41, 701–708. doi: 10.1111/j.1745-6584.2003.tb02408.x

Harvey, R. W., and Ryan, J. N. (2004). Use of PRD1 bacteriophage in groundwater viral transport, inactivation, and attachment studies. *FEMS Microbiol. Ecol.* 49, 3–16. doi: 10.1016/j.femsec.2003.09.015

Hassard, F., Gwyther, C. L., Farkas, K., Andrews, A., Jones, V., Cox, B., et al. (2016). Abundance and distribution of enteric bacteria and viruses in coastal and estuarine sediments—a review. *Front. Microbiol.* 7:1692. doi: 10.3389/fmicb.2016.01692

Helton, R. R., Liu, L., and Wommack, K. E. (2006). Assessment of factors influencing direct enumeration of viruses within estuarine sediments. *Appl. Environ. Microbiol.* 72, 4767–4774. doi: 10.1128/AEM.00297-06

Heuer, V., Inagaki, F., Morono, Y., Kubo, Y., Maeda, L., Bowden, S., et al. (2017). *Expedition 370 Scientists 2017 Temperature Limit of the Deep Biosphere off Muroto*. Available at: publications.iodp.org/preliminary_report/370/ (accessed September 26, 2017).

Hevia, A., Delgado, S., Margolles, A., and Sánchez, B. (2015). Application of density gradient for the isolation of the fecal microbial stool component and the potential use thereof. *Sci. Rep.* 5:16807. doi: 10.1038/srep16807

Hoshino, T., Kuratomi, T., Morono, Y., Hori, T., Oiwane, H., Kiyokawa, S., et al. (2015). Ecophysiology of zetaproteobacteria associated with shallow hydrothermal iron-oxyhydroxide deposits in nagahama Bay of Satsuma Iwo-Jima, Japan. *Front. Microbiol.* 6:1554. doi: 10.3389/fmicb.2015.01554

Inagaki, F., Hinrichs, K.-U., Kubo, Y., Bowles, M. W., Heuer, V. B., Hong, W.-L., et al. (2015). Exploring deep microbial life in coal-bearing sediment down to ∼2.5 km below the ocean floor. *Science* 349, 420–424. doi: 10.1126/science.aaa6882

John, S. G., Mendez, C. B., Deng, L., Poulos, B., Kauffman, A. K. M., Kern, S., et al. (2011). A simple and efficient method for concentration of ocean viruses by chemical flocculation. *Environ. Microbiol. Rep.* 3, 195–202. doi: 10.1111/j.1758-2229.2010.00208.x

Jover, L. F., Effler, T. C., Buchan, A., Wilhelm, S. W., and Weitz, J. S. (2014). The elemental composition of virus particles: implications for marine biogeochemical cycles. *Nat. Rev. Microbiol.* 12:519. doi: 10.1038/nrmicro3289

Kallmeyer, J., Pockalny, R., Adhikari, R. R., Smith, D. C., and D'hondt, S. (2012). Global distribution of microbial abundance and biomass in subseafloor sediment. *Proc. Natl. Acad. Sci. U.S.A.* 109, 16213–16216. doi: 10.1073/pnas.1203849109

Kinoshita, T., Bales, R. C., Maguire, K. M., and Gerba, C. P. (1993). Effect of pH on bacteriophage transport through sandy soils. *J. Contam. Hydrol.* 14, 55–70. doi: 10.1016/0169-7722(93)90041-P

Kobayashi, T., Koide, O., Mori, K., Shimamura, S., Matsuura, T., Miura, T., et al. (2008). Phylogenetic and enzymatic diversity of deep subseafloor aerobic microorganisms in organics- and methane-rich sediments off Shimokita Peninsula. *Extremophiles* 12, 519–527. doi: 10.1007/s00792-008-0157-7

Lipson, S. M., and Stotzky, G. (1983). Adsorption of reovirus to clay minerals: effects of cation-exchange capacity, cation saturation, and surface area. *Appl. Environ. Microbiol.* 46, 673–682.

Loveland, J., Ryan, J., Amy, G., and Harvey, R. (1996). The reversibility of virus attachment to mineral surfaces. *Colloids Surfaces A Physicochem. Eng. Aspects* 107, 205–221. doi: 10.1016/0927-7757(95)03373-4

Makita, H. (2017). *Yokosuka Cruise Report YK17-17 Elucidation of Microbial Ecosystems Utilizing Iron and other Environmental Factors to Support their Activity in "Iron-Dominated Flocculent Mats" at Tarama Knoll*. Natsushimacho: JAMSTEC.

Middelboe, M., Glud, R. N., and Filippini, M. (2011). Viral abundance and activity in the deep sub-seafloor biosphere. *Aquat. Microb. Ecol.* 63, 1–8. doi: 10.3354/ame01485

Miura, T., Masago, Y., Chan, Y.-M., Imai, T., and Omura, T. (2009). Detection of bacteria and enteric viruses from river and estuarine sediment. *J. Water Environ. Technol.* 7, 307–316. doi: 10.1128/mSystems.00025-18

Montanié, H., De Crignis, M. G., and Lavaud, J. (2015). Viral impact on prokaryotic and microalgal activities in the microphytobenthic biofilm of an intertidal mudflat (French Atlantic Coast). *Front. Microbiol.* 6:1214. doi: 10.3389/fmicb.2015.01214

Moore, G., Mikada, H., Moore, J., Becker, K., and Taira, A. (2005). "Legs 190 and 196 synthesis: deformation and fluid flow processes in the nankai trough accretionary prism," in *Proceedings of the Ocean Drilling Program: Scientific Results*, eds H. Mikada, G. F. Moore, A. Taira, K. Becker, J. C. Moore, and A. Klaus College Station, TX. doi: 10.2973/odp.proc.sr.190196.201.2005

Moore, R. S., Taylor, D. H., Sturman, L. S., Reddy, M. M., and Fuhs, G. W. (1981). Poliovirus adsorption by 34 minerals and soils. *Appl. Environ. Microbiol.* 42, 963–975.

Morono, Y., and Inagaki, F. (2016). Analysis of low-biomass microbial communities in the deep biosphere. *Adv. Appl. Microbiol.* 95, 149–178. doi: 10.1016/bs.aambs.2016.04.001

Morono, Y., Inagaki, F., Heuer, V., Kubo, Y., Maeda, L., Bowden, S., et al. (eds) (2017). "Expedition 370 methods," in *Proceedings of the International Ocean Discovery Program*, eds V. B. Heuer, F. Inagaki, Y. Morono, et al. (College Station, TX: International Ocean Discovery Program).

Morono, Y., Terada, T., Kallmeyer, J., and Inagaki, F. (2013). An improved cell separation technique for marine subsurface sediments: applications for high-throughput analysis using flow cytometry and cell sorting. *Environ. Microbiol.* 15, 2841–2849. doi: 10.1111/1462-2920.12153

Parikka, K. J., Le Romancer, M., Wauters, N., and Jacquet, S. (2017). Deciphering the virus-to-prokaryote ratio (VPR): insights into virus–host relationships in a variety of ecosystems. *Biol. Rev.* 92, 1081–1100. doi: 10.1111/brv.12271

Pecson, B. M., Decrey, L., and Kohn, T. (2012). Photoinactivation of virus on iron-oxide coated sand: enhancing inactivation in sunlit waters. *Water Res.* 46, 1763–1770. doi: 10.1016/j.watres.2011.12.059

Peduzzi, P. (2016). Virus ecology of fluvial systems: a blank spot on the map? *Biol. Rev.* 91, 937–949. doi: 10.1111/brv.12202

Pinto, F., Larsen, S., and Casper, P. (2013). Viriobenthos in aquatic sediments: variability in abundance and production and impact on the C-cycle. *Aquat. Sci.* 75, 571–579. doi: 10.1007/s00027-013-0301-z

Powelson, D. K., Simpson, J. R., and Gerba, C. P. (1991). Effects of organic matter on virus transport in unsaturated flow. *Appl. Environ. Microbiol.* 57, 2192–2196.

Rohwer, F., and Thurber, R. V. (2009). Viruses manipulate the marine environment. *Nature* 459:207. doi: 10.1038/nature08060

Ryan, J. N., Harvey, R. W., Metge, D., Elimelech, M., Navigato, T., and Pieper, A. P. (2002). Field and laboratory investigations of inactivation of viruses (PRD1 and MS2) attached to iron oxide-coated quartz sand. *Environ. Sci. Technol.* 36, 2403–2413. doi: 10.1021/es011285y

Schaub, S. A., and Sagik, B. P. (1975). Association of enteroviruses with natural and artificially introduced colloidal solids in water and infectivity of solids-associated virions. *Appl. Microbiol.* 30, 212–222.

Siem-Jørgensen, M., Glud, R. N., and Middelboe, M. (2008). Viral dynamics in a coastal sediment: seasonal pattern, controlling factors and relations to the pelagic–benthic coupling. *Mar. Biol. Res.* 4, 165–179. doi: 10.1080/17451000801888718

Sobsey, M. D., Dean, C. H., Knuckles, M. E., and Wagner, R. A. (1980). Interactions and survival of enteric viruses in soil materials. *Appl. Environ. Microbiol.* 40, 92–101.

Suttle, C. A. (2005). Viruses in the sea. *Nature* 437, 356–361. doi: 10.1038/nature04160

Suttle, C. A., and Fuhrman, J. A. (2010). "Enumeration of virus particles in aquatic or sediment samples by epifluorescence microscopy," in *Manual of Aquatic Viral Ecology*, eds S. W. Wilhelm, M. G. Weinbauer, and C. A. Suttle (Washington, DC: ASLO), 145–153.

Trubl, G., Solonenko, N., Chittick, L., Solonenko, S. A., Rich, V. I., and Sullivan, M. B. (2016). Optimization of viral resuspension methods for carbon-rich soils along a permafrost thaw gradient. *PeerJ* 4:e1999. doi: 10.7717/peerj.1999

Weinbauer, M. G., Bettarel, Y., Cattaneo, R., Luef, B., Maier, C., Motegi, C., et al. (2009). Viral ecology of organic and inorganic particles in aquatic systems: avenues for further research. *Aquat. Microb. Ecol. Int. J.* 57, 321–341. doi: 10.3354/ame01363

Wigington, C. H., Sonderegger, D., Brussaard, C. P. D., Buchan, A., Finke, J. F., Fuhrman, J. A., et al. (2016). Re-examination of the relationship between marine virus and microbial cell abundances. *Nat. Microbiol.* 1:15024. doi: 10.1038/nmicrobiol.2015.24

Williamson, K. E., Corzo, K. A., Drissi, C. L., Buckingham, J. M., Thompson, C. P., and Helton, R. R. (2013). Estimates of viral abundance in soils are strongly influenced by extraction and enumeration methods. *Biol. Fertil. Soils* 49, 857–869. doi: 10.1007/s00374-013-0780-z

Williamson, K. E., Wommack, K. E., and Radosevich, M. (2003). Sampling natural viral communities from soil for culture-independent analyses. *Appl. Environ. Microbiol.* 69, 6628–6633. doi: 10.1128/AEM.69.11.6628-6633.2003

Yanagawa, K., Morono, Y., Yoshida-Takashima, Y., Eitoku, M., Sunamura, M., Inagaki, F., et al. (2014). Variability of subseafloor viral abundance at the geographically and geologically distinct continental margins. *FEMS Microbiol. Ecol.* 88, 60–68. doi: 10.1111/1574-6941.12269

Yoshida-Takashima, Y., Nunoura, T., Kazama, H., Noguchi, T., Inoue, K., Akashi, H., et al. (2012). Spatial distribution of viruses associated with planktonic and attached microbial communities in hydrothermal environments. *Appl. Environ. Microbiol.* 78, 1311–1320. doi: 10.1128/AEM.06491-11

You, Y., Han, J., Chiu, P. C., and Jin, Y. (2005). Removal and inactivation of waterborne viruses using zerovalent iron. *Environ. Sci. Technol.* 39, 9263–9269. doi: 10.1021/es050829j

Zhu, B., Clifford, D. A., and Chellam, S. (2005). Virus removal by iron coagulation–microfiltration. *Water Res.* 39, 5153–5161. doi: 10.1016/j.watres.2005.09.035

Conflict of Interest Statement: The authors declare that the research was conducted in the absence of any commercial or financial relationships that could be construed as a potential conflict of interest.

frontiers in Microbiology

ORIGINAL RESEARCH
published: 16 July 2019
doi: 10.3389/fmicb.2019.01497

Hydrostatic Pressure Helps to Cultivate an Original Anaerobic Bacterium From the Atlantis Massif Subseafloor (IODP Expedition 357): *Petrocella atlantisensis* gen. nov. sp. nov.

*Marianne Quéméneur[1], Gaël Erauso[1], Eléonore Frouin[1], Emna Zeghal[1], Céline Vandecasteele[2], Bernard Ollivier[1], Christian Tamburini[1], Marc Garel[1], Bénédicte Ménez[3] and Anne Postec[1]**

[1] Aix-Marseille Université, Université de Toulon, CNRS, IRD, MIO UM110, Marseille, France, [2] INRA, US 1426, GeT-PlaGe, Genotoul, Castanet-Tolosan, France, [3] Université de Paris, Institut de Physique du Globe de Paris, CNRS UMR 7154, Paris, France

OPEN ACCESS

Edited by:
Isabelle Daniel,
Université Claude Bernard Lyon 1, France

Reviewed by:
Ida Helene Steen,
University of Bergen, Norway
Lotta Purkamo,
Geological Survey of Finland, Finland

***Correspondence:**
Anne Postec
anne.postec@univ-amu.fr

Specialty section:
This article was submitted to Extreme Microbiology, a section of the journal Frontiers in Microbiology

Received: 22 February 2019
Accepted: 14 June 2019
Published: 16 July 2019

Citation:
Quéméneur M, Erauso G, Frouin E, Zeghal E, Vandecasteele C, Ollivier B, Tamburini C, Garel M, Ménez B and Postec A (2019) Hydrostatic Pressure Helps to Cultivate an Original Anaerobic Bacterium From the Atlantis Massif Subseafloor (IODP Expedition 357): *Petrocella atlantisensis* gen. nov. sp. nov. Front. Microbiol. 10:1497. doi: 10.3389/fmicb.2019.01497

Rock-hosted subseafloor habitats are very challenging for life, and current knowledge about microorganisms inhabiting such lithic environments is still limited. This study explored the cultivable microbial diversity in anaerobic enrichment cultures from cores recovered during the International Ocean Discovery Program (IODP) Expedition 357 from the Atlantis Massif (Mid-Atlantic Ridge, 30°N). 16S rRNA gene survey of enrichment cultures grown at 10–25°C and pH 8.5 showed that *Firmicutes* and *Proteobacteria* were generally dominant. However, cultivable microbial diversity significantly differed depending on incubation at atmospheric pressure (0.1 MPa), or hydrostatic pressures (HP) mimicking the *in situ* pressure conditions (8.2 or 14.0 MPa). An original, strictly anaerobic bacterium designated 70B-A^T was isolated from core M0070C-3R1 (1150 meter below sea level; 3.5 m below seafloor) only from cultures performed at 14.0 MPa. This strain named *Petrocella atlantisensis* is a novel species of a new genus within the newly described family *Vallitaleaceae* (order *Clostridiales*, phylum *Firmicutes*). It is a mesophilic, moderately halotolerant and piezophilic chemoorganotroph, able to grow by fermentation of carbohydrates and proteinaceous compounds. Its 3.5 Mb genome contains numerous genes for ABC transporters of sugars and amino acids, and pathways for fermentation of mono- and di-saccharides and amino acids were identified. Genes encoding multimeric [FeFe] hydrogenases and a Rnf complex form the basis to explain hydrogen and energy production in strain 70B-A^T. This study outlines the importance of using hydrostatic pressure in culture experiments for isolation and characterization of autochthonous piezophilic microorganisms from subseafloor rocks.

Keywords: Atlantis Massif, subseafloor, oceanic crust, serpentinization, anaerobic culture, hydrostatic pressure

INTRODUCTION

The subseafloor biosphere remains largely unexplored, although estimated as a huge reservoir for prokaryotic life (Whitman et al., 1998; Orcutt et al., 2011; Kallmeyer et al., 2012). Exploration of the rock-hosted subseafloor biosphere is especially very challenging and carried out through costly ocean drilling programs, which still must face several technical difficulties, such as poor core recovery and microbial contamination. In addition, the very low microbial cell density, around 10^4 cells per gram of rock at North Pond (Jørgensen and Zhao, 2016) or even less in the Atlantis Massif (Früh-Green et al., 2018) (respectively 22 and 30°N along the Mid-Atlantic Ridge), the usually low growth rate, and the lack of knowledge on the physiology and metabolism of the prokaryotes living in these extreme environments, hamper the attempt at cultivating them. As a result, the subseafloor prokaryotic cultivability was estimated below 0.1% of total microscopically counted cells (D'Hondt et al., 2004). Moreover, the hydrostatic pressure is an important physical parameter of these deep-sea environments but was often neglected in previous subseafloor cultivation studies. To date, most of the enrichment tests performed on rocks recovered during ocean drilling programs were made at atmospheric pressure and failed to obtain microbial growth after first incubations or subcultures (Santelli et al., 2010; Hirayama et al., 2015). Both hydrostatic and lithostatic pressures in deep-sea and deep subseafloor environments (increasing by about 10 and 30 MPa km^{-1}, respectively (Schrenk et al., 2010)) have an impact on microbial growth, metabolism and physiology, thus on the cultivability of microorganisms (Bartlett et al., 2007; Lauro and Bartlett, 2007; Parkes et al., 2009; Takai, 2011; Picard and Daniel, 2013). Moreover, the importance of high HP for deep-sea microorganisms cultivation is now well established (Tamburini et al., 2013). In this work, HP incubation systems were used to cultivate and study physiology of microorganisms inhabiting the underexplored oceanic crustal biosphere.

The Atlantis Massif, a prominent underwater oceanic core complex of nearly 4 000 m high, hosts the famous Lost City Hydrothermal Field (LCHF) (Kelley et al., 2005). It is composed of deep crustal (gabbro) and upper mantle rocks (peridotite) that have been exposed at the ocean floor as a result of tectonic plates drifting and large active faulting (Früh-Green et al., 2018). Serpentinization of ultramafic mantle rocks by deeply circulating seawater produces heat and generates alkaline fluids enriched in hydrogen (H_2), methane (CH_4), short-chain alkanes and small organic acids, representing possible carbon and energy sources to fuel life in the absence of light and contributing to global biogeochemical cycles (Levin et al., 2016). Such environmental conditions and ecosystems may have prevailed on early Earth or other planets (Martin et al., 2008). In this context, the main objective of the IODP Expedition 357 "Atlantis Massif Serpentinization and Life" was to explore the extent and activity of the subseafloor biosphere in a young ultramafic substratum (Früh-Green et al., 2016, Früh-Green et al., 2017d). During this expedition, series of boreholes were drilled across the Atlantis Massif at different water depths and distances of LCHF (**Figure 1**), in order to evaluate how subseafloor microbial communities may vary depending on the age of the lithosphere, its alteration and the hydrothermal activity.

The emblematic LCHF located on top of the Atlantis Massif, at 800 meters below sea level (mbsl), exhibits high carbonate chimneys discharging alkaline hydrothermal fluids at moderate temperature (∼ pH 11 and 90°C) and high levels of dissolved H_2 (1-15 mM) and CH_4 (1-2 mM) as the most obvious manifestation of underground serpentinization reactions (Schrenk et al., 2013). The unique microbial communities living inside the porous chimney structures are dominated by a single *Methanosarcinales* phylotype (*Archaea*), with *Proteobacteria* and *Firmicutes* (*Bacteria*) (Schrenk et al., 2013). This peculiar ecosystem is assumed to picture an "open window on deep serpentinizing hydrothermal system" (Lang et al., 2018). However, due to the lack of core samples from the LCHF basement, direct experimental evidences supporting this assumption are missing. Only one study on the microbiology of the Atlantis Massif (IODP Expeditions 304-305, Hole U1309D) reports that the gabbroic layers host a low diversity of proteobacterial lineages (*Alpha-, Beta-* and *Gammaproteobacteria*) hypothetically degrading hydrocarbons and fixing carbon and nitrogen with the potential for anaerobic respiration of nitrate, sulfate and metals (Mason et al., 2010). To date no cultivated microorganism has been reported from these ecosystems to attest the occurrence of these metabolisms, and most of the deep-subsurface microorganisms detected so far were refractory to cultivation.

The primary goal of this study was to explore the diversity of cultivable prokaryotic communities of the Atlantis Massif subseafloor from a unique collection of rock cores composed in various proportions of carbonate, basalt, serpentinized peridotite and gabbro (**Figure 1** and **Supplementary Figure 1**). To increase our chance of success, we used a high-pressure incubation system (**Figure 1**) to mimic *in situ* HP at the sampling sites and the various anaerobic metabolisms likely to be present were targeted based on literature surveys (Mason et al., 2010; Schrenk et al., 2013). We used next-generation sequencing (NGS) of 16S rRNA gene amplicons to explore the cultivable microbial diversity of Atlantis Massif core samples incubated at atmospheric or *in situ* HP. We report novel anaerobes isolated from rock-hosted subseafloor ecosystems and describe the phenotypic and genomic features of strain 70B-A^T, the first isolate from the Atlantis Massif subseafloor obtained from high-pressure cultures. Finally, we propose it to represent a novel species of a new bacterial genus within the newly described family *Vallitaleaceae* (order *Clostridiales*, phylum *Firmicutes*).

MATERIALS AND METHODS

Rock Sample Collection

A unique set of rock samples was recovered during IODP Expedition 357 "Atlantis Massif Serpentinization and Life," which took place from October to December 2015 onboard the *RRS James Cook* (Früh-Green et al., 2016). Nine core samples were investigated in this study and were collected using two seabed rock drills (i.e., the British Geological Survey RockDrill2

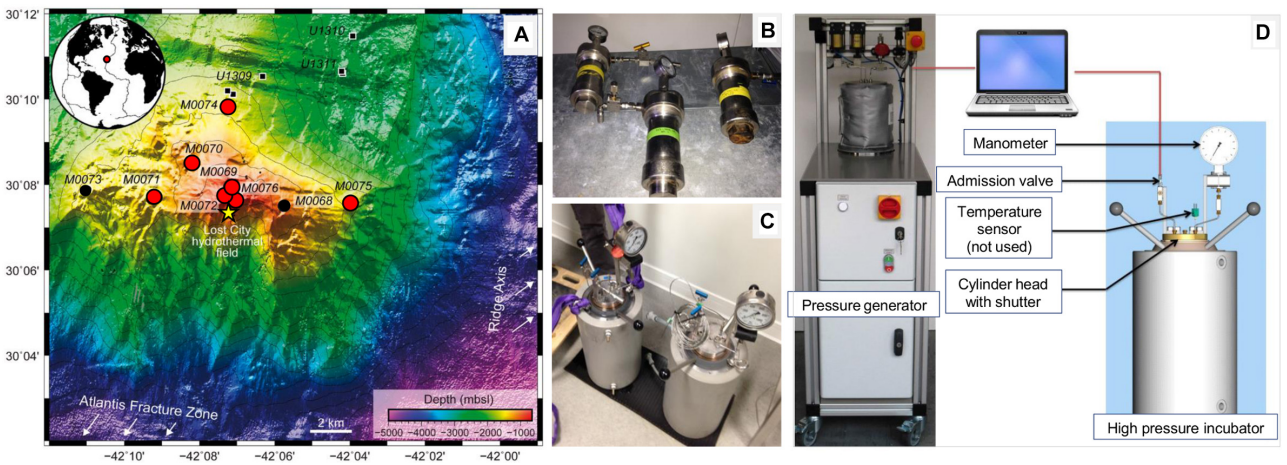

FIGURE 1 | Bathymetric map of the Atlantis Massif southern wall showing the location of the sites drilled during the IODP Expedition 357 [**A**; modified from (Rouméjon et al., 2018)] and the high-pressure devices used in this study **(B–D)**. On the map, the red circles indicate the sites considered in this study, the small black circles correspond to other holes drilled during the expedition, the small black squares show the Holes drilled during IODP Expeditions 304-305 (Site U1309) and the yellow star indicates the Lost City Hydrothermal Field. On the right, the photographs show high-pressure vessels (0.2 l in **B** or 5 l in **C**) used for storage and incubation, respectively. High-pressure vessels were connected to a piloted pressure generator **(D)** allowing linear increase for pressurization (or decrease for depressurization) of the hydrostatic pressure (0.5 MPa sec^{-1}) by the programmable computer-driven system [see details in (Tamburini et al., 2009)].

TABLE 1 | IODP expedition 357 samples used in this study (see photographs in **Supplementary Figure 1**).

Site	Hole	Core	Section	Interval (cm)		Depth (mbsf)		Lithology	Depth (mbsl)	Latitude, longitude
				Top	Bottom	Top	Bottom			
69	A	4	1	25	35	5.41	5.51	Foraminiferal carbonate sand	850	30.13240, −42.12003
69	**A**	**9**	**2**	**111**	**118.5**	**14.48**	**14.55**	**Serpentinized dunite with carbonate veins**	**850**	**30.13240,−42.12003**
70	**C**	**3**	**1**	**71**	**79**	**3.41**	**3.49**	**Carbonate-hosted basalt breccia**	**1,140.5**	**30.14240,−42.13657**
71	**C**	**5**	**CC**	**2**	**5**	**7.81**	**7.84**	**Serpentinized harzburgite**	**1,400**	**30.12860,−42.15312**
72	**B**	**7**	**1**	**106**	**119**	**10.05**	**10.18**	**Metagabbro**	**820**	**30.12990,−42.12205**
74	**A**	**1**	**1**	**50**	**60**	**0.50**	**0.60**	**Carbonate sand (highly disturbed during core recovery)**	**1,550**	**30.16442,−42.12192**
75	**B**	**3**	**1**	**54**	**74**	**4.52**	**4.72**	**Rubble: Talc schist, minor serpentinite**	**1,568**	**30.12750,−42.06617**
76	B	3	1	90	102	4.34	4.46	Metadolerite	760	30.12702, −42.11775

CC stands for core catcher, mbsf stands for meters below seafloor, mbsl stands for meters below sea level. Samples for which enrichment cultures succeeded are highlighted in bold.

(RD2) and the Meeresboden-Bohrgerät 70 (Mebo) from the Center for Marine Environmental Sciences, MARUM, University of Bremen, Germany). Drilling sites were located at varying distances away from LCHF and the ridge axis: one site drilled on the eastern part of the southern wall of the Atlantis Massif (Site M0075), three sites located in the central section <1 km north of Lost City (Sites M0069, M0072, and M0076), two sites located north toward the central dome of the massif (Sites M0070 and M0074), and one site on the western end (Site M0071) (**Table 1** and **Figure 1**). Drilled sites were located at a water depth ranging from 820 to 1 568 mbsl (**Table 1**). Sites M0070 and M0074 targeted the mafic, plutonic domain drilled during IODP Expeditions 304-305 at Site U1309 while the other sites targeted the serpentinite basement of the Atlantis Massif. Lithologies associated with each core sample are described in **Table 1** (photographs are shown in **Supplementary Figure 1**). During drilling, potential contamination was quantified using perfluorocarbon tracer and sampling was achieved under strict contamination controls onboard and offshore (Orcutt et al., 2017). Only samples with no detectable contamination were used for this study (Früh-Green et al., 2017c). Primary procedures, as well as core handling and processing used during the offshore and onshore phases of IODP Expedition 357 are detailed in (Früh-Green et al., 2017c). Details on studied sites according to their location on the Atlantis Massif are provided in (Früh-Green et al., 2017a,b,e,f).

Processing and Storage of Core Samples Used in This Study

Onboard, the processing of the core sample was done at 10°C. The exterior of the core sample was flamed to eliminate potential contaminants, then sliced and smashed into small pieces using a flamed chisel. These subsamples were crushed using a sterile stainless steel mortar and pestle, under sterile and anaerobic conditions. Approximately 5 cm^3 of the powdered rock sample were transferred into Hungate screw tubes, fully filled (~17 ml) with sterile artificial seawater (40 $g\,l^{-1}$ solution of Sea Salts, Sigma Aldrich) and stored in high pressure vessels (Top Industrie SA, France) at *in situ* HP conditions (from 8 to 17 MPa, depending on the water depths of the sites) by means of manual hydraulic pump and stored at 4°C until processing in the shore-based laboratory (**Figure 2**). Extra powder samples were transferred in 100 ml Schott bottles under a N_2 gas atmosphere, then stored at 4°C and atmospheric pressure (0.1 MPa) until processing in the onboard and shore-based laboratories (**Figure 2**). Details on HP devices are provided in (Tamburini, 2006; Tamburini et al., 2009, 2013).

Culture Media Preparation and Enrichment Culture Conditions

The composition of the culture media is detailed in the **Supplementary Table 1**. After dissolution of its components, the culture medium was boiled under a stream of O_2-free N_2 gas, cooled to room temperature, dispensed into Hungate tubes, flushed under N_2/CO_2 (80/20, v/v) and then sterilized by autoclaving. The media were completed by addition of sterile stock solutions of Na_2CO3 8% (w/v), $MgCl_26H_2O$ 50 g l^{-1}, Balch oligo elements solution, and Na_2S9H_2O 3% (w/v) injected through the tube septum (volumes are indicated in **Supplementary Table 1**).

Onboard, culture media were inoculated in duplicates in Hungate tubes at 0.1 MPa headspace of N_2/CO_2 or H_2/CO_2 (80/20, v/v) using approximately 0.5–1 cm^3 of rock as inoculum in 5 ml of anaerobic media (with the following abbreviations: F, for fermenters; MAcH2, MH2, MMet, for acetotrophic, hydrogenotrophic and methylotrophic methanogens; SAc and SH2, for acetotrophic and hydrogenotrophic sulfate reducers;

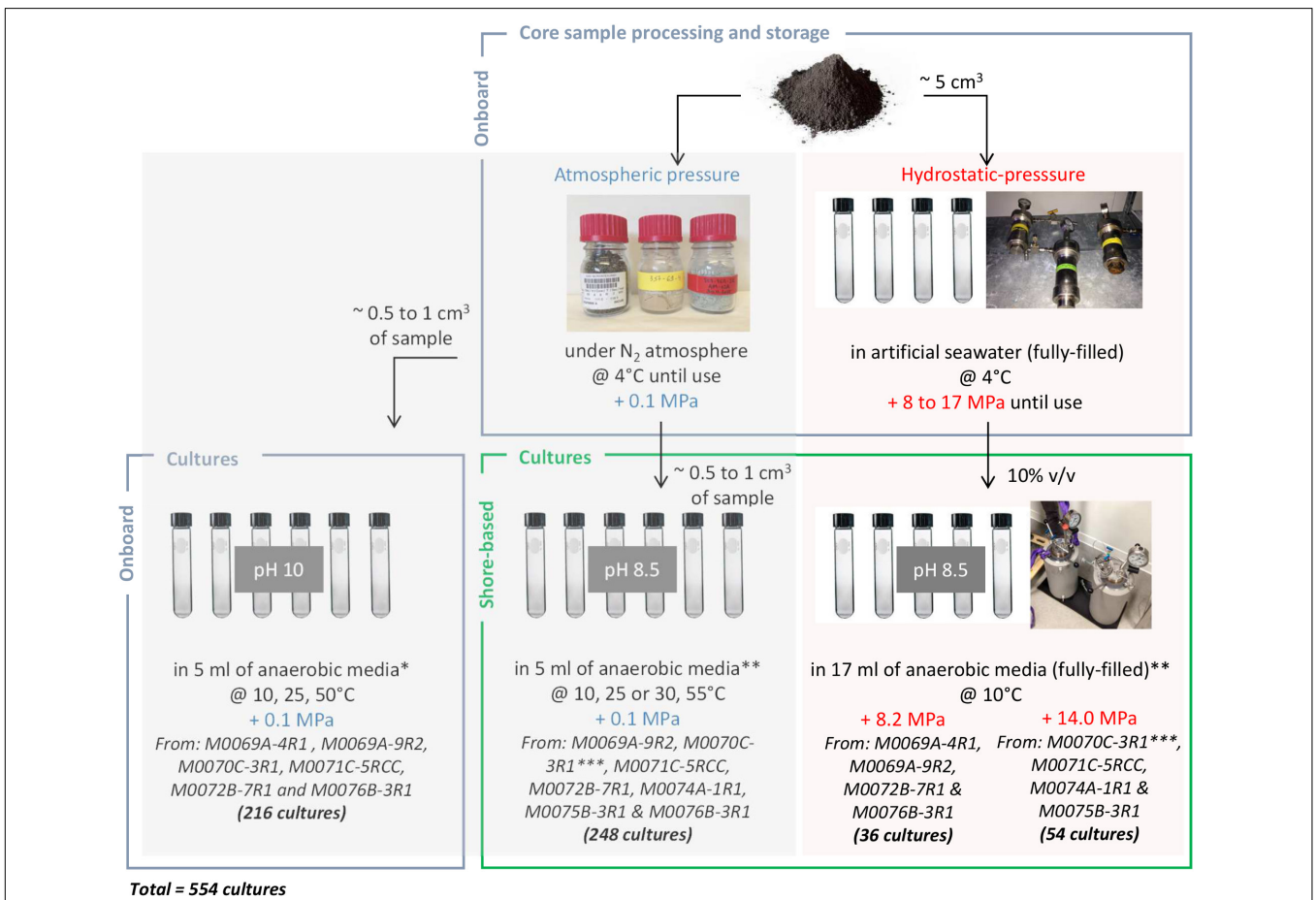

FIGURE 2 | Schematic view of the sampling processing and the cultures initiated at 0.1, 8.2 and 14.0 MPa, onboard and onshore. A total of 554 cultures was performed, in duplicate (except if too small rock quantity); controls were uninoculated tubes. *Fermentation (F); acetotrophic (MAcH2), hydrogenotrophic (MH2), and methylotrophic (MMet) methanogenesis; acetotrophic (SAc) and hydrogenotrophic (SH2) sulfate reduction. **Fermentation (F1), oligotrophy (F2), sulfate reduction from acetate or lactate (SRB1) and formate or H_2/CO_2 (SRB2), methanogenesis by acetoclasty or methylotrophy (MET1) and hydrogenotrophy (MET2), and iron reduction (FE) (**Supplementary Table 2**). ***Black basaltic and white carbonated parts dissociated.

Supplementary Table 1). Culture media pH were adjusted to 10 with 1M KOH as detailed in (Früh-Green et al., 2017c) and incubations were done at three temperatures: 10°C (the average temperature of sea bottom waters), 25 and 50°C (as we hypothesized a temperature gradient between hot hydrothermal fluid and cold subseafloor) A total of 216 tubes were inoculated with core samples M0069A-4R1, M0069A-9R2, M0070C-3R1, M0071C-5RCC, M0072B-7R1 and M0076B-3R1 (6 samples × 2 replicates × 3 temperatures × 6 media) (**Figure 2**).

In the shore-based laboratory (MIO), series of culture media (composition in **Supplementary Table 1**) were used to target the following metabolisms: fermentation (F1), oligotrophy (F2), sulfate reduction from acetate or lactate (SRB1) and formate or H_2/CO_2 (SRB2), methanogenesis by acetoclasty or methylotrophy (MET1) and hydrogenotrophy (MET2), and iron reduction (FE). The ISO 10390:2005 protocol, dedicated to measure soil pH, was used here for rock samples: powdered rocks were suspended in KCl 1M (1/5, v/v), and pH of the suspension was measured. The mean pH was 8.5 (below a pH of 10, which was the first assumption for onboard enrichment cultures) thus the pH of the shore-based culture media was accordingly adjusted to pH 8.5. Hungate tubes for incubation at 0.1 MPa contained 5 ml of medium, thus about 12 ml of gas headspace (N_2/CO_2 or H_2/CO_2, 80/20, v/v), while those used in HP incubation were filled with 17 ml of medium (no headspace) (Khelaifia et al., 2011). Cultures were run in duplicates, except for samples M0069A-4R1 and M0074A-1R1 due to the low amount of available material. 248 enrichment cultures at 0.1 MPa were incubated at 10°C, 25°C (or 30°C) and 55°C from core samples M0069A-9R2, M0070C-3R1 (black basaltic and white carbonated parts dissociated), M0071C-5RCC, M0072B-7R1, M0074A-1R1, M0075B-3R1, and M0076B-3R1 (8 samples × 2 replicates × 3 temperatures × 6 media -all except SRB2-, MET2 without replicate and only at 30°C). 36 enrichment cultures were launched at 8.2 MPa and 10°C from core samples M0069A-4R1, M0069A-9R2, M0072B-7R1 and M0076B-3R1 (the last two in duplicate) using the 6 onshore media (all except F2), while 54 enrichment cultures were launched at 14.0 MPa and 10°C from core samples M0070C-3R1 (black basaltic and white carbonated parts dissociated), M0071C-5RCC, M0074A-1R1 and M0075B-3R1 using the 6 onshore media (all except F2).

All cultures carried out under HP were incubated at 10°C (corresponding to the average temperature of sea bottom waters) (**Figure 2**). Shortly, culture tubes were placed for incubations in two HP 5 l inox incubators which were totally filled with distilled water, the septum transmitting the hydrostatic pressure inside the culture, before pressure was increased. A piloted pressure generator (see details in (Tamburini et al., 2009)) was used for accurate pressurization and depressurization (ramping rate = 3 MPa/min) (**Figure 1D**).

For each culture condition, a tube of medium not inoculated was incubated in parallel as negative control, to verify the absence of microbial contamination. The experimental procedure is summarized in **Figure 2**.

After 1 week incubation onboard and 1 month incubation (and more) in shore-lab experiments, the enrichment cultures were checked for growth by observation of cells stained with SYBR® Green I (Molecular Probes) 1X using an epifluorescence microscope Nikon ECLIPSE E600. The headspace gas, in the cultures that have one, were analyzed by gas chromatography (Shimadzu GC 8A instrument) to evaluate H_2 production or consumption and CH_4 production, as described in (Mei et al., 2014).

Strain Isolation and Analyses

Positive cultures were serially diluted at 1/10 of the volume up to 10^{-9} dilution in Hungate screw tubes containing 4.5 ml of anaerobic growth media plus agar (1.6% final) maintained liquid at 55°C in a water-bath. Inoculated tubes were then quickly cooled down while spinning using a tube spinner according to the roll-tube technique (Hungate, 1969). Colonies were picked up in an anaerobic gloves-box and used as an inoculum for the next series of dilution. This procedure was repeated three times before the strain culture was deemed pure. Morphological features of the isolates were examined using a microscope Nikon ECLIPSE E600 under phase contrast condition. Procedure for analyzing cell structures, the G+C content of genomic DNA, as well as cellular fatty acids and polar lipids composition, are given in **Supplementary Methods**.

Determination of Optimal Growth Conditions of Strain 70B-A^T

Experiments to determine growth ranges of strain 70B-A^T were performed in duplicates or in triplicates at 0.1 MPa using Hungate tubes containing 5 ml of F1 medium (for pH, temperature and salinity) or at 14.0 MPa using BM medium (i.e., mineral base of the F1 medium) supplemented with 0.2 g l^{-1} yeast extract and 20 mM glucose as sole carbon source. Potential substrates were tested in duplicates by addition into the BM medium (containing 0.5 g l^{-1} yeast extract). Details on experimental procedures are given in **Supplementary Methods**. Growth was determined by measuring optical density (OD) at 600 nm (Cary 50 UV-Vis spectrophotometer; Varian). End-products of metabolism were measured by high-performance liquid chromatography (HPLC) and gas phase chromatography after 2-weeks of incubation at 30°C (instruments details in (Mei et al., 2014)). Graphical and statistical analyzes of growth curves (OD *versus* time) of strain 70B-A^T were performed with XLSTAT 2018.6 (Microsoft Excel add-in program). After checking data normality, the parametric Student's *t*-test or non-parametric Mann-Whitney test were respectively used to estimate if the differences observed in maximum OD values (OD_{max}) or maximal growth rates between the cultures performed at 0.1 and 14.0 MPa were significant.

DNA Extraction and 16S rRNA Gene Sequencing

Fast DNA® kit for soil and FastDNA® kit were used respectively to extract DNA from enrichment cultures and isolated strain, according to the manufacturer recommendations

(MP Biomedical). DNA from enrichment cultures was used for PCR amplification targeting the V3-V4 region of the 16S rRNA gene using the primers Pro341F and Pro805R (Takahashi et al., 2014); amplicons were sequenced by Illumina MiSeq at MrDNA (TX, United States). 16S rRNA genes from isolated strains were amplified using the primers 27F and 1492R (Lane, 1991) and the PCR products were sent to GATC Biotech AG (Germany) for Sanger sequencing.

Whole Genome Sequencing of Strain 70B-A^T

For sequencing the genome of strain 70B-A^T, high molecular weight DNA was extracted from a 500 mL culture cell pellet by using a phenol-chloroform-isoamyl alcohol-based method as previously described (Marteinsson et al., 1995). Genomic sequencing was performed at the GenoToul platform (Toulouse, France) by combining long reads technology of Oxford Nanopore to ease assembling (GridION) and high coverage provided by short paired-end reads obtained with Illumina (MiSeq) technology. The methodological details on sequencing, read processing and *de novo* assembly of genome are provided in **Supplementary Methods**. The genome was annotated using the MicroScope plateform (Vallenet et al., 2017).

Bacterial Community Composition and Phylogenetic Analysis

Raw reads were first merged with PEAR v0.9.6 and trimmed when the quality scores were less than 20 for two consecutive bases. Only sequences with a length greater than 35 bp were retained for further analyses. Chimera sequences were identified and removed using vsearch (v2.3.4). The clustering to Operational Taxonomic Units (OTUs) (>97%) and their quality filtration were carried out using QIIME 1.9.1 (Caporaso et al., 2010) as described in (Frouin et al., 2018). Taxonomic assignment of the filtered OTUs was performed using the Uclust method against the SILVA database release for QIIME (v.123). Heatmap.3 package in R was used to build the heatmap (R Core Team, 2017).

Phylogenetic analyses and trees based on 16S rRNA gene sequences were conducted in MEGA7 (Kumar et al., 2016) using MUSCLE program (Edgar, 2004) for multiple alignment, as described by (Postec et al., 2015).

Data Deposition

MiSeq V3-V4 amplicons raw data were submitted to the Sequence Read Archive under SRA Study SRP148750, as part of the BioProject PRJNA448822. The GenBank/EMBL/DDBJ accession number for the 16S rRNA gene sequence (1490 bp) of strain 70B-A^T is KY969626. The genome sequence was deposited to the European Nucleotide Archive under study accession number PRJEB28585[1], and Genbank accession number LR130778. The type strain 70B-A^T was deposited in DSMZ and JCM culture collections under accession numbers DSM 105309^T = JCM 32078^T respectively.

[1]http://www.ebi.ac.uk/ena/data/view/PRJEB28585

RESULTS

Summary of Enrichment Cultures

A total of 554 anaerobic enrichment cultures were performed from IODP 357 core samples and monitored for about 1 year (**Figure 2**). Onboard, the first positive enrichment cultures were obtained after 2-week incubation from M0069A-9R2 using MAcH2 media at 25°C, 0.1 MPa and pH 10 (in the range of low temperature serpentinizing fluids pH values). No microbial growth was observed in other alkaliphilic cultures initiated onboard after 1-year regular monitoring, whatever the temperature and medium conditions tested. Back to the home lab, the first enrichment cultures at 0.1 MPa were obtained after 1-month incubation from M0070C-3R1 at 25°C in F1 and FE media, but only scarce cells were detected by epifluorescence microscopy from M0069A-9R2, M0071C-5RCC, M0072B-7R1 and M0074A-1R1 cultures after 2 months under similar conditions. Dividing cells were observed at 10°C in the same media than at 25°C but after longer incubation (≥2 months). No microbial growth was detected in any of the enrichment cultures at 55°C, neither from M0069A-4R1 (carbonate sand) or M0076B-3R1 (serpentinite) samples, in any conditions. At 14.0 MPa, active cells were observed from M0070C-3R1 sample after 1 month with all the tested media (more cells with F1 one), while scarce active cells were observed with M0075B-3R1 in F1 and SRB1 media. At 8.2 MPa, a slight growth was detected after 1-year incubation from M0072B-7R1 (using F1 and SRB1 media).

Phyla Diversity in Enrichment Cultures

Microbial diversity was analyzed by MiSeq 16S rRNA gene sequencing for a selection of 51 enrichment cultures, listed and described in **Supplementary Table 2**. A total of 462,162 sequences clustered in 415 OTUs was obtained.

Firmicutes and *Proteobacteria* were largely dominant in most conditions tested (**Figure 3**). *Actinobacteria*, *Bacteroidetes*, *Cyanobacteria* and *Deinococcus-Thermus* were also abundant in M0069A-9R2 cultures (MAcH2 and FE media, 10 and 25°C, 0.1 MPa) while *Acidobacteria*, *Chloroflexi*, *Saccharibacteria* and *Verrucomicrobia* were abundant in a M0071C-5RCC culture (FE medium, 25°C, 0.1 MPa). Enrichment cultures from M0072B-7R1, M0074A-1R1 and M0075B-3R1 contained only *Firmicutes* and *Proteobacteria*, except for sample M0072B-7R1 in FE medium at 25°C and 0.1 MPa culture containing also *Acidobacteria*, *Actinobacteria* and *Cyanobacteria*. In M0070C-3R1 cultures at 14.0 MPa, *Firmicutes* accounted for 74% to 99% of the microbial community (with the second most abundant phylum being *Proteobacteria*), while a more diverse community exhibiting *Bacteroidetes*, *Actinobacteria*, *Tennericutes* and *Cyanobacteria* members was detected at 0.1 MPa.

Archaea represented less than 0.2% of the total reads and were not detected in all cultures. *Methanosarcinales* affiliated to ANaerobic MEthane oxidizing *Archaea* (ANME-3) were found in M0069A-9R2, M0070C-3R1 and M0074A-1R1 [and already recognized in Lost City Hydrothermal chimneys (Brazelton et al., 2006)], together with rare OTUs assigned to the

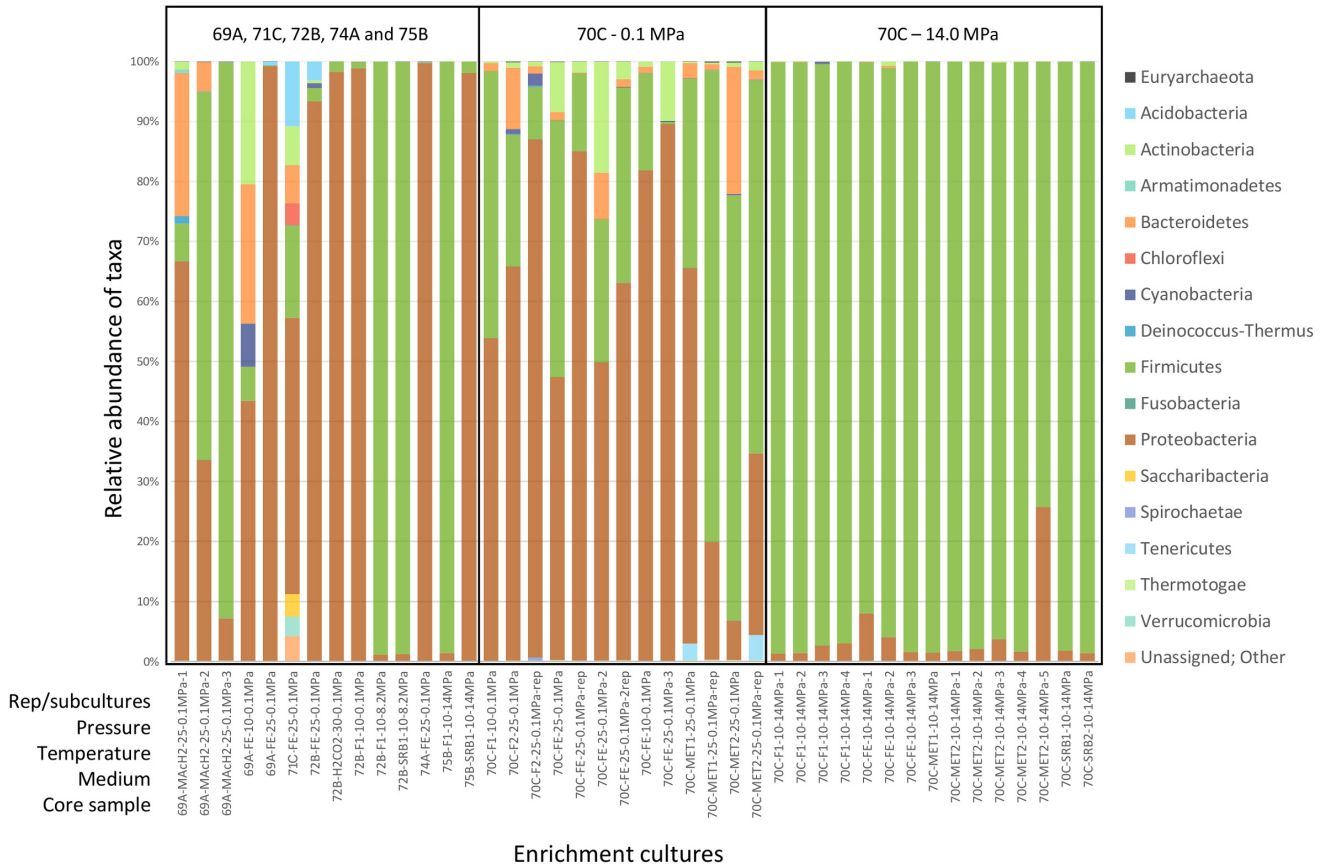

FIGURE 3 | Phylum-level microbial diversity in enrichment cultures from Atlantis Massif core samples. Analysis based on 16S rRNA gene sequences (V3–V4 region). 69A, 70C, 71C, 72B, 74A and 75B respectively stand for M0069A-9R2, M0070C-3R1, M0071C-5RCC, M0072B-7R1, M0074A-1R1 and M0075B-3R1 core samples. The sample names used in this study and their description in SRA (study SRP148750) are shown in **Supplementary Table 2**. Rep stands for replicate. Pressure is expressed in MPa, temperature in °C. F, SRB, FE, MET & MAcH2 correspond to culture media targeting fermenters, sulfate reducers, iron reducers and methanogens, respectively (**Supplementary Table 1**).

hyperthermophilic sulfur-reducing genus *Thermococcus* and the thermoacidophilic genus *Thermoplasma* (**Table 2**).

Dominant Cultivated Microorganisms: Abundant OTUs

Only the most abundant OTUs (>10% of total reads), representing the most likely cultivated members, are presented in **Figure 4**. Enrichment cultures from M0069A-9R2 were dominated at 25°C and 0.1 MPa by *Acinetobacter* (*Gammaproteobacteria*), *Bacillus* (*Bacilli*), *Sphingomonas* (*Alphaproteobacteria*) and *Sphingobacteriia (Bacteroidetes)*. Interestingly, an effect of the HP was observed for M0072B-7R1 cultures since *Tissierella* (*Clostridia*) largely dominated at 8.2 MPa while *Thalassospira* (*Alphaproteobacteria*; using H_2/CO_2), *Shewanella* and *Acinetobacter* (*Gammaproteobacteria*) were dominant at 0.1 MPa. Besides, *Marinilactibacillus* and *Halomonas*, also found in other deep ecosystems and including some piezophilic representatives (Kaye et al., 2004; Toffin et al., 2005), were cultivated at 14.0 MPa from M0075B-3R1 (**Figure 4**).

Most of the successful enrichment cultures were obtained from carbonate-hosted basalt breccia samples of M0070C-3R1 core (1150 mbsl, north of the Atlantis Massif). Marked differences in the microbial diversity of the cultures were observed depending on the incubation pressure. At 0.1 MPa, the dominant genera in M0070C-3R1 cultures were *Proteiniclasticum* (*Clostridia*), *Vibrio*, *Shewanella*, *Acinetobacter*, *Citrobacter* and *Pseudomonas* (belonging to *Gammaproteobacteria*) (**Figure 4**). *Sunxiuqinia* (*Cytophagia*) and *Tessaracoccus* (*Actinobacteria*; not shown, <10%), less abundant in the cultures, have been previously reported in deep biosphere environments, as well as *Shewanella* (Toffin et al., 2004; Finster et al., 2009; Picard and Daniel, 2013; Takai et al., 2013). In contrast, cultures from M0070C-3R1 incubated at 14.0 MPa were dominated mainly by 2 OTUs of an unknown genus, related to *Vallitalea* genus (*Clostridia*), representing up to 98% of the reads in a culture (**Figure 4**). *Proteiniclasticum, Alkalibacterium* (*Firmicutes*) with *Shewanella* were also found as dominant OTUs in M0070C-3R1 cultures at 14.0 MPa (also found at 0.1 MPa).

Most of the identified microorganisms seem to develop on heterotrophy in our enrichment cultures. Additionally, potential iron reducers (e.g., *Shewanella*) were identified as dominant, while potential H_2-consumers (*Hydrogenophaga, Thiobacillus*)

TABLE 2 | Relevant potential metabolisms/phenotypes of operational taxonomic units (OTUs) retrieved from anaerobic enrichment cultures from Atlantis Massif core samples (based on 16S rRNA gene analysis).

Potential metabolisms/phenotypes	OTUs affiliation (Genera)	Hole occurrences	Total reads abundance (%)
Hydrocarbon degraders	***Acinetobacter***, ***Halomonas***, *Marinobacter*, *Alcanivorax*, *Alicyclobacillus*, ***Sphingomonas***	69A, 70C, 71C, 72B, 74A, 75B	7.02
Iron reducers	***Shewanella***	69A, 70C, 72B	5.37
Thermophiles (hydrothermal origin)	*Caminicella*, *Desulfotomaculum*, *Desulfovibrio*, *Gaeilla*, *Mesoaciditoga*, *Thermicanus*, *Thermoanaerobacterium*, *Thermococcus**, *Thermoleophilia*, *Thermoplasma**, *Thermus*, *Thiomicrospira*, *Truepera*, *Vallitalea*	69A, 70C, 71C, 72B, 74A, 75B	1.44
Alkaliphiles	*Acetoanaerobium*, *Alkalibacterium*, *Alkaliphilus*, *Desulfonatronum*, *Thioalkalispira*	69A, 70C, 71C, 72B, 74A, 75B	0.55
Sulfate reducers	*Desulfacinum*, *Desulfobacter*, *Desulfovibrio*, *Desulfonauticus*, *Desulfonatronum*, *Desulfotomaculum*	69A, 70C, 71C, 72B, 74A	0.23
S-compounds oxidation	*Arcobacter*, *Sulfurimonas*, *Sulfurovum*, *Acidithiobacillus*, *Sulfitobacter*, *Thioalkalispira*, *Thiobacillus*, *Thiomicrospira*	69A, 70C, 71C, 72B, 74A, 75B	0.22
H_2 consumers	*Hydrogenophaga*, *Thiobacillus*, *Desulfotomaculum*	69A, 70C, 71C, 72B, 74A	0.06
Methyl or CH_4 consumers	Unknown genus *Methylococcales* (Marine Methylotrophic Group 1), *Methanosarcinales* (ANME-3)*	69A, 70C, 71C, 72B, 74A, 75B	0.03
Iron oxidizers	*Mariprofundus*, *Marinobacter*, *Thiobacillus*	69A, 70C, 71C, 72B, 74A, 75B	0.01

Dominant OTUs (>10% total reads) are indicated in bold and archaeal taxa using an asterisk. 69A, 70C, 71C, 72B, 74A, and 75B respectively stand for M0069A-9R2, M0070C-3R1, M0071C-5RCC, M0072B-7R1, M0074A-1R1, and M0075B-3R1 core samples.

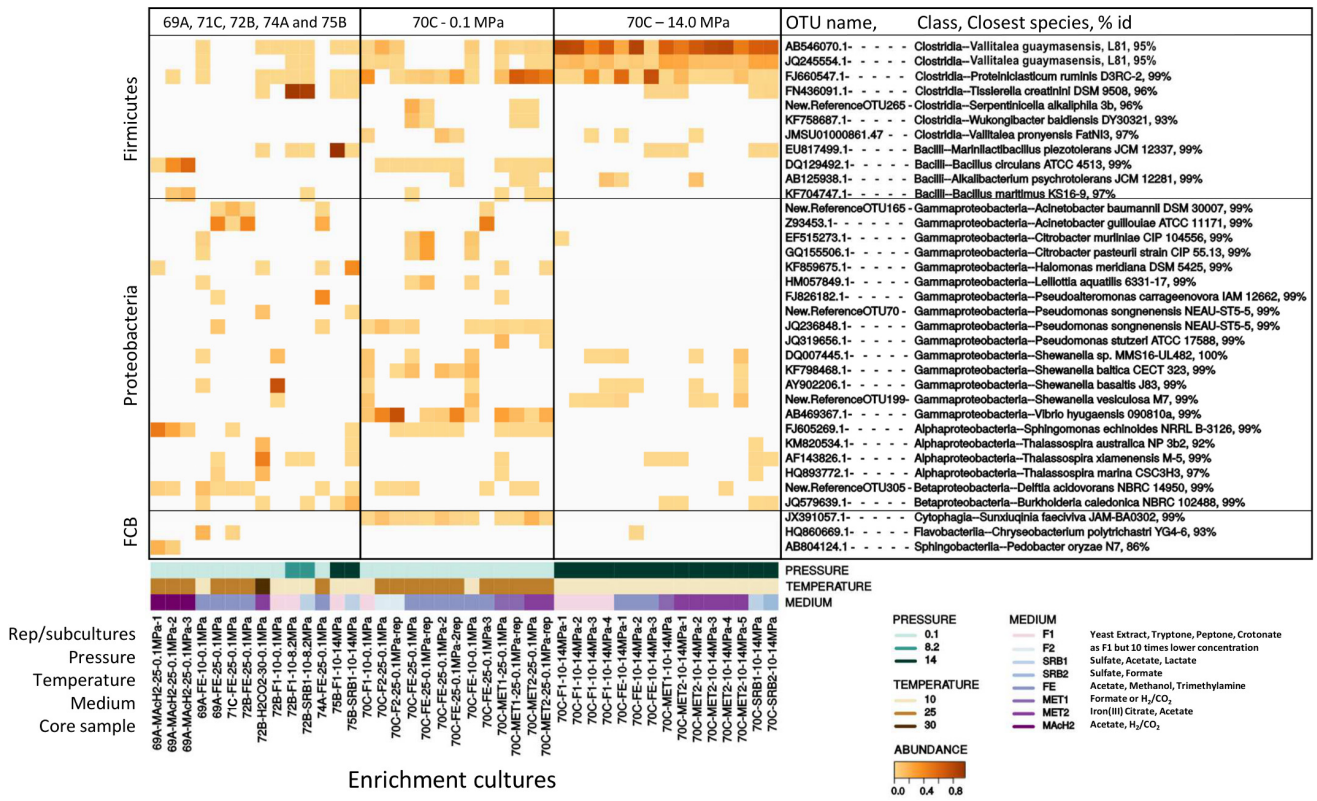

FIGURE 4 | Heatmap showing the distribution of dominant OTUs (>10% total reads) in anaerobic enrichment cultures from Atlantis Massif subseafloor rocks. OTU name, its class affiliation, name of its closest species and 16S rRNA gene percentage identity (% id) with this closest homolog are indicated on the right. 69A, 70C, 71C, 72B, 74A and 75B respectively stand for M0069A-9R2, M0070C-3R1, M0071C-5RCC, M0072B-7R1, M0074A-1R1 and M0075B-3R1 core samples. Rep stands for replicate. Pressure is expressed in MPa, temperature in °C. F, SRB, FE, MET & MAcH2 correspond to culture media targeting fermenters, sulfate reducers, iron reducers and methanogens, respectively (**Supplementary Table 1**). FCB stands for *Fibrobacteres/Bacteroidetes/Chlorobi* group.

and/or sulfate-reducers (*Desulfotomaculum*) were only observed as rare OTUs (**Table 2**).

Strain Isolation

In this study, a total of fourteen strains were isolated and affiliated to *Gammaproteobacteria*, *Actinobacteria*, *Bacillales* and *Clostridiales* (**Supplementary Figure 2**).

Three very similar isolates (100% 16S rRNA gene identity) affiliated to *Tissierella* genus (97% 16S rRNA gene identity with *T. creatinophila, Clostridiales*) were obtained from M0072B-7R1 cultures at 8.2 MPa using media SRB1 and F1 after 1-year incubation. At 25°C and 0.1 MPa, *Sphingobacteriia* initially enriched from M0069A-9R2 (in $MAcH_2$ medium) and accounting for 48% of the microbial community, was outcompeted by *Bacillus* after only two subcultures. A strain affiliated to *Bacillus circulans* (99% 16S rRNA gene identity) was finally isolated with LB-Tris medium from M0069A-9R2 (**Supplementary Figure 2B**).

The rest of the strains (10/14) were isolated from M0070C-3R1 subcultures. Among them, the strain 70-CrotoS2-10-2 isolated at 25°C and 0.1 MPa using F1 medium was closely affiliated to *Tessaracoccus oleiagri* and *T. profundii* (99% 16S rRNA gene identity). A positive enrichment culture at 25°C and 0.1 MPa with FE medium was also used as an inoculum for serial dilution on roll-tubes from which dark brown colonies, likely indicating iron reduction, formed after 4 days up to the dilution 10^{-7}. Four of these colonies were assigned to *Citrobacter freundii* (99% 16S rRNA gene identity) in the *Enterobacteriaceae* family (class *Gammaproteobacteria*). One of them, strain 70O-Fer25-B, is a motile coccobacillus shown in **Supplementary Figure 2A**.

Within *Firmicutes*, two strains closely affiliated to *Proteiniclasticum ruminis* (99% identity; type strain from yak rumen) were isolated at 10°C and 0.1 MPa in F1 medium. Finally, six isolates very closely related (sharing >99% 16S rRNA gene identity), were obtained from M0070C-3R1 cultures incubated at 14.0 MPa and 10°C in MET1, MET2 and F1 media. First colonies were obtained in roll-tubes after about 1 month incubation at 10°C and further purified by two additional series end-point dilution in roll-tubes before deemed pure. They were related to *Vallitalea* genus at <93% 16S rRNA gene identity and therefore represente new cultivated members of *Clostridiales* without close described species. One of them, called strain 70B-A^T, was chosen for complete characterization.

Characterization of Strain 70B-A^T

The 16S rRNA gene sequence of strain 70B-A^T was most closely related to members of *Vallitalea* and *Natranaerovirga* genera, with *V. guaymasensis* (Lakhal et al., 2013) and *N. pectinivora* (Sorokin et al., 2012) sharing respectively 92.6 and 90.2% 16S rRNA gene sequence identity with strain 70B-A^T (**Figure 5A**). Strain 70B-A^T genomic DNA contained 37.7 mol % of G+C.

The major cellular fatty acids of strain 70B-A^T were C16:1 w7c (35.6%), C16:0 (22.1%) and C16:1 w7c DMA (14.3%) (**Supplementary Table 3**). The main polar lipids consisted of nine phospholipids, one glycolipid, one phosphatidylglycerol and one phosphoglycolipid (**Table 3**).

Strain 70B-A^T cells rod shaped (0.4–0.7 μm in diameter and 2.0–12.0 μm in length) during the exponential growth phase (**Supplementary Figure 3A**) where it is motile through the action of observed polar and lateral monotrich flagella (data not shown). No spore formation was observed. Under unfavorable conditions (e.g., pH 11), morphology changed and showed inflated and deformed cells (**Supplementary Figure 3B**). The cell wall structure observed by transmission electron microscopy revealed a Gram-positive structure with the presence of a multilayered cell wall without an outer membrane as confirmed by Gram-staining (**Supplementary Figure 3C**).

Strain 70B-A^T grows under strict anaerobic conditions from 0 to 8% (w/v) NaCl (optimum at 2.5% (w/v) of NaCl; **Supplementary Figure 4B**), 10 to 35°C (optimum at 25°C;

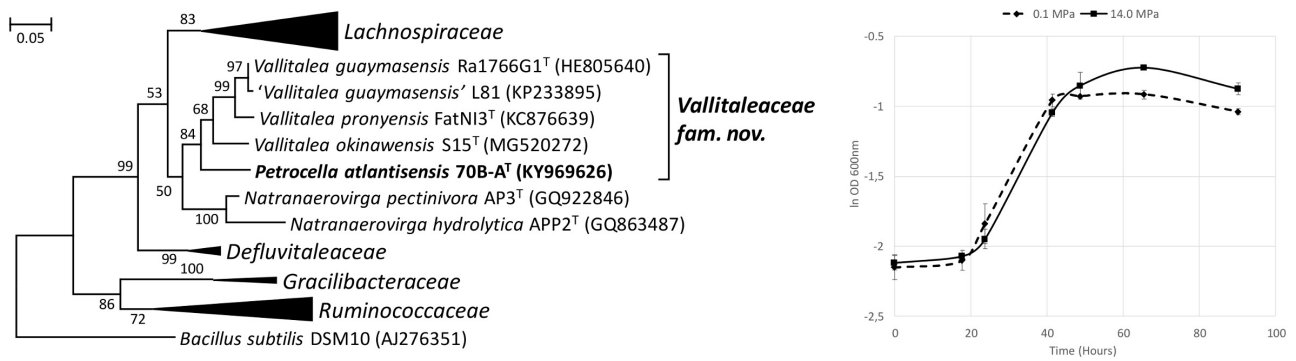

FIGURE 5 | Phylogenetic and physiological characteristics of strain 70B-A^T. **(A)** Maximum Likelihood phylogenetic tree based on 1203 aligned base pairs of 16S rRNA gene sequences showing the position of strain 70B-A^T in the *Clostridiales* order. The Kimura 2-parameter was used, and the analysis involved 34 sequences. *Bacillus subtilis* (AJ276351) was used as an outgroup. Bootstrap values higher than 50% (based on 1 000 replicates) are shown at branch nodes. Accession numbers of type species are indicated in brackets. Bar, 0.05 substitutions per nucleotide. **(B)** Growth curves of strain 70B-A^T at 0.1 and 14.0 MPa. Apart of hydrostatic pressure, all other culture conditions were identical (in Hungate tube with no headspace). The BM medium was supplemented with 0.2 g l^{-1} yeast extract and 20 mM glucose. The ln OD_{600nm} average from triplicates is shown here. Error bars are the associated standard deviation.

TABLE 3 | Differential phenotypic and genotypic characteristics between strain 70B-A^T and type strains of recognized *Vallitalea* species: *V. guaymasensis*^{T} (Kumar et al., 2016), *Natranaerovirga pectinivora*^{T} (Schrenk et al., 2010).

Characteristics	70B-A^T	*V. guaymasensis* Ra1766G1^T	*N. pectinivora* AP3^T
Origin	Atlantis Massif subseafloor	Sediment of Guaymas Basin	Soda soils
Temperature growth range (optimum) (°C)	10–35 (25)	20–40 (30–35)	≤43
pH growth range (optimum)	5.6–9.2 (7.8)	6.0–8.0 (6.5–7.5)	8.0–10.5 (9.5–9.7)
Salinity growth range (optimum) (%)	0–8 (2.5)	0.5–7.5 (2–3)	1.2–14.6 (2.0)
Gram	+	−	+
Motility	+	−	−
Spore	−	−	+
Main carbon sources	Carbohydrates	Carbohydrates	Galacturonic acid and pectin
Arabinose	−	+	−
Cellobiose	+	+	−
Fructose	+	−	−
Galactose	+	+	−
Glucose	+	+	−
Glycerol	+	−	−
Lactose	+	−	−
Maltose	+	+	−
Mannitol	+	+	−
Mannose	+	+	−
Pyruvate	+	+	−
Raffinose	+	+	−
Rhamnose	+	−	−
Sucrose	+	+	−
Xylose	−	+	−
Yeast extract	+	+	−
Polar lipids	PL, GL, PG, PGL	PG, DPG, PL, GL	PG, DPG, PL, GL, APL
Dominant fatty acids	C16:1 w7c, C16:0, C16:1 w7c DMA	Anteiso-C15:0, iso-C15:0, anteiso-C15:0 DMA, iso-C15:0 DMA	16:0, 16:1w7c, 18:1w7c
Main fermentation products	Acetate, H_2, CO_2, and formate	Acetate, H_2, and CO_2	Acetate and formate
Genomic features			
Size (base pair)	3,518,882	6,419,149	3,061,098
GC content	37.3%	31.2%	31.3%
Contig nb	1	7	29
Protein-coding genes (CDS)*	3,423	5,600	2,859
CDS with predicted function	2,904	4,043	2,251
rRNA genes (16S, 23S, 5S)	15	17	12
tRNA	56	56	50

Genomic features of V. guaymasensis *originated from strain L81 (no data available for the type strain) (Rouméjon et al., 2018). PL, phospholipids; GL, glycolipids; PG, phosphatidylglycerol; PGL, phosphoglycolipid; APL, aminophospholipids; DMA, dimethylacetals; CDS, coding DNA sequence. *Using MicroScope annotation platform and IMG-ER annotation platform for strain 70B-A^T and* V. guaymasensis *L81, respectively. Genomes accession numbers:* P. atlantisensis *70B-A^T: PRJEB28585;* V. guaymasensis *L81: NZ_QMDO00000000.1; and N. pectinovora AP3: IMG submission ID 191455.*

Supplementary Figure 4A), and pH 5.6 to 9.2 (optimum at pH 7.4-8.0). HP did not significantly improve its maximum specific growth rate: μ_{max} was in average 0.048 h^{-1} at 0.1 MPa and 0.045 h^{-1} at 14.0 MPa (**Figure 5B**). However, the maximum OD was significantly higher at 14.0 MPa (0.476 ± 0.016) than at 0.1 MPa (0.422 ± 0.011; Student *t*-test, $p = 0.003$).

Strain 70B-A^T was able to use cellobiose, fructose, galactose, glucose, glycerol, lactose, maltose, mannitol, mannose, pyruvate, raffinose, rhamnose, ribose, sucrose, trehalose, tryptone, yeast extract (YE), but not acetate, arabinose, butyrate, casaminoacids, citrate, crotonate, ethanol, formate, lactate, methanol, pectine, peptone, propionate, succinate, TMA, xylose. No growth was observed with only H_2/CO_2 or H_2/CO_2 and acetate as sole carbon sources. Strain 70B-A^T is strictly chemoorganotrophic as confirmed by HPLC analysis of substrate utilization. Growth on carbohydrates resulted in acetate as the main metabolic product, along with formate, H_2 and CO_2 (**Table 3**). Strain 70B-A^T was not able to use thiosulfate, sulfate, sulfite, nitrite, nitrate, Fe(III) citrate and elemental sulfur as electron acceptors. Under optimal conditions, the maximal growth rate (on BM medium plus glucose) was 0.048 h^{-1}.

Strain 70B-A^T has a lower growth temperature range than the type species of *Vallitalea* and *Natranaerovirga* (**Table 3**). While its pH and salinity ranges as well as its use of carbon source (mainly

carbohydrates) are similar to that of *V. guaymasensis*, strain 70B-A^T differs by its capacity to utilize fructose, glycerol, lactose and rhamnose (**Table 3**). Fatty acids profile resembles more that of *N. pectinovora* with abundant C16 and the absence of C15. Unlike the two other strains, 70B-A^T displays cell motility and a singular profile of polar lipids and a higher DNA G + C content (**Table 3**).

Genome Analysis of Strain 70B-A^T

The complete genome (one single contig) of strain 70B-A^T consists of a circular chromosome of 3 518 882 bp, with 37.3% GC content (**Table 3**). The chromosome contains 3 536 predicted genes, of which 3 423 are protein-coding. The size of the strain 70B-A^T genome is considerably smaller than that of *V. guaymasensis* L81, 6.42 Mb, and *V. okinawensis,* 5.86 Mb, but in the range of those of the *Natranaerovirga* genomes, 3.06 Mb for *N. pectinivora* and 2.98 Mb for *N. hydrolytica* (Schouw et al., 2018; Sun et al., 2018). Of the 3 423 protein-coding genes, 2 904 were given a predicted function (**Figure 6**). Carbohydrates and amino acids transport and metabolisms were among the most represented functional categories with respectively 6.3 and 6.1% of the function-predicted genes. In agreement with the culture-based conclusions on the metabolism, the genome of strain 70B-A^T encodes several glycosyl hydrolases (β-galactosidase, β-glucosidase, and α-amylase), proteases and peptidases. It contains numerous ABC-transporters of multi-sugars (pentose, hexose, and di-saccharides) and several sugars (mannose, fructose, lactose) phosphotransferase systems (PTS). A complete glycolysis (Embden-Meyerhof) and gluconeogenesis pathways were identified, as well as uncomplete Entner-Doudoroff and pentose phosphate pathways as observed in some Gram positive bacteria and archaea (Conway, 1992). The genes for the complete biosynthesis pathways of all the amino acids are present, except for the L-lysine and L-methionine which are incomplete and thus maybe not operational. Nevertheless, the genome encodes two oligo-peptides and, at least 12 amino-acids ABC transporters with all kind of specificity for polar amino-acids, branched-amino acids, lysine or arginine, and proline-betaine, suggesting these served as substrates for growth. The degradation pathways identified for L-alanine, L-cysteine, L-tryptophan, L-serine and L-threonine lead to pyruvate while those of L-aspartate, L-asparagine, L-Glutamate, and L-Glutamine generate oxaloacetate, fumarate or acetyl-CoA which could aliment an uncomplete citric acid (TCA) cycle (the succinyl-CoA synthase gene is lacking). Pyruvate could also be directly fermented in lactate (by a lactate dehydrogenase), acetate or ethanol (by an alcohol dehydrogenase) or via the common mixed acid fermentation pathway. A putative pyruvate: ferredoxin oxidoreductase catalyzes the formation of acetyl-CoA from the pyruvate, coupled to the reduction of ferredoxin (Fd). Thus, most of the reducing power of the diverse fermentations is transferred to NADH and reduced Fd electron carriers, and we postulate, as recently proposed for *V. guaymasensis* (Schouw et al., 2018), this fuels a hydrogenase to generate H_2. Indeed, genes for a tetrameric [Fe-Fe] hydrogenase are found as an

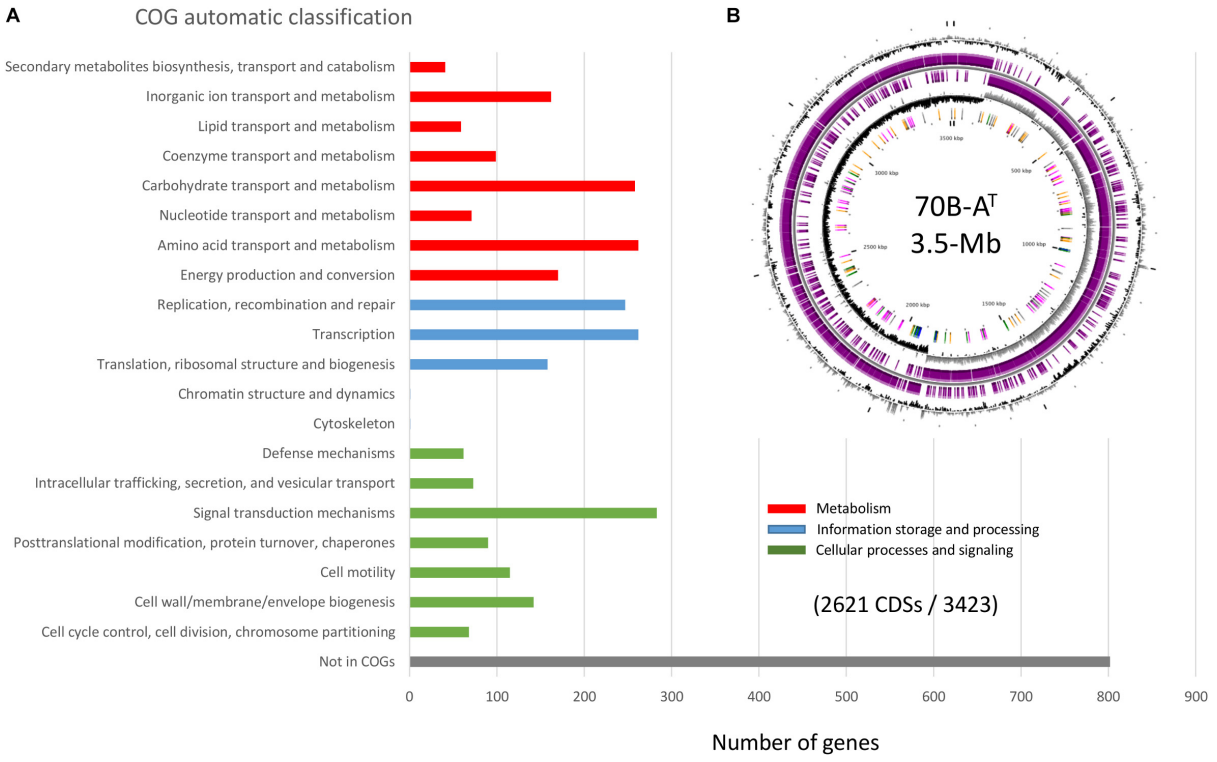

FIGURE 6 | Strain 70B-A^T genome analysis. **(A)** Functional categorization of 2621 Coding DNA Sequences (CDS) (out of 3423) based on the Clusters of Orthologous Groups (COGs) database (Galperin et al., 2015), **(B)** Circular genome view.

operon (PATL70BA_1019 to PATL70BA_1022) homologous to *hndA, hndB, hndC, hndD*, encoding a cytosolic NADP-reducing hydrogenase in *Desulfovibrio fructosivorans* (Dermoun et al., 2002). In this sulfate-reducing bacterium, this enzyme could either catalyzes H_2 oxidation during growth on H_2 as a sole energy source or produces H_2 when growing by fermentation of fructose in the absence of sulfate as a terminal electron acceptor. We assume that this tetrameric hydrogenase utilizes the mechanism of flavin-based electron bifurcation (FBEB) (Schuchmann et al., 2018): the exergonic electron flow from reduced Fd to H^+ drives endergonic electron flow from NADH to H^+. The archetype of such so-called bifurcative/confurcative hydrogenase was first described in *Thermotoga maritima* (Schut and Adams, 2009). Two additional hydrogenases-encoding genes are present, PATL70BA_1241 is homologous to a 4Fe-4S dicluster domain-containing, poorly characterized, periplasmic hydrogenase found in many anaerobic *Firmicutes*, and PATL70BA_2847, another homolog of the *hndA* subunit gene. Besides, the genes encoding a [FeFe] hydrogenase maturase (HydEFG), involved in the synthesis and incorporation of the di-iron center, were identified. The genome of strain 70B-A^T also contains an operon (*rnfC, rnfD, rnfG, rsxE, rsxA, rnfB*) encoding an Rnf complex coupling the translocation of proton/sodium ion across the membrane with the reversible oxidation of reduced ferredoxin with NAD^+ (Westphal et al., 2018). The Rnf complex could, therefore, serve to generate a proton/sodium gradient while equilibrating the pool of reductants (NADH) produced during sugars or amino-acids fermentation (Buckel and Thauer, 2018; Westphal et al., 2018).

The genome encodes both a V-type ATPase and an F-type of ATPase. The V-type ATPases use ATP to translocate protons across membranes, while F-type ATPases generate ATP *via* proton translocation (Perzov et al., 2001). The genome also contains a cluster of 9 genes (PATL70BA_2417 to 2426) encoding a nitrogenase (*nifH, nifD, nifK, nifE, nifB, nifV*) conferring this bacterium the ability to fix N_2, which may represent a selective advantage to survive in its challenging habitat. Several clusters of metal or metalloids (Fe, Zn, Cr, Ni, Ar, Hg) transporters genes were also found which could be involved in either import (iron siderophores) or export (detoxication) processes. Finally, the genome contains numerous transposases and integrases genes, of which many belong to putative prophages and two large conjugative integrated plasmids, also called integrons (Mazel, 2006), known as essential agents of bacterial genome evolution.

DISCUSSION

Today, our knowledge of subseafloor microbial ecosystems is mainly based on data from culture-independent methods such as 16S rRNA barcoding or metagenomics. Although these approaches have been proved incomparable to explore and describe the extent of microbial diversity and model the functioning of these ecosystems, they present only a partial view of the real picture since most of the microorganisms inhabiting these environments are uncultivated (Jungbluth et al., 2016). Subseafloor microorganisms have been mostly recalcitrant to cultivation in laboratory, making their physiological characterization complicated. Most of these microorganisms were isolated from sedimentary rock cores and included mostly aerobes or facultative anaerobes but a few strict anaerobes even though, passed the first tens centimeters depth below the seafloor, these environments are essentially anoxic (Toffin and Alain, 2014). Previous attempts at cultivating anaerobes from various subseafloor sediments often led to the isolation of the same few 'generalist' bacteria belonging to genera counting numerous species and strains encompassing a broad spectrum of environmental conditions (Ciobanu et al., 2014; Parkes et al., 2014).

In this study, our main goal was to cultivate anaerobic microorganisms inhabiting the rocky subseafloor associated with active serpentinization characterized by circulation of high pH fluids enriched in H_2, CH_4 and other organic molecules abiotically produced. To the best of our knowledge, the only cultivated anaerobes were isolated by our team from a shallow submarine serpentinite-hosted hydrothermal system, analogous to the LCHF, located in the Prony bay (New Caledonia) (Ben Aissa et al., 2014, 2015; Mei et al., 2014, 2016; Bes et al., 2015). In the present study, putative moderately halo-alkaliphilic bacteria (related to *Alkalibacterium*, *Halomonas*, *Tissierella* and the proposed genus *Petrocella*) were enriched and in some case isolated in cultures carried out at pH 8.5, while the only isolate obtained from the cultures at pH 10 (in the common range of pH values observed in low temperature serpentinizing systems) was a strain of *Bacillus circulans*, a facultative anaerobe, spore-forming, frequently detected in soils, but no obligate alkaliphile as targeted by the pH conditions. These results may be explained by the relatively low pH values (7.82–7.87) measured in the hole bottom waters, with maximum values of pH 7.98 recorded in Hole M0070C (Früh-Green et al., 2018). Anaerobic H_2-consumers, sulfate-reducers or methanogens (main metabolisms detected at LCHF) were not abundant in cultures despite the use of various culture conditions targeting these metabolisms and the elevated H_2 and CH_4 levels measured in bottom waters (5-73 and 2-5 nM, respectively, at Site M0070 where gas bubbles were observed issuing from the hole, see Figure 13 in Früh-Green et al. (2018)).

In such rock-hosted subseafloor ecosystems, cell abundance is well known to be exceptionally low making contamination a crucial issue, and cultivation of indigenous microorganism very challenging. Cell abundance in the IODP 357 core samples was very low ranging from tens to thousands of cells cm^{-3} with a maximum in Hole M0069A sediments (up to 1.6×10^4 cells cm^{-3}), before decreasing rapidly to $<10^2$ cells cm^{-3} in the underlying basement rocks (Früh-Green et al., 2018). In this study, growth was observed after a relatively short incubation time (1 month) in M0069A-9R2 and M0070C-3R1 enrichment cultures at 0.1 MPa and 25°C which may be due to contamination as suggested by the affiliation (at 99% identity) of the dominant OTU to genus or species corresponding to ubiquitous bacteria (*Citrobacter freundii, Proteiniclasticum ruminis, Bacillus circulans*; **Figure 4** and **Supplementary Figures 2A,B**) found in a wide range of habitats not specific of the deep biosphere or serpentinizing systems. In contrast with cultures at 0.1 MPa, utilization of HP induced a drastic change in the structure of

the bacterial communities for all combination of samples and cultures conditions (medium and incubation temperature), even at modest HP of 8.2 MPa, when compared to their counterpart incubated at atmospheric pressure (0.1 MPa gas headspace) as shown in **Figure 3**. Such phenomena has been since confirmed in our lab (Garel et al., 2019). Thus, one may assume that even moderately elevated HP inhibits growth of surface waters microorganisms and other contaminants that in these conditions are outcompeted by true deep sea/rock inhabitants. HP allowed the cultivation of novel microorganisms such as a potential new *Tissierella* species obtained at 8.2 MPa from M0072B-7R1 core (metagabbro) and a new *Clostridiales* lineage obtained at 14.0 MPa with M0070C-3R1 core sample (carbonate-cemented basaltic breccia) (**Figure 4** and **Supplementary Figures 2A,B**). Moreover, the isolate 70B-A^T, representing this new lineage, exhibits a strict anaerobic growth at 14.0 MPa making it very unlikely to originate from seawater or drilling equipment, but instead it may come from anoxic subseafloor. Strain 70B-A^T, as well as its closest neighbors belonging to the *Vallitalea* genus, were adapted to live in the deep-sea and subseafloor environments, both impacted by various kinds of hydrothermal activity in different geographical and geodynamic area (Arctic Mid-Ocean Ridge, Northeast and Southwest Pacific Ocean, East China Sea and now Mid-Atlantic Ridge). Here, strain 70B-A^T displayed maximum cell density (OD_{max}) under HP conditions (at 14 MPa). Knowing that the maximum population density (OD_{max}) can strongly influence the definition of the optimal growth conditions (Martini et al., 2013), strain 70B-A^T can therefore be considered as a piezophile even if further studies are needed to characterize its lifestyle under HP.

Mason et al. (2010) gave the first insight into the microbial community inhabiting the Atlantis Massif subseafloor using molecular approaches. They identified bacteria usually related to hydrocarbon-rich environment and recognized hydrocarbon degraders (Mason et al., 2010). Here, potential hydrocarbon degraders (*Halomonas*, *Sphingomonas*) were also detected as dominant in our anaerobic enrichments. The hydrocarbons detected in rocks of the Atlantis Massif may have a marine origin but might also originate from abiotic organic synthesis associated with serpentinization (Delacour et al., 2008; Hickok et al., 2018; Ménez et al., 2018), which may potentially sustain the endolithic microbial community. Interestingly, the closest neighbors of strain 70B-A^T belonging to *Vallitalea* genus originated from (i) the serpentinizing hydrothermal system of Prony (PHF; New Caledonia) (Ben Aissa et al., 2014), (ii) the Guaymas basin, a deep hydrothermally influenced ecosystem rich in hydrocarbons (Lakhal et al., 2013) and (iii) Loki's Castle, a hydrocarbon-rich hydrothermal field (Schouw et al., 2016). However, the role of these microorganisms in hydrocarbon degradation (Schouw et al., 2016) has not yet been established (Schouw et al., 2018). Culture experiments showed that strain 70B-A^T, like strains *V. guaymasensis* Ra1766G1^T and L81, and *V. pronyensis* strain FatNI3^T, does not use alkanes for growth but, instead, can degrade various carbohydrates and proteinaceous compounds, suggesting this is a metabolic feature common to members of the novel *Vallitaleaceae* family. Genome analysis of strain 70B-A^T confirmed the utilization of sugars which are fermented mostly in acetate, CO_2 and H_2 *via* the glycolysis and suggests that strain 70B-A^T is able to import oligo-peptides and amino acids and to convert them to acetate *via* oxidation to pyruvate and acetyl-CoA. The presence of a putative electron bifurcative/confurcative hydrogenase and an ion-motive Rnf complex, enabling ferredoxin-based pathways, seems to be crucial for energy conservation in members of the proposed family *Vallitaleaceae*. Interestingly, the closest homologs of this novel hydrogenase, and Rnf complex were detected in the same metagenome-assembled genomes (MAG) of dominant uncultivated *Firmicutes* from deep terrestrial subsurface sediments (Hernsdorf et al., 2017).

In conclusion, this study shows that hydrostatic pressure helps to enrich novel anaerobes from subseafloor rocks. The new isolate *Petrocella atlantisensis* 70B-A^T is considered to represent a novel species of a novel genus within a novel proposed family *Vallitaleaceae*. It is a halotolerant, psychrotolerant, mesophilic and piezophilic chemoheterotroph able to use carbohydrates, proteinaceous compounds and potentially amino acids. Strain 70B-A^T represents the first cultivated and characterized representative of the Atlantis Massif and will constitute a model strain to further study microbial adaptation to the deep subseafloor in a context of serpentinizing ultramafic rocks.

Description of *Vallitaleaceae* fam. nov.

Cells were rod shaped, obligately anaerobic, mesophilic, neutrophilic and marine. Capable of fermentation (no electron acceptor identified), using cellobiose, galactose, glucose, maltose, mannose, raffinose, sucrose and yeast extract, but not acetate (contrarily to both *Natranaerovirga* species). Originating from hydrothermal fields and/or deep oceanic subsurface habitats rich in hydrocarbon or related to serpentinization process. The family contains the type genus *Vallitalea* and the genus *Petrocella*.

Description of *Petrocella* gen. nov.

Petrocella (Pe.tro.cel'la N. L. n. *petra* a rock, stone; L. fem. n. *cella* a cell; N. L. fem. n. *Petrocella* a rod isolated from a rock). Gram-positive, motile, non-sporulating, marine and mesophilic rods. Fermentative and obligate anaerobe, able to use a wide range of sugars. It belongs to the order *Clostridiales* (phylum *Firmicutes*). The DNA G+C content of the type strain of the type species is 37.7 mol%. The type species is *Petrocella atlantisensis*.

Description of *Petrocella atlantisensis* sp. nov.

Petrocella atlantisensis (a.tlan.tis.en'sis. N. L. fem. adj. *atlantisensis* originated from the Atlantis Massif). It displays the following features in addition to those listed for the genus description. Cells are approximately 2–12 μm long and 0.4–0.7 μm wide, occurring singly or in pairs. Cells are motile and possess polar or lateral monotrich flagella. No spore was observed. Growth occurs at 10–35°C (optimum 25°C), at pH 5.6–9.2 (optimum pH 7.4–8.0) and with 0–8% (w/v) NaCl (optimum 2.5%). Yeast extract is required for growth. Cellobiose, fructose, galactose, glucose, glycerol, lactose, maltose, mannitol, mannose, pyruvate,

raffinose, rhamnose, ribose, sucrose, trehalose, tryptone and yeast extract are used as electron donors, but not acetate, arabinose, butyrate, casamino acids, citrate, crotonate, ethanol, formate, H_2/CO_2, H_2/CO_2 + acetate, lactate, methanol, pectine, peptone, propionate, succinate, TMA, xylose. None of the following electron acceptors was used: elemental sulfur, sulfate, thiosulfate, sulfite, nitrate and nitrite. The major fatty acids are C16:1 w7c, C16:0 and C16:1 w7c DMA. The type strain, 70B-A^T, (= DSM 105309^T = JCM 32078^T) was isolated from rocks drilled in the Atlantis Massif (Mid-Atlantic Ridge, 30° N).

DATA AVAILABILITY

The datasets generated for this study can be found in SRA, and ENA or Genbank, SRP148750 (MiSeq V3-V4 amplicons raw data), and PRJEB28585 or LR130778 (whole genome sequence of strain 70B-A^T).

AUTHOR CONTRIBUTIONS

AP wrote the manuscript in collaboration with MQ. MQ, GE, and AP designed the experiments. MQ collected the samples. MQ, AP, EZ, MG, and CT carried out the high-pressure experiments. EF performed the microbial diversity analyses. CV performed the genome sequencing. All authors contributed to the discussion and the writing of the manuscript.

FUNDING

This project was financially supported by the deepOASES ANR project (ANR-14-CE01-0008-06 and ANR-14-CE01-0008-01). Samples have been obtained from the International Ocean Discovery Program (IODP). Sequencing work in GeT Toulouse was funded as part of "Investissement d'avenir" program managed by Agence Nationale pour la Recherche (contract ANR-10-INBS-09). The project leading to this publication has received funding from European FEDER Fund under project 1166-39417.

ACKNOWLEDGMENTS

This research used samples and data provided by the International Ocean Discovery Program (IODP). We thank the co-chief scientists Prof. Gretchen Früh-Green and Dr. Beth Orcutt of IODP 357 "Atlantis Massif Serpentinization and Life" expedition that took place in 2015 (26 October–11 December 2015), and the staff of the drillship RRS James Cook carrying the BGS Rockdrill2 and the MARUM-MeBo seafloor drills. We also thank the other members of the shipboard scientific team (especially Y. Morono, M. O. Schrenk, and K. I. Twing) who enabled the collection and photography of the samples used in this study. We also thank M. Bartoli (MIO) for the electron microscopy photographs of strain 70B-A^T and H. Gaussier for correcting English in the text. This work was performed in collaboration with the GeT core facility, Toulouse, France (http://get.genotoul.fr) and was supported by France Génomique National Infrastructure; C. Roques and A. Castinel are especially thanked.

SUPPLEMENTARY MATERIAL

The Supplementary Material for this article can be found online at: https://www.frontiersin.org/articles/10.3389/fmicb.2019.01497/full#supplementary-material

REFERENCES

Bartlett, D. H., Lauro, F. M., and Eloe, E. A. (2007). "Microbial adaptation to high pressure," in *Physiology and Biochemistry of Extremophiles*, eds C. Gerday and N. Glandsdorf (Washington, DC: American Society for Microbiology Press), 333–348. doi: 10.1128/9781555815813.ch25

Ben Aissa, F., Postec, A., Erauso, G., Payri, C., Pelletier, B., Hamdi, M., et al. (2014). *Vallitalea pronyensis* sp nov., isolated from a marine alkaline hydrothermal chimney. *Int. J. Syst. Evol. Microbiol.* 64, 1160–1165. doi: 10.1099/ijs.0.055756-0

Ben Aissa, F., Postec, A., Erauso, G., Payri, C., Pelletier, B., Hamdi, M., et al. (2015). Characterization of *Alkaliphilus hydrothermalis* sp. nov., a novel alkaliphilic anaerobic bacterium, isolated from a carbonaceous chimney of the prony hydrothermal field, New Caledonia. *Extremophiles* 19, 183–188. doi: 10.1007/s00792-014-0697-y

Bes, M., Merrouch, M., Joseph, M., Quemeneur, M., Payri, C., Pelletier, B., et al. (2015). *Acetoanaerobium pronyense* sp. nov., an anaerobic alkaliphilic bacterium isolated from a carbonate chimney of the prony hydrothermal field (New Caledonia). *Int. J. Syst. Evol. Microbiol.* 65, 2574–2580. doi: 10.1099/ijs.0.000307

Brazelton, W. J., Schrenk, M. O., Kelley, D. S., and Baross, J. A. (2006). Methane- and sulfur-metabolizing microbial communities dominate the lost city hydrothermal field ecosystem. *Appl. Environ. Microbiol.* 72, 6257–6270. doi: 10.1128/AEM.00574-06

Buckel, W., and Thauer, R. K. (2018). Flavin-based electron bifurcation, ferredoxin, flavodoxin, and anaerobic respiration with protons (Ech) or NAD+ (Rnf) as electron acceptors: a historical review. *Front. Microbiol.* 9:401. doi: 10.3389/fmicb.2018.00401

Caporaso, J. G., Kuczynski, J., Stombaugh, J., Bittinger, K., Bushman, F. D., Costello, E. K., et al. (2010). QIIME allows analysis of high-throughput community sequencing data. *Nat. Methods* 7, 335–336. doi: 10.1038/nmeth.f.303

Ciobanu, M.-C., Burgaud, G., Dufresne, A., Breuker, A., Redou, V., Ben Maamar, S., et al. (2014). Microorganisms persist at record depths in the subseafloor of the canterbury Basin. *ISME J.* 8, 1370–1380. doi: 10.1038/ismej.2013.250

Conway, T. (1992). The entner-doudoroff pathway: history, physiology and molecular biology. *FEMS Microbiol. Rev.* 9, 1–27. doi: 10.1111/j.1574-6968.1992.tb05822.x

Delacour, A., Früh-Green, G. L., Bernasconi, S. M., Schaeffer, P., and Kelley, D. S. (2008). Carbon geochemistry of serpentinites in the lost city hydrothermal system (30 degrees N, MAR). *Geochim. Cosmochim. Acta* 72, 3681–3702. doi: 10.1016/j.gca.2008.04.039

Dermoun, Z., De Luca, G., Asso, M., Bertrand, P., Guerlesquin, F., and Guigliarelli, B. (2002). The NADP-reducing hydrogenase from *Desulfovibrio fructosovorans*: functional interaction between the C-terminal region of HndA and the N-terminal region of HndD subunits. *Biochim. Biophys. Acta* 1556, 217–225. doi: 10.1016/S0005-2728(02)00364-X

D'Hondt, S., Jørgensen, B. B., Miller, D. J., Batzke, A., Blake, R., Cragg, B. A., et al. (2004). Distributions of microbial activities in deep subseafloor sediments. *Science* 306, 2216–2221. doi: 10.1126/science.1101155

Edgar, R. C. (2004). MUSCLE: multiple sequence alignment with high accuracy and high throughput. *Nucliec Acids Res.* 32, 1792–1797. doi: 10.1093/nar/gkh340

Finster, K. W., Cockell, C. S., Voytek, M. A., Gronstal, A. L., and Kjeldsen, K. U. (2009). Description of *Tessaracoccus profundi* sp.nov., a deep-subsurface actinobacterium isolated from a chesapeake impact crater drill core (940 m depth). *Antonie van Leeuwenhoek* 96, 515–526. doi: 10.1007/s10482-009-9367-y

Frouin, E., Bes, M., Ollivier, B., Quéméneur, M., Postec, A., Debroas, D., et al. (2018). Diversity of rare and abundant prokaryotic phylotypes in the prony hydrothermal field and comparison with other serpentinite-hosted ecosystems. *Front. Microbiol.* 9:102. doi: 10.3389/fmicb.2018.00102

Früh-Green, G. L., Orcutt, B. N., Green, S., Cotterill, C., and the Expedition 357 Scientists (2016). "Expedition 357 preliminary report: atlantis massif serpentinization and Life," in *Proceedings of the International Ocean Discovery Program*, College Station, TX.

Früh-Green, G. L., Orcutt, B. N., Green, S. L., Cotterill, C., and the Expedition 357 Scientists (2017a). "Central sites," in *Proceedings of the International Ocean Discovery Program*, College Station, TX.

Früh-Green, G. L., Orcutt, B. N., Green, S. L., Cotterill, C., and the Expedition 357 Scientists (2017b). "Eastern sites," in *Proceedings of the International Ocean Discovery Program*, College Station, TX.

Früh-Green, G. L., Orcutt, B. N., Green, S. L., Cotterill, C., and the Expedition 357 Scientists (2017c). "Expedition 357 methods," in *Proceedings of the International Ocean Discovery Program*, College Station, TX.

Früh-Green, G. L., Orcutt, B. N., Green, S. L., Cotterill, C., and the Expedition 357 Scientists (2017d). "Expedition 357 summary," in *Proceedings of the International Ocean Discovery Program*, College Station, TX.

Früh-Green, G. L., Orcutt, B. N., Green, S. L., Cotterill, C., and the Expedition 357 Scientists (2017e). "Northern sites," in *Proceedings of the International Ocean Discovery Program*, College Station, TX.

Früh-Green, G. L., Orcutt, B. N., Green, S. L., Cotterill, C., and the Expedition 357 Scientists (2017f). "Western sites," in *Proceedings of the International Ocean Discovery Program*, College Station, TX.

Früh-Green, G. L., Orcutt, B. N., Rouméjon, S., Lilley, M. D., Morono, Y., Green, S., et al. (2018). Magmatism, serpentinization and life: insights through drilling the Atlantis massif (IODP expedition 357). *Lithos* 323, 137–155. doi: 10.1016/j.lithos.2018.09.012

Galperin, M. Y., Makarova, K. S., Wolf, Y. I., and Koonin, E. V. (2015). Expanded microbial genome coverage and improved protein family annotation in the COG database. *Nucleic Acids Res.* 43, D261–D269. doi: 10.1093/nar/gku1223

Garel, M., Bonin, P., Martini, S., Guasco, S., Roumagnac, M., Nagib, B., et al. (2019). Pressure-retaining sampler and high-pressure systems to study deep-sea microbes under *in situ* conditions. *Front. Microbiol.* 10:453. doi: 10.3389/fmicb.2019.00453

Hernsdorf, A. W., Amano, Y., Miyakawa, K., Ise, K., Suzuki, Y., Anantharaman, K., et al. (2017). Potential for microbial H_2 and metal transformations associated with novel bacteria and archaea in deep terrestrial subsurface sediments. *ISME J.* 11, 1915–1929. doi: 10.1038/ismej.2017.39

Hickok, K. A., Nguyen, T. B., and Lang, S. Q. (2018). Assessment of apolar lipids in subseafloor rocks and potential contaminants from the Atlantis Massif (IODP expedition 357). *Org. Geochem.* 122, 68–77. doi: 10.1016/j.orggeochem.2018.05.003

Hirayama, H., Abe, M., Miyazaki, J., Sakai, S., Nagano, Y., and Takai, K. (2015). "Data report: cultivation of microorganisms from basaltic rock and sediment cores from the north pond on the western flank of the mid-atlantic ridge, IODP expedition 336," in *Proceedings of the IODP (Integrated Ocean Drilling Program Management International, Inc.)*, eds K. J. Edwards, W. Bach, A. Klaus, and the Expedition 336 Scientists Tokyo. doi: 10.2204/iodp.proc.336.204.2015

Hungate, R. E. (1969). "A roll tube method for the cultivation of strict anaerobes," in *Methods in Microbiology*, eds J. R. Norris and D. W. Ribbons (London: Academic Press), 117–132. doi: 10.1016/s0580-9517(08)70503-8

Jørgensen, S. L., and Zhao, R. (2016). Microbial inventory of deeply buried oceanic crust from a young ridge flank. *Front. Microbiol.* 7:820. doi: 10.3389/fmicb.2016.00820

Jungbluth, S. P., Bowers, R. M., Lin, H.-T., Cowen, J. P., and Rappé, M. S. (2016). Novel microbial assemblages inhabiting crustal fluids within mid-ocean ridge flank subsurface basalt. *ISME J.* 10, 2033–2047. doi: 10.1038/ismej.2015.248

Kallmeyer, J., Pockalny, R., Adhikari, R. R., Smith, D. C., and D'Hondt, S. (2012). Global distribution of microbial abundance and biomass in subseafloor sediment. *Proc. Natl. Acad. Sci. U.S.A.* 109, 16213–16216. doi: 10.1073/pnas.1203849109

Kaye, J. Z., Márquez, M. C., Ventosa, A., and Baross, J. A. (2004). *Halomonas neptunia* sp. nov., *Halomonas sulfidaeris* sp. nov., *Halomonas axialensis* sp. nov. and *Halomonas hydrothermalis* sp. nov.: halophilic bacteria isolated from deep-sea hydrothermal-vent environments. *Int. J. Syst. Evol. Microbiol.* 54, 499–511. doi: 10.1099/ijs.0.02799-0

Kelley, D. S., Karson, J. A., Früh-Green, G. L., Yoerger, D. R., Shank, T. M., Butterfield, D. A., et al. (2005). A serpentinite-hosted ecosystem: the lost city hydrothermal field. *Science* 307, 1428–1434. doi: 10.1126/science.1102556

Khelaifia, S., Fardeau, M.-L., Pradel, N., Aussignargues, C., Garel, M., Tamburini, C., et al. (2011). *Desulfovibrio piezophilus* sp. nov., a piezophilic, sulfate-reducing bacterium isolated from wood falls in the mediterranean Sea. *Int. J. Syst. Evol. Microbiol.* 61, 2706–2711. doi: 10.1099/ijs.0.028670-0

Kumar, S., Stecher, G., and Tamura, K. (2016). MEGA7: molecular evolutionary genetics analysis version 7.0 for bigger datasets. *Mol. Biol. Evol.* 33, 1870–1874. doi: 10.1093/molbev/msw054

Lakhal, R., Pradel, N., Postec, A., Hamdi, M., Ollivier, B., Godfroy, A., et al. (2013). *Vallitalea guaymasensis* gen. nov., sp. nov., isolated from marine sediment. *Int. J. Syst. Evol. Microbiol.* 63(Pt 8), 3019–3023. doi: 10.1099/ijs.0.045708-0

Lane, D. J. (1991). "16S/23S rRNA sequencing," in *Nucleic Acid Techniques in Bacterial Systematics*, eds E. Stackebrandt and M. Goodfellow (New York, NY: John Wiley and Sons), 115–175.

Lang, S. Q., Früh-Green, G. L., Bernasconi, S. M., Brazelton, W. J., Schrenk, M. O., and McGonigle, J. M. (2018). Deeply-sourced formate fuels sulfate reducers but not methanogens at lost city hydrothermal field. *Sci. Rep.* 8:755. doi: 10.1038/s41598-017-19002-5

Lauro, F., and Bartlett, D. (2007). Prokaryotic lifestyles in deep sea habitats. *Extremophiles* 12, 15–25. doi: 10.1007/s00792-006-0059-5

Levin, L. A., Baco, A. R., Bowden, D. A., Colaco, A., Cordes, E. E., Cunha, M. R., et al. (2016). Hydrothermal vents and methane seeps: rethinking the sphere of influence. *Front. Mar. Sci.* 3:72. doi: 10.3389/fmars.2016.00072

Marteinsson, V., Watrin, L., Prieur, D., Caprais, J.-C., Raguenes, G., and Erauso, G. (1995). Sulfur-metabolizing hyperthermophilic anaerobic archaea isolated from hydrothermal vents in the southwestern pacific ocean. *Int. J. Syst. Bacteriol.* 45, 623–632. doi: 10.1099/00207713-45-4-623

Martini, S., Al Ali, B., Garel, M., Nerini, D., Grossi, V., Pacton, M., et al. (2013). Effects of hydrostatic pressure on growth and luminescence of a moderately-piezophilic luminous bacteria *Photobacterium phosphoreum* ANT-2200. *PLoS One* 8:e66580. doi: 10.1371/journal.pone.0066580

Martin, W., Baross, J., Kelley, D., and Russell, M. J. (2008). Hydrothermal vents and the origin of life. *Nat. Rev. Microbiol.* 6, 805–814. doi: 10.1038/nrmicro1991

Mason, O. U., Nakagawa, T., Rosner, M., Van Nostrand, J. D., Zhou, J., Maruyama, A., et al. (2010). First investigation of the microbiology of the deepest layer of ocean crust. *PLoS One* 5:e15399. doi: 10.1371/journal.pone.0015399

Mazel, D. (2006). Integrons: agents of bacterial evolution. *Nat. Rev. Microbiol.* 4:608. doi: 10.1038/nrmicro1462

Mei, N., Postec, A., Erauso, G., Joseph, M., Pelletier, B., Payri, C., et al. (2016). *Serpentinicella alkaliphila* gen. nov., sp. nov., a novel alkaliphilic anaerobic bacterium isolated from the serpentinite-hosted prony hydrothermal field, New Caledonia. *Int. J. Syst. Evol. Microbiol.* 66, 4464–4470. doi: 10.1099/ijsem.0.001375

Mei, N., Zergane, N., Postec, A., Erauso, G., Oilier, A., Payri, C., et al. (2014). Fermentative hydrogen production by a new alkaliphilic *Clostridium* sp (strain PROH2) isolated from a shallow submarine hydrothermal chimney in prony bay, New Caledonia. *Int. J. Hydrogen Energy* 39, 19465–19473. doi: 10.1016/j.ijhydene.2014.09.111

Ménez, B., Pisapia, C., Andreani, M., Jamme, F., Vanbellingen, Q. P., Brunelle, A., et al. (2018). Abiotic synthesis of amino acids in the recesses of the oceanic lithosphere. *Nature* 564, 59–63. doi: 10.1038/s41586-018-0684-z

Orcutt, B. N., Bergenthal, M., Freudenthal, T., Smith, D., Lilley, M. D., Schnieders, L., et al. (2017). Contamination tracer testing with seabed drills: IODP expedition 357. *Sci. Dril.* 23, 39–46. doi: 10.5194/sd-23-39-2017

Orcutt, B. N., Sylvan, J. B., Knab, N. J., and Edwards, K. J. (2011). Microbial ecology of the dark ocean above, at, and below the seafloor. *Microbiol. Mol. Biol. Rev.* 75, 361–422. doi: 10.1128/MMBR.00039-10

Parkes, R. J., Cragg, B., Roussel, E., Webster, G., Weightman, A., and Sass, H. (2014). A review of prokaryotic populations and processes in sub-seafloor sediments, including biosphere:geosphere interactions. *Mar. Geol.* 352, 409–425. doi: 10.1016/j.margeo.2014.02.009

Parkes, R. J., Sellek, G., Webster, G., Martin, D., Anders, E., Weightman, A. J., et al. (2009). Culturable prokaryotic diversity of deep, gas hydrate sediments: first use of a continuous high-pressure, anaerobic, enrichment and isolation system for subseafloor sediments (DeepIsoBUG). *Environ. Microbiol.* 11, 3140–3153. doi: 10.1111/j.1462-2920.2009.02018.x

Perzov, N., Padler-Karavani, V., Nelson, H., and Nelson, N. (2001). Features of V-ATPases that distinguish them from F-ATPases. *FEBS Lett.* 504, 223–228. doi: 10.1016/S0014-5793(01)02709-0

Picard, A., and Daniel, I. (2013). Pressure as an environmental parameter for microbial life — a review. *Biophys. Chem.* 183, 30–41. doi: 10.1016/j.bpc.2013.06.019

Postec, A., Quemeneur, M., Bes, M., Mei, N., Benaissa, F., Payri, C., et al. (2015). Microbial diversity in a submarine carbonate edifice from the serpentinizing hydrothermal system of the Prony Bay (New Caledonia) over a 6-year period. *Front. Microbiol.* 6:857. doi: 10.3389/fmicb.2015.00857

R Core Team (2017). *A Language and Environment for Statistical Computing*. Available at: https://www.R-project.org/ (accessed July, 2018).

Rouméjon, S., Früh-Green, G. L., Orcutt, B. N., and Zhao, R. (2018). Alteration heterogeneities in peridotites exhumed on the southern wall of the atlantis massif (IODP expedition 357). *J. Petrol.* 59, 1329–1358. doi: 10.1093/petrology/egy065

Santelli, C. M., Banerjee, N., Bach, W., and Edwards, K. J. (2010). Tapping the subsurface ocean crust biosphere: low biomass and drilling-related contamination calls for improved quality controls. *Geomicrobiol. J.* 27, 158–169. doi: 10.1080/01490450903456780

Schouw, A., Leiknes Eide, T., Stokke, R., Pedersen, R. B., Steen, I. H., and Bødtker, G. (2016). *Abyssivirga alkaniphila* gen. nov., sp. nov., an alkane-degrading, anaerobic bacterium from a deep-sea hydrothermal vent system, and emended descriptions of *Natranaerovirga pectinivora* and *Natranaerovirga hydrolytica*. *Int. J. Syst. Evol. Microbiol.* 66, 1724–1734. doi: 10.1099/ijsem.0.000934

Schouw, A., Vulcano, F., Roalkvam, I., Hocking, W., Reeves, E., Stokke, R., et al. (2018). Genome analysis of *Vallitalea guaymasensis* strain L81 isolated from a deep-sea hydrothermal vent system. *Microorganisms* 6:63. doi: 10.3390/microorganisms6030063

Schrenk, M. O., Brazelton, W. J., and Lang, S. Q. (2013). "Serpentinization, carbon, and deep life," in *Reviews Mineral Geochem*, eds R. M. Hazen, A. P. Jones, and J. A. Baross (Chantilly, VA: Mineralogical Society of America), 575–606. doi: 10.1515/9781501508318-020

Schrenk, M. O., Huber, J. A., and Edwards, K. J. (2010). Microbial provinces in the subseafloor. *Annu. Rev. Mar. Sci.* 2, 279–304. doi: 10.1146/annurev-marine-120308-081000

Schuchmann, K., Chowdhury, N. P., and Müller, V. (2018). Complex multimeric [FeFe] hydrogenases: biochemistry, physiology and new opportunities for the hydrogen economy. *Front. Microbiol.* 9:2911. doi: 10.3389/fmicb.2018.02911

Schut, G. J., and Adams, M. W. W. (2009). The iron-hydrogenase of *Thermotoga maritima* utilizes ferredoxin and NADH synergistically: a new perspective on anaerobic hydrogen production. *J. Bact.* 191, 4451–4457. doi: 10.1128/JB.01582-08

Sorokin, D., Tourova, T., Panteleeva, A., Kaparullina, E., and Muyzer, G. (2012). Anaerobic utilization of pectinous substrates at extremely haloalkaline conditions by *Natranaerovirga pectinivora* gen. nov., sp. nov., and *Natranaerovirga hydrolytica* sp. nov., isolated from hypersaline soda lakes. *Extremophiles* 16, 307–315. doi: 10.1007/s00792-012-0431-6

Sun, Y.-T., Zhou, N., Wang, B.-J., Liu, X.-D., Jiang, C.-Y., Ge, X., et al. (2018). *Vallitalea okinawensis* sp. nov., isolated from okinawa trough sediment and emended description of the genus Vallitalea. *Int. J. Syst. Evol. Microbiol.* 69, 404–410. doi: 10.1099/ijsem.0.003158

Takahashi, S., Tomita, J., Nishioka, K., Hisada, T., and Nishijima, M. (2014). Development of a prokaryotic universal primer for simultaneous analysis of Bacteria and Archaea using next-generation sequencing. *PLoS One* 9:e105592. doi: 10.1371/journal.pone.0105592

Takai, K. (2011). "Limits of life and the biosphere: lessons from the detection of microorganisms in the deep sea and deep subsurface of the Earth," in *Origins and Evolution of Life: An Astrobiological Perspective*, eds M. Gargaud, P. López-Garcìa, and H. Martin (Cambridge: Cambridge Univeristy Press), 469–486. doi: 10.1017/cbo9780511933875.030

Takai, K., Abe, M., Miyazaki, M., Koide, O., Nunoura, T., Imachi, H., et al. (2013). *Sunxiuqinia faeciviva* sp. nov., a facultatively anaerobic organoheterotroph of the *Bacteroidetes* isolated from deep subseafloor sediment. *Int. J. Syst. Evol. Microbiol.* 63, 1602–1609. doi: 10.1099/ijs.0.044065-0

Tamburini, C. (2006). "Life under pressure. Deep-sea microbial ecology," in *Life As We Know It*, ed. J. Seckbach (Dordrecht: Springer), 650.

Tamburini, C., Boutrif, M., Garel, M., Colwell, R. R., and Deming, J. W. (2013). Prokaryotic responses to hydrostatic pressure in the ocean – a review. *Environ. Microbiol.* 15, 1262–1274. doi: 10.1111/1462-2920.12084

Tamburini, C., Goutx, M., Guigue, C., Garel, M., Lefèvre, D., Charrière, B., et al. (2009). Effects of hydrostatic pressure on microbial alteration of sinking fecal pellets. *Deep Sea Res. Part 2 Top. Stud. Oceanogr.* 56, 1533–1546. doi: 10.1016/j.dsr2.2008.12.035

Toffin, L., and Alain, K. (2014). "Technological state of the art and challenges. Cultivation of marine subseafloor microorganisms: state-of-the-art solutions and major issues," in *Microbial Life of the Deep Biosphere*, eds J. Kallmeyer and D. Wagner (Berlin: Walter De Gruyter), 83–89.

Toffin, L., Bidault, A., Pignet, P., Tindall, B. J., Slobodkin, A., Kato, C., et al. (2004). *Shewanella profunda* sp. nov., isolated from deep marine sediment of the nankai trough. *Int. J. Syst. Evol. Microbiol.* 54, 1943–1949. doi: 10.1099/ijs.0.03007-0

Toffin, L., Zink, K., Kato, C., Pignet, P., Bidault, A., Bienvenu, N., et al. (2005). *Marinilactibacillus piezotolerans* sp. nov., a novel marine lactic acid bacterium isolated from deep sub-seafloor sediment of the nankai trough. *Int. J. Syst. Evol. Microbiol.* 55, 345–351. doi: 10.1099/ijs.0.63236-0

Vallenet, D., Calteau, A., Cruveiller, S., Gachet, M., Lajus, A., Josso, A., et al. (2017). MicroScope in 2017: an expanding and evolving integrated resource for community expertise of microbial genomes. *Nucleic Acids Res.* 45, D517–D528. doi: 10.1093/nar/gkw1101

Westphal, L., Wiechmann, A., Baker, J., Minton, N. P., and Müller, V. (2018). The Rnf complex is an energy coupled transhydrogenase essential to reversibly link cellular NADH and ferredoxin pools in the acetogen *Acetobacterium woodii*. *J. Bacteriol.* 200:e357-18. doi: 10.1128/jb.00357-18

Whitman, W. B., Coleman, D. C., and Wiebe, W. J. (1998). Prokaryotes: the unseen majority. *Proc. Natl. Acad. Sci. U.S.A.* 95, 6578–6583. doi: 10.1073/pnas.95.12.6578

Conflict of Interest Statement: The authors declare that the research was conducted in the absence of any commercial or financial relationships that could be construed as a potential conflict of interest.

frontiers in Microbiology

ORIGINAL RESEARCH
published: 26 July 2019
doi: 10.3389/fmicb.2019.01729

Origin of Short-Chain Organic Acids in Serpentinite Mud Volcanoes of the Mariana Convergent Margin

Philip Eickenbusch[1], Ken Takai[2], Olivier Sissman[3], Shino Suzuki[4], Catriona Menzies[5,6], Sanae Sakai[2], Pierre Sansjofre[7], Eiji Tasumi[2], Stefano M. Bernasconi[8], Clemens Glombitza[1,9], Bo Barker Jørgensen[10], Yuki Morono[4] and Mark Alexander Lever[1]**

[1] Institute of Biogeochemistry and Pollutant Dynamics, ETH Zürich, Zurich, Switzerland, [2] SUGAR Program, Institute for Extra-Cutting-Edge Science and Technology Avant-Garde Research (X-star), Japan Agency for Marine-Earth Science Technology, Yokosuka, Japan, [3] IFP Energies Nouvelles, Rueil-Malmaison, France, [4] Geomicrobiology Research Group, Kochi Institute for Core Sample Research, Japan Agency for Marine-Earth Science and Technology, Kochi, Japan, [5] Ocean and Earth Science, National Oceanography Centre, University of Southampton, Southampton, United Kingdom, [6] Department of Geology and Petroleum Geology, University of Aberdeen, Aberdeen, United Kingdom, [7] Laboratoire Géosciences Océan UMR 6538, Université de Bretagne Occidentale, Brest, France, [8] Geological Institute, ETH Zürich, Zurich, Switzerland, [9] NASA Ames Research Center, Moffett Field, CA, United States, [10] Department of Bioscience, Center for Geomicrobiology, Aarhus University, Aarhus, Denmark

OPEN ACCESS

Edited by:
Dawn Cardace, University of Rhode Island, United States

Reviewed by:
Timothy Ferdelman, Max Planck Institute for Marine Microbiology (MPG), Germany
Craig Lee Moyer, Western Washington University, United States

***Correspondence:**
Philip Eickenbusch
philipeickenbusch@gmail.com
Mark Alexander Lever
mark.lever@usys.ethz.ch

Specialty section:
This article was submitted to Extreme Microbiology, a section of the journal Frontiers in Microbiology

Received: *01 May 2019*
Accepted: *12 July 2019*
Published: *26 July 2019*

Citation:
Eickenbusch P, Takai K, Sissman O, Suzuki S, Menzies C, Sakai S, Sansjofre P, Tasumi E, Bernasconi SM, Glombitza C, Jørgensen BB, Morono Y and Lever MA (2019) Origin of Short-Chain Organic Acids in Serpentinite Mud Volcanoes of the Mariana Convergent Margin. Front. Microbiol. 10:1729. doi: 10.3389/fmicb.2019.01729

Serpentinitic systems are potential habitats for microbial life due to frequently high concentrations of microbial energy substrates, such as hydrogen (H_2), methane (CH_4), and short-chain organic acids (SCOAs). Yet, many serpentinitic systems are also physiologically challenging environments due to highly alkaline conditions (pH > 10) and elevated temperatures (>80°C). To elucidate the possibility of microbial life in deep serpentinitic crustal environments, International Ocean Discovery Program (IODP) Expedition 366 drilled into the Yinazao, Fantangisña, and Asùt Tesoru serpentinite mud volcanoes on the Mariana Forearc. These mud volcanoes differ in temperature (80, 150, 250°C, respectively) of the underlying subducting slab, and in the porewater pH (11.0, 11.2, 12.5, respectively) of the serpentinite mud. Increases in formate and acetate concentrations across the three mud volcanoes, which are positively correlated with temperature in the subducting slab and coincide with strong increases in H_2 concentrations, indicate a serpentinization-related origin. Thermodynamic calculations suggest that formate is produced by equilibrium reactions with dissolved inorganic carbon (DIC) + H_2, and that equilibration continues during fluid ascent at temperatures below 80°C. By contrast, the mechanism(s) of acetate production are not clear. Besides formate, acetate, and H_2 data, we present concentrations of other SCOAs, methane, carbon monoxide, and sulfate, δ^{13}C-data on bulk carbon pools, and microbial cell counts. Even though calculations indicate a wide range of microbial catabolic reactions to be thermodynamically favorable, concentration profiles of potential energy substrates, and very low cell numbers suggest that microbial life is scarce or absent. We discuss the potential roles of temperature, pH, pressure, and dispersal in limiting the occurrence of microbial life in deep serpentinitic environments.

Keywords: limits of life, deep biosphere, serpentinization, abiotic synthesis, formate, acetate, methane, International Ocean Discovery Program

INTRODUCTION

Since the 1950s, advances in sampling techniques have extended explorations of subseafloor life from ∼8 meters below seafloor (mbsf) (Morita and Zobell, 1955) to ∼2,500 mbsf (Inagaki et al., 2015). Today, the subseafloor microbial biosphere is estimated to account for 0.18–3.6% of total living biomass on Earth (Kallmeyer et al., 2012), and to persist in many places despite low energy supply and harsh environmental conditions, such as high temperature, pressure, salinity, and/or pH (Takai, 2011; Hoehler and Jørgensen, 2013; Lever et al., 2015). These variables affect the power requirements of microbial life, e.g., by increasing rates of biomolecule damage, and consequently also raise the power required by cells to maintain and repair essential biomolecules (Lever et al., 2015). As a result, the presence and abundance of microorganisms within subseafloor habitats varies greatly with location as a result of stark differences in cell-specific power supply and cell-specific power demand (Inagaki et al., 2015; Lever et al., 2015; Møller et al., 2018; Heuer et al., 2019).

In subseafloor sediments, most microorganisms are chemoorganotrophic and rely on the breakdown of photosynthetically fixed organic matter (OM) and *in situ*-produced microbial necromass as power sources (Canfield et al., 2005; Lomstein et al., 2012). Under anaerobic conditions, SCOAs, such as formate, acetate, propionate, butyrate, and lactate, in addition to H_2, are important metabolic intermediates, being the end products of microbial fermentation and acetogenesis reactions (Stams, 1994; Wellsbury et al., 2002; Worm et al., 2010). In addition, SCOAs are key energy substrates for microorganisms involved in terminal oxidation reactions to carbon dioxide (CO_2) and CH_4 involving nitrate, manganese(IV), iron(III), sulfate, and CO_2 as electron acceptors (Froelich et al., 1979; Sørensen et al., 1981; Canfield et al., 1993; Finke and Jørgensen, 2008). Microbial production and turnover of SCOAs has been reported from 0 (Finke et al., 2007) to 80°C (Wellsbury et al., 1997; Parkes et al., 2007), and pH values of <4 (Goodwin and Zeikus, 1987; Koschorreck, 2008) to >12 (Yu et al., 2013), and to sediment depths of ∼800 mbsf (Wellsbury et al., 2002).

In addition to being degraded by microorganisms, photosynthetically fixed OM, and microbial necromass can be broken down at high temperature by thermochemical or "thermogenic" reactions (Wellsbury et al., 1997; Egeberg and Barth, 1998). Elevated temperatures in petroleum and gas reservoirs, hydrothermal sediments, or deeply buried sediment layers produce many of the same intermediates and end products released during the microbial breakdown of OM, including SCOAs, H_2, and CH_4 (Wellsbury et al., 1997; Parkes et al., 2007). Field and laboratory experiments show that thermogenic SCOA pools are typically dominated by acetate (e.g., Cooles et al., 1987; Lundegard and Kharaka, 1990; Barth and Bjørlykke, 1993; Kharaka et al., 1993; Shebl and Surdam, 1996), and in exceptional cases by propionate (Carothers and Kharaka, 1978). Furthermore, in thermogenic environments with temperatures >100°C in the presence of sulfate, significant fractions of the SCOAs, H_2, and hydrocarbons produced by thermogenic breakdown of OM can be removed through thermochemical sulfate reduction (e.g., Mottl et al., 1979; Kiyosu and Krouse, 1990; Worden et al., 2000; Cross et al., 2004; Truche et al., 2009).

In addition to the breakdown of photosynthetically fixed and necromass bound OM, SCOAs can be synthesized via the abiotic reduction of inorganic carbon with electron donors released by serpentinization reactions (Holm and Andersson, 1998; McCollom and Seewald, 2007; Schrenk et al., 2013; Früh-Green et al., 2014; Preiner et al., 2018). Serpentinization reactions include chemical reactions whereby water reacts with ultramafic rocks rich in iron(II)-containing minerals, such as olivine and pyroxene, to release H_2 (McCollom and Bach, 2009; Preiner et al., 2018). This H_2 can then reduce inorganic carbon to formate, with which it forms a metastable equilibrium between 175 and 300° (McCollom and Seewald, 2001, 2003a). Mineral surface-catalyzed Sabatier-type and Fischer-Tropsch type reactions can furthermore cause H_2 to react abiotically with CO or CO_2 to form methanol, CH_4, and SCOAs and hydrocarbons with ≥2 C atoms (Sabatier and Senderens, 1899; Fischer and Tropsch, 1926; McCollom and Seewald, 2003a, 2007; Holm and Neubeck, 2009). Rates of serpentinization and FTT reactions strongly depend on temperature, availability of suitable catalysts, and H_2 and CO partial pressures (Van Der Laan and Beenackers, 1999), with H_2 release peaking at ∼300°C and CH_4 production peaking at 320°C in batch experiments ranging from 200 to 320°C (McCollom et al., 2016). Importantly, while the production of CH_4 and hydrocarbons with ≥2 C atoms by FTT in the presence of a gas phase is generally accepted, recent studies have challenged earlier reports of CH_4 production by FTT in water-saturated serpentinitic systems at 200–300°C (McDermott et al., 2015; McCollom, 2016; Wang et al., 2018). Instead stable and clumped isotopic compositions point toward synthesis of these hydrocarbons at ≥400°C from magmatic volatiles that are trapped within fluid-vapor inclusions. Alteration of mantle rocks by serpentinization then releases these compounds into circulating fluids.

A typical indicator of serpentinization reactions is the presence of fluids with pH >10 and high formate concentrations (Mottl et al., 2003; McCollom and Bach, 2009; Schrenk et al., 2013). In some places, large macrofaunal populations are present where serpentinite-influenced fluids mix with seawater at the seafloor (Kelley et al., 2005; Fryer, 2012; Ohara et al., 2012; Joseph, 2017). These macrofauna feed on abundant chemotrophic microbiota which are sustained by abiotically produced H_2, CH_4, and SCOAs as energy donors and seawater-derived O_2 and sulfate as electron acceptors. It has been suggested that the same abiotically produced compounds might also support microbial communities in the upper mantle and in subseafloor basaltic ocean crust (Früh-Green et al., 2004; Lever et al., 2013; Bach, 2016; Smith et al., 2019).

Well-known sites of serpentinization in the marine environment include the Lost City Hydrothermal Field (LCHF; Früh-Green et al., 2003, 2014; Kelley et al., 2005; Proskurowski et al., 2008; Konn et al., 2009; Lang et al., 2010, 2018) and the Mariana Forearc (Fryer et al., 2003, 2018b; Mottl et al., 2003; Hulme et al., 2010; Fryer, 2012). The LCHF is located on the Atlantis Massif, an oceanic core complex, 15 km west of the Mid-Atlantic Ridge and is a model environment for rock-hosted

serpentinitic marine systems. In contrast, serpentinite mud volcanoes of the Mariana forearc are located in a subduction zone. Here, highly alkaline serpentinite muds, produced >10 kmbsf in the mantle wedge by alteration of mantle rock with fluids liberated from the underlying subducting plate, are transported to the seafloor (Hulme et al., 2010; Fryer, 2012). Geochemical profiles and membrane lipids in muds of the top 20 mbsf indicate the presence of metabolically active microbial life that is dominated by Archaea (Mottl et al., 2003; Curtis et al., 2013; Aoyama et al., 2018; Kawagucci et al., 2018). Comparing 16S rRNA gene sequences of Curtis et al. (2013) with published sequences (M. Lever, *unpubl.*) indicates the presence of Lokiarchaeota with close relatives in methane hydrates, methane seeps, and anoxic subseafloor sediments, and of aerobic nitrifying Marine Group I Thaumarchaeota with close relatives in diverse deep sea benthic surface habitats. Cultivation studies have resulted in the isolation of alkaliphilic bacteria (*Marinobacter alkaliphilus*), which grow at a pH of 6.5 to 10.8–11.4 using organic substrates as electron donors, and O_2, nitrate, or fumarate as electron acceptors (Takai et al., 2005).

Distinguishing microbial, thermogenic, and abiotic origins of SCOAs remains a challenge in many locations because these processes overlap in temperature, pressure, and redox ranges and can, in theory, co-occur in the same environments (Holm and Andersson, 1998; Schrenk et al., 2013). Furthermore, as mentioned earlier, microbially, thermogenically, and abiotically produced SCOAs can also be removed by microbial, thermogenic, and abiotic processes. Thus, accumulation of SCOAs is not a reliable indicator of origin. Even if microbial, thermogenic, and abiotic processes are spatially separated, fluids may contain products of all three processes if they are mixtures with multiple origins. Fortunately, in some cases SCOA origin can be revealed by concentration, isotopic, and thermodynamic analyses of natural educts and products (Heuer et al., 2009; Lang et al., 2010, 2018; Lever et al., 2010).

Here we investigate the origin of SCOAs in three serpentinite mud volcanoes (Yinazao, Fantangisña, and Asùt Tesoru) of the Mariana forearc system based on mud and extracted pore fluids that were obtained during IODP Expedition 366 in 2016/2017. We compare depth-related trends in SCOA concentrations to those observed for other microbial energy substrates (H_2, CO, CH_4), and electron acceptors (SO_4^{2-}, DIC), to stable isotopic compositions of bulk carbon pools [DIC, total organic carbon (TOC), dissolved organic carbon (DOC)], and to cell counts. Furthermore, we present results of incubation experiments and of thermodynamic calculations to elucidate likely SCOA sources. Despite high concentrations of SCOAs and other microbial substrates and low temperatures of samples (<10°C), microbial activity and microbial populations are around the detection limit. This (near-)absence of active microbial populations is likely due to elevated temperature (~80–250°C) in the slab and/or high pH (pH 11.0–12.5) of serpentinite mud, and due to absence of significant microbial colonization of serpentinite mud during ascent from the mantle wedge to the seafloor. Due to the absence of a clear microbial imprint, the mud fluids sampled during Expedition 366 provide a unique window into the reactions that produce microbial energy substrates deep within subduction zones.

MATERIALS AND METHODS

Site Description

IODP Expedition 366 (8 December 2016 to 7 February 2017) onboard the *R/V JOIDES Resolution* drilled into the Yinazao (previously known as Blue Moon), Fantangisña (previously known as Celestial), and Asùt Tesoru (previously known as Big Blue) serpentinite mud volcanoes on the Mariana forearc (Fryer et al., 2018b). These mud volcanoes are located to the west of the Mariana Trench and differ in distance to the trench and temperature of the underlying subducting slab (**Figure 1**). The three mud volcanoes also differ in geographic location, i.e., Fantagisña is located ~90 km north of Yinazao, and ~170 km south of Asùt Tesoru (Fryer et al., 2018b). Yet, distance to trench, which only differs by 17 km, and associated changes in the slab temperature, which varies from 80°C to around 250°C, are more important drivers of deep geochemical processes (Hulme et al., 2010). For this reason we schematically represent the three mud volcanoes as a transect in **Figure 1**.

All three mud volcanoes are formed as fluids, liberated during the subduction of both sediments and crustal rock from the Pacific plate, hydrate the overlying plate's mantle and drive serpentinization, whereby mud is produced by rock-alteration and breakdown, and the pH of fluids becomes highly alkaline (Mottl et al., 2003; Fryer, 2012). Due to volume expansion and corresponding density changes, this mud wells up via conduits, which are likely related to fault intersections, to the seafloor (Früh-Green et al., 2004), where it forms serpentinite mud volcanoes with heights and diameters of multiple kilometers (Fryer et al., 2018b). Maximum vertical mud flow velocities at Yinazao and Asùt Tesoru have been estimated to be 10.3 and 36.3 cm yr^{-1}, respectively (Hulme et al., 2010; no data for Fantangisña), which correspond to ascent times of ~130,000 (Yinazao) and ~50,000 years (Asùt Tesoru) from the décollement to the seafloor. Detailed site data from IODP Expedition 366 are publicly available on the IODP homepage (Fryer et al., 2018b).

Sampling

Table 1 provides an overview of drilled sites included in this study. Most samples were obtained using a Half-Length Advanced Piston Corer. Site U1492C Core 1 was obtained by a full-length Advanced Piston Corer. Site U1498 samples were obtained using a Rotary Core Barrel. Based on estimated temperature gradients for all flank and summit sites, *in situ* temperatures of all cores were <10°C. For further details, we refer to Fryer et al. (2018a).

Porewater

Interstitial water samples were extracted by squeezing water out of inner parts of cores using Carver presses (Manheim, 1966) with filtering through prewashed 11 µm cellulose filters (Whatman, Cat.-No. 1001090). Water samples were then filtered through 0.45 µm PES syringe filters (GE Puradisc, Cat-No. 6780.2504) during splitting into aliquots. pH, and concentrations

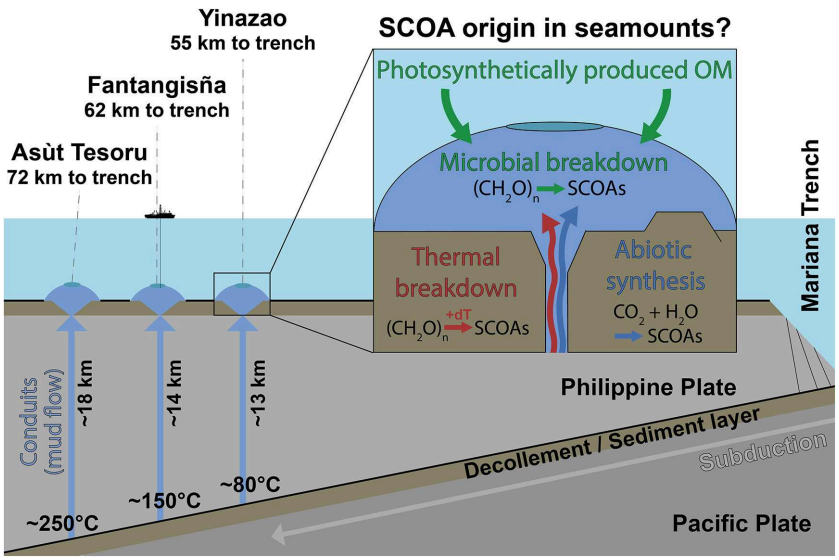

FIGURE 1 | Schematic dissection of the Yinazao, Fantangisña, and Asùt Tesoru mud volcanoes in relation to the Mariana Trench, which is formed by subduction of the Pacific Plate under the Philippine Plate. The Pacific Plate and its sediment cover are exposed to increasing temperatures as they are subducted. The Yinazao, Fantangisña, and Asùt Tesoru mud volcanoes are shown in blue due to the distinct blue color of the dominant lithology, upwelling serpentinite mud. Investigating how SCOA compositions, and origins (microbial, thermogenic, abiotic) change both horizonally and vertically between and within these mud volcanoes provides insights into the controls on carbon transformation reactions in the deep subseafloor.

of [$Mg_{(aq)}$], sulfate, DIC and DOC were determined onboard as described in Fryer et al. (2018a). All data are available online (Fryer et al., 2018b,c).

SCOA Quantification

Porewater samples for SCOA quantification were stored at −80°C in baked vials (6 h at 450°C) immediately after retrieval and were quantified in the home laboratory using two-dimensional ion chromatography as described in Glombitza et al. (2014).

DIC and DOC Concentrations

DIC and DOC concentrations were measured onboard with the OI Analytical Aurora 1030C TOC analyzer, consisting of a syringe module, a sample-stripping manifold, and an infrared CO_2 analyzer. Porewater samples (1 mL per injection) were acidified with 0.2 mL of 2 M HCl. The CO_2 released during this acid addition step was stripped and injected into the CO_2 analyzer. Subsequently, any remaining carbon in the sample was combusted, and the DOC was obtained by difference. The CO_2 Beer-Lambert absorption law was integrated to determine the total CO_2 released from the sample (Fryer et al., 2018a).

δ^{13}C-DOC Values

Porewater samples for δ^{13}C-DOC analyses were stored at −80°C in baked vials (6 h at 450°C). Isotopic compositions were measured after wet-chemical oxidation of DOC with persulfate (1 h at 100°C) on decarbonized subsamples (acidification to pH < 3 with 85% H_3PO_4). Two to four ml of headspace were then transferred into He flushed vials and analyzed using isotope-ratio mass spectrometry as described in Lang et al. (2012).

δ^{13}C-DIC Values

Porewater samples for δ^{13}C-DIC analyses were preserved by adding $HgCl_2$ and stored at 4°C. Depending on the concentration, 1–2 ml of sample were injected into He-flushed exetainers containing 150 µl of 85% phosphoric acid to lower the pH and convert all DIC into CO_2. CO_2 was then measured after equilibration using isotope-ratio mass spectrometry. Standardization was accomplished by measuring Na-bicarbonate solutions of different concentrations prepared from a Na-bicarbonate powder, for which the $\delta^{13}C$ was determined by digestion with phosporic acid, and by comparison to calcium carbonate standards as described in Breitenbach and Bernasconi (2011).

Serpentinite Mud

Cell Counts

To determine cell abundances, 2 cm^3 of mud were subsampled from central portions of cores using sterile cut-off syringes in an ultra clean air environment (KOACH T-500f, Koken, Ltd., Morono et al., 2018). Samples were immediately fixed with 2% paraformaldehyde in 3-(cyclohexylamino)-1-propanesulfonic acid (CAPS) buffer solution adjusted to pH 11. The fixed samples were stored at 4°C until the analysis at the home laboratory, whereby slurry samples were subjected to cell detachment and separation steps at the super clean room in Kochi Core Center, Japan (Morono et al., 2013, 2017). In brief, 1 mL of fixed mud slurry was mixed with 1.4 mL of 2.5% NaCl, 300 µL of detergent mix (100 mM ethylenediamine tetra-acetic acid [EDTA], 100 mM sodium pyrophosphate, 1% [v/v] Tween-80), and 300 µL of pure methanol, and homogenized on a Shake Master (Bio Medical Science, Japan) at 500 rpm for 60 min. Samples were

TABLE 1 | Background information on drilled holes during IODP Expedition 366.

Hole	Seamount	Location	Latitude	Longitude	Water depth (mbsl)	Coring	Total penetration (m)	Distance to trench (km)	Distance to slab (km)	Temperature at slab (°C)
U1492C	Yinazao	Summit	15°42.5590′N	147°10.6001′E	3666.47	APC/HLAPC	139.1	55	13	~80
U1493B	Asùt Tesoru	Flank	17°59.1665′N	147°06.0060′E	3358.92	HLAPC	32.6	72	18	~250
U1494A	Asùt Tesoru	Flank	18°3.0896′N	147°6.0003′E	2199.80	HLAPC	39	72	18	~250
U1495A	Asùt Tesoru	Flank	18°05.6693′N	147°06.0004′E	1405.81	HLAPC	10.7	72	18	~250
U1495B	Asùt Tesoru	Flank	18°05.6788′N	147°05.9901′E	1401.89	HLAPC	10.8	72	18	~250
U1496A	Asùt Tesoru	Summit	18°6.5936′N	147°6.0999′E	1243.38	HLAPC	44.8	72	18	~250
U1496B	Asùt Tesoru	Summit	18°6.6205′N	147°6.0998′E	1240.18	HLAPC	36	72	18	~250
U1497A	Fantangisña	Summit	16°32.2536′N	147°13.2642′E	2019.24	HLAPC	34.2	62	14	~150
U1497B	Fantangisña	Summit	16°32.2528′N	147°13.2606′E	2018.22	HLAPC	23.8	62	14	~150
U1498A	Fantangisña	Flank	16°27.0898′N	147°09.8502′E	3496.21	RCB	181.6	62	14	~150
U1498B	Fantangisña	Flank	16°27.3716′N	147°10.1166′E	3284.70	RCB	260	62	14	~150

All data from Fryer et al. (2018c), except distance to trench (from Hulme et al., 2010), and distance to slab data (Oakley, 2008; from Oakley et al., 2007, 2008).

then sonicated at 160 W for 30 s for 10 cycles (Bioruptor UCD-250HSA; Cosmo Bio, Japan), followed by loading onto density layers composed of 30% Nycodenz (1.15 g/cm^3), 50% Nycodenz (1.25 g/cm^3), 80% Nycodenz (1.42 g/cm^3), and 67% sodium polytungstate (2.08 g/cm^3), and centrifugation at 10,000×g for 1 h at 25°C with swinging rotors. The light density layer was collected, whereas the heavy fraction was subjected to a second round of separation after washing with 5 mL of 2.5% NaCl. The recovered supernatants were then pooled and passed through a 0.22 μm polycarbonate membrane filter. Cells on the membrane filter were stained with SYBR Green I staining solution (1/40 of SYBR Green I in Tris-EDTA [TE] buffer). The number of SYBR Green I–stained cells was enumerated by automated epifluorescence microscopic counting (Morono et al., 2009; Inagaki et al., 2015). To quantify procedural contamination, blank controls involving 1 mL of 2.5% NaCl solution were also subjected to the above cell separation and staining procedures. The procedural contamination was on average 1.0 cells per counted membrane ($n = 10$), which corresponds to a minimum quantification limit of 24 cells/cm^3 (average plus three times the standard deviation of blank counts).

Gas Analyses

To quantify concentrations of H_2, CH_4, and CO, 1 cm^3 of mud was collected from cut ends of core sections immediately after core arrival. Samples were placed in 20 cm^3 glass vials with 3 mL of distilled water and a small amount of $HgCl_2$ to prevent microbial activity. Vials were sealed with Teflon-coated butyl rubber septa and crimped aluminum caps and then placed in an oven at 80°C for 30 min. A 0.5 cm^3 aliquot of the headspace was sampled with a standard gas syringe and automatically injected into a GL Science GC4000 GC equipped with a helium ionization detector set at 250°C. The column (2 mm inner diameter; 6.3 mm outer diameter) was packed with carbosieve (Agilent/Hewlett Packard). The GC oven program was set to 40°C during the initial 5 min with a subsequent rise to 250°C at 20°C/min. A second 0.5 cm^3 aliquot of the headspace was then automatically injected into an Agilent/Hewlett Packard 6890 Series II gas chromatograph (GC) equipped with a flame ionization detector set at 250°C. The column (2 mm inner diameter; 6.3 mm outer diameter) was packed with 80/100 mesh HayeSep (Restek). The GC oven program was set to 80°C for 8.25 min with a subsequent rise to 150°C at 40°C/min. All measurements were calibrated using two different gas standards.

Total Organic Carbon (TOC) and δ^{13}C-TOC

Analyses were performed on solid residue samples after porewater squeezing. TOC and $\delta^{13}C_{org}$ were analyzed using an elemental analyzer (EA, Flash 2000; Thermo Scientific) coupled to a Delta V+ isotope ratio mass spectrometer (Thermo Scientific) at the Pôle de Spectrométrie Océan (PSO, Brest, France). Approximately 25 mg of decarbonated samples were loaded into tin capsules and introduced into an autosampler. Flash combustion was performed using an 8 s injection time of dioxygen at a flux of 240 mL min^{-1}. Carbon isotope ratios were obtained against reference standards (SED-IVA reference number: 33802151) and in-house standards

(Acetanilide: reference number 274462 from Thermo Fisher; CAP (leaf litter) and LIPG (yeast) from Institut de Physique du Globe de Paris, France). δ^{13}C-TOC values are given as the per mil (‰) difference from the PDB standard. TOC was measured using the thermal conductivity detector of the Flash 2000 instrument. Routine replicate measurements had internal deviations of 0.15‰ for δ^{13}C-TOC and <5% for TOC.

Thermodynamic Calculations

Gibbs energy yields (ΔG_r) of potential microbial, thermogenic, and abiotic reactions were calculated based on the equation

$$\Delta G_r = \Delta G^0_{r(T,p)} + RT\ ln\ Q_r \quad (1)$$

where $\Delta G^0_{r(T,p)}$ is the Gibbs energy (kJ mol^{-1} of reaction) at standard concentrations (1 M per each reactant and product, pH 7.0) corrected for *in situ* temperature T (K) and pressure p (bar), R is the universal gas constant (0.008314 kJ mol^{-1} K^{-1}), and Q_r the quotient of product and reactant activities. To obtain $\Delta G^0_{r(T,p)}$, the standard Gibbs energies of the reaction ΔG^0_r was corrected to estimated *in situ* slab temperature and pressure as outlined in Stumm and Morgan (1996). Standard Gibbs energies, standard enthalpies, and standard molal volumes of formation are shown in **Supplementary Table 1**. Calculations were done for activities of aqueous species, which were calculated using the activity coefficients $\gamma_{CO32-} = 0.038$ (Plummer and Sundquist, 1982), $\gamma_{CH4} = 1.24$ (Millero, 2000), $\gamma_{SO42-} = 0.104$ (Millero and Schreiber, 1982), and $\gamma_{HS-} = 0.685$ (Clegg and Whitfield, 1991). The activity coefficients of H_2 and CO were approximated with that of CH_4, those of SCOAs were approximated with that of HS^-, and those of glucose were set to 1.0. All concentrations were measured, except for glucose and HS^-, which were assumed to equal 1 nM and 1 mM, respectively. The ΔG_r was calculated for temperature, pressure, and pH in sediment cores and for temperature, pressure, and pH under slab conditions. The pH under slab conditions was 11.2 for Yinazao, 11.0 for Fantangisña, and 12.5 for Asùt Tesoru (based on Fryer et al., 2018b).

RESULTS

In the following sections we first compare geochemical background data (pH; magnesium, sulfate, DIC, and DOC concentrations; TOC contents) and cell counts on high-pH subsurface serpentinite mud fluids (pH 10.5–12.5) with shallow and adjacent samples, that are under stronger seawater or sedimentary influence and have moderate pH values (pH 7.8–10; **Figure 2**). We then examine how concentration profiles of potential microbial energy substrates (SCOAs, CH_4, H_2, CO; **Figure 3**) vary with pH within and across the three volcanoes. In the final part, we investigate how the relative contributions of different SCOAs to DOC change between and within mud volcanoes (**Figure 4**), how the concentrations of individual SCOAs change in high-pH samples with distance to the trench and with increasing slab temperature (**Figures 5**, **6**), and how δ^{13}C-isotopic values of DIC, DOC, and TOC change between and within mud volcanoes (**Figure 7**). Through this integrated analysis, we provide insights into the role of deep, tectonically driven reactions in determining the sources and chemical compositions of microbial energy substrates in mud volcanoes of the Mariana forearc.

Geochemical Setting

Porewater pH values increase downward from the seafloor (**Figure 2A**), where values approach those of seawater (pH 8.1). In samples with high fluid upflow, the pH stabilizes at values that increase with distance to trench (Yinazao: ∼10.7; Fantangisña: ∼11.2; Asùt Tesoru: ∼12.4) and at different sediment depths (Yinazao: ∼8 mbsf; Fantangisña: unclear but within top 66 mbsf; Asùt Tesoru: ∼4 mbsf). Within Fantangisña and Asùt Tesoru, fluids from flank sites or areas with less fluid upflow are clearly distinguishable from fluids in areas of higher upflow based on pH values closer to those in surface sediments (Mottl et al., 2003). For the sake of simplicity, we from now on refer to samples from boreholes with high upflow and pH>10.0 as "high-pH mud fluids," and samples from boreholes on flank sites and sites with less upflow and pH<10.0 as "moderate-pH mud fluids." We, moreover, distinguish between surface samples with a clear seawater influence, and subsurface samples, where pH values are constant at higher values.

Magnesium (Mg^{2+})concentrations are mostly below or close to the detection limit of 0.1 mM in subsurface high-pH mud fluids of all three mud volcanoes. In a few high-pH samples, concentrations of up to ∼5 mM are reached, which correspond to ∼10% of seawater values (∼54 mM). Drilling fluid (seawater) contamination is a likely source of these elevated Mg^{2+} values (**Figure 2B**) according to drilling fluid intrusion estimates based on perfluorocarbon tracer compounds (Fryer et al., 2017; Lever et al., in prep.). Mg^{2+} concentrations in high-pH fluids increase steeply near the seafloor, in the same intervals where pH values decrease, indicating significant fluid exchange, e.g., by diffusive mixing with seawater, in the top meters of sediment. By contrast, moderate-pH mud fluids show a gradual decrease but sustain significantly higher Mg^{2+} concentrations throughout the cored intervals. These Mg^{2+} concentrations cannot be explained with measured drilling fluid contamination (Fryer et al., 2017; Lever et al., in prep.) and indicate that moderate-pH pore fluids are a mixture of seawater and/or shallower sedimentary pore fluids and deeply-sourced serpentinitic fluids.

Sulfate concentrations in high-pH fluids (**Figure 2C**) show similar patterns to pH and magnesium, and in relation to chloride (**Supplementary Figure S1B**), i.e., changes toward seawater values (∼28 mM) in the upper meters, and steady profiles below. Chloride concentrations below those of seawater in high-pH fluids, moreover, indicate fluid freshening due to dewatering of deep clay-bearing minerals (**Supplementary Figure S1A**). There is no clear trend in sulfate concentrations with distance to trench, as is evident from the fact that high-pH fluids from Fantangisña are depleted in sulfate (∼4 mM), whereas those of Yinazao and Asùt Tesoru are only slightly lower (∼27 mM) or even higher (∼31 mM) than seawater values (28 mM; Mottl et al., 2003). By contrast, sulfate concentrations in moderate-pH fluids at Fantangisña show a striking variability, also in relation to chloride (**Supplementary Figure S1**), with values in

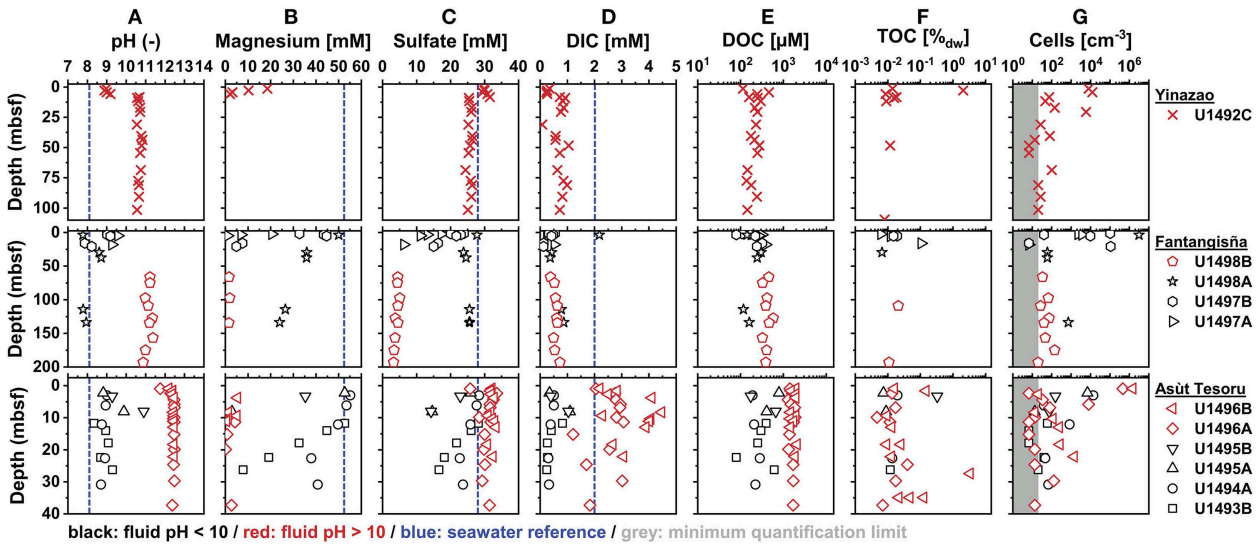

FIGURE 2 | Depth profiles of **(A)** pH, **(B)** magnesium (Mg^{2+}), **(C)** sulfate, **(D)** DIC, **(E)** DOC, **(F)** TOC, and **(G)** cell counts ordered in ascending distance to the Mariana Trench (top to bottom). All pH data, and magnesium (Mg^{2+}), sulfate, DIC, and DOC concentrations were measured shipboard and were obtained from Fryer et al. (2018b). TOC (% sample dry weight) and cell abundances are from this study (gray area indicates counts that are below the quantification limit of 20 cells cm^{-3}). Blue marks on the x-axis indicate seawater concentrations from Mottl et al. (2003). Red symbols indicate high-pH holes, black symbols indicate moderate-pH holes (see text for definitions).

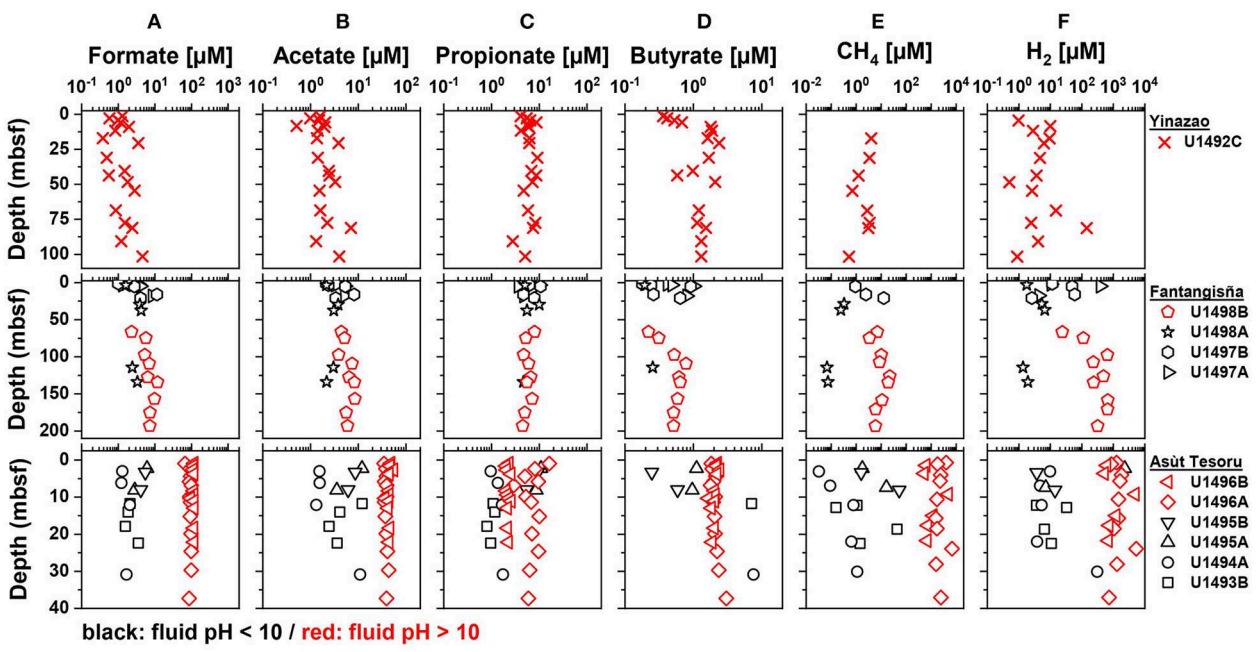

FIGURE 3 | Depth profiles of **(A)** formate, **(B)** acetate, **(C)** propionate, **(D)** butyrate, **(E)** CH4, and **(F)** H2 concentrations in the Yinazao, Fantangisña, and Asùt Tesoru mud volcanoes ordered in ascending distance to the Mariana Trench (top to bottom). Red symbols indicate high-pH holes with an average pH > 10, black symbols indicate moderate-pH holes with an average pH < 10.

holes U1497A and B decreasing steeply with sediment depth, while values from U1498A stabilize at ∼25 mM, which is ∼5-fold higher than in high-pH fluids of the same mud volcano. Sulfate concentration profiles on the flanks of Asùt Tesoru also vary between boreholes. Steep depth-related decreases to ∼14 mM occur in the top 12 mbsf at U1495A and B, while more moderate decreases to ∼15 mM and ∼22 mM at ∼30 mbsf occur at U1493B and U1494A, respectively. Unlike at Fantangisña,

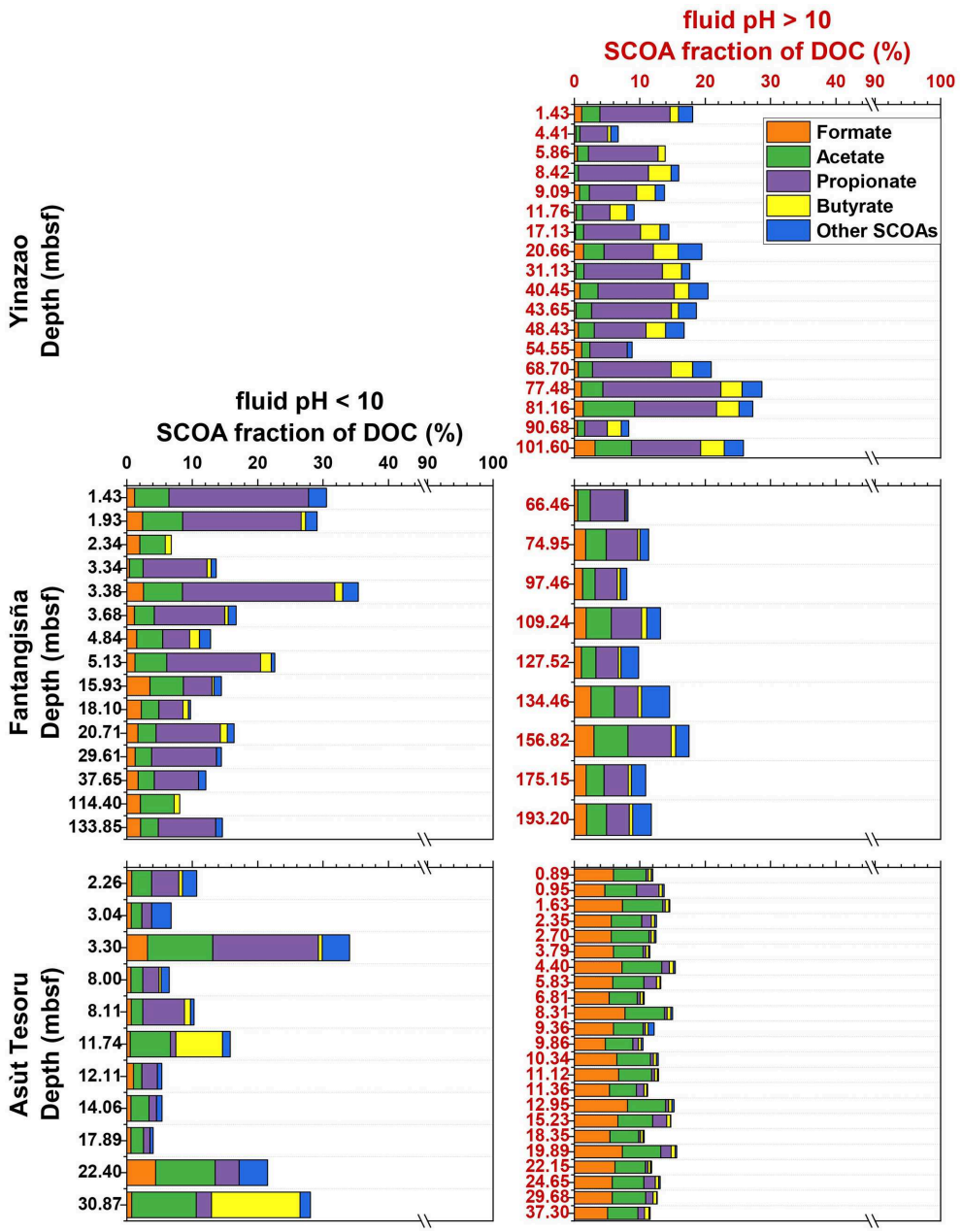

FIGURE 4 | SCOA percent fractions of DOC vs. depth at the Yinazao, Fantangisña, and Asùt Tesoru mud volcanoes. Black labeling indicates moderate pH fluids with an average pH < 10 **(Left)**, red labeling indicates high pH fluids with an average pH > 10 **(Right)**.

sulfate concentrations at Asùt Tesoru are higher in high-pH than in moderate-pH fluids.

DIC concentrations in high-pH fluids at Yinazao and Fantangisña remain mostly within a narrow range of 0 to 1 mM and are lower than those in seawater (Mottl et al., 2003; **Figure 2D**). By comparison, despite showing considerable scatter, measured DIC concentrations of high-pH fluids at Asùt Tesoru are higher (mostly 2–4 mM), in a range that is similar to or above seawater values. While DIC concentrations at shallow sediment depths and moderate-pH fluids at Fantangisña were in the same range as high-pH subsurface fluids, moderate-pH fluids at Asùt Tesoru consistently had 5–10-fold lower DIC concentrations than high-pH fluids.

DOC concentrations in high-pH fluids show straight subsurface profiles, with an increase in average concentration with distance to trench (Yinazao: 211 ± 51 μM; Fantangisña: 419 ± 79 μM; Yinazao: 1,684 ± 234 μM; **Figure 2E**). In moderate-pH fluids of Fantangisña and Asùt Tesoru, subsurface DOC concentrations also show no clear depth-related trends and have similar (Fantangisña; 317 ± 72 μM) or lower (Asùt Tesoru: 350

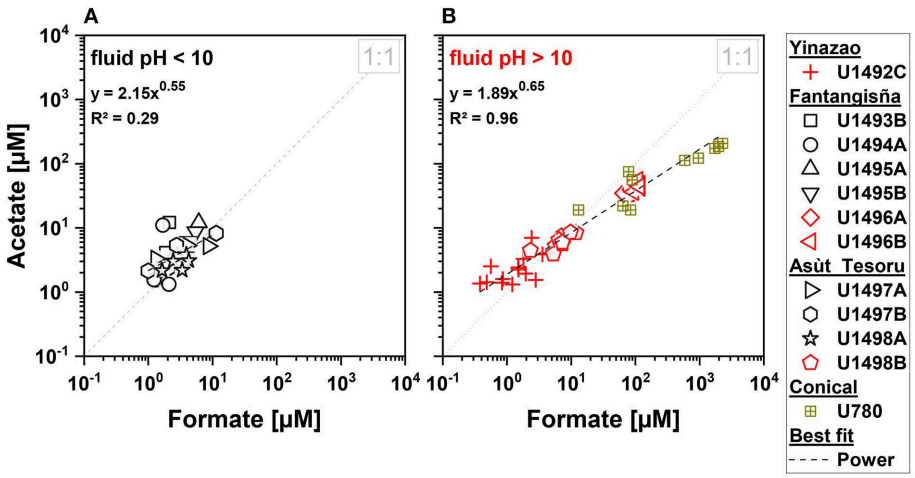

FIGURE 5 | Formate-to-acetate ratios for three serpentinite mud volcanoes drilled during IODP Expedition 366. Black symbols indicate moderate pH fluids with an average pH < 10 **(A)**, and red symbols indicate high pH fluids with an average pH > 10 **(B)**. Brown symbols indicate data on high pH fluids from Conical seamount from ODP Leg 125 (Haggerty and Fisher, 1992).

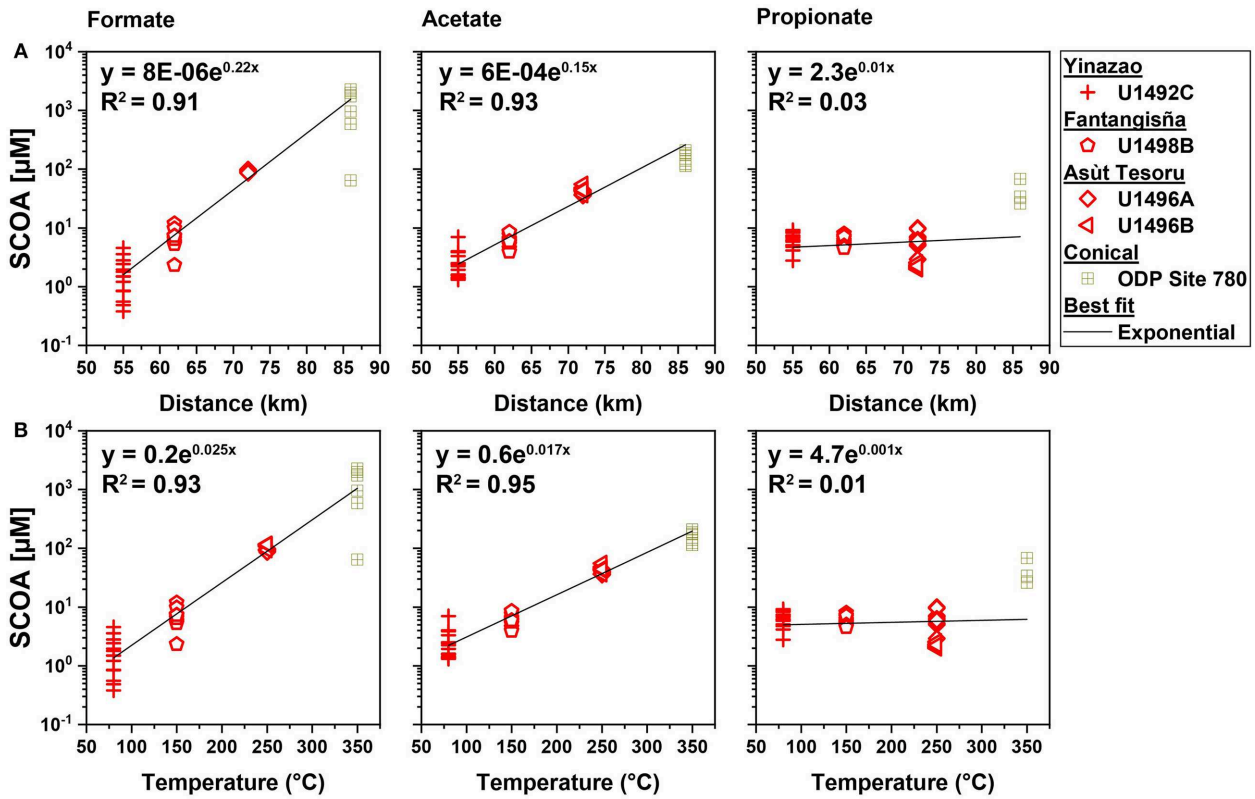

FIGURE 6 | Formate, acetate and propionate concentrations in high pH fluids vs. distance to trench **(A)** and vs. slab temperatures **(B)**. Regression includes data from Conical seamount, which was drilled during Ocean Drilling Program Leg 125 (Haggerty and Fisher, 1992).

± 195 µM) concentrations than in respective high-pH fluids. At Fantangisña, where measurements were also made in shallow sediment layers, there is a clear decrease in DOC concentrations toward the seafloor.

TOC contents in serpentinite muds are generally low, mostly scattering around ~0.01% dry weight, and do not show systematic differences between high- and moderate-pH fluids or between mud volcanoes (**Figure 2F**). Nonetheless,

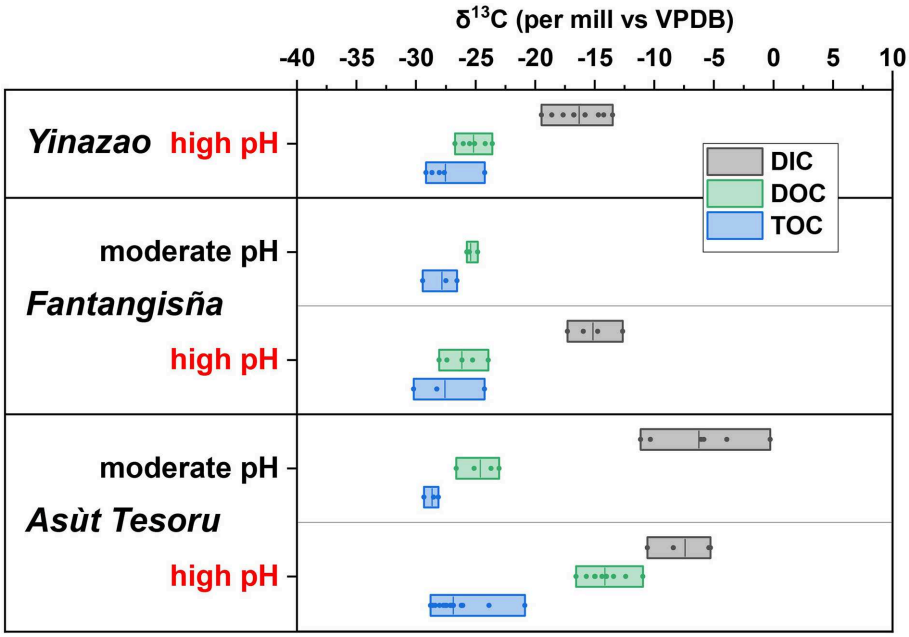

FIGURE 7 | Box plots of δ^{13}C-isotopic compositions of TOC, DOC, and DIC of moderate-pH and high-pH subsurface mud fluids. Boxes show the entire data range, vertical lines within boxes indicate the mean value.

there are several outliers, including values with 2.1% (U1492C 1H2; Yinazao) and 3.3% dry weight (U1496B 8XCC; Asùt Tesoru). Comparing porosity-corrected DOC to TOC contents in subsurface fluids, there are clear differences between and within mud volcanoes. DOC accounts for similar contributions of TOC in high-pH subsurface fluids at Yinazao (1.5 ± 0.7%) and at high-pH (∼2.0%) and moderate-pH (1.6 ± 1.3%) fluids of Fantangisña. By contrast, at Asùt Tesoru, the average DOC contribution to TOC is higher, i.e., 3.0 ± 1.2% in moderate-pH, and 13.1 ± 8.0% in high-pH subsurface fluids.

Cell counts reach values of $\sim 10^6$ cells cm^{-3} in the upper tens of meters, but are mostly below or within an order of magnitude above the quantification limit of 20 cells cm^{-3} in deeper layers, both in high-pH and moderate-pH muds (**Figure 2G**).

Concentration Profiles of Microbial Energy Substrates

Concentration profiles of potential microbial energy substrates show patterns with respect to depth below the seafloor and between high-pH and moderate-pH fluids that resemble those observed for pH, DIC, sulfate, and DOC.

Formate concentrations in high-pH fluids show straight subsurface profiles and increase with distance to trench (Yinazao: 1.8 ± 1.2 μM, Fantangisña: 7.0 ± 2.7 μM; Asùt Tesoru: 104 ± 11 μM; **Figure 3A**). Moderate-pH fluids from subsurface layers of Fantangisña are in a similar range (8.0 ± 3.7 μM) to high-pH fluids, and show the same characteristic decrease toward the seafloor that is also present in DOC concentrations. At Asùt Tesoru, however, moderate-pH, subsurface fluids have ∼40-fold lower concentrations (2.7 ± 1.7 μM) than high-pH fluids.

Acetate concentrations (**Figure 3B**) show similar trends to formate, except that the characteristic decrease toward the seafloor is absent from shallow sediments of Fantangisña, Moreover, the increase in high-pH fluids with distance to trench is not as strong as for formate. Average acetate concentrations range between 1 and 10 μM in high-pH (Yinazao: 2.4 ± 1.6 μM; Fantangisña: 6.2 ± 1.6 μM) and moderate-pH fluids (Fantangisña: 4.9 ± 4.0 μM; Asùt Tesoru: 5.6 ± 4.4 μM), except in high-pH subsurface fluids of Asùt Tesoru, where acetate concentrations are clearly elevated (42.0 ± 4.7 μM).

Propionate concentrations (**Figure 3C**) show no clear trends related to depth below the seafloor, fluid pH, or distance to trench, and range mostly from 1 to 10 μM both in high-pH (Yinazao: 6.3 ± 1.7 μM; Fantangisña: 5.9 ± 1.2 μM; Asùt Tesoru: 4.4 ± 2.8 μM) and in moderate-pH fluids (Fantangisña: 5.8 ± 2.5 μM; Asùt Tesoru: 3.5 ± 4.0 μM). Propionate concentrations are relatively uniform across boreholes at Fantangisña, but vary significantly in moderate-pH fluids of Asùt Tesoru, where U1493B and U1491A have 5–10 times lower concentrations than U1495A and B. Similarly, there is an offset among high-pH fluids of Asùt Tesoru (U1496), where hole B has ∼3 times lower concentrations than hole A.

Butyrate concentrations scatter in the submicromolar to low micromolar range (**Figure 3D**), showing no systematic relationship with depth below the seafloor, pH, or distance to trench. Average values of high-pH fluids are 1.5 ± 0.5 μM, 0.5 ± 0.2 μM, and 2.1 ± 0.3 μM at Yinazao, Fantangisña, and Asùt Tesoru, respectively. Average values of moderate-pH fluids are

0.6 ± 0.3 μM and 3.4 ± 3.6 μM at Fantangisña and Asùt Tesoru, respectively. The only notable trend is a linear decrease to the seafloor within the upper 10 mbsf at Fantangisña.

Other SCOAs were also detected in numerous samples (**Supplementary Figure S2**). Pyruvate was mainly detected in high-pH fluids of Asùt Tesoru (0.2 ± 0.1 μM). Valerate was detected in most high-pH fluid samples from Yinazao and Asùt Tesoru, with roughly 10-fold higher average concentrations in Asùt Tesoru (0.4 ± 0.2 μM vs. 0.04 ± 0.03 μM at Yinazao). Low (sub)micromolar concentrations of lactate were also present in most samples. Notably, lactate was the only SCOA with higher average concentrations in moderate-pH (1.5 ± 1.5 μM) than in high-pH fluids (0.7 ± 1.2 μM) of Asùt Tesoru.

Similar to formate, CH_4 concentrations (**Figure 3E**) in high-pH fluids show relatively straight downcore profiles and increase dramatically with distance to trench (Yinazao: 2.4 ± 1.4 μM, Fantangisña: 10.4 ± 6.3 μM; Asùt Tesoru: 2,170 ± 1,630 μM). CH_4 concentrations in moderate-pH subsurface fluids of Fantangisña and Asùt Tesoru are 10 to 100 times lower than in high-pH fluids from the same depths.

Similar to formate and CH_4, H_2 concentrations (**Figure 3F**) in high-pH fluids show a similar, strong increase with distance to trench (Yinazao: 16 ± 40 μM, Fantangisña: 380 ± 250 μM, Asùt Tesoru: 1,660 ± 1,560 μM). Compared to corresponding depths at Fantangisña and Asùt Tesoru, these H_2 concentrations are approximately two orders of magnitude higher than those in moderate-pH fluids (Fantangisña: 22.2 ± 32.4 μM; Asùt Tesoru: 225 ± 660 μM).

Carbon monoxide (CO) concentrations were barely detectable in high-pH fluids of Yinazao, but were clearly above detection in high-pH fluids of the other two mud volcanoes (Fantangisña: 11 ± 3 μM; Asùt Tesoru: 7 ± 2 μM; **Supplementary Figure S3**). Compared to high-pH fluids, CO concentrations in moderate-pH fluids of Fantangisña and Asùt Tesoru are in a similar range or slightly higher (Fantangisña: 13 ± 9 μM; Asùt Tesoru: 12 ± 3 μM).

Contribution of SCOAs to DOC

SCOAs make up ~10–30% of the C fraction of total DOC (**Figure 4**). The contribution of different SCOA species to the DOC pool varies with depth and pH. At Yinazao, the average SCOA fraction in high-pH fluids increases from ∼15% at the seafloor to ∼30% in the deepest samples. Propionate dominates the contribution in high-pH fluids (60–95% of SCOA C-pool), followed by acetate, butyrate, and then formate. Moderate pH-fluids at Fantangisña have trends similar to high-pH fluids at Yinazao, i.e., similar C contributions of SCOAs and propionate clearly dominating followed by acetate, but here the formate fraction is higher than the butyrate fraction. By comparison, SCOAs in high-pH fluids at Fantangisña account for a lower fraction of DOC, mainly due to a much lower C contribution of propionate, which barely exceeds acetate. The difference between moderate- and high-pH fluids is biggest at Asùt Tesoru. While moderate-pH fluid compositions fluctuate, and are variably dominated by acetate, propionate, and butyrate, high-pH fluids at Asùt Tesoru are consistently dominated by formate and acetate, which together account for 69–92% of the total SCOA-C.

Microbial Activity Within Samples Based on Incubation Experiments

To check for measurable microbial activity, we incubated high-pH muds of all three mud volcanoes at *in situ* pH in the laboratory using formate as an energy substrate and monitored concentrations of the metabolites formate, H_2, CH_4, and DIC for 6 weeks. None of the samples showed significant changes in metabolite concentrations over time or between formate incubations (100 μM ^{13}C-formate), killed controls (100 μM ^{13}C-formate + sodium azide), and negative controls (no formate).

SCOA Concentrations in High-PH Fluids in Relation to Distance to Trench and Slab Temperature

The very low cell numbers, the nearly constant concentration profiles of SCOAs in high-pH fluids, and the absence of measurable formate turnover in incubations raise the possibility that microbial activity is absent from high-pH subsurface muds. If so, then this raises the possibility that SCOAs measured in high-pH muds were thermogenically released from organic matter in the subducting slab and its sediments and/or produced by abiotic synthesis reactions linked to serpentinization of mantle rock of the Philippine Plate, and subsequently preserved over thousands of years during ascent. Under such a scenario, where all SCOAs in high-pH muds would be thermogenic or abiotic in origin, the changes in SCOA concentrations across mud volcanoes would reflect different environmental conditions deep within the subduction zone.

Our data are consistent with the possibility of SCOAs in high-pH fluids having deep origins. Cross-plots, in which previously measured formate and acetate concentrations from Conical Seamount (Haggerty and Fisher, 1992), a mud volcano that is located further away (86 km) from the Mariana Trench than Asùt Tesoru, are included, show that measured concentrations of formate and acetate in high-pH subsurface fluids are strongly correlated (power relationship; **Figure 5B**). Such a relationship is absent from moderate-pH samples (**Figure 5A**), or for propionate or butyrate in high-pH samples (*not shown*).

Next, we examined potential drivers behind the observed concentration trends in SCOAs in high-pH fluids across different mud volcanoes. Specifically, we investigated the relationship of formate, acetate, and propionate concentrations and mud volcano distance to the Mariana Trench, as a proxy for time since the initial subduction. Furthermore, we investigated the relationship between formate, acetate, and propionate concentrations and temperature in the subducting slab. The concentrations of formate and acetate, but not propionate, show a highly significant power relationship with distance to trench (**Figure 6**, upper panel) and with modeled *in situ* temperature in the underlying subducting slab (**Figure 6**, lower panel). Similarly, the ratios of formate to acetate, show strong power relationships with distance to trench and slab temperature (**Supplementary Figure S4**).

Stable Isotopic Compositions of Bulk Carbon Pools

As with most other analytes, the subsurface δ^{13}C-isotopic values of TOC, DOC, or DIC show no clear depth-related trends (**Supplementary Figure S5**), but instead indicate clear differences related to mud volcanoes and fluid pH (**Figure 7**).

Subsurface δ^{13}C-TOC values fall into a narrow range (Yinazao, high-pH: −27.5 ± 1.9‰; Fantangisña: moderate-pH: −27.8 ± 1.5‰; high-pH: −27.6 ± 3.0‰; Asùt Tesoru: moderate-pH: −28.7 ± 0.6‰; high-pH: −26.9 ± 2.0‰), and thus do not differ significantly between mud volcanoes or between pH-muds within mud volcanoes (Mann Whitney Test; $p > 0.05$).

All subsurface δ^{13}C-DOC data also fall within a narrow range, with the exception of high-pH fluids from Asùt Tesoru, where the average δ^{13}C-DOC is 11.1–12.1‰ higher than in all other mud volcano fluids (Yinazao, high-pH: −25.2 ± 1.2‰; Fantangisña: moderate-pH: −25.4 ± 0.4‰; high-pH: −26.2 ± 1.7‰; Asùt Tesoru: moderate-pH: −25.5 ± 2.3‰; high-pH: −14.1 ± 1.6‰). This difference in δ^{13}C-DOC between Asùt Tesoru high-pH fluids and all other mud volcano fluids is highly significant ($p < 0.01$).

Despite considerable scatter, subsurface δ^{13}C-DIC data show a clear division between Asùt Tesoru and the other two mud volcanoes. At Asùt Tesoru, moderate-pH and high-pH fluids have highly similar δ^{13}C-DIC ranges (moderate pH: −7.4 ± 3.6‰; high-pH: −7.6 ± 2.6‰). These values are significantly higher than in high-pH fluids of Yinazao (−16.3 ± 1.9‰) and Fantangisña (−15.3 ± 1.7‰; note: no data from moderate-pH fluids), which did not differ significantly from each other.

Comparing subsurface δ^{13}C-isotope data to each other reveals several trends. Overall, the mean δ^{13}C-DOC is consistently higher than the mean δ^{13}C-TOC. This difference is small (1.5–2.3‰) in muds of Yinazao and Fantangisña, and moderate-pH muds of Asùt Tesoru, but comparatively large (12.8‰) in high-pH muds of Asùt Tesoru (−14.1 ± 1.6‰ vs. −26.9 ± 2.0‰). Comparing δ^{13}C-DIC to δ^{13}C-TOC and δ^{13}C-DOC within each location and pH category shows that the δ^{13}C-DIC is consistently higher than the δ^{13}C-TOC and δ^{13}C -DOC. The average difference between δ^{13}C-DIC and δ^{13}C-TOC is lower in high-pH muds of Yinazao (−11.2‰) and Fantangisña (−12.3‰) compared to moderate-pH (−20.5‰) and high-pH muds (−19.3‰) at Asùt Tesoru. The average differences between δ^{13}C-DIC and δ^{13}C-DOC are in a similar range in high-pH muds of Yinazao (8.9‰) and Fantangisña (10.9‰) and in moderate-pH muds of Asùt Tesoru (18.1‰). The only exception is again high-pH mud of Asùt Tesoru, where the average δ^{13}C-DIC is only 6.6‰ higher than the average δ^{13}C-DOC.

DISCUSSION

Concentrations of potential microbial energy sources, such as formate, acetate, CH_4, H_2, and DOC, in deeply sourced high-pH fluids of Mariana forearc serpentinite mud volcanoes increase systematically with distance to the Mariana Trench and with underlying slab temperature. Yet, despite these increases, there are no clear indications of metabolically active microbial populations. Downward SCOA concentrations in high-pH subsurface muds of all three mud volcanoes show no clear changes, and neither do concentrations of other potential metabolites, such as sulfate, DIC, and DOC. Though an interpretation of the dissolved CH_4 and H_2 data is confounded by potential outgassing during core retrieval, these gases also show no clear depth-related production or consumption profiles. Microbial populations, quantified by microscopic counting, are mainly around the minimum quantification limit of 20 cells cm^{-3}. Local cell population peaks in subsurface high-pH fluids have to be interpreted with caution, given the local detection of millimolar concentrations of seawater-derived Mg^{2+}, and evidence of significant contamination of sediment porewater by drilling fluid (surface seawater) containing cell concentrations of 10^5-10^6 cells cm^{-3} (Lever et al., *in prep*.). Yet, even if the local peaks in cell counts accurately reflect *in situ* cell populations, these cells may not be metabolically active due to the highly alkaline *in situ* pH.

If significant microbial activity is absent, then this would mean that concentrations and compositions of potential microbial electron donors, such as SCOAs, CH_4, H_2, and CO, and electron acceptors, such as sulfate and DIC, in high-pH fluids could provide useful insights into deep, non-biological processes in the subducting slab and the overlying forearc mantle. For these high-pH fluids to be indeed informative, non-biological alterations of electron donor and acceptor compositions during the tens of thousands of years of mud fluid ascent would need to be absent or sufficiently slow to not overprint original trends. In the following sections we first investigate possible explanations for the absence of detectable microbial activity in this subseafloor environment, focusing on free energy yields of catabolic reactions and the environmental variables pressure, temperature, pH, and fluid mixing during ascent. Afterward we discuss possible deep sources and production mechanisms of measured SCOAs, as well as sulfate, methane, and bulk carbon pools, across the Mariana forearc.

Free Energies of Catabolic Reactions

To determine whether catabolic reactions are thermodynamically favorable, we calculated Gibbs energies for a range of reactions at *in situ* temperature, pressure, and pH in cores, as well as at estimated temperature, and pressure in the subducting slab using the *in situ* pH in the cores (**Table 2**). We include three respiration reaction types (methanogenesis, sulfate reduction, acetogenesis) that are important in marine serpentinitic systems (Brazelton et al., 2006; Quéméneur et al., 2014; Rempfert et al., 2017; Ijiri et al., 2018; Lang et al., 2018). Besides SCOAs, we include H_2, CO, and methane as substrates of microbial respiration, because of the ubiquitously high concentrations of H_2 and CH_4 and the detectable concentrations of CO in some of the high-pH muds. We also calculate free energy yields for the fermentative breakdown of propionate and butyrate, and the fermentative conversion of glucose to propionate and butyrate, as fermentation reactions are also likely to occur in serpentinitic environments (e.g., Kohl et al., 2016; Brazelton et al., 2017; Rempfert et al., 2017). While the currently known temperature limit of microbial life is 122°C (Takai et al., 2008), and thus

below the slab temperatures at Fantangisña and Asùt Tesoru, we nonetheless include calculations at all slab temperatures. This is because it cannot be ruled out that deep life exists at >122°C. Furthermore, many of the reactions in **Table 2** can also operate thermochemically or abiotically at high temperature and thus provide insights into potential non-biological sources and production pathways discussed later.

Our calculations indicate that the majority of reactions are thermodynamically favorable in all three mud volcanoes under both core and slab conditions (**Table 2**). Gibbs energies are mostly more negative than the theoretical minimum amount of energy that can be conserved per biochemical reaction (−20 to −10 kJ mol^{-1}; Schink and Thauer, 1988; Hoehler et al., 2001), also known as the "biological energy quantum" (BEQ; Thauer and Morris, 1984). Sulfate reduction is exergonic from all substrates, with reactions from SCOAs and CO in many cases being highly exergonic ($\Delta G_r < -100$ kJ mol^{-1}), especially at slab temperatures. Methanogenesis from formate, acetate, and CO is also always exergonic. By contrast, methanogenesis from H_2 ($+CO_3^{2-}$) is thermodynamically favorable under core conditions but in the range of the BEQ or even endergonic under slab conditions. Acetogenesis from formate, CO, and CO+H_2 is also always exergonic. Acetogenesis with H_2 ($+CO_3^{2-}$) or formate+H_2 as substrates is furthermore exergonic at core conditions, whereas the reverse reaction, acetate oxidation to H_2 ($+CO_3^{2-}$) or formate+H_2, is thermodynamically favorable under slab conditions. Fermentation of glucose to propionate or butyrate is highly favorable under all conditions, whereas propionate or butyrate fermentations to acetate are only clearly exergonic under slab conditions. The only reactions that are always endergonic, whether under core or slab conditions, are reactions involving the conversion of H_2+CO_3^{2-} or formate to CO ($\Delta G_r > +50$ kJ mol^{-1}). On the other hand, the reverse reaction is clearly exergonic, underscoring the potential for CO oxidation as a catabolic pathway in serpentinitic fluids (Morrill et al., 2014). Finally, the oxidation of formate to CO_3^{2-}+H_2 is close to thermodynamic equilibrium under core conditions, but exergonic under slab conditions.

In summary, given that many known catabolic reactions have significant free energy yields under core and slab conditions, the very low to absent microbial activity in high-pH fluids of the three mud volcanoes cannot be explained with absence of suitable substrates for energy-yielding catabolic reactions.

Potential Physiological Limits to Microbial Life in Subseafloor Serpentinites

Next we will discuss the potential roles of pressure, temperature, pH, and lack of fluid mixing as variables that limit the proliferation of microbial life in serpentinite mud volcanoes of the Mariana Forearc.

Among these variables, pressure alone is perhaps the least likely to be a strong limiting factor. We calculate *in situ* pressures of 2,740, 2,670–2,820, and 3,300–3,500 bar for the subducting slabs of Yinazao, Fantangisña, and Asùt Tesoru, respectively. While these values are higher than those in surface sediments of the deepest part of the world's oceans, the Mariana's Trench, or any subseafloor cores that have been recovered to date, laboratory experiments suggest that microbial life can remain metabolically active at >10,000 bar (Sharma et al., 2002) and survive even higher pressures (20,000–30,000 bar; Hazael et al., 2016). Furthermore, experiments suggest that the ability to survive high pressure (>10,000 bar) can evolve rapidly, even in microbial strains that are not pre-adapted to elevated pressure, such as *Escherichia coli* or *Shewanella oneidensis* (Vanlint et al., 2011; Hazael et al., 2014).

Temperature is a more likely limiting factor. As aforementioned, the slab temperatures at Fantangisña (150°C) and Asùt Tesoru (250°C) are above the known temperature limit of life (122°C; Takai et al., 2008). Furthermore, even though temperature in the subducting slab at Yinazao (80°C) is below this temperature limit, there is evidence that microbial life ceases at or below 80°C in energy-limited subsurface environments (Head et al., 2003; Inagaki et al., 2015; Møller et al., 2018; Heuer et al., 2019), despite heat-driven increases in the release of energy substrates from thermogenic (e.g., Wellsbury et al., 1997; Parkes et al., 2007) or abiotic reactions (e.g., McCollom and Seewald, 2001, 2003a). This lower temperature limit in the subsurface may exist for the following reasons. Rates of biomolecule-damage increase exponentially with temperature (e.g., Lindahl and Nyberg, 1972; Wolfenden et al., 1998; Steen et al., 2013). Cells may adjust their biomolecule compositions toward building blocks with higher thermal stability, e.g., DNA with higher GC content, and amino acids with lower racemization rates at elevated temperature. Yet, the resulting enhanced thermal stability is minor compared to the impact of temperature on biomolecule damage rates. For instance, over a temperature increase from 2 to 80°C, increases in racemization rates may vary by one order of magnitude between amino acids; yet this difference is small considering that racemization rates of all amino acids increase by ∼3–4 orders of magnitude over this temperature interval (Steen et al., 2013; Lever et al., 2015). Due to this dramatic increase in energy needed for biomolecule repair, it has been proposed that the upper temperature limit of microorganisms in energy-limited subsurface habitats is lower than in energy-replete environments, e.g., laboratory growth media or hydrothermal vent chimneys (Lever et al., 2015). Yet, crucially, the temperature argument only applies if the mud fluids remain free of microbial recolonization during ascent. If there is any significant microbial re-inoculation of cooled but presumably sterile serpentinite mud fluids from sediments or other fluids during ascent, then these microbial colonizers could potentially thrive as a result of the high concentrations of energy substrates and the high free energy yields of catabolic reactions. Indeed, geochemical data from our study, and from a study on a borehole observatory at the nearby South Chamorro Seamount (IODP Site 1200C; Kawagucci et al., 2018), suggest at most minimal recolonization of Mariana forearc serpentinite muds during ascent from the subducting slab.

The other potentially important factor is pH. Porewater pH values in high-pH fluids (Yinazao: ∼10.7; Fantangisña: ∼11.2; Asùt Tesoru: ∼12.4) and for the underlying subducting slab (Yinazao: ∼11.2; Fantangisña: ∼11.0; Asùt Tesoru: ∼12.5; Fryer et al., 2018c) are in the growth range of microbial pure cultures

TABLE 2 | Mean Gibbs energies (ΔG_r) (±standard deviation) of potential catabolic reactions in high-pH fluids of each mud volcano.

e^- donors by reaction type	Reaction	Yinazao		Fantangisña		Asùt Tesoru	
		2.6°C	80°C	3.5°C	150°C	2.2°C	250°C
Sulfate reduction							
H_2	$4\ H_2 + SO_4^{2-} + H^+ \rightarrow 4\ H_2O + HS^-$	−95 ± 16	−57 ± 20	−127 ± 10	−77 ± 15	−140 ± 6	−63 ± 12
Formate	$4\ HCOO^- + SO_4^{2-} \rightarrow HS^- + 4\ CO_3^{2-} + 3\ H^+$	−111 ± 10	−149 ± 9	−129 ± 5	−165 ± 5	−163 ± 3	−253 ± 5
Acetate	$CH_3COO^- + SO_4^{2-} \rightarrow HS^- + 2\ CO_3^{2-} + 2\ H^+$	−69 ± 3	−114 ± 4	−73 ± 2	−134 ± 1	−87 ± 1	−207 ± 3
Propionate	$2\ CH_3CH_2COO^- + 3\ SO_4^{2-} + 2\ H_2O \rightarrow 3\ HS^- + 6\ CO_3^{2-} + 2\ H_2 + 7\ H^+$	−230 ± 12	−379 ± 15	+225 ± 10	−449 ± 11	−252 ± 4	−677 ± 9
Butyrate	$2\ CH_3CH_2CH_2COO^- + 4\ SO_4^{2-} + 4\ H_2O \rightarrow 4\ HS^- + 8\ CO_3^{2-} + 4\ H_2 + 10\ H^+$	−310 ± 20	−533 ± 26	−277 ± 16	−604 ± 17	−322 ± 7	−947 ± 14
Carbon monoxide	$4\ CO + SO_4^{2-} + 4\ H_2O \rightarrow 4\ CO_3^{2-} + HS^- + 7\ H^+$	−322 ± 5	−397 ± 7	−370 ± 7	−444 ± 4	−399 ± 5	−552 ± 11
Methane	$CH_4 + SO_4^{2-} \rightarrow HS^- + CO_3^{2-} + H^+ + H_2O$	−27 ± 4	−43 ± 6	−32 ± 2	−58 ± 2	−52 ± 2	−117 ± 3
Methanogenesis							
H_2	$4\ H_2 + CO_3^{2-} + 2\ H^+ \rightarrow CH_4 + 3\ H_2O$	−68 ± 14	−10 ± 18	−95 ± 10	−15 ± 15	−88 ± 5	+59 ± 9
Formate	$4\ HCOO^- + H_2O \rightarrow CH_4 + 3\ CO_3^{2-} + 2\ H^+$	−84 ± 8	−102 ± 11	−98 ± 4	−103 ± 5	−112 ± 2	−130 ± 4
Acetate	$CH_3COO^- + H_2O \rightarrow CH_4 + CO_3^{2-} + H^+$	−42 ± 4	−66 ± 5	−41 ± 2	−72 ± 2	−36 ± 1	−84 ± 2
Carbon monoxide	$4\ CO + 5\ H_2O \rightarrow CH_4 + 3\ CO_3^{2-} + 6\ H^+$	−295 ± 5	−350 ± 6	−339 ± 6	−382 ± 5	−346 ± 6	−430 ± 9
Acetogenesis							
H_2	$4\ H_2 + 2\ CO_3^{2-} + 3\ H^+ \rightarrow CH_3COO^- + 4\ H_2O$	−25 ± 16	+57 ± 20	−53 ± 11	+59 ± 16	−52 ± 6	+145 ± 11
Formate	$4\ HCOO^- \rightarrow CH_3COO^- + 2\ CO_3^{2-} + H^+$	−42 ± 6	−35 ± 8	−56 ± 3	−29 ± 5	−76 ± 1	−45 ± 3
Formate + H_2	$2\ HCOO^- + 2\ H_2 + H^+ \rightarrow CH_3COO^- + 2\ H_2O$	−33 ± 8	+12 ± 10	−55 ± 6	+15 ± 10	−64 ± 3	+50 ± 6
Carbon monoxide	$4\ CO + 4\ H_2O \rightarrow CH_3COO^- + 2\ CO_3^{2-} + 5\ H^+$	−252 ± 4	−283 ± 5	−296 ± 5	−309 ± 4	−311 ± 4	−344 ± 9
Carbon monoxide + H_2	$2\ CO + 2\ H_2 \rightarrow CH_3COO^- + H^+$	−135 ± 8	−92 ± 10	−172 ± 5	−104 ± 8	−181 ± 4	−74 ± 8
Fermentation							
Propionate	$CH_3CH_2COO^- + 3\ H_2O \rightarrow CH_3COO^- + CO_3^{2-} + 3\ H_2 + 2\ H^+$	+2 ± 12	−59 ± 16	+25 ± 8	−64 ± 12	+32 ± 4	−116 ± 9
Butyrate	$CH_3CH_2CH_2COO^- + 2\ H_2O \rightarrow 2\ CH_3COO^- + 2\ H_2 + H^+$	−16 ± 3	−60 ± 11	+7 ± 5	−55 ± 7	−14 ± 3	−89 ± 6
Glucose to propionate	$C_6H_{12}O_6 + 5\ H_2O \rightarrow CH_3CH_2COO^- + 3\ CO_3^{2-} + 5\ H_2 + 7\ H^+$	−358 ± 21	−519 ± 26	−323 ± 15	−554 ± 20	−340 ± 7	−765 ± 14
Glucose to butyrate	$C_6H_{12}O_6 + 2\ H_2O \rightarrow CH_3CH_2CH_2COO^- + 2\ CO_3^{2-} + 2\ H_2 + 5\ H^+$	−365 ± 9	−467 ± 11	−361 ± 8	−512 ± 10	−375 ± 3	−659 ± 6
Carbon monoxide production							
H_2	$H_2 + CO_3^{2-} + 2\ H^+ \rightarrow CO + 2\ H_2O$	+57 ± 4	+85 ± 5	+61 ± 3	+92 ± 4	+65 ± 1	+122 ± 3
Formate	$HCOO^- + H^+ \rightarrow CO + H_2O$	+53 ± 2	+62 ± 2	+60 ± 1	+70 ± 1	+59 ± 1	+75 ± 2
Formate oxidation							
Formate	$HCOO^- + H_2O \rightarrow CO_3^{2-} + H_2 + H^+$	−4 ± 5	−23 ± 6	−1 ± 2	−22 ± 3	−6 ± 1	−47 ± 3

Calculations were done at in situ temperature, pressure, and pH of cores during sampling (left column) and under slab conditions (right column). Estimated pH values under slab conditions were 11.2 for Yinazao, 11.0 for Fantangisña, and 12.5 for Asùt Tesoru. In situ pressures were calculated based on hydrostatic pressure assuming a seawater density of 1.013 g cm^{-3} and a mud density of 1.8 g cm^{-3} (based on Fryer et al., 2018b). Thermodynamically unfavorable reactions with positive Gibbs energies are shaded.

(Takai et al., 2005; Suzuki et al., 2014; current record: pH 12.5, Takai et al., 2001; reviewed in Takai, 2019). Furthermore, there have been several enrichments of microorganisms and microbial DNA detections based on natural serpentinitic fluids with a pH≥12 (e.g., Crespo-Medina et al., 2014; Morrill et al., 2014; Kohl et al., 2016; Brazelton et al., 2017; Suzuki et al., 2017) including mud and borehole fluids of the nearby South Chamorro Seamount (Curtis et al., 2013; Kawagucci et al., 2018). Based on measured pH values, microbial life should therefore be possible in high-pH muds of the three mud volcanoes. Nonetheless, it is possible that the *in situ* pH is considerably higher than measured. The *in situ* pH in mud fluids at South Chamorro, which has the same measured pH value as Asùt Tesoru (12.5), has been estimated to be significantly higher (13.1; Mottl, 2009), and thus significantly above the known pH limit of microbial life. Furthermore, it is possible that high pH poses an effective barrier to microbial recolonization from sediment or other fluids during ascent, if colonizing cells are not adapted to such high pH.

In conclusion, elevated temperature (80–250°C) and extreme pH can explain the (near) absence of microbial life in ascending serpentinite mud fluids of the Yinazao, Fantangisña, and Asùt Tesoru mud volcanoes. If temperature functions as a natural sterilizing agent in the subducting slab, then this would indicate

minimal recolonization of fluids during their long ascent (Yinazao: ∼50,000 years, Asùt Tesoru: ∼130,000 years), during which their temperatures drop within the known limits of life (Fryer et al., 2018b; **Table 2**). The absence of recolonization could be due to recruitment limitation, e.g., no or only minimal mixing with other fluids or sediments containing microbial life. This notion is supported by the very low cell numbers and absence of clear microbial activity in moderate-pH fluids of the same three mud volcanoes. Alternatively, microbial life present in other fluids or sediments that come into contact with high-pH serpentinite fluids during ascent may not tolerate the high pH of serpentinite fluids.

Potential Sources and Production Mechanisms of Deep SCOAs

We document a strong increase in total SCOA concentrations and systematic shift in the composition of SCOAs in high-pH serpentinite muds that is correlated with distance to the Mariana Trench and slab temperature (**Figures 3–6**). The shift in SCOA compositions is mainly due to concentration increases of acetate and especially formate (**Figure 5**). Concentrations of propionate, which is the dominant SCOA at Yinazao, butyrate, or other SCOAs do not change substantially with distance to trench or slab temperature. Lactate (and CO) concentrations are even overall higher in moderate-pH compared to high-pH fluids.

The factors that are responsible for the strong changes in SCOA compositions are unclear. Distance to trench *per se* is an unlikely driver, but distance to trench is correlated with time since initial subduction and with pressure. SCOA compositions could evolve as production rates of different SCOAs change as a function of time and pressure. However, time and pressure effects are unlikely to be the main drivers behind the observed trends. Relative to Yinazao, distance to trench only changes by ∼13, ∼31, and ∼56% at Fantangisña, Asùt Tesoru, and Conical Seamount, respectively, and pressure also only increases by at most ∼30% from Yinazao to Asùt Tesoru (no data for Conical). By contrast, formate and acetate concentrations increase exponentially by ∼3 and ∼2 orders of magnitude, respectively, from Yinazao to Conical Seamount (**Figures 5**, **6**). This exponential increase is consistent with the well-known mathematical relationship between temperature and rates of chemical reactions (Arrhenius equation), and suggests that temperature is the main driver behind the observed differences in formate and acetate concentrations.

As slab temperatures increase, the sources of individual SCOAs and/or the balance between production and consumption of individual SCOAs appear to change. Concentrations of formate, acetate, butyrate, and CH_4 in the low micromolar and submicromolar range in high-pH muds of Yinazao are in the typical range of non-methanogenic marine sediments (Glombitza et al., 2014, 2015), and provide no indications of significant additional, non-diagenetic inputs. Only propionate and H_2 stand out, albeit only slightly. Propionate concentrations (∼5–10 μM) exceed those in typical marine sediments (≤2 μM; Glombitza et al., 2019), and are consistent with a low-temperature thermogenic propionate input (80°C; Carothers and Kharaka, 1978). H_2 concentrations (∼1–100 μM) are clearly higher than in typical marine sediments (<1 μM; e.g., Hoehler et al., 1998; Lin et al., 2012) and are consistent with a low-temperature serpentinization fluid input (Mayhew et al., 2013; Miller et al., 2017). Going from Yinazao (80°C) to Fantangisña (150°C), the clear increases in formate (to ∼10 μM) and especially H_2 concentrations (to ∼100–1,000 μM) are consistent with temperature-driven increases in serpentinization rates. By contrast, a significant stimulation of thermogenic processes, which would be expected to clearly increase concentrations of others SCOAs, is not evident.

A big shift in SCOA compositions occurs from Fantangisña (150°C) to Asùt Tesoru (250°C), where formate and acetate concentrations increase 15- and 7-fold, and methane and H_2 concentrations increase ∼200- and 4-fold, respectively (**Figure 3**). The observed increases in formate and acetate concentrations continue as temperatures increase further from Asùt Tesoru to Conical Seamount (350°C). For reasons, that we discuss in the next paragraphs, we believe that these strong increases in formate and acetate concentrations are driven by serpentinization.

High formate concentrations are a common feature of serpentinizing systems (Mottl et al., 2003; McCollom and Bach, 2009; Schrenk et al., 2013), and are attributed to a metastable equilibrium of formate with H_2 and CO_3^{2-} (McCollom and Seewald, 2001, 2003a). Hereby high formate concentrations result from the chemical reaction of H_2, produced during reactions of iron(II)-rich minerals with water, with CO_3^{2-} and H^+. This reaction is equivalent to the reversal of biological formate oxidation, which is shown in **Table 2**. While earlier studies suggest that formate equilibration with $H_2+CO_3^{2-}+H^+$ takes place at 175–300°C (McCollom and Seewald, 2001, 2003a), recent laboratory incubations of olivine-rich rocks indicate significant formate production from H_2+CO_2 at only 100°C (Miller et al., 2017). These data are in line with our calculations, which suggest that formate is at or near thermodynamic equilibrium with $H_2+CO_3^{2-}+H^+$ in cores, but not under estimated slab temperature, pressure, and pH (**Table 2**). The fact that this is even true for Yinazao, suggests that equilibration between formate and $H_2+CO_3^{2-}+H^+$ continues at temperatures significantly below 80°C.

The elevated acetate concentrations at Asùt Tesoru and Conical Seamount are more difficult to interpret than the elevated formate concentrations, as acetate is produced by serpentinization-related processes (Miller et al., 2017), and also is the dominant SCOA produced by thermogenic breakdown of OM (e.g., Kharaka et al., 1993; Shebl and Surdam, 1996; Dhillon et al., 2005). Though thermogenic acetate could be produced by thermal breakdown of OM from subducting sediment or mantle rock during serpentinitic alteration (Kelley and Früh-Green, 2001; McDermott et al., 2015), we consider abiotic synthesis processes to be the most likely source. This is because high rates of thermogenic acetate production are typically accompanied by significant increases in propionate and/or butyrate concentrations, which were not observed. Furthermore, isotopic data from Asùt Tesoru (Sissmann et al., *in preparation*) support an abiotic serpentinization-related production of acetate

(and formate), as δ^{13}C-values of both vary from ∼0 to ∼5‰, which is in the range of DIC, but considerably higher than the δ^{13}C values of TOC and DOC (**Figure 7**).

Geochemical Trends in Sulfate, Methane, and Bulk Organic Carbon Pools

Besides the increase in H_2 and formate concentrations, a striking change between Yinazao and Fantangisña high-pH mud fluids is the 80% decrease in sulfate concentrations, from close to seawater values (25 mM) at Yinazao to <5 mM at Fantangisña. This decrease is consistent with anhydrite ($CaSO_4$) precipitation, which has been proposed to remove most or all seawater sulfate from fluids during subduction in the Mariana forearc, and is only partially reversed by re-dissolution during fluid ascent (Kawagucci et al., 2018). By comparison, sulfate removal by thermochemical sulfate reduction, which is thermodynamically favorable in all mud volcanoes (**Table 2**), is an unlikely driver, both based on previous studies, which suggest that this process is inhibited in high-pH, serpentinitic systems (Seyfried et al., 2007), and given that sulfate concentrations increase again at higher temperatures. This strong increase in sulfate concentrations to values that exceed those in seawater in high-pH fluids of Asùt Tesoru (∼31 mM; this study) and Conical Seamount (up to ∼47 mM; Shipboard Scientific Party, 1990) is enigmatic. A possible source is redissolution of anhydrite during fluid ascent. Furthermore, antigorite, which forms at >200°C above the slab at Asùt Tesoru (Debret et al., 2019), and breaks down during serpentinization to generate oxidizing conditions that lead to sulfate production (Debret and Sverjensky, 2017), might explain the high sulfate concentrations in high-pH fluids of Asùt Tesoru and Conical Seamount. This same mechanism of antigorite breakdown could also explain the increase in DIC concentrations at Asùt Tesoru (**Figure 2D**) and the high alkalinities of 33–62 meq kg^{-1} in high-pH subsurface pore fluids of Conical Seamount (Shipboard Scientific Party, 1990).

As mentioned earlier, average CH_4 concentrations in high-pH subsurface fluids increase ∼200-fold from Fantangisña to Asùt Tesoru. Earlier data on high-pH fluids from Conical Seamount suggest that CH_4 concentrations are within the range of Asùt Tesoru (Shipboard Scientific Party, 1990), which would indicate no substantial further increases in CH_4 release as slab temperatures increase from 250 to 350°C. The sources of these very high CH_4 concentrations are controversial, and could in principle be abiotic or thermogenic. Although our SCOA data suggest that thermogenic breakdown of OM is not a dominant process of C cycling in high-pH fluids of Asùt Tesoru or Conical Seamount, potential mechanisms of abiotic CH_4 production are also unclear. Our thermodynamic calculations indicate that abiotic CH_4 formation from H_2 ($+CO_3^{2-}$) under aqueous conditions in the slab is an endergonic process (**Table 2**). By contrast, production of CH_4 by thermal decarboxylation of acetate, a reaction that has the same stoichiometry as biological methanogenesis from acetate (Kharaka et al., 1993) and is catalyzed by magnetite (McCollom and Seewald, 2003b), is thermodynamically favorable (**Table 2**). Yet, this reaction would require the production of millimolar acetate concentrations, and for >95% of this acetate to then be decarboxylated to CH_4 + CO_3^{2-}. If recent field studies on multiple submarine locations and laboratory experiments with olivine are a good indication, then it is more likely that most of the CH_4 in serpentinitic fluids of Asùt Tesoru and Conical Seamount is released from fluid inclusions within serpentinized mantle rock (McDermott et al., 2015; McCollom, 2016; Wang et al., 2018). In addition, CH_4 could form in thermodynamically distinct chemical microenvironments with H_2-rich vapors, e.g., serpentinization fronts (McCollom et al., 2016), rock fractures, or rock pores (Etiope and Whiticar, 2019). Akin to CH_4 from fluid inclusions, abiotically produced CH_4 from these microenvironments could then be liberated into mud fluids as a result of serpentinitic rock-alteration.

The TOC, DOC, and DIC isotopic compositions provide general insights into the sources of organic and inorganic carbon at Yinazao, Fantangisña, and Asùt Tesoru. Similar δ^{13}C-values (range: −21 to −30‰, with most values between −26 to −30 ‰) and similar, for the most part very low (0.01 wt. %) TOC contents indicate similar origins of TOC across all three mud volcanoes, including high-pH and moderate-pH muds (**Figure 7**, **Supplementary Figure S5**). These values are mostly lower than TOC of marine phytoplankton and suggest that—if they are of sedimentary origin—there is a significant terrestrial TOC contribution. While δ^{13}C-values of sedimentary TOC in the Mariana Trench are dominated by marine phytoplankton-derived organic carbon with higher isotopic values (−19 to −21‰), local layers with potentially significant terrestrial contributions (−24 to −25‰) were noted previously (Luo et al., 2017). Thus, it is possible that terrestrial TOC or certain ^{13}C-enriched marine TOC fractions are selectively enriched during subduction, as a result of greater resistance to microbial and heat-driven degradation processes. Alternatively, given that the TOC contents and δ^{13}C values are in the same range as those from other oceanic basement rocks [mostly 0–0.02 wt. %, −25 to −30‰; compiled in (Delacour et al., 2008)], it is also possible that most of the TOC is indigenous to the overlying plate. Heat-driven serpentinitic alteration would then release soluble fractions of mantle rock-bound TOC into solution and drive the increase in DOC concentrations in high-pH fluids from Yinazao to Asùt Tesoru. At Asùt Tesoru, the 4-fold increase in DOC concentrations compared to Fantangisña can, however, only in part be explained by release of rock-bound indigenous organic carbon. Here the strong isotopic offset (∼+10‰) of DOC relative to TOC suggests that a major fraction of DOC derives from a source that is significantly heavier than TOC. The contributions of formate and acetate, which account for ∼10–12% of the DOC and have ^{13}C-isotopic values in the range of DIC at Asùt Tesoru, can only explain an isotopic offset of ∼+2‰. Thus, the origin of a major component of the DOC pool in high-pH fluids of Asùt Tesoru remains unknown.

CONCLUSIONS

Our study produces novel insights into the controls on the production of microbial energy substrates, in particular SCOAs, in deeply buried subducting slab environments. Despite the

presence of high microbial energy substrate concentrations and significant Gibbs energy yields of a wide range of catabolic reactions, microorganisms are rare or absent, and no unequivocal evidence for microbial activity could be detected. This has implications for our understanding of deeply buried serpentinitic environments as potential habitats or even deep hotspots of microbial life, and suggests that the combination of temperature, highly alkaline pH, and dispersal limitation may strongly limit microbial population size in these environments. Instead, due to the absence of strong diagenetic alteration during fluid ascent over tens of millennia, high-pH fluids from mud volcanoes offer a unique window into the abiotic production mechanisms of microbial energy substrates by serpentinization and by serpentinization-related processes within subduction zones. Future studies will reveal the mechanisms by which some of these energy compounds, e.g., acetate, CH_4, are produced, which unknown sources contribute to the strongly elevated DOC concentrations in high-temperature, high-pH fluids, and what the origins of the still enigmatic moderate-pH fluids are.

DATA AVAILABILITY

The datasets generated for this study are available on request to the corresponding author.

AUTHOR CONTRIBUTIONS

PE and ML designed the study. PE, KT, OS, SSu, CM, SSa, PS, ET, and ML took samples, performed measurements, and/or contributed data analyses. SB, CG, BJ, and YM provided technical advice and support with the analyses. PE and ML wrote the manuscript with input from all co-authors.

FUNDING

This research used samples and/or data provided by the International Ocean Discovery Program (IODP). Additional support for the participation in IODP Expedition came from SwissDrilling (www.swissdrilling.ch), which is funded by the Swiss National Science Foundation (SNSF; www.snf.ch) project No. 182091 and by the Deep Carbon Observatory (www.deepcarbon.net). Funding for this research was provided by ETH Zurich. CG and BJ were supported by the Danish National Research Foundation [DNRF104], the European Research Council [ERC Advanced Grant #294200], and the Danish Council for Independent Research [DFF−7014-00196]. CM was supported by a NERC UK IODP Phase 2 Moratorium Award [NE/P020909/1].

ACKNOWLEDGMENTS

We thank Madalina Jaggi for laboratory support. PS thanks the Laboratoire d'Excellence LabexMER (ANR-10-LABX-19) and the GPI Laboratories, Inc. (Grand Rapids, MI, USA) for funding and analyses. OS thanks IODP-France for funding.

SUPPLEMENTARY MATERIAL

The Supplementary Material for this article can be found online at: https://www.frontiersin.org/articles/10.3389/fmicb.2019.01729/full#supplementary-material

Supplementary Figure S1 | (A) Chloride concentration depth profiles at all three mud volcanoes. **(B)** Depth profiles of sulfate-to-chloride concentration ratios (both mM). High-pH fluids (summit sites) are indicated by red marker symbols, moderate-pH fluids (flank sites) by black marker symbols. The dashed gray vertical lines indicate typical seawater chloride concentrations (559 mM) and seawater sulfate-to-chloride ratios [0.0517; assumes [sulfate] = 28.9 mM]. The dashed red vertical lines indicate chloride concentration asymptotes for high-pH fluids [Yinazao: 460 mM; Fantangisña: 480 mM; Asùt Tesoru (U1496A): 540 mM]. Chloride concentrations in high-pH fluids that are significantly below those in seawater indicate a potential freshwater contribution from dewatering of deeply buried clay minerals.

Supplementary Figure S2 | Concentration profiles of pyruvate, lactate, and valerate across boreholes of the three mud volcanoes.

Supplementary Figure S3 | Concentration profiles of CO across boreholes of the three mud volcanoes.

Supplementary Figure S4 | Concentration ratios of formate-to-acetate, formate-to-propionate, and acetate-to-propionate vs. temperature in the subducting slab (upper panel) and distance to the Mariana Trench (lower panel).

Supplementary Figure S5 | δ^{13}C-isotopic compositions of TOC, DOC, and DIC from moderate-pH (left column) and high-pH (right column) mud fluids of three serpentinite mud volcanoes drilled during IODP Expedition 366.

REFERENCES

Aoyama, S., Nishizawa, M., Miyazaki, J., Shibuya, T., Ueno, Y., and Takai, K. (2018). Recycled Archean sulfur in the mantle wedge of the Mariana Forearc and microbial sulfate reduction within an extremely alkaline serpentine seamount. *Earth Planet. Sci. Lett.* 491, 109–120. doi: 10.1016/j.epsl.2018.03.002

Bach, W. (2016). Some compositional and kinetic controls on the bioenergetic landscapes in oceanic basement. *Front. Microbiol.* 7:107. doi: 10.3389/fmicb.2016.00107

Barth, T., and Bjørlykke, K. (1993). Organic acids from source rock maturation: generation potentials, transport mechanisms and relevance for mineral diagenesis. *Appl. Geochem.* 8, 325–337. doi: 10.1016/0883-2927(93)90002-X

Brazelton, W. J., Schrenk, M. O., Kelley, D. S., and Baross, J. A. (2006). Methane- and sulfur-metabolizing microbial communities dominate the Lost City hydrothermal field ecosystem. *Appl. Environ. Microbiol.* 72, 6257–6270. doi: 10.1128/AEM.00574-06

Brazelton, W. J., Thornton, C. N., Hyer, A., Twing, K. I., Longino, A. A., Lang, S. Q., et al. (2017). Metagenomic identification of active methanogens and methanotrophs in serpentinite springs of the Voltri Massif, Italy. *PeerJ* 5:e2945. doi: 10.7717/peerj.2945

Breitenbach, S. F. M., and Bernasconi, S. M. (2011). Carbon and oxygen isotope analysis of small carbonate samples (20 to 100 µg) with a GasBench II preparation device. *Rapid Commun. Mass Spectrometry* 25, 1910–1914. doi: 10.1002/rcm.5052

Canfield, D. E., Jørgensen, B. B., Fossing, H., Glud, R., Gundersen, J., Ramsing, N. B., et al. (1993). Pathways of organic carbon oxidation in three continental margin sediments. *Mar. Geol.* 113, 27–40. doi: 10.1016/0025-3227(93)90147-N

Canfield, D. E., Kristensen, E., and Thamdrup, B. (2005). "Heterotrophic carbon metabolism," in *Advances in Marine*

Biology, eds E. K. Donald, E. Canfield, and T. Bo (Cambridge, MA: Academic Press), 129–166. doi: 10.1016/S0065-2881(05)48005-0

Carothers, W. W., and Kharaka, Y. K. (1978). Aliphatic Acid Anions in Oil-Field Waters–Implications for Origin of Natural Gas. *AAPG Bull.* 62, 2441–2453. doi: 10.1306/C1EA5521-16C9-11D7-8645000102C1865D

Clegg, S. L., and Whitfield, M. (1991). "Activity coefficients in natural waters," in *Activity Coefficients in Electrolyte Solutions,* ed. K.S. Pitzer. (Boca Raton, FL: CRC Press), 279–434. doi: 10.1201/9781351069472-6

Cooles, G. P., Mackenzie, A. S., and Parkes, R. J. (1987). Non-hydrocarbons of significance in petroleum exploration: volatile fatty acids and non-hydrocarbon gases. *Miner. Magaz.* 51, 483–493. doi: 10.1180/minmag.1987.051.362.03

Crespo-Medina, M., Twing, K. I., Kubo, M. D. Y., Hoehler, T. M., Cardace, D., McCollom, T., et al. (2014). Insights into environmental controls on microbial communities in a continental serpentinite aquifer using a microcosm-based approach. *Front. Microbiol.* 5:604. doi: 10.3389/fmicb.2014.00604

Cross, M. M., Manning, D. A. C., Bottrell, S. H., and Worden, R. H. (2004). Thermochemical sulphate reduction (TSR): experimental determination of reaction kinetics and implications of the observed reaction rates for petroleum reservoirs. *Organic Geochem.* 35, 393–404. doi: 10.1016/j.orggeochem.2004.01.005

Curtis, A. C., Wheat, C. G., Fryer, P., and Moyer, C. L. (2013). Mariana forearc serpentinite mud volcanoes harbor novel communities of extremophilic archaea. *Geomicrobiol. J.* 30, 430–441. doi: 10.1080/01490451.2012.705226

Debret, B., Albers, E., Walter, B., Price, R., Barnes, J. D., Beunon, H., et al. (2019). Shallow forearc mantle dynamics and geochemistry: new insights from IODP Expedition 366. *Lithos* 326–327, 230–245. doi: 10.1016/j.lithos.2018.10.038

Debret, B., and Sverjensky, D. A. (2017). Highly oxidising fluids generated during serpentinite breakdown in subduction zones. *Sci. Rep.* 7:10351. doi: 10.1038/s41598-017-09626-y

Delacour, A., Früh-Green, G. L., Bernasconi, S. M., Schaeffer, P., and Kelley, D. S. (2008). Carbon geochemistry of serpentinites in the Lost City hydrothermal system (30 degrees N, MAR). *Geochim. Cosmochim. Acta* 72, 3681–3702. doi: 10.1016/j.gca.2008.04.039

Dhillon, A., Lever, M., Lloyd, K. G., Albert, D. B., Sogin, M. L., and Teske, A. (2005). Methanogen diversity evidenced by molecular characterization of methyl coenzyme M reductase A (mcrA) genes in hydrothermal sediments of the Guaymas Basin. *Appl. Environ. Microbiol.* 71, 4592–4601. doi: 10.1128/AEM.71.8.4592-4601.2005

Egeberg, P. K., and Barth, T. (1998). Contribution of dissolved organic species to the carbon and energy budgets of hydrate bearing deep sea sediments (Ocean Drilling Program Site 997 Blake Ridge). *Chem. Geol.* 149, 25–35. doi: 10.1016/S0009-2541(98)00033-3

Etiope, G., and Whiticar, M. J. (2019). Abiotic methane in continental ultramafic rock systems: Towards a genetic model. *Appl. Geochem.* 102, 139–152. doi: 10.1016/j.apgeochem.2019.01.012

Finke, N., and Jørgensen, B. B. (2008). Response of fermentation and sulfate reduction to experimental temperature changes in temperate and Arctic marine sediments. *ISME J.* 2, 815–829. doi: 10.1038/ismej.2008.20

Finke, N., Vandieken, V., and Jørgensen, B. B. (2007). Acetate, lactate, propionate, and isobutyrate as electron donors for iron and sulfate reduction in Arctic marine sediments, Svalbard. *FEMS Microbiol. Ecol.* 59, 10–22. doi: 10.1111/j.1574-6941.2006.00214.x

Fischer, F., and Tropsch, H. (1926). Über die direkte Synthese von Erdöl-Kohlenwasserstoffen bei gewöhnlichem Druck. (Erste Mitteilung). *Berichte Deutsch Chem Gesellschaft* 59, 830–831. doi: 10.1002/cber.19260590442

Froelich, P. N., Klinkhammer, G. P., Bender, M. L., Luedtke, N. A., Heath, G. R., Cullen, D., et al. (1979). Early oxidation of organic matter in pelagic sediments of the eastern equatorial Atlantic: suboxic diagenesis. *Geochim. Cosmochim. Acta* 43, 1075–1090. doi: 10.1016/0016-7037(79)90095-4

Früh-Green, G., Andreani, M., Baross, J., Bernasconi, S. M., Boschi, C., Brazelton, W., et al. (2014). "Serpentinization and life: biogeochemical and tectono-magmatic processes in young mafic and ultramafic seafloor," ed. G. Fruh-Green. Available online at: http://www.eso.ecord.org/docs/357/758-Full2_Fruh-Green.pdf: ECORD Science Operator.

Früh-Green, G. L., Connolly, J. A. D., Plas, A., Kelley, D. S., and Grobéty, B. (2004). Serpentinization of oceanic peridotites: implications for geochemical cycles and biological activity. *Geophys. Monogr. Ser.* 144, 119–136. doi: 10.1029/144GM08

Früh-Green, G. L., Kelley, D. S., Bernasconi, S. M., Karson, J. A., Ludwig, K. A., Butterfield, D. A., et al. (2003). 30,000 years of hydrothermal activity at the lost city vent field. *Science* 301, 495–498. doi: 10.1126/science.1085582

Fryer, P. (2012). Serpentinite mud volcanism: observations, processes, and implications. *Annu. Rev. Mar. Sci.* 4, 345–373. doi: 10.1146/annurev-marine-120710-100922

Fryer, P., Mottl, M. J., Wheat, G., Moyer, C. L., Moore, G., Goodliffe, A., et al. (2003). "Mariana convergent margin: geochemical, tectonic, and biological processes at intermediate depths of an active subduction factory," ed. P. Fryer. Available online at: http://iodp.tamu.edu/scienceops/precruise/mariana/505-Full5.pdf:~IODP.

Fryer, P., Wheat, C. G., Williams, T., Albers, E., Bekins, B., Debret, B. P. R., et al. (2018a). "Expedition 366 methods," in *Proceedings of the International Ocean Discovery Program*, Vol. 366, ed. S. C. Lewis (College Station, TX: International Ocean Discovery Program). doi: 10.14379/iodp.proc.366.102.2018

Fryer, P., Wheat, C. G., Williams, T., Albers, E., Bekins, B., Debret, B. P. R., et al. (2018b). "Mariana convergent margin and south chamorro seamount," in *Proceedings of the International Ocean Discovery Program,* ed. S.C. Lewis (College Station, TX: International Ocean Discovery Program). doi: 10.14379/iodp.proc.366.2018

Fryer, P., Wheat, C. G., Williams, T., Albers, E. J., Bekins, B., Debret, B. P. R., et al. (2018c). "Expedition 366 summary," in *Proceedings of the International Ocean Discovery Program*, Vol. 366, ed S.C. Lewis (College Station, TX: International Ocean Discovery Program). doi: 10.14379/iodp.proc.366.101.2018

Fryer, P., Wheat, G., Williams, T., and the Expedition 366 Scientists (2017). Expedition 366 preliminary report: mariana convergent margin and south chamorro seamount. *Int. Ocean Discov. Progr.* 1–40. doi: 10.14379/iodp.pr.366.2017

Glombitza, C., Egger, M., Røy, H., and Jørgensen, B. B. (2019). Controls on volatile fatty acid concentrations in marine sediments (Baltic Sea). *Geochim. Cosmochim. Acta* 258, 226–241. doi: 10.1016/j.gca.2019.05.038

Glombitza, C., Jaussi, M., Roy, H., Seidenkrantz, M. S., Lomstein, B. A., and Jorgensen, B. B. (2015). Formate, acetate, and propionate as substrates for sulfate reduction in sub-arctic sediments of Southwest Greenland. *Front. Microbiol.* 6:846. doi: 10.3389/fmicb.2015.00846

Glombitza, C., Pedersen, J., Røy, H., and Jørgensen, B. B. (2014). Direct analysis of volatile fatty acids in marine sediment porewater by two-dimensional ion chromatography-mass spectrometry. *Limnol. Oceanogr. Methods* 12, 455–468. doi: 10.4319/lom.2014.12.455

Goodwin, S., and Zeikus, J. G. (1987). Ecophysiological adaptations of anaerobic bacteria to low pH: analysis of anaerobic digestion in acidic bog sediments. *Appl. Environ. Microbiol.* 53:57.

Haggerty, J. A., and Fisher, J. B. (1992). "Short-chain organic acids in interstitial waters from mariana and bonin forearc serpentines: leg 125," in *Proceedings of the Ocean Drilling Program* (College Station, TX), 125. doi: 10.2973/odp.proc.sr.125.125.1992

Hazael, R., Foglia, F., Kardzhaliyska, L., Daniel, I., Meersman, F., and Mcmillan, P. (2014). Laboratory investigation of high pressure survival in Shewanella oneidensis MR-1 into the gigapascal pressure range. *Front. Microbiol.* 5:612. doi: 10.3389/fmicb.2014.00612

Hazael, R., Meersman, F., Ono, F., and McMillan, P. F. (2016). Pressure as a limiting factor for life. *Life* 6:34. doi: 10.3390/life6030034

Head, I. M., Jones, D. M., and Larter, S. R. (2003). Biological activity in the deep subsurface and the origin of heavy oil. *Nature* 426, 344–352. doi: 10.1038/nature02134

Heuer, V. B., Lever, M. A., Morono, Y., and Teske, A. (2019). The limits of life and the biosphere in Earth's interior. *Oceanography* 32, 208–211. doi: 10.5670/oceanog.2019.147

Heuer, V. B., Pohlman, J. W., Torres, M. E., Elvert, M., and Hinrichs, K.-U. (2009). The stable carbon isotope biogeochemistry of acetate and other dissolved carbon species in subseafloor sediments at the northern Cascadia Margin. *Geochim. Cosmochim. Acta* 73, 3323–3336. doi: 10.1016/j.gca.2009.03.001

Hoehler, T. M., Alperin, M. J., Albert, D. B., and Martens, C. S. (1998). Thermodynamic control on hydrogen concentrations in anoxic sediments. *Geochim. Cosmochim. Acta* 62, 1745–1756. doi: 10.1016/S0016-7037(98)00106-9

Hoehler, T. M., and Jørgensen, B. B. (2013). Microbial life under extreme energy limitation. *Nat. Rev. Microbiol.* 11, 83–94. doi: 10.1038/nrmicro2939

Hoehler, T. M., Martens, C. S., Albert, D. B., and Alperin, M. J. (2001). Apparent minimum free energy requirements for methanogenic Archaea and sulfate-reducing bacteria in an anoxic marine sediment. *FEMS Microbiol. Ecol.* 38, 33–41. doi: 10.1111/j.1574-6941.2001.tb00879.x

Holm, N. G., and Andersson, E. M. (1998). "Hydrothermal systems," in *The Molecular Origins of Life: Assembling Pieces of the Puzzle*, ed. A. Brack (Cambridge: Cambridge University Press), 86–99. doi: 10.1017/CBO9780511626180.006

Holm, N. G., and Neubeck, A. (2009). Reduction of nitrogen compounds in oceanic basement and its implications for HCN formation and abiotic organic synthesis. *Geochem. Trans.* 10:9. doi: 10.1186/1467-4866-10-9

Hulme, S. M., Wheat, C. G., Fryer, P., and Mottl, M. J. (2010). Pore water chemistry of the Mariana serpentinite mud volcanoes: A window to the seismogenic zone. *Geochem. Geophys. Geosyst.* 11:1. doi: 10.1029/2009GC002674

Ijiri, A., Inagaki, F., Kubo, Y., Adhikari, R. R., Hattori, S., Hoshino, T., et al. (2018). Deep-biosphere methane production stimulated by geofluids in the Nankai accretionary complex. *Sci. Adv.* 4:6. doi: 10.1126/sciadv.aao4631

Inagaki, F., Hinrichs, K. U., Kubo, Y., Bowles, M. W., Heuer, V. B., Hong, W. L., et al. (2015). Exploring deep microbial life in coal-bearing sediment down to 2.5 km below the ocean floor. *Science* 349, 420–424. doi: 10.1126/science.aaa6882

Joseph, A. (2017). "Chapter 6 - seafloor hot chimneys and cold seeps: mysterious life around them," in *Investigating Seafloors and Oceans,* ed. A. Joseph (Amsterdam: Elsevier), 307–375. doi: 10.1016/B978-0-12-809357-3.00006-0

Kallmeyer, J., Pockalny, R., Adhikari, R. R., Smith, D. C., and D'hondt, S. (2012). Global distribution of microbial abundance and biomass in subseafloor sediment. *Proc. Natl. Acad. Sci. U.S.A.* 109, 16213–16216. doi: 10.1073/pnas.1203849109

Kawagucci, S., Miyazaki, J., Morono, Y., Seewald, J. S., Wheat, C. G., and Takai, K. (2018). Cool, alkaline serpentinite formation fluid regime with scarce microbial habitability and possible abiotic synthesis beneath the South Chamorro Seamount. *Prog. Earth Planet. Sci.* 5:74. doi: 10.1186/s40645-018-0232-3

Kelley, D. S., and Früh-Green, G. L. (2001). Volatile lines of descent in submarine plutonic environments: insights from stable isotope and fluid inclusion analyses. *Geochim. Cosmochim. Acta* 65, 3325–3346. doi: 10.1016/S0016-7037(01)00667-6

Kelley, D. S., Karson, J. A., Fruh-Green, G. L., Yoerger, D. R., Shank, T. M., Butterfield, D. A., et al. (2005). A serpentinite-hosted ecosystem: the Lost City hydrothermal field. *Science* 307, 1428–1434. doi: 10.1126/science.1102556

Kharaka, Y. K., Lundegard, P. D., Ambats, G., Evans, W. C., and Bischoff, J. L. (1993). Generation of aliphatic acid anions and carbon dioxide by hydrous pyrolysis of crude oils. *Appl. Geochem.* 8, 317–324. doi: 10.1016/0883-2927(93)90001-W

Kiyosu, Y., and Krouse, H. R. (1990). The role of organic acid in the abiogenic reduction of sulfate and the sulfur isotope effect. *Geochem. J.* 24, 21–27. doi: 10.2343/geochemj.24.21

Kohl, L., Cumming, E., Cox, A., Rietze, A., Morrissey, L., Lang, S. Q., et al. (2016). Exploring the metabolic potential of microbial communities in ultra-basic, reducing springs at The Cedars, CA, USA: Experimental evidence of microbial methanogenesis and heterotrophic acetogenesis. *J. Geophys. Res. Biogeosci.* 121, 1203–1220. doi: 10.1002/2015JG003233

Konn, C., Charlou, J. L., Donval, J. P., Holm, N. G., Dehairs, F., and Bouillon, S. (2009). Hydrocarbons and oxidized organic compounds in hydrothermal fluids from Rainbow and Lost City ultramafic-hosted vents. *Chem. Geol.* 258, 299–314. doi: 10.1016/j.chemgeo.2008.10.034

Koschorreck, M. (2008). Microbial sulphate reduction at a low pH. *FEMS Microbiol. Ecol.* 64, 329–342. doi: 10.1111/j.1574-6941.2008.00482.x

Lang, S. Q., Bernasconi, S. M., and Früh-Green, G. L. (2012). Stable isotope analysis of organic carbon in small (μg C) samples and dissolved organic matter using a GasBench preparation device. *Rapid Commun. Mass Spectrometry* 26, 9–16. doi: 10.1002/rcm.5287

Lang, S. Q., Butterfield, D. A., Schulte, M., Kelley, D. S., and Lilley, M. D. (2010). Elevated concentrations of formate, acetate and dissolved organic carbon found at the Lost City hydrothermal field. *Geochim. Cosmochim. Acta* 74, 941–952. doi: 10.1016/j.gca.2009.10.045

Lang, S. Q., Früh-Green, G. L., Bernasconi, S. M., Brazelton, W. J., Schrenk, M. O., and Mcgonigle, J. M. (2018). Deeply-sourced formate fuels sulfate reducers but not methanogens at Lost City hydrothermal field. *Sci. Rep.* 8:755. doi: 10.1038/s41598-017-19002-5

Lever, M. A., Heuer, V. B., Morono, Y., Masui, N., Schmidt, F., Alperin, M. J., et al. (2010). Acetogenesis in deep subseafloor sediments of the Juan de Fuca Ridge Flank: a synthesis of geochemical, thermodynamic, and gene-based evidence. *Geomicrobiol. J.* 27, 183–211. doi: 10.1080/01490450903456681

Lever, M. A., Rogers, K. L., Lloyd, K. G., Overmann, J., Schink, B., Thauer, R. K., et al. (2015). Life under extreme energy limitation: a synthesis of laboratory- and field-based investigations. *FEMS Microbiol. Rev.* 39, 688–728. doi: 10.1093/femsre/fuv020

Lever, M. A., Rouxel, O. J., Alt, J., Shimizu, N., Ono, S., Coggon, R. M., et al. (2013). Evidence for microbial carbon and sulfur cycling in deeply buried ridge flank basalt. *Science* 339, 1305–1308. doi: 10.1126/science.1229240

Lin, Y.-S., Heuer, V. B., Goldhammer, T., Kellermann, M. Y., Zabel, M., and Hinrichs, K.-U. (2012). Towards constraining H2 concentration in subseafloor sediment: a proposal for combined analysis by two distinct approaches. *Geochim. Cosmochim. Acta* 77, 186–201. doi: 10.1016/j.gca.2011.11.008

Lindahl, T., and Nyberg, B. (1972). Rate of depurination of native deoxyribonucleic acid. *Biochemistry* 11, 3610–3618. doi: 10.1021/bi00769a018

Lomstein, B. A., Langerhuus, A. T., D'Hondt, S., Jorgensen, B. B., and Spivack, A. J. (2012). Endospore abundance, microbial growth and necromass turnover in deep sub-seafloor sediment. *Nature* 484, 101–104. doi: 10.1038/nature10905

Lundegard, P. D., and Kharaka, Y. K. (1990). "Geochemistry of organic acids in subsurface waters," in *Chemical Modeling of Aqueous Systems II. American Chemical Society* (Washington, DC), 169–189. doi: 10.1021/bk-1990-0416.ch013

Luo, M., Gieskes, J., Chen, L., Shi, X., and Chen, D. (2017). Provenances, distribution, and accumulation of organic matter in the southern Mariana Trench rim and slope: implications for carbon cycle and burial in hadal trenches. *Mar. Geol.* 386, 98–106. doi: 10.1016/j.margeo.2017.02.012

Manheim, F. T. (1966). A hydraulic squeezer for obtaining interstitial water from consolidated and unconsolidated sediments. *US Geol. Survey Professional Paper* 550, 171–174

Mayhew, L. E., Ellison, E. T., McCollom, T. M., Trainor, T. P., and Templeton, A. S. (2013). Hydrogen generation from low-temperature water–rock reactions. *Nat. Geosci.* 6, 478–484. doi: 10.1038/ngeo1825

McCollom, T. M. (2016). Abiotic methane formation during experimental serpentinization of olivine. *Proc. Natl. Acad. Sci.* 113, 13965–13970. doi: 10.1073/pnas.1611843113

McCollom, T. M., and Bach, W. (2009). Thermodynamic constraints on hydrogen generation during serpentinization of ultramafic rocks. *Geochim. Cosmochim. Acta* 73, 856–875. doi: 10.1016/j.gca.2008.10.032

McCollom, T. M., Klein, F., Robbins, M., Moskowitz, B., Berquó, T. S., Jöns, N., et al. (2016). Temperature trends for reaction rates, hydrogen generation, and partitioning of iron during experimental serpentinization of olivine. *Geochim. Cosmochim. Acta* 181, 175–200. doi: 10.1016/j.gca.2016.03.002

McCollom, T. M., and Seewald, J. S. (2001). A reassessment of the potential for reduction of dissolved CO2 to hydrocarbons during serpentinization of olivine. *Geochim. Cosmochim. Acta* 65, 3769–3778. doi: 10.1016/S0016-7037(01)00655-X

McCollom, T. M., and Seewald, J. S. (2003a). Experimental constraints on the hydrothermal reactivity of organic acids and acid anions: I. Formic acid and formate. *Geochim. Cosmochim. Acta* 67, 3625–3644. doi: 10.1016/S0016-7037(03)00136-4

McCollom, T. M., and Seewald, J. S. (2003b). Experimental study of the hydrothermal reactivity of organic acids and acid anions: II. Acetic acid, acetate, and valeric acid. *Geochim. Cosmochim. Acta* 67, 3645–3664. doi: 10.1016/S0016-7037(03)00135-2

McCollom, T. M., and Seewald, J. S. (2007). Abiotic synthesis of organic compounds in deep-sea hydrothermal environments. *Chem. Rev.* 107, 382–401. doi: 10.1021/cr0503660

McDermott, J. M., Seewald, J. S., German, C. R., and Sylva, S. P. (2015). Pathways for abiotic organic synthesis at submarine hydrothermal fields. *Proc. Natl. Acad. Sci.* 112, 7668–7672. doi: 10.1073/pnas.1506295112

Miller, H. M., Mayhew, L. E., Ellison, E. T., Kelemen, P., Kubo, M., and Templeton, A. S. (2017). Low temperature hydrogen production during experimental

hydration of partially-serpentinized dunite. *Geochim. Cosmochim. Acta* 209, 161–183. doi: 10.1016/j.gca.2017.04.022

Millero, F. (2000). The activity coefficients of non-electrolytes in seawater. *Mar. Chem.* 70, 5–22. doi: 10.1016/S0304-4203(00)00011-6

Millero, F. J., and Schreiber, D. R. (1982). Use of the ion pairing model to estimate activity coefficients of the ionic components of natural waters. *Am. J. Sci.* 282, 1508–1540. doi: 10.2475/ajs.282.9.1508

Møller, M. H., Glombitza, C., Lever, M. A., Deng, L., Morono, Y., Inagaki, F., et al. (2018). D:L-amino acid modeling reveals fast microbial turnover of days to months in the subsurface hydrothermal sediment of Guaymas Basin. *Front. Microbiol.* 9:967. doi: 10.3389/fmicb.2018.00967

Morita, R. Y., and Zobell, C. E. (1955). Occurrence of bacteria in pelagic sediments collected during the mid-Pacific expedition. *Deep Sea Res.* 3, 66–73. doi: 10.1016/0146-6313(55)90036-8

Morono, Y., Hoshino, T., Terada, T., Suzuki, T., Sato, T., Yuasa, H., et al. (2018). Assessment of capacity to capture DNA aerosols by clean filters for molecular biology experiments. *Microbes Environ.* 33, 222–226. doi: 10.1264/jsme2.ME18012

Morono, Y., Inagaki, F., Heuer, V. B., Kubo, Y., Maeda, L., Bowden, S., et al. (2017). "Expedition 370 methods," in *Proceedings of the International Ocean Discovery Program,* Vol. 370, ed S. C. Lewis (College Station, TX: International Ocean Discovery Program).

Morono, Y., Terada, T., Kallmeyer, J., and Inagaki, F. (2013). An improved cell separation technique for marine subsurface sediments: applications for high-throughput analysis using flow cytometry and cell sorting. *Environ. Microbiol.* 15, 2841–2849. doi: 10.1111/1462-2920.12153

Morono, Y., Terada, T., Masui, N., and Inagaki, F. (2009). Discriminative detection and enumeration of microbial life in marine subsurface sediments. *ISME J.* 3, 503–511. doi: 10.1038/ismej.2009.1

Morrill, P. L., Brazelton, W. J., Kohl, L., Rietze, A., Miles, S. M., Kavanagh, H., et al. (2014). Investigations of potential microbial methanogenic and carbon monoxide utilization pathways in ultra-basic reducing springs associated with present-day continental serpentinization: the Tablelands, NL, CAN. *Front. Microbiol.* 5:613. doi: 10.3389/fmicb.2014.00613

Mottl, M. J. (2009). Highest pH. *Geochem. News* 141:9.

Mottl, M. J., Holland, H. D., and Corr, R. F. (1979). Chemical exchange during hydrothermal alteration of basalt by seawater—II. Experimental results for Fe, Mn, and sulfur species. *Geochim. Cosmochim. Acta* 43, 869–884. doi: 10.1016/0016-7037(79)90225-4

Mottl, M. J., Komor, S. C., Fryer, P., and Moyer, C. L. (2003). Deep-slab fluids fuel extremophilic Archaea on a Mariana forearc serpentinite mud volcano: Ocean Drilling Program Leg 195. *Geochem. Geophys. Geosyst.* 4:9009. doi: 10.1029/2003GC000588

Oakley, A. J. (2008). *A multi-channel seismic and bathymetric investigation of the central Mariana convergent margin* (Ph.D. thesis). University of Hawai'i at Manoa.

Oakley, A. J., Taylor, B., and Moore, G. F. (2008). Pacific Plate subduction beneath the central Mariana and Izu-Bonin fore arcs: new insights from an old margin. *Geochem. Geophys. Geosyst.* 9, 1–28. doi: 10.1029/2007GC001820

Oakley, A. J., Taylor, B., Moore, G. F., Fryer, P., Goodliffe, A. M., and Morgan, J. K. (2007). Emplacement, growth, and gravitational deformation of serpentinite seamounts on the Mariana forearc. *Geophys. J. Intern.* 170, 615–634. doi: 10.1111/j.1365-246X.2007.03451.x

Ohara, Y., Reagan, M. K., Fujikura, K., Watanabe, H., Michibayashi, K., Ishii, T., et al. (2012). A serpentinite-hosted ecosystem in the Southern Mariana Forearc. *Proc. Natl. Acad. Sci.* 109, 2831–2835. doi: 10.1073/pnas.1112005109

Parkes, R. J., Wellsbury, P., Mather, I. D., Cobb, S. J., Cragg, B. A., Hornibrook, E. R. C., et al. (2007). Temperature activation of organic matter and minerals during burial has the potential to sustain the deep biosphere over geological timescales. *Organic Geochem.* 38, 845–852. doi: 10.1016/j.orggeochem.2006.12.011

Plummer, L. N., and Sundquist, E. T. (1982). Total individual ion activity coefficients of calcium and carbonate in seawater at 25°C and 35%. salinity, and implications to the agreement between apparent and thermodynamic constants of calcite and aragonite. *Geochim. Cosmochim. Acta* 46, 247–258. doi: 10.1016/0016-7037(82)90252-6

Preiner, M., Xavier, J. C., Sousa, F. L., Zimorski, V., Neubeck, A., Lang, S. Q., et al. (2018). Serpentinization: connecting geochemistry, ancient metabolism and industrial hydrogenation. *Life (Basel)* 8:E41. doi: 10.3390/life8040041

Proskurowski, G., Lilley, M. D., Seewald, J. S., Früh-Green, G. L., Olson, E. J., Lupton, J. E., et al. (2008). Abiogenic hydrocarbon production at Lost City hydrothermal field. *Science* 319, 604–607. doi: 10.1126/science.1151194

Quéméneur, M., Bes, M., Postec, A., Mei, N., Hamelin, J., Monnin, C., et al. (2014). Spatial distribution of microbial communities in the shallow submarine alkaline hydrothermal field of the Prony Bay, New Caledonia. *Environ. Microbiol. Rep.* 6, 665–674. doi: 10.1111/1758-2229.12184

Rempfert, K. R., Miller, H. M., Bompard, N., Nothaft, D., Matter, J. M., Kelemen, P., et al. (2017). Geological and geochemical controls on subsurface microbial life in the Samail Ophiolite, *Oman. Front. Microbiol.* 8:56. doi: 10.3389/fmicb.2017.00056

Sabatier, P., and Senderens, J. B. (1899). Action of hydrogen on acetylene in presence of nickel. *Comptes Rendus Hebdomadais Seances l'Acad. Sci.* 128:1173.

Schink, B., and Thauer, R. K. (1988). "Energetics of syntrophic methane formation and the influence of aggregation," in *Granular Anaerobic Sludge: Microbiology and Technology*, eds G. Lettinga et al. (Wageningen: Pudoc), 5–17.

Schrenk, M. O., Brazelton, W. J., and Lang, S. Q. (2013). Serpentinization, carbon, and deep life. *Rev. Mineral. Geochem.* 75, 575–606. doi: 10.2138/rmg.2013.75.18

Seyfried, W. E., Foustoukos, D. I., and Fu, Q. (2007). Redox evolution and mass transfer during serpentinization: an experimental and theoretical study at 200°C, 500bar with implications for ultramafic-hosted hydrothermal systems at Mid-Ocean Ridges. *Geochim. Cosmochim. Acta* 71, 3872–3886. doi: 10.1016/j.gca.2007.05.015

Sharma, A., Scott, J. H., Cody, G. D., Fogel, M. L., Hazen, R. M., Hemley, R. J., et al. (2002). Microbial activity at gigapascal pressures. *Science* 295, 1514–1516. doi: 10.1126/science.1068018

Shebl, M. A., and Surdam, R. C. (1996). Redox reactions in hydrocarbon clastic reservoirs: experimental validation of this mechanism for porosity enhancement. *Chem. Geol.* 132, 103–117. doi: 10.1016/S0009-2541(96)00045-9

Shipboard Scientific Party (1990). "Site 780," in *Proceedings of the Ocean Drilling Program, Initial Reports 125*, ed. S. K. Steward (College Station, TX: Ocean Drilling Program), 147–178.

Smith, A. R., Kieft, B., Mueller, R., Fisk, M. R., Mason, O. U., Popa, R., et al. (2019). Carbon fixation and energy metabolisms of a subseafloor olivine biofilm. *ISME J.* 13, 1737–1749. doi: 10.1038/s41396-019-0385-0

Sørensen, J., Christensen, D., and Jørgensen, B. B. (1981). Volatile fatty acids and hydrogen as substrates for sulfate-reducing bacteria in anaerobic marine sediment. *Appl. Environ. Microbiol.* 42, 5–11.

Stams, A. J. M. (1994). Metabolic interactions between anaerobic bacteria in methanogenic environments. *Antonie Van Leeuwenhoek* 66, 271–294. doi: 10.1007/BF00871644

Steen, A. D., Jørgensen, B. B., and Lomstein, B. A. (2013). Abiotic racemization kinetics of amino acids in marine sediments. *PLoS ONE* 8:e71648. doi: 10.1371/journal.pone.0071648

Stumm, W., and Morgan, J. J. (1996). *Aquatic Chemistry Chemical Equilibria and Rates in Natural Waters*. New York, NY: Wiley.

Suzuki, S., Ishii, S. I., Hoshino, T., Rietze, A., Tenney, A., Morrill, P. L., et al. (2017). Unusual metabolic diversity of hyperalkaliphilic microbial communities associated with subterranean serpentinization at The Cedars. *ISME J.* 11, 2584–2598. doi: 10.1038/ismej.2017.111

Suzuki, S., Kuenen, J. G., Schipper, K., Van Der Velde, S., Ishii, S. I., Wu, A., et al. (2014). Physiological and genomic features of highly alkaliphilic hydrogen-utilizing Betaproteobacteria from a continental serpentinizing site. *Nat. Commun.* 5:3900. doi: 10.1038/ncomms4900

Takai, K. (2011). "Limits of life and the biosphere: lessons from the detection of microorganisms in the deep sea and deep subsurface of the Earth," in *Origins and Evolution of Life: An Astrobiological Perspective,* eds H. Martin, M. Gargaud, and P. López-Garcìa (Cambridge: Cambridge University Press), 469–486. doi: 10.1017/CBO9780511933875.030

Takai, K. (2019). "Limits of terrestrial life and biosphere," in *Astrobiology: From the Origins of Life to the Search for Extraterrestrial Intelligence*, eds A. Yamagishi, T. Kakegawa, and T. Usui (Singapore: Springer Singapore), 323–344. doi: 10.1007/978-981-13-3639-3_20

Takai, K., Moyer, C. L., Miyazaki, M., Nogi, Y., Hirayama, H., Nealson, K. H., et al. (2005). *Marinobacter alkaliphilus* sp. nov., a novel alkaliphilic bacterium isolated from subseafloor alkaline serpentine mud from Ocean Drilling Program Site 1200 at South Chamorro Seamount, Mariana Forearc. *Extremophiles* 9, 17–27. doi: 10.1007/s00792-004-0416-1

Takai, K., Nakamura, K., Toki, T., Tsunogai, U., Miyazaki, M., Miyazaki, J., et al. (2008). Cell proliferation at 122°C and isotopically heavy CH4 production by a hyperthermophilic methanogen under high-pressure cultivation. *Proc. Natl. Acad. Sci.* 105, 10949–10954. doi: 10.1073/pnas.0712334105

Takai, K., Spoelstra, N., Fredrickson, J. K., Moser, D. P., Pfiffner, S. M., Onstott, T. C., et al. (2001). *Alkaliphilus transvaalensis* gen. nov., sp. nov., an extremely alkaliphilic bacterium isolated from a deep South African gold mine. *Int. J. Syst. Evol. Microbiol.* 51, 1245–1256. doi: 10.1099/00207713-51-4-1245

Thauer, R. K., and Morris, G. (1984). "Metabolism of chemotrophic anaerobes: old views and new aspects," in *The Microbe, Part II, Prokaryotes and Eukaryotes,* eds M. Florkin and H. S. Mason. (New York, NY: Cambridge University Press), 123–168.

Truche, L., Berger, G., Destrigneville, C., Pages, A., Guillaume, D., Giffaut, E., et al. (2009). Experimental reduction of aqueous sulphate by hydrogen under hydrothermal conditions: implication for the nuclear waste storage. *Geochim. Cosmochim. Acta* 73, 4824–4835. doi: 10.1016/j.gca.2009.05.043

Van Der Laan, G. P., and Beenackers, A. A. C. M. (1999). Kinetics and selectivity of the fischer–tropsch synthesis: a literature review. *Catal. Rev.* 41, 255–318. doi: 10.1081/CR-100101170

Vanlint, D., Mitchell, R., Bailey, E., Meersman, F., Mcmillan, P. F., Michiels, C. W., et al. (2011). Rapid acquisition of gigapascal-high-pressure resistance by *Escherichia coli*. *mBio* 2:10. doi: 10.1128/mBio.00130-10

Wang, D. T., Reeves, E. P., Mcdermott, J. M., Seewald, J. S., and Ono, S. (2018). Clumped isotopologue constraints on the origin of methane at seafloor hot springs. *Geochim. Cosmochim. Acta* 223, 141–158. doi: 10.1016/j.gca.2017.11.030

Wellsbury, P., Goodman, K., Barth, T., Cragg, B. A., Barnes, S. P., and Parkes, R. J. (1997). Deep marine biosphere fuelled by increasing organic matter availability during burial and heating. *Nature* 388, 573–576. doi: 10.1038/41544

Wellsbury, P., Mather, I., and Parkes, R. J. (2002). Geomicrobiology of deep, low organic carbon sediments in the Woodlark Basin, Pacific Ocean. *FEMS Microbiol. Ecol.* 42, 59–70. doi: 10.1111/j.1574-6941.2002.tb00995.x

Wolfenden, R., Lu, X., and Young, G. (1998). Spontaneous hydrolysis of glycosides. *J. Am. Chem. Soc.* 120, 6814–6815. doi: 10.1021/ja9813055

Worden, R. H., Smalley, P. C., and Cross, M. M. (2000). The influence of rock fabric and mineralogy on thermochemical sulfate reduction: khuff formation, Abu Dhabi. *J. Sediment. Res.* 70, 1210–1221. doi: 10.1306/110499701210

Worm, P., Müller, N., Plugge, C., Stams, A. M., and Schink, B. (2010). "Syntrophy in methanogenic degradation," in *(Endo)Symbiotic Methanogenic Archaea,* ed. J. H. P. Hackstein (Berlin Heidelberg: Springer), 143–173. doi: 10.1007/978-3-642-13615-3_9

Yu, H., Wang, Z., Wang, Q., Wu, Z., and Ma, J. (2013). Disintegration and acidification of MBR sludge under alkaline conditions. *Chem. Eng. J.* 231, 206–213. doi: 10.1016/j.cej.2013.07.012

Conflict of Interest Statement: The authors declare that the research was conducted in the absence of any commercial or financial relationships that could be construed as a potential conflict of interest.

frontiers in Earth Science

ORIGINAL RESEARCH
published: 31 July 2019
doi: 10.3389/feart.2019.00196

Establishment of the Deep Mine Microbial Observatory (DeMMO), South Dakota, USA, a Geochemically Stable Portal Into the Deep Subsurface

Magdalena R. Osburn[1], Brittany Kruger[2], Andrew L. Masterson[1], Caitlin P. Casar[1] and Jan P. Amend[3]*

[1] Department of Earth and Planetary Sciences, Northwestern University, Evanston, IL, United States, [2] Division of Hydrologic Sciences, Desert Research Institute, Las Vegas, NV, United States, [3] Departments of Earth Sciences and Biological Sciences, University of Southern California, Los Angeles, CA, United States

Identifying temporal trends in deep subsurface geomicrobiology is challenging as it requires both in-depth knowledge of *in situ* geochemistry and innovative sampling techniques. Subsurface microbial dynamics can only be understood in the context of accompanying geochemistry, and thus, it is imperative to first characterize available microbial habitats and their temporal evolution. Also, samples must be acquired in a clean and consistent manner to avoid artifacts stemming from surface microbes, atmospheric contamination, or external temporal variability. To facilitate these ends, we established the Deep Mine Microbial Observatory (DeMMO) in the Sanford Underground Research Facility (SURF), Lead, SD, USA to sample naturally draining fracture fluids at six spatially distributed sites from the shallowest (800 ft) to the deepest accessible (4,850 ft) depths. Here we report on the installation and subsequent two-year aqueous geochemical monitoring campaign of the DeMMO network. DeMMO fluids have distinct geochemical compositions showing differences with respect to depth, proximity to mine workings, and host rock geology. Most measurements were remarkably stable through the two-year sampling window, illustrating temporal stability of the water sources to each site, including over induced perturbations such as drilling. Interestingly, there was a lack of seasonality even at shallowest sites, indicating limited direct communication with modern meteoric waters. Patterns of fluid geochemistry are distinct between sites, and largely predictable based upon our understanding of the lithology and inorganic geochemistry of the host rocks. Thermodynamic calculations suggest that both inorganic and organic redox reactions can yield energy to, respectively, lithotrophic and heterotrophic microorganisms in this system, although the yields vary considerably by site. We conclude that each DeMMO site represents a unique window into the deep subsurface of SURF, accessing distinct fluid pockets, aqueous geochemistry, and dissolved gas geochemistry – providing stable conditions that facilitate long-term habitation of subsurface fractures and water pockets by distinct microbial communities.

Keywords: deep subsurface, mine geochemistry, Sanford Underground Research Facility, subsurface life, reaction energetics

OPEN ACCESS

Edited by:
Dawn Cardace,
University of Rhode Island,
United States

Reviewed by:
Brandy Marie Toner,
University of Minnesota Twin Cities,
United States
Andrew Elwood Madden,
University of Oklahoma, United States

****Correspondence:***
Magdalena R. Osburn
maggie@northwestern.edu

Specialty section:
This article was submitted to Biogeoscience, a section of the journal Frontiers in Earth Science

Received: *13 February 2019*
Accepted: *16 July 2019*
Published: *31 July 2019*

Citation:
Osburn MR, Kruger B, Masterson AL, Casar CP and Amend JP (2019) Establishment of the Deep Mine Microbial Observatory (DeMMO), South Dakota, USA, a Geochemically Stable Portal Into the Deep Subsurface. Front. Earth Sci. 7:196. doi: 10.3389/feart.2019.00196

INTRODUCTION

The continental deep subsurface biosphere has garnered considerable research attention in the past three decades owing to its significance to water resources, carbon fluxes, and its identification as a reasonable astrobiological analog (Fredrickson and Onstott, 2001; Pedersen, 2001; Cavicchioli, 2002; Amend and Teske, 2005; Colwell and D'Hondt, 2013; Colman et al., 2017). A large number of studies focusing on sedimentary aquifers and igneous systems revealed diverse and active microbial populations that vary in abundance based on fluid type and host lithology (Murphy et al., 1992; Stevens and McKinley, 1995; Colwell and Lehman, 1997; Magot et al., 2000; Pedersen, 2001; Vető et al., 2004; Flynn et al., 2008; Fry et al., 2009; Griebler and Lueders, 2009; Küsel et al., 2016; Simkus et al., 2016; Probst et al., 2016, 2018). For example, Stevens and McKinley (1995) proposed that the ecosystem of the Columbia river flood basalt is supported solely by chemolithoautotrophic primary producers, although this was subsequently vigorously debated (Nealson et al., 2005). The arguments for surface-independent subsurface ecosystems are complicated by and challenged by considerable sample-to-sample variability in cell density and input of fossil and surficial organic carbon.

Deep igneous and metamorphic terranes have emerged as arguably the most relevant to astrobiology. This is due to their long-term isolation from surficial water and organic carbon inputs and the possibility of life existing, and even thriving, on chemical disequilibria produced through water-rock interactions alone. In the most extreme examples, fluids may be have been isolated for billions of years, even preserving signatures of early Earth (Holland et al., 2013; Li et al., 2016). Geochemical and geomicrobiological surveys into the Fendoscandian shield revealed depth gradients of microbial populations, presumably taking advantage of redox disequilibria at different horizons (Nyyssonen et al., 2013; Kietavainen et al., 2017). Sites in the South African shield revealed remarkably low diversity ecosystems dominated by only the metabolically-flexible organism *Desulforudis audaxviator* (Chivian et al., 2008; Magnabosco et al., 2015). Recent extrapolation reveals similar microbial ecotones in deep continental systems globally (Purkamo et al., 2016; Momper et al., 2017a).

As the state of the art has evolved past samples of opportunity, an effort is being made to set up long-term monitoring sites to study deep subsurface microbiology. Established sites include the Äspö Hard Rock Laboratory (Sweden); ONKALO (Finland); Mont Terri Rock Laboratory (Switzerland); Sudbury Neutrino Observatory Laboratory and Kidd Creek Mine (Canada); Soudan Underground laboratory, Permafrost Tunnel Research Laboratory, and Coast Range Ophiolite Microbial Observatory (United States); and the Boulby Underground Laboratory (United Kingdom) (Pedersen, 1996; Stroes-Gascoyne et al., 2007; Cardace et al., 2013; Pedersen et al., 2014). These observatories cover a large range of host lithology, water age, and interaction with surficial inputs and outputs. The purpose of this communication is to expand this list to include the deep metamorphic aquifers of South Dakota, United States, and to provide geochemical context within which to investigate the resident microbial communities and their metabolic activities.

THE SANFORD UNDERGROUND RESEARCH FACILITY (SURF)

The Sanford Underground Research Facility (SURF) is hosted in the former Homestake Gold Mine in Lead, South Dakota, United States. The Homestake Mine was active between 1876 and 2001, reaching a depth of over 8100 ft (2469 m) below land surface, and producing 1,101 metric tons of gold (Caddey, 1991; Mitchell, 2009; Heise, 2015). The site was donated to the state of South Dakota in 2006 and was ultimately developed into a dedicated science facility. The core of SURF infrastructure is on the 4850 ft (1478 m) level (below surface) including several large particle physics detectors (Heise, 2015). Active pumping maintains water levels well below the 5000 ft levels, although the facility was flooded to the 4100 ft level between the end of mining and the establishment of new science facilities. Note that the level depths are given in feet in accordance with the facility naming scheme.

SURF is hosted in heavily deformed, iron-rich, Paleoproterozoic metasediments with a complex geological history. Lithological units accessed within the mine workings in ascending stratigraphic order are the Poorman Formation, the Homestake Formation, and the Ellison Formation that collectively document voluminous oceanic volcanism and subsequent infilling of the marine basin. The Poorman Formation contains a distinct basal metaigneous member called the Yates Unit followed by up to 1000 m of metasedimentary deposits of mostly well banded sericite-biotite phyllites, carbonate-bearing phyllites, and graphitic phyllites. The ore-bearing Homestake Formation is a thin metamorphosed carbonate-type iron formation with abundant sulfides and mineralogy dependent on metamorphic grade. The overlying Ellison Formation is similar to the Poorman Formation comprising mostly sericite-biotite schists, quartzites, and tuffaceous igneous components with a more continental character (Caddey, 1991). The depositional age of these metasediments is constrained to less than 1.97 Ga by a zircon age from a tuff in the Ellison Formation (Caddey, 1991). This sequence is crosscut by tertiary-aged rhyolitic and phonolitic dikes and sills. Ore mineralization is concentrated primarily within the Homestake Formation and occurred largely contemporaneously with regional metamorphism and striking ductile deformation circa 1.84 Ga, potentially associated with emplacement of large granitic bodies (Caddey, 1991). While the mine infrastructure exists to facilitate retrieval of gold ore, only 3% by volume of host rocks are ore bearing (Caddey, 1991), leaving substantial swaths of undisturbed habitat for subsurface microbes. Both the Precambrian age and iron-rich character of the rocks at SURF affect the chemistry of the borehole fluids, contributing to the diverse array of microbial inhabitants (Osburn et al., 2014).

Previous geochemical and geomicrobiological work at SURF has focused on the ore formation and emplacement

(Caddey, 1991; Morelli et al., 2010; Steadman and Large, 2016), hydrology (Murdoch et al., 2011; Kennedy et al., 2015), and geomicrobiology of mine biofilms and soils largely in the context of bioprospecting (Rastogi et al., 2009, 2010, 2013; Waddell et al., 2010). In 2013 the NASA Astrobiology Institute Team *Life Underground* began work at SURF, characterizing geochemistry, microbiology, and redox reaction energetics at key sites with an eye toward habitability (Osburn et al., 2014). This was followed by detailed DNA sequencing of microbes contained within rock and fluid samples identifying key lithophilic taxa (Momper et al., 2017b) and a metagenomic investigation of two sites resulting in large scale genome assembly and metabolic assessment (Momper et al., 2017a). These studies collectively reveal distinct populations of subsurface microbes, many from wholly uncultivated lineages, with interesting metabolic strategies tailored to subsurface, rock-associated habitats.

Our initial work at SURF revealed the need for dedicated sampling infrastructure to effectively monitor flowing boreholes through time. While samples of opportunity provided a glimpse of interesting microbial ecosystems, replicability of these samples were limited and contamination of fracture samples with mine atmosphere and microbial inhabitants was a constant threat. To alleviate these problems, we sought to establish an observatory of sites through the mine where access could be controlled, fluids could be collected cleanly and consistently, and long-term experimental apparatus could be deployed for the long timescales over which many subsurface organisms grow. Monitoring of each site for geochemical and microbiological parameters before and after modification was a key goal. Here we report on a two-year time series of aqueous and gas geochemical monitoring. The microbial ecology of these sites and temporal dynamics therein is beyond the scope of this manuscript.

MATERIALS AND METHODS

Borehole Modification

Many hundreds of exploratory boreholes were drilled over the 125 years of mining operations and more subsequently as underground science facilities were built. Of these, six diamond drill holes were chosen for the DeMMO network based on host lithology, fluid flow rate, accessibility by monitoring teams, and fluid chemistry. Each of the six sites featured unique challenges and was modified as deemed possible and safe by SURF personnel. Two locations (D1 and D2) were inaccessible for drilling and were instead modified with hand tools and fitted with simple drain packers to restrict the inflow of mine atmosphere and channelize outflow. Three holes (D3, D4, and D5) were drilled with a diamond bit and fitted with custom designed expandable packers (**Figure 1**). Drilling was conducted in May 2016 by SURF personnel using legacy jackleg drilling methods, in which historic 2″ exploration holes (previously filled with concrete to control water outflow) were re-drilled with a 3″ diameter reaming bit to a depth of 5–6′. As such, foreign material was removed, unimpeded water outflow was restored, and fresh, smooth, rock surface was exposed to ensure appropriate contact with expandable packer surfaces. We will subsequently refer to this as borehole outlet modification. The last site (D6) was left in its original form with a steel manifold as it was not safe to modify.

Packers were custom built from acetal holopolymer material (Delrin) following a commercially available design (Margo Packer). It was deemed essential to avoid metal components in the packers, because many metals can influence microbially relevant aqueous redox chemistry. Stock Delrin components (McMaster Carr) were machined as needed (Princeton University, Geosciences Machine Shop) to create the nested-component design illustrated in **Figure 1**. In short, a hollow inner tube allows for the continuous outflow of fracture fluids accessed by the borehole, while an outer, mobile sleeve serves to compress four polyurethane bushings (Shore hardness = 60A, custom poured by PSI Urethanes, Inc.), thereby creating a seal with the borehole wall to eliminate communication with the local mine atmosphere. To control and sample outflowing fluid, a custom 5-port sampling manifold (Delrin) outfitted with polypropylene ball valves (Parker, US Plastic Corp.) was attached to each installed packer. Once installed, the packers and manifolds were not removed. Each DeMMO site was sampled upon each visit to SURF, including before, during, and after hole modification, creating a two-year time series from December 2015 to November 2017.

Field Methods

Site visits were conducted within a 4-day window in accordance with underground access schedules and necessary transit times. At each site temperature, pH, conductivity, total dissolved solids (TDS), and oxidation reduction potential (ORP) were measured with a portable Myron Ultrameter II. For D6 which needed to be opened, fluids were allowed to run for 2–5 min to stabilize prior to measurement. Samples were collected for major anions and cations, dissolved organic carbon (DOC), dissolved inorganic carbon (DIC), and dissolved gas geochemistry. All samples collected on site were preserved as appropriate (cool, frozen, or on dry ice) before transport back to the laboratory for analysis.

Redox sensitive ions were measured on site using a portable Hach DR1900 Spectrophotometer and associated reagent kits as described below. Hydrogen sulfide was measured by the methylene blue colorimetric method (Hach 8131). Ferrous iron concentrations were measured using the 1,10 phenanthroline method (Hach method 8146). Nitrate concentrations were measured using the NitraVer5 cadmium reduction method (Hach method 8039) and ammonia concentrations were measured using the Salicylate colorimetric method (Hach method 8155). Dissolved oxygen (DO) concentrations were also measured with low and high range ampules (Indigo Carmine Method, Hach methods 8316 and 8166, respectively), but poor reproducibility of these data on duplicate samples calls into questions its accuracy, and we report only averages. All kit-based measurements were conducted according to manufacturer instructions, and dilutions were performed with deionized water as necessary.

Aqueous Geochemistry

Filtrate (<0.22 μm) was collected in lab-supplied plastic bottles with nitric acid preservative or new plastic tubes for ICP-MS

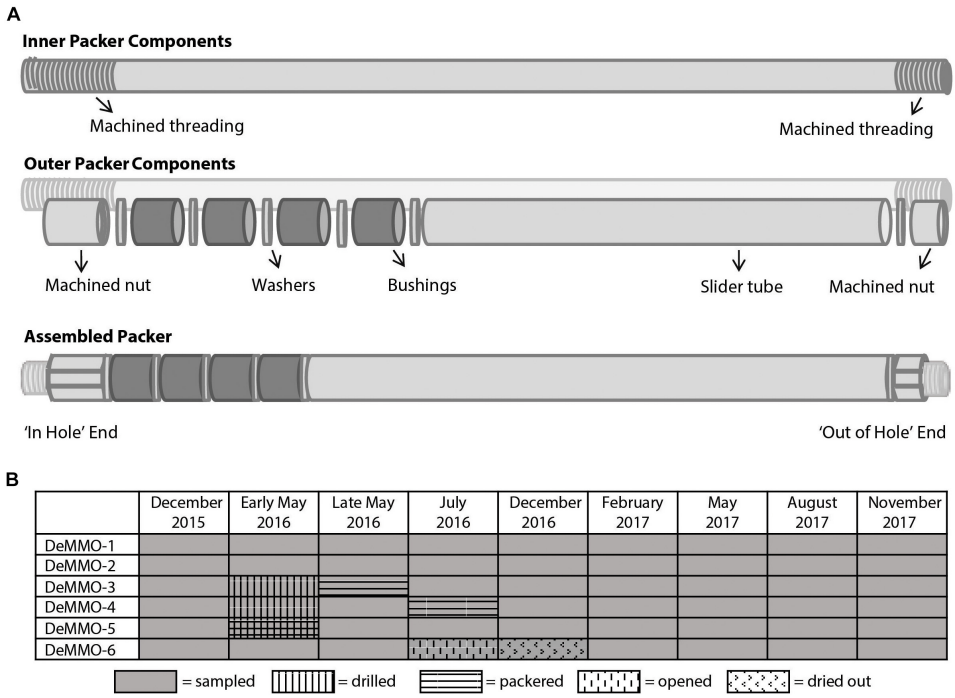

FIGURE 1 | (A) Packer design used to modify DeMMO 3, 4, and 5 illustrating the inner components, outer components, and assembled design. Dark gray bushings are expanded to create the seal with the borehole. **(B)** Timeline of sampling and hole modification.

(EPA method M200.7) and IC (EPA Method M300.0) analysis of major dissolved cations and anions, respectively, by ACZ laboratories. For IC methods, Br^-, Cl^-, F^-, and sulfate were analyzed and had minimum detectable levels of 0.25, 2, 0.25, and 2 mg/L, respectively. For ICP methods we analyzed (minimum detectable levels in ppm), Al (0.03), Ar (0.04), Ba (0.02), B (0.01), Cd (0.005), Ca (0.1), Cr (0.01), Cu (0.01), Fe (0.02), Pb (0.03), Li (0.008), Mg (0.2), Mn (0.005), Mo (0.02), Ni (0.008), Se (0.05), Si (0.1), Ag (0.01), Na (0.02), and Zn (0.01). Filtrate samples for DOC concentrations were collected in acid-washed (4 h in 10% HCl, DI rinsed) and combusted (4.5 h at 450°C) amber glass VOC vials with PTFE lined acid-washed caps, brought to pH ∼2 with 6N HCl, and stored at 4°C until measured by Anatek Labs, using method SM 5310B (non-purgeable organic carbon).

Samples for DIC and its respective $\delta^{13}C$ value ($\delta^{13}C_{DIC}$) were taken in ashed, helium-flushed, and evacuated Exetainers® and measured in house at the Northwestern Stable Isotope Facility via continuous flow on a ThermoFisher GasBench II, coupled to a Delta V Plus isotope ratio mass-spectrometer (CF-IRMS). Approximately 1 mL aliquots of each sample were syringe-injected into acidified (103% H_3PO_4) and helium-purged Exetainer® vials. The samples were then re-weighed to determine exact quantity, placed in the thermostated block of the GasBench II, and carbon dioxide allowed to evolve at 25°C for a minimum of 12 h. Sample carbon dioxide is sub-sampled by a PAL autosampler and $\delta^{13}C$ values determined by averaging 8 separate injections of ∼100 μL each. The isotopic composition, $\delta^{13}C_{DIC}$, is corrected using the periodic sampling of carbon dioxide from the H_3PO_4-acidified $CaCO_3$ standards NBS18 and NBS19 (respectively, $\delta^{13}C_{VPDB} = -5.014‰$, ≡1.95‰), and samples reported on the VPDB scale. Estimated precision (1 standard deviation) on total Dissolved Inorganic Carbon concentration ([DIC]) and $\delta^{13}C_{DIC}$ are ± 40 μM and ± 0.1‰, respectively.

Dissolved Gas Geochemistry

Dissolved gas samples were collected using the bubble stripping method of Chapelle et al. (2002) modified by Alter and Steiof (2005). In short, borehole fluid was directed through a glass gas sampling bulb, a 10 mL bubble of pure Ar was introduced into the chamber and the system was allowed to reach equilibrium while monitoring flow rate and temperature. The sample bubble was then removed and stored in an Ar-flushed and evacuated 10 mL Serum bottle previously capped with solid butyl rubber stoppers and crimped tin seals. Gas samples were analyzed on a Shimadzu GC-2014ATF Headspace GC equipped with Haysep 80/100 (5 m) and MS-5A 60/80 (2.5 m) molecular sieve columns and TCD and FID detectors. Dissolved gas concentrations were calculated from equilibrated gases based on solubility constants of each gas at the collection temperature and pressure as well as in reference to analytical standards.

RESULTS

Description of DeMMO

The selection of sites for the DeMMO network was undertaken with consideration of long-term accessibility, adequate fluid flow,

host lithology, and depth. The six chosen sites span a range of depths (800–4,850 ft), flow conditions, and host lithologies (**Table 1** and **Figures 2A,B**).

Two sites (D1, D2) are on the 800 ft level (**Figure 2A**). While, on the same horizontal plane, these boreholes intersect very different areas of mine geology and have different histories. D1 (historical name 10-1) was the tenth diamond borehole drilled at the Homestake Mine circa 1910. It is 1400 ft long (427 m) drilled eastward, away from any documented mining excavations. The bit drifted upward during drilling, terminating near Whitewood Creek. This borehole starts in Ellison Formation lithologies of chlorite-mica-garnet schists and phyllites, transitioning into unidentified metaigneous amphibolites, and subsequently tertiary intrusive rhyolites. The borehole log notes intersecting a water course at the hole terminus, which may be the current source of abundant flow (averages 2.5 L/min). The proximity of this water source to the surface could leave open the possibility of seasonal influence at this site, which we will evaluate below. In contrast, D2 (historical name #19223) intersects a complex region of folded Ellison, Homestake, and Poorman formations in an area with extensive sulfide mineralization and mined stopes. The hole begins in well-banded tan, brown, and gray phyllites of the Ellison Formation, followed by yellow-banded and mineral-rich Homestake Formation phyllites, gray – green and brown Poorman Formation phyllites, and rhyolitic to porphyritic intrusive igneous rocks. Significant minerals noted on the bore hole logs are graphite, sericite, cummingtonite, chlorite, chert, siderite, carbonate, biotite, quartz, fluorite, pyrrhotite, pyrite, and arsenopyrite. Fluids from both D1 and D2 are fresh, with conductivities <1 mS and relatively cool, with average temperatures of 10.3 and 12.5°C, respectively.

D3 (historical name #24790) is uniquely situated in a remote region of the 2000 ft level (**Figure 2A**) and was drilled in 1999 during the final phase of mining and exploration of the working Homestake Mine. This is a relatively short borehole (398 ft; 121 m) drilled at a steep upward angle. Intersected lithologies include gray to tan banded sericite, graphite, chert-bearing phyllites (Poorman Formation); gray green and white massive to banded Homestake Formation with biotite, sericite, chlorite, chert, vein quartz, graphite, siderite, pyrite, pyrrhotite, and arsenopyrite, and poorly banded sericite, graphite, and biotite phyllites (Ellison Formation). These rocks were not visibly intruded by tertiary volcanism. Currently the hole has strong flow (∼1.5 L/min) and features periodic eruptions of gas bubbles and particulate iron oxides. Measured ORP is consistently high (average −28 mV) but dissolved oxygen is undetectable. The fluids are consistently brackish with an average conductivity of 3 mS.

D4 (historical name #24228) is on the 4100 ft level very near, but not intersecting the Ross Shaft. This hole is unusual in that it was drilled at a downward angle (**Figure 2A**) that, importantly for the geochemistry and habitability, limits contamination with oxygen from the mine atmosphere. The drilling log is relatively simple, spanning 941 ft (287 m) and featuring primarily Poorman Formation banded graphite-biotite phyllites that variably include carbonate, sericite, chlorite, and garnets. Pyrrhotite and pyrite mineralization is noted throughout the core.

D5 (historical name #11938) and D6 (historical name DUSEL B) are both on the 4850 ft level, but as with D1 and D2, intersect very different rocks and feature different fluid chemistry. D5 (hole #11938) was drilled in 1978 during excavation of the 17-ledge mining area (see **Figure 2A**). It is 943 ft (287 m) long and intersects a wide range of lithologies. Notably this hole is in a drift with very significant modern fluid flow through both old boreholes and other fractures, commonly featuring abundant growth of white microbial biofilms and streamers. The trajectories of D4 and D5 trend toward a similar source area, between areas of significant excavation. We will evaluate the potential for similar hydrological source areas of D4 and D5 below. D5, however, intersects a much more diverse range of host lithologies, including the Poorman, Homestake, and Ellison formations as well as transitional facies between those units.

D6 was drilled in 2009 in preparation for construction of the proposed Deep Underground Science and Engineering Laboratory (DUSEL) facilities. This hole, along with its sister holes, in the same drift (DUSEL C, D, J, and 3A, not sampled), intersect the Yates Unit metabasalts with periodic rhyolitic tertiary dikes. D6 is 603 ft (184 m) long and was intentionally drilled in a direction of very limited mining influence where very significant fluid pressures were encountered. In contrast to the other fluids, those from D6 are much more saline, up to ∼8 mS. Logistical concerns prevented re-packering of this hole to a continuous flow system similar to the other DeMMO sites, however, we did install continuous flow experiments at this site in July 2016, changing this from a closed system to an open system. After 6 months of continuous

TABLE 1 | Site characteristics of DeMMO and surrounding rocks.

DeMMO site	Depth (ft)	Depth (m)	Host lithology*	Temp. (°C)+	Cond. (μS)	ORP (mV)	TDS (ppm)
D1	800	244	PF, YU, tP-Y, Ti	10.3 ± 0.3	966 ± 34	−90 ± 31	694 ± 26
D2	800	244	EF, HF, PF, Ti	12.5 ± 0.1	619 ± 8	−125 ± 36	438 ± 6
D3	2000	610	PF, tP-H, HF, EF	16.2 ± 0.2	3036 ± 15	−28 ± 35	2312 ± 13
D4	4100	1250	PF, tP-H	22.6 ± 0.3	1781 ± 42	−217 ± 46	1302 ± 34
D5	4850	1478	PF, tP-H, HF, EF	31.8 ± 0.6	1545 ± 10	−213 ± 59	1112 ± 8
D6	4850	1478	YF, Ti	21.6 ± 1.2	7925 ± 53	−244 ± 68	6602 ± 50

YY, Yates Unit; PF, Poorman Formation; HF, Homestake Formation; EF, Ellison Formation; Ti, Tertiary intrusive; tP-Y, transitional facies between Yates Unit and Poorman Formation; tP-H, transitional facies between Poorman and Homestake formations. +Geochemical data presented as averages over the two-year period plus or minus the standard deviation of those measurements.

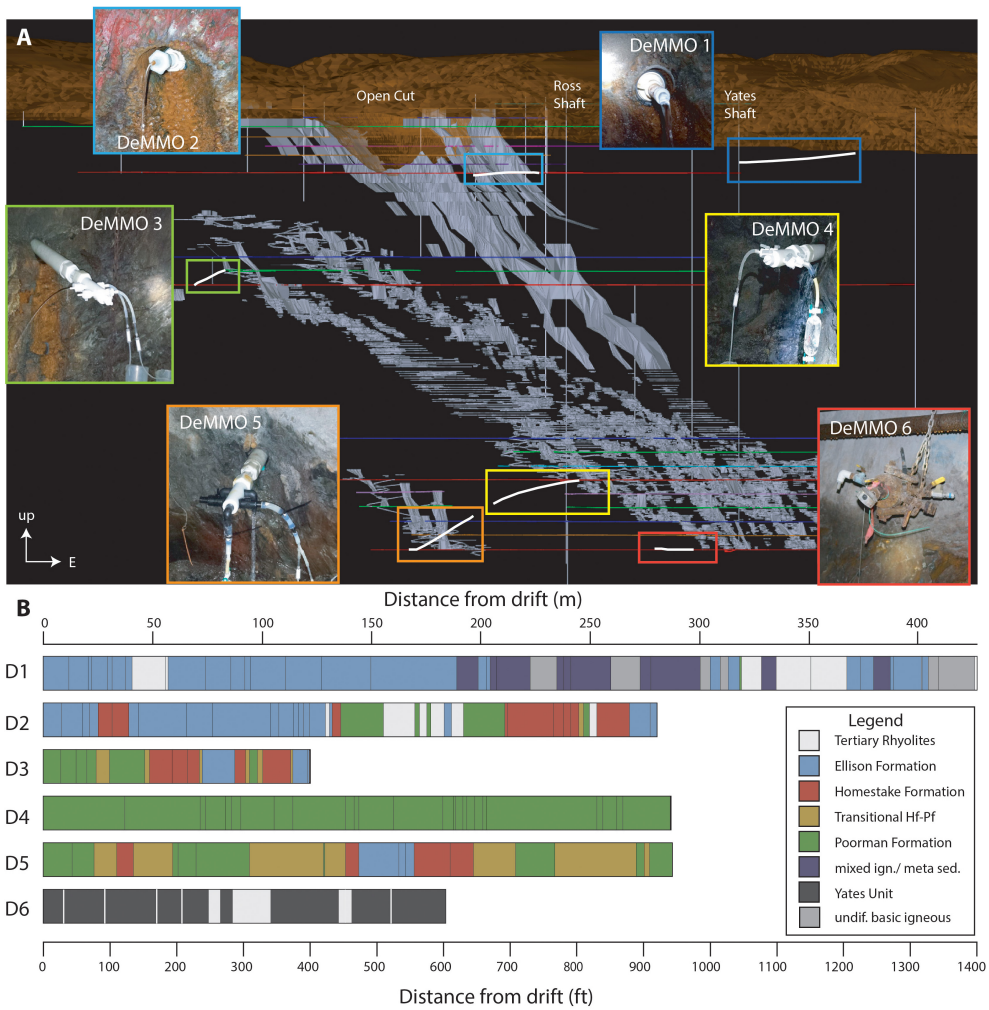

FIGURE 2 | Overview of SURF superstructure and borehole placement, trajectories, and intersecting lithologies. **(A)** A 3D georeferenced map of SURF and picture of each site. View is looking from south to north (map made by Kathy Hart using Vulcan Software printed with permission from SURF). Mined stopes shown in gray, borehole trajectories in white, mining levels in colored horizontal lines, and shafts in vertical gray lines. **(B)** Lithological units in boreholes from origin (0) to terminus compiled from each borehole log report.

flow, the hole ran dry and was closed and is now only opened for sampling trips and by safety personnel to mitigate pressure buildup.

Water Isotopes

The isotopic compositions of hydrogen and oxygen in water are often used as a first line of evidence regarding the original source of groundwater (Gat, 1996; Criss, 1999). We employ this classical technique as a means of both assessing the original source of fluids and also for identification of seasonal variability. **Figure 3A** shows isotopic data for DeMMO fluids plotted with the meteoric water line (MWL) and Online Isotopes in Precipitation Calculator (OIPC) estimates for month local precipitation (Welker, 2000; Bowen and Revenaugh, 2003; Bowen et al., 2005; Bowen, 2018). Strong seasonality in the climate above SURF produces distinct trends in the water isotope composition of precipitation driven primarily by temperature and vapor sources. The most depleted values occur in December, January, and February produced by cold temperatures and significant snowfall, whereas the most enriched values occur in August. The average isotope composition of annual precipitation approximates that which occurs between September and October of a given year.

Conservative Aqueous Geochemistry

Ternary diagrams of aqueous geochemistry at the six sites (**Figure 4**) reveal a broad range of cationic compositions, a fairly narrow range of anionic compositions, and extremely consistent behavior of individual sites through time. In fact, individual sites are so consistent that most data points plot within analytical error of each other, and thus long-term variability in this chemistry will not be discussed.

The cation data (**Figure 4A**) show separation by station depth, with considerable differences between the deepest

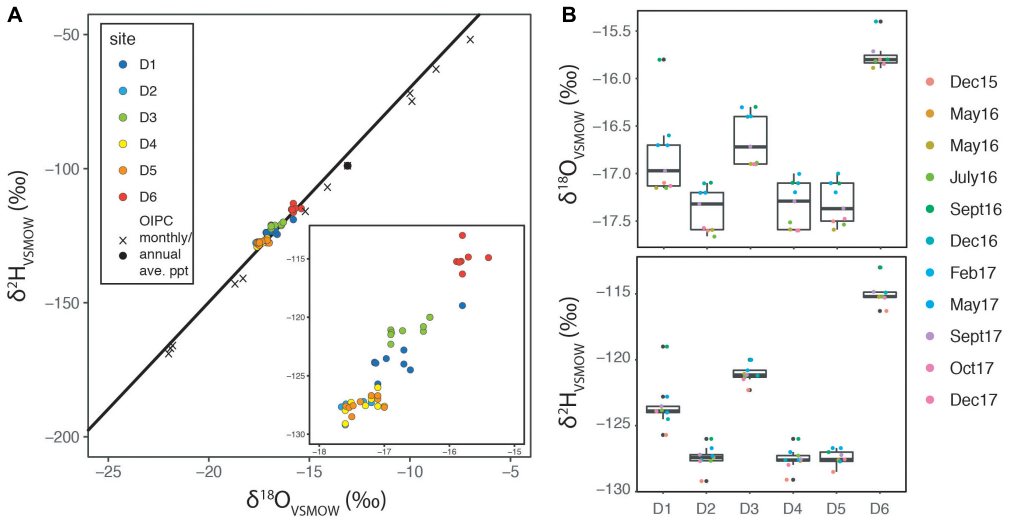

FIGURE 3 | Water isotopes of DeMMO sites and overlying land **(A)** Plot of water isotopes for DeMMO sites plotted on the meteoric water line and OIPC estimates of monthly average and annual precipitation. Inset expands borehole data range. **(B)** Box plots showing variability with time in both $\delta^{18}O$ and $\delta^{2}H$ where points are colored by the sampling date.

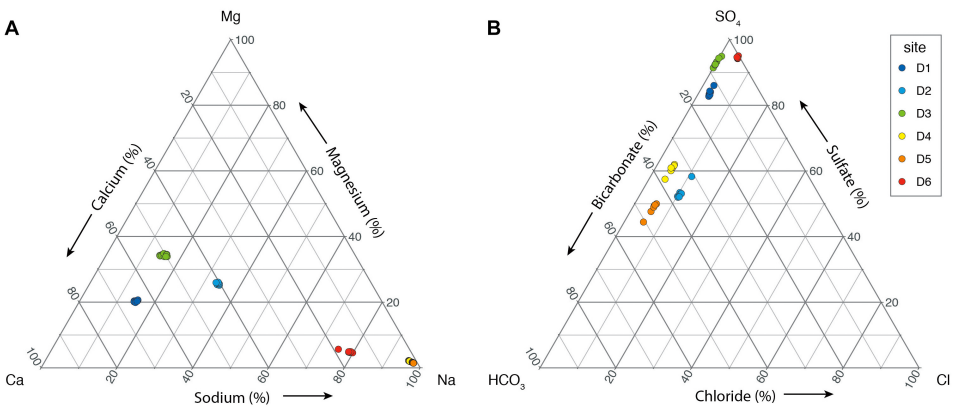

FIGURE 4 | Ternary diagrams illustrating the distribution of major cations **(A)** and anions **(B)** from each DeMMO site.

three, and the shallowest three samples. Deep samples (D4–D6) are sodium-type waters, whereas shallow samples (D1–D3) contain significantly more calcium and to a lesser extent magnesium. The anion data (**Figure 4B**) show that D1, D3, and D6 are sulfate-type waters, whereas D2, D4, and D5 have approximately even concentrations of sulfate and bicarbonate. Chloride is a minor component in these waters.

Each site is characterized by a distinct aqueous geochemistry. D4 and D5 are the most similar, with indistinguishable cation and chloride levels, and minor variations along the SO_4-HCO_3 axis. D1 and D3 are also similar, but with distinct calcium-magnesium and SO_4-HCO_3 signatures. D2 is consistently intermediate to the other samples and uniquely contains appreciable (although still low) levels of Cl^-. We hypothesize that these distinct chemistries result from different lithological composition present in the water source area for each site and also residence time of water through those rocks and will evaluate this hypothesis below.

Redox Sensitive Geochemistry

Measurements of redox sensitive ions are relatively rare in geochemical datasets owing, in part, to the difficulty of performing these measurements in the field. However, these are also the ions most likely to be cycled by microbes, and are thus their quantification is critical to characterizing lithotrophic habitability. Using portable meters, we monitored ferrous iron, nitrate, ammonium, and sulfide, as well as ORP at all time points after the December 2015 trip. The concentrations of all measured redox sensitive ions and ORP are temporally quite stable, despite potential notable uncertainties in the colorimetry techniques.

As with conservative ions, redox sensitive ions produce distinct fingerprints for each site. We observe broad covariation between nitrate, ammonium, and sulfide concentrations,

particularly at D4 and D5, which have consistently high ammonium and sulfide values, and correspondingly negative ORPs. Ferrous iron is elevated in D1, D3, and D6, presumably from interactions with mafic volcanic rocks and/or steel in previously mined cavities. Note in **Figure 5** that ferrous iron levels at D6 increase with time; a similar range (0.7–3.0 mg/L) was previously observed in Osburn et al. (2014). In the dataset described here, the low values correspond to times when the steel manifold was closed, and the high values to times when fluid was continually flowing. This is opposite to what would be predicted if the manifold itself was the source of ferrous iron.

Dissolved Gases

Dissolved gas concentrations exhibit significant variability through time and between sites (**Figure 6**). Carbon dioxide is the most stable and distinct measurement between sites, with decreasing average concentrations observed with depth for D1, D2, D4, D5, and D6. The outlier is D3, with consistently twofold (or more) higher concentrations. Field observations of the fluid streams at D3 confirm visible bubbles in the fluid stream from this site, which, based on these data, are likely mostly carbon dioxide. Concentrations of carbon monoxide and hydrogen are low (<1 nM) and exhibit no significant trends. Levels of helium, methane, and ethane covary, with elevated concentrations at D4, D6, and to a lesser extent D5. The methane/ethane ratios average 24, 76, 192 for D4, D5, and D6, respectively. Dissolved oxygen was measured colorimetrically and are of variable quality, with many analyses strongly affected by rapid oxidation post-sampling. The dissolved oxygen measurements should therefore be taken as maximum values, and we do not plot them with

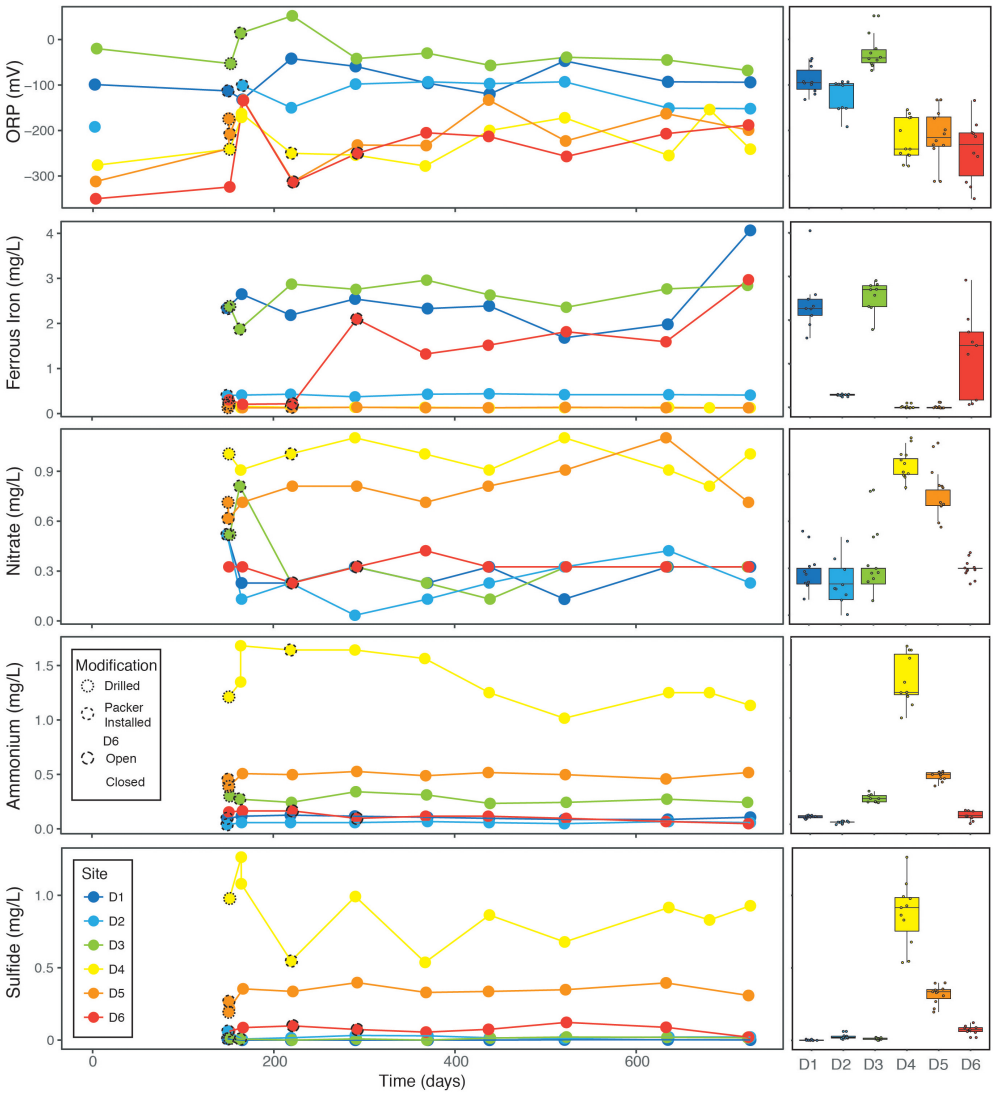

FIGURE 5 | Combined line plots and box plots of redox sensitive geochemical measurements showing change with time and aggregated site averages, interquartile ranges, and data points.

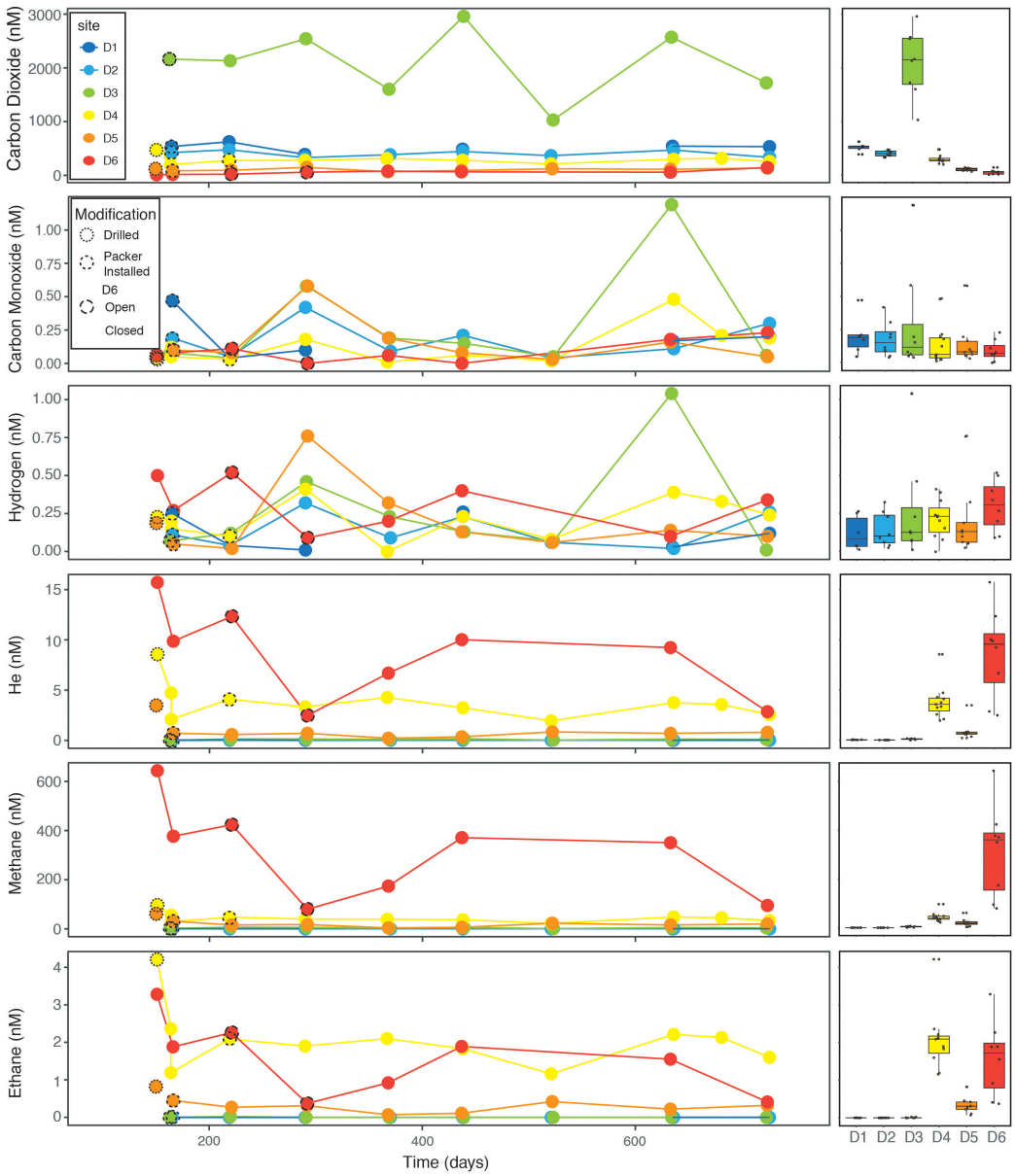

FIGURE 6 | Dissolved gas concentrations by site through time (left) and aggregate box plots illustrating average, interquartile range, and data points (right).

time; instead, we rely on ORP to record oxidation states of these fluids.

Carbon Chemistry ([DIC], $\delta^{13}C_{DIC}$, DOC)

Concentrations of DIC and DOC vary considerably among the DeMMO sites, but they are temporally quite stable (**Figure 7**). DIC levels are highest in D4, D5, and D3 (generally >10 mM), and much lower in D1, D2, and D6 (<5 mM). These differences do not appear to correlate with pH or dissolved carbon dioxide, suggesting distinct sources rather than equilibrium partitioning. The isotopic differences in DIC (**Figure 7**) follow a similar site pattern, with more enriched values in D3, D4, and D5 and slightly more depleted values in the others, particularly D6. Of note is the unusual trend at D3, where the earliest value is very enriched, but then decreases steadily to −8‰.

It can be seen in **Figure 7** that DOC concentrations vary broadly along a depth gradient, with additional variation in D6 through known perturbations. The shallowest sites, D1 and D2, have relatively high DOC levels (∼0.035 mM), but this is still quite low compared to surface oligotrophic fluids, which typically range closer to 1 mM (Leenheer et al., 1974). DOC concentrations are lower in D3, D4, and D5, with a slight depth relationship. D6 has extremely variable DOC concentrations ranging from near those of the shallow sites to the lowest observed values (0.01 mM). The significant drop in concentration at the beginning corresponds to when the systems transitioned

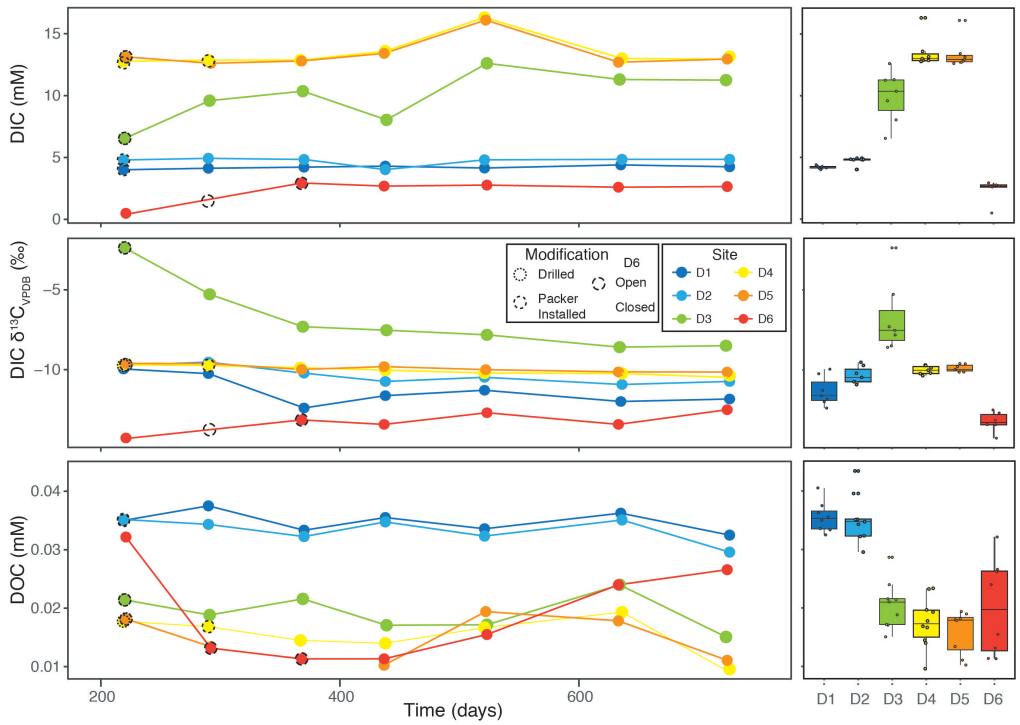

FIGURE 7 | Box and line plots of DIC, $\delta^{13}C_{DIC}$, and DOC.

from a closed manifold to an open flowing system. The hole at D6 eventually drained and was subsequently left sealed except to sample. The DOC concentration there appears to be rebounding after this change in protocol.

DISCUSSION

Relationship Between Different Sites

Determining Water Source

Taken together, the suite of geochemical data at SURF can point to relationships between sampling sites, the relative age of the fluids, and likely fluid flow paths. Our water isotope data (**Figure 3**) suggest a relatively unaltered meteoric signal with limited hydrothermal input for all DeMMO sites. While there is variability with time at each sample location (1‰ in $\delta^{18}O$ and ~5‰ in $\delta^{2}H$), there does not appear to be seasonal variation at any site. For instance, samples from D1 taken in December 2015, May 2016, and September 2016 are all similar (and depleted) despite the fact that corresponding relative monthly precipitation isotope values span a much larger range. This suggests that even at the site with the shallowest likely water input, the fluid source is integrated over a >1 year time frame. Furthermore, all sites are depleted relative to the annual average precipitation values, instead centering between March and April precipitation estimates, suggesting reservoir recharge is biased by spring rains and snow melt rather than a fully integrated annual precipitation signal. The lack of strongly enriched isotope values stands in considerable contrast to those from the older deep fluids reported from the South African and Canadian Cratons, where water-rock interaction and hydrothermal alteration drive waters to extreme values (Onstott et al., 2006; Sherwood Lollar et al., 2007) and the ultimate values of fracture fluids reflect mixing between these and paleometeoric fluids.

Murdoch et al. (2011) present a hydrological model for SURF that predicts different water ages in different areas of the mine. On the south side of the mine and within the main workings, even at depths exceeding 5000 ft, the putative ages are young, <10–100 years. On the north side, away from the main ledge, the ages can be much older, ranging from <100 years at shallow depths to >10,000 years below ~3000 ft. Our water isotope data (**Figure 3**) appear to reflect these predicted residence times. For instance, D4, D5, and D2 produced similar water isotope patterns and based on Murdoch's model are predicted to be very young fluids with locations on the far south side (D4 and D5) and near the open cut (D2). In contrast, D1, D3, and D6 show relative enrichment reflecting incorporation of older water draining from the surrounding region that has been captured by the hydrological depression of the mine. This is consistent with their locations on the east side (D1 and D6) and far northwest side (D3) of the mine. Longer water residence times facilitate increased water-rock interaction and should be reflected in geochemical fingerprints, particularly at D1, D3, and D6.

Borehole logs and broad geological maps document host geology that, combined with ion composition data, paint a complex picture of fluid flow and water-rock interactions. As noted above, fluids at D1, D2, and D3 are enriched in calcium and magnesium relative to fluids at D4, D5, and D6, which are

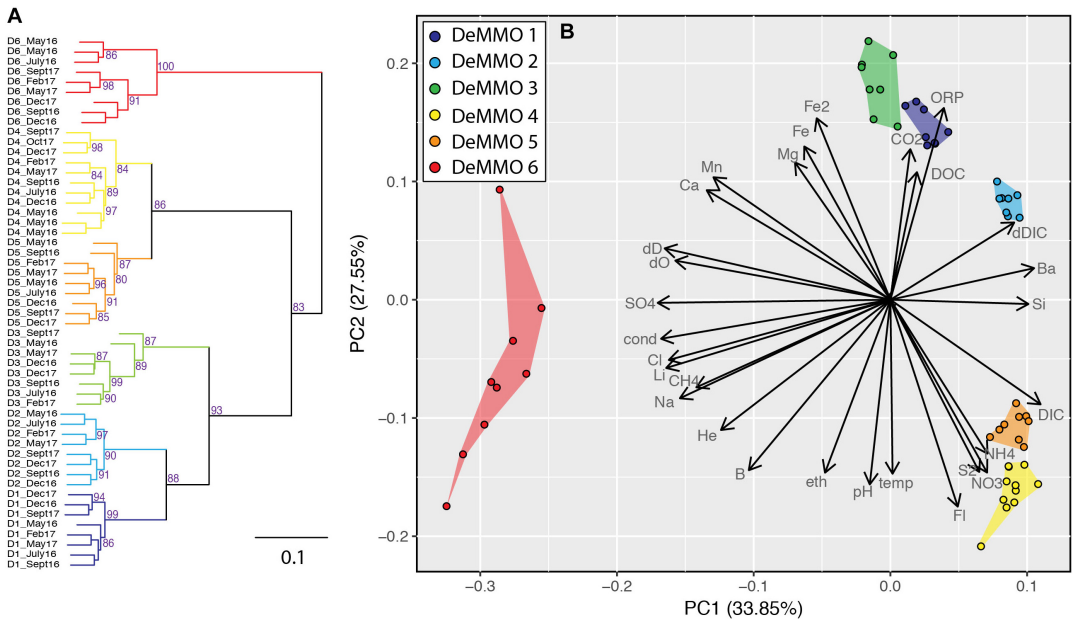

FIGURE 8 | Hierarchical clustering and PCA analysis of sites based on geochemistry inputs. **(A)** Wards Clustering and Euclidean distance matrix. Bootstrap values > 80 for higher order nodes shown in purple. **(B)** Principle components analysis produced in R with the prcomp() command and visualized using the ggfortify package. Envelopes containing all the points for a given site are highlighted for emphasis. Vectors illustrate the loading of different geochemical parameters on PC1 and PC2.

dominated by Na. The high calcium values in D1 and D2 are consistent with the presence of intermediate to mafic volcanic intrusions, which, as recorded in the drilling logs, are rich in calcium-plagioclase. The source of calcium in D3 is less clear, but perhaps records interactions with rocks beyond those observed in the drill logs. This is also suggested by the high levels of ferrous iron, which cannot be explained by either the presence of a steel packer or volcanic rocks in the borehole trajectory. Particularly curious is the lack of divalent cations in D6. This site is drilled into the Yates Unit, an amphibolite composed of ∼80% hornblende and 20% intermediate plagioclase, both of which should supply abundant calcium to fluids. Yet, D6 is almost 80% Na, suggesting that fluids spend much of their long residence time interacting with more sodium-rich rocks. One interpretation is that the D6 source fluid is traveling primarily along tertiary rhyolitic dykes rather than the very massive metabasalt. An additional option is that cation exchange within clay minerals has significantly altered the fluid geochemistry, replacing Ca and Mg in shallow fluids with Na at depth.

It can be seen in **Figure 4B** that all of the fluids are sulfate-rich and chloride-poor, but D2, D4, and D5 are best characterized as mixed carbonate-sulfate fluids. The presence and metamorphic grade of the Homestake Formation can account for the bicarbonate. At low metamorphic grade identified at D2, D4, and D5, Homestake Formation contains abundant siderite, a ferrous iron carbonate. At higher grades, as recorded at D3, Homestake Formation instead contains grunerite, an iron silicate. The lack of covariation between calcium and carbonate also supports a siderite origin for the carbonate ion as opposed to sedimentary calcium carbonate cements or veins. Thermodynamic calculations of mineral saturation state reveal that calcite and aragonite are only weakly oversaturated in D2–D6 although dolomite is weakly oversaturated at all sites (see **Supplementary Data**). Lastly, in addition to relatively high sulfate concentrations, the fluids at D1, D3, and D6 also contain abundant ferrous iron. This combination suggests a similar source, such as the dissolution of iron sulfide minerals or leaching of mafic volcanic rocks.

Statistical Evaluation of Similarity

Regardless of the specific flow paths and water-rock interactions, the geochemical fingerprints of each DeMMO fluid is distinct. Statistical analysis of variance can be used to evaluate how strongly these fingerprints are supported through time and evaluate the dominant parameters responsible for these groupings. Two visual representations of these relationships are portrayed in **Figure 8**. Hierarchical clustering of all sites based on variance of all parameters at each time point are illustrated in **Figure 8A**. The predominantly high bootstrap values indicate a strong level of support of each node. We observe clear clustering of data from each site through time with strong statistical support and no exceptions. D6 is the most divergent, branching away from all other sites at the first node. As predicted from broad geochemical signals, D4 and D5 cluster together, but importantly are separated with high statistical support. The notable differences in dissolved gas concentrations are the only major chemical differences between D4 and D5. This may be explained by temperature and hole geometry as D4 is relatively cool (average 25.3°C)

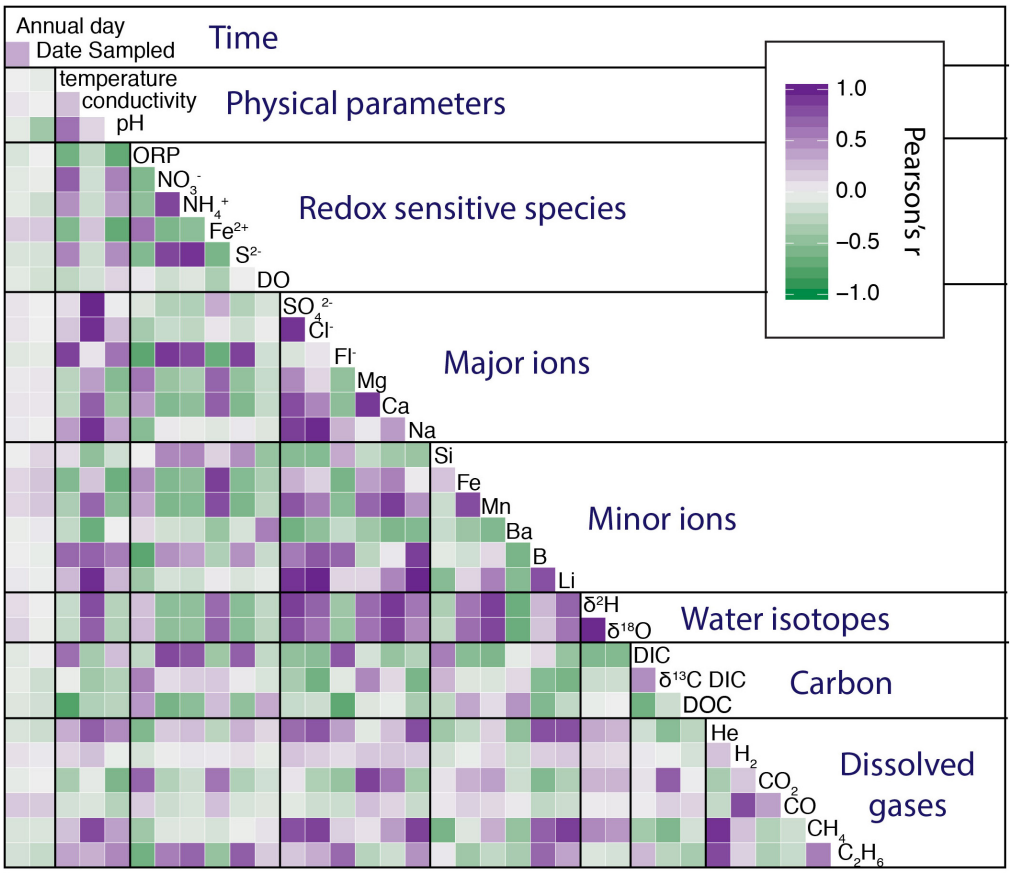

FIGURE 9 | Correlogram of all geochemical data showing Pearson's r correlation between variables with color. Correlogram was generated with GGally r package.

and drilled downward, both of which serve to promote higher dissolved gas concentrations. In contrast, D5 is warm (average 31.7°C) and drilled upward, limiting the storage capacity of dissolved gases. The shallower sites D1, D2, and D3 branch away from the deeper ones in a single node and D1 and D2 branch separately from D3. This clustering strongly supports our conclusion of distinct and stable geochemistry of each DeMMO site through time.

The principal components analysis (PCA) in **Figure 8B** illustrates the same associations seen in hierarchical clustering analysis, but additionally allows for comparison of how the geochemical parameters themselves plot in the sample ordination, and thus, which parameters are most responsible for separation. Variations in PC1 show positive loading of DIC, Ba, Si, $\delta^{13}C_{DIC}$, and ammonium and negative loading with sulfate, conductivity, water isotopes, lithium, and Cl^-. These parameters effectively separate D6 from all other samples. PC2 shows strong positive loading with ORP, iron, carbon dioxide, DOC and magnesium and negative loading with fluorine, temperature, pH, ethane, and nitrate. Variation in PC2 shows clear separation of D1, D2, and D3 from D4 and D5 based on nutrient concentrations, redox balance, and carbon sources. This plot is also useful for observing that even with variance between points for a given site, each remains distinct from even their closest spatial and geochemical neighbors.

Relationship Between Geochemical Parameters

In addition to understanding the relationship between sites, it is also useful to compare the relationship between geochemical parameters in this large dataset. To achieve this, we present a correlogram of pairwise correlation coefficients (**Figure 9**). We see strong positive (purple) and negative (green) correlations between many parameters. Some of these are very intuitive and expected, for instance the correlation between $\delta^{18}O$ and $\delta^{2}H$ in water isotopes which could be predicted by the meteoric water line. Another proof of concept is the positive correlation of major ions with both minor ions and conductivity. The correlations between water isotopes, major and minor ions, and conductivity support our identification of discrete water masses, where water isolation time modulates all of these variables. Other relationships are less intuitive and perhaps more informative, such as the lack of correlation between either annual day or date sampled and any geochemical parameter. This supports our conclusion that, as a whole, there are no long-term secular or seasonal trends in the data. An additional notable observation is that temperature

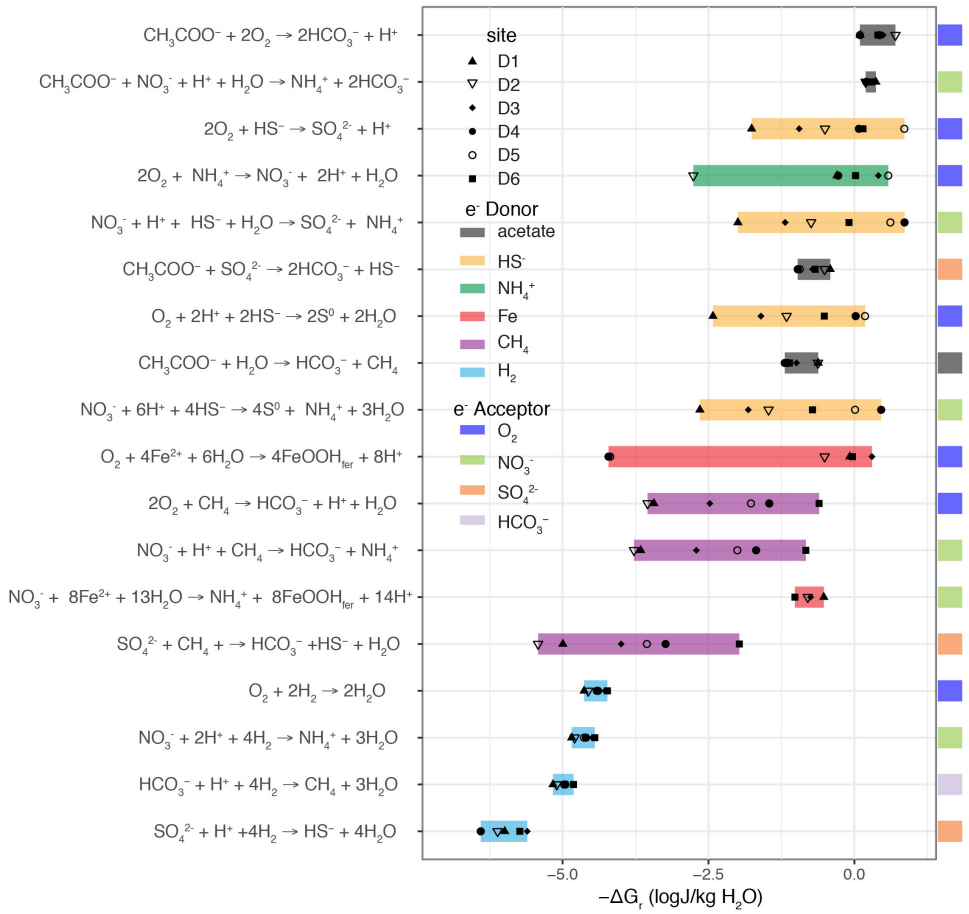

FIGURE 10 | Gibbs energy density of possible metabolic reactions for each DeMMO site. Full reactions are written on the left. Calculations for each site are indicated in by symbols where the full range observed for all sites is highlighted in a color bar corresponding to the e- donor. e- acceptor is indicated in the color bar on the far right.

has a strong negative correlation with DOC ($r = -0.75$). This relationship is as strong as the correlation between DOC and depth ($r = -0.77$). We might conclude that temperature is related to isolation age of the fluid and this represents a long-term utilization gradient. However, this is not supported by the relatively young expected age of D5 (based on water isotopes and mine geometry), which is also the warmest. Instead this correlation suggests more rapid utilization of DOC at higher temperatures. Another interesting observation is the relationship between helium, methane, and ethane. While both abiotic and biotic mechanisms of methane production produce ethane (albeit with at different ratios, e.g., Sherwood Lollar et al., 2007), there is no biotic helium production mechanism. This combined with the observed variable methane/ethane ratios, suggest both biotic and abiotic sources of methane in different ratios at different sites.

Trajectories With Time

Overall, we observe strong temporal consistency and large differences between study sites. This stability was not necessarily expected and has important implications for the use of mines as deep subsurface biosphere sampling points and our conclusions toward this biosphere as a whole. The SURF facility itself is dynamic, with strong seasonal changes in drainage into the mine based on local precipitation events and snow melt. We know that in sampling mine boreholes we are incorporating fluids coming from isolated fractures reflective of the greater deep subsurface and also those percolating through mine workings. It would be reasonable to expect that significant drainage events might impact at least the shallowest sites and/or the proportion of fracture fluid vs. mine-derived fluid in any site. The strong stability in major and minor ions, water isotopes, and physical parameters argues against any change in the fluid source to the DeMMO sites for a 2-year time period. This gives credence to our use of these sites as portals into the deep subsurface and gives a minimum integration timescale of >1 year to even the shallowest sites.

Site-specific trends in our data relate primarily to direct physical perturbation of the systems by either drilling borehole outlets or opening and closing of sampling manifolds. Sites D3, D4, and D5 were significantly modified by removal of concrete plugs. This produced large and obvious changes to the flow rates and redox sensitive geochemical measurements. For instance,

ORP values at 150–225 days, the time during and immediately after modification, varied considerably from values recorded both before and afterward (see **Figure 5**). Modification also appears to have affected ammonium in D4, which spiked at the perturbation and then returned to the pre-perturbation value after ∼1 year (**Figure 5**). Perhaps surprisingly, borehole outlet modification does not appear to have affected the conservative ion chemistry of the three drilled sites at all, suggesting the fluid itself emerges much deeper within the borehole. D6 was also significantly altered over the course of this dataset despite limited modification of the manifold itself. At this site, opening the sampling port to allow for the installation of continuous flow experiments in July 2016, changed this from a closed system to an open system. After 6 months of continuous flow, the hole ran dry and was then returned to a closed system state that has subsequently refilled (**Figure 1**). Remarkably, despite these substantial perturbations, most of the observed chemistry did not significantly change from before to after perturbation. DOC, ferrous iron, dissolved gas concentrations, and ORP do vary through time and may be related to the biogeochemical implications of packering the systems.

Habitability Potential of Each Site

Each DeMMO site presents a unique window into the deep subsurface with a distinct chemical buffet available to microorganisms. While the microbial ecology of these sites is beyond the scope of this manuscript, the geochemical data described here can be used to calculate redox energetics and posit potential metabolisms. As we observe strong concentration differences in both electron acceptors and electron donors available for microbial metabolisms, we can expect that different sites might be habitable to a different subset of microbes. Here we present values of Gibbs energy of reaction as energy density (J per kg of water) for key microbial metabolisms following the approach of Osburn et al. (2014). We use only species directly measured in this study, testing pairwise reactions of electron acceptors O_2, nitrate, sulfate, and HCO_3^- to oxidize electron donors hydrogen, ferrous iron, ammonium, sulfide, methane, and acetate. Reactions that were exergonic at least at one site are shown in **Figure 10**. In systems with limited flow (and therefore limited recharge of reactants and removal of products), energy densities are arguably more informative than energies per mole, which assume a constant, and hence unlikely resupply of oxidants and limiting reactants (Osburn et al., 2014).

Using this analysis, we can posit which metabolisms are possible and most profitable at each of the DeMMO sites, informing their habitability. Our calculations indicate that, unlike in most surface environments, oxygen and nitrate utilizing reactions are similarly energy-rich, and nitrate is the most consistently exergonic electron acceptor at D4. Sulfate reduction with hydrogen, methane, or acetate as electron donor are all exergonic, with the highest energy density deriving from acetate oxidation. Both acetoclastic and hydrogenotrophic methanogenesis are energy yielding at all sites. Hydrogenotrophic methanogenesis is the more exergonic on a per mole electrons basis, but due to low hydrogen concentrations, acetoclastic methanogenesis is more exergonic when evaluating energy density. Our results are extremely consistent with those of Osburn et al. (2014) which showed that reactions including sulfide, sulfur, ferrous iron, manganese, and ammonium to be the most exergonic. The previous study, however, didn't not address heterotrophic reactions.

Acetate oxidation yields energy at all six sites, and it is the most exergonic process at D1, D2, D3, and D6. This suggests that significant heterotrophic activity is possible even at great depth in the subsurface. In contrast, at D4 and D5, oxidation of sulfide to either elemental sulfur or to sulfate with either oxygen or nitrate are the most exergonic reactions. Visual evidence of these processes are the luxuriant white, sulfur-bearing microbial mats found at these sites (**Figure 11A**). Also, Osburn et al. (2014) found numerous putative sulfide oxidizing microbes based on DNA sequencing at BH8 which is equivalent to D5. Iron oxidation could be an important metabolism at D1, D2, D3, and D6. Again, we see evidence for these metabolisms in the red, iron-rich biofilms formed at the borehole outlets. Visualization of these iron oxides via scanning electron microscopy further reveals that they are composed almost exclusively of the distinctive twisted stalks (**Figure 11B**) produced by direct microbial iron oxidation by Gallionella-like species (Emerson and Moyer, 1997). Osburn et al. (2014) identified putative iron

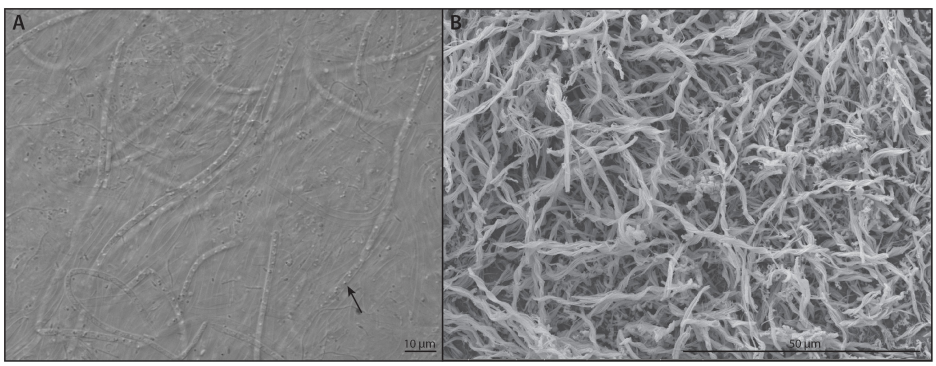

FIGURE 11 | Microscopic images indicating microbial metabolisms. **(A)** light microscopy image of a putative sulfide oxidizing filamentous bacterium with intracellular S^0 globules (arrow) taken from the outflow of D5 **(B)** SEM image of a twisted iron oxide stalk from the outflow of D3 produced by putative iron oxidizing bacteria.

oxidizers in BH2 (D1), BH5 (D2) although not Manifold B (D6). Ammonium oxidation is a viable metabolism at all sites but D2, where it is exergonic but has very low energy density. Methanogenesis generally has low energy density, but is viable at D6 and to a lesser degree at D4 and D5. Interestingly, these calculations correspond quite well to where and in what concentrations we observe methane (see **Figure 6**) although methanogens were found only in very low abundance by Osburn et al. (2014). In summary, the close agreement between our calculations and tangible observations yields confidence in this approach to defining habitability. We find that there is a rich assortment of both lithotrophic and heterotrophic metabolisms are possible at each site, although these vary considerably between sites, creating a distinct habitability fingerprint for each of these windows into the deep subsurface.

CONCLUSION

The now-established Deep Mine Microbial Observatory (DeMMO) is a new portal into the deep subsurface biosphere. The two-year time series presented here establishes baseline geochemical conditions of each site, identifies variability, and characterizes inherent controls on habitability. We observe distinct yet remarkably stable geochemical profiles at each site, suggesting a separate water source for each. Water isotopes and conductivity measurements support the presence of relatively young fluids at D2, D4, and D5 compared to relatively older fluids at D1, D3, and D6. Cationic compositions do not always correspond in a straightforward way to the lithologies encountered in each borehole log. We suggest that this may indicate longer than predicted fluid flow paths, channelized flow within intrusive rocks or quartz veins, and/or clay exchange. Using this timeseries, we are able to observe the changes induced by outlet modification of historical boreholes. Redox sensitive ions were the most sensitive to these anthropogenic perturbations and stabilized after $\sim$<1 year, whereas major ions were largely insensitive to these changes. We suggest this might inform future efforts within the community to modify and sample other deep subsurface sites. Energetic calculations identify a number of profitable sources of energy available to subsurface inhabitants of the DeMMO network, particularly sulfide and iron oxidation as well as heterotrophic reactions. We hope that this baseline serves to introduce the community to DeMMO such that it may be a resource for future queries into the deep subsurface environment.

DATA AVAILABILITY

All datasets generated for this study are included in the manuscript and/or the **Supplementary Files**.

AUTHOR CONTRIBUTIONS

MO designed the study and wrote the manuscript. BK was the field manager of the project and directed each field expedition. CC was a graduate student working at the site who collected most of the samples and performed microscopy. AM was our isotope lab manager who produced DIC concentration and isotope data. JA was PI of NAI Life Underground which funded most of this work. All authors contributed to the creation of the manuscript and study design.

FUNDING

This work was funded with NAI grant #NNAI3AA92A to JA (PI) and MO (Co-I) and NASA Exobiology grant #NNX15AM086 to MO.

ACKNOWLEDGMENTS

Many people contributed to the successful completion of this project. We thank Pratixaben Savalia for producing dissolved gas measurements and George Rose for machining the packer components. In addition, we thank Jaret Heise, Tom Reagan, and Kathy Hart from SURF for their assistance with field expeditions, access to maps and drill logs, and for permission to publish **Figure 2**.

SUPPLEMENTARY MATERIAL

The Supplementary Material for this article can be found online at: https://www.frontiersin.org/articles/10.3389/feart.2019.00196/full#supplementary-material

REFERENCES

Alter, M. D., and Steiof, M. (2005). Optimized method for dissolved hydrogen sampling in groundwater. *J. Contam. Hydrol.* 78, 71–86. doi: 10.1016/j.jconhyd.2005.03.002

Amend, J. P., and Teske, A. (2005). Expanding frontiers in deep subsurface microbiology. *Palaeogeogr. Palaeoclimatol. Palaeoecol.* 219, 131–155. doi: 10.1016/j.palaeo.2004.10.018

Bowen, G. (2018). *The Online Isotopes in Precipitation Calculator, version 3.1*.

Bowen, G. J., and Revenaugh, J. (2003). Interpolating the isotopic composition of modern meteoric precipitation. *Water Resour. Res.* 39:1299. doi: 10.1029/2003WR002086

Bowen, G. J., Wassenaar, L. I., and Hobson, K. A. (2005). Global application of stable hydrogen and oxygen isotopes to wildlife forensics. *Oecologia* 143, 337–348. doi: 10.1007/s00442-004-1813-y

Caddey, S. W. (1991). *The Homestake Gold Mine, an Early Proterozoic iron-formation-hosted gold deposit, Lawrence County, South Dakota*. Reston, VA: U.S. Geological Survey.

Cardace, D., Hoehler, T., McCollom, T., and Schrenk, M. (2013). Establishment of the coast range ophiolite microbial observatory (CROMO): drilling objectives and preliminary outcomes. *Sci. Drill.* 16, 45–55. doi: 10.5194/sd-16-45-2013

Cavicchioli, R. (2002). Extremophiles and the search for extraterrestrial life. *Astrobiology* 2, 281–292. doi: 10.1089/153110702762027862

Chapelle, F. H., O'neill, K., Bradley, P. M., Methé, B. A., Ciufo, S. A., Knobel, L. L., et al. (2002). A hydrogen-based subsurface microbial community dominated by methanogens. *Nature* 415, 312–315. doi: 10.1038/415312a

Chivian, D., Brodie, E. L., Alm, E. J., Culley, D. E., Dehal, P. S., DeSantis, T. Z., et al. (2008). Environmental genomics reveals a single-species ecosystem deep within Earth. *Science* 322, 275–278. doi: 10.1126/science.1155495

Colman, D. R., Poudel, S., Stamps, B. W., Boyd, E. S., and Spear, J. R. (2017). The deep, hot biosphere: twenty-five years of retrospection. *PNAS* 114, 6895–6903. doi: 10.1073/pnas.1701266114

Colwell, F. S., and D'Hondt, S. (2013). Nature and extent of the deep biosphere. *Rev. Mineral. Geochem.* 75, 547–574. doi: 10.2138/rmg.2013.75.17

Colwell, F. S., and Lehman, R. M. (1997). Carbon source utilization profiles for microbial communities from hydrologically distinct zones in a basalt aquifer. *Microb. Ecol.* 33, 240–251. doi: 10.1007/s002489900027

Criss, R. E. (1999). *Principles of Stable Isotope Distribution*. Oxford: Oxford University Press.

Emerson, D., and Moyer, C. (1997). Isolation and characterization of novel iron-oxidizing bacteria that grow at circumneutral pH. *Appl. Environ. Microbiol.* 63, 4784–4792.

Flynn, T. M., Sanford, R. A., and Bethke, C. M. (2008). Attached and suspended microbial communities in a pristine confined aquifer. *Water Resour. Res.* 44, 832–837. doi: 10.1029/2007WR006633

Fredrickson, J. K., and Onstott, T. C. (2001). "Biogeochemical and geological significance of subsurface microbiology," in *Subsurface Microbiology and Biogeochemistry*, ed. J. K. Fredrickson (Hoboken, NJ: Wiley-Liss), 3–37.

Fry, J. C., Horsfield, B., Sykes, R., Cragg, B. A., Heywood, C., Kim, G. T., et al. (2009). Prokaryotic populations and activities in an interbedded coal deposit, including a previously deeply buried section (1.6–2.3 km) Above 150 Ma basement rock. *Geomicrobiol. J.* 26, 163–178. doi: 10.1080/01490450902724832

Gat, J. R. (1996). Oxygen and hydrogen isotopes in the hydrologic cycle. *Annu. Rev. Earth Planet. Sci.* 24, 225–262. doi: 10.1146/annurev.earth.24.1.225

Griebler, C., and Lueders, T. (2009). Microbial biodiversity in groundwater ecosystems. *Freshw. Biol.* 54, 649–677. doi: 10.1111/j.1365-2427.2008.02013.x

Heise, J. (2015). The sanford underground research facility at homestake. *J. Phys. Conf. Ser.* 606, 12015–12026. doi: 10.1088/1742-6596/606/1/012015

Holland, G., Lollar, B. S., Li, L., Lacrampe-Couloume, G., Slater, G. F., and Ballentine, C. J. (2013). Deep fracture fluids isolated in the crust since the Precambrian era. *Nature* 497, 357–360. doi: 10.1038/nature12127

Kennedy, J. R., Koth, K. R., and Carruth, R. (2015). *Surface and Subsurface Microgravity Data in the Vicinity of Sanford Underground Research Facility, Lead, South Dakota*. U.S. Geological Survey: Reston, VA

Kietavainen, R., Ahonen, L., Niinikoski, P., Nykänen, H., and Kukkonen, I. T. (2017). Abiotic and biotic controls on methane formation down to 2.5 km depth within the Precambrian Fennoscandian Shield. *Geochim. Cosmochim. Acta* 202, 124–145. doi: 10.1016/j.gca.2016.12.020

Küsel, K., Totsche, K. U., Trumbore, S. E., Lehmann, R., Steinhäuser, C., and Herrmann, M. (2016). How deep can surface signals be traced in the critical zone? merging biodiversity with biogeochemistry research in a Central German Muschelkalk Landscape. *Front. Earth Sci.* 4:32. doi: 10.3389/feart.2016.00032

Leenheer, J. A., Malcolm, R. L., and McKinley, P. W. (1974). Occurrence of dissolved organic carbon in selected ground-water samples in the united states. *J. Res. U.S. Geol.* 2, 361–369.

Li, L., Wing, B. A., Bui, T. H., McDermott, J. M., Slater, G. F., Wei, S., et al. (2016). Sulfur mass-independent fractionation in subsurface fracture waters indicates a long-standing sulfur cycle in Precambrian rocks. *Nat. Commun.* 516, 1–9. doi: 10.1038/ncomms13252

Magnabosco, C., Ryan, K., Lau, M. C. Y., Kuloyo, O., Lollar, B. S., Kieft, T. L., et al. (2015). A metagenomic window into carbon metabolism at 3 km depth in Precambrian continental crust. *Nat. Publish. Group* 10, 730–741. doi: 10.1038/ismej.2015.150

Magot, M., Ollivier, B., and Patel, B. (2000). Microbiology of petroleum reservoirs. *Antonie Van Leeuwenhoek* 77, 103–116.

Mitchell, S. T. (2009). *Nuggets to Neutrinos: The Homestake Story*. Bloomington, IN: Xlibris Corporation.

Momper, L., Jungbluth, S. P., Lee, M. D., and Amend, J. P. (2017a). Energy and carbon metabolisms in a deep terrestrial subsurface fluid microbial community. *ISME J.* 11, 2319–2333. doi: 10.1038/ismej.2017.94

Momper, L., Kiel Reese, B., Zinke, L., Wanger, G., Osburn, M. R., Moser, D., et al. (2017b). Major phylum-level differences between porefluid and host rock bacterial communities in the terrestrial deep subsurface. *Environ. Microbiol. Rep.* 9, 501–511. doi: 10.1111/1758-2229.12563

Morelli, R. M., Bell, C. C., Creaser, R. A., and Simonetti, A. (2010). Constraints on the genesis of gold mineralization at the Homestake Gold Deposit, Black Hills, South Dakota from rhenium–osmium sulfide geochronology. *Miner. Deposita* 45, 461–480. doi: 10.1007/s00126-010-0284-9

Murdoch, L. C., Germanovich, L. N., Wang, H., Onstott, T. C., Elsworth, D., Stetler, L., et al. (2011). Hydrogeology of the vicinity of Homestake mine, South Dakota, USA. *Hydrogeol. J.* 20, 27–43. doi: 10.1007/s10040-011-0773-7

Murphy, E. M., Schramke, J. A., Fredrickson, J. K., Bledsoe, H. W., Francis, A. J., Sklarew, D. S., et al. (1992). The influence of microbial activity and sedimentary organic carbon on the isotope geochemistry of the middendoff aquifer. *Water Resour. Res.* 28, 723–740. doi: 10.1029/91wr02678

Nealson, K., Inagaki, F., and Takai, K. (2005). Hydrogen-driven subsurface lithoautotrophic microbial ecosystems (SLiMEs): do they exist and why should we care? *Trends Microbiol.* 13, 405–410. doi: 10.1016/j.tim.2005.07.010

Nyyssonen, M., Hultman, J., Ahonen, L., Kukkonen, I., Paulin, L., Laine, P., et al. (2013). Taxonomically and functionally diverse microbial communities in deep crystalline rocks of the Fennoscandian shield. *ISME J.* 8, 126–138. doi: 10.1038/ismej.2013.125

Onstott, T. C., Lin, L. H., Davidson, M., Mislowack, B., Borcsik, M., Hall, J., et al. (2006). The origin and age of biogeochemical trends in deep fracture water of the Witwatersrand Basin, South Africa. *Geomicrobiol. J.* 23, 369–414. doi: 10.1080/01490450600875688

Osburn, M. R., LaRowe, D. E., Momper, L. M., and Amend, J. P. (2014). Chemolithotrophy in the continental deep subsurface: Sanford underground research facility (SURF), USA. *Front. Microbiol.* 5:610. doi: 10.3389/fmicb.2014.00610

Pedersen, K. (1996). 16S rRNA gene diversity of attached and unattached bacteria in boreholes along the access tunnel to the Äspö hard rock laboratory, Sweden. *FEMS Microbiol. Ecol.* 19, 249–262. doi: 10.1016/0168-6496(96)00017-7

Pedersen, K. (2001). "Diversity and activity of microorganisms in deep igneous rock aquifers of the Fennoscandian Shield," in *Subsurface Microbiology and Biogeochemistry*, eds J. K. Fredrickson and M. Fletcher (Hoboken, NJ: Wiley-Liss), 97–139.

Pedersen, K., Bomberg, M., and Itävaara, M. (2014). *Summary Report Microbiology of Olkiluoto and ONKALO Groundwater. Report number: Posiva report 2012-42*. Eurajoki: Posiva Oy.

Probst, A. J., Castelle, C. J., Singh, A., Brown, C. T., Anantharaman, K., Sharon, I., et al. (2016). Genomic resolution of a cold subsurface aquifer community provides metabolic insights for novel microbes adapted to high CO2 concentrations. *Environ. Microbiol.* 19, 459–474. doi: 10.1111/1462-2920.13362

Probst, A. J., Ladd, B., Jarett, J. K., Geller-McGrath, D. E., Sieber, C. M. K., Emerson, J. B., et al. (2018). Differential depth distribution of microbial function and putative symbionts through sediment-hosted aquifers in the deep terrestrial subsurface. *Nat. Microbiol.* 3, 328–336. doi: 10.1038/s41564-017-0098-y

Purkamo, L., Bomberg, M., Kietäväinen, R., Salavirta, H., Nyyssönen, M., Nuppunen-Puputti, M., et al. (2016). Microbial co-occurrence patterns in deep Precambrian bedrock fracture fluids. *Biogeosciences* 13, 3091–3108. doi: 10.5194/bg-13-3091-2016

Rastogi, G., Gurram, R. N., Bhalla, A., Gonzalez, R., Bischoff, K. M., Hughes, S. R., et al. (2013). Presence of glucose, xylose, and glycerol fermenting bacteria in the deep biosphere of the former Homestake gold mine, South Dakota. *Front. Microbiol.* 4:18. doi: 10.3389/fmicb.2013.00018

Rastogi, G., Osman, S., Kukkadapu, R., Engelhard, M., Vaishampayan, P. A., Andersen, G. L., et al. (2010). Microbial and mineralogical characterizations of soils collected from the deep biosphere of the Former Homestake Gold Mine, South Dakota. *Microb. Ecol.* 60, 539–550. doi: 10.1007/s00248-010-9657-y

Rastogi, G., Stetler, L. D., Peyton, B. M., and Sani, R. K. (2009). Molecular analysis of prokaryotic diversity in the deep subsurface of the former Homestake gold mine, South Dakota, USA. *J Microbiol.* 47, 371–384. doi: 10.1007/s12275-008-0249-1

Sherwood Lollar, B., Voglesonger, K., Lin, L. H., Lacrampe-Couloume, G., Telling, J., Abrajano, T. A., et al. (2007). Hydrogeologic controls on episodic H_2 release from precambrian fractured rocks—energy for deep subsurface life on earth and mars. *Astrobiology* 7, 971–986. doi: 10.1089/ast.2006.0096

Simkus, D. N., Slater, G. F., Lollar, B. S., Wilkie, K., Kieft, T. L., Magnabosco, C., et al. (2016). Variations in microbial carbon sources and cycling in the deep continental subsurface. *Geochim. Cosmochim. Acta* 173, 264–283. doi: 10.1016/j.gca.2015.10.003

Steadman, J. A., and Large, R. R. (2016). Synsedimentary, diagenetic, and metamorphic pyrite, pyrrhotite, and marcasite at the homestake BIF-Hosted Gold Deposit, South Dakota, USA: insights on Au-As ore genesis from textural and LA-ICP-MS trace element studies. *Econ. Geol.* 111, 1731–1752. doi: 10.2113/econgeo.111.7.1731

Stevens, T. O., and McKinley, J. P. (1995). Lithoautotrophic microbia, ecosystems in deep basalt aquifers. *Science* 270, 450–454. doi: 10.1126/science.270.5235.450

Stroes-Gascoyne, S., Schippers, A., Schwyn, B., Poulain, S., Sergeant, C., Simonoff, M., et al. (2007). Microbial community analysis of opalinus clay drill core samples from the mont terri underground research laboratory, Switzerland. *Geomicrobiol. J.* 24, 1–17. doi: 10.1080/01490450601134275

Vető, I., Futó, I., Horváth, I., and Szántó, Z. (2004). Late and deep fermentative methanogenesis as reflected in the H-C-O-S isotopy of the methane-water system in deep aquifers of the Pannonian Basin (SE Hungary). *Organ. Geochem.* 35, 713–723. doi: 10.1016/j.orggeochem.2004.02.004

Waddell, E. J., Elliott, T. J., Vahrenkamp, J. M., Roggenthen, W. M., Sani, R. K., Anderson, C. M., et al. (2010). Phylogenetic evidence of noteworthy microflora from the subsurface of the former Homestake gold mine, Lead, South Dakota. *Environ. Technol.* 31, 979–991. doi: 10.1080/09593331003789511

Welker, J. M. (2000). Isotopic (d18O) characteristics of weekly precipitation collected across the USA: an initial analysis with application to water source studies. *Hydrol. Process.* 14, 1449–1464. doi: 10.1002/1099-1085(20000615)14:8<1449::aid-hyp993<3.0.co;2-7

Conflict of Interest Statement: The authors declare that the research was conducted in the absence of any commercial or financial relationships that could be construed as a potential conflict of interest.

frontiers in Microbiology

ORIGINAL RESEARCH
published: 28 August 2019
doi: 10.3389/fmicb.2019.01983

Ecology of Subseafloor Crustal Biofilms

Gustavo A. Ramírez[1†], Arkadiy I. Garber[2], Aurélien Lecoeuvre[3,4†], Timothy D'Angelo[3], C. Geoffrey Wheat[5] and Beth N. Orcutt[3]*

[1] Graduate School of Oceanography, University of Rhode Island, Narragansett, RI, United States, [2] Division of Biological Sciences, University of Montana, Missoula, MT, United States, [3] Bigelow Laboratory for Ocean Sciences, East Boothbay, ME, United States, [4] Université de Bretagne Occidentale, UFR Sciences et Techniques, Brest, France, [5] Institute of Marine Science, University of Alaska Fairbanks, Fairbanks, AK, United States

OPEN ACCESS

Edited by:
Sabin Zahirovic, University of Sydney, Australia

Reviewed by:
James F. Holden, University of Massachusetts Amherst, United States
Ruiyong Zhang, Federal Institute For Geosciences and Natural Resources, Germany
Craig Lee Moyer, Western Washington University, United States

***Correspondence:**
Beth N. Orcutt
borcutt@bigelow.org

†Present address:
Gustavo A. Ramírez, Department of Marine Sciences, University of North Carolina at Chapel Hill, Chapel Hill, NC, United States; College of Veterinary Medicine, Western University of Health Sciences, Pomona, CA, United States
Aurélien Lecoeuvre, Université de Paris, Institut de Physique du Globe de Paris, Paris, France

Specialty section:
This article was submitted to Extreme Microbiology, a section of the journal Frontiers in Microbiology

Received: *02 May 2019*
Accepted: *13 August 2019*
Published: *28 August 2019*

Citation:
Ramírez GA, Garber AI, Lecoeuvre A, D'Angelo T, Wheat CG and Orcutt BN (2019) Ecology of Subseafloor Crustal Biofilms. Front. Microbiol. 10:1983. doi: 10.3389/fmicb.2019.01983

The crustal subseafloor is the least explored and largest biome on Earth. Interrogating crustal life is difficult due to habitat inaccessibility, low-biomass and contamination challenges. Subseafloor observatories have facilitated the study of planktonic life in crustal aquifers, however, studies of life in crust-attached biofilms are rare. Here, we investigate biofilms grown on various minerals at different temperatures over 1–6 years at subseafloor observatories in the Eastern Pacific. To mitigate potential sequence contamination, we developed a new bioinformatics tool – *TaxonSluice*. We explore ecological factors driving community structure and potential function of biofilms by comparing our sequence data to previous amplicon and metagenomic surveys of this habitat. We reveal that biofilm community structure is driven by temperature rather than minerology, and that rare planktonic lineages colonize the crustal biofilms. Based on 16S rRNA gene overlap, we partition metagenome assembled genomes into planktonic and biofilm fractions and suggest that there are functional differences between these community types, emphasizing the need to separately examine each to accurately describe subseafloor microbe-rock-fluid processes. Lastly, we report that some rare lineages present in our warm and anoxic study site are also found in cold and oxic crustal fluids in the Mid-Atlantic Ridge, suggesting global crustal biogeography patterns.

Keywords: deep biosphere, subseafloor, oceanic crust, Juan de Fuca, CORK, FLOCS, low biomass

INTRODUCTION

Sediment-buried oceanic crust is one of the most inaccessible and understudied habitats on Earth (Orcutt et al., 2011b; Edwards et al., 2012). Upper oceanic crust, with an estimated volume of 10^{18} cubic meters (Fisk et al., 1998), hosts a global subseafloor aquifer (Fisher and Becker, 2000) that cycles through the crust at a water volume-equivalent to that of the planet's oceans every 10^5 to 10^6 years (Elderfield and Schultz, 1996; Wheat et al., 2003). This creates a water-rock thermodynamic disequilibrium that may power chemolithoautotrophy (Bach and Edwards, 2003; Edwards et al., 2005). The large volume of this habitat, despite lower biomass loads compared to overlying sediments (Kallmeyer et al., 2012), makes relatively small contributions of *in situ* dark autotrophy potentially significant to the local and global carbon cycle (McCarthy et al., 2010; Edwards, 2011; Orcutt et al., 2015).

A major challenge to ecological studies of subseafloor crust is containing and mitigating inadvertent contamination of low biomass samples during seafloor drilling (Lever et al., 2006, 2013; Masui et al., 2008; Santelli et al., 2010; Labonte et al., 2017). To this end, subseafloor observatories called CORKs (Davis et al., 1992; Wheat et al., 2010) were used successfully in microbiological

studies of crustal fluids at the eastern flank of the Juan de Fuca (JdF) Ridge (Cowen et al., 2003; Jungbluth et al., 2013, 2014, 2016, 2017a; Robador et al., 2014) and at North Pond (NP) on the western flank of the Mid-Atlantic Ridge (Meyer et al., 2016; Shah Walter et al., 2018; Tully et al., 2018). These studies show that plankton communities in warm and anoxic JdF crustal fluids change over time and are comprised of unique lineages within the Firmicutes, Deltaproteobacteria, Aminicenantes/OP8, and Thermotogae, that are rare in other marine systems. In contrast, the cool and oxic crustal plankton communities at NP are enriched in Gamma- and Epsilon-proteobacteria and are more similar in structure to bottom seawater. Recent metagenomic analysis suggests that NP crustal fluid planktonic communities are functionally stable despite temporal shifts in dominant taxonomic groups (Tully et al., 2018).

Despite progress in the study of crustal fluid plankton, the nature of crust-attached biofilms in this habitat is less well understood. Mineral colonization experiments using Flow-through Osmotic Colonization Systems [FLOCS, (Orcutt et al., 2010)] deployed within CORK observatories have grown biofilms *in situ* from crustal fluid inoculant (Orcutt et al., 2011a; Smith et al., 2011, 2016; Baquiran et al., 2016). These studies suggest that FLOCS-grown biofilms (contaminant-free proxies of natural crustal biofilms) are more similar to each other than the surrounding fluids seeding them, suggesting structural and potentially functional distinctions between crustal biofilm and plankton. The driving environmental factors and ecological effects of these differences are unknown. To our knowledge, metagenomic analysis of native subseafloor crustal biofilm communities has not be successful to date, although there are two recent metagenomic assessments of biofilms formed during incubations with subseafloor rocks *in vitro* (Zhang et al., 2016) and *in situ* (Smith et al., 2019). These studies suggest potential for carbon fixation by biofilm communities using the Wood-Ljundahl reductive TCA cycle, and also the potential for dissimilatory nitrate reduction. In oxic *in vitro* incubations of subseafloor basalts, iron cycling pathways appear to be prevalent (Zhang et al., 2016) whereas in an *in situ* iron-rich olivine incubation within anoxic sediment buried crust, sulfate reduction is more prevalent (Smith et al., 2019). Prior studies suggest that mineralogy is a driving factor influencing biofilm community structure on seafloor and subseafloor minerals (Toner et al., 2013; Smith et al., 2016), and one study also suggests that temperature is another important factor (Baquiran et al., 2016).

To further examine the nature of biofilms in the subseafloor crust, we assess biofilm community response to different environmental conditions through microbe-mineral incubation experiments within CORKs at the JdF Ridge flank (**Figure 1**). The incubations varied in mineral substrates, deployment temperature, and time, but all accessed the same subsurface crustal aquifer fluids. 16S rRNA gene amplicon sequence analysis of these low-biomass samples required the development of a new bioinformatics tool – *TaxonSluice* – for robust elimination of potential contaminant sequences. By comparing biofilm amplicon datasets recovered from our incubations to previously published metagenomic datasets from JdF and NP crustal fluids, as well as a metagenome from a subseafloor incubation of olivine at JdF, genetic differences with respect to potential activities of crust-attached biofilm and planktonic communities are assessed and the extent of biogeographical connectivity of the subseafloor crust is explored.

MATERIALS AND METHODS

Study Site

The four JdF subseafloor observatories targeted in this study include a transect of cased boreholes with CORKs that penetrate into ∼3.5 Ma year-old sediment-covered basaltic crust along a fluid flow path (**Figure 1** and **Supplementary Table S1**), as described elsewhere (Expedition 327 Scientists, 2011a). This configuration allows subseafloor conditions to return to a pre-drilling hydrogeological state by stopping bottom water intake (Fisher et al., 2011). Two observatories in the transect (Holes 1026B and U1301A) were previously used for mineral incubation studies (Orcutt et al., 2011a; Smith et al., 2011; Baquiran et al., 2016). The other two observatories, with upgraded materials to prevent corrosion, were installed during Integrated Ocean Drilling Program (IODP) Expedition 327 in 2010 (Fisher et al., 2011; Jungbluth et al., 2016). Overall, fluid conditions in the subsurface crust at this site are characterized as warm (64°C), anoxic, and sulfate-replete (Wheat et al., 2011; Neira et al., 2016).

Experiment Design

Colonization experiments were deployed at depth in the observatories during IODP Expedition 327 in 2010 and at the observatory wellheads on cruise AT26-03 in 2013 (**Figure 1B** and **Supplementary Table S2**). All samples were recovered in August 2014 during cruise AT26-18 of the R/V *Atlantis* (Woods Hole Oceanographic Institution). FLOCS deployed at depth downhole were exposed to *in situ* conditions within the anoxic 64°C crustal subseafloor aquifer, whereas FLOCS deployed at the wellhead are inoculated with the same crustal fluid sourced from below but are chilled in the surrounding 2°C oxic bottom water at the seafloor (**Figure 1B** and **Supplementary Table S1**). Wellhead FLOCS conditions are therefore cold and may have trace levels of oxygen from diffusion across FLOCS plastic materials, as discussed elsewhere (Baquiran et al., 2016). Briefly, FLOCS used in this study consisted of sterile massive basalts (previously cored from JdF Holes 1027B/U1301B) and commercially available pyrite (FeS_2, Ward's Science, Catalogue 466448) crushed (<250 μm grain size) and autoclaved prior to deployment as described elsewhere (Fisher et al., 2011). For additional details on FLOCS deployment configuration and recovery, see **Supplementary Information**.

Microscopy, Geochemical, and DNA Analyses

Methods used for sample preservation, scanning electron microscopy (SEM), geochemical analyses of the fluids exiting the FLOCS units, DNA extraction, quantitative polymerase chain reaction analysis of the small subunit ribosomal RNA

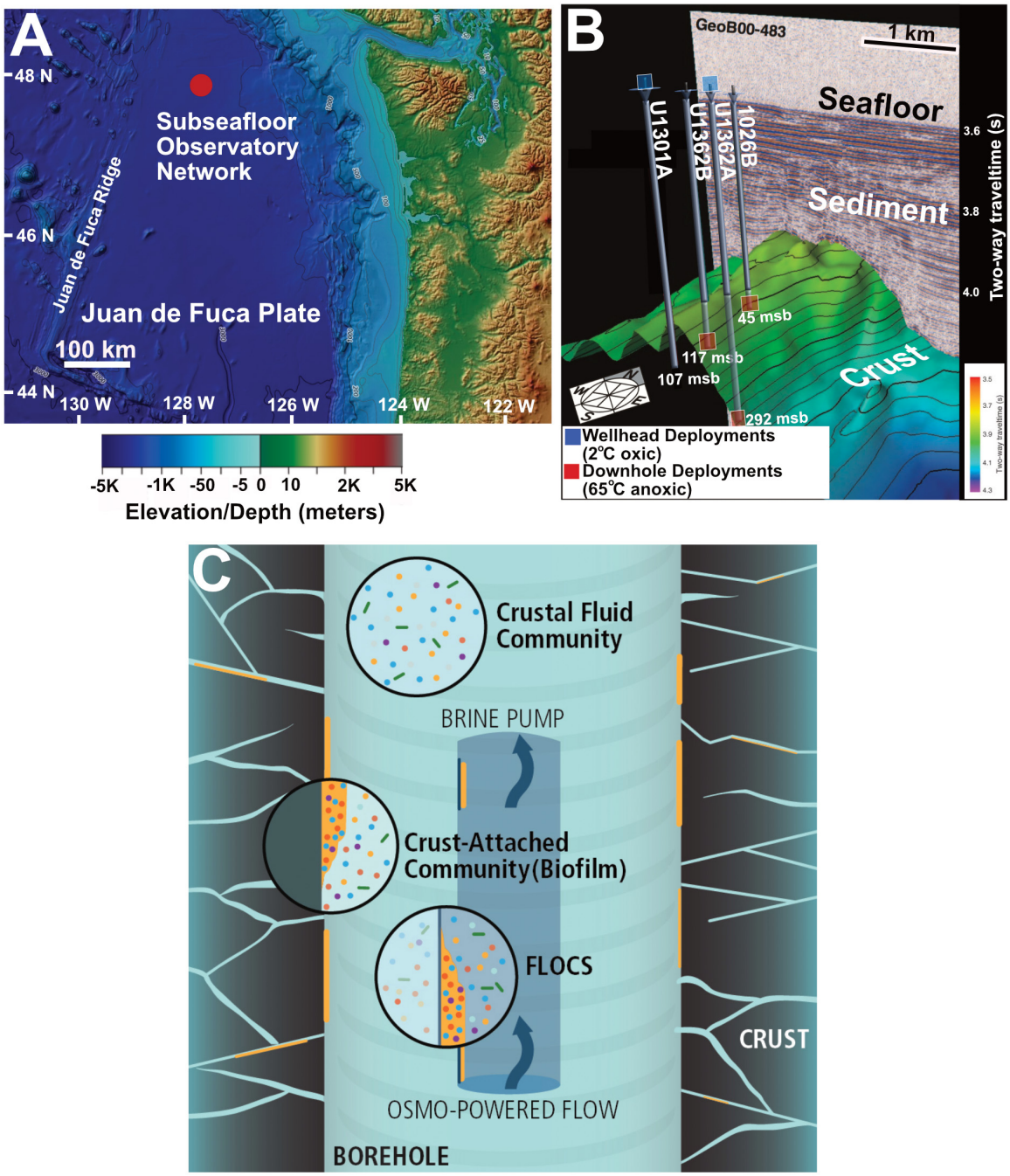

FIGURE 1 | (A) Location of Juan de Fuca Ridge CORK observatory sites in the northeastern Pacific Ocean. **(B)** Overview of subsurface crustal topography and penetration of CORK observatories used for experiment deployment in this study. IODP originated figure modified from Expedition 327 Scientists (2011b). **(C)** Schematic of FLOCS *in situ* deployment highlighting the differences in planktonic and crust-attached communities.

(16S rRNA) gene, 16S rRNA gene amplicon sequencing via Illumina, and data processing steps are described in detail in the **Supplementary Material**. Due to low DNA concentrations in the extracts (**Supplementary Table S3**), replicate extracts from similar experiments and minerals were pooled according to sample identity and further concentrated prior to 16S rRNA gene amplification. Extracts from procedural blanks were also pooled and sequenced to address2 inadvertent contamination, as described below. Sequence data was processed with *mothur* (Schloss et al., 2009) at the 97% or greater sequence similarity level defining an Operational Taxonomic Unit (OTU). All new sequence data from this study are

publicly available in the NCBI Short Read Archive under BioProject PRJNA472057; BioSample accession numbers: SAMN09228041–SAMN09228055.

Correcting for Potential Contaminant 16S rRNA Gene Sequences: *TaxonSluice*

As the amount of material available for analysis was limited, and the incubation settings are low biomass environments [*i.e.*: roughly 10^4 cells ml^{-1} (Jungbluth et al., 2013)], significant effort was invested in evaluating protocol blanks to assess for possible contamination in the sequence data, as recommended elsewhere (Sheik et al., 2018). To identify contaminant sequences in low-biomass samples, we developed a new bioinformatic tool: *TaxonSluice*. The code, sample datasets (data used for this study), validation efforts on mock communities, and additional user information (dependencies and user-set parameters) for this tool are publicly available on GitHub[1]. Briefly, *TaxonSluice* implements a novel heuristic algorithm (**Supplementary Material** and **Supplementary Figure S1**) with OTU tables and user input to specify blanks to identify potential contaminant sequences based on a user-defined abundance threshold (10% default). In this study, extraction blanks were incorporated in each batch of sample extractions, enabling assessment of multiple blanks across the dataset. Algorithm outputs include a summary of all "flagged" OTUs (**Supplementary Figure S1**) along with percent identity, percent coverage, *e*-value and environmental source for the 10 closest matches in the SILVA database. The user validates output prior to culling any of the flagged OTUs from the data. This multiple-blank approach is advantageous because each blank represents independent biological data, outside the single sample and sample-specific blank couple.

Linking Biofilm Amplicons and Metagenomic Data

To assess taxonomic overlap between the biofilm communities in this study with crustal fluid communities and other biofilm studies, biofilm 16S rRNA gene amplicon sequences recovered from our FLOCS incubations were used to recruit metagenomic reads from crustal fluids from JdF (Jungbluth et al., 2017a) and NP (Tully et al., 2018) as well as from a subseafloor incubation of olivine at JdF (Smith et al., 2019). Thus, we highlight that differentiation of biofilm and planktonic cells in these comparisons is exclusively done *in silico*. These publicly available metagenomes were downloaded from the NCBI Sequence Read Archive: JdF crustal fluid (NCBI BioSamples SAMNO3166137 and SAMO3166138 for Hole U1362A and U1362B fluids, respectively), NP crustal fluid [NCBI BioSamples SAMN07571231–SAMN07571245 for Holes U1382A and U1383C at various sampling times and depths, see Tully et al. (2018)], and JdF olivine [NCBI BioProject number PRJNA264811 (Smith et al., 2019)]. Metagenomes were assembled into contigs and binned into metagenome-assembled genomes (MAGs) following a pipeline described in the **Supplementary Information**.

To link functional potential of reconstructed MAGs to our FLOCS biofilms, 16S rRNA gene amplicons generated from biofilms were queried against the subset of MAGs containing full-length or near full-length 16S rRNA genes using BLASTn v2.2.30 + (Altschul et al., 1990), with the following parameters: -qcov_hsp_perc 0.9 -perc_identity 99.0. Crustal fluid MAGs with 16S rRNA genes meeting this alignment threshold were considered "biofilm-linked" (i.e., they are hypothesized to represent planktonic groups, or closest relatives, that transitioned from planktonic to biofilm lifestyles, see **Figure 2**). MAGs that had 16S rRNA genes not matching any of the FLOCS biofilm 16S rRNA gene amplicons were considered "planktonic". We note that 16S rRNA genes are notoriously difficult to reconstruct from metagenomic data (Yuan et al., 2015) and consequently, not all of the reconstructed MAGs had them. To minimize biases, MAGs lacking 16S rRNA gene sequences were excluded from subsequent genomic comparisons of planktonic vs. biofilm-linked fractions. For quality, assembly of 16S rRNA genes was assessed by mapping metagenome reads to the reconstructed 16S rRNA sequences using Bowtie2 v2.3.4.1 (Langmead and Salzberg, 2012), and manually examining the uniformity of read coverage. We also compared the overall read coverage among each reconstructed 16S rRNA gene and the contig from which each gene was predicted. MAGs with 16S rRNA genes with highly variable gene coverage profiles were excluded from all downstream analyses. MAGs were annotated using GhostKOALA (Kanehisa et al., 2016b). KEGG (Kanehisa et al., 2016a) assignments for each set of MAGs (biofilm-linked vs. planktonic) were normalized to total number of predicted ORFs and the resulting gene counts compared. For estimation of metabolic potential, a library of custom and publically available (Anantharaman et al., 2016) hidden Markov models (HMMs) was queried against each set of MAGs. The HMM library and associated scripts are available in GitHub: https://github.com/Arkadiy-Garber/taxonsluice/tree/master/custom_scripts_and_libs.

RESULTS

Summary of Deployment Conditions and Chemical Analyses

FLOCS were deployed for periods of one and 4 years (**Table 1**). Despite the different locations, temporal records of dissolved magnesium and sulfur (sulfate) indicate that subsurface crustal fluids were pulled into all of the FLOCS chambers (**Supplementary Figure S2**). After an initial period of mixing of the crustal fluid with the sterile deployment solutions, the concentrations of these ions reach concentrations that are expected for this environment (Wheat et al., 2010). These chemical records confirm the structural and functional integrity of our experiments throughout the deployment periods and indicate that intrusion of bottom seawater did not occur.

[1]https://github.com/Arkadiy-Garber/taxonsluice

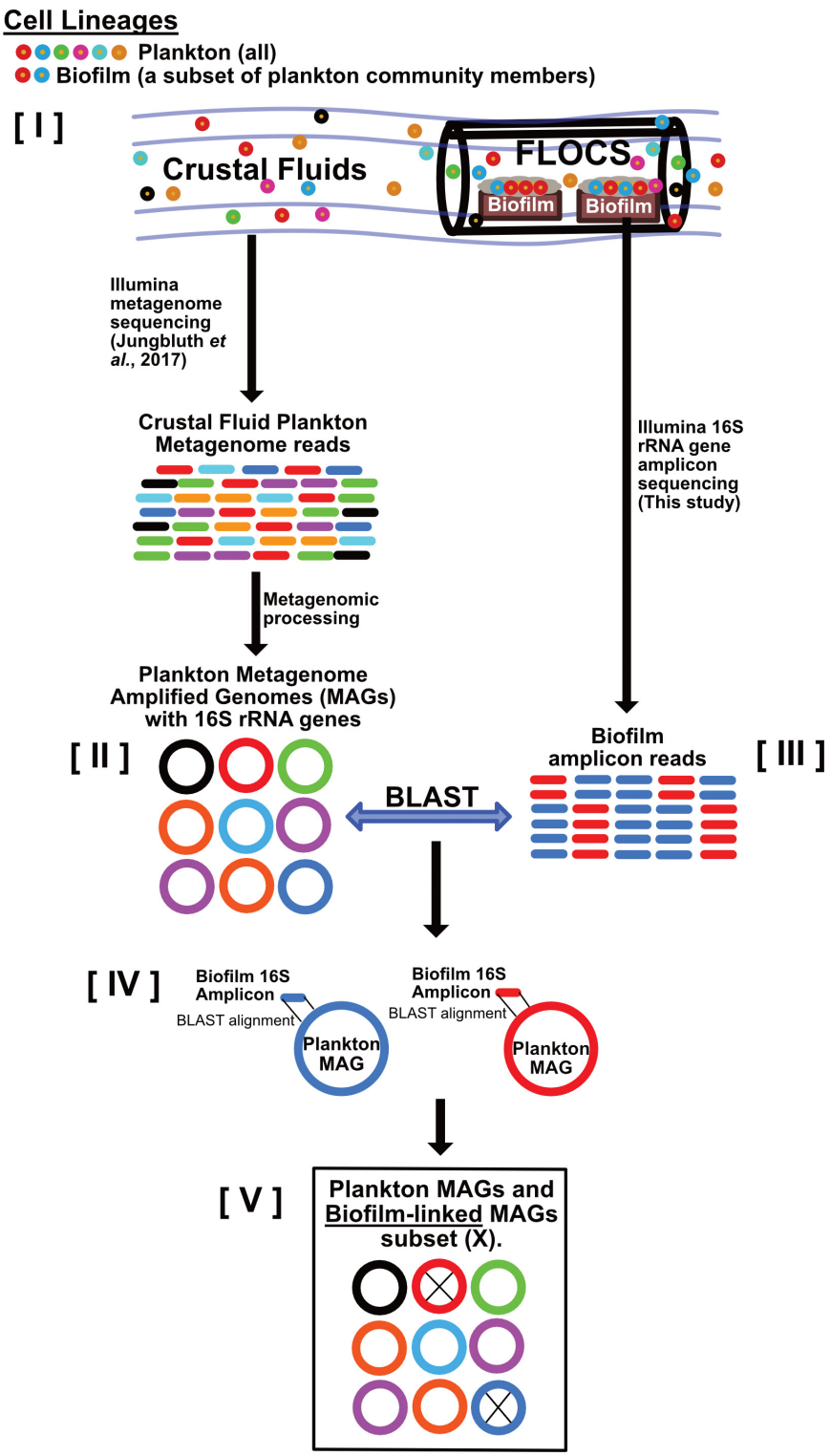

FIGURE 2 | Schematic depicting our strategy for linking crustal fluid plankton MAGs to biofilm lineages. This workflow begins with the assumption that **[I]** all biofilm community members are also part of the crustal fluid community because FLOCS biofilms arise from crustal fluid inoculation. Metagenomic data from crustal fluid is processed into MAGs representing planktonic lineages **[II]**. Amplicons (16S rRNA gene) sequences from FLOCS biofilm **[III]** also represent planktonic lineages; however, these lineages transitioned from planktonic to biofilm lifestyles. Stringent local alignments **[IV]** between biofilm amplicons and the subset of plankton MAGs containing 16S rRNA genes reveal which planktonic lineages also reside in FLOCS biofilm and are thus considered "biofilm-linked" **[V]**.

TABLE 1 | Presence of genes involved in various metabolic pathways in the biofilm and planktonic categories constructed from crustal fluid metagenome from the Juan de Fuca crustal subsurface (from Jungbluth et al., 2017a).

Metabolism	Function	Gene	Biofilm	Plankton
Carbon fixation	Wood Ljungdahl	codhCD	✓	✓
	Calvin cycle	Rubisco		✓
Nitrogen	Nitrate assimilation	NasA	✓	✓
	Nitrate reduction	NapAB	✓	✓
	Nitrate reduction	NarGH	✓	✓
	Dissimilatory nitrite reduction	NirBD	✓	
	Denitrification	NirS	✓	
	Nitrite reduction	NrfH	✓	
	Nitric oxide reduction	NorB	✓	✓
	Nitrous oxide reduction	NosZD		✓
Sulfur	Sulfate reduction	SopT	✓	✓
	Sulfate reduction	ApsK	✓	✓
	Sulfate reduction	CysN	✓	
	Sulfate reduction	AprA	✓	
	Sulfite reduction	AsrB		✓
	Sulfite reduction	dsrABCMK/dsrD	✓	
	Sulfur oxidation	dsrEFHCMK		✓
	Thiosulfate oxidation	SoxYZ	✓	
Iron	Iron reduction/oxidation	MtrA	✓	
Hydrogen	Hydrogen oxidation	Hydrogenases (various)	✓	✓
Oxygen	Oxygen reduction	Various	✓	✓
CO	Carbon monoxide oxidation	CO dehydrogenase	✓	✓

Microscopic Evidence of Microbial Colonization

SEM confirmed mineral colonization and was primarily useful for looking at secondary mineral precipitates (**Figure 3**, and **Supplementary Figures S3–S6**), which can have characteristic shapes (Toner et al., 2009) in this environment. Cell morphologies observed included straight, sheath-like stalks (some with external encrustation), coccoid shaped cells, and some structures that resembled "Y" shaped stalked cells. The composition and origin of the sheath features is unknown, but morphologically they resemble stalks known to be made by some microaerophilic iron oxidizing bacteria (Barco et al., 2017). Notably absent are twisted stalks enriched in iron oxyhydroxides previously observed in JdF mineral colonization experiments that had been exposed to bottom seawater (Orcutt et al., 2011a).

DNA Extraction, Gene Quantification, Sequencing, and OTU Quality Filtering

Bacterial 16S rRNA gene abundance varied from 2×10^2 to 1×10^6 gene copies per gram of rock; however, some samples were below the detection limit (**Supplementary Table S3**). The highest 16S rRNA gene abundances were observed on basalts enriched at wellheads. Illumina 16S rRNA gene sequencing resulted in 791,077 high quality sequences that were clustered into OTUs (**Supplementary Table S3**). *TaxonSluice* flagged 22 OTUs as potential sequence contaminants from kits. Ultimately, after assessing the *TaxonSluice* output, 17 of these 22 suspects were culled from further analyses. In sum, after implementing *TaxonSluice*, 401 Bacterial OTUs, representing 69.9% of the initial high-quality sequences, were further characterized.

Bacterial Community Composition, Diversity and Structure

Communities recovered from downhole incubations had more diverse taxonomic groups (Phylum-level) than those observed from wellhead deployments (**Figure 4**). While this may reflect the longer incubation time of the downhole incubations (**Supplementary Table S2**), we note that the DNA extracts were pooled from multiple samples and, therefore, cannot assess potential inter-sample variability. We thus interpret our community diversity survey as a qualitative rather than quantitative assessment. Proteobacteria comprised between 5–98% of the community of all incubations. All wellhead sequences grouped within Gamma- and Epsilon-proteobacteria. Firmicutes, Deltaproteobacteria, Aminicenantes (OP8), Thermotogae, Deferribacteres, Actinobacteria, Chloroflexi, Bacteroidetes, and Spirochetes were recovered from downhole 64°C anoxic incubations. The temperature-driven differential enrichment of Gamma- and Epsilon-proteobacterial lineages in wellhead deployments from warm the downhole crustal fluid communities is significant (Wald Test, P_{val} = 0.01, **Supplementary Figure S12**). Ordination patterns show communities recovered from different mineral substrates as similar (*e.g.*: 1362A_W_EnrBas associating with 1301A_W_Bas and 1362B_D_Pyr associating with 1026B_D_Bas; **Figure 4C** and **Supplementary Figure S13**). The first axis PCoA separated

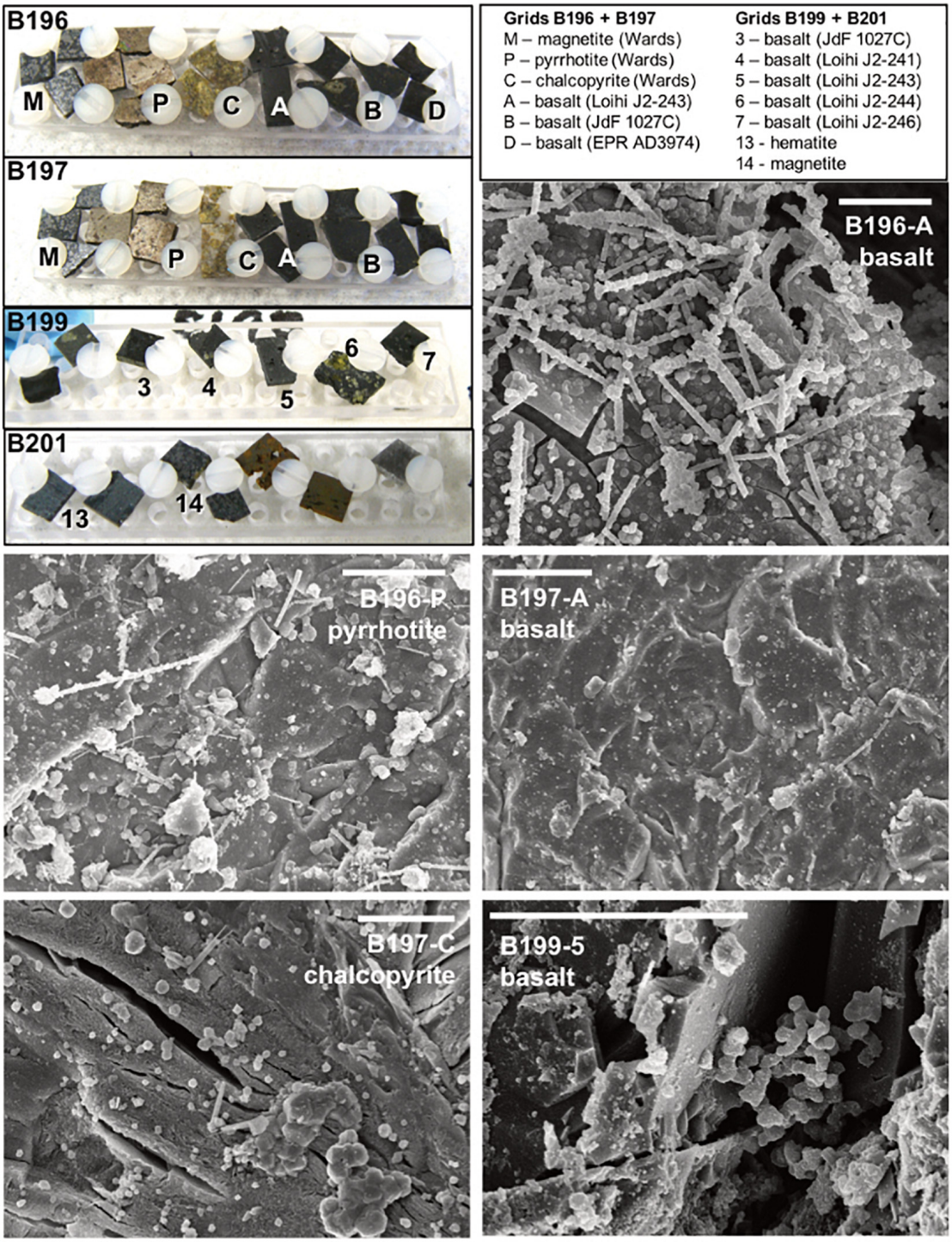

FIGURE 3 | Select scanning electron micrographs (SEM) from rock chips incubated downhole at Hole U1362B (see **Supplementary Figures S3**–**S6** for additional images). The upper left panel shows photographs of the rock chips before deployment on IODP Exp. 327, with grid labels and rock chip types indicated in the legend. Basalt chips were created from field samples collected previously from the East Pacific Rise (EPR, a glassy basalt collected on Alvin dive 3974), from Juan de Fuca Ridge flank (JdF, from ODP Hole 1027C), and from the Loihi Seamount (two highly vesicular aphyric basalts from ROV Jason dives J2-241 and J2-243, and two olivine-phyric basalt from dives J2-244 and J2-246). The metal sulfides chips were prepared from commercially available samples from Wards Geology. Representative scanning electron microscopy (SEM) micrographs from three basalt samples and two metal sulfides are shown; scale bars in each are 10 μm.

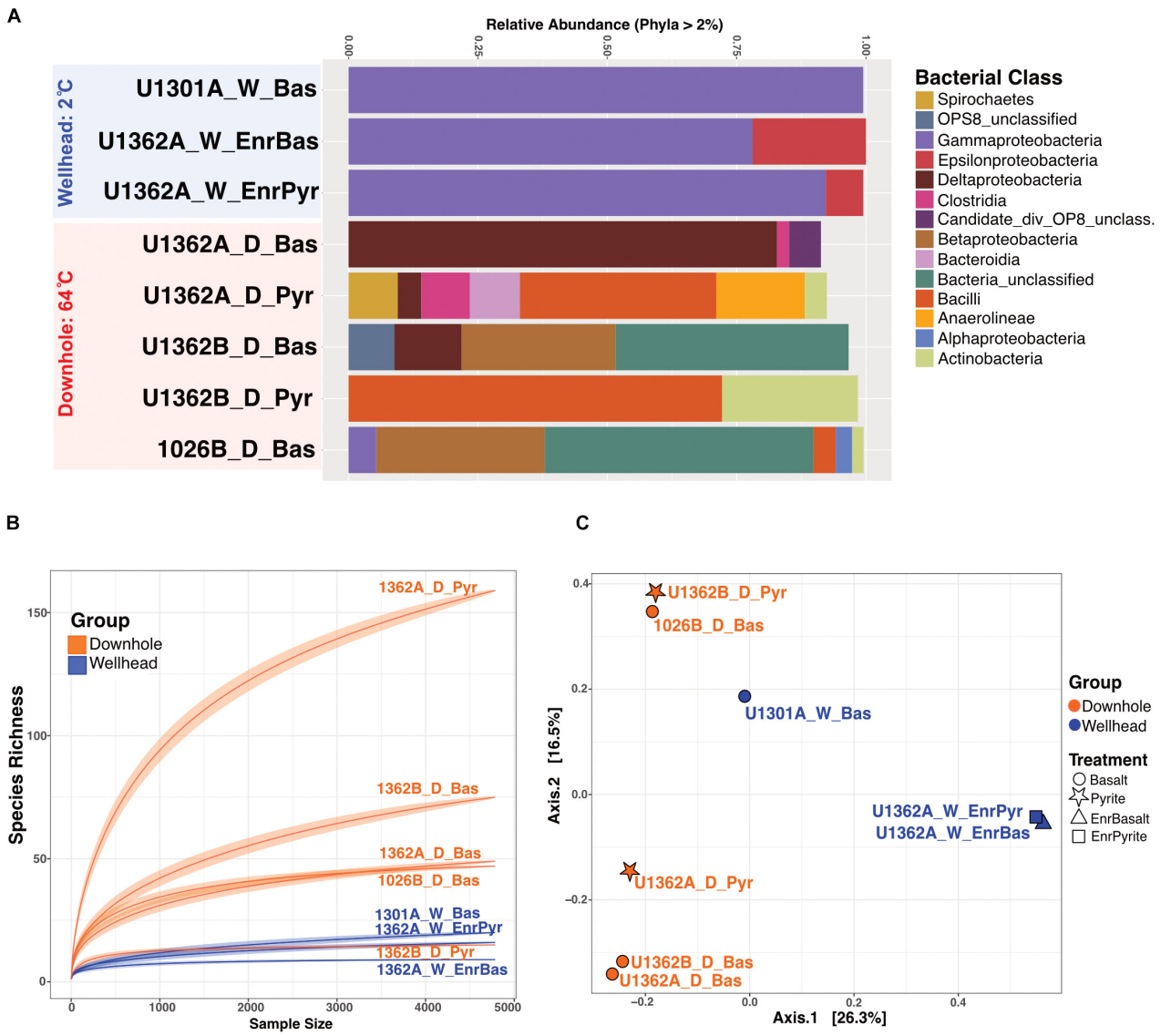

FIGURE 4 | Overview of the 16S rRNA gene diversity in rock chip biofilms from Juan de Fuca CORK subseafloor observatories FLOCS experiments. **(A)** Relative abundance of 16S rRNA gene sequences in various bacterial groups (at the class level as shown in legend, for groups >2% of sequences) for the wellhead (blue) and downhole (red) FLOCS samples. **(B)** Rarefaction analysis of the same sequence data reveals the greater diversity in most of the downhole biofilms. **(C)** Principal Coordinate Analysis (PCoA) of the same sequence data grouped by deployment location (color) and treatment type (symbols; as shown in the legend) reveals the clustering of microbial communities based on deployment location.

wellhead from downhole enrichments, implying that incubation environment (cool wellhead vs. warm downhole), rather than mineralogy, defined community structure.

Phylogenic Comparisons

There was nearly no overlap between OTUs from cold (2°C) wellhead and warm (64°C) downhole incubations (**Figure 5** and **Supplementary Figures S7–S9**). Phylogenetic analysis of our amplicons does not indicate matches to bottom seawater groups (**Supplementary Figure S7**), further corroborating chemical records (**Supplementary Figure S2**) and suggesting that bottom seawater intrusion did not occur. Wellhead incubations enriched Gamma- and Epsilon-proteobacteria lineages not observed in the downhole incubations (**Figures 5A,B** and **Supplementary Figure S7A**). These Gammaproteobacteria OTUs were related to sequences from ODP Hole 896A crustal fluids (Nigro et al., 2012). Epsilonproteobacteria were exclusive to wellhead deployments (**Figure 5B**). These sequences were classified to the genus *Arcobacter* and were highly similar to sequences from previous Hole U1301A wellhead enrichments (Baquiran et al., 2016).

Downhole incubations were dominated by lineages related to anaerobic thermophiles (**Figures 5C,D** and **Supplementary Figures S7–S9**). Firmicutes comprised between 6–87% of downhole samples (**Figure 4A**). Two high abundance OTUs,

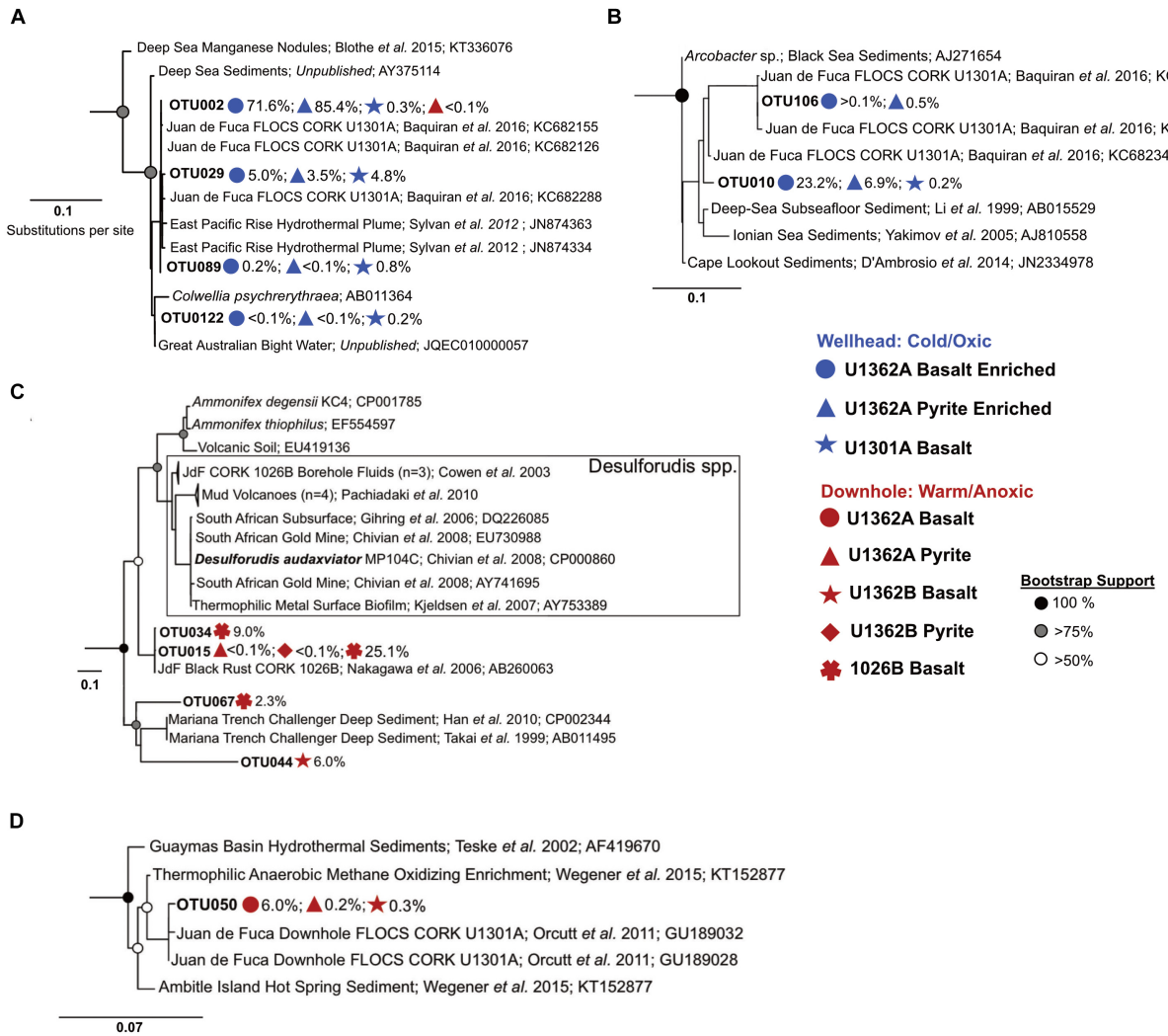

FIGURE 5 | Maximum likelihood phylogenetic trees of abundant 16S rRNA gene OTUs recovered in this study compared to close environmental relatives (based on 100 bootstrap replications) show different dominant groups between the wellhead and downhole rock chip incubations. **(A)** Gammaproteobacteria tree. **(B)** Deltaproteobacteria tree. **(C)** Firmicutes tree. **(D)** Aminicenantes (candidate phylum OP8) tree. Colored icons show FLOCS deployment site and substrate for each recovered OTU portrayed. Gray scale circles show bootstrap support per branch. Scale bars indicate substitutions per site. More detailed trees provided in **Supplementary Figures S7–S9**.

lineages within the class Clostridia, had high sequence identity (>99%) with a JdF observatory rust clone (Nakagawa et al., 2005) classified as *Ammonifex* sp. The Aminicenantes (OP8), reported in JdF crustal fluid communities (Huber et al., 2006; Jungbluth et al., 2013) and previous *in situ* mineral incubations (Orcutt et al., 2011a), were recovered from downhole incubated basalts (**Figure 5D** and **Supplementary Figure S8A**). Deltaproteobacteria predominantly clustered into 4 abundant lineages distantly related to cultured obligate thermophiles (**Supplementary Figure S7B**). Thermotogae, an anaerobic thermophilic phylum (Nesbo et al., 2015) reported previously in JdF crustal fluids (Jungbluth et al., 2016) and *in situ* enrichments (Orcutt et al., 2011a), was represented by two OTU lineages in downhole basalt incubations (**Supplementary Figure S8B**). Gammaproteobacteria, related to lineages from deep-sea and sediment environments, were recovered from downhole incubations (**Supplementary Figure S7A**). Other anaerobic thermophilic clades, some previously observed in substrate incubations and crustal fluids at this location (Orcutt et al., 2011a; Jungbluth et al., 2013, 2016), were detected in downhole deployments (**Supplementary Figure S9**).

Functional Analyses of Crust-Attached Biofilm Versus Crustal Fluid Plankton

To assess possible functional differences between rock-attached biofilms versus the planktonic phase in the warm and anoxic JdF crustal subsurface, we compared our biofilm amplicon dataset to published JdF crustal fluid metagenomic libraries

(Jungbluth et al., 2017a) through amplicon-based recruitment. A total of 79 metagenome assembled genomes (MAGs) with completeness levels ranging from 99 to 10% were reconstructed from the JdF crustal fluid metagenome assemblies (see **Supplementary File 2** for stats of all MAGs). Twenty three of these MAGs contained Bacterial 16S rRNA genes that overlapped with the region amplified by our amplicon primers. Assemblies of 16S rRNA genes from MAGs were validated by read coverage across the length of each gene and in comparison to the contig in which it is encoded. Twelve of these 23 MAGs contained 16S rRNA genes with a at least 99% identity over at least 90% coverage of our biofilm 16S rRNA amplicon length (**Supplementary Figures S10**, **S11**). We interpret these 12 bins as "biofilm-linked", representing planktonic taxa that have preferentially colonized FLOCS substrates (**Figure 2**). The remaining 11 reconstructed 16S rRNA genes do not meet our alignment threshold (i.e., they have substantially lower sequence identities to our biofilm amplicons; mean = 81.25%; maximum = 93.75%) and thus represent "planktonic" taxa that did not colonize FLOCS substrates. The phylogenetic affiliations of these bins, estimated by PhyloSift, and the closest NCBI matches to their 16S rRNA genes are reported in **Supplementary Figure S10** and **Supplementary File S1**, respectively.

We did a similar comparison of our amplicon dataset to a metagenome that was recently published (Smith et al., 2019) from a biofilm formed on olivine in this same habitat. In our reassembly of this JdF olivine metagenome, we detected eight metagenome bins with 16S rRNA genes with matches to our biofilm OTUs (**Supplementary Table S4**). Of these eight, two of them (OTUs 50 and 120) were also detected in the JdF crustal fluid metagenome, and one of them (OTU 122) was detected in a metagenome from NP crustal fluids.

Based on the partitioning of the 23 MAGs from JdF crustal fluid metagenomes into biofilm or planktonic categories, we examined the relative abundance of functional genes in each metagenome set (see **Supplementary File S2** for the full analysis). For major metabolic pathways, there are only minor differences in the relative abundance for annotations related to carbon fixation, nitrogen cycling and energy metabolism. We observed a higher relative abundance of pathways associated with sulfur and carbohydrate metabolisms in the planktonic fraction (**Figure 6A**). The biofilm-linked MAGs had a higher relative abundance of genes related to biofilm formation and lipopolysaccharide biosynthesis (**Figures 6B,C**) and planktonic MAGs had a higher relative abundance of genes related to flagellar assembly (**Figure 6D**).

Hidden Markov Models were used to further evaluate the genetic potential of the JdF MAGs grouped into biofilm and plankton fractions (**Table 1**). Genetic markers associated with carbon fixation via the Wood-Ljungdahl pathway are detected in both fractions. Various sulfate and dissimilatory sulfite reductases (*i.e., dsrABCMK* and *dsrD*) were also observed in both categories, while a polysulfide-carrier heterodimer (*soxYZ*) associated with the *sox* thiosulfate oxidation pathway (Gregersen et al., 2011) is only detected in the biofilm fraction. Genes for three types of oxygen reductases (*ccoNOP*, *coxAB*, and *cydAB*) and dissimilatory nitrate reductases (*napA*, *narG*) are observed in both fractions, while dissimilatory nitrite reduction (*nirBD*) and denitrification (*nirS*) genes are only observed in the biofilm-linked MAGs. Five groups of hydrogenases (Groups 1, 3b, 3c 3d, 4) are also observed in both biofilm and plankton fractions. Genes associated with the dissimilarity iron reduction and oxidation were absent from the planktonic and biofilm fractions.

Comparing Rock-Attached Biofilm Community Overlap With Crustal Fluid Metagenomes

Biofilm communities in the downhole FLOCS incubations (i.e., sourcing subsurface crustal fluids and incubated within the JdF warm and anoxic subsurface) recruit metagenomic 16S rRNA gene reads from the JdF crustal fluids (Jungbluth et al., 2017b) exclusively (**Figure 7**). By contrast, FLOCS deployed at CORK wellheads (*i.e.*, sourcing subsurface JdF crustal fluids but incubated under cold conditions at the observatory wellhead) recruit metagenomic 16S rRNA gene reads mostly from the cool and oxic NP crustal fluids (Tully et al., 2018).

DISCUSSION

Both rock-attached biofilms and free-floating plankton live in the crustal subseafloor; therefore, assessing the factors governing plankton recruitment onto crustal surfaces and, subsequently, differences in composition and potential activities of biofilm and plankton is necessary for a comprehensive ecological description of this habitat. In this study, we examine the influence of incubation conditions on subseafloor rock-attached biofilm composition (**Figure 1**). Further, we examine the partitioning of microbial groups into biofilms from the planktonic phase. Our results indicate that this process is influenced by environmental conditions (**Figures 4**, **5**, **7**), resulting in potential functional differences between these crustal community types (**Figure 6**).

Biofilm Development on Mineral Surfaces Deployed in Crustal Fluids for 1–6 Years

Biofilms formed on the substrate colonization experiments to a cell density of up to 10^3–10^6 cells per gram of rock based on quantitative PCR analysis of 16S rRNA genes in pooled DNA extracts (**Supplementary Table S3**). Some samples had DNA concentrations that were below quantification limits. Thus, the biofilms had relatively low biomass, which is expected for a subsurface ecosystem (Orcutt et al., 2011a; Smith et al., 2011, 2016), as compared to 10^7–10^9 gene copies per gram of seafloor-exposed basalt (Santelli et al., 2008).

We confirmed substrate colonization with SEM and observed various cell and mineral precipitate morphologies (**Figure 3**). In contrast to earlier experiments at this

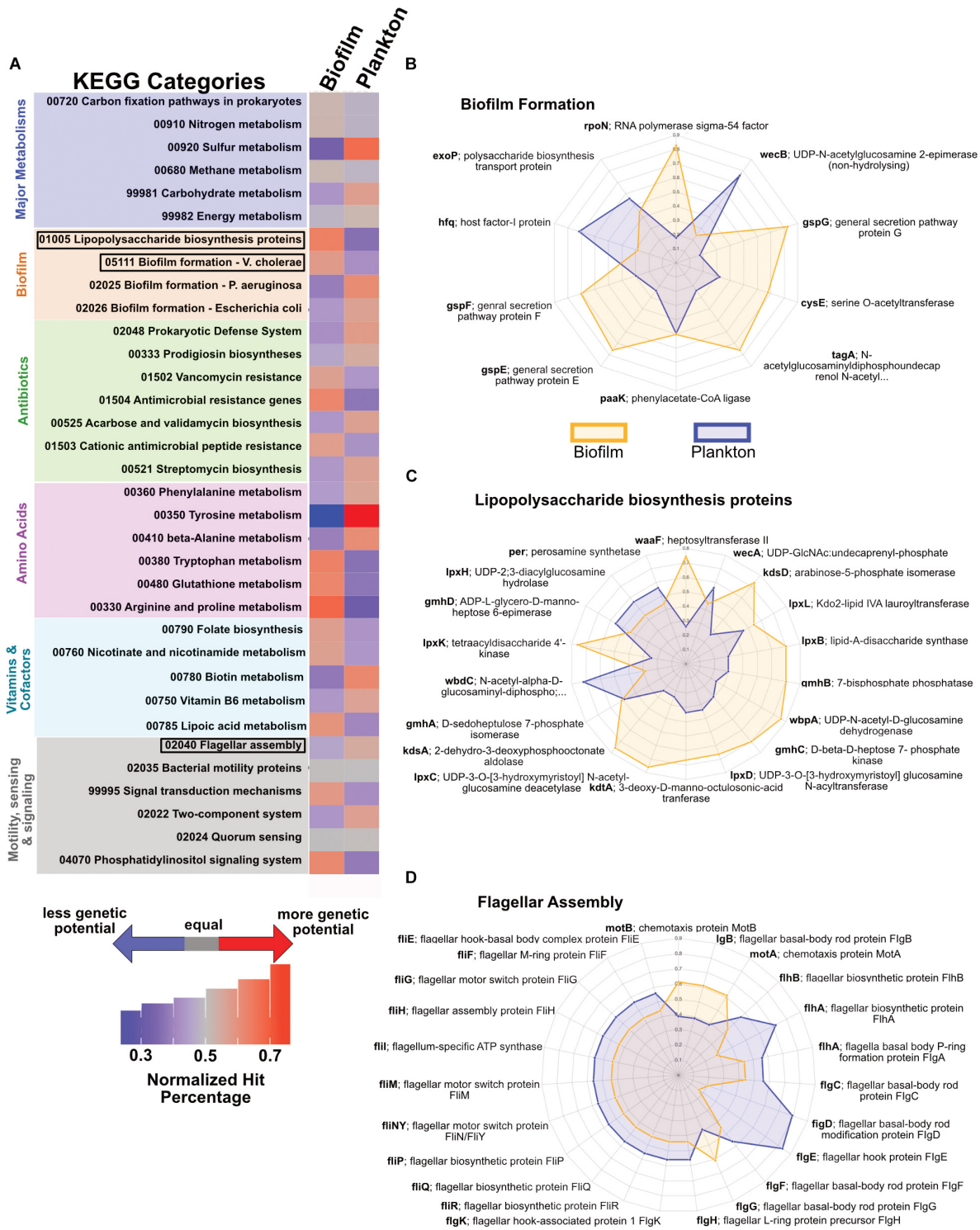

FIGURE 6 | Potential functional differences between biofilm-linked and planktonic MAG fractions. **(A)** Relative abundance (per legend) of metagenomic reads binning into different KEGG categories between the biofilm-linked and plankton fractions, where gray indicates equal abundance in the two fractions, red indicates a higher percentage (i.e., more genetic potential in KEGG category), and blue indicates a lower percentage (i.e., less genetic potential). **(B–D)** Spider plots indicating the relative abundance (from 0 in the center to 1 on the outer edge) in the biofilm-linked (orange) and plankton (blue) fractions of particular genes in KEGG categories for biofilm formation **(B)**, lipopolysaccharide biosynthesis **(C)**, and flagellar assembly **(D)**.

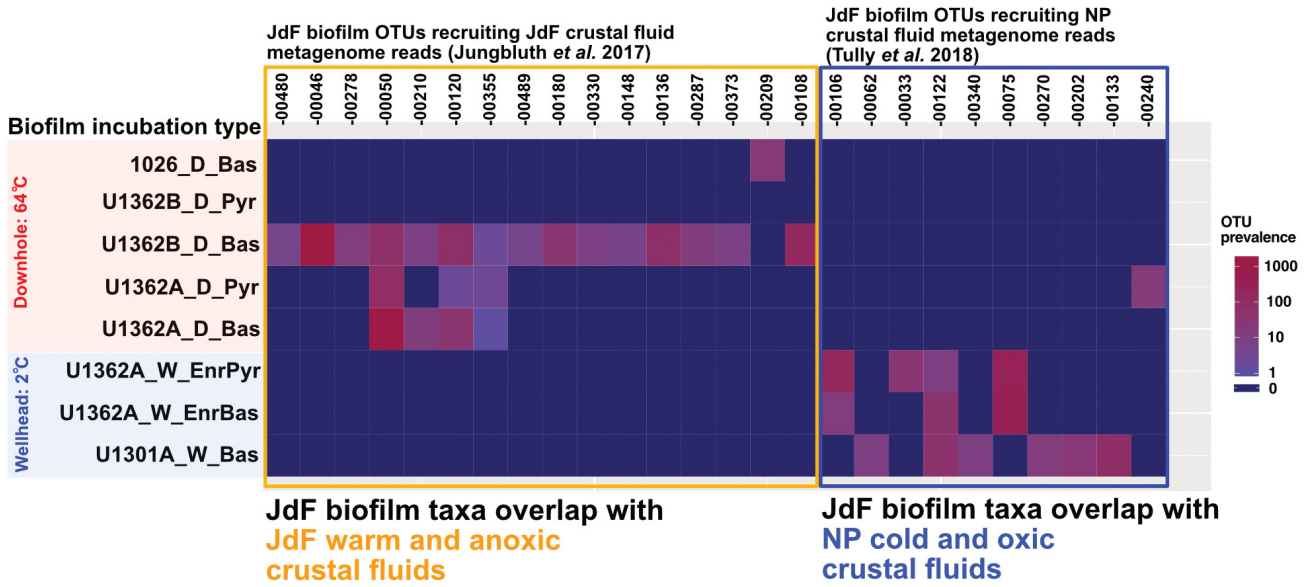

FIGURE 7 | Heatmap depicting the prevalence of JdF biofilm OTUs recruiting metagenomic reads from crustal fluids [Juan de Fuca (JdF) and North Pond (NP)] across all incubation types and substrates in our experiments. Numbers across x-axis refer to JdF biofilm OTUs recruiting crustal fluid metagenome reads. The y-axis shows the prevalence of OTUs with crustal fluid metagenomic matches across all substrate types and incubation conditions in this study. OTUs recovered from JdF downhole deployments recruit metagenomic reads from the warm and anoxic JdF crustal fluid but not the cool and oxic NP crustal fluid. In contrast, OTUs from the JdF wellhead deployments recruit metagenomic reads from the cold and oxic NP crustal fluids almost exclusively.

location (Orcutt et al., 2011a), twisted iron oxyhydroxide stalk morphotypes (previously attributed to iron oxidizing bacteria) were not observed. In the previous study, intrusion of oxygen-rich bottom seawater into the subsurface environment, due to leaky borehole conditions, was hypothesized to favor microaerophilic iron oxidation. Temporal records of dissolved ions do not indicate oxygen intrusion in these new experiments (**Supplementary Figure S2**), explaining the absence of the twisted-stalk morphotype. The origin of the morphotypes in the current experiments cannot be explained by this dataset alone.

Assessing Possible Sequence Contamination in Low Biomass Subsurface Samples

Low biomass in this environment is a common issue (Salter et al., 2014; Morono and Inagaki, 2016; Labonte et al., 2017; Sheik et al., 2018); thus, our 16S RNA gene sequence datasets needed to be rigorously evaluated for possible sequence contamination. Having sequenced multiple DNA extraction blanks, we were able to screen our libraries for spurious sequences following the philosophy espoused in a recent study of other low biomass subsurface samples (Sheik et al., 2018). This led to the development of a new analysis pipeline – *TaxonSluice* – to enable automated and reproducible screening of amplicon datasets with corresponding sequence blanks. Applying the *TaxonSluice* algorithm to our dataset culled 30.4% percent of high-quality sequences from incubation samples as potential contaminants (**Supplementary Table S3**) which are excluded in the ecological analysis below.

Environmental Factors Influencing Biofilm Development in the Crustal Subsurface

JdF crustal fluid taxa composition exhibits variability (Jungbluth et al., 2013; Tully et al., 2018). Despite this variability, the microbial clades comprising downhole biofilm are related to anaerobic thermophilic groups previously observed in crustal fluids at this site; *e.g.,* Firmicutes, Deltaproteobacteria, Aminicenantes/OP8, and Thermotogae (**Figures 4**, **5**, and **Supplementary Figures S7–S9**). In contrast, the biofilms seeded by the same crustal fluid but incubated in cold (2°C) conditions were comprised of psychrophilic Gamma- and Epsilon-proteobacteria as reported before (Baquiran et al., 2016). These groups are also common in other environments, where crustal rocks are exposed to bottom seawater (Sylvan et al., 2013). Remarkably, there is also overlap between our JdF wellhead incubation communities and taxa in cool and oxic crustal fluids from NP on the Mid-Atlantic Ridge (**Figure 7**). These observations indicate that temperature, and possibly oxygen, is a major environmental factor driving rock-attached biofilm community assembly in crustal ecosystems. This ecosystem structuring driver has also been proposed at a global level (Edwards et al., 2012).

Other possible ecological drivers of rock-attached biofilm community structure are less clear. The warmer downhole incubations have higher species richness compared to the cooler

downhole incubations (**Figure 4B**), suggesting reduced niche space in the cooler conditions. Downhole incubations lasted several years longer than the cooler incubations (**Supplementary Table S2**), so time may play a role in the diversification of the warmer biofilms, as suggested elsewhere (Santelli et al., 2008, 2009). Ordination patterns are not driven by rock substrate type (*i.e.*, basalts versus metal sulfides; **Figure 4C**), regardless of incubation location. This is consistent with earlier analyses of similar subseafloor mineral incubations (Orcutt et al., 2011a) but different than prior indications that mineralogy structures rock-attached microbial communities (Toner et al., 2013; Smith et al., 2016). Thus, the role of mineralogy on crustal ecosystem development is unclear and requires further investigation.

Common Microbial Groups Across Crustal Subsurface Ecosystems

Similarities between wellhead biofilm members and taxa in crustal fluids from a different cool and oxic crustal subsurface ecosystem (**Figures 5**, **7**) suggests that some lineages (e.g., *Colwellia* and *Arcobacter*) represent globally distributed denizens of the crustal subsurface biosphere. Although rare in the anoxic warm JdF crustal fluids, these cold-adapted aerobic groups are present in the aquifer and respond to changing environmental conditions (e.g., temperature) to dominate wellhead incubations (**Figure 4A** and **Supplementary Figure S12**). The consistency of biofilm community structure developing under cool wellhead conditions [i.e., the similarity of the *Colwellia* and *Arcobacter* spp. between this study and that of Baquiran et al. (2016)], and observations of these groups at this site previously (Huber et al., 2006; Jungbluth et al., 2013), suggests that some groups are consistently rare and responsive in the highly geochemically and thermally altered JdF crustal fluids. A taxonomic inventory of rocks from the cool and oxic subsurface at NP (Jorgensen and Zhao, 2016) also indicates an enrichment in Alteromonadales Gammaproteobacteria (the family in which *Colwellia* spp. reside) on subsurface basalts. We hypothesize that these microbial groups are sourced from bottom seawater and persist even in highly altered crustal fluids to rebound when conditions become favorable again.

Within the Firmicutes group, we note that the marine *Ca.* Desulfopertinax/terrestrial *Ca.* Desulforudis lineage, commonly observed in JdF crustal fluids and terrestrial subsurface sites (Jungbluth et al., 2017b), was not detected in our incubations (**Figure 5C**). Genetic repertoires of these closely related candidate taxa suggest the potential for flagellar-based motility. Glycosyltransferases and diphosphate-sugar epimerases, genes involved in biofilm formation, are detected in the genome of the marine *Ca.* Desulfopertinax cowenii and are absent in its terrestrial subsurface counterpart *Ca.* Desulforudis audaxviator. Our observations indicate that this lineage, despite having the genetic potential for biofilm colonization, may favor a planktonic rather than rock-attached lifestyle in our incubation conditions. However, the recent metagenomic analysis of a biofilm formed on olivine in the JdF crustal subsurface did detect this group (Smith et al., 2019), perhaps indicating that their presence in biofilms is dictated by specific mineral types.

Variable Functional Potential Between Rock-Attached and Planktonic Crustal Communities

Our partitioning of crustal fluid metagenomes into "biofilm-linked" and "planktonic" categories (**Figure 2**), suggests some functional differences between these compositionally distinct yet inter-related crustal communities (**Figure 6**). While this is an imperfect comparison, the observation that genes related to biofilm formation are more abundant in the biofilm fraction, while the abundance of motility-related genes is higher in the planktonic fraction, lends confidence to our approach. Also, our biofilm amplicon sequences matched 16S rRNA genes from 16S rRNA gene-bearing MAGs from a biofilm formed on olivine in the JdF crustal subsurface (**Supplementary Table S4**), with overlap with the groups identified from the JdF crustal metagenome (**Figure 7**), corroborating our interpretation of the biofilm lifestyle of these groups. It should be noted, however, that the functional potential encoded in MAGs lacking 16S rRNA genes, and missing genetic information from incomplete MAGs is not considered here, so this is a qualitative assessment.

Following this approach, we observe genes for multiple carbon fixation pathways (Wood-Ljungdahl, 3HP, 3HP/4HB) present in both biofilm and planktonic fractions in similar relative abundances, with the Calvin cycle gene RuBisCO only observed in plankton (**Table 1**). Prior studies have documented carbon fixation potential in cool and oxic subsurface crustal fluids (Meyer et al., 2016), in seafloor-exposed basalt biofilms (Orcutt et al., 2015) and in the anoxic subsurface of the JdF (Carr et al., 2019; Smith et al., 2019). Stable isotope assays suggest that carbon fixation in JdF crustal fluids can occur (McCarthy et al., 2010) although the system is net heterotrophic with a loss of organic matter (Lang et al., 2006; Lin et al., 2012). Our results support the potential for carbon fixation, performed by both biofilm and plankton communities, in the JdF subsurface crust.

By contrast, genes involved in sulfur cycling, despite being present in both fractions, may be relatively enriched in the plankton fraction (**Figure 6** and **Table 1**). Sulfate is the dominant oxidant in this system (Wheat et al., 2010), thus sulfate reduction would be expected as a dominant process if appropriate electron donors were available. Microbial sulfate reduction and microbial groups associated with this process have been detected in JdF crustal fluids (Robador et al., 2014); however, *in situ* rates of this process are unknown. The potential for microbial sulfate reduction on the rocks has also been documented by sulfur stable isotopes (Lever et al., 2013), and recent metagenomic analysis of a biofilm formed on olivine in the JdF subsurface detected sulfate reduction capability in several MAGs (Smith et al., 2019).

Determining the genetic potential for iron cycling processes in this environment is challenging due to the dearth of fully characterized iron cycling pathways (He et al., 2017). The recent metagenomic study of a biofilm on olivine did not detect the *cyc2* genes (Smith et al., 2019). These genes are thought to be indicative of neutrophilic, microaerobic iron oxidation (Barco et al., 2015;

Chan et al., 2018); which would be consistent with their absence from the anaerobic JdF crustal system. We detect *cyc2* in the JdF crustal fluid metagenome (data not shown); however, the subset of MAGs used in our analyses did not contain this gene. Iron is relatively abundant in the host rocks, as iron oxides comprise roughly 10% of the basalt (by weight) in this system, and iron oxyhydroxides are the second most abundant mineral alteration product. These phases indicate the potential for iron oxidation/reduction. Thermodynamic calculations suggest that utilization of iron is energetically favorable (Boettger et al., 2013). Theoretical calculations suggest that iron oxidation could potentially support chemolithoautotrophy in basalt ecosystems (Bach and Edwards, 2003), but further work is needed to fully characterize iron cycling processes in the crustal ecosystem.

The possibility of nitrate/nitrite oxidation/reduction in the Juan de Fuca crustal subsurface is controversial. Nitrate concentrations in crustal fluids from this environment are extremely low, near limits of detection [high nM to low μM; (Lin et al., 2012)] and are argued to be artifacts of drilling (Wheat et al., 2010) as nitrate is quickly lost from recharging fluids that enter this crustal outcrop system (Wheat et al., 2013). Despite this, Nitrospirae (nitrate oxidizers) are commonly detected in this crustal ecosystem (Jungbluth et al., 2017a). Here, we observe genes involved in denitrification in the biofilm-linked MAGs (**Table 1**), and a recent metagenomic study of a JdF olivine biofilm also detects nitrate reduction pathways genes (Smith et al., 2019) suggesting that cryptic nitrogen cycling at this site may be a possible metabolic feature, although it is unclear if this preferentially occurs in crust-attached biofilms.

The reductant-oxidant pairs in the JdF subsurface that fuel chemotrophy are unclear. Hydrogen and methane in JdF fluids could provide very low levels of free energy when coupled to various electron acceptors (Lin et al., 2012, 2014; Boettger et al., 2013; Robador et al., 2016). We detect Group 1 hydrogenases (hydrogen oxidation) typical of hydrogen consuming microorganisms (Peters et al., 2015) in the biofilm-linked metagenomic fraction. We did not detect methane cycling genes; however, 16S rRNA gene-containing MAGs used in this study only targeted Bacteria; thus, putative archaeal methanotrophs were not included in the analysis. Interestingly, uncultivated Archaea containing genes associated with methyl cycling (*mtrH*) but lacking *mrcA* have been recently reported from JdF crustal fluids (Carr et al., 2019). We detected genes coding for carbon monoxide dehydrogenase (**Table 1**). Furthermore, we observe genes associated with carbon monoxide oxidation in the biofilm-linked metagenomic fraction, expanding the potential for carboxydotrophy, recently reported for uncultivated Archaea in this system (Carr et al., 2019), to the Domain Bacteria. Carbon monoxide is known as an energy rich reductant in other subsurface ecosystems (Canovas et al., 2017).

The use of amino acids (**Figure 6A**) is supported by the consistent observation of the uncultivated Aminicenantes/OP8 group at this site (Orcutt et al., 2011a; Jungbluth et al., 2013, 2016; Smith et al., 2016). This group, also observed in terrestrial deep biosphere sites (Farag et al., 2014), is suggested to be involved in amino acid metabolism and peptide scavenging from cadaverous cells (Rinke et al., 2013; Sharon et al., 2015; Robbins et al., 2016). Amino acid and carbohydrate utilization potential is also detected in an olivine biofilm incubated at this site (Smith et al., 2019). Thus, despite the relatively minor contribution of necromass as a component of overall energy in deep marine sedimentary ecosystems (Bradley et al., 2018), its assimilation may support heterotrophy in marine and terrestrial crustal deep biosphere environments.

CONCLUSION

The nature of biofilm cellular recruitment from plankton in subseafloor crust is explored in this study. We show that temperature, and possibly redox state, drive recruitment of planktonic cells from crustal fluids into mineral-attached biofilms, supporting prior hypotheses about the global ecological structuring of this habitat (Edwards et al., 2012). Comparisons of biofilm communities from this study against crustal fluid communities from JdF and NP reveal global crustal biosphere connectivity by identifying related microbial groups that persist through changing environmental conditions in different subseafloor crustal aquifers. Further, despite many similarities, emergent genetic differences between rock-attached biofilm and planktonic communities inhabiting subseafloor crust are highlighted. Overall, we address a major gap in deep biosphere ecology by reporting the community drivers and genetic potential for geomicrobiological activity localized to biofilms attached to subseafloor crust, the largest contiguous habitat on Earth. As estimates of global biomass in ocean crust are beginning to emerge (Heberling et al., 2010; Bar-On et al., 2018), we emphasize that biomass partitioning into plankton and biofilm in this habitat, each community type existing at a different cellular density, is necessary for overall estimate robustness and proper ecological interpretation.

DATA AVAILABILITY

The datasets generated for this study can be found in NCBI Short Read Archive, BioProject PRJNA472057; BioSample accession numbers: SAMN09228041–SAMN09228055.

AUTHOR CONTRIBUTIONS

BO and CW conceived the study. GR, BO, and CW conducted the field deployments/recoveries. GR, BO, CW, AL, and TD performed the sample analyses. GR and AG performed the bioinformatic analyses and developed the software tools. GR, AG, CW, and BO interpreted the data. GR wrote the manuscript with input from all authors.

FUNDING

GR was supported by an U.S. National Science Foundation (NSF) Graduate Research Fellowship and a postdoctoral fellowship from the Center for Dark Energy Biosphere Investigations

(C-DEBI, funded by NSF award OCE-0939564). This work was supported by grants from the NSF (OCE-1030061 and OCE-1260548 to CW and OCE-1536539, OCE-1737017, and OCE-1233226 to BO), the National Aeronautics and Space Administration (NASA) Astrobiology Institute (NNA13AA92A subaward to BO), C-DEBI, and the International Ocean Discovery Program. This is C-DEBI contribution number 455.

ACKNOWLEDGMENTS

This manuscript is dedicated to the memory of our friend, colleague, and mentor Dr. Katrina J. Edwards, who inspired these experiments. We thank the science parties and crews of IODP Expedition 327 and cruises AT26-03 and AT26-18 on the R/V *Atlantis* for their support in the deployment and recovery of the FLOCS experiments, in particular, Andrew Fisher as chief scientist of IODP Expedition 327 and AT26-03. We also thank Peter Countway for providing a 16S rRNA gene qPCR standard, Steven D'Hondt, Sean McAllister, Michael D. Lee, Jean-Paul Baquiran, and Steffen L. Jørgensen for providing support for this project, and Josh Wood of the Deep Carbon Observatory for assistance with figure preparation.

SUPPLEMENTARY MATERIAL

The Supplementary Material for this article can be found online at: https://www.frontiersin.org/articles/10.3389/fmicb.2019.01983/full#supplementary-material

REFERENCES

Altschul, S., Gish, W., Miller, W., Myers, E., and Lipman, D. (1990). Basic local alignment search tool. *J. Mol. Biol.* 215, 403–410. doi: 10.1006/jmbi.1990.9999

Anantharaman, K., Brown, C. T., Hug, L. A., Sharon, I., Castelle, C. J., Probst, A. J., et al. (2016). Thousands of microbial genomes shed light on interconnected biogeochemical processes in an aquifer system. *Nat. Commun.* 7:13219. doi: 10.1038/ncomms13219

Bach, W., and Edwards, K. J. (2003). Iron and sulfide oxidation within the basaltic ocean crust: implications for chemolithoautotrophic microbial biomass production. *Geochim. Cosmochim. Acta* 67, 3871–3887. doi: 10.1016/s0016-7037(03)00304-301

Baquiran, J. P., Ramírez, G. A., Haddad, A. G., Toner, B. M., Hulme, S., Wheat, C. G., et al. (2016). Temperature and redox effect on mineral colonization in juan de fuca ridge flank subsurface crustal fluids. *Front. Microbiol.* 7:396. doi: 10.3389/fmicb.2016.00396

Barco, R. A., Emerson, D., Sylvan, J. B., Orcutt, B. N., Jacobson Meyers, M. E., Ramirez, G. A., et al. (2015). New insight into microbial iron oxidation as revealed by the proteomic profile of an obligate iron-oxidizing chemolithoautotroph. *Appl. Environ. Microbiol.* 81, 5927–5937. doi: 10.1128/AEM.01374-1315

Barco, R. A., Hoffman, C. L., Ramirez, G. A., Toner, B. M., Edwards, K. J., and Sylvan, J. B. (2017). In-situ incubation of iron-sulfur mineral reveals a diverse chemolithoautotrophic community and a new biogeochemical role for Thiomicrospira. *Environ. Microbiol.* 19, 1322–1337. doi: 10.1111/1462-2920.13666

Bar-On, Y., Phillips, R., and Milo, R. (2018). The biomass distribution on Earth. *PNAS* 115, 6506–6511. doi: 10.1073/pnas.1711842115

Boettger, J., Lin, H.-T., Cowen, J. P., Hentscher, M., and Amend, J. P. (2013). Energy yields from chemolithotrophic metabolisms in igneous basement of the Juan de Fuca ridge flank system. *Chemical. Geology.* 33, 11–19. doi: 10.1016/j.chemgeo.2012.10.053

Bradley, J. A., Amend, J. P., and Larowe, D. E. (2018). Necromass as a Limited Source of Energy for Microorganisms in Marine Sediments. *J. Geophys. Res. Biogeosci.* 123, 577–590. doi: 10.1002/2017jg004186

Canovas, P. A., Hoehler, T., and Shock, E. L. (2017). Geochemical bioenergetics during low-temperature serpentinization: an example from the Samail ophiolite, Sultanate of Oman. *J. Geophys. Res. Biogeosci.* 122, 1821–1847. doi: 10.1002/2017jg003825

Carr, S. A., Jungbluth, S. P., Eloe-Fadrosh, E. A., Stepanauskas, R., Woyke, T., Rappe, M. S., et al. (2019). Carboxydotrophy potential of uncultivated Hydrothermarchaeota from the subseafloor crustal biosphere. *ISME J.* 13, 1457–1468. doi: 10.1038/s41396-019-0352-9

Chan, C., Mcallister, S. M., Garber, A., Hallahan, B. J., and Rozovsky, S. (2018). Fe oxidation by a fused cytochrome-porin common to diverse Fe-oxidizing bacteria. *bioRxiv*

Cowen, J. P., Giovannoni, S. J., Kenig, F., Johnson, H. P., Butterfield, D., Rappé, M. S., et al. (2003). Fluids from aging crust that support microbial life. *Science* 299, 120–123. doi: 10.1126/science.1075653

Davis, E., Becker, K., Pettigrew, T., Carson, B., and Macdonald, R. (1992). "CORK: a hydrologic seal and downhole observatory for deep-ocean boreholes," in *Proceedings of the Ocean Drilling Program, Initial Reports*, eds E. E. Davis M. J. Mottl A. T. Fisher P. A. Baker K. Becker M. Boni et al. (College Station, TX: Ocean Drilling Program), Vol. 139. 43–53.

Edwards, K. J. (2011). Oceanography: carbon cycle at depth. *Nat. Geosci.* 4, 9–11. doi: 10.1038/ngeo1028

Edwards, K. J., Bach, W., and Mccollom, T. M. (2005). Geomicrobiology in oceanography: microbe-mineral interactions at and below the seafloor. *Trends Microbiol.* 13, 449–456. doi: 10.1016/j.tim.2005.07.005

Edwards, K. J., Fisher, A. T., and Wheat, C. G. (2012). The deep subsurface biosphere in igneous ocean crust: frontier habitats for microbiological exploration. *Front. Microbiol.* 3:8. doi: 10.3389/fmicb.2012.00008

Elderfield, H., and Schultz, A. (1996). Mid-ocean ridge hydrothermal fluxes and the chemical composition of the ocean. *Ann. Rev. Earth Planet. Sci.* 24, 191–224. doi: 10.1146/annurev.earth.24.1.191

Expedition 327 Scientists (2011a). Site U1362, in *Proceedings of IODP Integrated Ocean Drilling Program Management International, Inc.*, eds A. T. Fisher T. Tsuji K. Petronotis (Tokyo: Scientific Drilling), vol. 327, 4–8. doi: 10.2204/iodp.proc.327.103.2011

Expedition 327 Scientists (2011b). Expedition 327 summary, in *Proceedings of IODP Integrated Ocean Drilling Program Management International, Inc.*, eds A. T. Fisher T. Tsuji K. Petronotis (Tokyo: Scientific Drilling). doi: 10.2204/iodp.proc.327.101.2011

Farag, I. F., Davis, J. P., Youssef, N. H., and Elshahed, M. S. (2014). Global patterns of abundance, diversity and community structure of the aminicenantes (candidate phylum OP8). *PLoS One* 9:e92139. doi: 10.1371/journal.pone.0092139

Fisher, A. T., and Becker, K. (2000). Channelized fluid flow in oceanic crust reconciles heat-flow and permeability data. *Nature* 403, 71–74. doi: 10.1038/47463

Fisher, A. T., Wheat, C. G., Becker, K., Cowen, J., Orcutt, B. N., Hulme, S., et al. (2011). Design, deployment, and status of borehole observatory systems used for single-hole and cross-hole experiments, IODP Expedition 327, eastern flank of Juan de Fuca Ridge. In *Proceedings of the Integrated Ocean Drilling Program*, eds A.T. Fisher T. Tsuji and K. Petronotis (Tokyo).327

Fisk, M. R., Giovannoni, S. J., and Thorseth, I. H. (1998). Alteration of Oceanic volcanic glass: textural evidence of microbial activity. *Science* 281, 978–980. doi: 10.1126/science.281.5379.978

Gregersen, L. H., Bryant, D. A., and Frigaard, N. U. (2011). Mechanisms and evolution of oxidative sulfur metabolism in green sulfur bacteria. *Front. Microbiol.* 2:116. doi: 10.3389/fmicb.2011.00116

He, S., Barco, R. A., Emerson, D., and Roden, E. E. (2017). comparative genomic analysis of neutrophilic iron(II) oxidizer genomes for candidate genes in

extracellular electron transfer. *Front. Microbiol.* 8:1584. doi: 10.3389/fmicb.2017.01584

Heberling, C., Lowell, R. P., Liu, L., and Fisk, M. R. (2010). Extent of the microbial biosphere in the oceanic crust. *Geochem. Geophy. Geosyst.* 11, 1–15. doi: 10.1029/2009gc002968

Huber, J. A., Johnson, H. P., Butterfield, D. A., and Baross, J. A. (2006). Microbial life in ridge flank crustal fluids. *Environ. Microbiol.* 8, 88–99. doi: 10.1111/j.1462-2920.2005.00872.x

Jorgensen, S. L., and Zhao, R. (2016). Microbial Inventory of deeply buried oceanic crust from a young ridge flank. *Front. Microbiol.* 7:820. doi: 10.3389/fmicb.2016.00820

Jungbluth, S. P., Amend, J. P., and Rappe, M. S. (2017a). Metagenome sequencing and 98 microbial genomes from juan de fuca ridge flank subsurface fluids. *Sci. Data* 4:170037. doi: 10.1038/sdata.2017.37

Jungbluth, S. P., Glavina Del Rio, T., Tringe, S. G., Stepanauskas, R., and Rappe, M. S. (2017b). Genomic comparisons of a bacterial lineage that inhabits both marine and terrestrial deep subsurface systems. *PeerJ* 5, e3134. doi: 10.7717/peerj.3134

Jungbluth, S. P., Bowers, R. M., Lin, H. T., Cowen, J. P., and Rappe, M. S. (2016). Novel microbial assemblages inhabiting crustal fluids within mid-ocean ridge flank subsurface basalt. *ISME J.* 10, 2033–2047. doi: 10.1038/ismej.2015.248

Jungbluth, S. P., Grote, J., Lin, H. T., Cowen, J. P., and Rappe, M. S. (2013). Microbial diversity within basement fluids of the sediment-buried Juan de Fuca Ridge flank. *ISME J.* 7, 161–172. doi: 10.1038/ismej.2012.73

Jungbluth, S. P., Lin, H. T., Cowen, J. P., Glazer, B. T., and Rappe, M. S. (2014). Phylogenetic diversity of microorganisms in subseafloor crustal fluids from Holes 1025C and 1026B along the Juan de Fuca Ridge flank. *Front. Microbiol.* 5:119. doi: 10.3389/fmicb.2014.00119

Kallmeyer, J., Pockalny, R., Adhikari, R. R., Smith, D. C., and D'hondt, S. (2012). Global distribution of microbial abundance and biomass in subseafloor sediment. *Proc. Natl. Acad. Sci. U.S.A.* 109, 16213–16216. doi: 10.1073/pnas.1203849109

Kanehisa, M., Sato, Y., Kawashima, M., Furumichi, M., and Tanabe, M. (2016a). KEGG as a reference resource for gene and protein annotation. *Nucleic Acids Res.* 44, D457–D462. doi: 10.1093/nar/gkv1070

Kanehisa, M., Sato, Y., and Morishima, K. (2016b). BlastKOALA and GhostKOALA: KEGG tools for functional characterization of genome and metagenome sequences. *J. Mol. Biol.* 428, 726–731. doi: 10.1016/j.jmb.2015.11.006

Labonte, J. M., Lever, M. A., Edwards, K. J., and Orcutt, B. N. (2017). Influence of igneous basement on deep sediment microbial diversity on the eastern juan de fuca ridge flank. *Front. Microbiol.* 8:1434. doi: 10.3389/fmicb.2017.01434

Lang, S. Q., Butterfield, D. A., Lilley, M. D., Paul Johnson, H., and Hedges, J. I. (2006). Dissolved organic carbon in ridge-axis and ridge-flank hydrothermal systems. *Geochim. Cosmochim. Acta* 70, 3830–3842. doi: 10.1016/j.gca.2006.04.031

Langmead, B., and Salzberg, S. L. (2012). Fast gapped-read alignment with bowtie 2. *Nat. Methods* 9, 357–359. doi: 10.1038/nmeth.1923

Lever, M., Alperin, M., Engelen, B., Inagaki, F., Nakagawa, S., Steinsbu, B., et al. (2006). Trends in basalt and sediment core contamination during iodp expedition 301. *Geomicrobiol. J.* 23, 517–530. doi: 10.1080/01490450600897245

Lever, M. A., Rouxel, O., Alt, J. C., Shimizu, N., Ono, S., Coggon, R. M., et al. (2013). Evidence for microbial carbon and sulfur cycling in deeply buried ridge flank basalt. *Science* 339, 1305–1308. doi: 10.1126/science.1229240

Lin, H.-T., Cowen, J. P., Olson, E. J., Amend, J. P., and Lilley, M. D. (2012). Inorganic chemistry, gas compositions and dissolved organic carbon in fluids from sedimented young basaltic crust on the juan de fuca ridge flanks. *Geochim. Cosmochim. Acta* 85, 213–227. doi: 10.1016/j.gca.2012.02.017

Lin, H.-T., Cowen, J. P., Olson, E. J., Lilley, M. D., Jungbluth, S. P., Wilson, S. T., et al. (2014). Dissolved hydrogen and methane in the oceanic basaltic biosphere. *Earth Planet. Sci. Lett.* 405, 62–73. doi: 10.1016/j.epsl.2014.07.037

Masui, N., Morono, Y., and Inagaki, F. (2008). microbiological assessment of circulation mud fluids during the first operation of riser drilling by the deep-earth research vesselchikyu. *Geomicrobiol. J.* 25, 274–282. doi: 10.1080/01490450802258154

McCarthy, M. D., Beaupré, S. R., Walker, B. D., Voparil, I., Guilderson, T. P., and Druffel, E. R. M. (2010). Chemosynthetic origin of 14C-depleted dissolved organic matter in a ridge-flank hydrothermal system. *Nat. Geosci.* 4, 32–36. doi: 10.1038/ngeo1015

Meyer, J. L., Jaekel, U., Tully, B. J., Glazer, B. T., Wheat, C. G., Lin, H. T., et al. (2016). A distinct and active bacterial community in cold oxygenated fluids circulating beneath the western flank of the mid-atlantic ridge. *Sci. Rep.* 6, 22541. doi: 10.1038/srep22541

Morono, Y., and Inagaki, F. (2016). Analysis of low-biomass microbial communities in the deep biosphere. *Adv. Appl. Microbiol.* 95, 149–178. doi: 10.1016/bs.aambs.2016.04.001

Nakagawa, S., Takai, K., Inagaki, F., Chiba, H., Ishibashi, J., Kataoka, S., et al. (2005). Variability in microbial community and venting chemistry in a sediment-hosted backarc hydrothermal system: impacts of subseafloor phase-separation. *FEMS Microbial. Ecol.* 54, 141–155. doi: 10.1016/j.femsec.2005.03.007

Neira, N. M., Clark, J. F., Fisher, A. T., Wheat, C. G., Haymon, R. M., and Becker, K. (2016). Cross-hole tracer experiment reveals rapid fluid flow and low effective porosity in the upper oceanic crust. *Earth Planet. Sci. Lett.* 450, 355–365. doi: 10.1016/j.epsl.2016.06.048

Nesbo, C. L., Swither, K. S., Dahle, H., Haverkamp, T. H., and Birkeland, N. K. (2015). Evidence for extensive gene flow and Thermotoga subpopulations in subsurface and marine environments. *ISME J.* 9, 1532–1542. doi: 10.1038/ismej.2014.238

Nigro, L. M., Harris, K., Orcutt, B. N., Hyde, A., Clayton-Luce, S., Becker, K., et al. (2012). Microbial communities at the borehole observatory on the costa rica rift flank (ocean drilling program hole 896A). *Front. Microbiol.* 3:232. doi: 10.3389/fmicb.2012.00232

Orcutt, B., Wheat, C. G., and Edwards, K. J. (2010). Subseafloor ocean crust microbial observatories: development of FLOCS (FLow-through osmo colonization system) and evaluation of borehole construction materials. *Geomicrobiol. J.* 27, 143–157. doi: 10.1080/01490450903456772

Orcutt, B. N., Bach, W., Becker, K., Fisher, A. T., Hentscher, M., Toner, B. M., et al. (2011a). Colonization of subsurface microbial observatories deployed in young ocean crust. *ISME J.* 5, 692–703. doi: 10.1038/ismej.2010.157

Orcutt, B. N., Sylvan, J. B., Knab, N. J., and Edwards, K. J. (2011b). Microbial ecology of the dark ocean above, at, and below the seafloor. *Microbiol. Mol. Biol. Rev.* 75, 361–422. doi: 10.1128/MMBR.00039-10

Orcutt, B. N., Sylvan, J. B., Rogers, D. R., Delaney, J., Lee, R. W., and Girguis, P. R. (2015). Carbon fixation by basalt-hosted microbial communities. *Front. Microbiol.* 6:904. doi: 10.3389/fmicb.2015.00904

Peters, J. W., Schut, G. J., Boyd, E. S., Mulder, D. W., Shepard, E. M., Broderick, J. B., et al. (2015). [FeFe]- and [NiFe]-hydrogenase diversity, mechanism, and maturation. *Biochim. Biophys. Acta* 1853, 1350–1369. doi: 10.1016/j.bbamcr.2014.11.021

Rinke, C., Schwientek, P., Sczyrba, A., Ivanova, N. N., Anderson, I. J., Cheng, J. F., et al. (2013). Insights into the phylogeny and coding potential of microbial dark matter. *Nature* 499, 431–437. doi: 10.1038/nature12352

Robador, A., Jungbluth, S. P., Larowe, D. E., Bowers, R. M., Rappe, M. S., Amend, J. P., et al. (2014). Activity and phylogenetic diversity of sulfate-reducing microorganisms in low-temperature subsurface fluids within the upper oceanic crust. *Front. Microbiol.* 5:748. doi: 10.3389/fmicb.2014.00748

Robador, A., Larowe, D. E., Jungbluth, S. P., Lin, H. T., Rappe, M. S., Nealson, K. H., et al. (2016). Nanocalorimetric characterization of microbial activity in deep subsurface oceanic crustal fluids. *Front. Microbiol.* 7:454. doi: 10.3389/fmicb.2016.00454

Robbins, S. J., Evans, P. N., Parks, D. H., Golding, S. D., and Tyson, G. W. (2016). Genome-centric analysis of microbial populations enriched by hydraulic fracture fluid additives in a coal bed methane production well. *Front. Microbiol.* 7:731. doi: 10.3389/fmicb.2016.00731

Salter, S., Cox, M., Turek, E., Calus, S., Cookson, W. O., and Moffatt, M. (2014). Reagent and laboratory contaminantion can critically impact sequence-based microbiome analyses. *BMC Biol.* 12:87. doi: 10.1186/s12915-014-0087-z

Santelli, C. M., Banerjee, N., Bach, W., and Edwards, K. J. (2010). Tapping the subsurface ocean crust biosphere: low biomass and drilling-related contamination calls for improved quality controls. *Geomicrobiol. J.* 27, 158–169. doi: 10.1080/01490450903456780

Santelli, C. M., Edgcomb, V. P., Bach, W., and Edwards, K. J. (2009). The diversity and abundance of bacteria inhabiting seafloor lavas positively correlate with rock alteration. *Environ. Microbiol.* 11, 86–98. doi: 10.1111/j.1462-2920.2008.01743.x

Santelli, C. M., Orcutt, B. N., Banning, E., Bach, W., Moyer, C. L., Sogin, M. L., et al. (2008). Abundance and diversity of microbial life in ocean crust. *Nature* 453, 653–656. doi: 10.1038/nature06899

Schloss, P. D., Westcott, S. L., Ryabin, T., Hall, J. R., Hartmann, M., Hollister, E. B., et al. (2009). Introducing mothur: open-source, platform-independent, community-supported software for describing and comparing microbial communities. *Appl. Environ. Microbiol.* 75, 7537–7541. doi: 10.1128/AEM.01541-1549

Shah Walter, S. R., Jaekel, U., Osterholz, H., Fisher, A. T., Huber, J. A., Pearson, A., et al. (2018). Microbial decomposition of marine dissolved organic matter in cool oceanic crust. *Nat. Geosci.* 11, 334–339. doi: 10.1038/s41561-018-0109-5

Sharon, I., Kertesz, M., Hug, L. A., Pushkarev, D., Blauwkamp, T. A., Castelle, C. J., et al. (2015). Accurate, multi-kb reads resolve complex populations and detect rare microorganisms. *Genome Res.* 25, 534–543. doi: 10.1101/gr.183012.114

Sheik, C. S., Reese, B. K., Twing, K. I., Sylvan, J. B., Grim, S. L., Schrenk, M. O., et al. (2018). Identification and removal of contaminant sequences from ribosomal gene databases: lessons from the census of deep life. *Front. Microbiol.* 9:840. doi: 10.3389/fmicb.2018.00840

Smith, A., Popa, R., Fisk, M., Nielsen, M., Wheat, C. G., Jannasch, H. W., et al. (2011). In situ enrichment of ocean crust microbes on igneous minerals and glasses using an osmotic flow-through device. *Geochem. Geophys. Geosyst.* 12, 1–19. doi: 10.1029/2010gc003424

Smith, A. R., Fisk, M. R., Thurber, A. R., Flores, G. E., Mason, O. U., Popa, R., et al. (2016). Deep crustal communities of the juan de fuca ridge are governed by mineralogy. *Geomicrobiol. J.* 34, 147–156. doi: 10.1080/01490451.2016.1155001

Smith, A. R., Kieft, B., Mueller, R., Fisk, M. R., Mason, O. U., Popa, R., et al. (2019). Carbon fixation and energy metabolisms of a subseafloor olivine biofilm. *ISME J.* 13, 1737–1749. doi: 10.1038/s41396-019-0385-0

Sylvan, J. B., Sia, T. Y., Haddad, A. G., Briscoe, L. J., Toner, B. M., Girguis, P. R., et al. (2013). Low temperature geomicrobiology follows host rock composition along a geochemical gradient in lau basin. *Front. Microbiol.* 4:61. doi: 10.3389/fmicb.2013.00061

Toner, B. M., Lesniewski, R. A., Marlow, J. J., Briscoe, L. J., Santelli, C. M., Bach, W., et al. (2013). Mineralogy drives bacterial biogeography of hydrothermally inactive seafloor sulfide deposits. *Geomicrobiol. J.* 30, 313–326. doi: 10.1080/01490451.2012.688925

Toner, B. M., Santelli, C. M., Marcus, M. A., Wirth, R., Chan, C. S., Mccollom, T., et al. (2009). Biogenic iron oxyhydroxide formation at mid-ocean ridge hydrothermal vents: juan de Fuca Ridge. *Geochim. Cosmochim. Acta* 73, 388–403. doi: 10.1016/j.gca.2008.09.035

Tully, B. J., Wheat, C. G., Glazer, B. T., and Huber, J. A. (2018). A dynamic microbial community with high functional redundancy inhabits the cold, oxic subseafloor aquifer. *ISME J.* 12, 1–16. doi: 10.1038/ismej.2017.187

Wheat, C. G., Hulme, S. M., Fisher, A. T., Orcutt, B. N., and Becker, K. (2013). Seawater recharge into oceanic crust: IODP Exp 327 Site U1363 grizzly bare outcrop. *Geochem. Geophys. Geosyst.* 14, 1957–1972. doi: 10.1002/ggge.20131

Wheat, C. G., Jannasch, H. W., Fisher, A. T., Becker, K., Sharkey, J., and Hulme, S. (2010). Subseafloor seawater-basalt-microbe reactions: continuous sampling of borehole fluids in a ridge flank environment. *Geochem. Geophys. Geosyst.* 11, 1–18. doi: 10.1029/2010gc003057

Wheat, C. G., Jannasch, H. W., Kastner, M., Hulme, S., Cowen, J., Edwards, K. J., et al. (2011). Fluid sampling from oceanic borehole observatories: design and methods for CORK activities (1990-2010). *Proc. Integr. Ocean Drill. Program* 327, doi: 10.2204/iodp.proc.327.109.2011

Wheat, C. G., Mcmanus, J., Mottl, M. J., and Giambalvo, E. (2003). Oceanic phosphorus imbalance: magnitude of the mid-ocean ridge flank hydrothermal sink. *Geophys. Res. Lett.* 30, 1–4. doi: 10.1029/2003gl017318

Yuan, C., Lei, J., Cole, J., and Sun, Y. (2015). Reconstructing 16S rRNA genes in metagenomic data. *Bioinformatics* 31, i35–i43. doi: 10.1093/bioinformatics/btv231

Zhang, X., Feng, X., and Wang, F. (2016). Diversity and metabolic potentials of subsurface crustal microorganisms from the western flank of the mid-atlantic ridge. *Front. Microbiol.* 7:363. doi: 10.3389/fmicb.2016.00363

Conflict of Interest Statement: The authors declare that the research was conducted in the absence of any commercial or financial relationships that could be construed as a potential conflict of interest.

frontiers in Earth Science

PERSPECTIVE
published: 04 September 2019
doi: 10.3389/feart.2019.00225

Exploring the Deep Marine Biosphere: Challenges, Innovations, and Opportunities

Anaïs Cario[1,2], Gina C. Oliver[1] and Karyn L. Rogers[1,3]**

[1] Department of Earth and Environmental Sciences, Rensselaer Polytechnic Institute, Troy, NY, United States, [2] CNRS, Univ. Bordeaux, Bordeaux INP, ICMCB, Pessac, France, [3] Rensselaer Astrobiology Research and Education Center, Rensselaer Polytechnic Institute, Troy, NY, United States

The deep marine biosphere is one of the largest, and yet least explored, microbial habitats on the planet. Quantifying the extent, diversity, and activity of subsurface microbial communities is a crucial part of understanding their role in global biogeochemical cycles. Even though deep biosphere habitats can vary widely in chemistry, temperature, turnover rates, and energy sources, all subsurface microbes inherently experience high pressures. While not all subsurface microbes require elevated pressures, for many high pressures are essential to their cellular function and metabolism. Thus, when targeting this elusive portion of the biosphere, it is critical to maintain *in situ* pressure while sampling and cultivating subsurface microorganisms. In this perspective paper we highlight the sampling and cultivation technologies available to study these communities under *in situ* conditions. Maintaining elevated pressures throughout sampling, transfer, cultivation, and isolation is challenging, and more often than not samples are decompressed at some point during sample handling, potentially leading to biases in both community diversity and isolate physiology. The development of devices that maintain *in situ* pressures during sampling and allow for sample transfer without decompression have begun to address this challenge (like the PUSH – Pressurized Underwater Sample Handler). Such vessels can be used for both retrieval and enrichment of deep subsurface samples, as well as high-pressure growth and physiology experiments, thus expanding possibilities for deep biosphere exploration. Finally, we discuss the significant need to develop and share high-pressure facilities across the deep biosphere community, in order to expand the opportunities to discover novel piezophiles from the deep subsurface.

Keywords: deep biosphere, high-pressure microbiology, decompression, sampling, cultivation

OPEN ACCESS

Edited by:
Sabin Zahirovic,
University of Sydney, Australia

Reviewed by:
Bernhard Wehrli,
ETH Zürich, Switzerland
William Patrick Gilhooly III,
Indiana University–Purdue University Indianapolis, United States

****Correspondence:***
Anaïs Cario
anais.cario@cnrs.fr
Karyn L. Rogers
rogerk5@rpi.edu

Specialty section:
This article was submitted to Biogeoscience, a section of the journal Frontiers in Earth Science

Received: *31 May 2019*
Accepted: *16 August 2019*
Published: *04 September 2019*

Citation:
Cario A, Oliver GC and Rogers KL (2019) Exploring the Deep Marine Biosphere: Challenges, Innovations, and Opportunities. Front. Earth Sci. 7:225. doi: 10.3389/feart.2019.00225

UNVEILING THE INVISIBLE MAJORITY: THE DEEP MARINE BIOSPHERE

In this communication we consider the deep biosphere to include all environments at and above 10 MPa in the water column (10 MPa/km), subseafloor sediments (15 MPa/km) and all the potential reservoirs in the continental and oceanic crust (25 MPa/km) (Jannasch and Taylor, 1984; Oger and Jebbar, 2010; Picard and Daniel, 2013), though we focus primarily on marine environments. The deep-sea, defined as waters and sediments beneath 1000 m depth, is the Earth's largest ecosystem,

representing 65% of the planet's surface and encompassing 88% of the global biosphere (Jannasch and Taylor, 1984). The ocean has an average depth of 3800 m and an average pressure of 38 MPa (Herring and Clarke, 1971), and even the deepest waters (Mariana Trench at 11 km, 110 MPa) are known to host life (Glud et al., 2013; Nunoura et al., 2015; Tarn et al., 2016). The habitable zones of the continental crust are similarly vast and underexplored, and also host unique microbial communities (Stevens and McKinley, 1995; Takai et al., 2001; Moser et al., 2005; Lollar et al., 2006; Lavalleur and Colwell, 2013; Borgonie et al., 2015). This remote and dark biosphere hosts a range of subsurface habitats typically characterized by extreme conditions (Jørgensen and Boetius, 2007). They are mostly nutrient-poor – excluding the hot spots (e.g., hydrothermal vents) – and have slow or transient energy fluxes supplied by water-rock reactions and circulating crustal fluids (Orcutt et al., 2011). Despite harsh conditions, these ecosystems define the largest microbial habitat on Earth (Whitman et al., 1998; Kallmeyer et al., 2012; Bar-On et al., 2018). The subsurface is estimated to hold ∼15% of the total terrestrial biomass (Bar-On et al., 2018), and resident microbial communities potentially play an important role in mediating global biogeochemical cycles (D'Hondt et al., 2004; D'Hondt et al., 2009). However, only 5% of the oceans have been investigated using remote instruments and less than 0.01% has been sampled and studied (Ramirez-Llodra et al., 2010). Despite being such a large fraction of Earth's biomass the microbial diversity, activity and distribution, metabolic pathways, and energy fluxes of the subsurface biosphere are poorly understood because access is limited by technical and economic challenges. Over the past decade, international drilling programs (IODP – International Ocean Discovery Program, ICDP – International Continental Scientific Drilling Program), as well as national submersible facilities have expanded subsurface microbiology research to better understand how intra-terrestrial life inhabiting the deep crust and deep oceans plays a role within the deep biosphere. Subsurface technologies and recent advances in this field are well documented in Schrenk et al. (2010), Edwards et al. (2011), and Edwards et al. (2012).

A majority of prokaryotes live under high-pressure conditions, and thus pressure is a governing factor for the distribution of life (Picard and Daniel, 2013), and subsurface microorganisms are classified by their physiological responses (e.g., growth rates, cell yields) to pressure (Abe, 2007; Fang et al., 2010). Usually, well-adapted surface microorganisms are negatively impacted by high-pressure conditions (piezosensitive), even though some can grow at elevated pressures (piezotolerant). Likewise, microorganisms isolated from the subsurface often grow optimally at high-pressure (piezophiles), and obligate piezophiles are unable to grow at ambient (surface) pressures. In the case of the deep marine biosphere, evidence suggests that decompression can deleteriously impact cellular viability, including morphological changes (Chastain and Yayanos, 1991), membrane cell rupture (Park and Clark, 2002), and piezophile inactivation (Yayanos and Dietz, 1982; Yayanos and Dietz, 1983). Furthermore, significant shifts in community composition and gene expression have been noted as a result of sample decompression (La Cono et al., 2015; Edgcomb et al., 2016). To date, the number of facultative and obligate piezophiles is limited to ∼56 (**Figure 1A** and **Supplementary Table S2**) (Picard and Daniel, 2013; Jebbar et al., 2015). Among the obligate piezophiles, *Colwellia marinimaniae* has the highest optimum growth pressure at 120 MPa (Kusube et al., 2017). This psychrophile and the hyperthermophilic *Pyrococcus yayanosii* (Zeng et al., 2009), currently claim the highest pressure limits of growth (140 and 120 MPa, respectively). Although the majority of currently known piezophiles were isolated following decompression, these isolates may be notable exceptions, representing only the fraction of the subsurface biosphere tolerant of decompression. Indeed a much broader microbial community has been identified in the subsurface through alternative methods, including genetic and molecular approaches (Orsi et al., 2013), *in situ* metabolic rate measurements (Jørgensen et al., 1992; Kallmeyer and Boetius, 2004; Kallmeyer et al., 2012), intact polar lipid analysis (Zink et al., 2003; Lipp et al., 2008), stable isotope enrichments (Morono et al., 2011), cell counts (Parkes et al., 1994), and growth of viable cultures (D'Hondt et al., 2004; Smith et al., 2011). It should be noted that many of these observations were made on decompressed samples. While such results of ambient pressure experiments might extend our view of the deep biosphere, they are nonetheless biased toward surface pressures and likely do not reflect microbial processes at *in situ* pressure conditions.

The limited number of piezophilic isolates also hinders our ability to investigate the effects of high-pressure on metabolism and physiology (Tamburini, 2006). Piezophiles exhibit different strategies to cope with elevated pressure and maintain cell integrity over a wide pressure range (Bartlett, 2002; Abe, 2007; Oger and Jebbar, 2010) including (i) cell wall and lipid membrane biochemistry (DeLong and Yayanos, 1985; Allen and Bartlett, 2002; Cario et al., 2015); (ii) intracellular salt content and osmolyte regulation (Martin et al., 2002; Cario et al., 2016b); (iii) specific high-pressure gene expressions (Kato and Qureshi, 1999; Campanaro et al., 2005; Simonato et al., 2006; Vannier et al., 2015; Michoud and Jebbar, 2016); and (iv) macromolecule structural modulation (Kawano et al., 2004; Rosenbaum et al., 2012). These unique piezophilic strategies have been identified via a limited number of high-pressure cultivation experiments, but there are diverse, uncultured species within the deep biosphere that undoubtedly have unknown metabolic and physiological strategies. In the absence of additional isolates, these unknown functions have been probed with high-pressure experiments conducted on bulk samples from the deep biosphere (e.g., sediments, fluids, enrichment cultures). Among these >200 varied experiments one general trend that has emerged is that retrieval depth is broadly correlated with a positive response to elevated pressure (**Figure 1B**). These results suggest that decompression and/or ambient pressure conditions are a challenge for subsurface organisms, and that incorporating elevated pressure conditions into sampling and experimental protocols could greatly improve experimental outcomes. Below we review the sampling and cultivation techniques commonly adopted in marine subsurface biosphere research, the limitations inherent to these approaches, and strategies to improve

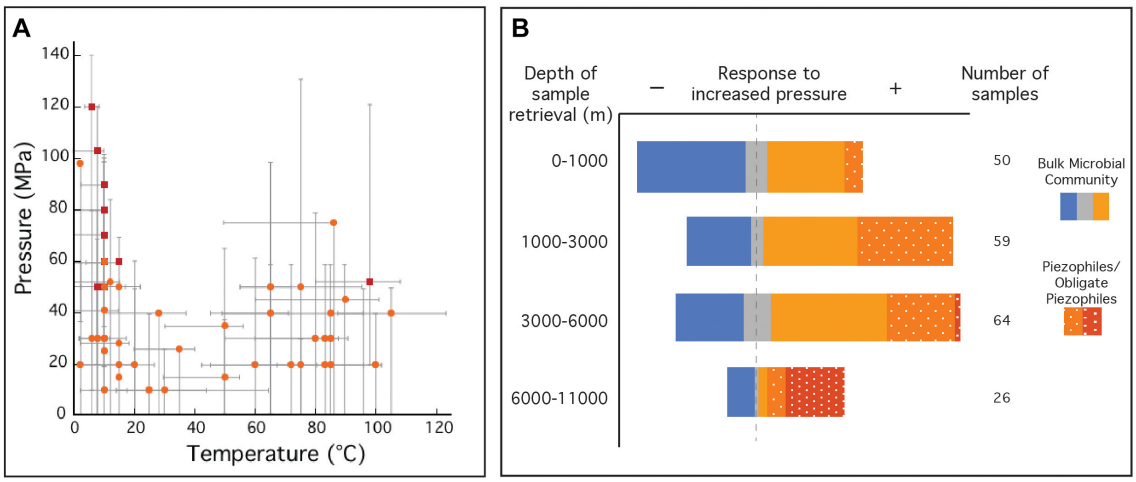

FIGURE 1 | (A) Optimal temperature and pressure growth conditions for known piezophiles (light orange circles) and obligate piezophiles (red squares). Gray bars indicate the reported temperature and pressure growth ranges for each isolate. **(B)** Collection of natural samples and isolates with sample origins at various depths and their response to elevated pressure compared to ambient pressure (0.1 MPa). Natural samples (solid), where metabolic activity was monitored, was reported to have either a negative (solid blue), neutral (solid gray) or positive (solid orange) response to increased pressure compared to growth at 0.1 MPa. Isolated piezophiles (dotted orange) are described here as having optimum growth at pressures above 0.1 MPa and obligate piezophiles (dotted red) are those that require elevated pressures for growth and cannot grow at 0.1 MPa. This figure is not an exhaustive list of all natural samples taken from the deep biosphere with reported pressure tolerances and does not include piezotolerant organisms (optimum growth pressure at 0.1 MPa). Temperature and pressure data for isolates in **A**,**B** were collected from references listed in **Supplementary Table S2**. Data for natural samples were extracted from Picard and Daniel (2013).

subsurface exploration through technology development and new collaborative models (**Figure 2**).

HOW DO WE EXPLORE THE PIEZOSPHERE?

Since the discovery of deep-sea and subsurface microbial life (Zobell, 1952; Corliss et al., 1979; Parkes et al., 1994), the development of advanced instrumentation for observing, retrieving, and manipulating samples has illuminated some of the key characteristics of the deep geosphere and biosphere (Tengberg et al., 1995; Ramirez-Llodra et al., 2010). International collaboration and national efforts are the hallmarks of subsurface exploration, including drilling and submersibles. Similarly large international programs support the research communities that explore the deep biosphere and improve our knowledge of the subsurface microbiome (cf. ICOMM – International Census of Marine Microbes; C-DEBI – Center for Dark Energy Biosphere Investigations; and DCO – Deep Carbon Observatory). Only three human expeditions have explored the deepest part of the ocean (Mariana Trench, 11 km) (Oppenheimer and Zobell, 1952; Gallo et al., 2015; Fitzherbert, 2019), leaving 95% of the ocean unexplored directly (Ramirez-Llodra et al., 2010), even though other HOVs (human occupied vehicles), like the *Shinkai 6500* and *Nautile* that reach up to 6500 m, allow for indirect exploration of nearly 98% of the ocean floor. Moreover, a veritable army of landers, ROVs (remotely operated vehicles), and AUVs (autonomous underwater vehicles) enable much of today's deep ocean exploration (**Supplementary Table S1**) (Tengberg et al., 1995; Reysenbach and Götz, 2001; Yayanos, 2001; Tamburini, 2006), while a new class of Internet operated vehicles (IOVs) and mobile platforms provide extended monitoring of both the seafloor and the water column (Aguzzi et al., 2019).

While drilling and exploration vehicles remain few, instruments to obtain subsurface samples are more numerous (**Supplementary Table S1**). The paltry list of isolated piezophiles reflects the difficulty of both retrieving and cultivating piezophiles from subsurface samples. Because decompression affects cellular viability, and because most samples are decompressed during sample handling, it remains possible that most piezophilic strains elude current sampling and culturing techniques. Therefore, several pressure-retaining devices have been developed to enable sampling without decompression (Jannasch et al., 1973; Yayanos, 1977; Bianchi et al., 1999; Tamburini et al., 2013). Recently, Tamburini's team used a pressure-retaining sampler in the bathypelagic zone to measure prokaryote activity under *in situ* pressure conditions, and demonstrated that decompression suppresses both piezophilic metabolisms and water column community composition (Garel et al., 2019). A similar pressure-retaining sampler was developed as part of DCO's PRIME (Piezophile Research Instrumentation for Microbial Exploration) Facility. The Pressurized Underwater Sample Handler System (PUSH) is similar to Bianchi's sampler (Bianchi et al., 1999), and uses a floating piston system to enable sampling, transport, transfer, and cultivation of high-pressure fluids without decompression (Rogers et al., 2016b).

Accessing the deep marine biosphere and retrieving samples at *in situ* pressures has proven a significant technological challenge for deep biosphere exploration, but these improvements can

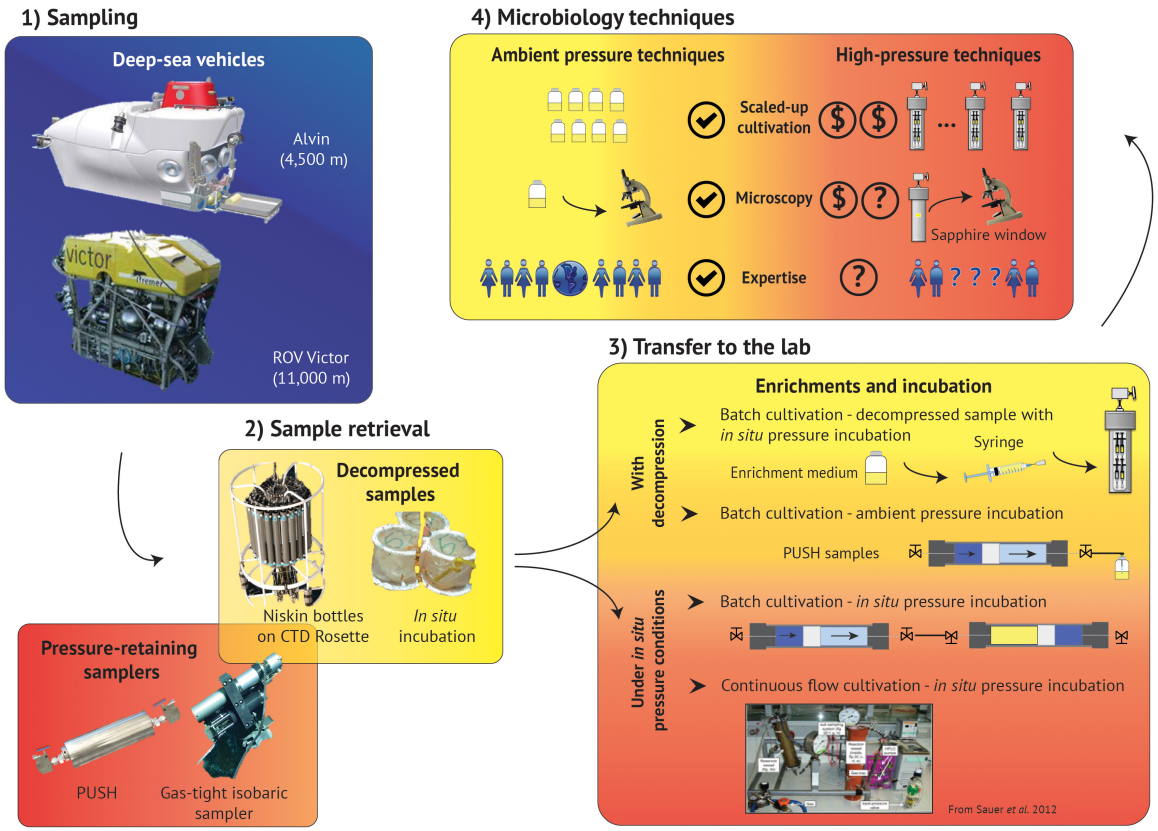

FIGURE 2 | Summary schematic of the deep-sea exploration workflow, from sampling to laboratory experiments. Access to deep marine environments is enabled with submersibles (1 – Sampling), along with the various devices that support 2 – Sample retrieval. 3 – Transfer to the lab and subsequent cultivation techniques often include batch cultivation, but can also accommodate continuous flow methods, though many of these techniques require sample decompression. 4 – Microbiology techniques are much more robust for ambient pressure conditions, and high-pressure analogs of these methods require technology development, high-pressure expertise, and can also increase the costs, and thus decrease the accessibility, of many of these protocols. (Box 1: Alvin picture is reprinted from Woods Hole Oceanographic Institution website (link: https://www.whoi.edu/oceanus/feature/building-the-next-generation-alvin-submersible/) 2019 Copyright WHOI, ROV Victor picture is reprinted from Ifremer website (link: https://wwz.ifremer.fr/grands_fonds/Les-moyens/Les-engins/Les-robots/Robots-Ifremer/Le-Victor-6000) 2019 Copyright IFREMER; Box 2: PUSH is a personal picture, Isobaric sampler picture is reprinted from Woods Hole Oceanographic Institution website (link: https://www.whoi.edu/press-room/news-release/surprisingly-productive-microbes-fuel-deep-sea-ecosystem/) 2019 Copyright WHOI, CTD rosette picture is Reprinted from NOAA website (link: https://oceanexplorer.noaa.gov) 2019 Copyright NOAA, *in situ* incubation is reprinted with permission from Rassa et al. (2009). Copyright 2019 Taylor & Francis Group; Box 3: Reprint with permission from Sauer et al. (2012). © 2012 Sauer, Glombitza, and Kallmeyer (CC BY-NC 3.0). 2019.)

be amplified if subsequent laboratory studies, particularly cultivation experiments, maintain high-pressure conditions. It is particularly important to maintain *in situ* pressure conditions during sampling, transfer to the laboratory, and throughout cultivation and storage, in order to avoid decompression bias. When targeting novel deep biosphere microbes, replicating *in situ* environmental conditions (i.e., pressure, temperature, pH, volatile composition, low nutrients concentrations) and subsampling without decompression are crucial aspects of the cultivation process. Since traditional laboratory culturing techniques are not easily adapted to high-pressure, customized devices and protocols have been developed. Yayanos and colleagues, the pioneers of high-pressure microbiology, developed early high-pressure cultivation apparatus (Yayanos and Pollard, 1969; Yayanos et al., 1979; Yayanos et al., 1982; Yayanos et al., 1984; Yayanos, 1986; DeLong et al., 1997), and these have since been expanded (Taylor and Jannasch, 1976; Bernhardt et al., 1987; Nauhaus et al., 2002; Takai et al., 2008). Cultivating piezophiles requires expertise in both high-pressure equipment (e.g., hydrostatic pumps, high-pressure vessels) (Kato et al., 2008; Kato, 2011) as well as manipulating high-pressure cultures. Most of these high-pressure devices are batch reactors, using a compressible reaction container in static high-pressure vessels. Typically, a stoppered syringe containing inoculated growth medium will be pressurized in a hydrostatic pressure vessel (e.g., Takai et al., 2008). Unfortunately, this setup requires decompression during subsampling, potentially suppressing growth rates and cell viability (Cario et al., 2016a; Rogers et al., 2016a, Oliver, 2019). Variable-volume reactors, like the PUSH and others (Seyfried et al., 1979; Bianchi et al., 1999; Cario et al., 2016a; Rogers et al., 2016b; Garel et al., 2019; Oliver, 2019; **Supplementary Table S1**), can overcome this limitation, and have recently been used for batch cultivation without decompression, identifying two pressure-tolerant

strains previously thought to be pressure-sensitive (Cario et al., 2016a; Oliver, 2019). This technology has been extended to allow for high-pressure transfer (Oliver, 2019), a crucial step in replicating traditional liquid culture microbial cultivation and expanding the possibilities for high-pressure isolation from enrichment cultures. A further improvement that better replicates natural geological environments are continuous flow-through systems. Jannasch and colleagues first developed a high-pressure (71 MPa maximum) continuous culture system for low temperatures (Jannasch et al., 1996). Sauer et al. designed a flow-through bioreactor (120°C and 60 MPa) that allows for volatile equilibration of the culture medium, subsampling without decompression, and the inclusion of a solid phase (Sauer et al., 2012). Recently, in the Rogers' lab, a similar continuous flow reactor was built that extended this pressure range to 100 MPa and incorporated a module for sample fixation prior to decompression (**Supplementary Table S1**).

Deep ocean sediments can also host a significant portion of the subsurface biosphere (Jørgensen and Boetius, 2007; Kallmeyer et al., 2012; Lloyd et al., 2013); However, retrieving deep ocean sediments and maintaining *in situ* pressures during cultivation and transfer of sediment present additional challenges. High-pressure sediments have been retrieved during drilling with pressure-coring systems (Reed et al., 2002; Kubo et al., 2014), but only the DeepIsoBUG system (Parkes et al., 2009) can transfer sediment under pressure for subsequent cultivation. Otherwise, most methods developed for high-pressure incubation and enrichment of sediments require decompression. Nonetheless, these devices can accommodate general batch cultivation, enhanced volatile concentrations, and flow-through conditions, and have confirmed that microbial metabolic rates are faster at elevated pressures in the presence of increased volatile substrate concentrations (Nauhaus et al., 2002; Bowles et al., 2011; Sauer et al., 2012). Given the extent of the subsurface microbiome contained in deep-sea sediments, the deleterious impact of decompression, and the documented importance of elevated pressure on growth and metabolism, expansion and improvement of high-pressure sediment manipulation remains ripe for high-impact technological developments.

WHAT ARE THE LIMITS?

In the modern era of microbiology, the capabilities of Earth's extremophiles have far outpaced our ability to conceive of the bounds of habitability. For each perceived limit – temperature, pressure, pH, energy flux, etc. – a novel and hard-to-imagine extremophile has surpassed expectations and extended the reach of potential habitable environments. In contrast, our technological capabilities have not kept pace with this ever-expanding habitable envelope. Even with the current known temperature and pressure limits of life, we have not yet explored most of the habitable subsurface. The primary limitations are the expense of drilling and oceanographic expeditions, together with technological limitations for sampling and sample manipulation. In the deepest parts of the ocean, pressures can reach 110 MPa, and access to these environments is limited to only a few ROVs and landers. Recently, Bartlett and colleagues developed a modular lander capable of sampling these hadal trenches at depths greater than 6000 m (Peoples et al., 2019). While spatially limited, these regions nonetheless represent 45% of the depth range of the ocean (Jamieson, 2015). Sampling at these pressures also poses technological challenges, as most samplers are designed to access meso- and bathypelagic zones (200–1000 and 1000–4000 m, respectively), and only a few are designed to reach deeper zones. Access to subsurface crustal and sedimentary ecosystems is limited by drilling technology, and high-pressure retrieval of solid-phase samples is rare. To our knowledge only fluid samples have been collected from deep crustal aquifers at *in situ* pressures (Hatanpää et al., 2005; Hallbeck and Pedersen, 2008) and high-pressure sediment retrieval is pressure-limited (Kubo et al., 2014). These latter examples highlight one of the more daunting challenges to understanding the deep biosphere, which is the scarcity of samples. Subsurface sampling is not only sparse, but often targets specific kinds of environments (e.g., hydrothermal systems, trenches, etc.), resulting in a lack of coverage for the "average" deep subsurface. Therefore, it is difficult to extrapolate across the entire subsurface biosphere, leaving large errors on our estimates for subsurface biomass, as well as metabolic, physiologic and genetic diversity.

CHALLENGES, INNOVATIONS AND OPPORTUNITIES

The last few decades have witnessed a dramatic increase in subsurface exploration and research, extending our access to and understanding of the deep biosphere, nonetheless, sampling and analysis challenges remain. Here we focus on four areas of opportunity for innovation (**Figure 2**): (i) sampling at *in situ* pressure conditions; (ii) high-pressure cultivation techniques; (iii) dissemination of high-pressure skills among the community; and (iv) increasing participation and/or incorporation of high-pressure sampling into deep-sea and drilling expeditions. We propose that community priorities going forward focus on deepening our knowledge of the deep biosphere and its role in global biogeochemical cycles, particularly by addressing technology development and implementing novel management and collaborative models to increase community access to high-pressure samples and devices.

Despite the ubiquity of prokaryotes within the deep biosphere, only a limited number have been cultivated (e.g., 0.1%) (D'Hondt et al., 2004). Illustrative of this point is the distribution of the isolated piezophiles (**Figure 1A**), with pressure maxima among the psychrophiles of the hadal zones and vent hyperthermophiles. The moderate temperature and pressure regime (e.g., ∼20 –60°C and ∼40–80 MPa) lacks piezophilic isolates despite the prevalence of such conditions within deep-sea sediments (Picard and Daniel, 2013). Similarly, the moderate pressure extent of the isolated hyperthermophilic piezophiles (P_{opt} < 80 MPa) reflects the conditions of the most accessible fluids from mid-ocean ridge high-temperature vents. Ecosystems at higher pressures and more moderate temperatures (e.g., subduction zones, crust off-axis of spreading centers) are among the least accessed habitats

of the subsurface. Exploring the full breadth of the piezosphere will require new drilling and sampling techniques targeting high-pressure retrieval and manipulations of rock and sediment samples. More broadly across the piezosphere, better cultivation methods that mimic *in situ* environmental conditions (i.e., temperature, pressure, chemical composition), could improve enrichment and isolation of novel piezophiles. Targeting several metabolic and physiologic niches requires scaling up high-pressure cultivation either by vastly increasing the number of pressure vessels or developing new technologies for multiplexing techniques (Kallmeyer et al., 2003). The deep biosphere also hosts microbial communities with slow metabolic rates surviving on minimal energy sources (D'Hondt et al., 2002). Traditional enrichment and isolation techniques favor fast growth under high-energy conditions, and are less likely to capture the slow pace of the deep biosphere microbiome. *In situ* or long-term incubations could help target the deep slow biosphere, but these require innovations for long-term incubations and high-pressure retrieval. While it is clear that every microbiological and molecular tool should be brought to bear to understand the deep biosphere, many of these need to be adapted to accommodate the elevated pressures of the subsurface. For example, monitoring metabolic rates during controlled incubations often relies on radiolabeled substrates (Frank et al., 2015), but adding radioactive material to pressure vessels introduces significant shipboard and laboratory safety concerns. Electrochemical monitoring of *in situ* chemistry during laboratory cultivation is also quite common in benchtop microbiology, but a more significant technological challenge when incubations are conducted at elevated pressures. Visualizing cells and microbial communities with high-pressure microscopy can be accomplished via specialized equipment (e.g., DACs), but is hardly as routine as it is in the traditional microbiology workflow. Even the most basic methods like dilution-to-extinction isolation protocols, proteomic analyses, or compound-specific stable isotope measurements, require either large numbers or larger volumes of high-pressure devices, limiting wide-spread use.

Molecular techniques, which are often used to give a more robust picture of microbial diversity compared to cultivation-based approaches, have indeed revealed that subsurface microbial diversity is broader than that represented by the cultivated piezophiles (Orsi et al., 2013). However, recent work suggests that even molecular techniques can suffer from decompression bias (Garel et al., 2019). Nonetheless, continued application of next-generation *–omics* techniques could further elucidate the diversity and activity of the subsurface microbiome (Nunoura et al., 2010), and be used to improve culturing efforts. For example, GeoChip-based high-throughput metagenomics have highlighted metabolic functions within dynamic microbial communities (He et al., 2007; Wang et al., 2009). Furthermore, the combination of stable-isotope probing (Webster et al., 2010; Lin et al., 2013; Fortunato and Huber, 2016), FISH-SIMS (Behrens et al., 2008) and single-cell sorting (Lasken, 2007) could further elucidate the links between microbial diversity, environmental conditions, and ecosystem processes, and develop more robust models of the deep biosphere and its connection to long-term biogeochemical processes.

Finally, we believe that sharing high-pressure expertise and equipment within the deep biosphere community, and expanding the scope of high-pressure microbial research, will advance our understanding of the deep biosphere. The number of facilities that can sample and manipulate subsurface samples at *in situ* pressures is considerably smaller than the number of research groups that regularly sample and study the deep subsurface. The barrier to entry (expense and expertise) into high-pressure techniques is high, but better coordination and new collaborative models can change this paradigm. The DCO, via the PRIME facility, supported the purchase of several PUSH samplers to share within the community, with the goal of isolating and characterizing more piezophilic microorganisms. However, equipment sharing will only be successful if it is accompanied by the requisite personnel and expertise. Therefore, new collaborative models that include equipment, personnel, and funding need to be developed to keep community-wide facilities successful and sustainable.

The Earth's deep biosphere not only represents a crucial segment of the global biosphere and modern biogeochemical cycles, but it also serves as a window into Earth's habitable environments throughout its history. Furthermore, as the exploration for life beyond Earth shifts to other solar system bodies, including the subsurface of Mars (Stamenković et al., 2019), or the subsurface ocean worlds of Europa, Enceladus and other moons, understanding how these environments can foster life becomes crucial to this exploration. Therefore, the technology developed to explore Earth's modern deep biosphere will eventually become a key component of missions to these bodies to search for signatures of extant extraterrestrial life or its remnant biosignatures.

DATA AVAILABILITY

The datasets generated for this study are available on request to the corresponding author.

AUTHOR CONTRIBUTIONS

AC, GO, and KR conceived the study. AC wrote the original draft. KR and GO wrote sections of the manuscript. GO and AC created the tables and figures. All authors contributed to the revisions of the manuscript, tables, and figures, and approved the submitted version.

FUNDING

Funding for this work was provided by NASA (NNX13AP2G9 and 80NSSC17K0252 to KR), the Deep Carbon Observatory (Subawards: 10371-07, 10561-01, and 10311-11 to KR), an NSF Graduate Fellowship (FAIN 1247271 and 1744655 to GO), and a GSA Research Grant to GO. Additional support was provided by startup funds from Rensselaer Polytechnic Institute to KR.

ACKNOWLEDGMENTS

The development of the PUSH devices and PRIME facility originated at the DCO Sandpit Workshop on Bioreactors, convened by Isabelle Daniel and sponsored by the Deep Carbon Observatory. We appreciate the contributions from the workshop participants and the entire DCO community in support of this initiative. We further thank Isabelle Daniel, Hervé Cardon, Bruce Watson, and Chris Hoff for technical support. Finally, we thank the two reviewers for helpful comments.

SUPPLEMENTARY MATERIAL

The Supplementary Material for this article can be found online at: https://www.frontiersin.org/articles/10.3389/feart.2019.00225/full#supplementary-material

REFERENCES

Abe, F. (2007). Exploration of the effects of high hydrostatic pressure on microbial growth, physiology and survival: perspectives from piezophysiology. *Biosci. Biotechnol. Biochem.* 71, 2347–2357. doi: 10.1271/bbb.70015

Aguzzi, J., Chatzievangelou, D., Marini, S., Fanelli, E., Danovaro, R., Flögel, S., et al. (2019). New high-tech flexible networks for the monitoring of deep-sea ecosystems. *Environ. Sci. Technol.* 53, 6616–6631. doi: 10.1021/acs.est.9b00409

Allen, E. E., and Bartlett, D. H. (2002). Structure and regulation of the omega-3 polyunsaturated fatty acid synthase genes from the deep-sea bacterium *Photobacterium profundum* strain SS9. *Microbiology* 148, 1903–1913. doi: 10.1099/00221287-148-6-1903

Bar-On, Y. M., Phillips, R., and Milo, R. (2018). The biomass distribution on Earth. *Proc. Natl. Acad. Sci. U.S.A.* 115, 6506–6511. doi: 10.1073/pnas.1711842115

Bartlett, D. H. (2002). Pressure effects on *in vivo* microbial processes. *Biochim. Biophys. Acta* 1595, 367–381. doi: 10.1016/s0167-4838(01)00357-0

Behrens, S., Lösekann, T., Pett-Ridge, J., Weber, P. K., Ng, W.-O., Stevenson, B. S., et al. (2008). Linking microbial phylogeny to metabolic activity at the single-cell level by using enhanced element labeling-catalyzed reporter deposition fluorescence in situ hybridization (EL-FISH) and NanoSIMS. *Appl. Environ. Microbiol.* 74, 3143–3150. doi: 10.1128/AEM.00191-08

Bernhardt, G., Jaenicke, R., and Lüdemann, H.-D. (1987). High-pressure equipment for growing methanogenic microorganisms on gaseous substrates at high temperature. *Appl. Environ. Microbiol.* 53, 1876–1879.

Bianchi, A., Garcin, J., and Tholosan, O. (1999). A high-pressure serial sampler to measure microbial activity in the deep sea. *Deep Sea Res. I Oceanogr. Res. Papers* 46, 2129–2142. doi: 10.1016/s0967-0637(99)00039-4

Borgonie, G., Linage-Alvarez, B., Ojo, A., Mundle, S., Freese, L. B., Van Rooyen, C., et al. (2015). Eukaryotic opportunists dominate the deep-subsurface biosphere in South Africa. *Nat. Commun.* 6:8952. doi: 10.1038/ncomms9952

Bowles, M. W., Samarkin, V. A., and Joye, S. B. (2011). Improved measurement of microbial activity in deep-sea sediments at *in situ* pressure and methane concentration. *Limnol. Oceanogr. Methods* 9, 499–506. doi: 10.4319/lom.2011.9.499

Campanaro, S., Vezzi, A., Vitulo, N., Lauro, F., D'Angelo, M., Simonato, F., et al. (2005). Laterally transferred elements and high pressure adaptation in *Photobacterium profundum* strains. *BMC Genomics* 6:122.

Cario, A., Daniel, I., and Rogers, K. L. (2016a). "Increased pressure tolerance of a marine bacterium when cultivated under high-pressure conditions without subsampling decompression," in *Proceedings of the 11th International Congress on Extremophiles 2016*, Kyoto.

Cario, A., Jebbar, M., Thiel, A., Kervarec, N., and Oger, P. M. (2016b). Molecular chaperone accumulation as a function of stress evidences adaptation to high hydrostatic pressure in the piezophilic archaeon *Thermococcus barophilus*. *Sci. Rep.* 6:29483. doi: 10.1038/srep29483

Cario, A., Grossi, V., Schaeffer, P., and Oger, P. M. (2015). Membrane homeoviscous adaptation in the piezo-hyperthermophilic archaeon *Thermococcus barophilus*. *Front. Microbiol.* 6:1152. doi: 10.3389/fmicb.2015.01152

Chastain, R. A., and Yayanos, A. A. (1991). Ultrastructural changes in an obligately barophilic marine bacterium after decompression. *Appl. Environ. Microbiol.* 57, 1489–1497.

Corliss, J. B., Dymond, J., Gordon, L. I., Edmond, J. M., von Herzen, R. P., Ballard, R. D., et al. (1979). Submarine thermal springs on the Galapagos Rift. *Science* 203, 1073–1083. doi: 10.1126/science.203.4385.1073

DeLong, E., Franks, D., and Yayanos, A. (1997). Evolutionary relationships of cultivated psychrophilic and barophilic deep-sea bacteria. *Appl. Environ. Microbiol.* 63, 2105–2108.

DeLong, E. F., and Yayanos, A. (1985). Adaptation of the membrane lipids of a deep-sea bacterium to changes in hydrostatic pressure. *Science* 228, 1101–1103. doi: 10.1126/science.3992247

D'Hondt, S., Jørgensen, B. B., Miller, D. J., Batzke, A., Blake, R., Cragg, B. A., et al. (2004). Distributions of microbial activities in deep subseafloor sediments. *Science* 306, 2216–2221. doi: 10.1126/science.1101155

D'Hondt, S., Rutherford, S., and Spivack, A. J. (2002). Metabolic activity of subsurface life in deep-sea sediments. *Science* 295, 2067–2070. doi: 10.1126/science.1064878

D'Hondt, S., Spivack, A. J., Pockalny, R., Ferdelman, T. G., Fischer, J. P., Kallmeyer, J., et al. (2009). Subseafloor sedimentary life in the South Pacific Gyre. *Proc. Natl. Acad. Sci.* 106, 11651–11656. doi: 10.1073/pnas.0811793106

Edgcomb, V. P., Taylor, C., Pachiadaki, M. G., Honjo, S., Engstrom, I., and Yakimov, M. (2016). Comparison of Niskin vs. *in situ* approaches for analysis of gene expression in deep Mediterranean Sea water samples. *Deep Sea Res. II Top. Stud. Oceanogr.* 129, 213–222. doi: 10.1016/j.dsr2.2014.10.020

Edwards, K., Fisher, A., and Wheat, C. G. (2012). The deep subsurface biosphere in igneous ocean crust: frontier habitats for microbiological exploration. *Front. Microbiol.* 3:8. doi: 10.3389/fmicb.2012.00008

Edwards, K. J., Wheat, C. G., and Sylvan, J. B. (2011). Under the sea: microbial life in volcanic oceanic crust. *Nat. Rev. Microbiol.* 9, 703–712. doi: 10.1038/nrmicro2647

Fang, J., Zhang, L., and Bazylinski, D. A. (2010). Deep-sea piezosphere and piezophiles: geomicrobiology and biogeochemistry. *Trends Microbiol.* 18, 413–422. doi: 10.1016/j.tim.2010.06.006

Fitzherbert, S. (2019). *Deepest Submarine Dive in History, Five Deeps Expedition Conquers Challenger Deep*. Dallas, TX: FiveDeepsPress, 1–7.

Fortunato, C. S., and Huber, J. A. (2016). Coupled RNA-SIP and metatranscriptomics of active chemolithoautotrophic communities at a deep-sea hydrothermal vent. *ISME J.* 10, 1925–1938. doi: 10.1038/ismej.2015.258

Frank, K. L., Rogers, K. L., Rogers, D. R., Johnston, D. T., and Girguis, P. R. (2015). Key factors influencing rates of heterotrophic sulfate reduction in active seafloor hydrothermal massive sulfide deposits. *Front. Microbiol.* 6:1449. doi: 10.3389/fmicb.2015.01449

Gallo, N. D., Cameron, J., Hardy, K., Fryer, P., Bartlett, D. H., and Levin, L. A. (2015). Submersible-and lander-observed community patterns in the Mariana and New Britain trenches: influence of productivity and depth on epibenthic and scavenging communities. *Deep Sea Res. I Oceanogr. Res. Papers* 99, 119–133. doi: 10.1016/j.dsr.2014.12.012

Garel, M., Bonin, P., Martini, S., Guasco, S., Roumagnac, M., Bhairy, N., et al. (2019). Pressure-retaining sampler and high-pressure systems to study deep-sea microbes under *in situ* conditions. *Front. Microbiol.* 10:453. doi: 10.3389/fmicb.2019.00453

Glud, R. N., Wenzhöfer, F., Middelboe, M., Oguri, K., Turnewitsch, R., Canfield, D. E., et al. (2013). High rates of microbial carbon turnover in sediments in the deepest oceanic trench on Earth. *Nat. Geosci.* 6, 284–288. doi: 10.1038/ngeo1773

Hallbeck, L., and Pedersen, K. (2008). Characterization of microbial processes in deep aquifers of the Fennoscandian Shield. *Appl. Geochem.* 23, 1796–1819. doi: 10.1016/j.apgeochem.2008.02.012

Hatanpää, E., Manninen, P., and Apilo, S. (2005). *Representativity of Gas Samples Taken with the Pressurized Water Sampling System (PAVE) 1995-2004*, Vol. 44. Eurajoki: Posiva Oy, 123.

He, Z., Gentry, T. J., Schadt, C. W., Wu, L., Liebich, J., Chong, S. C., et al. (2007). GeoChip: a comprehensive microarray for investigating biogeochemical, ecological and environmental processes. *ISME J.* 1, 67–77. doi: 10.1038/ismej.2007.2

Herring, P. J., and Clarke, M. R. (1971). *Deep Oceans*. London: Barker.

Jamieson, A. (2015). *The Hadal Zone: Life in the Deepest Oceans*. Cambridge: Cambridge University Press.

Jannasch, H. W., and Taylor, C. D. (1984). Deep-sea microbiology. *Annu. Rev. Microbiol.* 38, 487–487.

Jannasch, H. W., Wirsen, C. O., and Doherty, K. W. (1996). A pressurized chemostat for the study of marine barophilic and oligotrophic bacteria. *Appl. Environ. Microbiol.* 62, 1593–1596.

Jannasch, H. W., Wirsen, C. O., and Winget, C. L. (1973). A bacteriological pressure-retaining deep-sea sampler and culture vessel. *Deep Sea Res. Oceanogr. Abstracts* 20, 661–664. doi: 10.1016/0011-7471(73)90033-8

Jebbar, M., Franzetti, B., Girard, E., and Oger, P. (2015). Microbial diversity and adaptation to high hydrostatic pressure in deep-sea hydrothermal vents prokaryotes. *Extremophiles* 19, 721–740. doi: 10.1007/s00792-015-0760-3

Jørgensen, B. B., and Boetius, A. (2007). Feast and famine—microbial life in the deep-sea bed. *Nat. Rev. Microbiol.* 5, 770–781. doi: 10.1038/nrmicro1745

Jørgensen, B. B., Isaksen, M. F., and Jannasch, H. W. (1992). Bacterial sulfate reduction above 100°C in deep-sea hydrothermal vent sediments. *Science* 258, 1756–1757. doi: 10.1126/science.258.5089.1756

Kallmeyer, J., and Boetius, A. (2004). Effects of temperature and pressure on sulfate reduction and anaerobic oxidation of methane in hydrothermal sediments of Guaymas Basin. *Appl. Environ. Microbiol.* 70, 1231–1233. doi: 10.1128/aem.70.2.1231-1233.2004

Kallmeyer, J., Ferdelman, T. G., Jansen, K.-H., and Jørgensen, B. B. (2003). A high-pressure thermal gradient block for investigating microbial activity in multiple deep-sea samples. *J. Microbiol. Methods* 55, 165–172. doi: 10.1016/s0167-7012(03)00138-6

Kallmeyer, J., Pockalny, R., Adhikari, R. R., Smith, D. C., and D'Hondt, S. (2012). Global distribution of microbial abundance and biomass in subseafloor sediment. *Proc. Natl. Acad. Sci.* 109, 16213–16216. doi: 10.1073/pnas.1203849109

Kato, C. (2011). "Cultivation methods for piezophiles," in *Extremophiles Handbook*, ed. K. Horikoshi (Tokyo: Springer), 719–726. doi: 10.1007/978-4-431-53898-1_34

Kato, C., Nogi, Y., and Arakawa, S. (2008). "Isolation, cultivation, and diversity of deep-sea piezophiles," in *High-Pressure Microbiology*, eds C. Michiels, D. Bartlett, and A. Aersten (Washington, DC: ASM Press), 203–217. doi: 10.1128/9781555815646.ch12

Kato, C., and Qureshi, M. H. (1999). Pressure response in deep-sea piezophilic bacteria. *J. Mol. Microbiol. Biotechnol.* 1, 87–92.

Kawano, H., Nakasone, K., Matsumoto, M., Yoshida, Y., Usami, R., Kato, C., et al. (2004). Differential pressure resistance in the activity of RNA polymerase isolated from *Shewanella violacea* and *Escherichia coli*. *Extremophiles* 8, 367–375. doi: 10.1007/s00792-004-0397-0

Kubo, Y., Mizuguchi, Y., Inagaki, F., Yamamoto, K., Schultheiss, P., Grigar, K., et al. (2014). new hybrid pressure-coring system for the drilling vessel Chikyu. *Sci. Drill.* 17, 37–43. doi: 10.5194/sd-17-37-2014

Kusube, M., Kyaw, T. S., Tanikawa, K., Chastain, R. A., Hardy, K. M., Cameron, J., et al. (2017). *Colwellia marinimaniae* sp. nov., a hyperpiezophilic species isolated from an amphipod within the Challenger Deep, Mariana Trench. *Int. J. Syst. Evol. Microbiol.* 67, 824–831. doi: 10.1099/ijsem.0.001671

La Cono, V., Smedile, F., La Spada, G., Arcadi, E., Genovese, M., Ruggeri, G., et al. (2015). Shifts in the meso-and bathypelagic archaea communities composition during recovery and short-term handling of decompressed deep-sea samples. *Environ. Microbiol. Rep.* 7, 450–459. doi: 10.1111/1758-2229.12272

Lasken, R. S. (2007). Single-cell genomic sequencing using multiple displacement amplification. *Curr. Opin. Microbiol.* 10, 510–516. doi: 10.1016/j.mib.2007.08.005

Lavalleur, H. J., and Colwell, F. S. (2013). Microbial characterization of basalt formation waters targeted for geological carbon sequestration. *FEMS Microbiol. Ecol.* 85, 62–73. doi: 10.1111/1574-6941.12098

Lin, Y. S., Lipp, J. S., Elvert, M., Holler, T., and Hinrichs, K. U. (2013). Assessing production of the ubiquitous archaeal diglycosyl tetraether lipids in marine subsurface sediment using intramolecular stable isotope probing. *Environ. Microbiol.* 15, 1634–1646. doi: 10.1111/j.1462-2920.2012.02888.x

Lipp, J. S., Morono, Y., Inagaki, F., and Hinrichs, K.-U. (2008). Significant contribution of Archaea to extant biomass in marine subsurface sediments. *Nature* 454, 991–994. doi: 10.1038/nature07174

Lloyd, K. G., May, M. K., Kevorkian, R. T., and Steen, A. D. (2013). Meta-analysis of quantification methods shows that archaea and bacteria have similar abundances in the subseafloor. *Appl. Environ. Microbiol.* 79, 7790–7799. doi: 10.1128/AEM.02090-13

Lollar, B. S., Lacrampe-Couloume, G., Slater, G., Ward, J., Moser, D., Gihring, T., et al. (2006). Unravelling abiogenic and biogenic sources of methane in the Earth's deep subsurface. *Chem. Geol.* 226, 328–339. doi: 10.1016/j.chemgeo.2005.09.027

Martin, D., Bartlett, D. H., and Roberts, M. F. (2002). Solute accumulation in the deep-sea bacterium *Photobacterium profundum*. *Extremophiles* 6, 507–514. doi: 10.1007/s00792-002-0288-1

Michoud, G., and Jebbar, M. (2016). High hydrostatic pressure adaptive strategies in an obligate piezophile *Pyrococcus yayanosii*. *Sci. Rep.* 6:27289. doi: 10.1038/srep27289

Morono, Y., Terada, T., Nishizawa, M., Ito, M., Hillion, F., Takahata, N., et al. (2011). Carbon and nitrogen assimilation in deep subseafloor microbial cells. *Proc. Natl. Acad. Sci.* 108, 18295–18300. doi: 10.1073/pnas.1107763108

Moser, D. P., Gihring, T. M., Brockman, F. J., Fredrickson, J. K., Balkwill, D. L., Dollhopf, M. E., et al. (2005). *Desulfotomaculum* and *Methanobacterium* spp. dominate a 4-to 5-kilometer-deep fault. *Appl. Environ. Microbiol.* 71, 8773–8783. doi: 10.1128/aem.71.12.8773-8783.2005

Nauhaus, K., Boetius, A., Krüger, M., and Widdel, F. (2002). *In vitro* demonstration of anaerobic oxidation of methane coupled to sulphate reduction in sediment from a marine gas hydrate area. *Environ. Microbiol.* 4, 296–305. doi: 10.1046/j.1462-2920.2002.00299.x

Nunoura, T., Takaki, Y., Hirai, M., Shimamura, S., Makabe, A., Koide, O., et al. (2015). Hadal biosphere: insight into the microbial ecosystem in the deepest ocean on Earth. *Proc. Natl. Acad. Sci.* 112, E1230–E1236. doi: 10.1073/pnas.1421816112

Nunoura, T., Takaki, Y., Kakuta, J., Nishi, S., Sugahara, J., Kazama, H., et al. (2010). Insights into the evolution of Archaea and eukaryotic protein modifier systems revealed by the genome of a novel archaeal group. *Nucleic Acids Res.* 39, 3204–3223. doi: 10.1093/nar/gkq1228

Oger, P., and Jebbar, M. (2010). The many ways of coping with pressure. *Res. Microbiol.* 161, 799–809. doi: 10.1016/j.resmic.2010.09.017

Oliver, G. C. (2019). *Exploring Microbial Growth of a Model Extremophile, Archaeoglobus Fulgidus, at Elevated Pressures*. Ph.D. dissertation, Rensselaer Polytechnic Institute, Troy, NY, 142.

Oppenheimer, C. H., and Zobell, C. E. (1952). The growth and viability of 63 species of marine bacteria as influenced by hydrostatic pressure. *J. Mar. Res.* 11, 10–18.

Orcutt, B. N., Sylvan, J. B., Knab, N. J., and Edwards, K. J. (2011). Microbial ecology of the dark ocean above, at, and below the seafloor. *Microbiol. Mol. Biol. Rev.* 75, 361–422. doi: 10.1128/MMBR.00039-10

Orsi, W. D., Edgcomb, V. P., Christman, G. D., and Biddle, J. F. (2013). Gene expression in the deep biosphere. *Nature* 499, 205–208. doi: 10.1038/nature12230

Park, C. B., and Clark, D. S. (2002). Rupture of the cell envelope by decompression of the deep-sea methanogen *Methanococcus jannaschii*. *Appl. Environ. Microbiol.* 68, 1458–1463. doi: 10.1128/aem.68.3.1458-1463.2002

Parkes, R. J., Cragg, B. A., Bale, S. J., Getlifff, J. M., Goodman, K., Rochelle, P. A., et al. (1994). Deep bacterial biosphere in Pacific Ocean sediments. *Nature* 371, 410–413. doi: 10.1038/371410a0

Parkes, R. J., Sellek, G., Webster, G., Martin, D., Anders, E., Weightman, A. J., et al. (2009). Culturable prokaryotic diversity of deep, gas hydrate sediments: first use of a continuous high-pressure, anaerobic, enrichment and isolation system for subseafloor sediments (DeepIsoBUG). *Environ. Microbiol.* 11, 3140–3153. doi: 10.1111/j.1462-2920.2009.02018.x

Peoples, L. M., Norenberg, M., Price, D., McGoldrick, M., Novotny, M., Bochdansky, A., et al. (2019). A full-ocean-depth rated modular lander and pressure-retaining sampler capable of collecting hadal-endemic microbes under

in situ conditions. *Deep Sea Res. I Oceanogr. Res. Papers* 143, 50–57. doi: 10.1016/j.dsr.2018.11.010

Picard, A., and Daniel, I. (2013). Pressure as an environmental parameter for microbial life—a review. *Biophys. Chem.* 183, 30–41. doi: 10.1016/j.bpc.2013.06.019

Ramirez-Llodra, E., Brandt, A., Danovaro, R., De Mol, B., Escobar, E., German, C., et al. (2010). Deep, diverse and definitely different: unique attributes of the world's largest ecosystem. *Biogeosciences* 7, 2851–2899. doi: 10.5194/bg-7-2851-2010

Rassa, A. C., Mcallister, S., Safran, S., and Moyer, C. (2009). Zeta-Proteobacteria dominate the colonization and formation of microbial mats in low-temperature hydrothermal vents at Loihi Seamount, Hawaii. *Geomicrobiol. J.* 26, 623–638. doi: 10.1080/01490450903263350

Reed, D. W., Fujita, Y., Delwiche, M. E., Blackwelder, D. B., Sheridan, P. P., Uchida, T., et al. (2002). Microbial communities from methane hydrate-bearing deep marine sediments in a forearc basin. *Appl. Environ. Microbiol.* 68, 3759–3770. doi: 10.1128/aem.68.8.3759-3770.2002

Reysenbach, A.-L., and Götz, D. (2001). Methods for the study of hydrothermal vent microbes. *Methods Microbiol.* 30, 639–656. doi: 10.1016/s0580-9517(01)30066-1

Rogers, K. L., Cario, A., Cardon, H., and Daniel, I. (2016a). "Experimental high-pressure cultivation with the PUSH50: increased pressure tolerance of a marine bacterium without subsampling decompression," in *Proceedings of the 5th International Workshop on Deep-Sea Microbiology*, Kyoto, 10.

Rogers, K. L., Cario, A., Cardon, H., and Daniel, I. (2016b). "Introducing the PUSH50: A New Instrument to Extend Microbial Exploration within the Deep Biosphere," in *Proceedings of the 11th International Congress on Extremophiles*, Kyoto.

Rosenbaum, E., Gabel, F., Durá, M. A., Finet, S., Cléry-Barraud, C., Masson, P., et al. (2012). Effects of hydrostatic pressure on the quaternary structure and enzymatic activity of a large peptidase complex from *Pyrococcus horikoshii*. *Arch. Biochem. Biophys.* 517, 104–110. doi: 10.1016/j.abb.2011.07.017

Sauer, P., Glombitza, C., and Kallmeyer, J. (2012). A system for incubations at high gas partial pressure. *Front. Microbiol.* 3:25. doi: 10.3389/fmicb.2012.00025

Schrenk, M. O., Huber, J. A., and Edwards, K. J. (2010). Microbial provinces in the subseafloor. *Annu. Rev. Mar. Sci.* 2, 279–304. doi: 10.1146/annurev-marine-120308-081000

Seyfried, W., Gordon, P., and Dickson, F. (1979). A new reaction cell for hydrothermal solution equipment. *Am. Mineral.* 64, 646–649.

Simonato, F., Campanaro, S., Lauro, F., Vezzi, A., D'Angelo, M., Vitulo, N., et al. (2006). Piezophilic adaptation: a genomic point of view. *J. Biotechnol.* 126, 11–25. doi: 10.1016/j.jbiotec.2006.03.038

Smith, A., Popa, R., Fisk, M., Nielsen, M., Wheat, C. G., Jannasch, H. W., et al. (2011). *In situ* enrichment of ocean crust microbes on igneous minerals and glasses using an osmotic flow-through device. *Geochem. Geophys. Geosyst.* 12:Q06007.

Stamenković, V., Beegle, L., Zacny, K., Arumugam, D., Baglioni, P., Barba, N., et al. (2019). The next frontier for planetary and human exploration. *Nat. Astronomy* 3, 116–120.

Stevens, T. O., and McKinley, J. P. (1995). Lithoautotrophic microbial ecosystems in deep basalt aquifers. *Science* 270, 450–455.

Takai, K., Komatsu, T., Inagaki, F., and Horikoshi, K. (2001). Distribution of archaea in a black smoker chimney structure. *Appl. Environ. Microbiol.* 67, 3618–3629. doi: 10.1128/aem.67.8.3618-3629.2001

Takai, K., Nakamura, K., Toki, T., Tsunogai, U., Miyazaki, M., Miyazaki, J., et al. (2008). Cell proliferation at 122°C and isotopically heavy CH4 production by a hyperthermophilic methanogen under high-pressure cultivation. *Proc. Natl. Acad. Sci.U.S.A.* 105, 10949–10954. doi: 10.1073/pnas.0712334105

Tamburini, C. (2006). "Life under pressure. *Deep-sea microbial ecology*," in *Life as We Know it Series: Cellular Origin and Life in Extreme Habitats and Astrobiology*, ed. J. Seckbach (Berlin: Springer), 1–17.

Tamburini, C., Boutrif, M., Garel, M., Colwell, R. R., and Deming, J. W. (2013). Prokaryotic responses to hydrostatic pressure in the ocean–a review. *Environ. Microbiol.* 15, 1262–1274. doi: 10.1111/1462-2920.12084

Tarn, J., Peoples, L. M., Hardy, K., Cameron, J., and Bartlett, D. H. (2016). Identification of free-living and particle-associated microbial communities present in hadal regions of the Mariana Trench. *Front. Microbiol.* 7:665. doi: 10.3389/fmicb.2016.00665

Taylor, C. D., and Jannasch, H. W. (1976). Subsampling technique for measuring growth of bacterial cultures under high hydrostatic pressure. *Appl. Environ. Microbiol.* 32, 355–359.

Tengberg, A., De Bovee, F., Hall, P., Berelson, W., Chadwick, D., Ciceri, G., et al. (1995). Benthic chamber and profiling landers in oceanography—a review of design, technical solutions and functioning. *Prog. Oceanogr.* 35, 253–294. doi: 10.1016/0079-6611(95)00009-6

Vannier, P., Michoud, G., Oger, P., þór Marteinsson, V., and Jebbar, M. (2015). Genome expression of *Thermococcus barophilus* and *Thermococcus kodakarensis* in response to different hydrostatic pressure conditions. *Res. Microbiol.* 166, 717–725. doi: 10.1016/j.resmic.2015.07.006

Wang, F., Zhou, H., Meng, J., Peng, X., Jiang, L., Sun, P., et al. (2009). GeoChip-based analysis of metabolic diversity of microbial communities at the Juan de Fuca Ridge hydrothermal vent. *Proc. Natl. Acad. Sci.* 106, 4840–4845. doi: 10.1073/pnas.0810418106

Webster, G., Rinna, J., Roussel, E. G., Fry, J. C., Weightman, A. J., and Parkes, R. J. (2010). Prokaryotic functional diversity in different biogeochemical depth zones in tidal sediments of the Severn Estuary, UK, revealed by stable-isotope probing. *FEMS Microbiol. Ecol.* 72, 179–197. doi: 10.1111/j.1574-6941.2010.00848.x

Whitman, W. B., Coleman, D. C., and Wiebe, W. J. (1998). Prokaryotes: the unseen majority. *Proc. Natl. Acad. Sci.* 95, 6578–6583. doi: 10.1073/pnas.95.12.6578

Yayanos, A., and Pollard, E. (1969). A study of the effects of hydrostatic pressure on macromolecular synthesis in *Escherichia coli*. *Biophysics* 9, 1464–1482. doi: 10.1016/s0006-3495(69)86466-0

Yayanos, A. A. (1977). Simply actuated closure for a pressure vessel: design for use to trap deep-sea animals. *Rev. Sci. Instr.* 48, 786–789. doi: 10.1063/1.1135150

Yayanos, A. A. (1986). Evolutional and ecological implications of the properties of deep-sea barophilic bacteria. *Proc. Natl. Acad. Sci.* 83, 9542–9546. doi: 10.1073/pnas.83.24.9542

Yayanos, A. A. (2001). Deep-sea piezophilic bacteria. *Methods Microbiol.* 30, 615–637. doi: 10.1016/s0580-9517(01)30065-x

Yayanos, A. A., and Dietz, A. S. (1982). Thermal inactivation of a deep-sea barophilic bacterium, isolate CNPT-3. *Appl. Environ. Microbiol.* 43, 1481–1489.

Yayanos, A. A., and Dietz, A. S. (1983). Death of a hadal deep-sea bacterium after decompression. *Science* 220, 497–498. doi: 10.1126/science.220.4596.497

Yayanos, A. A., Dietz, A. S., and Vanboxtel, R. (1979). Isolation of a deep-sea barophilic bacterium and some of its growth characteristics. *Science* 205, 808–810. doi: 10.1126/science.205.4408.808

Yayanos, A. A., Dietz, A. S., and Vanboxtel, R. (1982). Dependence of reproduction rate on pressure as a hallmark of deep-sea bacteria. *Appl. Environ. Microbiol.* 44, 1356–1361.

Yayanos, A. A., Vanboxtel, R., and Dietz, A. S. (1984). High-pressure-temperature gradient instrument - Use for determining the temperature and pressure limits of bacterial growth. *Appl. Environ. Microbiol.* 48, 771–776.

Zeng, S., Birrien, J., Fouquet, Y., Cherkashov, G., Jebbar, M., Querellou, J., et al. (2009). *Pyrococcus* CH1, an obligate piezophilic hyperthermophile: extending the upper pressure-temperature limits for life. *ISME J.* 3, 873–876. doi: 10.1038/ismej.2009.21

Zink, K.-G., Wilkes, H., Disko, U., Elvert, M., and Horsfield, B. (2003). Intact phospholipids—microbial "life markers" in marine deep subsurface sediments. *Organic Geochem.* 34, 755–769. doi: 10.1016/s0146-6380(03)00041-x

Zobell, C. E. (1952). Bacterial life at the bottom of the Philippine trench. *Science* 115, 507–508. doi: 10.1126/science.115.2993.507

Conflict of Interest Statement: The authors declare that the research was conducted in the absence of any commercial or financial relationships that could be construed as a potential conflict of interest.

frontiers in Earth Science

ORIGINAL RESEARCH
published: 11 October 2019
doi: 10.3389/feart.2019.00263

Deep Carbon Cycling Over the Past 200 Million Years: A Review of Fluxes in Different Tectonic Settings

Kevin Wong[1,2], Emily Mason[2], Sascha Brune[3,4], Madison East[5], Marie Edmonds[2] and Sabin Zahirovic[5]*

[1] School of Earth and Environment, University of Leeds, Leeds, United Kingdom, [2] Department of Earth Sciences, University of Cambridge, Cambridge, United Kingdom, [3] GFZ German Research Centre for Geosciences, Potsdam, Germany, [4] Institute of Geosciences, University of Potsdam, Potsdam, Germany, [5] EarthByte Group, School of Geosciences, The University of Sydney, Sydney, NSW, Australia

Carbon is a key control on the surface chemistry and climate of Earth. Significant volumes of carbon are input to the oceans and atmosphere from deep Earth in the form of degassed CO_2 and are returned to large carbon reservoirs in the mantle via subduction or burial. Different tectonic settings (e.g., volcanic arcs, mid-ocean ridges, and continental rifts) emit fluxes of CO_2 that are temporally and spatially variable, and together they represent a first-order control on carbon outgassing from the deep Earth. A change in the relative importance of different tectonic settings throughout Earth's history has therefore played a key role in balancing the deep carbon cycle on geological timescales. Over the past 10 years the *Deep Carbon Observatory* has made enormous progress in constraining estimates of carbon outgassing flux at different tectonic settings. Using plate boundary evolution modeling and our understanding of present-day carbon fluxes, we develop time series of carbon fluxes into and out of the Earth's interior through the past 200 million years. We highlight the increasing importance of carbonate-intersecting subduction zones over time to carbon outgassing, and the possible dominance of carbon outgassing at continental rift zones, which leads to maxima in outgassing at 130 and 15 Ma. To a first-order, carbon outgassing since 200 Ma may be net positive, averaging ∼50 Mt C yr^{-1} more than the ingassing flux at subduction zones. Our net outgassing curve is poorly correlated with atmospheric CO_2, implying that surface carbon cycling processes play a significant role in modulating carbon concentrations and/or there is a long-term crustal or lithospheric storage of carbon which modulates the outgassing flux. Our results highlight the large uncertainties that exist in reconstructing the corresponding in- and outgassing fluxes of carbon. Our synthesis summarizes our current understanding of fluxes at tectonic settings and their influence on atmospheric CO_2, and provides a framework for future research into Earth's deep carbon cycling, both today and in the past.

Keywords: deep carbon cycle, carbonate assimilation, solid Earth degassing, plate reconstructions, carbon dioxide, subduction zone

OPEN ACCESS

Edited by:
Jacob B. Lowenstern, United States Geological Survey, United States

Reviewed by:
Esther M. Schwarzenbach, Freie Universität Berlin, Germany
Barbara Ratschbacher, California Institute of Technology, United States

****Correspondence:***
Kevin Wong
eekw@leeds.ac.uk

Specialty section:
This article was submitted to Volcanology, a section of the journal Frontiers in Earth Science

Received: *05 June 2019*
Accepted: *24 September 2019*
Published: *11 October 2019*

Citation:
Wong K, Mason E, Brune S, East M, Edmonds M and Zahirovic S (2019) Deep Carbon Cycling Over the Past 200 Million Years: A Review of Fluxes in Different Tectonic Settings. Front. Earth Sci. 7:263. doi: 10.3389/feart.2019.00263

INTRODUCTION

The deep carbon cycle of the Earth connects the exospheric (atmosphere, hydrosphere, biosphere) reservoirs of carbon to those in the crust and mantle (e.g., Dasgupta and Hirschmann, 2010). The non-anthropogenic concentration of atmospheric CO_2 is modulated by outgassing from the crust and mantle at plate boundary and intraplate settings (e.g., Self et al., 2005; van der Meer et al., 2014) and metamorphic carbon release (e.g., Skelton, 2011). Ingassing returns carbon to the crust and mantle through processes such as silicate weathering (e.g., Dessert et al., 2003) and subduction of altered oceanic crust, serpentinized lithospheric mantle, and seafloor sediments (e.g., Alt and Teagle, 1999; Alt et al., 2013; Plank, 2014).

Past work on links between tectonic parameters and carbon fluxes have often focused solely on the present day (e.g., Dasgupta and Hirschmann, 2010; Kelemen and Manning, 2015), or on the importance of specific tectonic settings through time (e.g., van der Meer et al., 2014; McKenzie et al., 2016; Brune et al., 2017). Early attempts at reconciling both present-day fluxes and past tectonically driven carbon cycling have been qualitative due to the immense uncertainties in quantifying present-day carbon degassing (e.g., Kerrick, 2001), or have attempted to tackle carbon cycling on a coarse scale for the entirety of Earth history (e.g., Dasgupta, 2013).

Through the *DECADE* program of the *Deep Carbon Observatory*, we now have a much improved understanding of the present-day outgassing rate of carbon, and its variability, in a range of tectonic settings. In tandem with the rapid increase in observations of carbon outgassing, progress has been made in modeling plate tectonics over geological time, e.g., through the development of open-source and community tools like *GPlates* (e.g., Gurnis et al., 2012; Müller et al., 2018), which allow reconstruction and quantification of tectonic plate boundary lengths, slab fluxes, and other tectonic parameters during much of the Phanerozoic (e.g., Matthews et al., 2016). In this study, we compile and review estimates of carbon fluxes into and out of the mantle over the past 200 Ma at plate boundaries, by combining our understanding of present-day fluxes with plate tectonic reconstructions. In doing so, we assess the effects of plate tectonics on the deep carbon cycle, and the implications for the surface environment.

BACKGROUND AND METHODS

Carbon enters the mantle through the subduction of carbon-bearing phases in the oceanic lithosphere at subduction zones, and is returned to Earth's surface during magmatic or tectonic activity (**Figure 1**). Therefore, the global distribution of plate boundaries is a primary control on the magnitude of solid Earth carbon degassing. To model tectonic parameters over geological time, we use *GPlates*, an open-source software for plate reconstructions (Müller et al., 2018 and references therein). In addition to illustrating past tectonic plate distributions up to 1000 Ma (e.g., Matthews et al., 2016; Müller et al., 2016; Merdith et al., 2017, 2019), *GPlates* has been previously used as a basis to extrapolate paleogeography (Cao et al., 2017b), past seafloor sediment thicknesses (Dutkiewicz et al., 2017), and the distribution of continental flood basalts and oceanic plateaus (Johansson et al., 2018). We utilize the open access global plate motion model of Müller et al. (2016) to analyze plate boundary length (**Figure 2**), which captures the past 200 million years of plate tectonic evolution based on paleomagnetic data, seafloor isochrons, and other plate motion indicators (e.g., ocean island chains). Alongside this model we use the subduction history data of East et al. (2019) to determine subduction flux parameters. Plate boundary lengths and other parameters from these models provide a basis for our tectonic carbon flux estimates in 1 Myr intervals. These parameters are provided in **Supplementary Table S1**. Uncertainties are determined through standard error propagation of uncertainties within present-day carbon flux measurements (see **Table 1**) and the standard deviation of computed tectonic parameters.

In this synthesis, we contrast the quantity of carbon that is outgassed at various tectonic settings against the carbon returned to deep Earth at subduction zones (**Figure 1**). Hence, processes such as decarbonation efficiency in the subducted slab beneath the crust-mantle boundary (e.g., Johnston et al., 2011), biogeochemical cycling (e.g., Lenton et al., 2018), and carbon drawdown from silicate weathering at the surface Earth (e.g., Dessert et al., 2003; Johansson et al., 2018) are not considered.

RESULTS

Carbon Ingassing

The carbon entering the mantle at subduction zones can be subdivided into three constituent components which comprise the total carbon in a subducting oceanic lithosphere slab: the carbon locked within altered oceanic crust, the carbon present within serpentinized mantle, as well as organic and inorganic carbon present in deep-sea sediments (Kelemen and Manning, 2015). During subduction, carbon may be liberated from the slab through metamorphic decarbonation (e.g., Kerrick and Connolly, 2001), by dissolution of carbonate phases directly into a supercritical fluid (Manning, 2004; Facq et al., 2014) or through the formation of carbonatitic melts (Poli, 2015), thereby entering the mantle wedge. Carbon may also be subducted deeper into the mantle (e.g., Thomson et al., 2014, 2016).

Liberated slab carbon, alongside other volatile components, enters the overlying mantle as a low density, volatile-rich fluid phase. Such fluids depress the solidus of peridotite, and can promote melting in asthenospheric mantle (e.g., Dasgupta and Hirschmann, 2006, 2010), in which case carbon partitions into the melt and is later released as CO_2 gas during volcanic eruptions. However, carbon-bearing fluids may also stall in the lithosphere as a result of this solidus depression, and subsequently freeze to form metasomatic layers and veins beneath the continents (e.g., McKenzie, 1989; Rooney et al., 2017).

The presence of surface-derived carbon in the deep mantle is inferred from the isotopic composition of superdeep diamonds (from sub-lithospheric depths of >250 km). Many superdeep

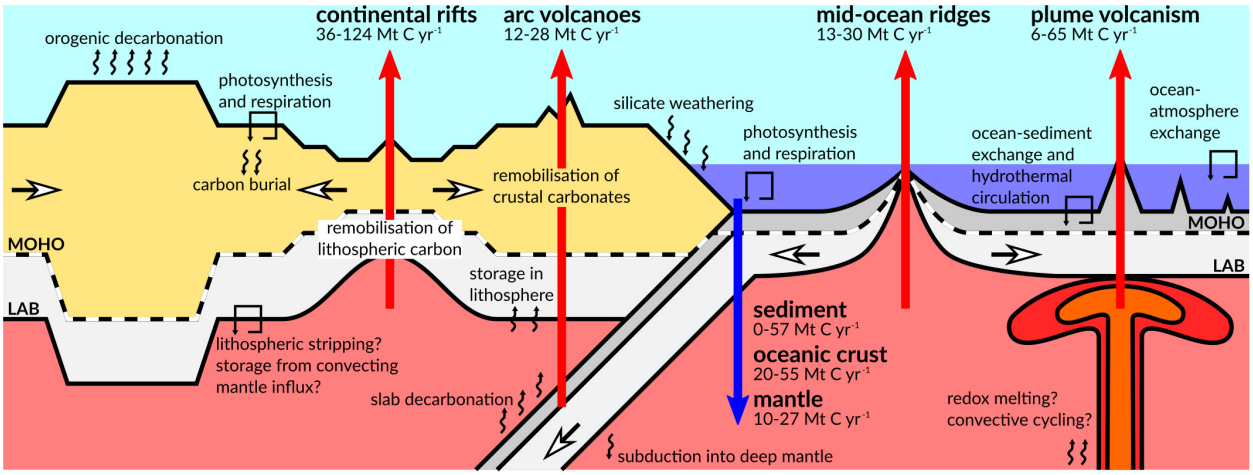

FIGURE 1 | Cartoon illustrating major fluxes of carbon to, from, and within the Earth's exogenic and endogenic systems. The fluxes discussed in this paper are highlighted as large colored arrows; the small arrows represent other processes occurring within each system that are not considered in this study. Values give the maximum and minimum fluxes since 200 Ma for each setting discussed. The two major boundaries highlighted are the Mohorovičić discontinuity (crust-mantle boundary; Moho) and the lithosphere-asthenosphere boundary (LAB).

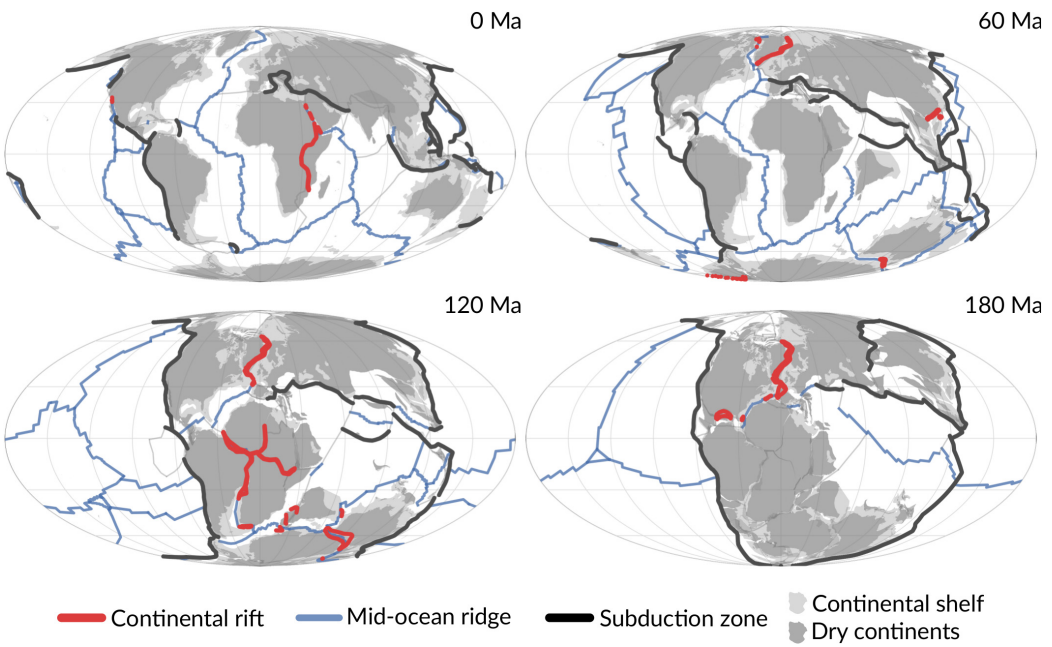

FIGURE 2 | Plate tectonic reconstructions of key plate boundary types at 60 Myr intervals from the present-day using the model of Müller et al. (2016).

diamonds host carbon and oxygen isotope ratios indicative of a biogenic endmember (Thomson et al., 2014; Burnham et al., 2015) and mafic inclusions with similar compositions to mid-ocean ridge basalt (MORB) (Thomson et al., 2016), which may suggest the existence of a thermal/compositional barrier to deep carbon subduction. While light carbon isotope ratios can arise from fractionation both prior to and during diamond growth (e.g., Cartigny et al., 2001), Smart et al. (2011) demonstrated that Rayleigh fractionation cannot produce extreme $\delta^{13}C$ values, instead invoking the presence of recycled organic matter during diamond synthesis. Material subducted into the convecting mantle can therefore return to the surface, illustrating the vast scale of deep carbon cycling.

Altered Oceanic Crust

Carbon, sourced from magmatic fluids and dissolved inorganic and organic components in seawater, is fixed into oceanic crust as carbonate and carbon-bearing minerals during hydrothermal alteration at mid-ocean ridges largely during the first few tens of millions of years after crust formation (Alt and Teagle, 1999;

TABLE 1 | Summary table presenting data and conversion factors used in this study.

Quantity	Input data	Conversion factors	References
Altered oceanic crust	Crustal carbon concentration, subduction zone length, subduction rate	–	Müller et al., 2016; Müller and Dutkiewicz, 2018
Serpentinized mantle	Serpentinite carbon concentration and extent, subduction zone length, subduction rate	681 ± 45 ppm (average serpentinite carbon concentration); 20 ± 10%, 13.5 ± 1.5 km (serpentinization degree and extent)	Kelemen and Manning, 2015; Müller et al., 2016; East et al., 2019
Carbonate sediment	Subducted carbonate sediment	–	Dutkiewicz et al., 2018
Continental rifts	Rift length, average rift carbon flux	2.5 ± 2.0 kt C km^{-1} yr^{-1} (rift carbon length flux)	Müller et al., 2016; Brune et al., 2017; Hunt et al., 2017
Mid-ocean ridges	Mid-ocean ridge length, present-day mid-ocean ridge carbon flux	0.37 ± 0.23 kt C km^{-1} yr^{-1} (ridge carbon length flux)	Müller et al., 2016
Plume volcanoes	LIP area, basalt carbon concentration	6.0 ± 3.0 Mt C yr^{-1} (baseline plume flux); 0.8 ± 0.3 wt% (primary plume basalt CO_2 concentration)	Müller et al., 2016; Johansson et al., 2018; Hauri et al., 2019; Werner et al., 2019
Arc volcanoes	Subduction zone length, carbonate platform distribution, present-day arc flux, expected carbonate-intersecting and non-carbonate-intersecting volcanic carbon fluxes	27 ± 16 Mt C yr^{-1} (present-day arc flux); $10^{7.4-8.0}$ mol km^{-1} yr^{-1} (range for carbonate-intersecting arcs); $10^{0.0-6.4}$ mol km^{-1} yr^{-1} (range for non-carbonate-intersecting arcs)	Kelemen and Manning, 2015; Müller et al., 2016; Pall et al., 2018; Werner et al., 2019

Input data in italics are provided by GPlates modeling. Density of basaltic rock is taken as 2800 kg m^{-3}. A full table detailing plate tectonic parameters used in concordance with these conversion factors is given as ***Supplementary Table S1****. Note that 3.67 t of CO_2 contain 1 t of pure carbon.*

Shilobreeva et al., 2011; Coogan et al., 2016). The amount of carbon fixed into oceanic crust and accumulated in the overlying sediments is a function of multiple variables. The spreading rate of a mid-ocean ridge determines the rate at which carbonate from sedimentary material leaches into crust; older oceanic crust will host more carbonate than younger crust; higher bottom water temperatures change the chemistry of seawater, promoting higher seawater Ca concentrations and encouraging carbonate precipitation (Gillis and Coogan, 2011; Coogan and Gillis, 2013; Coogan and Dosso, 2015). In addition, erupted basalts in the uppermost part of oceanic crust gain higher carbon concentrations than crustal gabbros through this mechanism (Staudigel et al., 1989; Gillis and Coogan, 2011).

Our understanding of carbon in altered oceanic crust results from ocean crust drilling (e.g., Staudigel et al., 1989; Alt and Teagle, 1999). Using the data collected from such programs, Müller and Dutkiewicz (2018) determined the magnitude of subducted carbon in oceanic crust by determining oceanic crust carbon concentrations as a function of crustal age, and bottom water temperature. From this parameterization of crustal carbon concentrations, the mean oceanic carbon concentration and its standard deviation can be determined for the past 200 Myrs. This model is used in our synthesis to account for subducted crustal carbon (**Figure 3**).

Serpentinized Mantle

Bending of a plate at the outer rise before subduction at the trench produces normal faults that cut through the brittle lithosphere (e.g., Christensen and Ruff, 1988). These faults permit the infiltration of water into the lithospheric mantle and promote hydrous alteration and serpentinization (Ranero et al., 2003; Lefeldt et al., 2012); such alteration is evident from lower seismic velocities than those measured in unaltered mantle (e.g., van Avendonk et al., 2011). Models of outer rise serpentinization have shown that the extent of faulting, and hence serpentinization, are dependent on multiple parameters including crustal age, plate velocity, and coupling between the downgoing and overriding plate (Rüpke et al., 2004; Naliboff et al., 2013).

Serpentinites may host a significant amount of carbon (Alt et al., 2013). Present-day serpentinized mantle carbon ingassing flux is likely of the same order of magnitude to carbon subducted in altered crust (Alt et al., 2013; Dasgupta, 2013; Kelemen and Manning, 2015), and is hence an important contributing factor to the total carbon ingassing flux. We adopt the average serpentinite carbon concentration value of 681 ± 45 ppm of Kelemen and Manning (2015) to estimate subducted serpentinized mantle carbon through time using the model of Müller et al. (2016) (**Figure 3**). In addition, we take a serpentinization extent of 20 ± 10% and a serpentinized mantle thickness of 10.5 ± 3.5 km to determine total altered mantle contributions during subduction (Kelemen and Manning, 2015).

In addition to serpentinization immediately prior to subduction, mantle peridotite may also be serpentinized near mid-ocean ridges. Mantle peridotite is exposed at slow- and ultra-slow spreading ridges (White et al., 2001), and constitutes as much as 25% of oceanic crust produced at these settings (Alt et al., 2013). Carbon fixation into exposed seafloor serpentinite has been estimated at 1.1–2.7 Mt C yr^{-1} (Schwarzenbach et al., 2013). However, plate reconstructions suggest that the global root-mean-square ridge spreading rates in the past 200 Ma were rarely lower than the present-day (Seton et al., 2012; Müller et al., 2016). The subduction of exposed serpentinized peridotite has therefore contributed only a small and likely unchanging proportion of carbon to the ingassing flux, such that the contribution from serpentinized peridotites at slow-spreading ridges lies within calculated error of our flux from altered crust and serpentinized mantle estimates. More detailed work is

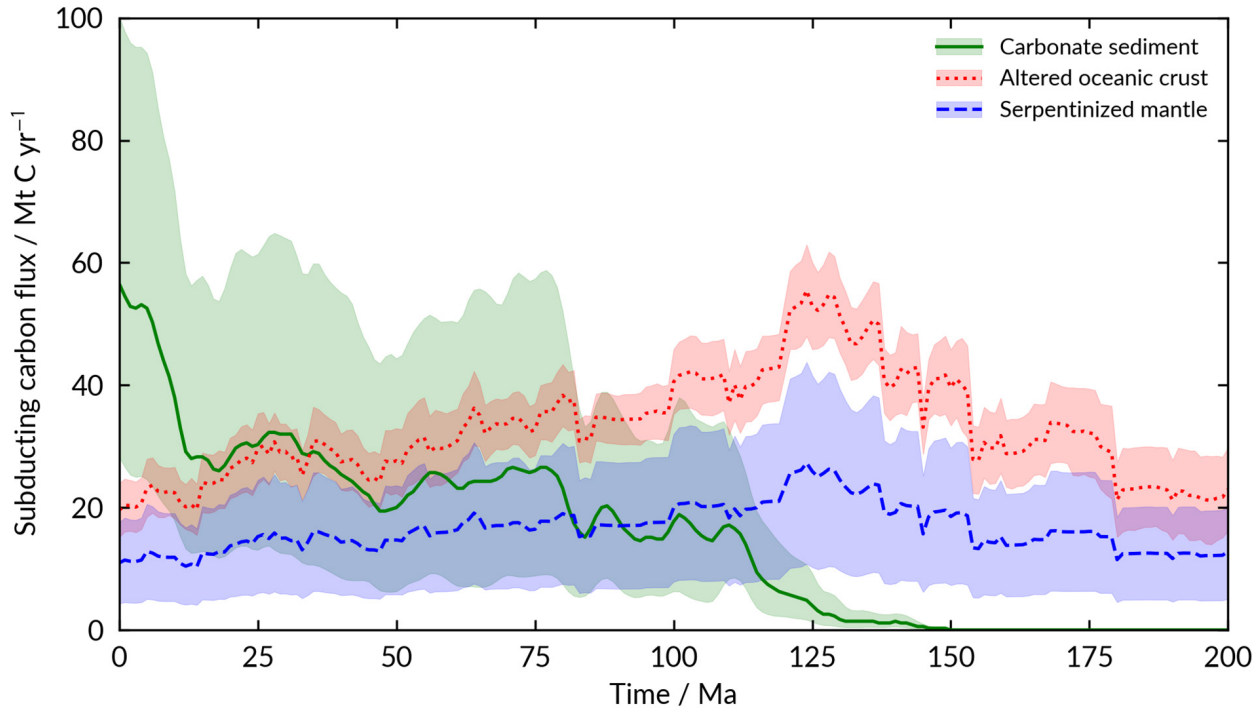

FIGURE 3 | Estimated input of carbon into subduction zones since 200 Ma, divided into the different source lithologies (altered crust, sedimentary carbonate, and serpentinized mantle). The time series for altered crust and sedimentary carbonate are from Müller and Dutkiewicz (2018) and Dutkiewicz et al. (2018), respectively. The increase in sedimentary carbonate arising from the Mesozoic Marine Revolution is included from 150 Myr onward, when sedimentary carbonate input commenced due to an evolutionary radiation of biomineralizing metazoans (e.g., Edmond and Huh, 2003).

required to reduce the uncertainties related to serpentinization processes throughout the plate reconstruction timeframe.

Carbonate Sediments

The composition and distribution of pelagic ocean sediments are highly variable (Plank and Langmuir, 1998; Plank, 2014; Dutkiewicz et al., 2015, 2016; Clift, 2017). A significant proportion of seafloor sediments are carbon-bearing (e.g., Plank, 2014), and are derived from the weathering of continental crust, accumulation of the skeletal components of biomineralizing organisms, and unreduced biological material (e.g., Dutkiewicz et al., 2015). A major control on the quantity of carbon sequestered within sediments is the carbonate compensation depth (CCD), the water depth at which carbonate dissolution exceeds carbonate deposition (e.g., van Andel, 1975; Ridgwell and Zeebe, 2005). The CCD is known to be well-buffered against carbon cycle perturbations, but may be subject to major changes in carbon cycle dynamics (Pälike et al., 2012). One such change during the Oligocene resulted in a deepening of the global CCD of more than a kilometer (van Andel, 1975).

The depth of the CCD is dependent on several factors, including the rate and composition of terrestrial sediment flux (Walling and Fang, 2003), biological productivity (Kumar et al., 1995; Sarmiento et al., 2004), and sea-surface temperature and salinity (Dutkiewicz et al., 2016). Sediment composition can additionally be considered a function of latitude as a result of increased biological productivity and continental weathering at lower latitudes, which has been suggested to have a direct influence on the CO_2 degassed from arc volcanism (Plank, 2014; Aiuppa et al., 2017; Clift, 2017). The compositional and lateral heterogeneity of sediments affects the role subducted sediment can play in the deep carbon cycle.

In addition, the evolution of ocean phytoplankton must be considered. Although carbonate-biomineralizing metazoans are known from the Neoproterozoic (e.g., Grant, 1990), it was not until the mid-Mesozoic that the marine carbonate cycle became more representative of the present-day. The Mesozoic Marine Revolution (MMR) at ∼150 Ma saw an evolutionary radiation in biomineralizing faunas and calcareous plankton which affected the operation of ocean geochemistry (Falkowski et al., 2004; Ridgwell, 2005; Erba, 2006). Edmond and Huh (2003) suggest that prior to the MMR little sedimentary carbonate could be contributed to subduction zones, with sedimentation instead dominated by opal.

Carbon fractions and mass fluxes in subduction zone sediments have been characterized through ocean drilling programs (Rea and Ruff, 1996; Plank and Langmuir, 1998; Plank, 2014). The average present-day subducted sediment is taken as GLOSS II by Plank (2014), which comprises 3.07 ± 0.23 wt% CO_2 (0.84 ± 0.06 wt% C). Carbon and helium isotope systematics have also previously been used to differentiate between sources of carbon contributing to arc volcanic CO_2 emissions (Sano and Williams, 1996; Hilton et al., 2002). This method considers three principal sources of carbon at subduction

zones: the mantle, marine carbonates, and organic carbon, however, it does not distinguish the role of carbon present in arc crust (Mason et al., 2017).

Such methods have yielded estimates of carbonate subduction at the present-day. The review of Kelemen and Manning (2015) utilizes a flux of 13–23 Mt C yr^{-1} at the present-day after Plank (2014). Clift (2017), on the other hand, suggests a much larger present-day flux of ∼60 Mt C yr^{-1} which additionally accounts for subduction accretion processes, of which ∼48 Mt C yr^{-1} is carbonate and the rest, organic carbon. By considering the factors controlling the position of the CCD and hence the proportion of carbon within ocean sediments, Dutkiewicz et al. (2018) determined subducted sedimentary carbonate fluxes for the past 120 Myr, including a present-day estimate of 57 Mt C yr^{-1}. Here, we adopt the model of Dutkiewicz et al. (2018) to estimate carbonate subduction through geological time (**Figure 3**). To account for the MMR, we assume that the sedimentary carbonate flux prior to 150 Ma is negligible as an extreme case.

Like Dutkiewicz et al. (2018), we do not consider accretion of sediments onto arc crust. While accretionary prism growth could account for removal of as much as 70% of sediment entering the trench at present-day subduction zones (von Huene and Scholl, 1991), Dutkiewicz et al. (2018) note that accretionary processes are difficult to constrain for the geological past. We therefore follow their reasoning in assuming all sediment entering subduction zone trenches enters the mantle. Modeling organic carbon sediment subduction is beyond the scope of this paper, but can be considered significant; organic carbon may comprise as much as 1 wt% of carbonate-free sediments (e.g., Kelemen and Manning, 2015). The present-day organic carbon flux is thought to contribute ∼20% of the total subducting carbon sediment flux (Clift, 2017). While our percentage uncertainties for carbonate subduction are typically greater than 20% and may encompass the uncertainty in organic carbon subduction, we acknowledge that the total carbon subducted within sediments has not been completely accounted for.

Carbon Outgassing

Volcanoes are traditionally considered to be the principal natural sources of carbon to the atmosphere, whereas tectonic degassing along fault systems is considered to be an additional, possibly substantial source of CO_2 (Kerrick, 2001). Over the past few decades, significant progress has been made in estimating the total flux and provenance of carbon from volcanic regions (e.g., Burton et al., 2013; Aiuppa et al., 2017, 2019; Werner et al., 2019), which has allowed the semi-permanent instrumentation of >20 of the top outgassing volcanoes worldwide (Carn et al., 2016, 2017), as well as large number of campaign measurements (e.g., Aiuppa et al., 2017, 2019). Recent studies highlight the importance of diffuse carbon outgassing away from volcanic centers for the outgassing carbon budget (Lee et al., 2016; Tamburello et al., 2018). In this case, carbon-bearing fluids are transported through faults and fractures. This link between faulting, fluid migration and carbon degassing has been documented in continental rifts and along transform faults (Kennedy et al., 1997; Ring et al., 2016) and is further supported by the occurrence of deep earthquake swarms detected in continental rifts worldwide (Ibs-von Seht et al., 2008).

Volcanic Degassing

There are numerous challenges associated with the estimation of volcanic carbon fluxes (Burton et al., 2013; Werner et al., 2019). Owing to the large background concentration of CO_2 in our atmosphere, CO_2 fluxes from volcanoes cannot yet be measured directly. If SO_2 is also emitted from the volcano, the SO_2 flux can be measured using spectroscopy (e.g., UV camera, Differential Optical Absorption Spectroscopy), then combined with the molar C/S in volcanic gases to yield CO_2 flux (Aiuppa et al., 2006, 2017, 2019; Carn et al., 2017). If there is no SO_2 (e.g., in low temperature, geothermal areas, or areas of diffuse CO_2 emissions), then spatially integrated methods of CO_2 flux estimation must be used (Chiodini et al., 1998; Werner et al., 2019), or methods that consider the petrology of erupted magmas (Aiuppa et al., 2019). Fluxes must be based, in many cases, on short timescale periods of measurement, over just a segment of a volcanic region (rift or arc). Each carbon flux measurement captures only a snapshot of the outgassing behavior of each volcano, and may not be representative of the flux averaged over longer timescales.

Magmatic CO_2 can be constrained through study of melt inclusions in mineral phases (e.g., Wallace, 2005; Blundy et al., 2010), however, the concentration of carbon trapped in magmas is dependent on several factors, such as the pressure at which CO_2 begins to degas, and also the degree to which the magma has undergone crystallization. Melt inclusions can therefore provide only a minimum bound to arc carbon fluxes (Wallace, 2005; Wallace et al., 2015). Estimates from melt inclusions are further complicated by the spatial heterogeneity of carbon present in the Earth's upper mantle which is sampled during magmatism, resulting in variable concentrations of CO_2 in mantle-derived magmas (Helo et al., 2011; Le Voyer et al., 2017; Hauri et al., 2019). Carbon fluxes and concentrations averaged both over time and large spatial regions (e.g., over entire arc systems) therefore provide the most robust representation of that region's relative contribution to total carbon outgassing as a whole.

Finally, both active and diffuse degassing of volcanic regions must be considered. A significant proportion of carbon emissions is expected to be released away from active volcanic vents and plumes at both actively erupting and dormant settings by diffuse porous flow (e.g., Armstrong McKay et al., 2014; Werner et al., 2019). Furthermore, the proportion of CO_2 that is absorbed into groundwater in volcanic regions is largely unknown, yet contributes significantly to surface carbon reservoirs (Tamburello et al., 2018).

Alongside CO_2, carbon is degassed as other species. The role of methane (CH_4) in the global carbon cycle has been highlighted by Etiope et al. (2008). Methane emitted from volcanic settings is minor compared to CO_2 (typically more than two orders of magnitude lower (e.g., Fischer, 2008), so we consider here only the CO_2 emissions from volcanic settings. Other carbon-bearing species (e.g., CO, OCS, CS_2) contribute negligible amounts of carbon to the atmosphere and may be ignored (Burton et al., 2013).

The total CO_2 flux from volcanoes and volcanic regions is estimated to lie in the range 250–375 Mt CO_2 yr^{-1} (70 to 100 Mt C yr^{-1}, Werner et al., 2019), which is slightly lower than that estimated by Burton et al. (2013) (540 Mt CO_2 yr^{-1}; 150 Mt C yr^{-1}). We consider below the individual contributions from magmatism at continental rifts, mid-ocean ridges, plume volcanoes, and subduction zones.

Continental Rifts

The importance of continental rifting to the deep carbon cycle, especially rifting occurring in East Africa, has been highlighted by several authors (Lee et al., 2016; Brune et al., 2017; Foley and Fischer, 2017; Hunt et al., 2017). Magmatism during rifting liberates carbon and other volatiles stored in sub-continental lithospheric mantle (e.g., Rooney et al., 2017) and continental crust (e.g., Parks et al., 2013), allowing it to be transported to the surface. Extensional faults may then become localized within rifting zones as deformation continues (Muirhead et al., 2016); these faults can facilitate and focus the transport of magma and exsolved CO_2 to the surface from the mantle (e.g., Faulkner et al., 2010; Tamburello et al., 2018).

Sources of outgassing carbon may be differentiated through carbon and helium isotope ratios, as each source component has a distinct isotopic composition. Carbon isotope studies by Lee et al. (2016) on the Magadi-Natron Basin of the Eastern branch of the East African Rift suggest that the mantle is the dominant source of carbon during the early stages of rifting; this is supported by similar results from the Western branch (Botz and Stoffers, 1993) and from the Central European Eger Rift (Weinlich et al., 1999; Kämpf et al., 2013; Bräuer et al., 2018). The destabilization and degassing of mantle-derived carbon is hence an important contributor during continental rifting.

Continental rifts show a large degree of spatial variability as they transition from fault-bounded basins to oceanic spreading ridges (e.g., Ebinger, 2005). The diffuse carbon flux from a continental rift may match this variability along its length; previous estimates of carbon fluxes from the East African Rift, for example, based on extrapolation, vary from 5.0 ± 3.9 to 19.4 ± 9.0 Mt C yr^{-1} depending on the rift sector sampled (Lee et al., 2016; Hunt et al., 2017). Individual sectors of a continental rift may show significant intrinsic heterogeneity in their carbon fluxes both along and across rift strike (Hunt et al., 2017). Finally, the many influences on continental rift development result in a considerable range of continental rift basin areal fluxes of 3–120 t C km^{-2} yr^{-1} worldwide (Brune et al., 2017 and references therein). This variability might be related to several processes and parameters: the amount of decompression melting as a function of extension rate (Bown and White, 1995) or the existence of a mantle plume beneath the rift (White and McKenzie, 1995), the age of the lithosphere and maturity of the rift (Foley and Fischer, 2017), spatio-temporal changes of the stress field (Tamburello et al., 2018), or local episodes of magmatic and seismic activity (Bräuer et al., 2018). Identifying the relative impact of these controls at specific sites, which is expected to lead to a reduction of the uncertainty on the CO_2 flux, is a topic of ongoing research, which goes beyond the scope of this paper.

Brune et al. (2017) give rift mean areal fluxes and rift flux standard deviations of 49 ± 53 t C km^{-2} yr^{-1}, or 63 ± 44 t C km^{-2} yr^{-1} if both mean and standard deviation are weighted by rift basin area. If the recent Main Ethiopian Rift estimate of Hunt et al. (2017) is included (an areal flux of 122 t CO_2 km^{-2} yr^{-1} over 20,000 km^2), the mean and area-weighted mean are 46 ± 46 and 52 ± 38 t C km^{-2} yr^{-1}, respectively. We choose an areal flux of 50 ± 40 t C km^{-2} yr^{-1} for rift basins to capture the full uncertainty in present-day continental rift carbon flux and rifting styles (**Figure 4**). Continental rift length histories are based on the plate tectonic model of Müller et al. (2016), complemented by a compilation of rifts preserved in the geological record (Şengör and Natal'in, 2001). We retain the assumed continental rift basin width of 50 km used by Brune et al. (2017) as such a width is typical of a developing rift zone on strong continental lithosphere (e.g., Copley and Woodcock, 2016).

We do not account for the individual active fluxes of rift volcanoes such as Nyiragongo and Nyamuragira, two rift volcanoes that are known to be major carbon degassers (e.g., Aiuppa et al., 2019). Their combined flux of 1.6 ± 1.1 Mt C yr^{-1} (Aiuppa et al., 2019) is minor compared to the overall diffuse flux, and is accounted for by the uncertainty in the diffuse estimate.

Mid-Ocean Ridges

The flux of CO_2 from mid-ocean ridges is almost entirely delivered into ocean water (Le Voyer et al., 2018). A fraction of this CO_2 is precipitated into seafloor lithologies in the form of carbonate in crustal veins and serpentinites, or fixed into organic matter during photosynthesis (e.g., Alt and Teagle, 1999; Le Voyer et al., 2018); in addition, oceanic carbon reaches equilibrium with atmospheric carbon over short timescales (e.g., Zeebe, 2012). We must therefore consider mid-ocean ridge fluxes through time, as ridges are a significant contributor to Earth's exogenic reservoirs.

There is a substantial range in previously published estimates of carbon fluxes from mid-ocean ridges (**Figure 5**). This is due to the challenge of estimating carbon fluxes in mid-ocean ridge settings with much less accessibility relative to other volcanic settings, and the subsequent difficulty in measurement of ridge carbon directly. Variability in spreading rate, mantle carbon concentrations and magma flux also produce notable differences in carbon flux along different mid-ocean ridge segments; CO_2 fluxes are known to vary by at least two orders of magnitude as a result of this (Le Voyer et al., 2017, 2018; Hauri et al., 2019). In addition, there is uncertainty as to whether mantle volatiles liberated during decompression melting beneath mid-ocean ridges are focused toward the ridge axis or distributed along the base of the lithosphere (e.g., Keller et al., 2017). The method we apply must therefore account for uncertainty in past estimates and spatial heterogeneities in present-day ridge carbon fluxes.

The low solubility of carbon in mid-ocean ridge basalts (e.g., Dixon et al., 1995) means that few samples collected at the surface are undegassed. Carbon flux estimates for MOR are therefore obtained through the measurement of ratios of CO_2 in basaltic glass relative to lithophile trace elements that partition in a similar manner during melting and crystallization, such as Ba, Nb, and Rb, as this allows for the correction of degassed samples

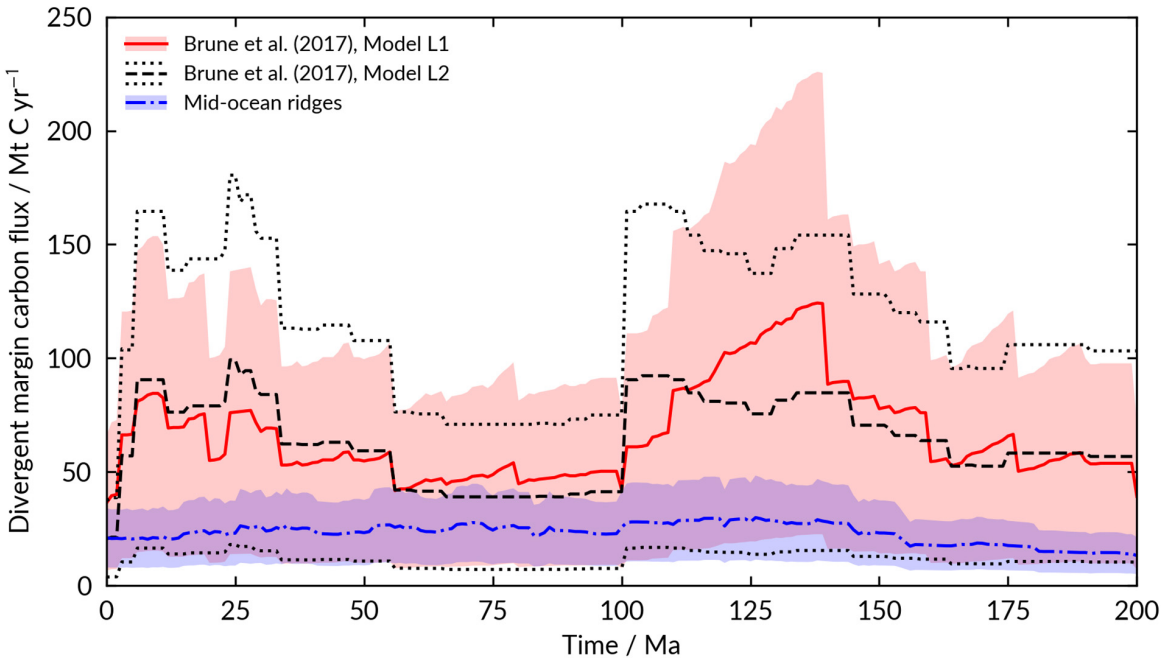

FIGURE 4 | The carbon flux and uncertainty from divergent plate boundaries since 200 Ma. For continental rifts, the two models from Brune et al. (2017) are used, where L1 uses continent-scale rifts in concordance with rifts from the geological record, while L2 offers an alternate model using geologically inferred rifts alone. Mid-ocean ridge carbon outgassing flux is determined using a present-day estimate of 21 ± 13 Mt C yr^{-1}, which encompasses most recent estimates and their uncertainties.

assuming a constant CO_2 to incompatible element ratio (e.g., Saal et al., 2002; Rosenthal et al., 2015). However, Matthews et al. (2017) suggest that CO_2/Ba and CO_2/Nb ratios may also be influenced by the pressure at which degassing occurs, followed by mixing. Other approaches linking CO_2 to ^{3}He in mid-ocean ridge basalts must additionally correct for degassing of He from mantle-derived melts (e.g., Marty and Tolstikhin, 1998).

As it is difficult to account for uncertainty in these methods and results, we consider a simple approach in extrapolating mid-ocean ridge flux through time. We take the modern mid-ocean ridge flux and divide it by modern mid-ocean ridge length to obtain a mean carbon flux per unit length of ridge. This constant is then multiplied by ridge length as computed according to our reference plate tectonic model. This approach allows for the extrapolation of present-day carbon fluxes through geological time, but neglects both magma production fluxes and primary mantle carbon concentrations (Le Voyer et al., 2017, 2018; Hauri et al., 2019). We select a present-day total mid-ocean ridge carbon flux of 21 ± 13 Mt C yr^{-1}, which overlaps with most previous estimates and their uncertainties (**Figure 5**). In addition, this estimate accounts for the range suggested by the recent estimate of Le Voyer et al. (2018), who sum individual ridge segment fluxes across the entire global ridge system based on MORB glass data. This extrapolation is shown in **Figure 4**.

Plume-Related Volcanism

Volcanism related to active mantle upwelling is a significant contributor of carbon to exogenic Earth. As an example, recent measurements of carbon fluxes from Katla volcano on Iceland suggest that basaltic plume-related volcanoes may constantly contribute a significant quantity of carbon to the atmosphere (∼5 kt C day^{-1}, or ∼2 Mt C yr^{-1}, Ilyinskaya et al., 2018). However, it remains uncertain whether such high emissions are representative of steady state diffuse degassing or pre-eruptive melt degassing; increased CO_2 fluxes prior to eruption are known to correlate with an increase in magmatic flux, complicating our ability to estimate an "average" flux from plume volcanoes (e.g., CO_2 fluxes reached >20 kt day^{-1} prior to the 2008 summit eruption at Kilauea Volcano, rising above a "background" flux of ≤300 t day^{-1} during the 1995 East Rift eruption; Gerlach et al., 2002; Poland et al., 2012).

The carbon released at plume settings is of uncertain origin, and is likely derived from multiple sources in the crust and mantle (Black and Gibson, 2019). While radiogenic isotope ratios (e.g., ^{3}He/^{4}He) suggest that mantle plume material may originate from a deep, primordial carbon reservoir (e.g., Marty et al., 2013), convecting mantle materials such as subducted slabs are likely to be entrained during plume upwellings, additionally contributing to the chemical composition of the plume and its carbon contribution (e.g., Sobolev et al., 2011). Plume-related magmas often indicate a geochemical contribution from lithospheric mantle (e.g., Gibson et al., 2006; Rooney, 2017), a known sink and source for mantle carbon (e.g., Foley and Fischer, 2017). Finally, crustal carbon-bearing rocks may be decarbonated during the emplacement of intrusive or extrusive plume magmas, which can cause extensive release of CO_2 and CH_4 (e.g., Ganino and Arndt, 2009; Svensen and Jamtveit, 2010).

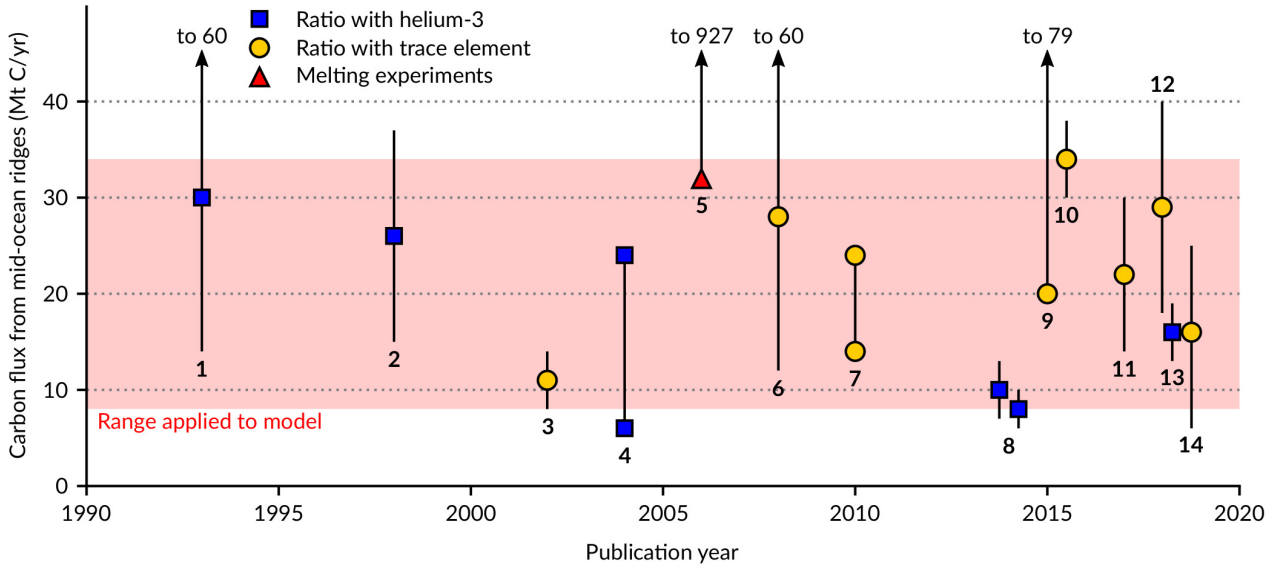

1. Zhang and Zindler, 1993
2. Marty and Tolstikhin, 1998
3. Saal et al., 2002
4. Resing et al., 2004
5. Dasgupta and Hirschmann, 2006
6. Cartigny et al., 2008
7. Shaw et al., 2010
8. Chavrit et al., 2014 (two estimates)
9. Rosenthal et al., 2015
10. Michael and Graham, 2015
11. Le Voyer et al., 2017
12. Hauri et al., 2018
13. Tucker et al., 2018
14. Le Voyer et al., 2018

FIGURE 5 | Comparison of previous ridge carbon flux estimates, plotted against year of publication (symbols and lines), and the range employed in this paper (red area). The symbols denote the method used to derive the estimate. Where two symbols are given a range of estimates is reported; a line to one or both sides of a point marks the uncertainty in the estimate. The flux estimates of Javoy and Pineau (1991) and Aubaud et al. (2004) are not shown as they extend beyond the range of the figure (180 Mt C yr^{-1} and $160^{+60}/_{-30}$ Mt C yr^{-1} respectively), as do the uncertainties of Zhang and Zindler (1993) and Cartigny et al. (2008), and the maximum bounds of Dasgupta and Hirschmann (2006) and Rosenthal et al. (2015). Chavrit et al. (2014) provide a minimum and maximum estimate and error based on the geochemical data availability of the mid-ocean ridge samples analyzed. The other literature estimates compiled are Marty and Tolstikhin (1998), Saal et al. (2002), Resing et al. (2004), Shaw et al. (2010), Michael and Graham (2015), Hauri et al. (2017), Le Voyer et al. (2017, 2018), Tucker et al. (2018).

The carbon liberated by a plume is likely to vary over its lifetime as a result of the temporal and spatial evolution it undergoes (e.g., Black and Gibson, 2019). In addition, neither the intrinsic properties of a mantle plume (e.g., potential temperature, buoyancy flux) nor the tectonic controls of melt generation (e.g., lithospheric thickness) appear to correlate with magmatic flux and degree of melting (Sleep, 1990), thereby affecting plume carbon fluxes, which, at the present-day, may differ between active plumes by several orders of magnitude (Werner et al., 2019). One possible method of generalizing plume fluxes is to establish a "baseline plume flux" at the present-day, and assume that this baseline has remained somewhat constant over the 200 Myr time period considered in this study.

Marty and Tolstikhin (1998) theorized that plume-related volcanism may contribute similar amounts of CO_2 to the atmosphere as mid-ocean ridges; subsequent estimates have suggested that the flux from plume volcanoes may be much smaller than mid-ocean ridge fluxes (e.g., Dasgupta and Hirschmann, 2010; Werner et al., 2019). A compilation of some plume-related volcanic carbon fluxes by Barry et al. (2014) suggests that 3–8 Mt C yr^{-1} may be degassed by plume-related volcanism. Hauri et al. (2019) suggest a Hawaiian flux of 0.9 Mt C yr^{-1} from melt inclusions, comparable to the flux from the Kilauea plume of 0.8 Mt C yr^{-1} (Werner et al., 2019). By reviewing melt inclusions from other ocean islands, Hauri et al. (2019) suggest an estimate of 2–4 Mt C yr^{-1} from ocean intraplate volcanism, which is smaller, but comparable, to mid-ocean ridge flux. The volcanic flux review of Werner et al. (2019) provides an estimate of 2–7 Mt C yr^{-1} for intraplate volcanism including Yellowstone; including the Ilyinskaya et al. (2018) Katla estimate, this becomes 3–9 Mt C yr^{-1}. Considering these estimates we suggest a present-day plume flux of 6 ± 3 Mt C yr^{-1}, which is dominated by the fluxes of Yellowstone and Katla, but does not account for all plume volcanoes. If we assume that the passive carbon flux from mantle plumes remains roughly constant through geological time (implying either that the number of mantle plumes has remained roughly constant over the past 200 Ma, or that the variable conditions affecting each plume average out to present-day values), we can use this present-day estimate as a baseline mantle plume carbon flux (**Figure 6**).

Plume-derived carbon fluxes are further complicated by temporal variability in volcanism, especially at their arrival at the surface. Large Igneous Provinces (LIPs) and flood-basalt volcanism are often associated with the impact of a plume head with the base of the lithosphere (e.g., Richards et al., 1989; White and McKenzie, 1989). Emplacement of LIPs into and onto continental and oceanic crust are often associated with large changes in atmospheric CO_2 and SO_2 resulting in mass

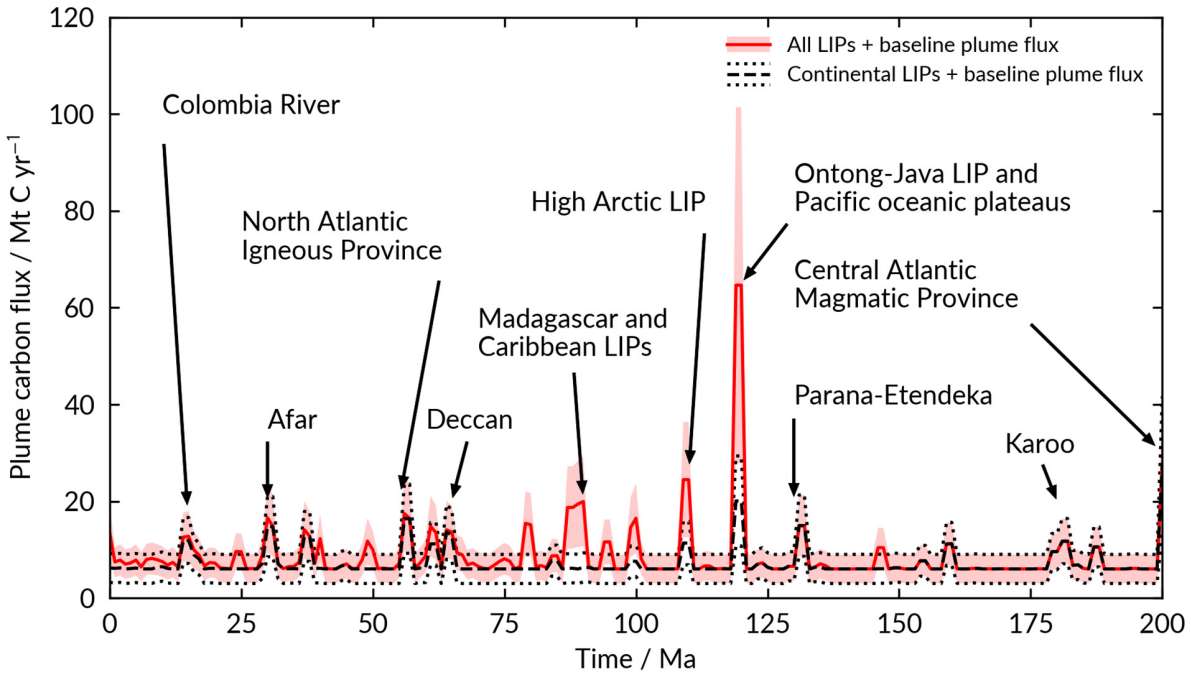

FIGURE 6 | Volcanic carbon flux from continental and oceanic plume volcanoes (black dashed line and dotted line uncertainty) and all plume volcanism (red and shaded red area) since 200 Ma. A baseline flux of 6 ± 3 Mt yr^{-1} is assumed from recent volcanic flux reviews, and including the recent flux measurement from Katla (Ilyinskaya et al., 2018). Major flood basalt eruptions are annotated. The plume eruptive volcanic volumes are derived from Johansson et al. (2018).

extinction events (e.g., Self et al., 2005, 2006; Ernst, 2014; Percival et al., 2015, 2017, 2018; Black and Manga, 2017; Johansson et al., 2018); these changes, much like the duration of volcanism, are short-term (1–5 Ma or less, e.g., Bryan and Ferrari, 2013) and associated spikes in atmospheric CO_2 concentration are buffered by rapid weathering feedbacks acting on time scales of ∼1 Myr (Dessert et al., 2001). Nevertheless, during periods of flood basalt emplacement, these volcanic eruptions provide substantial CO_2 contributions to the atmosphere.

Assimilation of carbon-rich material is additionally possible by LIP-related intrusions. Volatilization of organic carbon present in shales intruded by large igneous provinces could contribute significant proportions of CO_2 and CH_4 to the atmosphere over very short timescales, resulting in rapid climate change (Svensen et al., 2009; Svensen and Jamtveit, 2010; Jones et al., 2016 and references therein). While we note the importance of this assimilation to overall plume contributions, we do not consider them further in this study, as the timescales of these processes are likely too short for our modeling (∼100,000 year timescales, Svensen and Jamtveit, 2010).

Flood basalts likely degas completely as erupted products retain minimal carbon; by estimating the mass of erupted products we can estimate a carbon flux from estimated primary carbon concentrations (e.g., Self et al., 2006; Jones et al., 2016). However, the concentration of CO_2 in LIP magmas is known to range from 0.1 to 2 wt% (Black and Gibson, 2019.), limiting the resolution of our approach. We adapt the LIP erupted area per 1 Myr of Johansson et al. (2018) to determine an average annual area flux, which is converted into a corresponding LIP eruption volume flux using an average flood basalt thickness of 2 ± 1 km (which fits the average thickness of most flood basalts, Courtillot and Renne, 2003; Ross et al., 2005; Ernst, 2014). To predict the carbon which is degassed, we select an average intraplate primary CO_2 concentration of 0.8 ± 0.3 wt% (Hauri et al., 2019; **Figure 6**); this CO_2 concentration lies within the range suggested by Black and Gibson (2019). For our analysis we assume that oceanic and continental LIP basalts degas the entirety of their CO_2 on eruption.

Arc Volcanism

Carbon degassed at continental arc volcanoes is sourced from the mantle via fluids liberated from subducted slabs, from the mantle wedge, and from assimilation in the shallow crust (Marty et al., 2013; Aiuppa et al., 2017; Mason et al., 2017). There is an abundance of evidence to show that carbon from subducted material (sediments and crust) influences the carbon output of volcanoes in subduction zones (Sano and Marty, 1995; Sano and Williams, 1996; Hilton et al., 2002; Shaw et al., 2003; Fischer, 2008; Aiuppa et al., 2017). This is exemplified by the Central American Volcanic Arc, which displays along-arc trends in volatile emissions linked to the composition of slab material and fluids (Aiuppa et al., 2014; de Moor et al., 2017).

High latitude volcanoes, such as those of the Aleutian Arc, outgas low fluxes of carbon (Fischer, 2008; Aiuppa et al., 2017; Lopez et al., 2018); these volcanoes are associated with the subduction of seafloor sediments dominated by carbon-poor diatomaceous and terrigenous material (Johnston et al., 2011). The sedimentary composition is reflected in the carbon isotopic

composition, which lies within mantle values (Kodosky et al., 1991; Symonds et al., 2003; Fischer and Lopez, 2016). Latitude, a key control on sediment compositions, may therefore modulate the magnitude of carbon outgassing from arc volcanoes.

As well as carbon sourced from the subducting slab, it has become increasingly clear that some carbon is sourced from the overlying crust. The evolution of biomineralizing life led to growth and development of carbonate platforms built on continental margins, and the potential of these platforms to interact with percolating arc magmas at subduction zones (Pall et al., 2018; Lee et al., 2019). Models of magma intrusion into lower crustal hot zones predict substantial amounts of crustal melting where basaltic sills intrude amphibolite and other crustal rocks (Annen, 2011; Solano et al., 2012). This interaction provides the basis for assimilation of host rock chemistry, and is consistent with widespread geochemical signatures of assimilation (e.g., Hildreth and Moorbath, 1988; Goff et al., 2001; Chadwick et al., 2007; Iacono-Marziano et al., 2009). The decarbonation of crustal carbonates interacting with silicate magmas generates increased volumes of CO_2 relative to non-carbonate-intersecting arcs; this enhanced outgassing is observed in experiments (Iacono-Marziano et al., 2008, 2009; Deegan et al., 2010; Carter and Dasgupta, 2015, 2016, 2018), and is evident from isotopic signatures of shallow crustal assimilation of carbonate measured in arc volcanic gas emissions (Mason et al., 2017). The co-evolution of continental arc lengths and carbonate platforms must therefore be considered when considering arc carbon fluxes. Increased volcanic carbon outgassing fluxes are expected when continental arc lengths are longer than at the present-day, as the potential of crustal carbonate intersection is greater (Lee et al., 2013, 2015; Lee and Lackey, 2015; Pall et al., 2018).

We use subduction zone length as a proxy for arc length using as in Pall et al. (2018); this method permits us to capture periods of arc history that may not be considered through other methods (e.g., mantle tomography, van der Meer et al., 2014; detrital zircon age statistics, McKenzie et al., 2014, 2016; exposure of arc-related granitoid bodies, Cao et al., 2017a). The data for carbonate platform development through time from Pall et al. (2018) is also used for modeling the degree of carbonate intersection. In the model of Pall et al. (2018), multiple crustal decarbonation events are not considered. It is likely that a second magmatic intrusion in the same position as a prior intrusion will not liberate as much CO_2 as a first event, however, multiple factors (e.g., temperature, pressure, melt composition, carbonate platform thickness) affect the efficiency of decarbonation and hinder the simplicity of modeling multiple decarbonation events (Johnston et al., 2011).

It should be noted that the influence of carbonate, both in the shallow crust and from the subducted slab, is not the only significant control on volcanic carbon degassing. The specific dynamics of degassing play a critical role in the fluxes of all magmatic gases released at volcanoes. The highest carbon flux (Nyiragongo, Le Guern, 1987) recorded thus far was measured at an intra-plate (associated with a continental rift) open vent basaltic system with no evidence of shallow carbonate assimilation. Furthermore, the effect of localized mantle upwelling (as hypothesized under Italian volcanoes, e.g., Schiano et al., 2001), should be considered, as this will affect our extrapolation of arc fluxes through time when based solely on carbonate intersection. Understanding and integrating the complexity the above factors introduce through time is, however, beyond the scope of this work.

Kelemen and Manning (2015) estimate arc volcanic fluxes at the present-day as 18–43 Mt C yr^{-1}. Recent reviews of active and diffuse carbon fluxes places currently known arc emissions at 8–12 Mt C yr^{-1} (Aiuppa et al., 2019; Werner et al., 2019); this value does not account for total volcanic arc degassing, instead providing a minimum bound from arc volcano carbon fluxes which have been measured or monitored. Recent methods considering concentrations of CO_2 within magmatic material added to continental arcs have produced similar values at the present-day of 7.8 Mt C yr^{-1} (Ratschbacher et al., 2019), but do not account for differences in the carbon content of the subducted slab and overlying crust. We therefore use a present-day arc output of 27 $\pm$ 16 Mt C yr^{-1}, taking into account both recent estimates and the range suggested by Kelemen and Manning (2015). Werner et al. (2019) also note that the higher estimates may be skewed toward eruptive periods when active degassing is enhanced; we use this value as a suitable upper constraint for arc degassing.

In our study we distinguish between arcs that intersect crustal carbonates and those that do not. **Figure 7** shows the result of applying the average endmember values of $10^{8.0}$ mol km^{-1} yr^{-1} degassed from carbonate-intersecting arcs and $10^{6.3}$ mol km^{-1} yr^{-1} degassed from non-carbonate intersecting arcs to the model of Pall et al. (2018; see **Supplementary Material** for more details). Our results show that if arcs are treated as undifferentiated over time, then the carbon fluxes from continental arcs have remained relatively constant through the past 200 Ma, varying from 93 to 123% of the present-day value at most. If, however, we differentiate arcs into those that intersect carbonate and those that do not, we predict that carbon arc fluxes have increased over time as a result of increasing carbonate-intersection (from 43% of present-day values at the start of the Jurassic).

Our approach does not consider the influence of significant carbon-degassing volcanoes such as Etna and Popocatepétl, which together contribute at least 2 Mt C yr^{-1} to present-day global arc flux, or 5–15% (Werner et al., 2019). Both volcanoes are located on arcs intersecting crustal carbonates (Etna on the Calabrian Arc; Popocatepétl on the Trans-Mexican Volcanic Belt). de Moor et al. (2017) propose that the dominance of such volcanoes may indicate either immense short-scale compositional or geophysical variability in carbon subduction along arc segments or short-term variability in arc carbon fluxes; in addition we suggest that the lateral distribution of crustal carbonate may also be a factor in determining local carbon degassing rates.

DISCUSSION

Net Carbon Flux

In this analysis we have considered the balance of carbon degassed at different tectonic settings and the amount of carbon that is subducted into the deep Earth (**Figure 8**). The result of

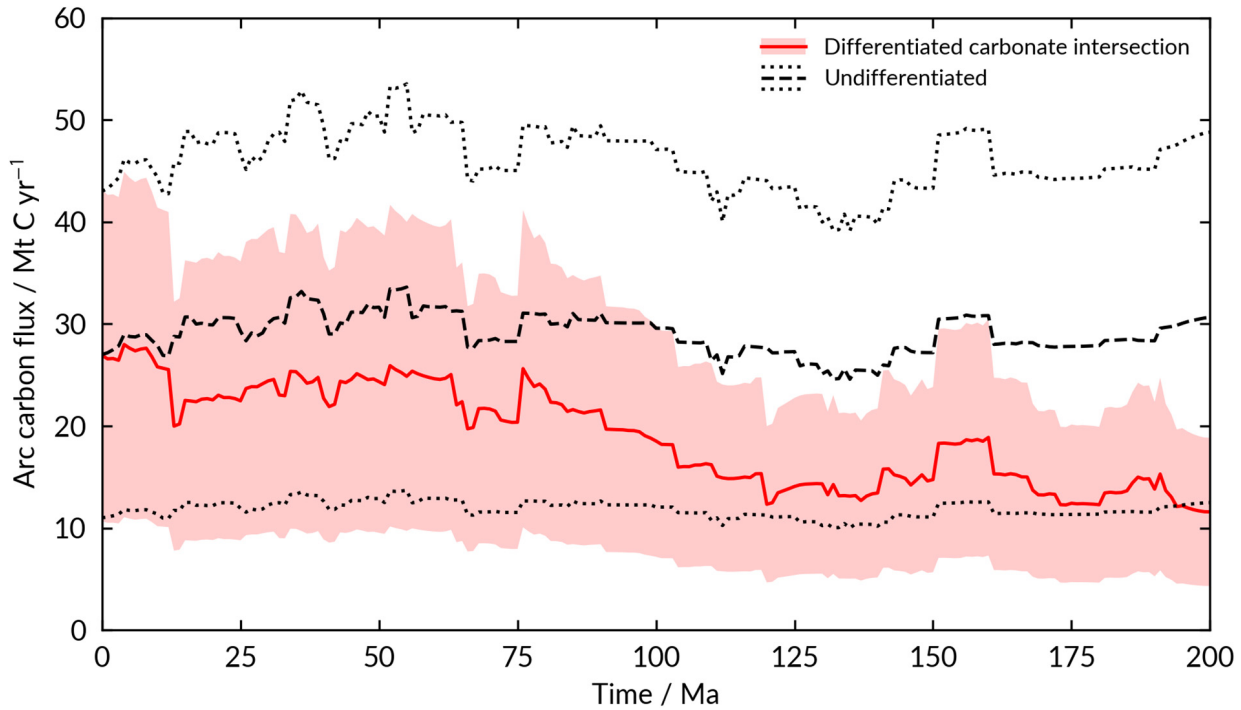

FIGURE 7 | Minimum, maximum, and mean arc carbon flux for volcanic arcs since 200 Ma. The red line and area illustrate the case where carbonate-intersecting subduction zone arcs and those that do not intersect carbonates are differentiated, producing $10^{8.0}$ mol km^{-1} yr^{-1} and $10^{6.3}$ mol km^{-1} yr^{-1} of carbon, respectively. The case where all arc lengths produce the same carbon flux (arcs are not differentiated into carbonate-intersecting and non-carbonate-intersecting) is included as the black dashed line and dotted uncertainty.

the analysis presented here is that while net outgassing flux has stayed close to zero for the last 200 Myr, for the majority of this time net outgassing of CO_2 has been slightly positive, at around 25–75 Mt C yr^{-1} (the equivalent of the CO_2 degassing of 5–15 Mount Etnas, Burton et al., 2013). This result therefore suggests that the carbon released from Earth's mantle is larger than the carbon returned to the mantle at subduction zones, and that there has been a net outgassing of carbon to the Earth's surface since 200 Ma.

We acknowledge that this first-order net degassing curve does not account for the subduction of organic carbon within sediments (as mentioned in section "Carbonate Sediments"), which may constitute a significant proportion of subducting carbon, however, we note that organic carbon subduction, if similar to the ∼20% of subducted sediment at the present-day (Clift, 2017), would not be sufficient to account for the difference between ingassing and outgassing fluxes. We additionally make note of the potential release of stored carbon within the crust and mantle during volcanism, such as at carbonate-intersecting arcs, which may bolster the net carbon outgassing curve.

Figure 9 shows the relative contribution of each tectonic setting to total degassing. Our results agree to a first order with those of Marty and Tolstikhin (1998), who suggest that the contributions from mid-ocean ridges, arcs, and plumes may contribute comparable fluxes of carbon; at the present-day and over the past 200 Ma the contributions from mid-ocean ridges, arcs, and plumes have been similar. More interestingly, our results highlight the vital role of rifting to the deep carbon cycle, consistent with previous studies (Brune et al., 2017; Foley and Fischer, 2017). Of the four plate tectonic settings considered in this study, continental rifts account for a significant portion of degassed carbon (**Figure 9**); the mean areal flux of 50 ± 40 t C km^{-2} yr^{-1} adopted suggests that continental rifts may consistently supply 50% of the total outgassing carbon from the deep Earth, with a maximum at ∼130 Ma linked to the rifting of the Pangaean supercontinent. However, such a large quantity may be an artifact of the uncertainties in capturing rift carbon fluxes; the minimum and maximum rift values would suggest consistent carbon contributions of 20 and 70%, respectively to Earth's surface (**Figure 9**). This observation highlights the necessity for a better understanding of carbon degassing within continental rift zones, and demonstrates that continental rifts may play the most important role in delivering non-anthropogenic carbon to the atmosphere. Oceanic divergent boundaries contribute a smaller, but not insubstantial amount of ∼20%, which remains fairly constant over the past 200 Myr.

Volcanic arc contributions to total outgassing have fluctuated between 10 and 30% of total net outgassing through time, reaching a maximum at the present-day, coincident with a minimum in rift carbon (**Figure 9**). This could illustrate the effect of millions of years of carbonate accumulation in the crust through geological time, and hence increasing arc carbonate assimilation; this could also be a result of the limitations of both the Pall et al. (2018) model and

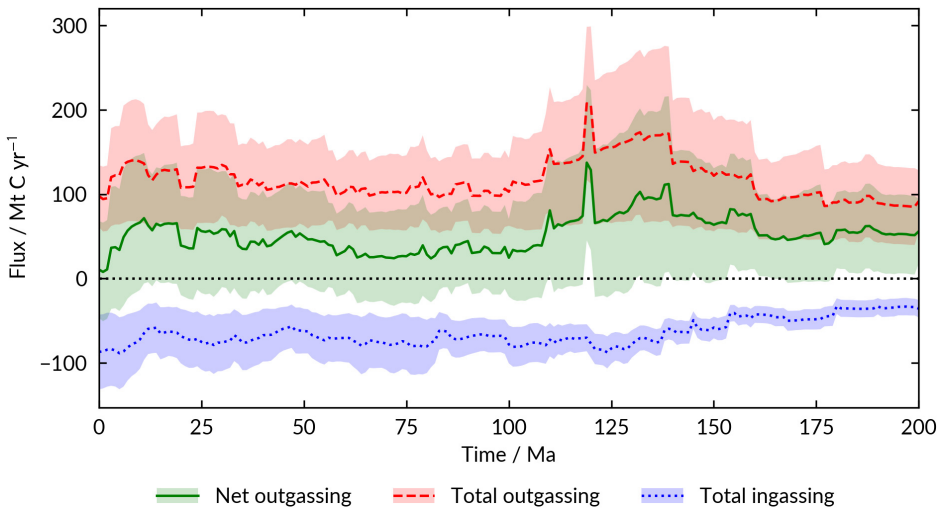

FIGURE 8 | Total outgassing (red), total ingassing (blue), and net outgassing (green) plotted against time. Total ingassing curve drawn assuming a symmetric uncertainty represented by the difference between the maximum carbonate sediment subduction and the mean carbonate sediment subduction, as opposed to the modeled asymmetric distribution. Total outgassing curve drawn assuming the continent scale rift history of Brune et al., 2017 (L1), and the differentiation of volcanic arcs into carbonate-intersecting and non-intersecting (Pall et al., 2018).

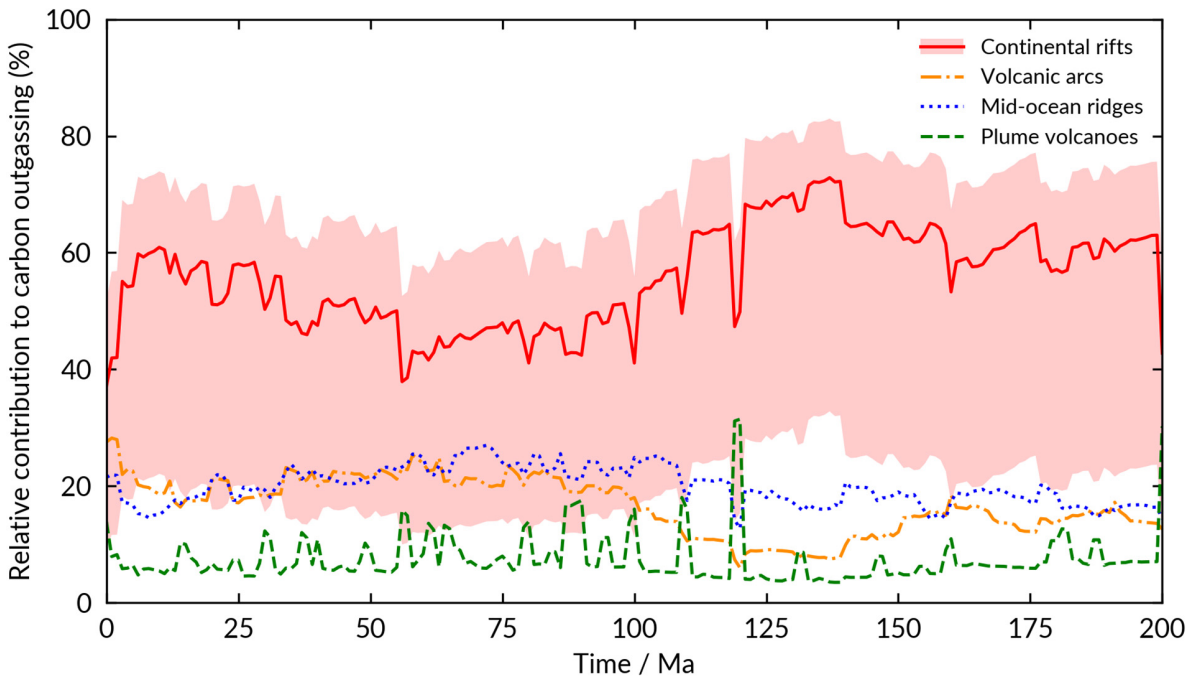

FIGURE 9 | Ratioed outgassing contributions from different tectonic settings. Rift maximum and minimum degassing is shown as the shaded red area. The contributions from arcs, plumes, and ridges are mean calculated values; uncertainty envelopes for these contributions are not shown.

our own assumptions, which both do not account for carbonate platform thicknesses or the effect of multiple decarbonation events.

Mantle plume volcanism contributes ∼10% of the total flux, with increased outgassing during LIP emplacement events (**Figure 9**). Our LIP carbon fluxes are in agreement with past estimates for carbon degassing for individual LIPs, including the Columbia River Basalt Group eruptions estimate of Armstrong McKay et al. (2014) (7.5–10 Mt C yr^{-1}) and the Deccan Traps estimate of Caldeira and Rampino (1990) (6 to 20 × 10^{16} moles over several hundred thousand years, or ∼7–20 Mt C yr^{-1}).

Figures 8, **9** therefore highlight the role of arc and rift magmatism in liberating vast quantities of carbon stored within the crust and mantle. Volatilized carbon-bearing phases at

these settings have played a vital role in tipping the balance between carbon subduction and degassing over the last 200 Myr, and new insights into the remobilization of stored carbon in continental crust and metasomatized lithospheric mantle will likely continue to prove a fruitful avenue for future research into the deep carbon cycle.

Links Between Carbon Fluxes and Atmospheric CO_2

Our total net outgassing curve is plotted against the proxy atmospheric CO_2 record of Foster et al. (2017) in **Figure 10**. There appears to be minimal first-order correlation between the two curves, albeit for occasional spikes corresponding to LIP eruptions (e.g., at 100–120 Ma). Similarly, there is little correlation between the outgassing/ingassing ratio and atmospheric CO_2 (**Figure 11A**). The noticeable lack of correlation between total net outgassing fluxes and atmospheric CO_2 concentrations highlights the importance of carbon cycling and storage within surface reservoirs, thereby maintaining Earth's climate.

One of the major surface processes we have not considered is carbon drawdown resulting from silicate weathering. Silicate weathering provides a negative feedback to elevated atmospheric CO_2 concentrations (e.g., Dessert et al., 2003; Jones et al., 2016). Carbon can chemically sequester in silicate materials to form clay minerals, which are preferentially removed during erosion and transported to the oceans (Colbourn et al., 2015). The drawdown of atmospheric CO_2 is dependent on available surface area for weathering, local erosion rates, and land surface reactivity (Rugenstein et al., 2019). Temperature, humidity, precipitation rates and acidity of the weathering environment all control erosion rates and are in turn controlled by climate; greater erosional rates and CO_2 drawdown is expected at lower latitudes where precipitation rates and temperature are higher (e.g., Amiotte Suchet et al., 2003). CO_2 drawdown by silicate weathering is further enhanced by the emplacement of large surface areas of mafic material onto the Earth's surface, which weather 5–10 times faster than granitic or gneissic material (Dessert et al., 2001, 2003). LIPs and basaltic eruptions therefore provide an immense sink for atmospheric carbon, considered a net sink by some studies (e.g., Jones et al., 2011), with a drawdown flux of $\sim 1.8 \pm 2.2$ Mt C km^{-2} yr^{-1} (average basaltic watershed CO_2 consumption rate, Dessert et al., 2003). The link between flood basalt area within low latitudes and atmospheric CO_2 has been explored previously by Johansson et al. (2018), who link downward atmospheric CO_2 trends to the transit and residence of major LIPs in the near-equatorial humid belt.

In addition, we have not considered the exsolution of CO_2 during the metamorphism of carbon-bearing rocks, such as limestones or shales (Bickle, 1996; Evans, 2011). The thermal breakdown of carbonates can liberate CO_2 contained within the carbonate structure, as can reaction with silica (e.g., Ague and Nicolescu, 2014). Vast amounts of CO_2 are therefore expected to be released during regional metamorphism in orogenic belts, such as the Himalayas (Kerrick and Caldeira, 1998; Evans et al., 2008), where reactions from greenschist facies onward can permit subsolidus decarbonation. Direct measurement of metamorphic carbon dioxide is often possible in orogenic belts through the analysis of riverine water and groundwaters (e.g., Becker et al., 2008; Evans et al., 2008; Frondini et al., 2008), chromatographic modeling of fluid reaction fronts (Skelton, 2011), and metamorphic phase diagram modeling (Groppo et al., 2017). Svensen and Jamtveit (2010) argue that owing to the long timescales related to orogenic processes there are unlikely to be substantial climate changes linked to orogenic decarbonation; however, present-day estimates of orogenic degassing are on a similar order of magnitude to that of mid-ocean ridges and

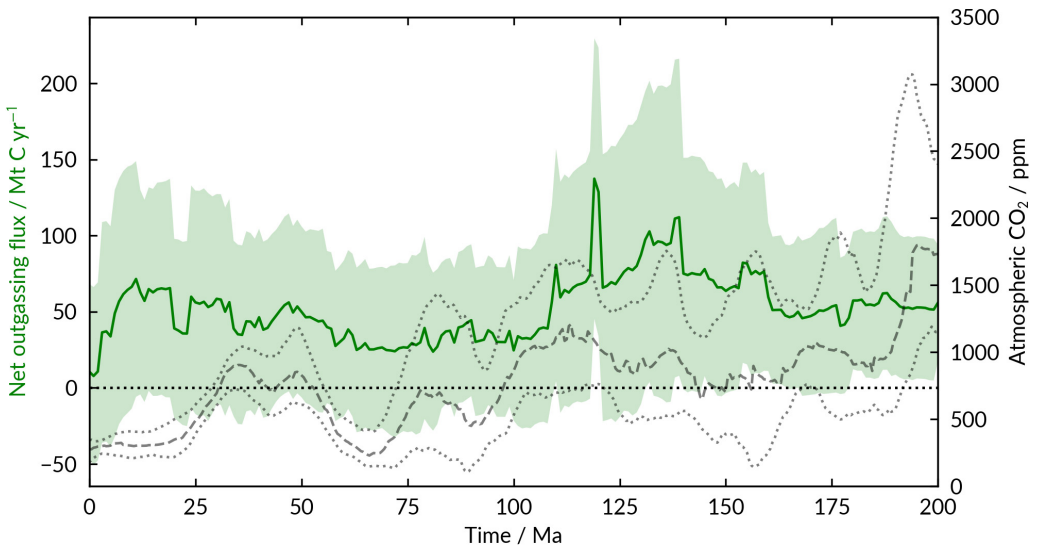

FIGURE 10 | Net carbon flux plotted against time (green line and green shaded area uncertainty). Atmospheric CO_2 curve of Foster et al. (2017) included (dashed gray line) with 2σ uncertainty (dotted gray lines).

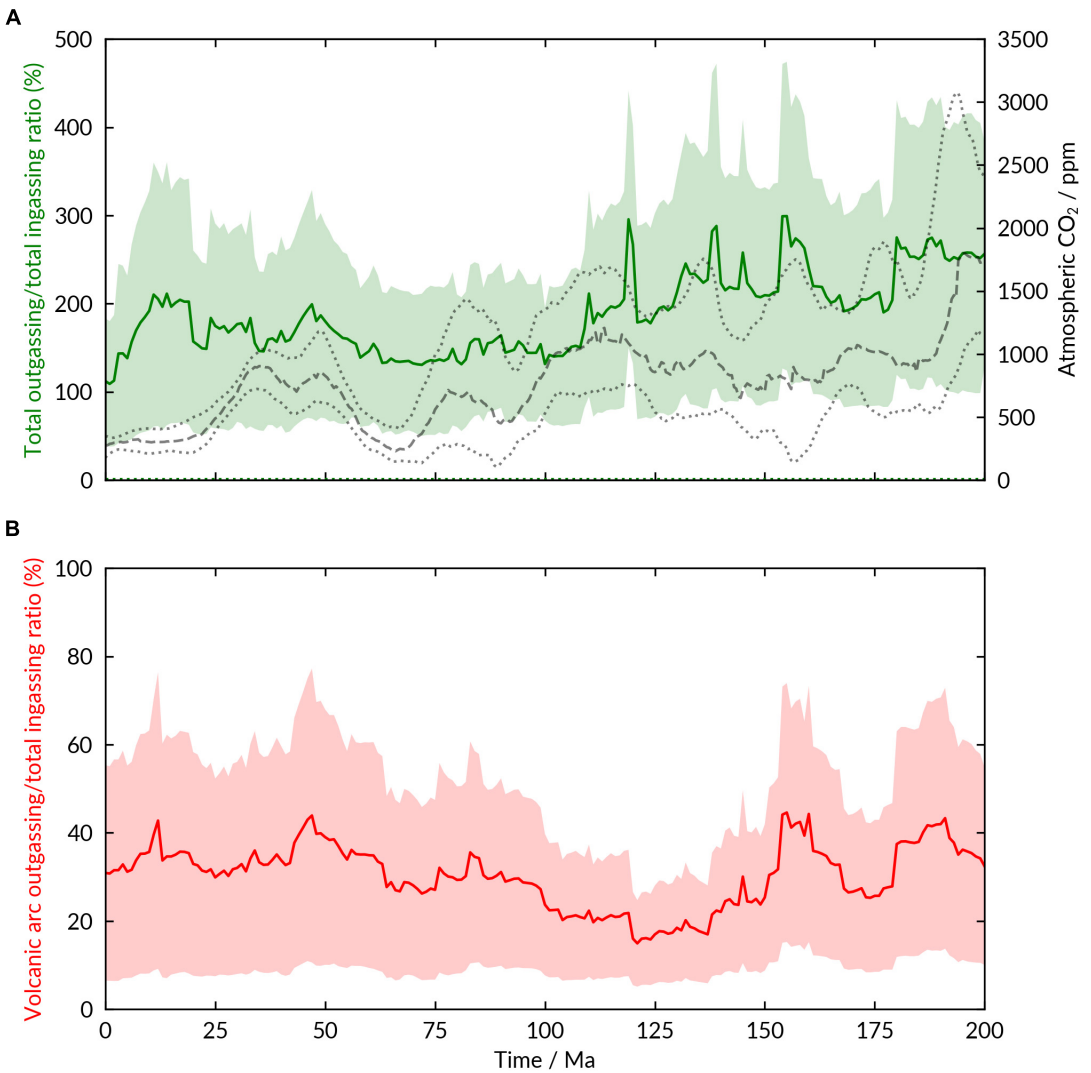

FIGURE 11 | (A) Gross carbon outgassing/ingassing ratio as percentage ingassing plotted against time (green line and shaded area). The atmospheric CO_2 curve and uncertainty of Foster et al. (2017) is included as the dashed and dotted gray lines. **(B)** Percentage of subducted material accounted for by outgassing at volcanic arcs, and uncertainty envelope.

plumes. As an example, measured Himalayan metamorphic carbon fluxes range from 0.132 to 0.408 Mt C yr^{-1} (Groppo et al., 2017) to 11 Mt C yr^{-1} (Becker et al., 2008). On the other hand, the erosion of orogenic belts has been linked to immense atmospheric drawdown as a result of silicate weathering (e.g., Raymo and Ruddiman, 1992).

The question as to whether total metamorphic degassing is balanced by drawdown resulting from silicate weathering of mountain belts remains a subject of debate. Some authors suggest that decarbonation and silicate weathering are in balance as a result of increased sedimentation expected from erosion of orogenic belts, and hence increased organic carbon burial (Galy et al., 2007; Gaillardet and Galy, 2008). Metamorphic contributions to carbon fluxing could therefore be ignored if this was indeed the case. In contrast, Huh (2010) estimates that the drawdown flux of the Tibetan Plateau at the present-day is substantially lower than suggested degassing rates listed above (e.g., Skelton, 2011), implying that metamorphic degassing and drawdown are decoupled (Evans, 2011).

Metamorphic degassing is dependent on the pressure and temperature of reaction, the initial composition of the rock and its volatile content, the porosity of the rock and the ease of degassing, and the rate at which metamorphic rocks undergo reaction (e.g., France-Lanord and Derry, 1997; Evans et al., 2008; Groppo et al., 2017). We therefore expect significant variations in metamorphic CO_2 degassing both across a single mountain range and between different ranges. In addition we anticipate large temporal variability in carbon exsolution over the lifetime of an orogenic belt. Without considering this full range in parameters it is difficult to accurately determine past metamorphic fluxes using our present-day analogs. One future avenue of research may be to determine orogenic belt areas from paleogeographical models

(e.g., Cao et al., 2017b), and utilize them alongside the rock record in estimating protolith compositions and hence metamorphic decarbonation and drawdown fluxes, however, such modeling is beyond the scope of this paper.

What Goes Down Is Mostly What Comes Up – The Norm or the Exception?

Kelemen and Manning (2015) suggest that ingassing and degassing carbon fluxes at present-day subduction zones are approximately in balance, or perhaps that outgassing fluxes are larger, implying that there is very little return of carbon to the deep mantle, and that some carbon sourced from the subducting slab may be stored in the lithosphere of the overriding plate. Other authors have argued that carbon subduction and mantle outgassing are in steady state over long timescales (e.g., Jarrard, 2003).

Our analysis suggests that at the present-day, most of the carbon entering the mantle at subduction zones is unaccounted for; only about 20–40% of subducted carbon is outgassed at arc volcanoes, implying that the remaining 60–80% of subducted material is returned to the mantle or trapped in lithospheric reservoirs (**Figure 11B**). Within the mantle, this 60% is likely either recycled back into the deep mantle or stored in the mantle lithosphere. In either case, convection, plumes, and continental rifting may liberate carbon from the mantle and return it to the surface. Our results additionally indicate that there has not been a period in the past 200 Myrs during which subduction fluxes have been perfectly balanced by arc emissions. Arc emissions have, for this time period, constituted less than 50% of the total subducted carbon. This result not only illustrates the relatively low efficiency of arcs in outgassing their subducted carbon, but also the role of continental rifts and mid-ocean ridges in maintaining the Earth's ingassing and outgassing balance.

The difference between our conclusions and those of Kelemen and Manning (2015) at the present-day is partly a result of new estimates of carbonate subduction. Recent estimates of carbonate subduction at the present-day of 48 Mt C yr^{-1} (Clift, 2017) and 57 Mt C yr^{-1} (Dutkiewicz et al., 2018) are significantly larger than the 13–23 Mt C yr^{-1} assumed for carbon-bearing sediments by Kelemen and Manning (2015). Likewise, present-day estimates for arc degassing are significantly lower than the values adopted by Kelemen and Manning (2015), Aiuppa et al. (2019) estimate a value of 8.0 ± 0.6 Mt C yr^{-1}, and the value we use of 27 ± 16 Mt C yr^{-1} to capture the range of estimates reflects these recent developments.

Finally, recent investigations into carbon sequestration in the Costa Rica subduction zone suggests that a significant portion of carbon may be stored as subsurface crustal calcite in the forearc region, implying that relatively little subducted carbon is then consumed and degassed at subduction zones (Barry et al., 2019). An alternate conclusion from our results could therefore be that a significant proportion of slab-derived carbon is removed by forearc processing prior to outgassing at subduction zones, however, further understanding of such processes will be necessary to differentiate between the effects of forearc storage and deep mantle subduction.

CONCLUSION

The relationships between the temporal change in plate boundary lengths and deep Earth carbon outgassing and ingassing have been the subject of several recent studies (Brune et al., 2017; Müller and Dutkiewicz, 2018; Pall et al., 2018). This study summarizes our understanding of carbon degassing at tectonic settings at the present-day, and the implications of current present-day estimates to temporal atmospheric carbon variability and climate change since the start of the Jurassic. We have highlighted recent advances made, particularly in the fields of plate reconstruction modeling and measurements of carbon degassing, but also the significant uncertainties and debates that are ongoing in the carbon cycling community. With this in mind a number of broad conclusions may be drawn:

(1) Net outgassing has been positive over the last 200 Ma, averaging ∼50 Mt C yr^{-1} more than ingassing at subduction zones (**Figure 8**). This result highlights the importance of surface sinks in regulating atmospheric CO_2, or the necessity of reactivation of sub-continental lithospheric storage, but may be accounted for when other carbon sequestering mechanisms are incorporated (e.g., silicate weathering, etc.).

(2) We build on previous work (e.g., Brune et al., 2017; Foley and Fischer, 2017) to show that rifts appear to be the dominant tectonic setting in terms of carbon degassing fluxes over the last 200 Ma (**Figure 9**), although significant uncertainty remains. However, the influence of carbonate-intersecting arcs increases with time (see **Figure 7**). The influence that this increase may or may not have had on atmospheric CO_2 over the last 200 Ma remains unclear. An implication of this conclusion is that outgassing at volcanic arcs does not completely account for the carbon ingassed at subduction zones (**Figure 11B**), and that some material is recycled back into the mantle, where it later contributes to carbon outgassed at rifts, ridges, and plume volcanoes.

(3) The net outgassing values (**Figure 10**) do not correlate well with atmospheric CO_2 concentrations over the last 200 Ma (**Figures 10**, **11A**). This should not be taken as implying that the approach of this work is incorrect, but that there are "missing" components in the model of ingassing and outgassing presented here.

(4) Our first-order outgassing curve is limited by our present-day understanding of deep carbon cycling processes. Further understanding of the mechanisms behind carbon production and release will be necessary to constrain carbon estimates at the present day. We highlight the following critical components which will be essential in understanding the global carbon balance through deep time: (a) Integration of orogenic controls on the deep carbon cycle, including metamorphic degassing and silicate weathering; (b) Sub-lithospheric storage of carbon, which may be critical for understanding the distribution of carbon on Earth but is yet unaccounted for in most models (including the one presented here); (c) Constraining the uncertainty in carbon fluxes arising from continental rifts.

DATA AVAILABILITY STATEMENT

The datasets generated for this study are available on request to the corresponding author.

AUTHOR CONTRIBUTIONS

SB, MrE, and SZ conceived the study. KW and EM performed the literature review with support from SB, MrE, and SZ. KW assembled net outgassing curve. MdE and SZ contributed data from *GPlates*. All authors contributed to interpretation and writing of the manuscript.

FUNDING

This work arose from a workshop funded by the Alfred P. Sloan Foundation at the University of Cambridge in 2018, under the auspices of the *Deep Carbon Observatory*. SB was supported through the Helmholtz Young Investigators Group *CRYSTALS* (VH-NG-1132). SZ and MdE were supported by Alfred P. Sloan grants G-2017-9997 and G-2018-11296 through the *Deep Carbon Observatory*, and SZ was also supported by Australian Research Council grant IH130200012.

ACKNOWLEDGMENTS

We thank R. Dietmar Müller for constructive comments on a draft of the manuscript, and feedback from colleagues who attended the Janet Watson Meeting at the Geological Society of London in 2019 and participate in the University of Leeds' Rocks, Melts, Fluids study group.

SUPPLEMENTARY MATERIAL

The Supplementary Material for this article can be found online at: https://www.frontiersin.org/articles/10.3389/feart.2019.00263/full#supplementary-material

REFERENCES

Ague, J. J., and Nicolescu, S. (2014). Carbon dioxide released from subduction zones by fluid-mediated reactions. *Nat. Geosci.* 7, 355–360. doi: 10.1038/ngeo2143

Aiuppa, A., Federico, C., Giudice, G., Gurrieri, S., Liuzzo, M., Shinohara, H., et al. (2006). Rates of carbon dioxide plume degassing from mount etna volcano. *J. Geophys. Res. Solid Earth* 111:B09207. doi: 10.1029/2006JB004307

Aiuppa, A., Fischer, T. P., Plank, T., and Bani, P. (2019). CO2 flux emissions from the Earth's most actively degassing volcanoes, 2005–2015. *Sci. Rep.* 9:5442. doi: 10.1038/s41598-019-41901-y

Aiuppa, A., Fischer, T. P., Plank, T., Robidoux, P., and Di Napoli, R. (2017). Along-arc, inter-arc and arc-to-arc variations in volcanic gas CO2/ST ratios reveal dual source of carbon in arc volcanism. *Earth Sci. Rev.* 168, 24–47. doi: 10.1016/j.earscirev.2017.03.005

Aiuppa, A., Robidoux, P., Tamburello, G., Conde, V., Galle, B., Avard, G., et al. (2014). Gas measurements from the costa rica–nicaragua volcanic segment suggest possible along-arc variations in volcanic gas chemistry. *Earth Planet. Sci. Lett.* 407, 134–147. doi: 10.1016/j.epsl.2014.09.041

Alt, J. C., Schwarzenbach, E. M., Früh-Green, G. L., Shanks, W. C., Bernasconi, S. M., Garrido, C. J., et al. (2013). The role of serpentinites in cycling of carbon and sulfur: seafloor serpentinization and subduction metamorphism. *Lithos* 178, 40–54. doi: 10.1016/j.lithos.2012.12.006

Alt, J. C., and Teagle, D. A. H. (1999). The uptake of carbon during alteration of ocean crust. *Geochim. Cosmochim. Acta* 63, 1527–1535. doi: 10.1016/S0016-7037(99)00123-4

Amiotte Suchet, P., Probst, J.-L., and Ludwig, W. (2003). Worldwide distribution of continental rock lithology: implications for the atmospheric/soil CO2 uptake by continental weathering and alkalinity river transport to the oceans. *Glob. Biogeochem. Cycles* 17, 1038–1051. doi: 10.1029/2002GB001891

Annen, C. (2011). Implications of incremental emplacement of magma bodies for magma differentiation, thermal aureole dimensions and plutonism–volcanism relationships. *Tectonophysics* 500, 3–10. doi: 10.1016/j.tecto.2009.04.010

Armstrong McKay, D. I., Tyrrell, T., Wilson, P. A., and Foster, G. L. (2014). Estimating the impact of the cryptic degassing of large igneous provinces: a mid-miocene case-study. *Earth Planet. Sci. Lett.* 403, 254–262. doi: 10.1016/j.epsl.2014.06.040

Aubaud, C., Pineau, F., Jambon, A., and Javoy, M. (2004). Kinetic disequilibrium of C, He, Ar and carbon isotopes during degassing of mid-ocean ridge basalts. *Earth Planet. Sci. Lett.* 222, 391–406. doi: 10.1016/j.epsl.2004.03.001

Barry, P. H., Hilton, D. R., Füri, E., Halldórsson, S. A., and Grönvold, K. (2014). Carbon isotope and abundance systematics of Icelandic geothermal gases, fluids and subglacial basalts with implications for mantle plume-related CO2 fluxes. *Geochim. Cosmochim. Acta* 134, 74–99. doi: 10.1016/j.gca.2014.02.038

Barry, P. H., Moor, J. M., de Giovannelli, D., Schrenk, M., Hummer, D. R., Lopez, T., et al. (2019). Forearc carbon sink reduces long-term volatile recycling into the mantle. *Nature* 568:487. doi: 10.1038/s41586-019-1131-5

Becker, J. A., Bickle, M. J., Galy, A., and Holland, T. J. B. (2008). Himalayan metamorphic CO2 fluxes: quantitative constraints from hydrothermal springs. *Earth Planet. Sci. Lett.* 265, 616–629. doi: 10.1016/j.epsl.2007.10.046

Bickle, M. J. (1996). Metamorphic decarbonation, silicate weathering and the long-term carbon cycle. *Terra Nova* 8, 270–276. doi: 10.1111/j.1365-3121.1996.tb00756.x

Black, B. A., and Gibson, S. A. (2019). Deep carbon and the life cycle of Large Igneous Provinces. *Elements* 15, 319–324. doi: 10.2138/gselements.15.5.319

Black, B. A., and Manga, M. (2017). Volatiles and the tempo of flood basalt magmatism. *Earth Planet. Sci. Lett.* 458, 130–140. doi: 10.1016/j.epsl.2016.09.035

Blundy, J., Cashman, K. V., Rust, A., and Witham, F. (2010). A case for CO2-rich arc magmas. *Earth Planet. Sci. Lett.* 290, 289–301. doi: 10.1016/j.epsl.2009.12.013

Botz, R. W., and Stoffers, P. (1993). Light hydrocarbon gases in lake tanganyika hydrothermal fluids (East-Central Africa). *Chem. Geol.* 104, 217–224. doi: 10.1016/0009-2541(93)90152-9

Bown, J. W., and White, R. S. (1995). Effect of finite extension rate on melt generation at rifted continental margins. *J. Geophys. Res. Solid Earth* 100, 18011–18029. doi: 10.1029/94JB01478

Bräuer, K., Kämpf, H., Niedermann, S., and Strauch, G. (2018). Monitoring of helium and carbon isotopes in the western eger rift area (Czech republic): relationships with the 2014 seismic activity and indications for recent (2000–2016) magmatic unrest. *Chem. Geol.* 482, 131–145. doi: 10.1016/j.chemgeo.2018.02.017

Brune, S., Williams, S. E., and Müller, R. D. (2017). Potential links between continental rifting, CO2 degassing and climate change through time. *Nat. Geosci.* 10, 941–946. doi: 10.1038/s41561-017-0003-6

Bryan, S. E., and Ferrari, L. (2013). Large igneous provinces and silicic large igneous provinces: progress in our understanding over the last 25 years. *GSA Bull.* 125, 1053–1078. doi: 10.1130/B30820.1

Burnham, A. D., Thomson, A. R., Bulanova, G. P., Kohn, S. C., Smith, C. B., and Walter, M. J. (2015). Stable isotope evidence for crustal recycling as recorded by

superdeep diamonds. *Earth Planet. Sci. Lett.* 432, 374–380. doi: 10.1016/j.epsl.2015.10.023

Burton, M. R., Sawyer, G. M., and Granieri, D. (2013). Deep carbon emissions from volcanoes. *Rev. Mineral. Geochem.* 75, 323–354. doi: 10.2138/rmg.2013.75.11

Caldeira, K., and Rampino, M. R. (1990). Carbon dioxide emissions from deccan volcanism and a K/T boundary greenhouse effect. *Geophys. Res. Lett.* 17, 1299–1302. doi: 10.1029/GL017i009p01299

Cao, W., Lee, C.-T. A., and Lackey, J. S. (2017a). Episodic nature of continental arc activity since 750 Ma: a global compilation. *Earth Planet. Sci. Lett.* 461, 85–95. doi: 10.1016/j.epsl.2016.12.044

Cao, W., Zahirovic, S., Flament, N., Williams, S. E., Golonka, J., and Müller, R. D. (2017b). Improving global paleogeography since the late paleozoic using paleobiology. *Biogeosciences* 14, 5425–5439. doi: 10.5194/bg-14-5425-2017

Carn, S. A., Clarisse, L., and Prata, A. J. (2016). Multi-decadal satellite measurements of global volcanic degassing. *J. Volcanol. Geotherm. Res.* 311, 99–134. doi: 10.1016/j.jvolgeores.2016.01.002

Carn, S. A., Fioletov, V. E., McLinden, C. A., Li, C., and Krotkov, N. A. (2017). A decade of global volcanic SO2 emissions measured from space. *Sci. Rep.* 7:44095. doi: 10.1038/srep44095

Carter, L. B., and Dasgupta, R. (2015). Hydrous basalt–limestone interaction at crustal conditions: implications for generation of ultracalcic melts and outflux of CO2 at volcanic arcs. *Earth Planet. Sci. Lett.* 427, 202–214. doi: 10.1016/j.epsl.2015.06.053

Carter, L. B., and Dasgupta, R. (2016). Effect of melt composition on crustal carbonate assimilation: implications for the transition from calcite consumption to skarnification and associated CO2 degassing. *Geochem. Geophys. Geosyst.* 17, 3893–3916. doi: 10.1002/2016GC006444

Carter, L. B., and Dasgupta, R. (2018). Decarbonation in the Ca-Mg-Fe carbonate system at mid-crustal pressure as a function of temperature and assimilation with arc magmas – Implications for long-term climate. *Chem. Geol.* 492, 30–48. doi: 10.1016/j.chemgeo.2018.05.024

Cartigny, P., Harris, J. W., and Javoy, M. (2001). Diamond genesis, mantle fractionations and mantle nitrogen content: a study of δ13C–N concentrations in diamonds. *Earth Planet. Sci. Lett.* 185, 85–98. doi: 10.1016/S0012-821X(00)00357-5

Cartigny, P., Pineau, F., Aubaud, C., and Javoy, M. (2008). Towards a consistent mantle carbon flux estimate: insights from volatile systematics (H2O/Ce, δD, CO2/Nb) in the North Atlantic mantle (14° N and 34° N). *Earth Planet. Sci. Lett.* 265, 672–685. doi: 10.1016/j.epsl.2007.11.011

Chadwick, J. P., Troll, V. R., Ginibre, C., Morgan, D., Gertisser, R., Waight, T. E., et al. (2007). Carbonate assimilation at merapi volcano, java, indonesia: insights from crystal isotope stratigraphy. *J. Petrol.* 48, 1793–1812. doi: 10.1093/petrology/egm038

Chavrit, D., Humler, E., and Grasset, O. (2014). Mapping modern CO2 fluxes and mantle carbon content all along the mid-ocean ridge system. *Earth Planet. Sci. Lett.* 387, 229–239. doi: 10.1016/j.epsl.2013.11.036

Chiodini, G., Cioni, R., Guidi, M., Raco, B., and Marini, L. (1998). Soil CO2 flux measurements in volcanic and geothermal areas. *Appl. Geochem.* 13, 543–552. doi: 10.1016/S0883-2927(97)00076-0

Christensen, D. H., and Ruff, L. J. (1988). Seismic coupling and outer rise earthquakes. *J. Geophys. Res. Solid Earth* 93, 13421–13444. doi: 10.1029/JB093iB11p13421

Clift, P. D. (2017). A revised budget for Cenozoic sedimentary carbon subduction. *Rev. Geophys.* 55, 97–125. doi: 10.1002/2016RG000531

Colbourn, G., Ridgwell, A., and Lenton, T. M. (2015). The time scale of the silicate weathering negative feedback on atmospheric CO2. *Glob. Biogeochem. Cycles* 29, 583–596. doi: 10.1002/2014GB005054

Coogan, L. A., and Dosso, S. E. (2015). Alteration of ocean crust provides a strong temperature dependent feedback on the geological carbon cycle and is a primary driver of the Sr-isotopic composition of seawater. *Earth Planet. Sci. Lett.* 415, 38–46. doi: 10.1016/j.epsl.2015.01.027

Coogan, L. A., and Gillis, K. M. (2013). Evidence that low-temperature oceanic hydrothermal systems play an important role in the silicate-carbonate weathering cycle and long-term climate regulation. *Geochem. Geophys. Geosyst.* 14, 1771–1786. doi: 10.1002/ggge.20113

Coogan, L. A., Parrish, R. R., and Roberts, N. M. W. (2016). Early hydrothermal carbon uptake by the upper oceanic crust: insight from in situ U-Pb dating. *Geology* 44, 147–150. doi: 10.1130/G37212.1

Copley, A., and Woodcock, N. (2016). Estimates of fault strength from the variscan foreland of the northern UK. *Earth Planet. Sci. Lett.* 451, 108–113. doi: 10.1016/j.epsl.2016.07.024

Courtillot, V. E., and Renne, P. R. (2003). On the ages of flood basalt events. *C. R. Geosci.* 335, 113–140. doi: 10.1016/S1631-0713(03)00006-3

Dasgupta, R. (2013). Ingassing, storage, and outgassing of terrestrial carbon through geologic time. *Rev. Mineral. Geochem.* 75, 183–229. doi: 10.2138/rmg.2013.75.7

Dasgupta, R., and Hirschmann, M. M. (2006). Melting in the Earth's deep upper mantle caused by carbon dioxide. *Nature* 440, 659–662. doi: 10.1038/nature04612

Dasgupta, R., and Hirschmann, M. M. (2010). The deep carbon cycle and melting in Earth's interior. *Earth Planet. Sci. Lett.* 298, 1–13. doi: 10.1016/j.epsl.2010.06.039

de Moor, J. M., Kern, C., Avard, G., Müller, C., Aiuppa, A., Saballos, A., et al. (2017). A new sulfur and carbon degassing inventory for the southern central american volcanic arc: the importance of accurate time-series data sets and possible tectonic processes responsible for temporal variations in arc-scale volatile emissions. *Geochem. Geophys. Geosyst.* 18, 4437–4468. doi: 10.1002/2017GC007141

Deegan, F. M., Troll, V. R., Freda, C., Misiti, V., Chadwick, J. P., McLeod, C. L., et al. (2010). Magma–carbonate interaction processes and associated CO2 release at merapi volcano, indonesia: insights from experimental petrology. *J. Petrol.* 51, 1027–1051. doi: 10.1093/petrology/egq010

Dessert, C., Dupré, B., François, L. M., Schott, J., Gaillardet, J., Chakrapani, G., et al. (2001). Erosion of deccan traps determined by river geochemistry: impact on the global climate and the 87Sr/86Sr ratio of seawater. *Earth Planet. Sci. Lett.* 188, 459–474. doi: 10.1016/S0012-821X(01)00317-X

Dessert, C., Dupré, B., Gaillardet, J., François, L. M., and Allègre, C. J. (2003). Basalt weathering laws and the impact of basalt weathering on the global carbon cycle. *Chem. Geol.* 202, 257–273. doi: 10.1016/j.chemgeo.2002.10.001

Dixon, J. E., Stolper, E. M., and Holloway, J. R. (1995). An experimental study of water and carbon dioxide solubilities in Mid-Ocean ridge basaltic liquids. Part I: calibration and solubility models. *J. Petrol.* 36, 1607–1631. doi: 10.1093/oxfordjournals.petrology.a037267

Dutkiewicz, A., Müller, R. D., Cannon, J., Vaughan, S., and Zahirovic, S. (2018). Sequestration and subduction of deep-sea carbonate in the global ocean since the early cretaceous. *Geology* 47, 91–94. doi: 10.1130/G45424.1

Dutkiewicz, A., Müller, R. D., O'Callaghan, S., and Jónasson, H. (2015). Census of seafloor sediments in the world's ocean. *Geology* 43, 795–798. doi: 10.1130/G36883.1

Dutkiewicz, A., Müller, R. D., Wang, X., O'Callaghan, S., Cannon, J., and Wright, N. M. (2017). Predicting sediment thickness on vanished ocean crust since 200 Ma. *Geochem. Geophys. Geosyst.* 18, 4586–4603. doi: 10.1002/2017GC007258

Dutkiewicz, A., O'Callaghan, S., and Müller, R. D. (2016). Controls on the distribution of deep-sea sediments. *Geochem. Geophys. Geosyst.* 17, 3075–3098. doi: 10.1002/2016GC006428

East, M., Müller, R. D., Williams, S. E., Zahirovic, S., and Heine, C. (2019). Subduction history reveals Cretaceous slab superflux as a possible cause for the mid-Cretaceous plume pulse and superswell events. *EarthArXiv*

Ebinger, C. (2005). Continental break-up: the east african perspective. *Astron. Geophys.* 46, 16–12. doi: 10.1111/j.1468-4004.2005.46216.x

Edmond, J. M., and Huh, Y. (2003). Non-steady state carbonate recycling and implications for the evolution of atmospheric pCO2. *Earth Planet. Sci. Lett.* 216, 125–139. doi: 10.1016/S0012-821X(03)00510-7

Erba, E. (2006). The first 150 million years history of calcareous nannoplankton: biosphere–geosphere interactions. *Palaeogeogr. Palaeoclimatol. Palaeoecol.* 232, 237–250. doi: 10.1016/j.palaeo.2005.09.013

Ernst, R. E. (2014). *Large Igneous Provinces*. Cambridge, CA: Cambridge University Press.

Etiope, G., Lassey, K. R., Klusman, R. W., and Boschi, E. (2008). Reappraisal of the fossil methane budget and related emission from geologic sources. *Geophys. Res. Lett.* 35. doi: 10.1029/2008GL033623

Evans, K. (2011). Metamorphic carbon fluxes: how much and how fast? *Geology* 39, 95–96. doi: 10.1130/focus012011.1

Evans, M. J., Derry, L. A., and France-Lanord, C. (2008). Degassing of metamorphic carbon dioxide from the Nepal Himalaya. *Geochem. Geophys. Geosyst.* 9:Q04021. doi: 10.1029/2007GC001796

Facq, S., Daniel, I., Montagnac, G., Cardon, H., and Sverjensky, D. A. (2014). In situ Raman study and thermodynamic model of aqueous carbonate speciation in equilibrium with aragonite under subduction zone conditions. *Geochim. Cosmochim. Acta* 132, 375–390. doi: 10.1016/j.gca.2014.01.030

Falkowski, P. G., Katz, M. E., Knoll, A. H., Quigg, A., Raven, J. A., Schofield, O., et al. (2004). The evolution of modern eukaryotic phytoplankton. *Science* 305, 354–360. doi: 10.1126/science.1095964

Faulkner, D. R., Jackson, C. A. L., Lunn, R. J., Schlische, R. W., Shipton, Z. K., Wibberley, C. A. J., et al. (2010). A review of recent developments concerning the structure, mechanics and fluid flow properties of fault zones. *J. Struct. Geol.* 32, 1557–1575. doi: 10.1016/j.jsg.2010.06.009

Fischer, T. P. (2008). Fluxes of volatiles (H2O, CO2, N2, Cl, F) from arc volcanoes. *Geochem. J.* 42, 21–38. doi: 10.2343/geochemj.42.21

Fischer, T. P., and Lopez, T. M. (2016). First airborne samples of a volcanic plume for δ13C of CO2 determinations. *Geophys. Res. Lett.* 43, 3272–3279. doi: 10.1002/2016GL068499

Foley, S. F., and Fischer, T. P. (2017). An essential role for continental rifts and lithosphere in the deep carbon cycle. *Nat. Geosci.* 10, 897–902. doi: 10.1038/s41561-017-0002-7

Foster, G. L., Royer, D. L., and Lunt, D. J. (2017). Future climate forcing potentially without precedent in the last 420 million years. *Nat. Commun.* 8:14845. doi: 10.1038/ncomms14845

France-Lanord, C., and Derry, L. A. (1997). Organic carbon burial forcing of the carbon cycle from Himalayan erosion. *Nature* 390, 65–67. doi: 10.1038/36324

Frondini, F., Caliro, S., Cardellini, C., Chiodini, G., Morgantini, N., and Parello, F. (2008). Carbon dioxide degassing from tuscany and Northern Latium (Italy). *Glob. Planet. Chang.* 61, 89–102. doi: 10.1016/j.gloplacha.2007.08.009

Gaillardet, J., and Galy, A. (2008). Himalaya–carbon sink or source? *Science* 320:1727. doi: 10.1126/science.1159279

Galy, V., France-Lanord, C., Beyssac, O., Faure, P., Kudrass, H., and Palhol, F. (2007). Efficient organic carbon burial in the Bengal fan sustained by the Himalayan erosional system. *Nature* 450:407. doi: 10.1038/nature06273

Ganino, C., and Arndt, N. T. (2009). Climate changes caused by degassing of sediments during the emplacement of large igneous provinces. *Geology* 37, 323–326. doi: 10.1130/G25325A.1

Gerlach, T. M., McGee, K. A., Elias, T., Sutton, A. J., and Doukas, M. P. (2002). Carbon dioxide emission rate of Kīlauea Volcano: implications for primary magma and the summit reservoir. *J. Geophys. Res. Solid Earth* 107, ECV 3-1–ECV 3-15. doi: 10.1029/2001JB000407

Gibson, S. A., Thompson, R. N., and Day, J. A. (2006). Timescales and mechanisms of plume–lithosphere interactions: 40Ar/39Ar geochronology and geochemistry of alkaline igneous rocks from the Paraná–Etendeka large igneous province. *Earth Planet. Sci. Lett.* 251, 1–17. doi: 10.1016/j.epsl.2006.08.004

Gillis, K. M., and Coogan, L. A. (2011). Secular variation in carbon uptake into the ocean crust. *Earth Planet. Sci. Lett.* 302, 385–392. doi: 10.1016/j.epsl.2010.12.030

Goff, F., Love, S. P., Warren, R. G., Counce, D., Obenholzner, J., Siebe, C., et al. (2001). Passive infrared remote sensing evidence for large, intermittent CO2 emissions at popocatépetl volcano, Mexico. *Chem. Geol.* 177, 133–156. doi: 10.1016/S0009-2541(00)00387-9

Grant, S. W. (1990). Shell structure and distribution of Cloudina, a potential index fossil for the terminal proterozoic. *Am. J. Sci.* 290, 261–294.

Groppo, C., Rolfo, F., Castelli, D., and Mosca, P. (2017). Metamorphic CO2 Production in collisional orogens: petrological constraints from phase diagram modeling of himalayan, scapolite-bearing, calc-silicate rocks in the NKC(F)MAS(T)-HC system. *J. Petrol.* 58, 53–83. doi: 10.1093/petrology/egx005

Gurnis, M., Turner, M., Zahirovic, S., DiCaprio, L., Spasojevic, S., Müller, R. D., et al. (2012). Plate tectonic reconstructions with continuously closing plates. *Comput. Geosci.* 38, 35–42. doi: 10.1016/j.cageo.2011.04.014

Hauri, E. H., Cottrell, E., Kelley, K. A., Tucker, J. M., Shimizu, K., Le Voyer, M., et al. (2019). "Carbon in the convecting mantle," in *Deep Carbon: Past to Present*, eds B. Orcutt, R. Dasgupta, and I. Daniel (Cambridge: Cambridge University Press).

Hauri, E. H., Maclennan, J., McKenzie, D., Gronvold, K., Oskarsson, N., and Shimizu, N. (2017). CO2 content beneath northern Iceland and the variability of mantle carbon. *Geology* 46, 55–58. doi: 10.1130/G39413.1

Helo, C., Longpré, M.-A., Shimizu, N., Clague, D. A., and Stix, J. (2011). Explosive eruptions at mid-ocean ridges driven by CO2-rich magmas. *Nat. Geosci.* 4, 260–263. doi: 10.1038/ngeo1104

Hildreth, W., and Moorbath, S. (1988). Crustal contributions to arc magmatism in the andes of central chile. *Contrib. Mineral. Petrol.* 98, 455–489. doi: 10.1007/BF00372365

Hilton, D. R., Fischer, T. P., and Marty, B. (2002). Noble gases and volatile recycling at subduction zones. *Rev. Mineral. Geochem.* 47, 319–370. doi: 10.2138/rmg.2002.47.9

Huh, Y. (2010). "Estimation of atmospheric CO2 uptake by silicate weathering in the himalayas and the tibetan plateau: a review of existing fluvial geochemical data," in *Monsoon Evolution and Tectonic-Climate Linkage in Asia*, eds P. D. Clift, R. Tada, and H. Zheng, (London: Geological Society).

Hunt, J. A., Zafu, A., Mather, T. A., Pyle, D. M., and Barry, P. H. (2017). Spatially variable CO2 degassing in the main Ethiopian rift: implications for magma storage, volatile transport, and rift-related emissions. *Geochem. Geophys. Geosyst.* 18, 3714–3737. doi: 10.1002/2017GC006975

Iacono-Marziano, G., Gaillard, F., and Pichavant, M. (2008). Limestone assimilation by basaltic magmas: an experimental re-assessment and application to Italian volcanoes. *Contrib. Mineral. Petrol.* 155, 719–738. doi: 10.1007/s00410-007-0267-8

Iacono-Marziano, G., Gaillard, F., Scaillet, B., Pichavant, M., and Chiodini, G. (2009). Role of non-mantle CO2 in the dynamics of volcano degassing: the mount vesuvius example. *Geology* 37, 319–322. doi: 10.1130/G25446A.1

Ibs-von Seht, M., Plenefisch, T., and Klinge, K. (2008). Earthquake swarms in continental rifts – A comparison of selected cases in America, Africa and Europe. *Tectonophysics* 452, 66–77. doi: 10.1016/j.tecto.2008.02.008

Ilyinskaya, E., Mobbs, S., Burton, R., Burton, M., Pardini, F., Pfeffer, M. A., et al. (2018). Globally significant CO2 emissions from Katla, a Subglacial Volcano in Iceland. *Geophys. Res. Lett.* 45, 332–310. doi: 10.1029/2018GL079096

Jarrard, R. D. (2003). Subduction fluxes of water, carbon dioxide, chlorine, and potassium. *Geochem. Geophys. Geosyst.* 4:8905. doi: 10.1029/2002GC000392

Javoy, M., and Pineau, F. (1991). The volatiles record of a "popping" rock from the Mid-atlantic ridge at 14°N: chemical and isotopic composition of gas trapped in the vesicles. *Earth Planet. Sci. Lett.* 107, 598–611. doi: 10.1016/0012-821X(91)90104-P

Johansson, L., Zahirovic, S., and Müller, R. D. (2018). The interplay between the eruption and weathering of large igneous provinces and the deep-time carbon cycle. *Geophys. Res. Lett.* 45, 5380–5389. doi: 10.1029/2017GL076691

Johnston, F. K. B., Turchyn, A. V., and Edmonds, M. (2011). Decarbonation efficiency in subduction zones: implications for warm cretaceous climates. *Earth Planet. Sci. Lett.* 303, 143–152. doi: 10.1016/j.epsl.2010.12.049

Jones, M. T., Hembury, D. J., Palmer, M. R., Tonge, B., Darling, W. G., and Loughlin, S. C. (2011). The weathering and element fluxes from active volcanoes to the oceans: a montserrat case study. *Bull. Volcanol.* 73, 207–222. doi: 10.1007/s00445-010-0397-0

Jones, M. T., Jerram, D. A., Svensen, H. H., and Grove, C. (2016). The effects of large igneous provinces on the global carbon and sulphur cycles. *Palaeogeogr. Palaeoclimatol. Palaeoecol.* 441, 4–21. doi: 10.1016/j.palaeo.2015.06.042

Kämpf, H., Bräuer, K., Schumann, J., Hahne, K., and Strauch, G. (2013). CO2 discharge in an active, non-volcanic continental rift area (Czech republic): characterisation (δ13C, 3He/4He) and quantification of diffuse and vent CO2 emissions. *Chem. Geol.* 339, 71–83. doi: 10.1016/j.chemgeo.2012.08.005

Kelemen, P. B., and Manning, C. E. (2015). Reevaluating carbon fluxes in subduction zones, what goes down, mostly comes up. *Proc. Natl. Acad. Sci. U.S.A.* 112, E3997–E4006. doi: 10.1073/pnas.1507889112

Keller, T., Katz, R. F., and Hirschmann, M. M. (2017). Volatiles beneath mid-ocean ridges: deep melting, channelised transport, focusing, and metasomatism. *Earth Planet. Sci. Lett.* 464, 55–68. doi: 10.1016/j.epsl.2017.02.006

Kennedy, B. M., Kharaka, Y. K., Evans, W. C., Ellwood, A., DePaolo, D. J., Thordsen, J., et al. (1997). Mantle fluids in the san andreas fault system, California. *Science* 278, 1278–1281. doi: 10.1126/science.278.5341.1278

Kerrick, D. M. (2001). Present and past nonanthropogenic CO2 degassing from the solid earth. *Rev. Geophys.* 39, 565–585. doi: 10.1029/2001RG000105

Kerrick, D. M., and Caldeira, K. (1998). Metamorphic CO2 degassing from orogenic belts. *Chem. Geol.* 145, 213–232. doi: 10.1016/S0009-2541(97)00144-7

Kerrick, D. M., and Connolly, J. A. D. (2001). Metamorphic devolatilization of subducted oceanic metabasalts: implications for seismicity, arc magmatism and volatile recycling. *Earth Planet. Sci. Lett.* 189, 19–29. doi: 10.1016/S0012-821X(01)00347-8

Kodosky, L. G., Motyka, R. J., and Symonds, R. B. (1991). Fumarolic emissions from Mount St. augustine, alaska: 1979–1984 degassing trends, volatile sources and their possible role in eruptive style. *Bull. Volcanol.* 53, 381–394. doi: 10.1007/BF00280228

Kumar, N., Anderson, R. F., Mortlock, R. A., Froelich, P. N., Kubik, P., Dittrich-Hannen, B., et al. (1995). Increased biological productivity and export production in the glacial Southern Ocean. *Nature* 378, 675–680. doi: 10.1038/378675a0

Le Guern, F. (1987). Mechanism of energy transfer in the lava lake of niragongo (Zaire), 1959–1977. *J. Volcanol. Geotherm. Res.* 31, 17–31. doi: 10.1016/0377-0273(87)90003-5

Le Voyer, M., Hauri, E. H., Cottrell, E., Kelley, K. A., Salters, V. J. M., Langmuir, C. H., et al. (2018). Carbon fluxes and primary magma CO2 contents along the global mid-ocean ridge system. *Geochem. Geophys. Geosyst.* 20, 1387–1424. doi: 10.1029/2018GC007630

Le Voyer, M., Kelley, K. A., Cottrell, E., and Hauri, E. H. (2017). Heterogeneity in mantle carbon content from CO2-undersaturated basalts. *Nat. Commun.* 8:14062. doi: 10.1038/ncomms14062

Lee, C.-T. A., Jiang, H., Dasgupta, R., and Torres, M. (2019). "A framework for understanding whole earth carbon cycling," in *Deep Carbon: Past to Present*, eds B. Orcutt, R. Dasgupta, and I. Daniel (Cambridge: Cambridge University Press).

Lee, C.-T. A., and Lackey, J. S. (2015). Global continental arc flare-ups and their relation to long-term greenhouse conditions. *Elements* 11, 125–130. doi: 10.2113/gselements.11.2.125

Lee, C.-T. A., Shen, B., Slotnick, B. S., Liao, K., Dickens, G. R., Yokoyama, Y., et al. (2013). Continental arc–island arc fluctuations, growth of crustal carbonates, and long-term climate change. *Geosphere* 9, 21–36. doi: 10.1130/GES00822.1

Lee, C.-T. A., Thurner, S., Paterson, S., and Cao, W. (2015). The rise and fall of continental arcs: interplays between magmatism, uplift, weathering, and climate. *Earth Planet. Sci. Lett.* 425, 105–119. doi: 10.1016/j.epsl.2015.05.045

Lee, H., Muirhead, J. D., Fischer, T. P., Ebinger, C. J., Kattenhorn, S. A., Sharp, Z. D., et al. (2016). Massive and prolonged deep carbon emissions associated with continental rifting. *Nat. Geosci.* 9, 145–149. doi: 10.1038/ngeo2622

Lefeldt, M., Ranero, C. R., and Grevemeyer, I. (2012). Seismic evidence of tectonic control on the depth of water influx into incoming oceanic plates at subduction trenches. *Geochem. Geophys. Geosyst.* 13:Q05013. doi: 10.1029/2012GC004043

Lenton, T. M., Daines, S. J., and Mills, B. J. W. (2018). COPSE reloaded: an improved model of biogeochemical cycling over Phanerozoic time. *Earth Sci. Rev.* 178, 1–28. doi: 10.1016/j.earscirev.2017.12.004

Lopez, T. M., Fischer, T. P., Plank, T. A., Malinverno, A., Rizzo, A. L., Rasmussen, D. J., et al. (2018). Tracing volatile cycling from subduction to outgassing along the Aleutian Arc, in *Proceedings of the V43I-0246 AGU Fall Meeting Abstracts*, Washington, DC.

Manning, C. E. (2004). The chemistry of subduction-zone fluids. *Earth Planet. Sci. Lett.* 223, 1–16. doi: 10.1016/j.epsl.2004.04.030

Marty, B., Alexander, C. M. O., and Raymond, S. N. (2013). Primordial origins of Earth's carbon. *Rev. Mineral. Geochem.* 75, 149–181. doi: 10.2138/rmg.2013.75.6

Marty, B., and Tolstikhin, I. N. (1998). CO2 fluxes from mid-ocean ridges, arcs and plumes. *Chem. Geol.* 145, 233–248. doi: 10.1016/S0009-2541(97)00145-9

Mason, E., Edmonds, M., and Turchyn, A. V. (2017). Remobilization of crustal carbon may dominate volcanic arc emissions. *Science* 357, 290–294. doi: 10.1126/science.aan5049

Matthews, K. J., Maloney, K. T., Zahirovic, S., Williams, S. E., Seton, M., and Müller, R. D. (2016). Global plate boundary evolution and kinematics since the late Paleozoic. *Glob. Planet. Chang.* 146, 226–250. doi: 10.1016/j.gloplacha.2016.10.002

Matthews, S., Shorttle, O., Rudge, J. F., and Maclennan, J. (2017). Constraining mantle carbon: CO2-trace element systematics in basalts and the roles of magma mixing and degassing. *Earth Planet. Sci. Lett.* 480, 1–14. doi: 10.1016/j.epsl.2017.09.047

McKenzie, D. (1989). Some remarks on the movement of small melt fractions in the mantle. *Earth Planet. Sci. Lett.* 95, 53–72. doi: 10.1016/0012-821X(89)90167-2

McKenzie, N. R., Horton, B. K., Loomis, S. E., Stockli, D. F., Planavsky, N. J., and Lee, C.-T. A. (2016). Continental arc volcanism as the principal driver of icehouse-greenhouse variability. *Science* 352, 444–447. doi: 10.1126/science.aad5787

McKenzie, N. R., Hughes, N. C., Gill, B. C., and Myrow, P. M. (2014). Plate tectonic influences on neoproterozoic–early Paleozoic climate and animal evolution. *Geology* 42, 127–130. doi: 10.1130/G34962.1

Merdith, A. S., Collins, A. S., Williams, S. E., Pisarevsky, S., Foden, J. D., Archibald, D. B., et al. (2017). A full-plate global reconstruction of the neoproterozoic. *Gondwana Res.* 50, 84–134. doi: 10.1016/j.gr.2017.04.001

Merdith, A. S., Williams, S. E., Brune, S., Collins, A. S., and Müller, R. D. (2019). Rift and plate boundary evolution across two supercontinent cycles. *Glob. Planet. Chang.* 173, 1–14. doi: 10.1016/j.gloplacha.2018.11.006

Michael, P. J., and Graham, D. W. (2015). The behavior and concentration of CO2 in the suboceanic mantle: inferences from undegassed ocean ridge and ocean island basalts. *Lithos* 23, 338–351. doi: 10.1016/j.lithos.2015.08.020

Muirhead, J. D., Kattenhorn, S. A., Lee, H., Mana, S., Turrin, B. D., Fischer, T. P., et al. (2016). Evolution of upper crustal faulting assisted by magmatic volatile release during early-stage continental rift development in the East African Rift. *Geosphere* 12, 1670–1700. doi: 10.1130/GES01375.1

Müller, R. D., Cannon, J., Qin, X., Watson, R. J., Gurnis, M., Williams, S., et al. (2018). GPlates: building a virtual earth through deep time. *Geochem. Geophys. Geosyst.* 19, 2243–2261. doi: 10.1029/2018GC007584

Müller, R. D., and Dutkiewicz, A. (2018). Oceanic crustal carbon cycle drives 26-million-year atmospheric carbon dioxide periodicities. *Sci. Adv.* 4:eaaq0500. doi: 10.1126/sciadv.aaq0500

Müller, R. D., Seton, M., Zahirovic, S., Williams, S. E., Matthews, K. J., Wright, N. M., et al. (2016). Ocean basin evolution and global-scale plate reorganization events since pangea breakup. *Ann. Rev. Earth Planet. Sci.* 44, 107–138. doi: 10.1146/annurev-earth-060115-012211

Naliboff, J. B., Billen, M. I., Gerya, T., and Saunders, J. (2013). Dynamics of outer-rise faulting in oceanic-continental subduction systems. *Geochem. Geophys. Geosyst.* 14, 2310–2327. doi: 10.1002/ggge.20155

Pälike, H., Lyle, M. W., Nishi, H., Raffi, I., Ridgwell, A., Gamage, K., et al. (2012). A Cenozoic record of the equatorial Pacific carbonate compensation depth. *Nature* 488, 609–614. doi: 10.1038/nature11360

Pall, J., Zahirovic, S., Doss, S., Hassan, R., Matthews, K. J., Cannon, J., et al. (2018). The influence of carbonate platform interactions with subduction zone volcanism on palaeo-atmospheric CO2; since the devonian. *Clim. Past* 14, 857–870. doi: 10.5194/cp-14-857-2018

Parks, M. M., Caliro, S., Chiodini, G., Pyle, D. M., Mather, T. A., Berlo, K., et al. (2013). Distinguishing contributions to diffuse CO2 emissions in volcanic areas from magmatic degassing and thermal decarbonation using soil gas 222Rn–δ13C systematics: application to santorini volcano. Greece. *Earth Planet. Sci. Lett.* 37, 180–190. doi: 10.1016/j.epsl.2013.06.046

Percival, L. M. E., Jenkyns, H. C., Mather, T. A., Dickson, A. J., Batenburg, S. J., Ruhl, M., et al. (2018). Does large igneous province volcanism always perturb the mercury cycle? comparing the records of oceanic anoxic event 2 and the end-cretaceous to other mesozoic events. *Am. J. Sci.* 318, 799–860. doi: 10.2475/08.2018.01

Percival, L. M. E., Ruhl, M., Hesselbo, S. P., Jenkyns, H. C., Mather, T. A., and Whiteside, J. H. (2017). Mercury evidence for pulsed volcanism during the end-Triassic mass extinction. *Proc. Natl. Acad. Sci. U.S.A.* 114, 7929–7934. doi: 10.1073/pnas.1705378114

Percival, L. M. E., Witt, M. L. I., Mather, T. A., Hermoso, M., Jenkyns, H. C., Hesselbo, S. P., et al. (2015). Globally enhanced mercury deposition during the end-pliensbachian extinction and toarcian OAE: a link to the karoo–ferrar large igneous Province. *Earth Planet. Sci. Lett.* 428, 267–280. doi: 10.1016/j.epsl.2015.06.064

Plank, T. (2014). "4.17 - the chemical composition of subducting sediments," in *Treatise on Geochemistry*, eds H. D. Holland, and K. K. Turekian, (Amsterdam: Elsevier).

Plank, T., and Langmuir, C. H. (1998). The chemical composition of subducting sediment and its consequences for the crust and mantle. *Chem. Geol.* 145, 325–394. doi: 10.1016/S0009-2541(97)00150-2

Poland, M. P., Miklius, A., Jeff Sutton, A., and Thornber, C. R. (2012). A mantle-driven surge in magma supply to Kīlauea Volcano during 2003–2007. *Nat. Geosci.* 5, 295–300. doi: 10.1038/ngeo1426

Poli, S. (2015). Carbon mobilized at shallow depths in subduction zones by carbonatitic liquids. *Nat. Geosci.* 8, 633–636. doi: 10.1038/ngeo2464

Ranero, C. R., Phipps Morgan, J., McIntosh, K., and Reichert, C. (2003). Bending-related faulting and mantle serpentinization at the middle America trench. *Nature* 425, 367–373. doi: 10.1038/nature01961

Ratschbacher, B. C., Paterson, S. R., and Fischer, T. P. (2019). Spatial and depth-dependent variations in magma volume addition and addition rates to continental arcs: application to global CO 2 fluxes since 750 Ma. *Geochem. Geophys. Geosyst.* 20, 2997–3018. doi: 10.1029/2018GC008031

Raymo, M. E., and Ruddiman, W. F. (1992). Tectonic forcing of late cenozoic climate. *Nature* 359, 117–122. doi: 10.1038/359117a0

Rea, D. K., and Ruff, L. J. (1996). Composition and mass flux of sediment entering the world's subduction zones: implications for global sediment budgets, great earthquakes, and volcanism. *Earth Planet. Sci. Lett.* 140, 1–12. doi: 10.1016/0012-821X(96)00036-2

Resing, J. A., Lupton, J. E., Feely, A., and Lilley, M. D. (2004). CO2 and 3He in hydrothermal plumes: implications for mid-ocean ridge CO2 flux. *Earth Planet. Sci. Lett.* 226, 449–464. doi: 10.1016/j.epsl.2004.07.028

Richards, M. A., Duncan, R. A., and Courtillot, V. E. (1989). Flood basalts and Hot-spot tracks: plume heads and tails. *Science* 246, 103–107. doi: 10.1126/science.246.4926.103

Ridgwell, A. (2005). A mid mesozoic revolution in the regulation of ocean chemistry. *Mar. Geol.* 217, 339–357. doi: 10.1016/j.margeo.2004.10.036

Ridgwell, A., and Zeebe, R. E. (2005). The role of the global carbonate cycle in the regulation and evolution of the Earth system. *Earth Planet. Sci. Lett.* 234, 299–315. doi: 10.1016/j.epsl.2005.03.006

Ring, U., Tonguç Uysal, I., Yüce, G., Ünal-Ýmer, E., Italiano, F., Ýmer, A., et al. (2016). Recent mantle degassing recorded by carbonic spring deposits along sinistral strike-slip faults, south-central Australia. *Earth Planet. Sci. Lett.* 454, 304–318. doi: 10.1016/j.epsl.2016.09.017

Rooney, T. O. (2017). The Cenozoic magmatism of East-Africa: part I – flood basalts and pulsed magmatism. *Lithos* 28, 264–301. doi: 10.1016/j.lithos.2017.05.014

Rooney, T. O., Nelson, W. R., Ayalew, D., Hanan, B., Yirgu, G., and Kappelman, J. (2017). Melting the lithosphere: metasomes as a source for mantle-derived magmas. *Earth Planet. Sci. Lett.* 461, 105–118. doi: 10.1016/j.epsl.2016.12.010

Rosenthal, A., Hauri, E. H., and Hirschmann, M. M. (2015). Experimental determination of C, F, and H partitioning between mantle minerals and carbonated basalt, CO2/Ba and CO2/Nb systematics of partial melting, and the CO2 contents of basaltic source regions. *Earth Planet. Sci. Lett.* 412, 77–87. doi: 10.1016/j.epsl.2014.11.044

Ross, P.-S., Ukstins Peate, I., McClintock, M. K., Xu, Y. G., Skilling, I. P., White, J. D. L., et al. (2005). Mafic volcaniclastic deposits in flood basalt provinces: a review. *J. Volcanol. Geotherm. Res.* 145, 281–314. doi: 10.1016/j.jvolgeores.2005.02.003

Rugenstein, J. K. C., Ibarra, D. E., and von Blanckenburg, F. (2019). Neogene cooling driven by land surface reactivity rather than increased weathering fluxes. *Nature* 571, 99–102. doi: 10.1038/s41586-019-1332-y

Rüpke, L. H., Morgan, J. P., Hort, M., and Connolly, J. A. D. (2004). Serpentine and the subduction zone water cycle. *Earth Planet. Sci. Lett.* 223, 17–34. doi: 10.1016/j.epsl.2004.04.018

Saal, A. E., Hauri, E. H., Langmuir, C. H., and Perfit, M. R. (2002). Vapour undersaturation in primitive mid-ocean-ridge basalt and the volatile content of Earth's upper mantle. *Nature* 419, 451–455. doi: 10.1038/nature01073

Sano, Y., and Marty, B. (1995). Origin of carbon in fumarolic gas from island arcs. *Chem. Geol.* 119, 265–274. doi: 10.1016/0009-2541(94)00097-R

Sano, Y., and Williams, S. N. (1996). Fluxes of mantle and subducted carbon along convergent plate boundaries. *Geophys. Res. Lett.* 23, 2749–2752. doi: 10.1029/96GL02260

Sarmiento, J. L., Gruber, N., Brzezinski, M. A., and Dunne, J. P. (2004). High-latitude controls of thermocline nutrients and low latitude biological productivity. *Nature* 427, 56–60. doi: 10.1038/nature02127

Schiano, P., Clocchiatti, R., Ottolini, L., and Busà, T. (2001). Transition of Mount Etna lavas from a mantle-plume to an island-arc magmatic source. *Nature* 412, 900–904. doi: 10.1038/35091056

Schwarzenbach, E. M., Früh-Green, G. L., Bernasconi, S. M., Alt, J. C., and Plas, A. (2013). Serpentinization and carbon sequestration: a study of two ancient peridotite-hosted hydrothermal systems. *Chem. Geol.* 351, 115–133. doi: 10.1016/j.chemgeo.2013.05.016

Self, S., Thordarson, T., and Widdowson, M. (2005). Gas fluxes from flood basalt eruptions. *Elements* 1, 283–287. doi: 10.2113/gselements.1.5.283

Self, S., Widdowson, M., Thordarson, T., and Jay, A. E. (2006). Volatile fluxes during flood basalt eruptions and potential effects on the global environment: a Deccan perspective. *Earth Planet. Sci. Lett.* 248, 518–532. doi: 10.1016/j.epsl.2006.05.041

Şengör, A. M. C., and Natal'in, B. A. (2001). "Rifts of the world," in *Mantle Plumes: Their Identification Through Time*, eds R. Ernst, and K. Buchan, (Boulder, CO: Geological Society of America), 389–482.

Seton, M., Müller, R. D., Zahirovic, S., Gaina, C., Torsvik, T., Shephard, G., et al. (2012). Global continental and ocean basin reconstructions since 200Ma. *Earth Sci. Rev.* 113, 212–270. doi: 10.1016/j.earscirev.2012.03.002

Shaw, A. M., Behn, M. D., Humphris, S. E., Sohn, R. A., and Gregg, P. M. (2010). Deep pooling of low degree melts and volatile fluxes at the 85°E segment of the gakkel ridge: evidence from olivine-hosted melt inclusions and glasses. *Earth Planet. Sci. Let.* 289, 311–322. doi: 10.1016/j.epsl.2009.11.018

Shaw, A. M., Hilton, D. R., Fischer, T. P., Walker, J. A., and Alvarado, G. E. (2003). Contrasting He–C relationships in nicaragua and costa rica: insights into C cycling through subduction zones. *Earth Planet. Sci. Lett.* 214, 499–513. doi: 10.1016/S0012-821X(03)00401-1

Shilobreeva, S., Martinez, I., Busigny, V., Agrinier, P., and Laverne, C. (2011). Insights into C and H storage in the altered oceanic crust: results from ODP/IODP Hole 1256D. *Geochim. Cosmochim. Acta* 75, 2237–2255. doi: 10.1016/j.gca.2010.11.027

Skelton, A. (2011). Flux rates for water and carbon during greenschist facies metamorphism. *Geology* 39, 43–46. doi: 10.1130/G31328.1

Sleep, N. H. (1990). Hotspots and mantle plumes: some phenomenology. *J. Geophys. Res. Solid Earth* 95, 6715–6736. doi: 10.1029/JB095iB05p06715

Smart, K. A., Chacko, T., Stachel, T., Muehlenbachs, K., Stern, R. A., and Heaman, L. M. (2011). Diamond growth from oxidized carbon sources beneath the Northern Slave Craton, Canada: a δ13C–N study of eclogite-hosted diamonds from the jericho kimberlite. *Geochim. Cosmochim. Acta* 75, 6027–6047. doi: 10.1016/j.gca.2011.07.028

Sobolev, S. V., Sobolev, A. V., Kuzmin, D. V., Krivolutskaya, N. A., Petrunin, A. G., Arndt, N. T., et al. (2011). Linking mantle plumes, large igneous provinces and environmental catastrophes. *Nature* 477, 312–316. doi: 10.1038/nature10385

Solano, J. M. S., Jackson, M. D., Sparks, R. S. J., Blundy, J. D., and Annen, C. (2012). Melt segregation in deep crustal hot zones: a mechanism for chemical differentiation, crustal assimilation and the formation of evolved magmas. *J. Petrol.* 53, 1999–2026. doi: 10.1093/petrology/egs041

Staudigel, H., Hart, S. R., Schmincke, H.-U., and Smith, B. M. (1989). Cretaceous ocean crust at DSDP Sites 417 and 418: carbon uptake from weathering versus loss by magmatic outgassing. *Geochim. Cosmochim. Acta* 53, 3091–3094. doi: 10.1016/0016-7037(89)90189-0

Svensen, H., and Jamtveit, B. (2010). Metamorphic fluids and global environmental changes. *Elements* 6, 179–182. doi: 10.2113/gselements.6.3.179

Svensen, H., Planke, S., Polozov, A. G., Schmidbauer, N., Corfu, F., Podladchikov, Y. Y., et al. (2009). Siberian gas venting and the end-Permian environmental crisis. *Earth Planet. Sci. Lett.* 277, 490–500. doi: 10.1016/j.epsl.2008.11.015

Symonds, R. B., Poreda, R. J., Evans, W. C., Janik, C. J., and Ritchie, B. E. (2003). *Mantle and Crustal Sources of Carbon, Nitrogen, and Noble Gases in Cascade-Range and Aleutian-Arc Volcanic Gases*. USGS Open File Report No. 03–436. Reston, VA: USGS.

Tamburello, G., Pondrelli, S., Chiodini, G., and Rouwet, D. (2018). Global-scale control of extensional tectonics on CO2 earth degassing. *Nat. Commun.* 9:4608. doi: 10.1038/s41467-018-07087-z

Thomson, A. R., Kohn, S. C., Bulanova, G. P., Smith, C. B., Araujo, D., Walter, M. J., et al. (2014). Origin of sub-lithospheric diamonds from the Juina-5 kimberlite (Brazil): constraints from carbon isotopes and inclusion compositions. *Contrib. Mineral. Petrol.* 168:1081. doi: 10.1007/s00410-014-1081-8

Thomson, A. R., Walter, M. J., Kohn, S. C., and Brooker, R. A. (2016). Slab melting as a barrier to deep carbon subduction. *Nature* 529, 76–79. doi: 10.1038/nature16174

Tucker, J. M., Mukhopadhyay, S., and Gonnermann, H. M. (2018). Reconstructing mantle carbon and noble gas contents from degassed mid-ocean ridge basalts. *Earth Planet. Sci. Lett.* 496, 108–119. doi: 10.1016/j.epsl.2018.05.024

van Andel, T. H. (1975). Mesozoic/cenozoic calcite compensation depth and the global distribution of calcareous sediments. *Earth Planet. Sci. Lett.* 26, 187–194. doi: 10.1016/0012-821X(75)90086-2

van Avendonk, H. J. A., Holbrook, W. S., Lizarralde, D., and Denyer, P. (2011). Structure and serpentinization of the subducting Cocos plate offshore nicaragua and Costa Rica. *Geochem. Geophys. Geosyst.* 12:Q06009. doi: 10.1029/2011GC003592

van der Meer, D. G., Zeebe, R. E., van Hinsbergen, D. J. J., Sluijs, A., Spakman, W., and Torsvik, T. H. (2014). Plate tectonic controls on atmospheric CO2 levels since the Triassic. *Proc. Natl. Acad. Sci. U.S.A.* 111, 4380–4385. doi: 10.1073/pnas.1315657111

von Huene, R., and Scholl, D. W. (1991). Observations at convergent margins concerning sediment subduction, subduction erosion, and the growth of continental crust. *Rev. Geophys.* 29, 279–316. doi: 10.1029/91RG00969

Wallace, P. J. (2005). Volatiles in subduction zone magmas: concentrations and fluxes based on melt inclusion and volcanic gas data. *J. Volcanol. Geotherm. Res.* 140, 217–240. doi: 10.1016/j.jvolgeores.2004.07.023

Wallace, P. J., Kamenetsky, V. S., and Cervantes, P. (2015). Melt inclusion CO2 contents, pressures of olivine crystallization, and the problem of shrinkage bubbles. *Am. Mineral.* 100, 787–794. doi: 10.2138/am-2015-5029

Walling, D. E., and Fang, D. (2003). Recent trends in the suspended sediment loads of the world's rivers. *Glob. Planet. Chang.* 39, 111–126. doi: 10.1016/S0921-8181(03)00020-1

Weinlich, F. H., Bräuer, K., Kämpf, H., Strauch, G., Tesaø, J., and Weise, S. M. (1999). An active subcontinental mantle volatile system in the western Eger rift, Central Europe: gas flux, isotopic (He, C, and N) and compositional fingerprints. *Geochim. Cosmochim. Acta* 63, 3653–3671. doi: 10.1016/S0016-7037(99)00187-8

Werner, C., Fischer, T. P., Aiuppa, A., Edmonds, M., Cardellini, C., Carn, S., et al. (2019). "Carbon dioxide emissions from subaerial volcanic regions: two decades in review," in *Deep Carbon: Past to Present*, eds B. Orcutt, R. Dasgupta, and I. Daniel (Cambridge: Cambridge University Press).

White, R. S., and McKenzie, D. P. (1989). Magmatism at rift zones: the generation of volcanic continental margins and flood basalts. *J. Geophys. Res. Solid Earth* 94, 7685–7729. doi: 10.1029/JB094iB06p07685

White, R. S., and McKenzie, D. P. (1995). Mantle plumes and flood basalts. *J. Geophys. Res. Solid Earth* 100, 17543–17585. doi: 10.1029/95JB01585

White, R. S., Minshull, T. A., Bickle, M. J., and Robinson, C. J. (2001). Melt generation at very slow-spreading oceanic ridges: constraints from geochemical and geophysical data. *J. Petrol.* 42, 1171–1196. doi: 10.1093/petrology/42.6.1171

Zeebe, R. E. (2012). History of seawater carbonate chemistry, atmospheric Co2, and ocean acidification. *Ann. Rev. Earth Planet. Sci.* 40, 141–165. doi: 10.1146/annurev-earth-042711-105521

Zhang, Y., and Zindler, A. (1993). Distribution and evolution of carbon and nitrogen in Earth. *Earth Planet. Sci. Lett.* 117, 331–345. doi: 10.1016/0012-821X(93)90088-Q

Conflict of Interest: The authors declare that the research was conducted in the absence of any commercial or financial relationships that could be construed as a potential conflict of interest.

frontiers in Earth Science

ORIGINAL RESEARCH
published: 22 October 2019
doi: 10.3389/feart.2019.00268

Wetting Behavior of Iron–Carbon Melt in Silicates at Mid-Mantle Pressures With Implications for Earth's Deep Carbon Cycle

Junjie Dong[1,2], *Jie Li*[1]* *and Feng Zhu*[1†]

[1] Department of Earth and Environmental Sciences, University of Michigan, Ann Arbor, MI, United States, [2] Department of Earth and Planetary Sciences, Harvard University, Cambridge, MA, United States

OPEN ACCESS

Edited by:
Sami Mikhail,
University of St Andrews,
United Kingdom

Reviewed by:
Geoffrey David Bromiley,
University of Edinburgh,
United Kingdom
Valerio Cerantola,
European X-Ray Free Electron Laser,
Germany

***Correspondence:**
Jie Li
jackieli@umich.edu

†Present address:
Feng Zhu,
Hawai'i Institute of Geophysics and Planetology, University of Hawai'i at Mānoa, Honolulu, HI, United States

Specialty section:
This article was submitted to Earth and Planetary Materials, a section of the journal Frontiers in Earth Science

Received: 31 May 2019
Accepted: 30 September 2019
Published: 22 October 2019

Citation:
Dong J, Li J and Zhu F (2019) Wetting Behavior of Iron–Carbon Melt in Silicates at Mid-Mantle Pressures With Implications for Earth's Deep Carbon Cycle. Front. Earth Sci. 7:268. doi: 10.3389/feart.2019.00268

Metallic melt containing iron (Fe) and carbon (C) may be present at depths greater than 250 km inside the Earth. Depending on its wetting behavior, such dense melt may be trapped locally or drain into deep mantle and core. Here, we report experimental data on the wetting behavior of Fe–C melt in silicates at the conditions of Earth's mid-mantle between 10 and 23 GPa and 1600 and 1800°C. The measured dihedral angles of Fe–C melt in olivine, ringwoodite or bridgmanite and ferropericlase matrixes are 117 ± 14°, 120 ± 14°, and 107 ± 16°, respectively, well above the critical value of 60° for complete wetting. The estimated percolation thresholds are at least 7% in volume, far exceeding the amount of metal in the mantle. Consequently, slab-derived Fe–C melt in the mid-mantle is expected to occur as isolated pockets and would not percolate through its silicate matrix.

Keywords: dihedral angle, metallic melt, percolation, ultra-low velocity zone, core growth

INTRODUCTION

Iron–carbon alloys represent reduced forms of carbon and are important components of Earth's long-term carbon cycle. Metallic iron may have been actively produced in the lower mantle (e.g., Frost et al., 2004), the mantle transition zone, and deep part of the upper mantle (e.g., Rohrbach et al., 2007), due to disproportionation of ferrous iron (Fe^{2+}) in silicates into iron metal (Fe^0) and ferric iron (Fe^{3+}). At depths greater than ~250 km, metallic iron may reduce subducted carbonates to produce elemental carbon or carbide ($MgCO_3 + 2\ Fe^0 = 3\ (Fe, Mg)O + C$, e.g., Rohrbach and Schmidt, 2011). Studies of diamond inclusions show that metallic melt containing Fe and C is present in the deep mantle (e.g., Kaminsky and Wirth, 2011; Smith et al., 2016). Depending on its wetting behavior, such melt may be trapped locally or drain into greater depths. Furthermore, carbon is a candidate for the light alloying element for the Earth's iron-rich core, which likely constitutes the predominant carbon reservoir of the planet (e.g., Wood et al., 2013; Li and Fei, 2014). If the Fe–C melt could form an interconnected network, it may eventually segregate to the core-mantle boundary (CMB), possibly merging into the liquid outer core. It has been proposed that slab-derived Fe–C melt in isolated patches can match seismically observed density and velocity features of some ultralow velocity zones (ULVZs) (Liu et al., 2016). For these reasons, knowledge of the wetting behavior of Fe–C is crucial for assessing the fate of slab-derived metallic liquid in deep Earth.

The wetting behavior of iron-rich melt containing sulfur, oxygen, and silicon at high pressures has been studied previously in order to understand the mechanisms of core formation (e.g., Takafuji et al., 2004; Terasaki et al., 2008; Shi et al., 2013). However, that of Fe–C melt in silicate matrix remains poorly understood. Experimental data on the wetting behavior of Fe–C melt at mid-mantle conditions is scarce and limited to <6 GPa (Duncan and Fei, 2017; Zhimulev et al., 2018). In this study, we conduct experiments to investigate the wetting behavior of Fe–C melt in a matrix of polycrystalline olivine polymorphs and bridgmanite/ferropericlase at the conditions of Earth's mid-mantle between 10 and 23 GPa and 1600 and 1800°C. The results are applied to assess the feasibility of percolative drainage of iron–carbon melt through the mantle.

MATERIALS AND METHODS

Experimental

High pressure experiments were carried out using the 1000-ton Walker-type multi-anvil press at the University of Michigan. Experiments at pressures up to 17 GPa used Toshiba-Tungaloy F-grade tungsten carbide (WC) cubes with 5 mm truncation edge length (TEL) and those at pressures up to 23 GPa used similar WC cubes with 3 mm TEL (**Figure 1**). Temperature was monitored using the power curves determined by previous multi-anvil experiments with type-C (W95Re5-W74Re26) thermocouples. The pressure uncertainty is estimated to be ±2 GPa and the temperature uncertainty is estimated to be ±100 K, on the basis of duplication experiments (Li and Li, 2015).

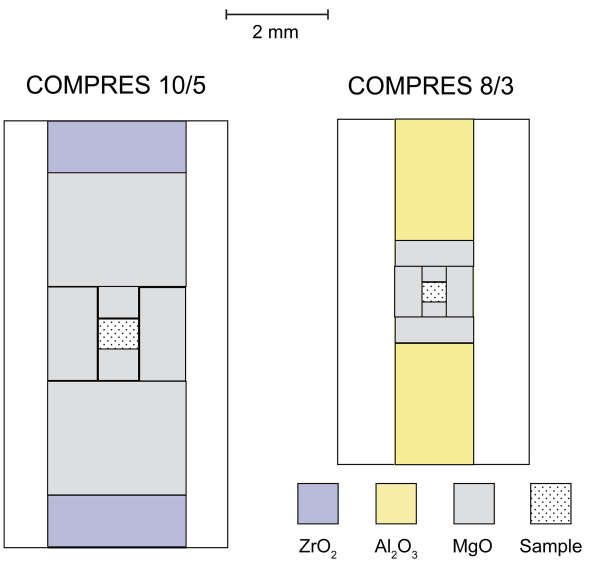

FIGURE 1 | Configurations of cell assemblies for high-pressure experiments. Left: cross-section of modified COMPRES 10/5 assembly showing the sample (dotted) with a MgO container (gray), MgO spacers (gray), and zirconia end-plugs (blue). Right: cross-section of modified COMPRES 8/3 assembly showing the sample (dotted) with a MgO container (gray), MgO spacers (gray), and alumina end-plugs (yellow).

The starting material of the experiments consists of a powder mixture of San Carlos olivine, iron, and graphite. The olivine powder was prepared by grinding natural grains under ethanol in an agate mortar for 1 h and then dried at 110°C. Its composition is approximately $(Mg_{0.9}Fe_{0.1})_2SiO_4$ with 2900 ppm Ni (Herzberg et al., 2016). An Fe–C mixture with 96 wt% Fe and 4 wt% graphite, corresponding to the eutectic composition of the Fe–C binary system at 10 GPa (Fei and Brosh, 2014) was homogenized and then mixed with the olivine power with a ratio of approximately 97:3 in volume. The volume fraction of Fe–C in the starting material was increased above 7% in one run for comparison. The sample was packed into a MgO capsule, which was dried at 950°C for approximately 2 h before loading to minimize trapped moisture. COMPRES 10/5 and 8/3 assemblies were used for experiments up to 17 GPa and those above 20 GPa, respectively (Leinenweber et al., 2012).

In each experiment, the sample was first pressurized to 5 GPa and then sintered at 800–1000°C for 8–12 h during further compression to the target pressure. Target temperature was set below the melting temperature of the silicate phase and above the melting temperature of the iron-rich mixture. The sample was held at target pressure and temperature for approximately 30 min and then quenched by cutting power to the heater and slowly decompressed to ambient pressure.

Analytical

Recovered experimental products were examined for texture, structure, and composition using optical microscopes, micro-Raman spectroscope, and scanning electron microscope (SEM) with energy dispersive spectrometer (EDS). The sample was first mounted in epoxy, sectioned and polished for analyses using optical microscopes. Raman analysis was then performed using a Renishaw inVia confocal Raman Microscope with a 532 nm continuous wave laser. The input laser power varied between 4 and 40 mW and the laser beam was focused through a 50× Mitutoyo objective lens to a diameter of 3–5 microns or through a 20× Olympus objective lens to a beam diameter of 7–12 microns. Raman signal was dispersed with an 1800 grooves/cm grating to achieve spectral resolution of 1–2 wave number (wn). The spectral window was centered at 520 wn. The signal was recorded with a Peltier cooled CCD. Acquisition time is typically 1 s per CCD window. Replicate measurements were conducted to evaluate heterogeneity. For composition and further texture analyses, the polished sample was aluminum-coated and examined using a JOEL 700FLV field emission SEM in the Central Campus Electron Microbeam Analysis Laboratory (EMAL) at the University of Michigan.

Apparent dihedral angles were measured from back scattered electron (BSE) images of the recovered samples by using the thresholding and protractor functions of the image processing software Fiji (Schindelin et al., 2012). To establish a consistent criterion and hence to increase reproducibility of dihedral angle measurement, the BSE images of the measured areas were converted into binary format. Each individual dihedral angle was measured by the "protractor" function in Fiji. The actual fraction of Fe–C in each experiment was estimated from the

polished cross-sections of recovered samples using the "Analyze Particles. . ." function in Fiji.

RESULTS AND DISCUSSION

Four experiments at pressures between 10 and 23 GPa and temperatures at 1600°C or 1800°C produced domains of quenched Fe–C melt dispersed in solid matrix (**Table 1** and **Figure 2**). The molten state of the Fe–C phase is inferred from the spherical shape and/or the dendritic texture of interspersed carbon-rich and carbon-poor domains. The solid state of the silicate or oxide is inferred from the euhedral or sub-hedral shapes. The coexistence of Fe–C melt with solid silicate and oxide at the experimental pressures and temperatures are consistent with known melting behavior of silicates and iron–carbon binary system (**Figure 3**).

In all experiments, the Fe–C melt after quench formed isolated pockets at the grain boundaries of silicate or silicate and oxide matrix. The volume fraction of the Fe–C melt ranged from 0.5 to 7.3%. At small melt fractions between 0.5 and 2.6%, the Fe–C melt assumed nearly spherical shape with a radius of $R = 0.2$–1 micron (R, radius of an equal area circle) and showed no connectivity at all (**Figure 2**, upper). The Fe–C sphere appear somewhat distorted at 17 and 23 GPa. Although some large melt domains ($R \geq 5$ micron) were formed at a melt fraction of 7.3%, the dihedral angles of the small isolated melt pockets ($R \leq 1$ micron) remained large and full connectivity was not developed (**Figure 2**, lower). All the textures suggest that Fe–C melt does not wet silicate or silicate plus oxide at the conditions of the mid-mantle.

Raman analyses showed that the olivine converted into ringwoodite at 17 GPa, and dissociated into bridgmanite and ferropericlase at 23 GPa (**Figure 4**). The carbon contents of the Fe–C melt phases were only estimated semi-quantitatively from EDS data because the domains are typically sub-micron in size. They are consistent with the expected 4 ± 2 wt%. The Fe–C melt phases sometimes contained a small amount of nickel, likely originating from San Carlos olivine in the starting materials.

Dihedral Angle of Fe–C Melt in Mantle Silicate

The apparent dihedral angles of Fe–C melt in silicate matrix at mid-mantle conditions are measured in cross-sections of

TABLE 1 | Summary of experimental conditions and results.

Exp. #	Pressure (GPa)	Temperature (°C)	Melt fraction (%)	Matrix	# of angles measured	Dihedral angles (°)
M053016	10	1600	2.6	Olivine	208	117 ± 14
M052416	17	1600	0.5	Ringwoodite	91	120 ± 14
M013017	23	1800	1.2	Bridgmanite/Ferropericlase	257	107 ± 16
M060316	23	1800	7.3	Bridgmanite/Ferropericlase	–	–

Pressure uncertainty is ±2 GPa and temperature uncertainty is ±100 K. In M060316, no clear triple junction is available for dihedral measurement. Melt fraction is estimated from a cross-section of the recovered sample for each run.

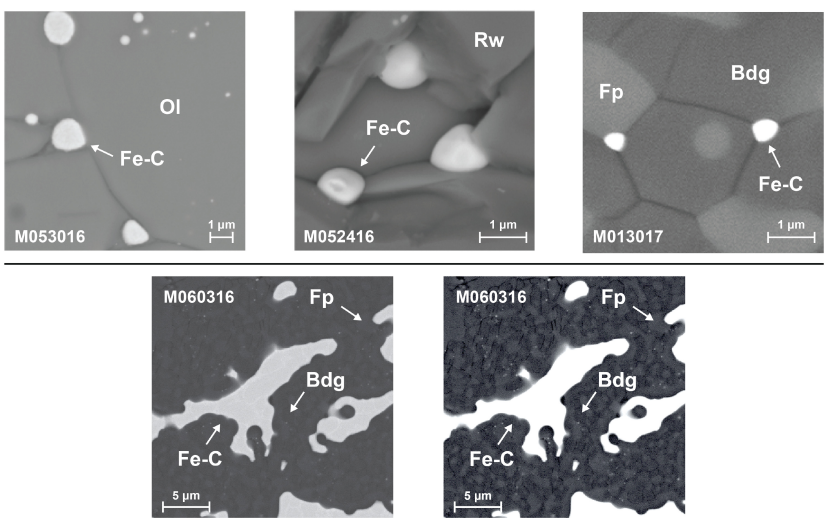

FIGURE 2 | Back scattered electron (BSE) image of the experimental products. Upper: products showing Fe–C melt (gray) dispersed in olivine (Ol) in M053016, ringwoodite (Rw) in M052417, and bridgmanite (Bdg) and ferropericlase (Fp) in M013017. Lower: product of experiment M060316 showing Fe–C melt (gray with dendritic texture on the left, bright on the right) in a matrix of bridgmanite (Bdg) and ferropericlase (Fp). Some Fe–C melt partially connected to form larger domains but small melt pockets remain trapped in the solid matrix.

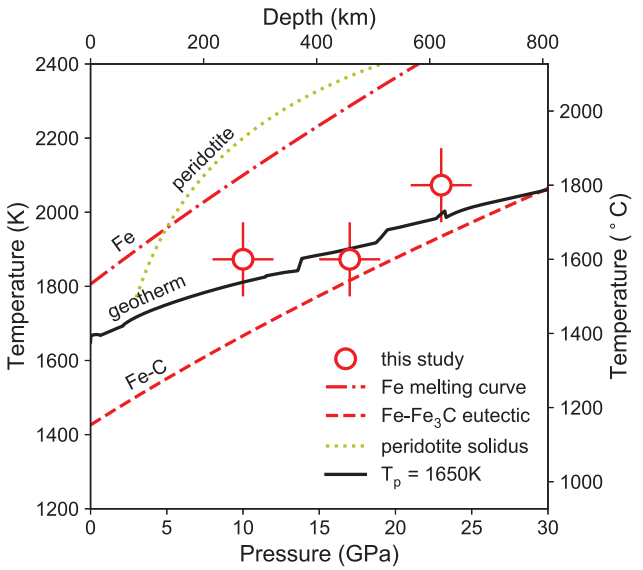

FIGURE 3 | Experimental pressures and temperatures with respect to the geotherm. The temperatures of the experiments (open circle with error bars) are near the estimated mantle temperatures (solid, Stixrude and Lithgow-Bertelloni, 2011) and fall between the melting curve of iron (dashed dotted, fitted from Williams et al., 1987) and the eutectic melting curve of Fe–C binary system (dashed, fitted from Hultgren et al., 1963; Hirayama et al., 1993; Lord et al., 2009; Fei and Brosh, 2014; Liu et al., 2016), and they are below the solidus of peridotite (dotted, Herzberg et al., 2000).

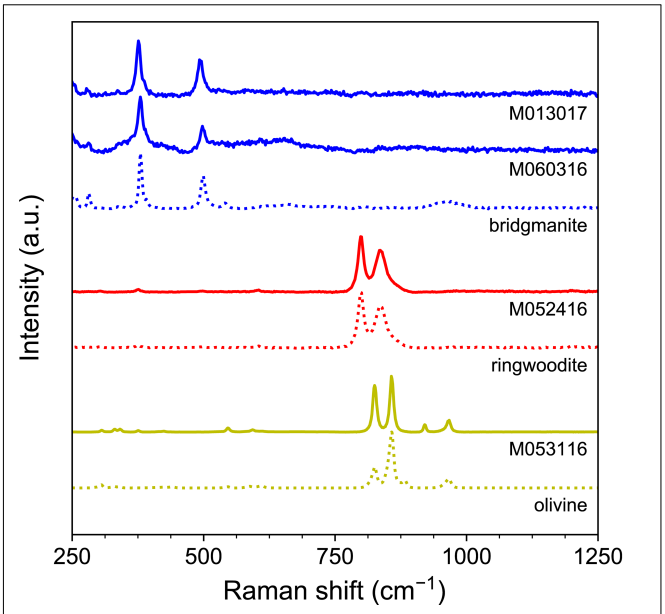

FIGURE 4 | Raman spectra of silicate phases in experimental products. Reference spectra (dashed) are plotted for comparison.

the experimental products. Dihedral angle is defined as the angle between the junction of two solid grains and melt pocket in the plane normal to the junction of the two solid grains (e.g., Porter et al., 2009). Previous studies suggested that a large number of measurements (50–100) are adequate to determine the effective dihedral angles reliably (Holness and Lewis, 1997). Here, between 91 and 257 measurements yielded distributions close to Gaussian (**Table 1** and **Figure 5**). The mean value of the apparent dihedral angle distribution is taken as the effective dihedral angle, with one standard deviation as the associated uncertainty. The dihedral angles of Fe–C melt in olivine, ringwoodite, and bridgmenite-ferropericlase are 117 ± 14° at 10 GPa, 120 ± 14° at 17 GPa, and 107 ± 16° at 23 GPa, respectively. In previous studies, the median is sometimes taken as the effective dihedral angle of the system when the distribution is not near Gaussian. For comparison, we also report the medians of the measured dihedral angles in each experiment with a 95% confidence interval around the medians (Stickels and Hucke, 1964), which are $116^{+4}{}_{-2}$° at 10 GPa, $119^{+4}{}_{-4}$° at 17 GPa, and $108^{+2}{}_{-2}$° at 23 GPa, respectively.

Textural Equilibrium

The measured dihedral angle is accurate only when the system has reached textural equilibrium so that with time the microstructures will only change in size but not in type or shape. At textural equilibrium, the distribution of the apparent dihedral angels formed by the liquid phase assumes a Gaussian pattern, with a single peak that drops off rapidly on both sides (Holzheid et al., 2000). Moreover, the distribution of grain sizes approaches the theoretically expected pattern, and the apparent angles formed by the solid grains at triple junction center around 120°, also dropping off rapidly above or below the mean value. Assuming that the effect of solid silicate matrixes is negligible, the dihedral angle measured in an equilibrated phase assembly is characteristic of the composition at specific pressure and temperature conditions.

Time series studies showed that iron-rich melt in solid silicate matrix reached steady-state texture within 12 min at 25 GPa and 2500 K (Takafuji et al., 2004) in laser-heated diamond anvil cells, and within 50 min at 14 GPa and 1700°C in multi-anvil apparatus (Shannon, 1998). In this study, the experiments were sintered at 5 GPa and 800–1000°C for 8–12 h and then held at 10–23 GPa and 1600–1800°C for about 30 min. The pressure and temperature conditions and experimental durations are comparable to the studies with demonstrated textural equilibrium. Moreover, the distributions of the apparent angles can be fitted by Gaussian curves (**Figure 5**), indicating sufficient approach to texture equilibrium. Equilibrium is further supported by the nearly 120° of dihedral angles at triple junctions of solid grains (**Figure 2**). Although the equilibrated triple junctions of solid grains may have formed at the pre-annealing or sintering stage, textural re-equilibration between solid grains at a slightly higher temperature would take shorter time than starting from ambient temperature, and the Fe–C melt is expected to establish textural equilibrium with the solid phases much faster than within the solid grains.

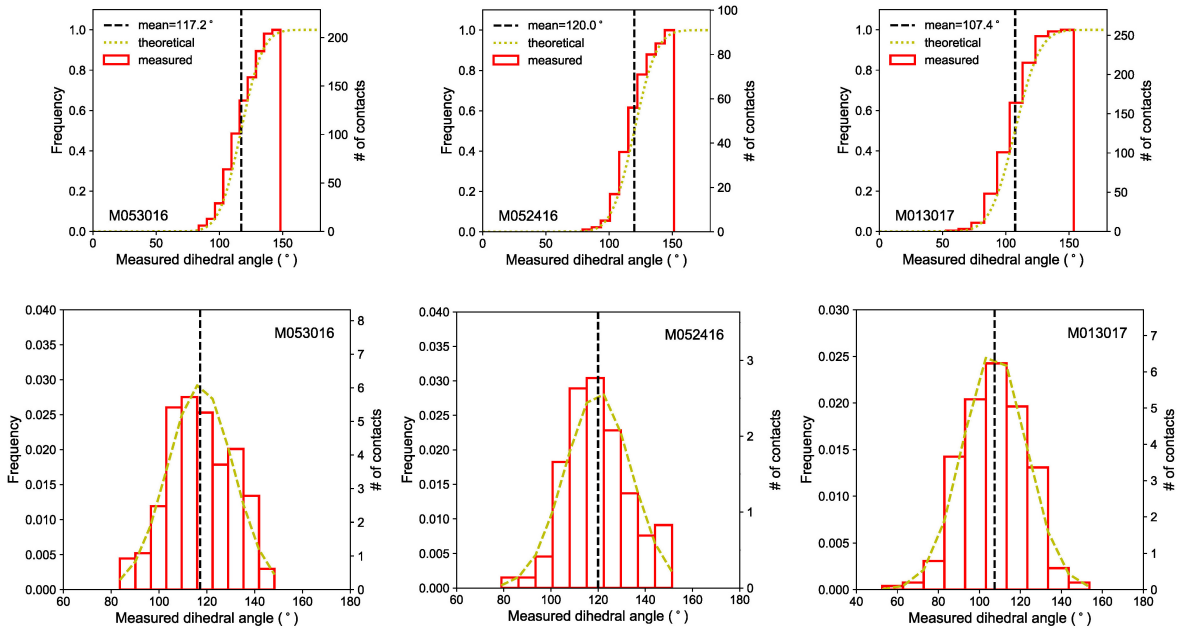

FIGURE 5 | Cumulative **(upper panel)** and simple **(lower panel)** frequency distributions of apparent dihedral angles. The apparent dihedral angles measured from the BSE images of the cross-section for each experiment (red solid line) are compared with the theoretical frequency curves (yellow dashed line). The vertical dashed lines represent the mean values of the apparent dihedral angle distributions.

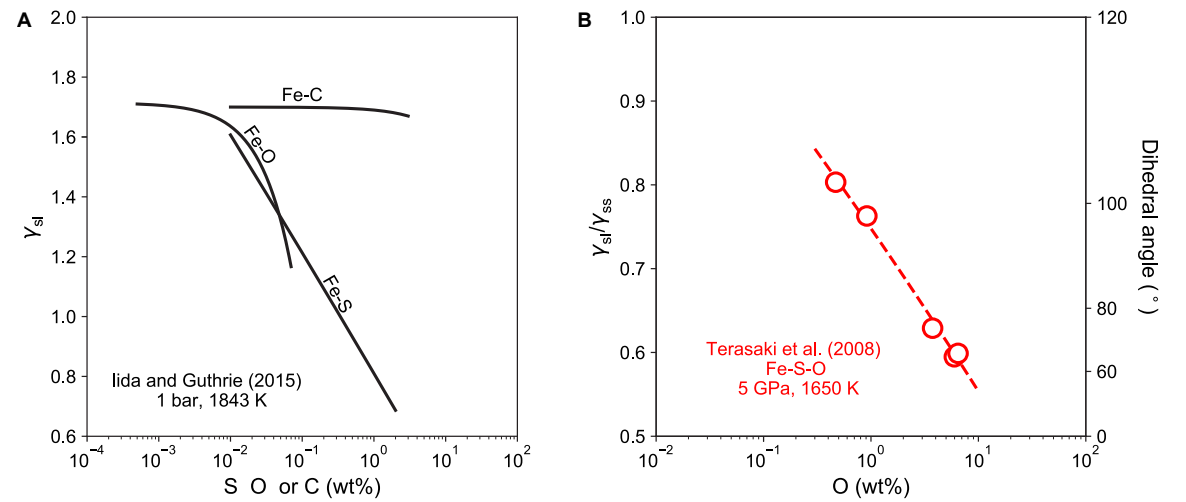

FIGURE 6 | (A) Surface tension of iron-rich melt on aluminum oxide surface as a function of the concentration of lighter alloying element at 1 bar and 1843 K (Halden and Kingery, 1955; Iida and Guthrie, 2015). **(B)** Ratio of surface tensions and dihedral angles of iron-rich melt in mantle silicate as a function of the concentration of lighter alloying element at 5 GPa and 1650 K (Terasaki et al., 2008).

Interfacial Energy and Surface Tension Between Fe–C Melt and Mantle Silicate

The measured dihedral angles allow us to estimate the interfacial energy and surface tension between Fe–C melt and various mantle silicate phases at high pressure and high temperature conditions. The dihedral angle of a liquid in a solid matrix is governed by the interfacial energy per unit area between the liquid and the solid, γ_{sl}, and that between the solid phases, γ_{ss}. In an isotropic system, force balance at the triple junction can be described by the Cahn's equation (e.g., Porter et al., 2009):

$$\frac{\gamma_{ss}}{\gamma_{sl}} = 2 \cdot \cos\frac{\theta}{2} \quad (1)$$

The interfacial energy between solid silicate grains (olivine) is estimated at about 0.9 J/m^2 with a relatively large uncertainty of ±30% (Stevenson, 1990). If this value is applicable to silicates

at high pressures and high temperatures, then the measured dihedral angles of 107–120° yield the interfacial energy between Fe–C melt and major mantle silicates at approximately 0.76–0.9 J/m^2 at 10–23 GPa. The surface tension of Fe–C melt on mantle silicate, which has the identical numerical value to the interfacial energy between liquid and solid (Shannon, 1998), is 0.76–0.9 N/m.

The relation $2\cdot\cos\theta/2 = \gamma_{ss}/\gamma_{sl}$ is derived for simple systems containing a single isotropic solid phase, and therefore it does not hold accurately for anisotropic mantle silicates such as olivine and bridgmanite. Laporte and Watson (1995) showed that with sufficiently high anisotropy the melt may form isolated plane-faced pockets at grain corners. A few experimental studies examined the anisotropy of γ_{sl} at olivine-basalt interface at low pressures (e.g., Schäfer and Foley, 2002), but the influence of anisotropy on the wetting behavior of iron-rich melt system remains to be explored.

According to the relationship between dihedral angle and interfacial energies, $\theta = 120°$ when $\gamma_{ss} = \gamma_{sl}$. Below 120°, θ decreases rapidly with the ratio and reaches the critical value of 60° when $\gamma_{ss} = \sqrt{3}\gamma_{sl} \sim 1.7\gamma_{sl}$ or $\gamma_{sl} \sim 0.6\gamma_{ss}$. This relationship can be applied to understand the effects of composition, pressure, temperature on the wetting properties of Fe–C melt, as will be discussed below.

Composition Effect on the Dihedral Angles of Iron-Rich Melt

Our results show that the measured dihedral angles of Fe–C melt in silicates remained near 120°, indicating that the Fe–C melt does not wet major silicate phases in the mantle. The surface-avoiding or surface-phobic behavior of carbon is similar to that observed in metallurgical studies at ambient pressure (Halden and Kingery, 1955; Iida and Guthrie, 2015). It has been shown that at ambient pressure adding carbon to an iron liquid has little effect on the surface tension of liquid iron, which remains high even with more than 10 wt% of carbon (**Figure 6A**). In contrast, metallurgical studies showed that the surface tension of iron-rich liquid on aluminum oxide is sensitive to the presence of alloying elements such as O and S. At 1 bar and 1843 K, adding 0.1 wt% oxygen rapidly reduces the surface tension of liquid iron on alumina to by about 35%, whereas adding the same amount of sulfur to liquid iron reduces the surface tension by 30% (**Figure 6A**). These elements are therefore known as surface-loving elements or surfactants.

At high pressures, the dihedral angle of iron-rich melt in silicate is also influenced by the presence of alloying elements such as O and S (**Figure 6B**). For example, adding oxygen to an Fe–S melt lowers its dihedral angle in silicate matrix, which could fall below the critical value of 60° at sufficiently high oxygen concentrations (Terasaki et al., 2005, 2007, 2008). Other non-metal elements, such as S (e.g., Terasaki et al., 2005), Si (e.g., Mann et al., 2008), and P (e.g., Terasaki et al., 2007) can also reduce the dihedral angle of iron-rich melt in silicate, although the effect is weaker than oxygen.

Previous studies found that oxidized starting material or moistures trapped in sample capsule may introduce oxygen to the melt, as revealed by the presence of tiny FeO blobs exsolved from iron-rich melt upon quench (e.g., Terasaki et al., 2005). Carbon and oxygen are likely incompatible in iron-rich melt (Fischer et al., 2015). In this study, no tiny blob was observed in the quenched Fe–C melt, suggesting little influence of oxygen on the measured dihedral angles.

Effect of Pressure on the Dihedral Angle of Fe–C Melt in Silicate

The results from this study show little pressure dependence of the dihedral angle of Fe–C melt in mantle silicate between 10 and 23 GPa, with the variations from 107 to 120° falling within the measurement uncertainty of ±14–16° (**Figure 7**). The measured angles are also comparable to the dihedral angle of 115° between Fe–C melt with 4.3 wt% carbon and olivine at 3 GPa and 1400°C (Duncan and Fei, 2017).

Pressure can influence the dihedral angle of Fe-rich melt in silicate in a number of ways (Shannon, 1998). Misalignment of crystal lattices produces excess volume or gap, which contributes to interfacial energy γ_{ss}. The excess volume between melt and crystal is likely smaller because atoms in the melt are not constrained by a lattice and hence moves more freely to fill space. Upon compression, the amount of lattice misalignment may change as a result of pressure-induced preferred orientation, polymorphic structural transformation, or

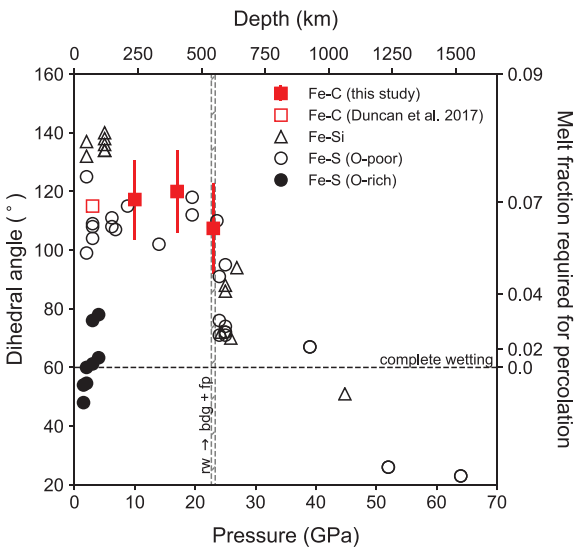

FIGURE 7 | Dihedral angle of Fe-rich melt in silicate or silicate plus oxide matrix as a function of pressure. The dihedral angles of Fe–C melt from this study (solid squares with error bar) and that of between an Fe–C melt containing 4.3 wt% carbon in olivine (open square, Duncan and Fei, 2017) are above 100°. Plotted for comparison are data on oxygen-poor Fe–S melt (open circles, Terasaki et al., 2008), oxygen-rich Fe–S melt (closed circle, Shannon and Agee, 1996, 1998; Shi et al., 2013), and Fe–Si melt (Open triangles, Takafuji et al., 2004; Mann et al., 2008). Dashed horizontal line marks the critical angle of 60° for complete wetting. The vertical bar marks the boundary where ringwoodite (Rw) breaks down to form bridgmanite (Bdg) and ferropericlase (Fp). The melt fraction required for percolation at a given dihedral angle, known as the percolation threshold, is marked on the right *Y*-axis.

even chemical reaction such as the breakdown of ringwoodite into bridgmanite and ferropericlase. Compression likely reduces the difference between the two excess volumes, leading to a smaller γ_{ss}/γ_{sl}, hence larger dihedral angle.

Compression may also affect the chemical properties of the interface such as the partitioning of surface-active elements between the coexisting melt and solid. For instance, significant chemical change such as enhanced solubility of oxygen in iron-rich alloy may have reduced γ_{sl}, thus lowering the dihedral angle (Terasaki et al., 2008). Even if the solubilities of surface-active elements remain constant, their surface activities may change with pressure (Shannon, 1998). The same amount of sulfur affects dihedral angle less significantly at high pressure (Shannon, 1998) than at 1 bar (Iida and Guthrie, 2015). Furthermore, segregation of certain species into the grain boundary may occur as a result of compression (Shannon, 1998). These changes could affect γ_{ss} and γ_{sl} and thus the dihedral angle.

The absence of pressure effect on the dihedral angle of Fe–C melt in mantle silicates suggests that ratio of interfacial energies remain nearly unchanged between 3 and 23 GPa, unless various pressure-induced effects on the ratio fortuitously offset each other. Within the pressure range of the upper mantle and transition zone, the dihedral angle of Fe–S melt with 12–14 wt% S in silicate also falls between 100 and 120°, showing little pressure dependence (**Figure 7**; Shannon and Agee, 1996). For Fe–Si melt in silicate, available data at pressure below 5 GPa do not show any pressure dependence either (**Figure 7**; e.g., Mann et al., 2008).

At higher pressures, diamond-anvil cell experiments on Fe–Si melt up to 47 GPa and 3000 K (Takafuji et al., 2004) and on Fe–S melt up to 64 GPa and 3300 K (Shi et al., 2013) showed that the dihedral angles of molten iron-alloys in bridgmanite matrix decreased rapidly with increasing pressure and temperature to below the critical value of 60° (**Figure 7**). The large negative pressure effect may be related to large deviatoric stress in solid phases, which would increase γ_{ss} significantly and therefore reducing θ (**Figure 5**; Rubie and Jacobson, 2016). Alternatively, significant chemical change such as enhanced solubility of oxygen in the iron-rich alloy may have reduced γ_{sl}, thus reducing the dihedral angle (Terasaki et al., 2008). It is also possible that temperature effect plays an important in the observed reduction of dihedral angle, as discussed below.

Effect of Temperature on the Wetting Behavior of Fe–C Melt in Mantle Silicate

No temperature effect on the dihedral angle of Fe–C melt in mantle silicate was observed between 1600 and 1800°C, at 10–23 GPa. Strong temperature dependence of surface tension was reported in metallurgical studies on iron alloys at 1 bar (e.g., Passerone and Sangiorgi, 1985). At 25 GPa, the dihedral angle of Fe–Si melt in bridgmanite decreases from 94° at 2400 K to 70° at 2800 K (Takafuji et al., 2004), also suggesting potentially significant temperature effect on the surface tension of compressed iron-rich melt, especially at temperatures approaching the melting point of the solid phase. In this study, the experimental temperatures were near the eutectic temperatures of Fe–C binary systems and far below the melting point of the silicate matrixes. The relatively low temperatures and small temperature range may explain the absence of temperature effect in our data.

At deep Earth conditions, it is often difficult to separate the effects of pressure, temperature, and composition on the dihedral angle. The temperature of a dihedral angle experiment must fall above the liquidus of iron-rich alloy and below the solidus of silicates, leaving a relatively narrow temperature range at which iron-rich melt coexists with solid silicate. This range usually shifts upward as pressure increases (**Figure 3**), and therefore it may be impossible to isolate the pressure and temperature effects. For Fe–S, the pressure rise from 25 to 64 GPa is accompanied by an increase of temperature from 2300 to 3300 K (Shi et al., 2013); thus it remains unclear if temperature, pressure, or both are responsible for the decrease in the dihedral angle of Fe–S in silicates.

Effect of Crystalline Structure on the Dihedral Angle of Fe–C Melt in Silicate

Our results show that the dihedral angle of Fe–C melt is not affected by pressure-induced polymorphic transition or decomposition of silicate at mid-mantle conditions. In the experiments, olivine powder grew in crystal size at 10 GPa, and transformed into ringwoodite at 17 GPa. At 23 GPa, ringwoodite broke down to form bridgmanite and ferropericlase. The measured dihedral angles of Fe–C melt remained near 115°. In contrast, the wetting behavior of Fe–S changed abruptly upon the break-down of ringwoodite, with the dihedral angle of Fe–S melt with 12–14 wt% S dropping from approximately 108° at upper mantle conditions to 71° at 25 GPa (Shannon and Agee, 1998). It is possible that the presence of ferropericlase increased the solubility of oxygen in the Fe–S melt, thus lowering its surface tension, whereas oxygen remains highly insoluble in the Fe–C melt, which is more reducing than the Fe–S melt.

Melt Connectivity and Percolation Threshold

The dihedral angles of Fe–C melt in silicate matrix at 3–23 GPa are well above the critical value of 60°, implying that Fe–C melt can only flow through mantle silicate when its volume fraction exceeds ∼7%. Dihedral angle measures the ability of liquid to wet a solid matrix. A dihedral angle of 60° or smaller implies complete wetting, where an interconnected network of liquid forms regardless of the melt fraction. A dihedral angle that is greater than 60° implies that a fraction of melt may be stranded in the solid matrix as isolated pockets. The minimum volume fraction of liquid to form a network that enables passage is known as the percolation threshold, f_p. For homogeneously distributed melt in solid matrix, f_p can be estimated from θ through the following relationship:

$$f_p \sim 0.009\sqrt{\theta - 60} \quad (2)$$

With θ ∼ 120°, the percolation threshold is estimated at ∼7 vol% (e.g., von Bargen and Waff, 1986; Stevenson, 1990). It should be noted that dihedral angle is a function of interfacial energy ratio (Eq. 1) while connectivity can be affected by both dihedral angle

and melt fraction. Full connectivity of Fe-rich melt in silicate will develop at a wetting angle of $>60°$ if the melt fraction is sufficiently large. However, at very low melt fractions, as relevant to the amount of metallic melt in the Earth's mantle, percolative drainage (forming an interconnected network) can only occur when the wetting angle of Fe-rich melt is below 60°.

Below the threshold, percolation of iron-rich melt through silicate may still occur if the silicate matrix becomes partially molten (e.g., Duncan and Fei, 2017) or deforms under shear stress (e.g., Todd et al., 2016). Although the presence of partial melt of silicate does not change the dihedral angles of iron-rich melt (e.g., Holzheid, 2013), droplets of dense iron-rich melt can sink through molten silicate, especially when the amount of silicate melt is large enough to create channels (Duncan and Fei, 2017). The presence of non-wetting silicate melt may also raise the percolation threshold of iron-rich melt (Yoshino et al., 2004).

A number of studies have investigated if shear deformation can enhance connectivity of iron-rich melt and facilitate its percolation through silicate, but the effect remains poorly constrained. Walte et al. (2011) suggested that deformation only promote Fe–S melt segregation at high strain rates, with no influence at geologically relevant strain rates. Todd et al. (2016) also showed that the ability of Fe–S melt to flow through olivine matrix did not change with the amount of shear deformation. Cerantola et al. (2015) further suggested that the onset of silicate melting nullifies any effect of deformation on melt segregation and may hinter segregation of Fe-rich melt by reducing its connectivity. In contrast, Berg et al. (2017) suggested that deformation aided percolation at high pressure over a very large range of strain rates.

Implications for Earth's Deep Carbon Cycle

The measured large dihedral angles and estimated high percolation thresholds imply that percolation may not be a viable mechanism to segregate Fe–C melt from the mantle into the core. The amount of Fe–C melt in the mid-mantle was estimated at no more than 1 wt% (Frost et al., 2004). This is well below the percolation threshold of ~7 vol%, and therefore the Fe–C melt is expected to be stranded as isolated pockets at the mid-mantle pressures.

The presence of other alloying elements such as sulfur, hydrogen, and/or oxygen may allow Fe–C melt to percolate through surrounding silicates toward greater depths. Metallic phases in diamond inclusions consist not only Fe and C but also S and H (Smith et al., 2016). Adding sulfur may reduce the interfacial energy of Fe–C melt and lower the percolation threshold. The effect of hydrogen is not known. While oxygen is effective in lowering the surface tension of iron-rich melt, its solubility in Fe–C melt is likely negligible because of the reducing condition.

Partial melt of silicates may also facilitate percolation of iron-rich melt (Duncan and Fei, 2017). However, the present-day

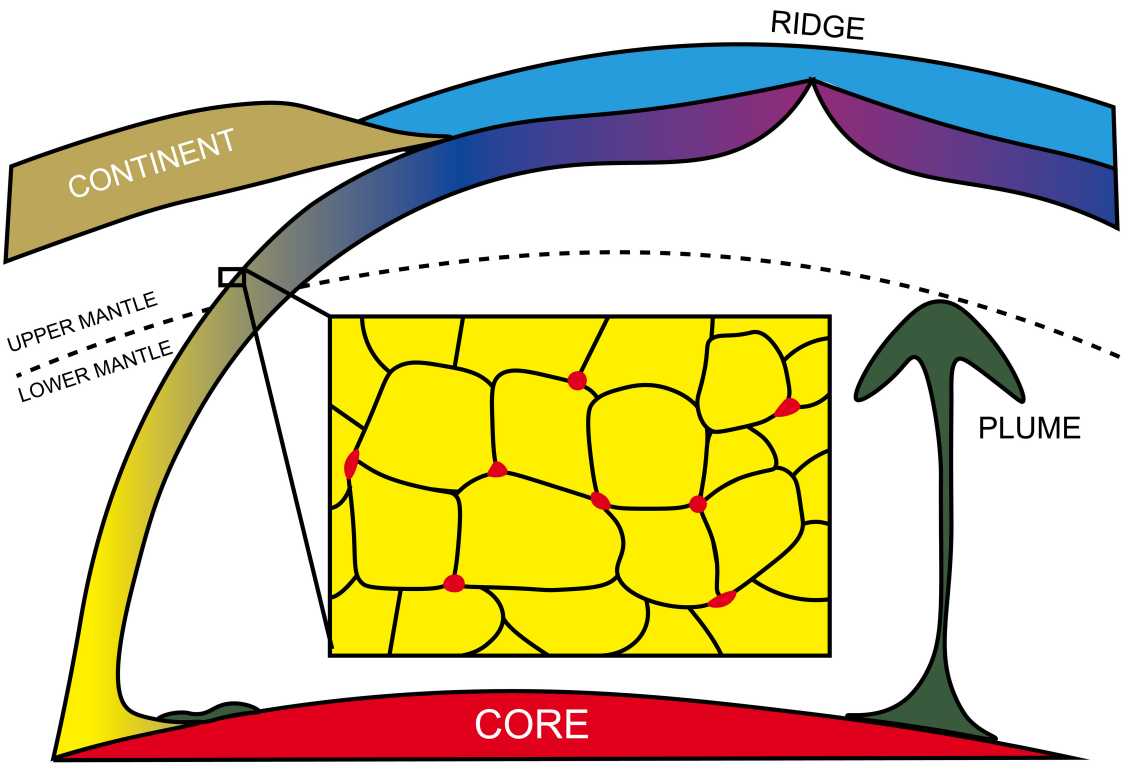

FIGURE 8 | In Earth's mid-mantle (up to 23 GPa), slab-derived Fe–C melt is expected to be trapped as isolated pockets and would not percolate through silicate matrix.

mantle temperature is too low to cause extensive melting of the silicates, thus segregation of Fe–C melt through channels of molten silicate is unlikely.

Given that the percolation threshold of Fe–C binary melt is much higher than the amount of Fe–C melt in the mid-mantle, and that partial melting of silicate matrix is unlikely with the present-day geotherm, we conclude that the slab-derived Fe–C melt is most likely to be retained within the subducting slab at mid-mantle depths during diamond growth, unless its wetting behavior is sufficiently modified by the presence of other alloying elements to allow percolation.

Although slab-derived Fe–C melt may not be able to percolate through the mantle, it may still reach the CMB if the sinking slab materials can survive viscous stirring associated with mantle plumes and remain largely unmixed with the ambient mantle. Liu et al. (2016) proposed that near the base of the mantle, the presence of slab-derived iron–carbon melt in isolated patches may explain seismically observed density excess and velocity features of some ULVZs. Here, we found that the dihedral angle of Fe–C in mid-mantle is larger than 100°. If applicable at the conditions near the CMB, then more than 10 vol% Fe–C is needed to match the ULVZ observations (Liu et al., 2016). This amount is, however, larger than the percolation threshold, implying that not enough Fe–C can be retained in silicate matrix to produce long-lived ULVZs, unless its drainage is hindered by the presence of silicate partial melt (Cerantola et al., 2015). Alternatively, metallic melt may be replenished through on-going subduction or infiltration of core melt back into ferropericlase matrix due to morphological instability (Otsuka and Karato, 2012).

Once at the CMB, Fe–C melt may segregate into the core if the high temperature at the base of the lower mantle lowers its dihedral angle and percolation threshold sufficiently. With an estimated 1 wt% Fe–C in the mantle (e.g., Wood et al., 2013), loss of Fe–C from 40% of the mantle corresponds to 0.8% growth in core mass at the expense of 0.4% reduction in mantle mass, which is equivalent to about 10-km expansion in core radius over Earth's history. This is insignificant for the iron-rich core but would be a major leak for carbon in the silicate Earth.

CONCLUSION

The wetting behavior of Fe–C melt in silicates at mid-mantle conditions have been studied using multi-anvil experiments. The dihedral angles of Fe–C melt in olivine, ringwoodite, and bridgmanite/ferropericlase matrixes are measured at 117° at 10 GPa, 120 ± 14° at 17 GPa, and 107 ± 16° at 23 GPa, respectively. Carbon is found to behave as a surface-avoiding element in silicates at pressures up to 23 GPa, consistent with the high surface tension of Fe–C melt on alumina at 1 bar. Within the experimental ranges, no effect of pressure or temperature was observed.

The measure dihedral angles and estimated percolation thresholds are applied to assess the behavior of Fe–C alloys at deep Earth conditions. The percolation threshold of Fe–C melt in silicates is estimated at 7 vol%, much larger than the amount produced in the mantle. Consequently, Fe–C melt is expected to be retained within subducting slabs at mid-mantle depths (**Figure 8**), unless its surface tension is sufficiently lowered by the presence of other alloying elements such as sulfur. The amount of Fe–C melt needed to match the low shear wave velocity of the ULVZs, however, exceeds the percolation threshold. As a result, continuous replenishment, dynamic stirring, or the presence of non-wetting silicate melt is needed to generate ULVZ through slab-derived metallic melt. The non-wetting behavior of Fe–C implies that active core growth through percolation is unlikely, even though limited draining of Fe–C to the core remains feasible and may cause significant carbon loss from the silicate Earth.

Further investigations are necessary to fully assess the wetting behavior of Fe–C melt during core formation and deep carbon cycle. This study only reached the pressure at the uppermost lower mantle. The wetting behavior of Fe–C melt in main stretch of the lower mantle remains to be studied. Additional work is also needed to demonstrate equilibrium texture through time-series experiments, quantify the composition of the Fe–C melt, evaluate the effect of temperature, and to explore the influence of anisotropy on the wetting behavior of iron-rich melts.

DATA AVAILABILITY STATEMENT

All datasets generated for this study are included in the manuscript/supplementary files.

AUTHOR CONTRIBUTIONS

JL and JD conceived the idea and designed the project. JD performed the experiments and analyzed the data, as part of his undergraduate honors thesis under the supervision of JL. JD and JL wrote the manuscript. FZ helped with the experiments.

FUNDING

This work was partially supported by the National Science Foundation Grants AST 1344133 and EAR 1763189, and the Alfred P. Sloan Foundation Deep Carbon Observatory Grant G-2017-9954 to JL; and a Turner Undergraduate Award from the Department of Earth and Environmental Sciences at University of Michigan, a James Mills Peirce Fellowship from the Graduate School of Arts and Sciences at Harvard University, open access publication funding from the Harvard Open-Access Publishing Equity (HOPE) office, and the Department of Earth and Planetary Sciences (EPS) at Harvard University to JD.

ACKNOWLEDGMENTS

We thank the reviewers, GB and VC, for their reviews that helped to improve and clarify the manuscript; Hidenori Terasaki, Shun-ichiro Karato, Rebecca A. Fischer, Wendy L. Mao, Carl B. Agee, and David (Dave) Walker for discussions and comments; and Paul Kelley, the Harvard Open-Access Publishing Equity (HOPE) office, and the Frontiers Wavier Office for providing open-access funding opportunities.

REFERENCES

Berg, M. T., Bromiley, G. D., Butler, I. B., Frost, M., Bradley, R., Carr, J., et al. (2017). Deformation-aided segregation of Fe-S liquid from olivine under deep earth conditions: implications for core formation in the early solar system. *Phys. Earth Planet. Inter.* 263, 38–54. doi: 10.1016/j.pepi.2017.01.004

Cerantola, V., Walte, N. P., and Rubie, D. C. (2015). Deformation of a crystalline olivine aggregate containing two immiscible liquids: implications for early core–mantle differentiation. *Earth Planet. Sci. Lett.* 417, 67–77. doi: 10.1016/j.epsl.2015.02.014

Duncan, M. S., and Fei, Y. (2017). "Experimental constraints on metal percolation through silicate: implications for core formation on asteroids and planetesimals," in *Lunar and Planetary Science Conference*, Vol. 48, (Houston, TX).

Fei, Y., and Brosh, E. (2014). Experimental study and thermodynamic calculations of phase relations in the Fe–C system at high pressure. *Earth Planet. Sci. Lett.* 408, 155–162. doi: 10.1016/j.epsl.2014.09.044

Fischer, R. A., Nakajima, Y., Campbell, A. J., Frost, D. J., Harries, D., Langenhorst, F., et al. (2015). High pressure metal–silicate partitioning of Ni, Co, V, Cr, Si, and O. *Geochim. Cosmochim. Acta* 167, 177–194. doi: 10.1073/pnas.1108544108

Frost, D. J., Liebske, C., Langenhorst, F., McCammon, C. A., Trønnes, R. G., and Rubie, D. C. (2004). Experimental evidence for the existence of iron-rich metal in the Earth's lower mantle. *Nature* 428, 409–412. doi: 10.1038/nature02413

Halden, F. A., and Kingery, W. D. (1955). Surface tension at elevated temperatures. II. Effect of C, N, O and S on liquid iron surface tension and interfacial energy with Al2O3. *J. Phys. Chem.* 59, 557–559. doi: 10.1021/j150528a018

Herzberg, C., Vidito, C., and Starkey, N. A. (2016). Nickel–cobalt contents of olivine record origins of mantle peridotite and related rocks. *Am. Mineral.* 101, 1952–1966. doi: 10.2138/am-2016-5538

Herzberg, C., Raterron, P., and Zhang, J. (2000). New experimental observations on the anhydrous solidus for peridotite KLB−1. *Geochem., Geophys., Geosyst.* 1:1051. doi: 10.1029/2000GC000089

Hirayama, Y., Fujii, T., and Kurita, K. (1993). The melting relation of the system, iron and carbon at high pressure and its bearing on the early stage of the Earth. *Geophys. Res. Let.* 20, 2095–2098. doi: 10.1029/93gl02131

Holness, M. B., and Lewis, S. (1997). The structure of the halite-brine interface inferred from pressure and temperature variations of equilibrium dihedral angles in the halite-H_2O-CO_2 system. *Geochim. Cosmochim. Acta* 61, 795–804. doi: 10.1016/s0016-7037(96)00370-5

Holzheid, A. (2013). Sulphide melt distribution in partially molten silicate aggregates: implications to core formation scenarios in terrestrial planets. *Eur. J. Mineral.* 25, 267–277. doi: 10.1127/0935-1221/2013/0025-2264

Holzheid, A., Schmitz, M. D., and Grove, T. L. (2000). Textural equilibria of iron sulfide liquids in partly molten silicate aggregates and their relevance to core formation scenarios. *J. Geophys. Res.: Solid Earth* 105, 13555–13567. doi: 10.1029/2000jb900046

Hultgren, R., Orr, R. L., Anderson, P. D., and Kelley, K. K. (1963). *Selected Values of Thermodynamic Properties of Metals and Alloys*. New York, NY: John Wiley and Sons, Inc, 107.

Iida, T., and Guthrie, R. I. (2015). *The Thermophysical Properties of Metallic Liquids: Fundamentals*, Vol. 1. Oxford: Oxford University Press.

Kaminsky, F. V., and Wirth, R. (2011). Iron carbide inclusions in lower-mantle diamond from Juina. Brazil. *Can. Mineral.* 49, 555–572. doi: 10.3749/canmin.49.2.555

Laporte, D., and Watson, E. B. (1995). Experimental and theoretical constraints on melt distribution in crustal sources: the effect of crystalline anisotropy on melt interconnectivity. *Chem. Geol.* 124, 161–184. doi: 10.1016/0009-2541(95)00052-n

Leinenweber, K. D., Tyburczy, J. A., Sharp, T. G., Soignard, E., Diedrich, T., Petuskey, W. B., et al. (2012). Cell assemblies for reproducible multi-anvil experiments (the COMPRES assemblies). *Am. Mineral.* 97, 353–368. doi: 10.2138/am.2012.3844

Li, J., and Fei, Y. (2014). Experimental constraints on core composition. *Treatise Geochem.* 2, 568–546.

Li, Z., and Li, J. (2015). Melting curve of NaCl to 20 GPa from electrical measurements of capacitive current. *Am. Mineral.* 100, 1892–1898. doi: 10.2138/am-2015-5248

Liu, J., Li, J., Hrubiak, R., and Smith, J. S. (2016). Origins of ultralow velocity zones through slab-derived metallic melt. *Proc. Natl. Acad. Sci. U.S.A.* 113, 5547–5551. doi: 10.1073/pnas.1519540113

Lord, O. T., Walter, M. J., Dasgupta, R., Walker, D., and Clark, S. M. (2009). Melting in the Fe–C system to 70 GPa. *Earth Planet. Sci. Lett.* 284, 157–167. doi: 10.1016/j.epsl.2009.04.017

Mann, U., Frost, D. J., and Rubie, D. C. (2008). The wetting ability of Si-bearing liquid Fe-alloys in a solid silicate matrix-percolation during core formation under reducing conditions? *Phys. Earth Planet. Int.* 167, 1–7. doi: 10.1016/j.pepi.2007.12.002

Otsuka, K., and Karato, S.-I. (2012). Deep penetration of molten iron into the mantle caused by a morphological instability. *Nature* 492, 243–246. doi: 10.1038/nature11663

Passerone, A., and Sangiorgi, R. (1985). Solid-liquid interfacial tensions by the dihedral angle method. A mathematical approach. *Acta Metallurgica* 33, 771–776. doi: 10.1016/0001-6160(85)90100-2

Porter, D. A., Easterling, K. E., and Sherif, M. (2009). *Phase Transformations in Metals and Alloys, (Revised Reprint)*. CRC press.

Rohrbach, A., Ballhaus, C., Golla–Schindler, U., Ulmer, P., Kamenetsky, V. S., and Kuzmin, D. V. (2007). Metal saturation in the upper mantle. *Nature* 449, 456–458. doi: 10.1038/nature06183

Rohrbach, A., and Schmidt, M. W. (2011). Redox freezing and melting in the Earth's deep mantle resulting from carbon–iron redox coupling. *Nature* 472, 209–212. doi: 10.1038/nature09899

Rubie, D. C., and Jacobson, S. A. (2016). Mechanisms and geochemical models of core formation. *Deep Earth: Physics and Chemistry of the Lower Mantle and Core* 217, 181–190. doi: 10.1002/9781118992487

Schäfer, F. N., and Foley, S. F. (2002). The effect of crystal orientation on the wetting behaviour of silicate melts on the surfaces of spinel peridotite minerals. *Contrib. Mineral. Petrol.* 143, 254–262. doi: 10.1007/s00410-001-0339-0

Schindelin, J., Arganda-Carreras, I., Frise, E., Kaynig, V., Longair, M., Pietzsch, T., et al. (2012). Fiji: an open-source platform for biological-image analysis. *Nat. Methods* 9, 676–682. doi: 10.1038/nmeth.2019

Shannon, M. C. (1998). *Percolation of Iron Melts Through Mantle Minerals at High Pressure: Implications for Core Formation*. Ph.D. Dissertation, Harvard University, Cambridge, MA.

Shannon, M. C., and Agee, C. B. (1996). High pressure constraints on percolative core formation. *Geophys. Res. Lett.* 23, 2717–2720. doi: 10.1029/96gl02817

Shannon, M. C., and Agee, C. B. (1998). Percolation of core melts at lower mantle conditions. *Science* 280, 1059–1061. doi: 10.1126/science.280.5366.1059

Shi, C. Y., Zhang, L., Yang, W., Liu, Y., Wang, J., Meng, Y., et al. (2013). Formation of an interconnected network of iron melt at Earth's lower mantle conditions. *Nat. Geosci.* 6, 971. doi: 10.1038/ngeo1956

Smith, E. M., Shirey, S. B., Nestola, F., Bullock, E. S., Wang, J., Richardson, S. H., et al. (2016). Large gem diamonds from metallic liquid in Earth's deep mantle. *Science* 354, 1403–1405. doi: 10.1126/science.aal1303

Stevenson, D. J. (1990). "Fluid Dynamics of Core Formation," in *Origin of the Earth*. Oxford: Oxford University Press, 231–249.

Stickels, C. A., and Hucke, E. E. (1964). Measurement of dihedral angles. *Trans. Metallurgical Soc. AIME* 230:795.

Stixrude, L., and Lithgow-Bertelloni, C. (2011). Thermodynamics of mantle minerals-II. Phase equilibria. *Geophys. J. Int.* 184, 1180–1213. doi: 10.1111/j.1365-246x.2010.04890.x

Takafuji, N., Hirose, K., Ono, S., Xu, F., Mitome, M., and Bando, Y. (2004). Segregation of core melts by permeable flow in the lower mantle. *Earth Planet. Sci. Lett.* 224, 249–257. doi: 10.1016/j.epsl.2004.05.016

Terasaki, H., Frost, D. J., Rubie, D. C., and Langenhorst, F. (2005). The effect of oxygen and sulphur on the dihedral angle between Fe–O–S melt and silicate minerals at high pressure: implications for Martian core formation. *Earth Planet. Sci. Lett.* 232, 379–392. doi: 10.1016/j.epsl.2005.01.030

Terasaki, H., Frost, D. J., Rubie, D. C., and Langenhorst, F. (2007). Interconnectivity of Fe–O–S liquid in polycrystalline silicate perovskite at lower mantle conditions. *Phys. Earth Planet. Int.* 161, 170–176. doi: 10.1016/j.pepi.2007.01.011

Terasaki, H., Frost, D. J., Rubie, D. C., and Langenhorst, F. (2008). Percolative core formation in planetesimals. *Earth Planet. Sci. Lett.* 273, 132–137. doi: 10.1073/pnas.1707580114

Todd, K. A., Watson, H. C., Yu, T., and Wang, Y. (2016). The effects of shear deformation on planetesimal core segregation: results from in-situ X-ray micro-tomography. *Am. Mineral.* 101, 1996–2004. doi: 10.2138/am-2016-5474

von Bargen, N., and Waff, H. S. (1986). Permeabilities, interfacial areas and curvatures of partially molten systems: results of numerical computations of equilibrium microstructures. *Journal of Geophysical Research: Solid Earth*, 91, 9261–9276. doi: 10.1029/JB091iB09p09261

Walte, N. P., Rubie, D. C., Bons, P. D., and Frost, D. J. (2011). Deformation of a crystalline aggregate with a small percentage of high-dihedral-angle liquid: implications for core–mantle differentiation during planetary formation. *Earth Planet. Sci. Lett.* 305, 124–134. doi: 10.1016/j.epsl.2011.02.049

Williams, Q., Jeanloz, R., Bass, J., Svendsen, B., and Ahrens, T. J. (1987). The melting curve of iron to 250 gigapascals: a constraint on the temperature at Earth's center. *Science* 236, 181–182. doi: 10.1126/science.236.4798.181

Wood, B. J., Li, J., and Shahar, A. (2013). Carbon in the core: its influence on the properties of core and mantle. *Rev. Mineral. Geochem.* 75, 231–250. doi: 10.1126/sciadv.1701840

Yoshino, T., Walter, M. J., and Katsura, T. (2004). Connectivity of molten Fe alloy in peridotite based on in situ electrical conductivity measurements: implications for core formation in terrestrial planets. *Earth Planet. Sci. Lett.* 222, 625–643. doi: 10.1016/s0012-821x(04)00182-7

Zhimulev, E. I., Chepurov, A. I., Sonin, V. M., Litasov, K. D., and Chepurov, A. A. (2018). Experimental modeling of percolation of molten iron through polycrystalline olivine matrix at 2.0–5.5 GPa and 1600°C. *High Press. Res.* 38, 153–164. doi: 10.1080/08957959.2018.1458847

Conflict of Interest: The authors declare that the research was conducted in the absence of any commercial or financial relationships that could be construed as a potential conflict of interest.

frontiers in Earth Science

ORIGINAL RESEARCH
published: 24 October 2019
doi: 10.3389/feart.2019.00264

Understanding Degassing Pathways Along the 1886 Tarawera (New Zealand) Volcanic Fissure by Combining Soil and Lake CO_2 Fluxes

Ery C. Hughes[1,2,3], Agnes Mazot[2], Geoff Kilgour[2], Cameron Asher[2], Marco Michelini[2,4], Karen Britten[2], Lauriane Chardot[2,5], Yves Feisel[2,6] and Cynthia Werner[7]*

[1] School of Earth Sciences, University of Bristol, Bristol, United Kingdom, [2] Wairakei Research Centre, GNS Science, Taupō, New Zealand, [3] Division of Geological and Planetary Sciences, California Institute of Technology, Pasadena, CA, United States, [4] Space Research Coordination Center, University of Pittsburgh, Pittsburgh, PA, United States, [5] Earth Observatory of Singapore, Nanyang Technological University, Singapore, Singapore, [6] Institute of Geosciences, Johannes Gutenberg-Universität Mainz, Mainz, Germany, [7] Private Contractor, New Plymouth, New Zealand

CO_2 flux measurements are often used to monitor volcanic systems, understand the cause of volcanic unrest, and map sub-surface structures. Currently, such measurements are incomplete at Tarawera (New Zealand), which erupted with little warning in 1886 and produced a ∼17 km long fissure. We combine new soil CO_2 flux and C isotope measurements of Tarawera with previous data from Rotomahana and Waimangu (regions also along the 1886 fissure) to fingerprint the CO_2 source, understand the current pathways for degassing, quantify the CO_2 released along the entire fissure, and provide a baseline survey. The total CO_2 emissions from the fissure are 1227 $t \cdot d^{-1}$ (742–3398 $t \cdot d^{-1}$ 90 % confidence interval), similar to other regions in the Taupō Volcanic Zone. The CO_2 flux from Waimangu and Rotomahana is far higher than from Tarawera (>549 vs. ∼4 $t \cdot d^{-1}$ CO_2), likely influenced by a shallow silicic body at depth and Okataina caldera rim faults increasing permeability at the southern end of the fissure. Highly localized regions of elevated CO_2 flux occur along the fissure and are likely caused by cross-cutting faults that focus the flow. One of these areas occurs on Tarawera, which is emitting ∼1 $t \cdot d^{-1}$ CO_2 with a $\delta^{13}CO_2$ of -5.5 ± 0.5 ‰, and comparison with previous observations shows that activity is declining over time. This region highlights the spatial and temporal complexity of degassing pathways at volcanoes and that sub-surface structures exert a primary control on the magnitude of CO_2 flux in comparison to the surface mechanism (i.e., CO_2 released through the soil or lake surface).

Keywords: Tarawera, Waimangu, Rotomahana, CO_2 flux, carbon isotopes, volcanic degassing, gas permeability

OPEN ACCESS

Edited by:
Artur Ionescu, Babeş-Bolyai University, Romania

Reviewed by:
Colin J. N. Wilson, Victoria University of Wellington, New Zealand
Dmitri Rouwet, National Institute of Geophysics and Volcanology (INGV), Italy

****Correspondence:***
Ery C. Hughes
ehughes@caltech.edu

Specialty section:
This article was submitted to Volcanology, a section of the journal Frontiers in Earth Science

Received: *25 May 2019*
Accepted: *24 September 2019*
Published: *24 October 2019*

Citation:
Hughes EC, Mazot A, Kilgour G, Asher C, Michelini M, Britten K, Chardot L, Feisel Y and Werner C (2019) Understanding Degassing Pathways Along the 1886 Tarawera (New Zealand) Volcanic Fissure by Combining Soil and Lake CO_2 Fluxes. Front. Earth Sci. 7:264. doi: 10.3389/feart.2019.00264

INTRODUCTION

Carbon dioxide (CO_2) is the second most abundant gas emitted from magma and, due to its low solubility, exsolves at relatively high pressures (mid-crust to potentially upper mantle) (e.g., Mysen et al., 1975; Blank and Brooker, 1994; Ni and Keppler, 2013; Edmonds and Wallace, 2017). CO_2 emerges at the surface both actively during eruption and passively during quiescent periods, either

through advection in volcanic plumes and fumaroles or diffusively through lakes and soils (e.g., Baubron et al., 1990; Allard et al., 1991; Burton et al., 2013). Areas of elevated CO_2 flux can be mapped to elucidate the magmatic and hydrothermal system, such as the occurrence of deep-seated structures or other preferential pathways, for instance dikes, faults, or variable geological units (e.g., Hernández et al., 2001; Werner and Cardellini, 2006; Carapezza et al., 2009; Mazot et al., 2011; Hutchison et al., 2015; Cardellini et al., 2017). Moreover, repeat measurements of CO_2 degassing in a volcanic area can be integrated over time to monitor changes, allowing for the discernment of potential causes of volcanic unrest (e.g., Baubron et al., 1991; Diliberto et al., 2002; Granieri et al., 2003; Badalamenti et al., 2004; Carapezza et al., 2008; Inguaggiato et al., 2011; Jácome Paz et al., 2016).

Here, we examine the CO_2 flux along the ∼17 km long fissure produced by the 10 June 1886 eruption of Tarawera volcano, New Zealand (e.g., Thomas, 1888; Cole, 1970; Nairn, 1979). In this explosive basaltic eruption, a fissure sliced through the pre-existing rhyolite domes (Tarawera Volcanic Complex) in the north-east, whilst in the south-west, the fissure intersected an active hydrothermal system. After The 1886 eruption, the craters from the fissure filled with water forming Lake Rotomahana and the Waimangu Geothermal System became established. Previous work has shown that the Waimangu-Rotomahana portion of the fissure has high CO_2 emissions (Hurst et al., 2006; Mazot et al., 2014), but there was no quantification for the Tarawera portion of the fissure. Hence, we present new soil CO_2 flux and isotope measurements collected on Tarawera, along the fissure created by the 1886 eruption. These data are combined with measurements of soil CO_2 flux at Waimangu (Hurst et al., 2006) and the surface CO_2 flux of Lake Rotomahana (Mazot et al., 2014). We use these data to understand the source of CO_2, investigate the controls on degassing pathways along the 1886 fissure, and calculate the total CO_2 emissions. Further, our baseline survey can now be compared to future measurements, especially during times of volcanic unrest.

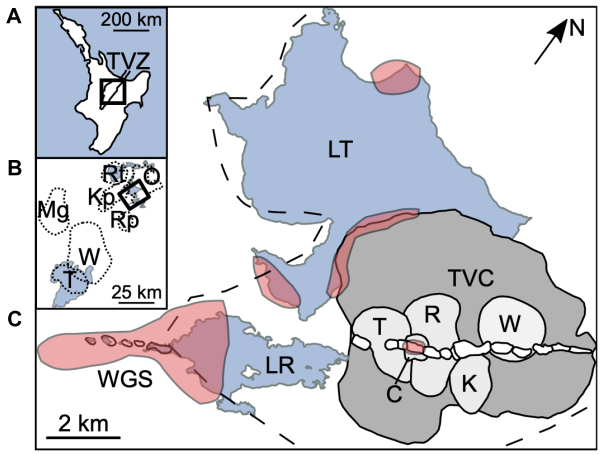

FIGURE 1 | (A) North island of New Zealand with the location of the Taupō Volcanic Zone (TVZ), where the black square shows the area covered in **(B)** caldera systems (black, dotted lines: Rt = Rotorua, O = Okataina, Kp = Kapenga, Rp = Reporoa, Mg = Mangakino, W = Whakamaru, and T = Taupō) and lakes (blue) within the Taupō Volcanic Zone, where the black square shows the area covered in **(C)** Waimangu Geothermal System (WGS), Lake Rotomahana (LR), and Tarawera Volcanic Complex (TVC, dark gray with black, solid outline), including the recent domes (light gray with black, solid outline: T = Tarawera, C = Crater, R = Ruawahia, K = Kanakana, and W = Wahanga) and 1886 fissure (white with black, solid outline), where lakes are in blue (LT = Lake Tarawera), red regions are areas of geothermal activity from Nairn (2002), and the black, dashed line indicates the Okataina caldera rim.

GEOLOGICAL AND VOLCANOLOGICAL SETTING

The Tarawera Linear Vent Zone is one of two linear vent zones in the Okataina Volcanic Centre, which is the most recently active rhyolitic centre in the Taupō Volcanic Zone, New Zealand (**Figures 1A,B**; Healy, 1962; Nairn, 2002). The most recent domes in the Tarawera Volcanic Complex were produced in the ∼1314 Kaharoa eruption, namely: Crater, Wahanga, Ruawahia, and Tarawera (**Figure 1C**; Nairn et al., 2001). The most recent eruption occurred on 10 June 1886, which was a basaltic Plinian eruption resulting in a ∼17 km long fissure and caused New Zealand's largest number of fatalities from a volcanic eruption at 108 people (Walker et al., 1984; Keam, 1988). The eruption lasted for 5 h with the fissure extending from Tarawera south-westwards to the area now occupied by Lake Rotomahana and the Waimangu Geothermal System (**Figure 1C**; Walker et al., 1984; Keam, 1988; Simmons et al., 1993). Pre-eruption, the Rotomahana area contained two smaller lakes (Rotomahana and Rotomakariri) and the sinter deposits of the Pink and White Terraces (Nairn, 1979). Phreatomagmatic eruptions occurred in the Waimangu-Rotomahana region and at the beginning and end of the eruption at Tarawera, whereas magmatic eruptions (Strombolian to Plinian in intensity) occurred on Tarawera itself during the main eruptive phase (Nairn, 1979; Walker et al., 1984; Sable et al., 2006, 2009). There was no thermal activity reported at Tarawera prior to the 1886 eruption and the eruption was preceded by little warning (Nairn, 2002). Since the 1886 eruption, most activity has been concentrated in Waimangu and Rotomahana (**Figure 1C**). Geothermal activity has been well-studied at Rotomahana, consisting of fumaroles, hot springs and geysers, as well as bubbling areas within the lake (e.g., Walker et al., 2015; Stucker et al., 2016). Waimangu consists of hot springs, crater lakes (such as Frying Pan and Inferno), steaming and altered ground, minor silica deposits, and has had hydrothermal eruptions since 1886 (e.g., Mongillo, 1994; Vandemeulebrouck et al., 2008).

For many months after the 1886 eruption, steam continued to be emitted from the fissure walls on Tarawera (Cole, 1970), but in more recent times activity has been relatively minor. Nairn (2002) describes five localities in Crater and Tarawera domes where steam rose from regions of warm ground and two low-pressure fumaroles, with temperatures of 55°C (1973) and 70°C (1980) for the Crater dome fumaroles (**Figure 1C**). These features are closely associated with outcrops of the 1886 basaltic dike and

their location and intensity remained constant over time (Nairn, 2002). In 1985, there were two small active steam vents in the deep crater between Ruawahia and Tarawera domes, although activity was reported to be waning (Nairn, 2002). Giggenbach et al. (1993) reported the temperature and gas compositions for a fumarole (Tarawera forest, 98°C) and spring (Tarawera swamp, 20°C) sampled in 1987/89, but the exact locations of the features are not given. These gas compositions suggest mixing between a MOR-type mantle component [R_M/R_A = 5.92–6.63, where R is the $^3He/^4He$ of the sample (M) and the present-day Earth's atmosphere (A)] and a CO_2-enriched component (CO_2 = 970–980 mmol/mol dry gas) from subducted marine sediments, which is consistent with other volcanic features in the Taupō Volcanic Zone (Giggenbach et al., 1993). The GNS Science Geothermal and Groundwater Database[1] lists three features in Tarawera consisting of two regions of steaming ground and one weakly steaming fumarole, which are all located in Crater J. There are also hot water seepages on the southern edge of Lake Tarawera consisting of warm springs (25–30 °C), gas bubbles, elevated lake floor temperatures, and a low resistivity region (**Figure 1C**; Bennie and Stagpoole, 1985; Whiteford et al., 1996; Nairn, 2002). This suggests that there is currently an ongoing heat and gas source beneath Tarawera (Nairn, 2002).

MATERIALS AND METHODS

Soil CO_2 Flux Measurements

Soil CO_2 flux measurements at Tarawera were made using the accumulation chamber method with a portable non-dispersive Infra-Red system (WS-LI820-CO2: West Systems © S.r.l., Pontedera (PI), Italy; Chiodini et al., 1998). Soil temperatures (∼15 cm below the surface) were made concurrently at each location. The ambient air pressure and temperature were measured at least at the beginning and end of each day, and linearly interpolated for each measurement. Measurements were conducted at least one day after any rainfall, as rain can influence the porosity and the CO_2 degassing to the surface (e.g., Reimer, 1980; Hinkle, 1994).

The 1886 fissure in Tarawera was surveyed during two field campaigns (a total of three days in February–April 2016 and nine days in February–March 2017), where 339 locations were measured (361 measurements in total, including repeats) covering Craters D–K (**Figure 2**). Crater floors, septa, and rims (apart from the northern rim of Wahanga dome, which is sacred to Ngāti Rangitihi iwi) were measured, whilst some areas were inaccessible (although these areas showed no visual indications of degassing). The ground tended to be covered in small scoria (which sometimes made creating a good seal around the chamber difficult) or thin soils (sufficiently deep to create a good seal around the chamber). The steep crater walls and survey scale prevented GPS from accurately recording measurement locations. Therefore, most localities were recorded by annotating and then digitizing Google Earth Images and high-resolution orthophotos, which were generated from a DEM created using a DJI Phantom 4 and Agisoft photoscan. These were combined with differential GPS to locate the measurements. Copies of the annotated maps are included in the **Supplementary Material** to show exact measurement locations. Craters A, B, C, and M were not surveyed as they are highly vegetated and outside the domes themselves. Crater J was surveyed in both 2016 and 2017.

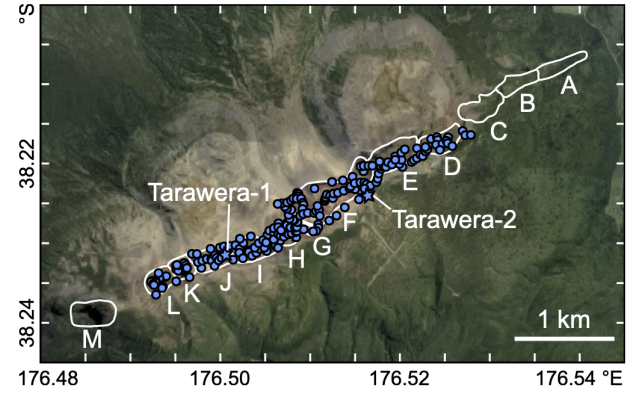

FIGURE 2 | Locations of CO_2 flux measurements at Tarawera with craters (white, solid outline) labeled after Sable et al. (2006). Stars indicate location of isotope samples (Tarawera-1 and Tarawera-2). Image from Google Maps.

Soil CO_2 flux (φ_{CO_2} in $g{\cdot}m^{-2}{\cdot}d^{-1}$) was calculated at each location using:

$$\varphi_{CO_2} = k\frac{V}{A}\frac{T_0}{T}\frac{P}{P_0}\frac{dc}{dt}$$

where dc/dt is the change in CO_2 concentration over time as CO_2 accumulates in the chamber during the measurement ($ppm{\cdot}s^{-1}$), k is a constant to convert to $g{\cdot}m^{-2}{\cdot}d^{-1}$ (155.87 $g{\cdot}d^{-1}$), P is the pressure (kPa), T is the temperature (K), V is the net global volume of the chamber (6.23×10^{-3} m^3), A is the area of the base of the chamber (3.14×10^{-2} m^2), T_0 is 298 K, and P_0 is 101.3 kPa. Where repeat measurements were taken, the average for that location was calculated. The detection limit for this system is ∼1 $g{\cdot}m^{-2}{\cdot}d^{-1}$. All data are available in the **Supplementary Material**.

Soil Gas $\delta^{13}CO_2$ Measurements

Gas samples for $\delta^{13}CO_2$ isotope analysis were collected by extracting gas from the accumulation chamber using a syringe at the beginning and end of a CO_2 flux measurement (Chiodini et al., 2008). One set of samples was collected where the highest CO_2 flux was measured on Tarawera (Tarawera-1), along with samples of ambient air, and one set of samples was collected over vegetation (Tarawera-2) (**Figure 2**). The samples were introduced into evacuated tubes filled with Helium. A Europa Geo 20-20 dual inlet at the National Isotope Centre, GNS Science, New Zealand, was used to measure the $\delta^{13}CO_2$ (reported in ‰ variation relative to VPDB), with a precision of 0.1 ‰.

Additional CO_2 Flux Data

We combine the Tarawera CO_2 flux data with previous surveys of Rotomahana (Mazot et al., 2014) and Waimangu

[1]http://ggw.gns.cri.nz/ggwdata/

(Hurst et al., 2006). The survey of Rotomahana consisted of 484 measurements covering the entire lake surface in 2010–2011, including $\delta^{13}CO_2$ measurements of the gas in bubble plumes (Mazot et al., 2014). The CO_2 flux was measured at the lake surface using the same accumulation chamber method as described in the section "Soil CO_2 Flux Measurements", except the chamber was floating on the lake surface (Mazot, 2005). The survey also measured the chemical and physical properties of the lake water in two vertical profiles and used an echo sounder to locate bubble plumes (Mazot et al., 2014). The survey of Waimangu consisted of 101 locations (102 measurements, including repeats) along two transects using the accumulation chamber method conducted in February 2006 (Hurst et al., 2006). These measurements were collected in conjunction with electrical resistivity measurements and 1 m depth ground temperatures (Hurst et al., 2006).

Data Processing

Graphical statistical analysis was used to separate the CO_2 flux data (excluding data below detection limit) into different log-normal distributions for Tarawera (this study) and Waimangu (Hurst et al., 2006) data separately (graphical statistical analysis for Rotomahana was calculated by Mazot et al., 2014) and the fissure as a whole (Fissure = Waimangu + Rotomahana + Tarawera). The proportion (x), arithmetic mean ($\bar{\varphi}$), and 90 % confidence interval (calculated using the Sichel T-test) of each population are estimated using Sinclair (1974; **Table 1**). The areas of Waimangu and Tarawera were calculated from the minimum bounding rectangle for the measurement locations using the getMinBBox function in the shotGroups package for R (R Core Team, 2018; Wollschlaeger, 2018) and the area of Rotomahana was the lake surface taken from Mazot et al. (2014; **Table 2**). The total CO_2 flux ($T^j_{CO_2}$) was calculated using:

$$T^j_{CO_2} = \sum_{i=A}^{n} x_i \cdot A_j \cdot \bar{\varphi}_i$$

where j refers to Waimangu or Tarawera with area A, and i is the population with proportion x and $\bar{\varphi}$ mean CO_2 flux (**Tables 1** and **2**). The CO_2 flux range is calculated using the lower and upper 90 % confidence interval for CO_2 flux instead of the mean. As the Tarawera data contained data below detection limit, the population proportions were recalculated to include data below detection limit. CO_2 flux measurements below detection limit were assumed to have 0–1 $g{\cdot}m^{-2}{\cdot}d^{-1}$ CO_2 flux. As the surveys were conducted at different spatial resolutions, and hence each measurement does not represent the same area in each region, the total CO_2 flux (and range) for the whole fissure was calculated by summing the individual total (and range) CO_2 fluxes.

Two methods were used to estimate the spatial distribution and total CO_2 flux for the Tarawera data. WinGslib was used to estimate the CO_2 flux for all Tarawera data (Deutsch and Journel, 1998). A variogram quantifies the spatial correlation of the CO_2 flux by comparing the CO_2 flux value at one location to those at other locations at set distances (defined by the lag spacing, which should be similar to the data spacing) and directions (defined by the azimuth and total azimuth for the range of angles considered) (**Figure 3**). For the Tarawera data, a variogram was produced using 65 lags, a lag spacing of 12 m, and an azimuth of 30° with a total azimuth of 30° (**Figure 3**). The variogram was fitted using an azimuth of 30°, a sill of 0.82 (value the variogram plateaus at), nugget of 0.30 (in the ideal case this would be 0 but measurement error elevates this value), and a range of 100 m (value where the data become spatially uncorrelated) (**Figure 3**). This variogram was used in the sequential Gaussian simulations, which were produced using simple kriging, a grid size of 34 × 34 m, a search radius of 40 m, and by averaging 100 simulations. Total CO_2 flux was calculated from the average of the simulations and the error was calculated from the variation between simulations. Only one area at Tarawera was found to

TABLE 1 | Results from graphical statistical analysis.

Population	Proportion (%)	Mean CO_2 flux ($g{\cdot}m^{-2}{\cdot}d^{-1}$)	CO_2 flux range ($g{\cdot}m^{-2}{\cdot}d^{-1}$)
Waimangu-A	7	449	364–684
Waimangu-B	8	119	99–171
Waimangu-C	85	22	20–26
Rotomahana-A[1]	5	1297	670–4343
Rotomahana-B[1]	94	25	23–28
Rotomahana-C[1]	1	0.1	0.06–0.26
Tarawera-A	3	611	246–1138
Tarawera-B	3	67	35–228
Tarawera-C	10	7	6–9
Tarawera-D	9	1	1–2
Tarawera-E	75	bdl	0–1
Fissure-A	3	4586	1600–29759
Fissure-B	8	161	124–201
Fissure-C	52	25	24–27
Fissure-D	3	4	4–5
Fissure-E	3	1	1–2
Fissure-F	30	bdl	0–1

Range is the 90 % confidence interval. [1]*Rotomahana data from Mazot et al. (2014). bdl = below detection limit (<1 $g{\cdot}m^{-2}{\cdot}d^{-1}$ CO_2 flux).*

TABLE 2 | Total CO_2 flux using graphical statistical analysis, sequential Gaussian simulations, and ordinary kriging.

		Total CO_2 flux (range) ($t{\cdot}d^{-1}$)		
Region	Area (km^2)	Graphical statistical analysis	Sequential Gaussian simulations	Ordinary kriging
Waimangu	1.10	66 (52–92)		
Rotomahana[1]	9.63	1113 (667–3211)	549 ± 72	
Tarawera	2.12	48 (20–95)	4.2 ± 2.4 (0.7–13.5)	
Crater J (all)				1.1
Crater J (2016)				0.5
Crater J (2017)				1.2
Fissure	12.85	1227 (742–3398)	>553 ± 72	

Range is 90 % confidence interval. Error is one standard deviation. [1]*Rotomahana data from Mazot et al. (2014). Fissure is calculated using the combined data from Waimangu, Rotomahana, and Tarawera.*

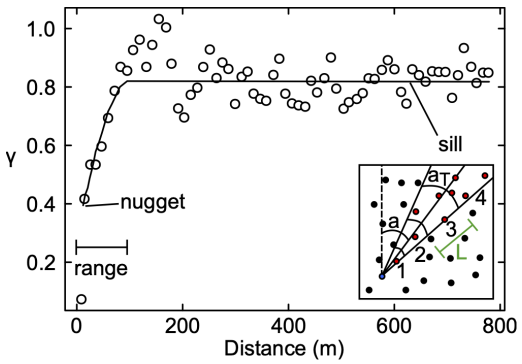

FIGURE 3 | Experimental (65 lags, a lag spacing of 12 m, and an azimuth of 30° with a total azimuth of 30°; white circles) and model (azimuth of 30°, a sill of 0.82, nugget of 0.30, and a range of 100 m; black line) semi-variogram (γ is the variogram value, where higher values indicate the data are more correlated) of Tarawera CO_2 flux normal scores used in the sequential Gaussian simulations. The inset illustrates how the variogram is calculated: the circles represent data points at different spatial locations. The spatial correlation of the blue data point to other data points (variogram) can be calculated considering the red data points which are at azimuth a and within total azimuth a_T. The lag number (*n*) is indicated in black (1, 2, 3, 4) and correlates to distances of L·n, where L is the lag spacing. This procedure was carried out for all data points to calculate the variogram.

be significantly emitting CO_2 (Crater J), and the region over which degassing occurred was much smaller than the grid size required to model the entire Tarawera dataset. Therefore, data from Crater J were interpolated using ordinary kriging with a 3 × 3 m grid spacing, to estimate the spatial variation and CO_2 flux for all, 2016, and 2017 data. The spatial distribution of the Waimangu data does not make interpolation appropriate (Hurst et al., 2006) and sequential Gaussian simulations were applied to the Rotomahana data by Mazot et al. (2014).

RESULTS

We observed no visual hydrothermal activity, such as fumaroles or steaming ground, at Tarawera. Our survey was in summer/spring when it would be less likely to observe low temperature, steaming ground but others (e.g., tour guides, iwi members) who visit the mountain regularly throughout the year have also not observed steaming ground in recent years. 75 % of Tarawera CO_2 flux measurements are below detection limit (bdl, <1 g·m^{-2}·d^{-1} CO_2 flux) (**Table 1**). Repeat measurements in Tarawera at the same location have a range in their variability (flux/mean flux) of ±2–146 % (8 locations) when measured on the same day and ±5–100 % (7 locations) when measured in consecutive years. The $\delta^{13}CO_2$ from the highest CO_2 flux area in Tarawera (within Crater J) is -5.5 ± 0.5 ‰ (**Table 3**). Soil temperatures range from 10–44°C at Tarawera, and soil temperatures do not correlate with CO_2 flux at Waimangu and weakly correlate at Tarawera (**Figure 4**).

Tarawera CO_2 flux can be described by four log-normal distributions (in order of decreasing mean CO_2 flux): Tarawera-A, Tarawera-B, Tarawera-C, and Tarawera-D, with an additional

TABLE 3 | $\delta^{13}CO_2$ isotopic data.

Location	Description	No. samples	CO_2 flux (g·m^{-2}·d^{-1})	$\delta^{13}CO_2$ (‰)
Waimangu[1]	Pools			−3.6 to −3.1
Rotomahana[2]	Bubbles			−2.88 to −2.39
Tarawera-1	Soil	3	3681	−5.5 ± 0.5
Tarawera-1	Air	2		−11.2 ± 1.1
Tarawera-2	Vegetation	4	7.8	−13.8 ± 1.6

Errors are one standard deviation of the repeat measurements for Tarawera data from this study, and other data are from [1]*Giggenbach (1995) and* [2]*Mazot et al. (2014).*

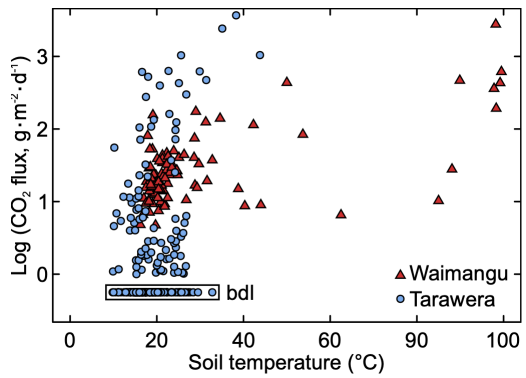

FIGURE 4 | Soil CO_2 flux against soil temperature at ∼1 m depth for Waimangu (red triangles) and ∼15 cm depth for Tarawera (blue circles). Data in the box are below detection limit (bdl, <1 g·m^{-2}·d^{-1} CO_2 flux).

group to include data below detection limit (Tarawera-E) (**Table 1** and **Figures 5B,E**). The total Tarawera CO_2 flux using graphical statistical analysis is 48 t·d^{-1} using an area of 2.12 km^2 for Craters D–K (20–95 t·d^{-1} 90 % confidence interval, **Table 2**). Waimangu CO_2 flux can be described using three log-normal distributions (in order of decreasing mean CO_2 flux): Waimangu-A, Waimangu-B, and Waimangu-C (**Table 1** and **Figures 5A,D**). The total Waimangu CO_2 flux is 66 t·d^{-1} using an area of 1.10 km^2 (52–92 t·d^{-1} 90 % confidence interval) (**Table 2**).

Alternatively, we can apply graphical statistical analysis to the entire fissure (Fissure; **Figure 5C**), including the Rotomahana data from Mazot et al. (2014). As the individual surveys (i.e., for Waimangu, Rotomahana, and Tarawera) have different spatial resolutions, each measurement does not represent the same area and hence the proportions are incorrect. These data are described by six groups (including a group for data below detection limit), compared to 11 required to describe Waimangu, Rotomahana, and Tarawera separately (**Table 1** and **Figure 5F**). By combining all the data, Fissure-A (highest mean CO_2 flux) consists of Waimangu-A, Rotomahana-A, and Tarawera-A; and Fissure-B consists of Waimangu-B and Tarawera-B (**Table 1** and **Figures 5D–F**). Fissure-C has similar characteristics to Waimangu-C and Rotomahana-B; whilst Fissure-D is Tarawera-C, Fissure-E is Tarawera-D, and Fissure-F (data below detection limit) includes Rotomahana-C

and Tarawera-E (**Table 1** and **Figures 5D–F**). The total CO_2 flux from the whole fissure is 1227 t·d^{-1} (742–3398 t·d^{-1} 90 % confidence interval) (**Table 2**).

The CO_2 flux distribution generated using sequential Gaussian simulations for Tarawera is shown in **Figure 6** and the total Tarawera CO_2 flux is 4.2 ± 2.4 t·d^{-1}, with a range of 0.7–13.5 t·d^{-1} (**Table 2**). All high CO_2 flux (Tarawera-A and Tarawera-B, **Table 1** and **Figure 5E**) is found in Crater J (**Figures 6**, **7**), where soil temperatures reach 44°C. Within Crater J, CO_2 degassing is highly localized reaching a maximum of 3200 g·m^{-2}·d^{-1} and decreasing in intensity away from the septum between Craters I and J, where there is an outcrop of basaltic dike from the 1886 eruption (**Figures 6**, **7**). The total CO_2 flux from Crater J is 1.1 t·d^{-1} for all data, 0.5 t·d^{-1} for 2016 data, and 1.2 t·d^{-1} for 2017 data (**Table 2**). Other areas of 1886 dike outcrop do not show elevated CO_2 flux (**Figure 6**). Combining the total CO_2 flux estimate for Rotomahana from Mazot et al. (2014) with Tarawera gives a minimum value of 553 ± 72 t·d^{-1} for the north-eastern section of the whole fissure (**Table 2**). Evaluating the total CO_2 emissions from the whole fissure using sequential Gaussian simulations is not possible as the flux from Waimangu is not fully constrained. The diverse range of features emitting CO_2, such as Frying Pan and Inferno lakes, make it very difficult to accurately quantify the total CO_2 flux in this area.

DISCUSSION

Sources of CO_2

The magnitude of CO_2 flux and its isotopic composition (and soil temperatures) can be combined to identify the source of

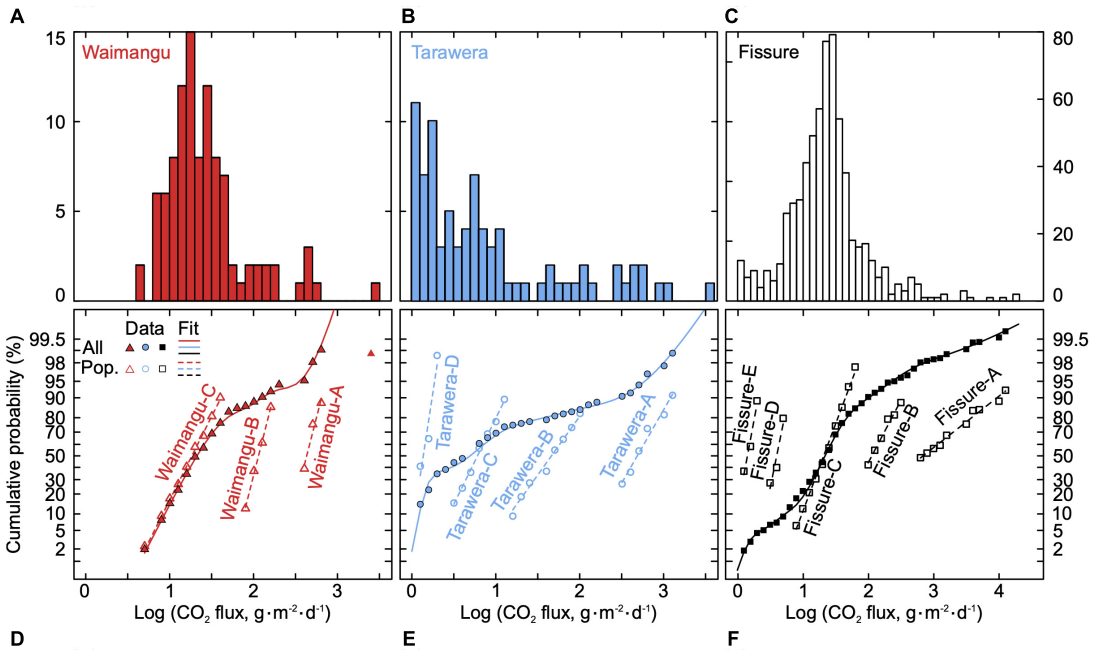

FIGURE 5 | CO_2 flux data for the 1886 fissure: histogram for **(A)** Waimangu, **(B)** Tarawera, and **(C)** the whole fissure (Fissure = Waimangu + Rotomahana + Tarawera); and probability plot for **(D)** Waimangu, **(E)** Tarawera, and **(F)** the whole fissure, where raw data are in closed symbols, populations (abbreviated to Pop.) are in open symbols (labeled according to **Table 1**), and fits are in dashed lines for populations and solid lines for all data. Waimangu data is from Hurst et al. (2006), Rotomahana data from Mazot et al. (2014), and Tarawera data from this study.

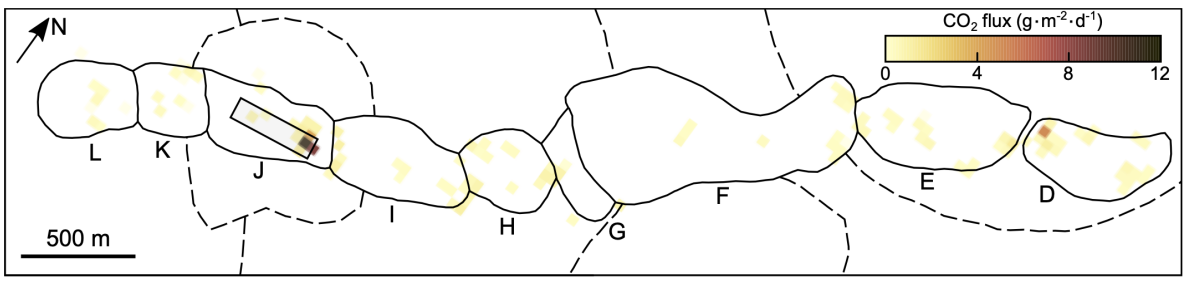

FIGURE 6 | Tarawera CO_2 flux distribution from sequential Gaussian simulations, where craters (solid black outline) and domes (dashed black outline) are from Sable et al. (2006). Location of **Figure 7** shown by gray box.

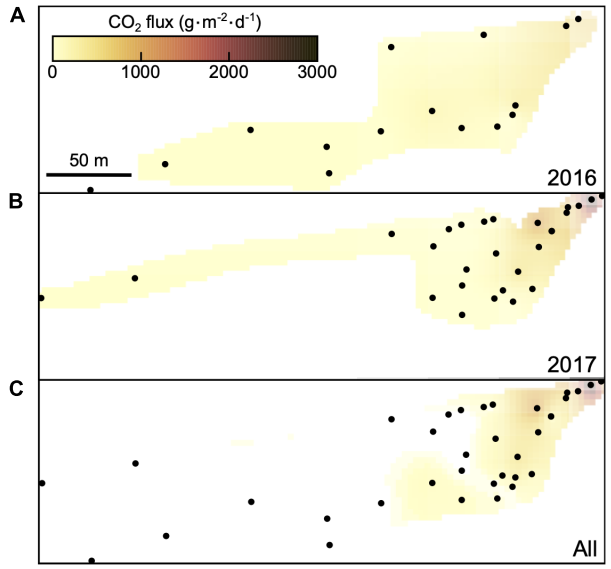

FIGURE 7 | Data from Crater J in Tarawera interpolated using simple kriging for **(A)** 2016, **(B)** 2017, and **(C)** all data, where black circles are the location of CO_2 flux measurements. Location within Crater J shown in **Figure 6** by gray box.

CO_2 (e.g., Chiodini et al., 2008). In general, background CO_2 is typically biogenic with low flux (0.2–21 g·m^{-2}·d^{-1} CO_2) and light isotopic signature (−35 to −7 ‰ $\delta^{13}CO_2$) (Raich and Schlesinger, 1992; Cheng, 1996; Raich and Tufekciogul, 2000; Chiodini et al., 2008). Magmatic CO_2 has higher fluxes (>400 g·m^{-2}·d^{-1} CO_2) and heavier isotopic signatures (>−5 ‰ $\delta^{13}C$) (Chiodini et al., 2008). Also, mixed populations (i.e., background + magmatic) occur.

The number of CO_2 flux groups decreases from 11 to 6 when Waimangu, Rotomahana, and Tarawera are combined (Fissure, **Table 1** and **Figures 5D–F**). This demonstrates there is overlap in the population distributions of the CO_2 flux between the three regions. Fissure-A and Fissure-B are due to magmatic/hydrothermal processes, as revealed by their high CO_2 fluxes (mean CO_2 flux 4586 g·m^{-2}·d^{-1} and 161 g·m^{-2}·d^{-1}, respectively) and $\delta^{13}CO_2$ isotopic signatures (−5.5 to −2.39 ‰, **Table 3**). Both populations occur in localized areas, likely focused by highly permeable pathways (e.g., Aiuppa et al., 2004; Hutchison et al., 2015). Fissure-A is the high flux area of Rotomahana, associated with the presence of sublacustrine vents and bubble plumes, and the equivalent sub-aerial process in Waimangu and Tarawera. Fissure B is degassing through the soil and is present in Waimangu and Tarawera. Fissure-C (mean CO_2 flux 25 g·m^{-2}·d^{-1}, found in Waimangu and Rotomahana) is not spatially localized and represents the mixture of the high- and low-flux populations. In Rotomahana this represents CO_2 diffusion at the air-water boundary, whilst at Waimangu this is diffuse degassing with a mixed hydrothermal-biogenic component. Fissure-D (mean CO_2 flux 4 g·m^{-2}·d^{-1}) and Fissure-E (mean CO_2 flux 1 g·m^{-2}·d^{-1}) represent the background CO_2 flux for Tarawera, which is likely biogenic in origin. The two rates of background CO_2 flux may be due to the difficulty in creating and maintaining soils resulting in less biological activity due to the steep crater walls in some areas of Tarawera. Fissure-F (Rotomahana and Tarawera) is below detection limit.

Volcanic eruptions within the Okataina Volcanic Centre have been overwhelming driven by rhyolitic magmas (e.g., Nairn, 2002), with limited volumes of basalt erupted as discrete events (e.g., Matahi Scoria: Pullar and Nairn, 1972) or as part of a potential trigger mechanism (e.g., Kaharoa eruption: Leonard et al., 2002). Previous work on rhyolitic eruptions in the Okataina Volcanic Centre has shown that the storage depths are ∼4–6 km, based on the volatile contents of phenocryst-hosted melt inclusions (Johnson et al., 2011). Additionally, magneto-telluric inversions delineate a highly conductive region >3.5 km depth under Waimangu and the southern end of Rotomahana, which is interpreted as a shallow silicic intrusion, but this conductive region is not present at the northern end of Rotomahana toward Tarawera (Heise et al., 2016). The low solubility of CO_2, especially in rhyolites, suggests that CO_2 is likely to decouple from magmas at greater depths than these shallow, rhyolitic intrusions (e.g., Mysen et al., 1975; Blank and Brooker, 1994; Ni and Keppler, 2013). This, in combination with the CO_2 isotopic signature, suggests that the source of the CO_2 across the entire fissure is either the mantle or deep-seated mafic magmas that are degassing in the lower crust (Mazot et al., 2014). For instance, geophysical data suggests zones of interconnected, partial melts occur at >10 km in the Okataina Volcanic Centre (e.g., Bannister et al., 2004; Heise et al., 2007, 2010; Villamor et al., 2011), which at these depths are likely to be basaltic in composition. Clinopyroxene geobarometry for the Tarawera basalt gives depths between 4–12 km (100–300 MPa, assuming a crustal density of 2500 kg·m^{-3}), although some pressures were >28 km (>700 MPa), which is within the mantle-crust boundary (15–21 or 25–30 km depth depending on the study) (e.g., Stratford and Stern, 2002; Bannister et al., 2004; Sable et al., 2009). This is supported by gas measurements of other features in the Tarawera Volcanic Complex (and Taupō Volcanic Zone), which point to a carbon-rich, MOR-type mantle source (Giggenbach, 1995) and the CO_2 flux from other areas in the Taupō Volcanic Zone (e.g., Rotorua), which are fed by deep seated magmas (Werner and Cardellini, 2006).

Spatial Variation in CO_2 Flux

The magmatic/hydrothermal CO_2 varies along the whole fissure, in both isotopic signature and magnitude (**Tables 1** and **3**). The calculated $\delta^{13}CO_2$ in equilibrium with the bubble plumes at Rotomahana is −2.88 to −2.39 ‰ (Mazot et al., 2014), consistent with a magmatic origin, but heavier than the values observed at Tarawera of −5.5 ± 0.5 ‰ (**Table 3**). Also, dissolved gas from Waimangu geothermal features (e.g., lakes and pools) are heavier with −3.6 to −3.1 ‰ $\delta^{13}CO_2$ (Giggenbach, 1995; **Table 3**). This could indicate different sources for the CO_2 occurring along the fissure or temporal variations in $\delta^{13}CO_2$ as these data were collected at different times (Waimangu in 1978/79, Rotomahana in 2012, and Tarawera in 2017). More likely, however, these variations reflect fractionation

during different processes effecting the CO_2 as it travels to reach the surface. For instance, CO_2 can become kinetically isotopically fractionated as it diffuses through the soil, resulting in CO_2 close to the soil-atmosphere interface being isotopically heavier than the true value (Camarda et al., 2007). Also, CO_2 undergoes equilibrium isotopic fractionation between free CO_2 and dissolved C-bearing species in water, which was corrected for in the Rotomahana data (+4.23 to +4.72 ‰ $\delta^{13}C_{TDIC}$ to −2.88 to −2.39 ‰ calculated $\delta^{13}CO_2$) but not for the Waimangu data (Mook et al., 1974; Inguaggiato et al., 2000).

The magmatic/hydrothermal CO_2 flux is heterogenous along the whole fissure (**Figure 8A**). Firstly, the total CO_2 flux from Waimangu and Rotomahana (1179 $t{\cdot}d^{-1}$ using graphical statistical analysis and >549 $t{\cdot}d^{-1}$ using sequential Gaussian simulations) is much higher than from Tarawera (48 $t{\cdot}d^{-1}$ using graphical statistical analysis and 4.2 $t{\cdot}d^{-1}$ using sequential Gaussian simulations) (**Table 2**). This is due to greater proportions of Fissure-A, Fissure-B, and Fissure-C CO_2 flux populations (focused and diffuse predominantly hydrothermal/magmatic CO_2 fluxes, **Table 1**) in Waimangu and Rotomahana compared to Tarawera. The discrepancy is likely larger as there is significant uncertainty in the Waimangu CO_2 flux, which is likely an underestimate as much of the degassing has not been measured (e.g., only two transects have been measured and fumarolic plumes/bubbles in the pools have not been measured) and the total CO_2 flux greatly depends on the area taken for Waimangu. Despite the uncertainty in the CO_2 flux from Waimangu, this shows that the fissure is heterogeneously degassing CO_2. This is a long-lived feature of the area, as prior to the 1886 eruption what is now Rotomahana contained extensive geothermal activity (e.g., the Pink and White terraces), whilst Tarawera was inactive (e.g., Nairn, 2002).

This could imply a difference in the CO_2 source between the Waimangu-Rotomahana and Tarawera areas, where shallow intrusions feed Waimangu-Rotomahana and deep intrusions feed Tarawera, but as discussed in the section "Sources of CO_2" this is unlikely due to the low solubility of CO_2 in rhyolites (e.g., Mysen et al., 1975; Blank and Brooker, 1994; Ni and Keppler, 2013). Therefore, the source of CO_2 in both regions is likely to be deep intrusions, but variations of the CO_2 flux at the surface are due to permeability differences in the overlying rock. This could be partly due to Rotomahana occurring on the caldera edge, whilst Tarawera lies within the caldera. The caldera edge contains rim faults, which likely explains the elevated heat and gas flux here, and the dikes and craters formed during the 1886 eruption could have extended this area outside the caldera rim into Waimangu. Additionally, the shallow intrusion may help to maintain the pathways to the surface (e.g., providing additional heat as the intrusion cools) and thus facilitates deep CO_2 reaching the surface in Waimangu and Rotomahana compared to Tarawera.

Secondly, the magmatic/hydrothermal CO_2 flux has broadly two different magnitudes (**Figure 8A**). The lower CO_2 flux (Fissure-C, **Table 1** and **Figure 5F**) occurs everywhere and is the mixture between the background and magmatic/hydrothermal fluxes. The higher CO_2 flux is spatially highly localized (Fissure-A and Fissure-B, **Table 1** and **Figure 5F**), which is degassing through vents and the surrounding soil, and is associated with elevated soil temperatures in Waimangu and Tarawera

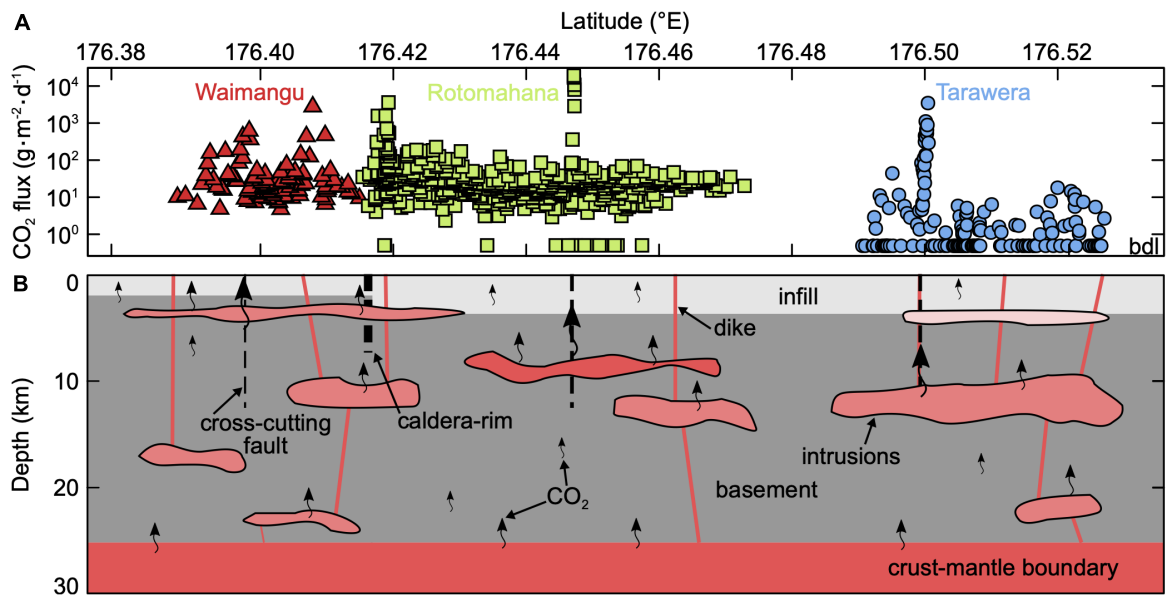

FIGURE 8 | (A) Raw CO_2 flux against latitude for Waimangu (red triangles) (Hurst et al., 2006), Rotomahana (green squares) (Mazot et al., 2014), and Tarawera (blue circles) (this study) where bdl is data below detection limit (< 1 $g{\cdot}m^{-2}{\cdot}d^{-1}$ CO_2 flux), and **(B)** a conceptual model of the sub-surface below the 1886 fissure, showing intrusions (pinks and reds) (approximate depths based on Bannister et al., 2004; Sable et al., 2009; Johnson et al., 2011; Cole et al., 2014; Heise et al., 2016, 2010), volcanic infill (light gray) (depths from Seebeck et al., 2010), basement (dark gray), crust-mantle boundary (red) (depth from Bannister et al., 2004), caldera-rim fault (thick, dashed, black line) (location based on Nairn, 2002), cross-cutting faults (thin, dashed, black lines) (locations based on this study), dikes (thin, pink, solid lines), and CO_2 degassing (curly arrows, where size indicates flux).

(maximum of 98 and 44°C, respectively). The difference between Fissure-A/Fissure-B and Fissure-C is likely a permeability control, rather than a change in source, because of the localized nature of Fissure-A/Fissure-B (∼1–10 m in width parallel to the fissure trend) and it is found throughout fissure (two regions in Waimangu, two in Rotomahana, and one in Tarawera). However, more data are needed for Waimangu to fully understand the spatial features in this area.

There are several potential explanations for these spatially localized areas of flux. The basaltic dikes from the 1886 eruption themselves could provide elevated permeable pathways for CO_2 (e.g., Nairn, 2002). Fluid pathways have been linked with the structure of domes, with elevated fluid flow along permeability pathways associated with domes, dike margins, conduit shear zones, and eruptive vents in both volcanic and hydrothermal areas (e.g., Werner and Cardellini, 2006; Rissmann et al., 2011; Gaunt et al., 2014). We observed a dike outcrop associated with the elevated CO_2 flux in Crater J (Nairn and Cole, 1981), which is also the centre of Crater dome (subsequently overlain by Ruawahia and Tarawera domes). However, there are many dike outcrops and domes in Tarawera which are not associated with elevated CO_2 flux, therefore there must be an additional factor influencing the location of increased degassing.

Elevated CO_2 fluxes within the fissure could be associated with faults, which provide pathways for fluids to reach the surface (e.g., Aiuppa et al., 2004; Werner and Cardellini, 2006; Hutchison et al., 2015). The 1886 fissure trends at 57°N due to extension of the Taupō Volcanic Zone, whilst dike outcrops within the fissure are aligned more easterly due to near surface stresses (Malahof, 1968; Nairn and Cole, 1981). This feature likely exerts a first order control on the CO_2 flux within the Tarawera Linear Vent Zone, although measurements have not been made outside the fissure. The CO_2 flux could be focused into the discrete regions at the intersection of faults that cross-cut the fissure and the fissure itself. Regional structures within the Taupō Volcanic Zone (but outside the Okataina Volcanic Centre) are aligned at ∼40°N, and structures outside the Taupō Volcanic Zone in the basement greywacke are typically aligned north-south (Nairn and Cole, 1981; Seebeck et al., 2010). For instance, the craters associated with the Rotokawau eruption are east-west aligned, indicating there are structural features at other orientations to the spreading direction in the Okataina Volcanic Centre (Nairn, 2002). On the other hand, these faults could be associated with Reidel shear, which are a set of faults at a high angle to the main fault (75°), or with steps in the main fault at depth, as the dikes for the 1886 fissure are en echelon. A conceptual model of the sub-surface beneath the 1886 fissure is shown in **Figure 8B**.

Temporal Variation in CO_2 Flux and Baseline Monitoring Data

The entire fissure was surveyed over 11 years; therefore, it is important to address whether these data can be combined. Previous repeat surveys at Rotorua conducted approximately a decade apart produced similar CO_2 flux maps, although local-scale changes were observed (Werner and Cardellini, 2006; Hanson et al., 2018). We assess the reproducibility of CO_2 flux measurements by comparing repeat measurements at the same location on the same day and approximately a year apart at Tarawera, and the surveying of Crater J in both 2016 and 2017. The variability between measurements at the same location made on the same day and a year apart are similar (±2–146 % and ±5–100 %, respectively). This variation is larger than that measured in a laboratory setting (±10 % for 0.2 to >10000 $g{\cdot}m^{-2}{\cdot}d^{-1}$ CO_2 flux) (Chiodini et al., 1998), but is in the range of those made in the field at the same location on the same day by different groups (±5–167 %) (Lewicki et al., 2005). Such temporal variations are a combination of error and natural changes in the flux (Lewicki et al., 2005). The total flux from Crater J in 2016 was 0.5 $t{\cdot}d^{-1}$ compared to 1.2 $t{\cdot}d^{-1}$ in 2017, which is twice the variability observed by Lewicki et al. (2005) (±41 vs. ±22 %, respectively) (**Table 2**). The same locations were not measured in Crater J both years and spatial variations can exist at the meter-scale (**Figure 7**). The highest CO_2 flux location was only measured in 2017 (622 vs. 3884 $g{\cdot}m^{-2}{\cdot}d^{-1}$ maximum measured CO_2 flux in 2016 and 2017, respectively) and the measurement density was higher in 2017. Hence, although the flux was lower in 2016 it occupied an apparently greater area of the crater floor, resulting in similar overall fluxes. These observations give confidence in combining the CO_2 flux data from different surveys.

Combining our data and observations with previous data implies that activity at Tarawera continues to decline over time (Cole, 1970; Nairn, 2002). Between 1973 and 1987 there were fumaroles with temperatures ranging from 50 to 98°C (Giggenbach et al., 1993; Nairn, 2002), whereas in 2016–2017 there was no evidence of any fumaroles. A region of warm ground remains (maximum 44°C soil temperature), but it is not hot enough to produce steam. This either implies that over time there has been a reduction in CO_2 and heat from the source (e.g., no new influx of magma for a long time, hence no new CO_2 or heat to reach the surface), or the pathways of CO_2 and heat are gradually sealing off (e.g., due to precipitation within the fluid pathways). This would be consistent with no thermal activity being visible at Tarawera prior to the 1886 eruption, even though the Kaharoa eruption occurred in ∼1314.

Our compiled baseline survey of the whole fissure is particularly relevant for determining any future unrest in the Okataina Volcanic Centre and understanding its cause, or more specifically along the Tarawera Linear Vent Zone. Sherburn and Nairn (2004) model the potential precursory activity to the next eruption from Tarawera and suggest that seismicity will be the first sign of unrest (∼5 years prior to eruption), with new springs and fumaroles appearing ∼1 year prior to eruption. Soil CO_2 emissions were not considered, but changes in gas emissions can reveal activity prior to seismicity (e.g., Poland et al., 2008; Werner et al., 2013). CO_2 emissions are invisible; therefore, measurements are typically made after seismic unrest begins or surface deformation is observed, but we now have a further method to monitor unrest using soil CO_2 flux and isotopic ratios. Our spatial coverage at Tarawera, combined with that of Waimangu and Rotomahana, show that there is large variability in the CO_2 flux across the fissure. Waimangu and Rotomahana CO_2 fluxes are more active than Tarawera, but future measurements could be collected across these features

and compared to the compiled baseline survey. For instance, the small area of degassing in Tarawera (compared to Waimangu and Rotomahana) coupled with the steady decline of this fumarole field makes any degassing changes relatively straightforward to delineate in Crater J. Future monitoring for increases in CO_2 flux, soil temperature, or area over which degassing occurs, as well changes in the isotopic composition of the CO_2, in Crater J could indicate changes in the source or depth of magma beneath Tarawera.

Total CO_2 Emissions

The total CO_2 emissions from the whole fissure are 1227 t·d^{-1} (742–3398 t·d^{-1} 90 % confidence interval) from graphical statistical analysis and a minimum of 553 ± 72 t·d^{-1} based on sequential Gaussian simulations estimates from Rotomahana and Tarawera. There is significant uncertainty in this value due to the limited data available from Waimangu. Mazot et al. (2014) estimated the total CO_2 emissions from Waimangu-Rotomahana as ∼1000 t·d^{-1} by using the average CO_2 flux from Rotomahana over the area of both Rotomahana and Waimangu (assumed to be 4.4 km^2). Additional data expanding the area measured at Waimangu, including measurements of the pools and other features, would especially help to constrain the area over which degassing occurs and its magnitude to refine this estimate. Along the 1886 fissure there is a lack of data connecting Rotomahana to Tarawera. As there are significant differences in the quantity of CO_2 being released in these two regions, data in this area would help understand where the change occurs. To further improve the estimate of the total CO_2 emissions, measurements outside the fissure (e.g., soil CO_2 emissions in transects perpendicular to the fissure) would help to constrain the total area degassing.

Despite this significant uncertainty, almost all the CO_2 is magmatic/hydrothermal as the other components have orders of magnitude lower CO_2 flux. Hence, this provides a minimum estimate of the magmatic/hydrothermal CO_2 flux in this area, which is a significant emission rate globally. For comparison, the Rotorua geothermal system produces 620 t·d^{-1} over 8.9 km^2, but emissions from the lake were not measured which would extend the area of emissions by one third. Including the emissions from the lake would result in an emission rate of ∼1000 t·d^{-1} (Werner and Cardellini, 2006), a similar value to our results across the fissure. Rotokawa is a non-volcanic, developed high-temperature geothermal field within the Taupō Volcanic Zone that emits 441 ± 84 t·d^{-1} over 2.88 km^2 (Bloomberg et al., 2014), which is a similar value if scaled to the same area as the fissure. Our value is also similar to Whakāri/White Island, New Zealand (1249 ± 117 t·d^{-1}, 0.61 km^2, Werner et al., 2004, 2008; Bloomberg et al., 2014; Christenson et al., 2017), which passively degasses CO_2 through a volcanic plume and the soil, but Tarawera is degassing over a much larger area.

CONCLUSION

We combine soil and lake CO_2 flux and $\delta^{13}CO_2$ measurements along the fissure created during the 1886 Tarawera eruption. The fissure is emitting 1227 t·d^{-1} (742–3398 t·d^{-1} 90 % confidence interval) CO_2, which is similar in magnitude to other regions in the Taupō Volcanic Zone The CO_2 degassing along the fissure is a combination of magmatic and biogenic CO_2, where the magmatic CO_2 is sourced from the mantle or deep-seated mafic magmas. There is significant variability in CO_2 degassing along the fissure, with elevated magmatic degassing at Waimangu and Rotomahana likely due to enhanced permeability where the fissure and caldera rim intersect and the presence of a shallow silicic body. Additionally, highly localized regions of very high flux are facilitated by faults that cross-cut the fissure. Activity along the fissure has changed over time since its creation, and future CO_2 flux and $\delta^{13}CO_2$ can be compared to this dataset in case of volcanic unrest.

DATA AVAILABILITY STATEMENT

All datasets generated and analyzed for this study are included in the manuscript/**Supplementary Materials**.

AUTHOR CONTRIBUTIONS

EH, AM, and GK contributed the conception and design of this study. CA and EH collected the photogrammetry data. CA processed the orthophotos. EH, AM, GK, CA, MM, KB, LC, and YF collected the Tarawera CO_2 flux data. EH processed the CO_2 flux data with the help of AM. EH wrote the first draft of the manuscript. All authors contributed to manuscript revision, read, and approved the submitted version.

FUNDING

EH was funded during an internship by GNS Science, NERC GW4+ DTP, and a GNS Science/NERC GW4+ DTP Ph.D. studentship [NE/L002434/1]. AM and GK are supported by the New Zealand Strategic Science Investment Fund (SSIF) from the New Zealand Ministry of Business, Innovation & Employment (MBIE).

ACKNOWLEDGMENTS

We would like to thank the Ruawahia 2B trust for welcoming us onto Mount Tarawera and permitting us to collect data on the mountain and especially Ken Raureti, Tīpene Marr, and Paul Warbrick for their support of this work; Andy Phillips (GNS Science) who ran the Tarawera $\delta^{13}CO_2$ analyses; and we also thank Colin Wilson, Dmitri Rouwet, and Valerio Acocella for their constructive and helpful comments, and Artur Ionescu for their editorial handling.

SUPPLEMENTARY MATERIAL

The Supplementary Material for this article can be found online at: https://www.frontiersin.org/articles/10.3389/feart.2019.00264/full#supplementary-material

REFERENCES

Aiuppa, A., Allard, P., D'Alessandro, W., Giammanco, S., Parello, F., and Valenza, M. (2004). Magmatic gas leakage at Mount Etna (Sicily, Italy): relationships with the volcano-tectonic structures, the hydrological pattern and the eruptive activity. *Geophys. Monogr. Am. Geophys. Union* 143, 129–146.

Allard, P., Carbonnelle, J., Dajlevic, D., Bronec, J., Le Morel, P., Robe, M. C., et al. (1991). Eruptive and diffuse emissions of CO_2 from Mount Etna. *Nature* 351, 387–391. doi: 10.1038/351387a0

Badalamenti, B., Bruno, N., Caltabiano, T., Di Gangi, F., Giammanco, S., and Salerno, G. (2004). Continuous soil CO_2 and discrete plume SO_2 measurements at Mt. Etna (Italy) during 1997–2000: a contribution to volcano monitoring. *Bull. Volcanol.* 66, 80–89. doi: 10.1007/s00445-003-0305-y

Bannister, S., Bryan, C. J., and Bibby, H. M. (2004). Shear wave velocity variation across the Taupo Volcanic Zone, New Zealand, from receiver function inversion. *Geophys. J. Int.* 159, 291–310. doi: 10.1111/j.1365-246X.2004.02384.x

Baubron, J.-C., Allard, P., Sabroux, J.-C., Tedesco, D., and Toutaln, J.-P. (1991). Soil gas emanations as precursory indicators of volcanic eruptions. *J. Geol. Soc. Lond.* 148, 571–576. doi: 10.1144/gsjgs.148.3.0571

Baubron, J. C., Allard, P., and Toutain, J. P. (1990). Diffuse volcanic emissions of carbon dioxide from Vulcano Island, Italy. *Nature* 344, 51–53. doi: 10.1038/344051a0

Bennie, S. L., and Stagpoole, V. M. (1985). *Waterborne Resistivity Measurements in the Rotorua Lakes Area of New Zealand*. Wellington: Department of Scientific and Industrial Research.

Blank, J. G., and Brooker, R. A. (1994). Experimental studies of carbon dioxide in silicate melts: solubility, speciation, and stable carbon isotope behaviour. *Rev. Mineral. Geochem.* 30, 157–186. doi: 10.1515/9781501509674-011

Bloomberg, S., Werner, C. A., Rissmann, C., Mazot, A., Horton, T., Gravley, D. M., et al. (2014). Soil CO_2 emissions as a proxy for heat and mass flow assessment, Taupō Volcanic Zone, New Zealand. *Geochem. Geophys. Geosystems* 15, 4885–4904. doi: 10.1002/2014GC005327

Burton, M. R., Sawyer, G. M., and Granieri, D. (2013). Deep carbon emissions from volcanoes. *Rev. Mineral. Geochem.* 75, 323–354. doi: 10.2138/rmg.2013.75.11

Camarda, M., De Gregorio, S., Favara, R., and Gurrieri, S. (2007). Evaluation of carbon isotope fractionation of soil CO_2 under an advective–diffusive regimen: a tool for computing the isotopic composition of unfractionated deep source. *Geochim. Cosmochim. Acta* 71, 3016–3027. doi: 10.1016/j.gca.2007.04.002

Carapezza, M. L., Lelli, M., and Tarchini, L. (2008). Geochemistry of the Albano and Nemi crater lakes in the volcanic district of Alban Hills (Rome, Italy). *J. Volcanol. Geotherm. Res.* 178, 297–304. doi: 10.1016/J.JVOLGEORES.2008.06.031

Carapezza, M. L., Ricci, T., Ranaldi, M., and Tarchini, L. (2009). Active degassing structures of Stromboli and variations in diffuse CO_2 output related to the volcanic activity. *J. Volcanol. Geotherm. Res.* 182, 231–245. doi: 10.1016/j.jvolgeores.2008.08.006

Cardellini, C., Chiodini, G., Frondini, F., Avino, R., Bagnato, E., Caliro, S., et al. (2017). Monitoring diffuse volcanic degassing during volcanic unrests: the case of Campi Flegrei (Italy). *Sci. Rep.* 7:6757. doi: 10.1038/s41598-017-06941-2

Cheng, W. (1996). Measurement of rhizosphere respiration and organic matter decomposition using natural ^{13}C. *Plant Soil* 183, 263–268. doi: 10.1007/BF00011441

Chiodini, G., Caliro, S., Cardellini, C., Avino, R., Granieri, D., and Schmidt, A. (2008). Carbon isotopic composition of soil CO_2 efflux, a powerful method to discriminate different sources feeding soil CO_2 degassing in volcanic-hydrothermal areas. *Earth Planet. Sci. Lett.* 274, 372–379. doi: 10.1016/J.EPSL.2008.07.051

Chiodini, G., Cioni, R., Guidi, M., Raco, B., and Marini, L. (1998). Soil CO_2 flux measurements in volcanic and geothermal areas. *Appl. Geochem.* 13, 543–552. doi: 10.1016/S0883-2927(97)00076-0

Christenson, B. W., White, S., Britten, K., and Scott, B. J. (2017). Hydrological evolution and chemical structure of a hyper-acidic spring-lake system on Whakaari/White Island, NZ. *J. Volcanol. Geotherm. Res.* 346, 180–211. doi: 10.1016/J.JVOLGEORES.2017.06.017

Cole, J. W. (1970). Structure and eruptive history of the Tarawera Volcanic Complex. *N. Z. J. Geol. Geophys.* 13, 879–902. doi: 10.1080/00288306.1970.10418208

Cole, J. W., Deering, C. D., Burt, R. M., Sewell, S., Shane, P. A. R., and Matthews, N. E. (2014). Okataina Volcanic Centre, Taupo Volcanic Zone, New Zealand: a review of volcanism and synchronous pluton development in an active, dominantly silicic caldera system. *Earth Sci. Rev.* 128, 1–17. doi: 10.1016/j.earscirev.2013.10.008

Deutsch, C. V., and Journel, A. G. (1998). *GSLIB: Geostatistical Software Library and User's Guide*. New York, NY: Oxford University Press.

Diliberto, I., Gurrieri, S., and Valenza, M. (2002). Relationships between diffuse CO_2 emissions and volcanic activity on the island of Vulcano (Aeolian Islands, Italy) during the period 1984–1994. *Bull. Volcanol.* 64, 219–228. doi: 10.1007/s00445-001-0198-6

Edmonds, M., and Wallace, P. J. (2017). Volatiles and exsolved vapor in volcanic systems. *Elements* 13, 29–34. doi: 10.2113/gselements.13.1.29

Gaunt, H. E., Sammonds, P. R., Meredith, P. G., Smith, R., and Pallister, J. S. (2014). Pathways for degassing during the lava dome eruption of Mount St. Helens 2004–2008. *Geology* 42, 947–950. doi: 10.1130/G35940.1

Giggenbach, W. F. (1995). Variations in the chemical and isotopic composition of fluids discharged from the Taupo Volcanic Zone, New Zealand. *J. Volcanol. Geotherm. Res.* 68, 89–116. doi: 10.1016/0377-0273(95)00009-J

Giggenbach, W. F., Sano, Y., and Wakita, H. (1993). Isotopic composition of helium, and CO_2 and CH_4 contents in gases produced along the New Zealand part of a convergent plate boundary. *Geochim. Cosmochim. Acta* 57, 3427–3455. doi: 10.1016/0016-7037(93)90549-C

Granieri, D., Chiodini, G., Marzocchi, W., and Avino, R. (2003). Continuous monitoring of CO_2 soil diffuse degassing at Phlegraean Fields (Italy): influence of environmental and volcanic parameters. *Earth Planet. Sci. Lett.* 212, 167–179. doi: 10.1016/S0012-821X(03)00232-2

Hanson, M. C., Oze, C., Werner, C. A., and Horton, T. W. (2018). Soil $\delta^{13}C$-CO_2 and CO_2 flux in the H_2S-rich Rotorua hydrothermal system utilizing cavity ring down spectroscopy. *J. Volcanol. Geotherm. Res.* 358, 252–260. doi: 10.1016/J.JVOLGEORES.2018.05.018

Healy, J. (1962). "Structure and volcanism in the Taupo Volcanic Zone, New Zealand," in *The Crust of the Pacific Basin, Geophysical Monograph Series*, eds W. E. Smith, G. A. Macdonald, and H. Kuno, (Washington, D.C: American Geophysical Union), 151–157. doi: 10.1029/GM006p0151

Heise, W., Bibby, H. M., Caldwell, T. G., Bannister, S. C., Ogawa, Y., Takakura, S., et al. (2007). Melt distribution beneath a young continental rift: the Taupo Volcanic Zone, New Zealand. *Geophys. Res. Lett.* 34:L14313. doi: 10.1029/2007GL029629

Heise, W., Caldwell, T. G., Bertrand, E. A., Hill, G. J., Bennie, S. L., and Palmer, N. G. (2016). Imaging the deep source of the Rotorua and Waimangu geothermal fields, Taupo Volcanic Zone, New Zealand. *J. Volcanol. Geotherm. Res.* 314, 39–48. doi: 10.1016/j.jvolgeores.2015.10.017

Heise, W., Caldwell, T. G., Bibby, H. M., and Bennie, S. L. (2010). Three-dimensional electrical resistivity image of magma beneath an active continental rift, Taupo Volcanic Zone, New Zealand. *Geophys. Res. Lett.* 37:L10301. doi: 10.1029/2010GL043110

Hernández, P. A., Salazar, J. M., Shimoike, Y., Mori, T., Notsu, K., and Pérez, N. (2001). Diffuse emission of CO_2 from Miyakejima volcano, Japan. *Chem. Geol.* 177, 175–185. doi: 10.1016/S0009-2541(00)00390-9

Hinkle, M. E. (1994). Environmental conditions affecting concentrations of He, CO_2, O_2 and N_2 in soil gases. *Appl. Geochem.* 9, 53–63. doi: 10.1016/0883-2927(94)90052-3

Hurst, T., Legaz, A., Revil, A., Vandemeulebrouck, J., and Werner, C. A. (2006). "Multi-electrode resistivity suveys around the hot lakes of the Waimangu geothermal area, New Zealand," in *Proceedings of the 28th New Zealand Geothermal Workshop*, Vancouver, WA.

Hutchison, W., Mather, T. A., Pyle, D. M., Biggs, J., and Yirgu, G. (2015). Structural controls on fluid pathways in an active rift system: a case study of the Aluto volcanic complex. *Geosphere* 11, 542–562. doi: 10.1130/GES01119.1

Inguaggiato, S., Pecoraino, G., and D'Amore, F. (2000). Chemical and isotopical characterisation of fluid manifestations of Ischia Island (Italy). *J. Volcanol. Geotherm. Res.* 99, 151–178. doi: 10.1016/S0377-0273(00)00158-X

Inguaggiato, S., Vita, F., Rouwet, D., Bobrowski, N., Morici, S., and Sollami, A. (2011). Geochemical evidence of the renewal of volcanic activity inferred from CO_2 soil and SO_2 plume fluxes: the 2007 Stromboli eruption (Italy). *Bull. Volcanol.* 73, 443–456. doi: 10.1007/s00445-010-0442-z

Jácome Paz, M. P., Taran, Y., Inguaggiato, S., and Collard, N. (2016). CO_2 flux and chemistry of El Chichón crater lake (México) in the period 2013–2015: evidence for the enhanced volcano activity. *Geophys. Res. Lett.* 43, 127–134. doi: 10.1002/2015GL066354

Johnson, E. R., Kamenetsky, V. S., McPhie, J., and Wallace, P. J. (2011). Degassing of the H_2O-rich rhyolites of the Okataina Volcanic Center, Taupo Volcanic Zone, New Zealand. *Geology* 39, 311–314. doi: 10.1130/G31543.1

Keam, R. F. (1988). *Tarawera: The Volcanic Eruption of 10 June 1886 A.D.* New Zealand: Physics Department, University of Auckland.

Leonard, G., Cole, J. W., Nairn, I. A., and Self, S. (2002). Basalt triggering of the c. AD 1305 Kaharoa rhyolite eruption, Tarawera Volcanic Complex, New Zealand. *J. Volcanol. Geotherm. Res.* 115, 461–486. doi: 10.1016/S0377-0273(01)00326-2

Lewicki, J. L., Bergfeld, D., Cardellini, C., Chiodini, G., Granieri, D., Varley, N., et al. (2005). Comparative soil CO_2 flux measurements and geostatistical estimation methods on Masaya volcano, Nicaragua. *Bull. Volcanol.* 68, 76–90. doi: 10.1007/s00445-005-0423-9

Malahof, A. (1968). "Origin of magnetic anomalies over the central volcanic region of New Zealand," in *The Crust and Upper Mantle of the Pacific Area, Geophysical Monograph Series*, eds L. Knopoff, C. L. Drake, and P. J. Hart, (Washington, D.C: American Geophysical Union), 218–240. doi: 10.1029/gm012p0218

Mazot, A. (2005). *CO_2 Degassing and Fluid Geochemistry at Papandayan and Kelud Volcanoes*. Brussels: Universite Libre de Bruxelles.

Mazot, A., Rouwet, D., Taran, Y., Inguaggiato, S., and Varley, N. (2011). CO_2 and He degassing at El Chichón volcano, Chiapas, Mexico: gas flux, origin and relationship with local and regional tectonics. *Bull. Volcanol.* 73, 423–441. doi: 10.1007/s00445-010-0443-y

Mazot, A., Schwandner, F. M., Christenson, B., de Ronde, C. E. J., Inguaggiato, S., Scott, B. J., et al. (2014). CO_2 discharge from the bottom of volcanic Lake Rotomahana, New Zealand. *Geochem. Geophys. Geosyst.* 15, 577–588. doi: 10.1002/2013GC004945

Mongillo, M. (1994). Aerial thermal infrared mapping of the Waimangu-Waiotapu geothermal region, New Zealand. *Geothermics* 23, 511–526. doi: 10.1016/0375-6505(94)90016-7

Mook, W. G., Bommerson, J. C., and Staverman, W. H. (1974). Carbon isotope fractionation between dissolved bicarbonate and gaseous carbon dioxide. *Earth Planet. Sci. Lett.* 22, 169–176. doi: 10.1016/0012-821X(74)90078-8

Mysen, B. O., Arculus, R. J., and Eggler, D. H. (1975). Solubility of carbon dioxide in melts of andesite, tholeiite, and olivine nephelinite composition to 30 kbar pressure. *Contrib. Mineral. Petrol.* 53, 227–239. doi: 10.1007/BF00382441

Nairn, I. A. (1979). Rotomahana-Waimangu eruption, 1886: base surge and basalt magma. *N. Z. J. Geol. Geophys.* 22, 363–378. doi: 10.1080/00288306.1979.10424105

Nairn, I. A. (2002). *Geology of the Okataina Volcanic Centre, Scale 1:50000*. Lower Hutt: Institute of Geological and Nuclear Sciences Limited.

Nairn, I. A., and Cole, J. W. (1981). Basalt dikes in the 1886 Tarawera Rift. *N. Z. J. Geol. Geophys.* 24, 585–592. doi: 10.1080/00288306.1981.10421534

Nairn, I. A., Self, S., Cole, J. W., Leonard, G. S., and Scutter, C. (2001). Distribution, stratigraphy, and history of proximal deposits from the c. AD 1305 Kaharoa eruptive episode at Tarawera volcano, New Zealand. *N. Z. J. Geol. Geophys.* 44, 467–484. doi: 10.1080/00288306.2001.9514950

Ni, H., and Keppler, H. (2013). Carbon in silicate melts. *Rev. Mineral. Geochem.* 75, 251–287.

Poland, M., Miklius, A., Orr, T., Sutton, J., Thornber, C., and Wilson, D. (2008). New episodes of volcanism at Kilauea volcano, Hawaii. *EOS* 89, 37–48. doi: 10.1029/2001JB000602

Pullar, W. A., and Nairn, I. A. (1972). Matahi basaltic tephra member, Rotoiti breccia formation. *N. Z. J. Geol. Geophys.* 15, 446–450. doi: 10.1080/00288306.1972.10422342

R Core Team, (2018). *R: A Language And Environment for Statistical Computing*. Vienna: R Foundation for Statistical Computing.

Raich, J. W., and Schlesinger, W. H. (1992). The global carbon dioxide flux in soil respiration and its relationship to vegetation and climate. *Tellus B* 44, 81–99. doi: 10.1034/j.1600-0889.1992.t01-1-00001.x

Raich, J. W., and Tufekciogul, A. (2000). Vegetation and soil respiration: correlations and controls. *Biogeochemistry* 48, 71–90. doi: 10.1023/A:1006112000616

Reimer, G. M. (1980). Use of soil-gas helium concentrations for earthquake prediction: limitations imposed by diurnal variation. *J. Geophys. Res. Solid Earth* 85, 3107–3114. doi: 10.1029/JB085iB06p03107

Rissmann, C., Nicol, A., Cole, J., Kennedy, B., Fairley, J., Christenson, B., et al. (2011). Fluid flow associated with silicic lava domes and faults, Ohaaki hydrothermal field, New Zealand. *J. Volcanol. Geotherm. Res.* 204, 12–26. doi: 10.1016/J.JVOLGEORES.2011.05.002

Sable, J. E., Houghton, B. F., Wilson, C. J. N., and Carey, R. J. (2006). Complex proximal sedimentation from Plinian plumes: the example of Tarawera 1886. *Bull. Volcanol.* 69, 89–103. doi: 10.1007/s00445-006-0057-6

Sable, J. E., Houghton, B. F., Wilson, C. J. N., and Carey, R. J. (2009). "Eruption mechanisms during the climax of the Tarawera 1886 basaltic Plinian eruption inferred from microtextural characteristics of the deposits," in *Studies in Volcanology: The Legacy of John Walker*, eds T. Thordarson, S. Self, G. Larsen, S. K. Rowland, and A. Hoskuldsson, (London: The Geological Society of London), 129–154. doi: 10.1144/iavcel002.7

Seebeck, H., Nicol, A., Stern, T. A., Bibby, H. M., and Stagpoole, V. (2010). Fault controls on the geometry and location of the Okataina Caldera, Taupo Volcanic Zone, New Zealand. *J. Volcanol. Geotherm. Res.* 190, 136–151. doi: 10.1016/J.JVOLGEORES.2009.04.011

Sherburn, S., and Nairn, I. A. (2004). Modelling geophysical precursors to the prehistoric c. AD1305 Kaharoa rhyolite eruption of Tarawera volcano, New Zealand. *Nat. Hazards* 32, 37–58. doi: 10.1023/B:NHAZ.0000026791.16566.96

Simmons, S. F., Keywood, M., Scott, B. J., and Keam, R. F. (1993). Irreversible change of the Rotomahana-Waimangu hydrothermal system (New Zealand) as a consequence of a volcanic eruption. *Geology* 21, 643–646.

Sinclair, A. J. (1974). Selection of threshold values in geochemical data using probability graphs. *J. Geochemical Explor.* 3, 129–149. doi: 10.1016/0375-6742(74)90030-2

Stratford, W. R., and Stern, T. A. (2002). Crust and upper mantle structure in a continental back-arc spreading zone: Central North Island, New Zealand. *EOS Trans. Am. Geophys. Union* 83, 32B–35B.

Stucker, V. K., de Ronde, C. E. J., Scott, B. J., Wilson, N. J., Walker, S. L., and Lupton, J. E. (2016). Subaerial and sublacustrine hydrothermal activity at Lake Rotomahana. *J. Volcanol. Geotherm. Res.* 314, 156–168. doi: 10.1016/J.JVOLGEORES.2015.06.017

Thomas, A. P. W. (1888). *Report on the Eruption of Tarawera and Rotomahana, NZ*. Wellington, NZ: Government Printer.

Vandemeulebrouck, J., Hurst, A. W., and Scott, B. J. (2008). The effects of hydrothermal eruptions and a tectonic earthquake on a cycling crater lake (Inferno Crater Lake, Waimangu, New Zealand). *J. Volcanol. Geotherm. Res.* 178, 271–275. doi: 10.1016/J.JVOLGEORES.2008.06.021

Villamor, P., Berryman, K. R., Nairn, I. A., Wilson, K., Litchfield, N., and Ries, W. (2011). Associations between volcanic eruptions from Okataina Volcanic Center and surface rupture of nearby active faults, Taupo rift, New Zealand: insights into the nature of volcano-tectonic interactions. *Geol. Soc. Am. Bull.* 123, 1383–1405. doi: 10.1130/B30184.1

Walker, G. P. L., Self, S., and Wilson, L. (1984). Tarawera 1886, New Zealand – a basaltic Plinian fissure eruption. *J. Volcanol. Geotherm. Res.* 21, 61–78. doi: 10.1016/0377-0273(84)90016-7

Walker, S. L., de Ronde, C. E. J., Fornari, D. J., Tivey, M. A., and Stucker, V. K. (2015). High-resolution water column survey to identify active sublacustrine hydrothermal discharge zones within Lake Rotomahana, North Island, New Zealand. *J. Volcanol. Geotherm. Res.* 314, 142–155. doi: 10.1016/j.jvolgeores.2015.07.037

Werner, C., Hurst, T., Scott, B., Sherburn, S., Christenson, B. W., Britten, K., et al. (2008). Variability of passive gas emissions, seismicity, and deformation during crater lake growth at White Island volcano, New Zealand, 2002–2006. *J. Geophys. Res.* 113:B01204. doi: 10.1029/2007JB005094

Werner, C. A., and Cardellini, C. (2006). Comparison of carbon dioxide emissions with fluid upflow, chemistry, and geologic structures at the Rotorua geothermal system, New Zealand. *Geothermics* 35, 221–238. doi: 10.1016/j.geothermics.2006.02.006

Werner, C. A., Christenson, B., Scott, B., Britten, K., and Kilgour, G. (2004). "Monitoring CO_2 emissions at White Island volcano, New Zealand: evidence

for total decrease in magmatic mass and heat output," in *Proceedings of the 11th International Symposium Water–Rock Interaction*, Boca Raton, FL.

Werner, C. A., Kelly, P. J., Doukas, M., Lopez, T., Pfeffer, M., McGimsey, R., et al. (2013). Degassing of CO_2, SO_2, and H_2S associated with the 2009 eruption of Redoubt Volcano, Alaska. *J. Volcanol. Geotherm. Res.* 259, 270–284. doi: 10.1016/J.JVOLGEORES.2012.04.012

Whiteford, P. C., Graham, D. J., and Risk, G. F. (1996). "Thermal activity beneath Lake Tarawera, New Zealand, outlined by temperature measurements," in *Proceedings of the 18th New Zealand Geothermal Workshop*, Wellington, NZ.

Wollschlaeger, D. (2018). *Shotgroups: Analyze Shot Group Data*. Vienna: R Foundation for Statistical Computing.

Conflict of Interest: The authors declare that the research was conducted in the absence of any commercial or financial relationships that could be construed as a potential conflict of interest.

frontiers in Astronomy and Space Sciences

ORIGINAL RESEARCH
published: 01 November 2019
doi: 10.3389/fspas.2019.00062

On the Role of the Urey Reaction in Extracting Carbon From the Earth's Atmosphere and Adding It to the Continental Crust

Louise H. Kellogg, Donald L. Turcotte and Harsha Lokavarapu*

Department of Earth and Planetary Sciences, University of California, Davis, Davis, CA, United States

Urey (1952a,b, 1956) introduced the Urey reaction to explain the origin of carbonates in the continental crust. The reaction extracts CO_2 from the atmosphere in acid rain that reacts with calcium silicates, the products are transported to the oceans where organic and inorganic processes results in the deposition of calcium carbonates. The origin of the CO_2 can be (1) the early atmosphere and (2) the mantle. The reaction removes almost all the atmospheric CO_2 that survived the formation of the Earth. If surface volcanism introduces more CO_2 than is lost by subduction, the CO_2 entering the atmosphere will be lost to the continental crust by the Urey reaction. Studies of carbon fluxes between surface reservoirs have demonstrated the importance of the Urey reaction in controlling the concentration of CO_2 in the atmosphere. At the present time the only surface reservoir with a large mass of carbon is the continental crust. In order to quantify the rate at which the Urey reaction removes CO_2 from the atmosphere we utilize data from the Paleocene-Eocene thermal maximum (PETM). This was a period of elevated global temperatures ($\Delta T = 4 - 5^{\circ}$C) at 56 Ma attributed to a pulse of volcanism and associated CO_2 in the north Atlantic. We utilize the decay time of this thermal anomaly to quantify the rate at which CO_2 is extracted from the atmosphere by the Urey reaction.

Keywords: Urey reaction, carbon, continental crust, atmosphere, early Earth

OPEN ACCESS

Edited by:
Sami Mikhail,
University of St Andrews,
United Kingdom

Reviewed by:
Fang Huang,
Rensselaer Polytechnic Institute,
United States
Nikolai Bagdassarov,
Goethe University Frankfurt, Germany

****Correspondence:***
Donald L. Turcotte
dlturcotte@ucdavis.edu

Specialty section:
This article was submitted to Earth and Planetary Materials, a section of the journal Frontiers in Astronomy and Space Sciences

Received: *30 April 2019*
Accepted: *13 September 2019*
Published: *01 November 2019*

Citation:
Kellogg LH, Turcotte DL and Lokavarapu H (2019) On the Role of the Urey Reaction in Extracting Carbon From the Earth's Atmosphere and Adding It to the Continental Crust. Front. Astron. Space Sci. 6:62. doi: 10.3389/fspas.2019.00062

1. INTRODUCTION

We first give a brief introduction to the distribution of carbon in the Earth. In doing this we will utilize the concept of carbon reservoirs. In some cases the definition of a carbon reservoir is well-defined. The Earth's atmosphere is an example. Carbon in the atmosphere is primarily in CO_2 and its concentration is relatively uniform. In other cases the definition of a carbon reservoir is arbitrary. The Earth's mantle is an example. The relatively uniform composition of mid-ocean ridge basalts (including CO_2) is taken as evidence of a near-uniform upper mantle reservoir. However, the variability of ocean-island and hot-spot basalts is evidence for a complex heterogeneous lower-mantle.

Houghton (2007) considered the present distribution of carbon in near-surface reservoirs including the atmosphere, oceans, ocean sediments, vegetation and soil, and fossil fuels. However, the near-surface reservoirs contain only a small fraction of the carbon in the Earth. The major reservoirs for carbon at the present are the core, the mantle, and the continental crust. It is generally accepted that a large fraction of the carbon resides in the core reservoir. Both during early core

formation and accretion, and during core formation after the moon-forming giant impact, carbon in the solid Earth was largely partitioned into the core. Dasgupta (2013) estimates that the mass of carbon in the core is ${}^cM_c = 4.44 \times 10^9$ Gt (1 Gt = 10^{12} kg) but there is certainly a large error bar. We suggest that a reasonable estimate for the present mass of carbon in the core is ${}^cM_c = (4 \pm 2) \times 10^9$ Gt.

A number of authors have studied the global carbon flux at mid-ocean ridges. These values can be used to estimate the composition of carbon in the mantle source region. Michael and Graham (2015) give a mass fraction ${}^cC_m = (34 \pm 20) \times 10^{-6}$ and Rosenthal et al. (2015) give a value ${}^cC_m = (75 \pm 40) \times 10^{-6}$. We suggest that a reasonable estimate for the composition of carbon in this source region is ${}^cC_m = (5 \pm 2.5) \times 10^{-5}$. Assuming the entire mantle to have this concentration, the mass of carbon in the mantle is ${}^cC_m = (2 \pm 1) \times 10^8$ Gt.

The third large reservoir for carbon at the present time is the continental crust. About 1% of the carbon in the Earth is in the continental crust; a large fraction of this carbon is in carbonates (limestones, marble, etc.) Wedepohl (1995) has given a comprehensive review of the composition of the continental crust with an emphasis on carbon. He gives a total carbon mass in the continental crust ${}^cM_{ccp} = 4.2 \times 10^7$ Gt. Of this total he attributes about 80% to sediments, almost entirely in carbonates. Hayes and Waldbauer (2006) have reviewed the literature on carbon in the crust and have given a range of masses and gave a preferred total carbon mass ${}^cM_{ccp} = 10^8$ Gt. In this paper we will accept the value given by Wedepohl (1995) as a representative value for the present mass of carbon in the continental crust ${}^cM_{ccp} = 4.2 \times 10^7$ Gt, but suggest that a reasonable range of acceptable values is ${}^cM_{ccp} = 2 \times 10^7$ – 2×10^8 Gt.

A list of the estimated present masses of carbon in the reservoirs we consider is given in **Table 1**. The estimated total mass of carbon in all of the reservoirs is ${}^cM = 4.68 \times 10^9$ Gt. With the mass of the Earth, 5.97×10^{24} kg, the concentration of carbon in the bulk Earth by mass is about 0.1%. These values are consistent with previous estimates (Dasgupta, 2013; DePaolo, 2015). We do not give error bars because the uncertainties of some values are difficult to specify.

A large fraction of the carbon in the surface reservoirs is in the continental crust, ∼99.99%. Much of this carbon is in the carbonates (limestones, marbles). Some 20–30% of the sediments in the continental crust are carbonates, independent of age (Mackenzie and Morse, 1992). Urey (1952a,b, 1956) proposed that a reaction between atmospheric CO_2 and calcium silicate was a major source of carbon in the continental crust. This reaction is now known as the Urey reaction. The principal purpose of this paper is to evaluate the role of the Urey reaction in terms of our present knowledge of the distribution of carbon in the Earth.

Two sources of the carbon in the continental crust are available. The first of these is the atmosphere. Today the atmosphere has very little carbon in it, however the atmosphere of Venus has a large mass of carbon as CO_2. It is quite possible that the early Earth also had a very high concentration of CO_2, the Urey reaction could have removed a significant fraction of this carbon to the continental crust. The second source of the carbon in the continental crust is the mantle. If the flux of carbon out of the mantle in surface volcanism exceeds the loss of carbon in subduction, the mantle could have lost carbon to the continental crust. The Urey reaction could have played an important role in this process.

TABLE 1 | Masses of carbon in the Earth's carbon reservoirs considered in this paper (1 Gt = 10^{12} kg).

Reservoir	Mass of carbon Gt	References
Core	4×10^9	Dasgupta, 2013
Mantle	2×10^8	This paper
Continental crust	4.2×10^7	Wedepohl, 1995
Oceans	3.8×10^4	Houghton, 2007
Atmosphere	8.5×10^2	NOAA, 2017
Total	4.24×10^9	

2. THE UREY REACTION

Urey (1952a,b, 1956) introduced the Urey reaction to explain the origin of calcium carbonates (limestones, marbles) in the continental crust. The basic reaction combines atmospheric CO_2 with a calcium silicate to generate a calcium carbonate plus silica. In order to include the role of acid rain in the process we write the Urey reaction in the form

$$\begin{aligned} CaSiO_3 + 2CO_2 + H_2O &\rightarrow Ca^{2+} + 2HCO_3^- + SiO_2 \\ &\rightarrow CaCO_3 + SiO_2 + CO_2 + H_2O \quad (1) \end{aligned}$$

The aqueous products are removed by calcium carbonate precipitation. Carbon dioxide (carbonic acid) in acid rain dissolves calcium silicate (wollastonite) sediments to give calcium, bicarbonate, and silica. The resulting calcium and bicarbonate ions flow in rivers to the oceans where either organic or inorganic precipitation produces the calcium carbonate. Blättler and Higgins (2017) have considered Urey's carbonate-silicate cycle in some detail utilizing measured calcium isotope ratios.

The role of the Urey reaction in maintaining a low concentration of CO_2 in the Earth's atmosphere was explicitly stated by Urey (1952b). "As carbon dioxide was formed it reacted with silicates to form limestone. Of course the silicates may have been a variety of minerals but the pressure of CO_2 was always kept at a low level by this reaction or similar reactions just as it is now."

Although the mass of carbon in the atmosphere today is small (∼ 850 Gt), the mass may have been much higher in the past. One of the major differences between Venus and the Earth is atmospheric composition. The atmospheric pressure on Venus is about a factor of 100 greater than the atmospheric pressure on Earth and is 96% carbon dioxide. The mass of carbon in the Venus atmosphere is ${}^cM_{ap} = 1.28 \times 10^8$ Gt. Scaling the atmospheric carbon masses to the overall masses of Venus and the Earth gives an estimate of the mass of carbon in the early

atmosphere of the Earth. The estimated value is ${}^cM_{ap} = 1.57 \times 10^8$ Gt (Kasting and Ackerman, 1986).

Another major difference between the Earth and Venus is the giant impact that is hypothesized to have been responsible for the origin of the moon. During the final stages of the Earth's accretion, a collision between the Earth and an astronomical body about the size of Mars occurred 20–100 Myrs after the origin of the solar system. A detailed review of the influence of this collision on the first several hundred million years of Earth evolution has been given by Zahnle et al. (2007). The intensity of the collision melted and vaporized significant fractions of the Earth and the incoming body. Some fraction of the incoming body (and some fraction of the Earth) subsequently accreted and cooled to form Earth's moon. It is estimated that the hot silicate atmosphere cooled and condensed over about a thousand years. A global magma ocean cooled and solidified much more slowly, possibly over tens of millions of years. Sleep and Zahnle (2001) and Sleep et al. (2011, 2014) have proposed that a substantial fraction of the CO_2 in the atmosphere was absorbed by the solid surface crust of the global magma ocean. Episodic foundering subduction of this dense crust transported the carbon into the Earth's mantle, removing CO_2 from the atmosphere.

An alternative to the mechanism proposed by Sleep and Zahnle (2001) is that carbon was directly transferred to the mantle during accretion (Li et al., 2016) or that carbon was transferred by tectonic processes during the Hadean. Shaw (2008) has provided a comprehensive review of CO_2 evolution in the Hadean to the early Proterzoic.

An important question concerning carbon is the origin of the carbon in the continental crust. One hypothesis is that they were extracted from the atmosphere by the Urey reaction relatively early in the Earth's history. This hypothesis was put forward by Kramers (2002) and by Lowe and Tice (2004). It should be noted that the potential mass of carbon in the early atmosphere, 1.57×10^8 Gt, is substantially larger than the estimated present mass of carbon in the continental crust ${}^cM_{ccp} = 4.2 \times 10^7$ Gt. Thus, a substantial fraction of the carbon in the continental crust could have been transferred from the atmosphere.

In order for the Urey reaction to extract CO_2 from the atmosphere the early Earth must have had continental crust in order to generate surface deposits of calcium silicates. In addition the Earth must of had oceans in order for the acid rain to catalyze the Urey reaction between atmospheric CO_2 and the surface deposits of calcium silicates. Little data is available for timing the initiation of the extraction of CO_2 from the atmosphere. We will assume that the process began at a time t_0 after the solidification of the magma ocean at about 4.5 Ga. We further assume that the Urey reaction extracted carbon from the atmosphere at a constant rate ${}^cJ_{a-cc}$ until the concentration of CO_2 in the atmosphere was reduced to a very low level. The rate of loss of carbon from the atmosphere is given by

$$\frac{d\,{}^cM_a}{dt} = -\,{}^cJ_{a-cc}. \tag{2}$$

We require ${}^cM_a = {}^cM_{a0}$ at $t = t_0$ and obtain

$${}^cM_a = {}^cM_{a0} - {}^cJ_{a-cc}(t - t_0) \tag{3}$$

This transport is completed at $t = \tau$ when ${}^cM_a = 0$ where

$$\tau = t_0 + \frac{{}^cM_{a0}}{{}^cJ_{a-cc}} \tag{4}$$

Taking ${}^cM_{a0} = 1, 2,$ and 3×10^7 Gt we give the dependence of the carbon flux ${}^cJ_{a-cc}$ on the flux time $\tau - t_0$ in **Figure 1**. Combining Equations (3) and (4) we find the time dependence of the mass of carbon in the atmosphere

$${}^cM_a = {}^cM_{a0}\left(1 - \frac{t - t_0}{\tau - t_0}\right) \tag{5}$$

for the period $t_0 < t < t_0 + \tau$. For $t_0 + \tau < t < t_0 + t_p$, we have added ${}^cM_{a0}$ to the continental crust.

Again taking ${}^cM_{a0} = 1, 2,$ and 3×10^7 Gt we give the mass of carbon in the continental crust ${}^cM_{cc}$ as a function of time t in **Figure 2** for $t_0 = 1$ Gyr and $\tau = 1$ and 3 Gyr. Carbon is lost from the atmosphere to the continental crust after plate tectonics provides the calcium silicate required for the Urey reaction to proceed.

In discussing the role of the Urey reaction we focus our attention on its role in the generation of carbonate sediments in the continental crust. Above we discussed how it could be directly responsible for the extraction of primordial CO_2 from the atmosphere. We now turn our attention to its indirect role in the addition of carbon from the mantle into the continental crust. Carbon is extracted from the mantle by volcanism and is returned to the mantle by subduction. If the rate of addition exceeds the rate of loss then the difference may be responsible for the origin of a large fraction of the carbon in the continental crust. Order of magnitude estimates of this process given by Hayes and Waldbauer (2006) demonstrated the plausibility of this mechanism.

A comprehensive model for the variability of atmosphere CO_2 over Phanerozoic times has been given by Berner and Kothavala (2001). This model, GEOCARB III, is complex and involves both organic and inorganic processes. Transport of

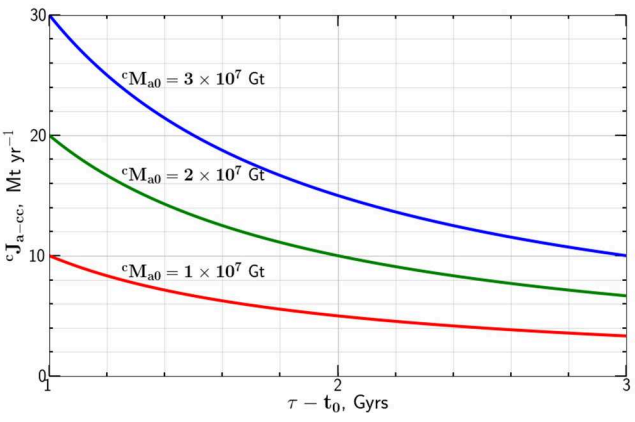

FIGURE 1 | Dependence of the constant mass flux of carbon from the atmosphere to the continental crust ${}^cJ_{a-cc}$ required to transfer the mass of carbon 1, 2, and 3×10^7 Gt to the continental crust in a time $\tau - t_0$.

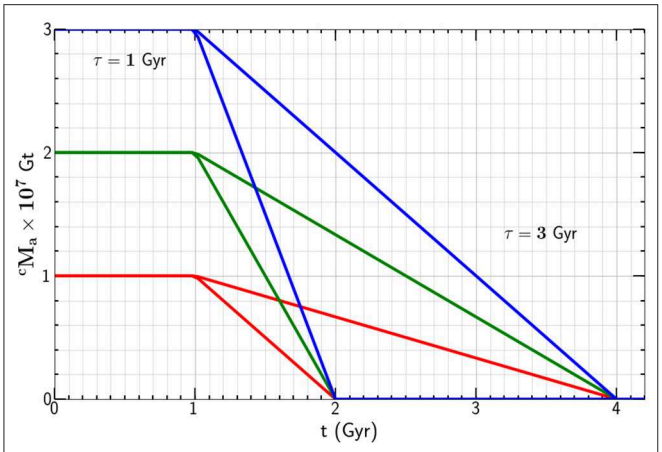

FIGURE 2 | Dependence of the mass of carbon in the atmosphere ^cM_a on time t for $t_0 = 1$ Gyr, $\tau =$ 1and 3 Gyr, and $^cM_{a0} = 1, 2, 3 \times 10^7$ Gt.

carbon between the atmosphere, oceans, and continental crust is quantified on the million year time scale. The balance is dominated by the exchange of carbon between carbonates in the continental crust and carbon in the surficial reservoirs (oceans and atmosphere) and organic carbon (Berner and Caldeira, 1997). This exchange occurs through the Urey reaction given in Equation (1). When erosion is high, the Urey reaction extracts CO_2 from the atmosphere adding carbonates to the continental crust. High erosion rates are associated with low sea level and large continental areas. When erosion is low, the Urey reaction operates in the opposite direction (from right to left in Equation 1) with carbonates decomposing to give CO_2. An example of this metamorphic process is the subduction of carbonate sediments and the generation and return of CO_2 to the atmosphere in subduction zone volcanics (Frezzotti et al., 2011).

We will next provide estimates for the rate at which surface volcanism transfers carbon from the mantle to the surface reservoirs. Volumetrically, surface volcanism is dominated by mid-ocean ridge volcanism. A number of authors have studied the global carbon flux from the mantle at mid-ocean ridges. Some studies involve direct measurements of CO_2 concentrations and others utilize correlations with other elements, such as barium. Hayes and Waldbauer (2006) summarized the early literature and gave a mid-ocean ridge global carbon flux $^cJ_{m-a} =$ 12 Mtyr^{-1}. Dasgupta and Hirschmann (2010) summarized the available data and gave a global carbon flux $^cJ_{m-a} = 36 \pm 24$ Mtyr^{-1}. Michael and Graham (2015) obtained an estimate of the carbon flux from mid-ocean ridges using measurements of CO_2/Ba ratios with published compilations of trace elements. They suggest that the global flux of carbon out of the mantle at mid-ocean ridges is $^cJ_{m-a} = 34 \pm 20$ Mtyr^{-1}. Rosenthal et al. (2015) used CO_2/Ba and CO_2/Nb systematics and conclude that the global flux of carbon is $^cJ_{m-a} = 50 \pm 30$ Mtyr^{-1}. Chavrit et al. (2014) carried out CO_2 vesicularity measurements on some 400 mid-ocean ridge glasses. These results were interpreted to give a global carbon flux $^cJ_{m-a} = 10 \pm 3.4$ Mtyr^{-1}. Since not all CO_2 would be expected to be in cavities, the actual carbon flux would be expected to be somewhat higher. Based on these previous studies we suggest that a reasonable choice for the carbon flux from the mantle at mid-ocean ridges is $^cJ_{m-a} = 36 \pm 24$ Mtyr^{-1}.

Flux estimates of carbon in ocean island basalts and hot spot volcanics have been reviewed by Hayes and Waldbauer (2006). Volumetrically this volcanism is about 10% of the mid-ocean ridges volcanism but some of this volcanism may be tapping a primitive lower mantle reservoir with higher concentrations of carbon. Considering the uncertainties we will neglect this source of carbon to the atmosphere in our modeling.

Just as carbon is lost from the mantle at mid-ocean ridges, carbon is returned to the mantle at subduction zones. A detailed study of carbon fluxes at subduction zones has been carried out by Kelemen and Manning (2015). These authors suggest that the downward flux of carbon at global subduction zones is 53 ± 13 Mtyr^{-1}. However, a substantial fraction of this carbon never makes it to the mantle. Carbon is returned to the oceans and atmosphere in subduction zone volcanism. Kelemen and Manning (2015) estimate the loss of carbon due to subduction zone volcanics is in the range 30 ± 12 Mtyr^{-1}. Taking the difference of these values, the present subduction flux of carbon to the mantle is $^cJ_{sp} = 24 \pm 24$ Mtyr^{-1}. Dasgupta and Hirschmann (2010) have also provided a comprehensive study of carbon subduction and conclude that $^cJ_{sp} = 36 \pm 12$ Mtyr^{-1} reach the mantle. An earlier review of carbon subduction was given by Hayes and Waldbauer (2006). These authors concluded that the input flux of carbon is 36 ± 12 Mtyr^{-1} and that the flux to the mantle is $^cJ_{sp} = 27 \pm 9$ Mtyr^{-1}.

We obtain an estimate for the net flux of carbon from the mantle required to produce a large mass of carbon in the continental crust assuming that this flux $^cJ_{m-cc}$ has been a constant during the period $t_p - t_0$ to t_p (present time). We use the relation

$$^cJ_{m-cc} = \frac{^c\Delta M_{m-cc}}{t_p - t_0} \tag{6}$$

Taking the carbon mass transported from the mantle to the continental crust $^c\Delta M_{m-cc} = 1, 2,$ and3×10^7 Gt we give the dependence of the carbon flux $^cJ_{m-cc}$ on the flux time $t_p - t_0$ in **Figure 3**. The results are essentially identical to those given in **Figure 1** for the transfer from the atmosphere. This is not surprising since Equation (6) is basically the same as Equation (3).

The time dependence of the mass $^cM_{m-cc}$ transferred from the mantle to the continental crust is given by

$$^cM_{m-cc} = ^c\Delta M_{m-cc}\frac{t - t_p}{t_p - t_0} \tag{7}$$

Again taking $^c\Delta M_{m-cc} = 1, 2,$ and3×10^7 Gt we give the dependence of the mass of carbon added to the continental crust $^cM_{a-cc}$ as a function of time t in **Figure 4** for $t_0 = 1.4$ Gyr.

When excess CO_2 in the atmosphere has been depleted by the Urey reaction an approximate steady state balance is established between the volcanic input of CO_2 and extraction by the Urey reaction. It has been argued by many authors that this balance is

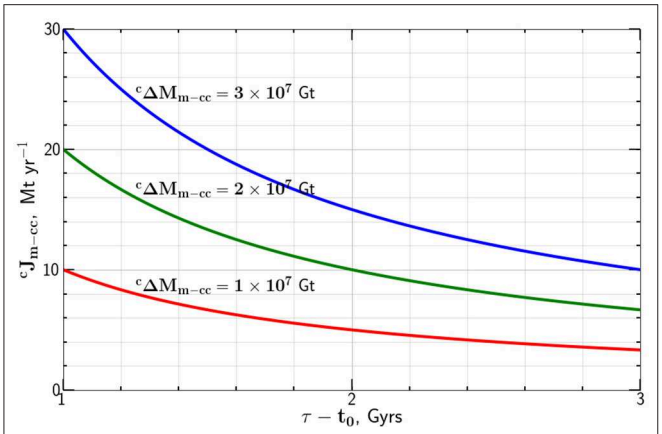

FIGURE 3 | Dependence of the present mass flux of carbon from the mantle to the continental crust $^{c}J_{(m-cc)p}$, required to generate $^{c}\Delta M_{m-cc}$ mass of carbon in the continental crust, in a time $t_p - t_0$, on this time difference.

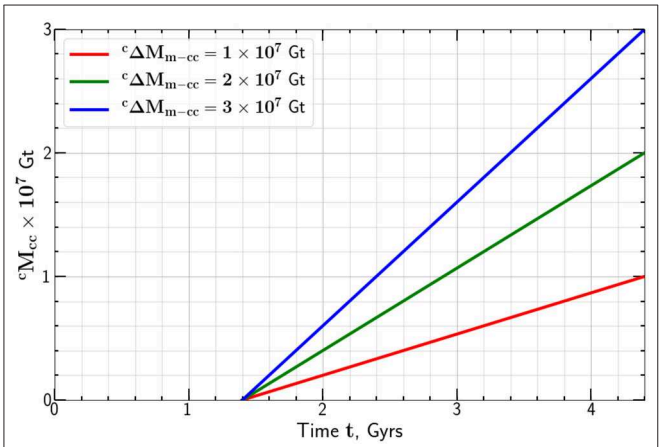

FIGURE 4 | Dependence of the mass of carbon added to the continental crust $^{c}M_{cc}$ on time, t for $t_0 = 1.4$ Gyrs.

controlled by the Urey reaction. We approximate this balance by the relation

$$^{c}J_{a-cc} = \frac{^{c}M_a}{\tau_{a-cc}} \tag{8}$$

where $^{c}J_{a-cc}$ is the rate of volcanic input of carbon into the atmosphere. We assume that the extraction rate is proportional to the mass of carbon in the atmosphere $^{c}M_a$. The rate at which the Urey reaction rate processes carbon τ_{a-cc} takes account of the rate at which acid rain can interact with calcium silicate sediments, clearly τ_{a-cc} can be a function of time.

3. PETM

As a further test of our approach to the use of the Urey reaction to explain variations in atmospheric CO_2 concentrations we will consider the Paleocene-Eocene thermal maximum (PETM). This was a period of elevated global temperatures that occurred at about 56 Ma. The elevated temperatures are attributed to increased concentrations of CO_2 and possibly methane in the atmosphere. The maximum increase in global surface temperatures is in the range $4 - 5^{\circ}$C and the period of excess temperatures lasted some 10^6 yrs. The occurrence of this period of high atmospheric CO_2 and temperatures was first documented by Kennett and Stott (1991) from an observation of large carbon and oxygen isotope ratios in an ocean drilling core.

A comprehensive review of the subsequent studies of this event was given by McInerney and Wing (2011). By the time this review paper was published some 400 research papers on a wide variety of aspects of PETM were included. The onset of the period of high atmosphere CO_2 and temperature was dated at 56.3 Ma, the onset lasted <10 ka, and the subsequent decay lasted some 120–220 ka. Observational data used to constrain the structure of the thermal pulse involves a variety of isotope measurements in drilling cores. One example is the temporal dependence of the observed δ^{13}C anomaly in a drilling core (Cui et al., 2011). A second example is the use of boron isotope data as a proxy for seawater (Gutjahr et al., 2017). Jones et al. (2013) have carried out a detailed study of the warming associated with the PETM. They conclude that the global mean surface anomaly is in the range 4–5°C.

Several sources of the carbon associated with the PETM have been proposed. These include methane clathrates and melting of permafrost. Storey et al. (2007) have made a very strong case for associating the PETM with the flood basalt volcanism resulting from the opening of the north Atlantic. This volcanism is documented in east Greenland and the Faroe Islands. The earliest of these flood basalts have an age of 56.1 ± 0.5 Ma. We support the hypothesis that a substantial fraction of the carbon responsible for the PETM was CO_2 entering the atmosphere from these flood basalts.

Studies of isotopic anomalies associated with the PETM systematically show a rapid increase at about 55.8 Ma with a subsequent decay of the anomaly over about 10^5 yrs. There is considerable scatter between drill sites. As an example of an isotopic anomaly we give data from the Deep Sea Drilling Project (DSDP) site 401 in the northeast Atlantic Ocean (Gutjahr et al., 2017). A strong negative carbon isotope anomaly was found in foraminifera *Morozovella subbotinae*. The observed $\delta^{13}C$ anomaly is given as a function of time t_{PETM} relative to the onset of the anomaly in **Figure 5**.

Gutjahr et al. (2017) have carried out an extensive modeling study using the available isotope data to provide estimates for the carbon generated during the PETM. We will utilize these values and take the total carbon added to the Earth's surface to be 12,000 Gt. Before and after the PETM we take the background carbon mass in the atmosphere to be $^{c}M_{ab} = 1,400$ Gt and the peak mass of carbon in the atmosphere during the PETM to be $^{c}M_{a0} = 3,050$ Gt.

We now carry out an approximate analysis of the decay of the PETM due to the loss of CO_2 from the atmosphere by the Urey reaction. We extend the balance given in Equation (8) to include the transient removal of carbon from the atmosphere and write

$$\frac{d^{c}M_a}{dt} = {}^{c}J_{(a-cc)b} - \frac{^{c}M_a}{\tau_{a-cc}} \tag{9}$$

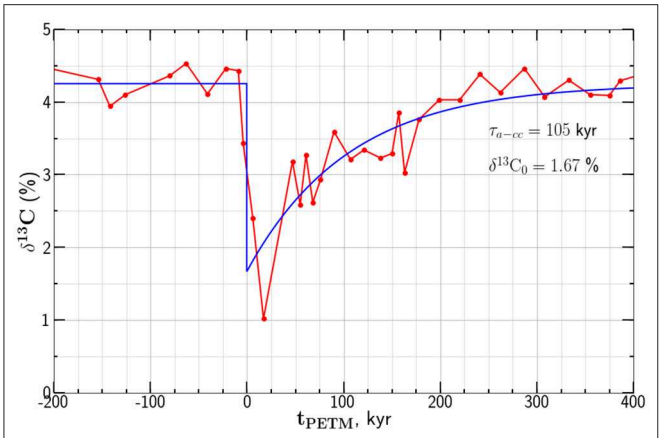

FIGURE 5 | An example of the carbon isotope anomaly associated with the PETM. The dependence of the $\delta^{13}C$ values on depositional time t_{PETM} relative to the onset of the anomaly are given. The data are from the DSDP site 401 with the carbon in foraminifera *M. subbotinae* (Gutjahr et al., 2017). Also shown is the least squares best fit of our relaxation model from Equation (12) with relaxation time $\tau_{a-cc} = 105$ kyr and $\delta^{13}C_0 = 1.67\%$.

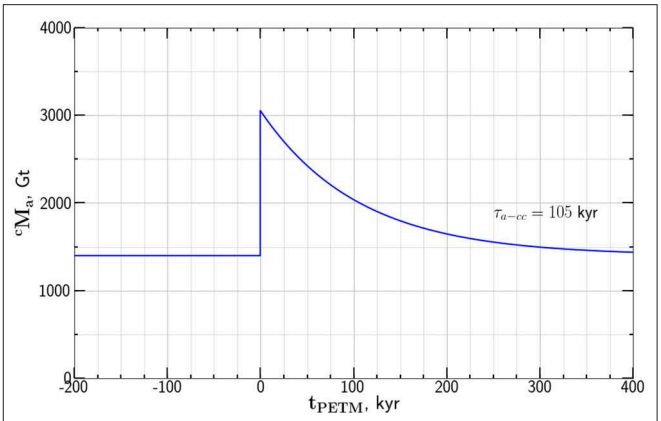

FIGURE 6 | Dependence of the atmosphere carbon mass values ^cM_a for the PETM anomaly on time t_{PETM} relative to the onset of the anomaly. The values are from our relaxation model give in Equation (11) with $^cM_{ab} = 1,400$ Gt and $^cM_{a0} = 3,050$ Gt.

From Equation (8) the background mass of carbon in the atmosphere is given by

$$^cM_{ab} = \tau_{a-cc}\, ^cJ_{(a-cc)b} \tag{10}$$

We prescribe an initial mass of carbon in the atmosphere at $t = 0, ^cM_{a0}$, with $^cM_{a0} > ^cM_{ab}$ and solve Equation (10) taking τ_{a-cc} to be constant with the result

$$^cM_a = (^cM_{a0} - ^cM_{ab})e^{-t/\tau_{a-cc}} + ^cM_{ab} \tag{11}$$

The excess mass of carbon in the atmosphere $^cM_{a0} - ^c M_{ab}$ decays exponentially as the Urey reaction extracts carbon from the atmosphere.

In order to estimate the value of the characteristic decay time τ_{a-cc} we assume that the negative carbon isotope anomaly is proportional to the mass of carbon in the atmosphere and write Equation (11) as

$$\delta^{13}C = \delta^{13}C_b - (\delta^{13}C_b - \delta^{13}C_0)e^{-t_{PETM}/\tau_{a-cc}} \tag{12}$$

where $\delta^{13}C_b$ is the background isotope ratio before and after PETM and $\delta^{13}C_0$ is the minimum isotope ratio prescribed at $t = 0$. Taking $\delta^{13}C_b = 4.25\%$ the dependence of $\delta^{13}C$ on t_{PETM} from Equation (12) is compared with the isotope anomaly values given in **Figure 5**. The least squares fit of the exponential decay to the data points in given taking $\tau_{a-cc} = 105$ kyr and $\delta^{13}C_0 = 1.67\%$.

We next use this value of τ_{a-cc} to obtain the dependence of atmosphere carbon mass on time during PETM based on the model dependence given in Equation (11). Taking the values $^cM_{ab} = 1,400$ Gt and $^cM_{a0} = 3,050$ Gt as given by Gutjahr et al. (2017) with $\tau_{a-cc} = 105$ kyr the model results are given in **Figure 6**.

We now return to Equation (10). This result relates the background atmospheric carbon mass $^cM_{ab}$ to the background rate of volcanic input of CO_2 carbon into the atmosphere $^cJ_{(a-cc)b}$ and the Urey decay time τ_{a-cc}. During the PETM we have taken the background carbon mass $^cM_{ab} = 1,400$ Gt. Taking $\tau_{a-cc} = 105$ kyr we find from Equation (12) that $^cJ_{(a-cc)b} = 13$ Mtyr^{-1}. This is an independent determination of the volcanic flux of carbon into the atmosphere. In **Figure 4** we gave volcanic the flux required to generate a specific mass of carbon in the continental crust

4. DISCUSSION

Urey (1952a) proposed the Urey reaction, Equation (1) to explain the origin of carbonates in the continental crust. He argued that the reaction would essentially remove all CO_2 from the atmosphere. It is now accepted that in analogy to Venus, there may have been a large mass of carbon in the Earth's early atmosphere, as much as 10^8 Gt. However, only a fraction of this may have survived the moon forming impact. We give a very simplified model for the extraction of carbon from the atmosphere to the continental crust, taking the extraction rate $^cJ_{a-cc}$ to be constant. There are basically no constraints on the variation of this rate with time. If a significant fraction of the carbon in the continental crust was extracted from the atmosphere, it is likely that it occurred early in Earth's history as illustrated in **Figure 1**.

The Urey reaction also controls the equilibrium mass of carbon in the atmosphere after the removal of any large initial concentration. The input of carbon to the atmosphere is from volcanism and we show that the equilibrium mass of carbon in the atmosphere $^cM_{ab}$ is proportional to the rate of volcanic injection $^cJ_{a-cc}$ divided by a characteristic Urey time τ_u. We quantify the value of τ_u by studying the observed relaxation of the Paleocene-Eocene thermal maximum, which occurred at 56 Ma, and the relaxation time is about $\tau_u = 10^5$ yrs.

We also give a simplified model for the extraction of carbon from the atmosphere to the continental crust. If the volcanic

loss of carbon from the mantle by volcanism exceeds the return of carbon by subduction, the difference is added to the continental crust. If the volcanic carbon enters the oceans organic precipitation creates carbonates. If the volcanic carbon enters the atmosphere it enters the continental crust by the Urey reaction. Current estimates of carbon fluxes from and to the mantle are sufficient to have produced all the carbon in the continental crust. At the present time it is not possible to quantify the relative importance of carbon addition to the continental crust from the early atmosphere and the mantle.

We have addressed two major questions concerning carbon in the atmosphere in this paper. The first is the origin of the carbon in the continental crust. We conclude that it is possible the carbon could have been extracted either from the early atmosphere or from the mantle over a longer period of time. Studies of the concentration of carbon in the atmosphere and continental crust over geologic time are required and should receive a high priority.

The second question we have addressed is the relaxation of injections of carbon into the atmosphere back to equilibrium values. We quantify this by studying the Paleocene-Eocene thermal maximum (PETM). This has obvious implications for the recovery from the process of anthropogenic injection of carbon into the atmosphere. We find the relaxation time to be about 50,000 yrs.

DATA AVAILABILITY STATEMENT

All datasets generated for this study are included in the manuscript/supplementary files.

AUTHOR CONTRIBUTIONS

All authors listed have made a substantial, direct and intellectual contribution to the work, and approved it for publication.

ACKNOWLEDGMENTS

The authors would like to acknowledge financial support from the Alfred P. Sloan Foundation under Grant G-2818-10087 through the Deep Carbon Observatory.

REFERENCES

Berner, R. A., and Caldeira, K. (1997). The need for mass balance and feedback in the geochemical carbon cycle. *Geology* 25, 955–956.

Berner, R. A., and Kothavala, Z. (2001). GEOCARB III: a revised model of atmospheric CO_2 over phanerozoic time. *Am. J. Sci.* 301, 182–204. doi: 10.2475/ajs.301.2.182

Blättler, C. L., and Higgins, J. A. (2017). Testing Urey's carbonate–silicate cycle using the calcium isotopic composition of sedimentary carbonates. *Earth Planet. Sci. Lett.* 479, 241–251. doi: 10.1016/j.epsl.2017.09.033

Chavrit, D., Humler, E., and Grasset, O. (2014). Mapping modern CO_2 fluxes and mantle carbon content all along the mid-ocean ridge system. *Earth Planet. Sci. Lett.* 387, 229–239. doi: 10.1016/j.epsl.2013.11.036

Cui, Y., Kump, L. R., Ridgwell, A. J., Charles, A. J., Junium, C. K., Diefendorf, A. F., et al. (2011). Slow release of fossil carbon during the Palaeocene–Eocene thermal maximum. *Nat. Geosci.* 4, 481–485. doi: 10.1038/ngeo1179

Dasgupta, R. (2013). Ingassing, storage, and outgassing of terrestrial carbon through geologic time. *Rev. Miner. Geochem.* 75, 183–229. doi: 10.2138/rmg.2013.75.7

Dasgupta, R., and Hirschmann, M. M. (2010). The deep carbon cycle and melting in Earth's interior. *Earth Planet. Sci. Lett.* 298, 1–13. doi: 10.1016/j.epsl.2010.06.039

DePaolo, D. J. (2015). Sustainable carbon emissions: the geologic perspective. *MRS Energy Sustain.* 2:E9. doi: 10.1557/mre.2015.10

Frezzotti, M. L., Selverstone, J., Sharp, Z. D., and Compagnoni, R. (2011). Carbonate dissolution during subduction revealed by diamond-bearing rocks from the Alps. *Nat. Geosci.* 4, 703–706. doi: 10.1038/ngeo1246

Gutjahr, M., Ridgwell, A., Sexton, P. F., Anagnostou, E., Pearson, P. N., Pälike, H., et al. (2017). Very large release of mostly volcanic carbon during the Palaeocene–Eocene thermal maximum. *Nature* 548, 573–577. doi: 10.1038/nature23646

Hayes, J. M., and Waldbauer, J. R. (2006). The carbon cycle and associated redox processes through time. *Philos. Trans. R. Soc. Lond. B Biol. Sci.* 361, 931–950. doi: 10.1098/rstb.2006.1840

Houghton, R. A. (2007). Balancing the global carbon budget. *Annu. Rev. Earth Planet. Sci.* 35, 313–347. doi: 10.1146/annurev.earth.35.031306.140057

Jones, T. D., Lunt, D. J., Schmidt, D. N., Ridgwell, A., Sluijs, A., Valdes, P. J., et al. (2013). Climate model and proxy data constraints on ocean warming across the Paleocene–Eocene thermal maximum. *Earth Sci. Rev.* 125, 123–145. doi: 10.1016/j.earscirev.2013.07.004

Kasting, J. F., and Ackerman, T. P. (1986). Climatic consequences of very high carbon dioxide levels in the Earth's early atmosphere. *Science* 234, 1383–1386. doi: 10.1126/science.11539665

Kelemen, P. B., and Manning, C. E. (2015). Reevaluating carbon fluxes in subduction zones, what goes down, mostly comes up. *Proc. Natl. Acad. Sci. U.S.A.* 112, E3997–E4006. doi: 10.1073/pnas.1507889112

Kennett, J. P., and Stott, L. D. (1991). Abrupt deep-sea warming, palaeoceanographic changes and benthic extinctions at the end of the Palaeocene. *Nature* 353:225.

Kramers, J. D. (2002). Global modelling of continent formation and destruction through geological time and implications for CO_2 drawdown in the Archaean eon. *Geol. Soc. Lond. Spec. Publ.* 199, 259–274. doi: 10.1144/GSL.SP.2002.199.01.13

Li, Y., Dasgupta, R., Tsuno, K., Monteleone, B., and Shimizu, N. (2016). Carbon and sulfur budget of the silicate earth explained by accretion of differentiated planetary embryos. *Nat. Geosci.* 9, 781–785. doi: 10.1038/ngeo2801

Lowe, D. R., and Tice, M. M. (2004). Geologic evidence for Archean atmospheric and climatic evolution: fluctuating levels of CO_2, CH_4, and O_2 with an overriding tectonic control. *Geology* 32, 493–496. doi: 10.1130/G20342.1

Mackenzie, F. T., and Morse, J. W. (1992). Sedimentary carbonates through phanerozoic time. *Geochim. Cosmochim. Acta* 56, 3281–3295. doi: 10.1016/0016-7037(92)90305-3

McInerney, F. A., and Wing, S. L. (2011). The Paleocene-Eocene thermal maximum: a perturbation of carbon cycle, climate, and biosphere with implications for the future. *Annu. Rev. Earth Planet. Sci.* 39, 489–516. doi: 10.1146/annurev-earth-040610-133431

Michael, P. J., and Graham, D. W. (2015). The behavior and concentration of CO_2 in the suboceanic mantle: inferences from undegassed ocean ridge and ocean island basalts. *Lithos* 236, 338–351. doi: 10.1016/j.lithos.2015.08.020

NOAA (2017). *Earth System Research Laboratory, Global Monitoring Division*. Available online at: www.esrl.noaa.gov/gmd/ccgg/trends/

Rosenthal, A., Hauri, E., and Hirschmann, M. (2015). Experimental determination of C, F, and H partitioning between mantle minerals and carbonated basalt, CO_2/Ba and CO_2/Nb systematics of partial melting, and the CO_2 contents of basaltic source regions. *Earth Planet. Sci. Lett.* 412, 77–87. doi: 10.1016/j.epsl.2014.11.044

Shaw, G. H. (2008). Earth's atmosphere–Hadean to early Proterozoic. *Chem. Erde Geochem.* 68, 235–264. doi: 10.1016/j.chemer.2008.05.001

Sleep, N. H., Bird, D. K., and Pope, E. C. (2011). Serpentinite and the dawn of life. *Philos. Trans. R. Soc. Lond. B Biol. Sci.* 366, 2857–2869. doi: 10.1098/rstb.2011.0129

Sleep, N. H., and Zahnle, K. (2001). Carbon dioxide cycling and implications for climate on ancient earth. *J. Geophys. Res. Planets* 106, 1373–1399. doi: 10.1029/2000JE001247

Sleep, N. H., Zahnle, K. J., and Lupu, R. E. (2014). Terrestrial aftermath of the moon-forming impact. *Philos. Trans. R. Soc. Lond. A Math. Phys. Eng. Sci.* 372:20130172. doi: 10.1098/rsta.2013.0172

Storey, M., Duncan, R. A., and Swisher, C. C. (2007). Paleocene-Eocene thermal maximum and the opening of the northeast atlantic. *Science* 316, 587–589. doi: 10.1126/science.1135274

Urey, H. C. (1952a). On the early chemical history of the earth and the origin of life. *Proc. Natl. Acad. Sci. U.S.A.* 38, 351–363. doi: 10.1073/pnas.38.4.351

Urey, H. C. (1952b). *The Planets: Their Origin and Development*. New Haven, CT: Yale University Press.

Urey, H. C. (1956). Regarding the early history of the earth's atmosphere. *Geol. Soc. Am. Bull.* 67, 1125–1128. doi: 10.1130/0016-7606(1956)67[1125:RTEHOT]2.0.CO;2

Wedepohl, K. H. (1995). The composition of the continental crust. *Geochim. Cosmochim. Acta* 59, 1217–1232. doi: 10.1016/0016-7037(95)00038-2

Zahnle, K., Arndt, N., Cockell, C., Halliday, A., Nisbet, E., Selsis, F., et al. (2007). Emergence of a habitable planet. *Space Sci. Rev.* 129, 35–78. doi: 10.1007/s11214-007-9225-z

Conflict of Interest: The authors declare that the research was conducted in the absence of any commercial or financial relationships that could be construed as a potential conflict of interest.

frontiers in Earth Science

ORIGINAL RESEARCH
published: 19 November 2019
doi: 10.3389/feart.2019.00297

Stability of Organic Carbon Components in Shale: Implications for Carbon Cycle

Sudeshna Basu[1], Alexander B. Verchovsky[2], Anna Bogush[1], Adrian P. Jones[1] and Anne-Lise Jourdan[1]*

[1] Department of Earth Sciences, University College London, London, United Kingdom, [2] Department of Planetary Sciences, Open University, Milton Keynes, United Kingdom

OPEN ACCESS

Edited by:
Sami Mikhail,
University of St Andrews,
United Kingdom

Reviewed by:
Vadim Reutsky,
V.S. Sobolev Institute of Geology and Mineralogy (RAS), Russia
Alberto Vitale Brovarone,
UMR 7590 Institut de Minéralogie, de Physique des Matériaux et de Cosmochimie (IMPMC), France

****Correspondence:***
Sudeshna Basu
Sudeshna.basu@ucl.ac.uk

Specialty section:
This article was submitted to Earth and Planetary Materials, a section of the journal Frontiers in Earth Science

Received: *16 June 2019*
Accepted: *29 October 2019*
Published: *19 November 2019*

Citation:
Basu S, Verchovsky AB, Bogush A, Jones AP and Jourdan A-L (2019) Stability of Organic Carbon Components in Shale: Implications for Carbon Cycle. Front. Earth Sci. 7:297. doi: 10.3389/feart.2019.00297

Stability and mobility of organic matter in shale is significant from the perspective of carbon cycle. Shale can only be an effective sink provided that the organic carbon present is stable and immobile from the host sites and, not released easily during geological processes such as low pressure-temperature burial diagenesis and higher pressure-temperature subduction. To examine this, three Jurassic shale samples of known mineralogy and total organic carbon content, with dominantly continental source of organic matter, belonging to the Haynesville-Bossier Formation were combusted by incremental heating from temperature of 200 to 1400°C. The samples were analyzed for their carbon and nitrogen release profiles, bulk $\delta^{13}C$ composition and C/N atomic ratio, based on which, at least four organic carbon components are identified associated with different minerals such as clay, carbonate, and silicate. They have different stability depending on their host sites and occurrences relative to the mineral phases and consequently, released at different temperature during combustion. The components identified are denoted as, C-1 (organic carbon occurring as free accumulates at the edge or mouth of pore spaces), C-2 (associated with clay minerals, adsorbed or as organomineral nanocomposites; with carbonate minerals, biomineralized and/or occluded), C-3(a) (occurring with silicate minerals, biomineralized and/or occluded) and C-3(b) (graphitized carbon). They show an increasing stability and decreasing mobility from C-1 to C-3(b). Based on the stability of the different OC components, shale is clearly an efficient sink for the long term C cycle as, except for C-1 which forms a very small fraction of the total and is released at temperature of ∼200°C, OC can be efficiently locked in shale surviving conditions of burial diagenesis and, subduction at fore arc regions in absence of infiltrating fluids. Under low fluid flux, C-3(b) can be efficiently retained as a refractory phase in the mantle when subducted. It is evident that the association and interaction of the organic matter with the different minerals play an important role in its retention in the shale.

Keywords: carbon cycle, carbon, nitrogen, clay minerals, carbonate, silicate

INTRODUCTION

Like many other elements, carbon cycles through different reservoirs on Earth including the atmosphere, mantle, hydrosphere (oceans and rivers), petrogenic reservoirs (mainly sedimentary rocks), soil and vegetal cover and biosphere (mainly as biomass). The carbon cycle has both slow and fast components referred to as the short and long term cycles respectively (**Appendix 1**) (Berner, 2003; Wallmann and Aloisi, 2012). The short term cycle includes photosynthesis, respiration and decomposition of biomass as well as air-ocean gas exchange. The carbon component in organic matter, referred to as the organic carbon (OC) can be incorporated in the plant biomass by photosynthesis. It subsequently cycles through the soil and oceanic sediments where, a fraction of it can be subject to decomposition. For the long term cycle, a fraction of the carbon subducted to the Earth's mantle is returned to the surface via degassing as CO_2 and CH_4 from mid-oceanic ridges (MORs) and hotspots within plate settings, arcs and forearc regions in subduction settings (Chiodini et al., 2010; Kelemen and Manning, 2015; Aiuppa et al., 2019; Voyer et al., 2019). For mid-oceanic ridges the CO_2 can be dissolved in the seawater as bicarbonate ions, although substantial release, to an extent diffuse, is also possible (Voyer et al., 2019). Contribution to degassing is restricted to shallow water areas where the ridge system is exposed above sea level. CO_2 degassing from volcanic front is well-constrained as compared to fore arc or back arc regions, possibly related to lack of obvious high emission sources in the area between the trench and the degassing volcanic arc front (Voyer et al., 2019). Emplacement of Large Igneous Provinces and mountain building can be associated with metamorphic degassing. For better understanding of such open system processes, it is necessary to constraint the fluid composition and constrain the absolute timings and duration of the fluid flow (Evans, 2011). The time scale of interest, relative to the processes involved will determine if the carbon cycle is in a steady state.

Beside the mantle, another effective carbon sink can be the different rock types where it can be locked in mineralized form as in sedimentary rocks as carbonates (biogenic and authigenic), or in hydrothermal calcite vein formed by low temperature alteration of the upper oceanic crust following chemical weathering of silicate rocks (Alt et al., 1999; Coogan et al., 2016). A recent study has shown that CO_2 maybe sequestered within the crust by calcite deposition or alternatively be incorporated into the biomass as inorganic carbon during microbial activity, consequently limiting the amount of C available for transfer to the deep mantle (Barry et al., 2019). OC is also contained in organic matter locked in ancient marine sediments represented by shale. The organic content in carbonaceous shale can be more than 20% by weight (Dayal, 2017). Given that sedimentary formations represent 66% of the rocks on the Earth's surface of which 50% is shale (Blatt and Jones, 1975), it is the largest reservoir in terms of the total mass of OC on Earth. Consequently, its contribution to the global carbon budget and the role that it plays in the carbon cycle cannot be neglected. While rocks like limestone are primarily constituted of carbonate minerals, in shale, they coexist with OC. The carbonate content in shale is variable, deposited by primary precipitation, biochemical processes or recrystallization during diagenesis. OC degradation by microbial sulfate reduction can be related to carbonate accumulation in anoxic sediments when sedimentary organic matter is converted to bicarbonate ions, accounting for the coexistence of carbonate minerals with organic matter (Wallmann and Aloisi, 2012; Zeng et al., 2018). The hydrocarbon fluid in the petroleum and natural gas reservoirs, mostly biogenic although abiogenic origin cannot be ruled out, is also a considerable carbon sink (Etiope and Sherwood-Lollar, 2013). Immiscible hydrocarbon fluids can be present in the expected range of pressure and temperature in subduction zone, providing a mechanism for the transfer of slab carbon to the deep mantle (Huang et al., 2017; Li, 2017; Vitale Brovarone et al., 2017).

The subduction of the carbonate minerals is distinct from, but operates in tandem with the OC (Cook-Kollars et al., 2014). Based on net flux estimates, carbon can be considered to be in steady state between subduction and mantle outgassing (Jarrard, 2003). Alternatively, there may be an increase in carbon at the Earth's surface over time or, a net flux to the mantle under the fore arcs controlled by the initial composition of the subducting material (Cook-Kollars et al., 2014; Kelemen and Manning, 2015; Clift, 2017). During fore arc metamorphism, subducted carbonate can be retained without any substantial decarbonation and loss of CO_2 under peak pressure-temperature conditions of ∼3 GPa and 600°C, at depth of 120 km (Collins et al., 2015). Carbonates reduced to graphitized form, at very high to lower temperature of 430°C, can be transported to deeper regions resulting in long term (Gyrs) removal of reduced, light carbon from surficial reservoirs of the Earth (Galvez et al., 2013; Duncan and Dasgupta, 2017). Degassing of graphitic OC can be substantial up to the chlorite zone but restricted at higher metamorphic grades (Zhang et al., 2018). A highly stable OC component in the graphitized form can be retained as a refractory phase under mantle conditions during subduction (Duncan and Dasgupta, 2017). Subduction of carbonates to the deep mantle beyond 660 km (transition zone) maybe inhibited due to melting of carbonate components (Thomson et al., 2016). When fluids circulate along sheared and brecciated domains and plate interfaces, substantial decarbonation and carbonate dissolution can occur at depth of 80–120 km in subducting slabs (Ague and Nicolescu, 2014; Cook-Kollars et al., 2014; Collins et al., 2015; Schwarzenbach et al., 2018). The large volume of infiltrating H_2O-rich fluid can be derived externally from underlying dehydrating mafic and ultramafic rocks.

We analyzed shale for carbon (and nitrogen) by stepwise combustion to decouple the different carbon components that are present. This study demonstrates that the stability of OC in shale is governed by their variable association with different mineral phases like carbonate, clay minerals and silicates related to how they are trapped/hosted with them. While free occurrence as accumulates, aggregated by clumping or binding renders them most unstable, a more stable and less mobile OC component occurs with silicate and carbonate minerals. It can occur as biominerals within the silicate walls of organisms such as diatoms or, within carbonate shells of corals or foraminifera. When

occluded, the OC is protected or blocked within the mineral frame of silicate or carbonate matrix (Keil and Mayer, 2014). The stability can be variable when associated with clay and carbonate minerals, depending on whether they are adsorbed, occluded or biomineralized.

OBJECTIVES OF THE STUDY

Shale can be an efficient, long term geological reservoir locking up carbon both in its organic and inorganic forms. Carbon can be released from it during weathering and transported to soil and rivers and finally to the oceans as inherited or 'old carbon' (Di-Giovanni et al., 2002). The later can be substantial and, is in addition to contribution from soil originating from present or post-glacial vegetal cover referred to as the 'new carbon' which is less resistant to microbial degradation. It is critical to understand how much of OC in shale is lost prior to release and eventual transportation to rivers and oceans. Over time, this fraction of the OC can be again locked for millions of years as they are redeposited and reconsolidated into rocks. The availability of OC from shales to contribute toward soil and river flux is largely controlled by how easily it can be degraded by geological processes such as oxidative weathering or altered during burial diagenesis. This will also control the exposure of shale organic matter to microorganisms in the weathering profile (Petsch et al., 2005). The breakdown of the liberated OC is facilitated by microbial oxidation in the presence of atmospheric oxygen. Its susceptibility toward alteration under action of different reagents, has been seen to be related to its stability and/or mobility from different host sites in shale (Zhu et al., 2016). This has implications for sediment subduction as well. Depending on its stability, the OC can be effectively subducted to the deeper mantle, unless incorporated in advecting sedimentary piles or buoyant metasedimentary diapirs to be transported to the hotter mantle wedge (Tsuno and Dasgupta, 2011; Tsuno et al., 2012; Kelemen and Manning, 2015).

It is evident that if the oxidation reactions proceed at a fast rate to enable degradation of the OC in shales to CO_2 following exposure to the atmosphere by uplift and erosion, it cannot be sequestered in re-sedimented rocks to be isolated from the surficial carbon reservoirs for long periods of time. In subduction zones, with increasing burial, if OC is resistant to remobilization by CO_2 formation, it cannot be released to the atmosphere by magmatic degassing but instead can be efficiently subducted in graphitized form by rhyolitic melt and sequestered in the deep mantle (Wallmann and Aloisi, 2012). In both these instances the fate of OC as to its susceptibility to oxidation, subsequently impacts the long term carbon cycle. This study aims to look into the effect of oxidation with increasing temperature on the mobility of carbon locked in shales, by combusting them with incremental heating. Depending on the host sites of different forms of carbon of various stability and their consequent mobility, their release during combustion will occur at different temperature. In the geological context, this has critical implication as stable and less mobile forms of carbon are more likely to be re-sedimented in marine rocks by escaping degradation or, if subducted, can be sequestered in the deep mantle.

BACKGROUND: DECOUPLING CARBON COMPONENTS IN A SHALE BY CONVENTIONAL METHODS

Different types of OC have different degrees of resistance to oxidative degradation depending on their type (Wallmann and Aloisi, 2012) and their host sites in rocks (Zhu et al., 2016). But, isolating these components in terms of their variable stability and mobility can be quite challenging. Conventionally organic and inorganic carbon components (carbonates) in shale are decoupled by acid treatment, where the mineralized inorganic carbon is converted to CO_2 during acidification. The OC is subsequently analyzed from the inorganic carbon free sample after injection into a TOC (total organic carbon) analyzer. The OC is then detected and measured after oxidizing it to CO_2 and releasing it from the sample. The inorganic carbon can be quantified by the carbon analyzer by measuring the total carbon content and the non-carbonate carbon fraction following leaching with hydrochloric acid. Some loss of volatile and soluble components of OC is known to occur during acid treatment (Saikkonen and Rautiainen, 1990). In the process of separating the organic and inorganic components prior to analyses, information in terms of OC-carbonate association is lost. Also, no discrimination between the different OC components present in different sites is possible.

The OC occurs as both low molecular weight (free) and high molecular weight (kerogen) forms. Solvent extraction can solvate the free compounds thereby isolating them from the relatively immobile kerogen and mineral matrix (Wright et al., 2015) again failing to provide information pertaining to host site, stability and mobility. The heterogeneity of organic matter can be monitored by petrographic and spectroscopic methods. Use of organic petrography and scanning electron microscopy can be used to distinguish between different organic components in terms of their differences in porosity and, association with each other and mineral components (Yang et al., 2017). Raman imaging can provide structural information in terms of the degree of organization indicating graphitization of the organic matter (Henry et al., 2019), but none of these methods by themselves can relate the occurrences of the carbon components to their stability and mobility in the shale or provide any quantification of the components.

Thermal decomposition method like loss on ignition (LOI), that oxidizes organic matter at temperature of 500–550°C followed by decomposition of carbonate at 900–1000°C, can be used for decoupling and quantifying OC and inorganic carbon components in clay-poor shale, but can be affected by sample size and breakdown of clay minerals (Smith, 2003). On the other hand, a combination of methods have shown to be more informative. For example, multi-step pyrolysis at temperature of 350, 600, and 1000°C coupled with Fourier transform infrared (FTIR) spectrophotometry was successfully applied to reveal information on the different speciation of OC in

terms of thermal maturity (Saikkonen and Rautiainen, 1990). In a different study, a combination of treatment with reagents after separation of clay-sized fractions, followed by pyrolysis and FTIR spectrophotometry revealed OC components having different stability/mobility levels, occurring at different sites in the shale (Zhu et al., 2016).

In this study, by simultaneously analyzing carbon and nitrogen in shale in small incremental steps for their concentration, isotopic ($\delta^{13}C$) and elemental composition (C/N), it has been possible to decouple the different carbon components based on their mobility/stability, without any acid treatment. Simultaneous analyses of carbon, and nitrogen enabled correlation with the carbonate and clay minerals. In addition, the organic $\delta^{13}C$ ($\delta^{13}C_{organic}$) and N/C elemental ratio helped to constrain the source (marine/lacustrine/continental) of the organic matter in these shales. Measurement by simultaneous thermal analyses (STA), was used to support the observed mineral breakdown from the combustion experiments.

METHODOLOGY

Three Jurassic shales from two different cores of the Haynesville-Bossier formation were analyzed by multiple step combustion for carbon and nitrogen concentration, C/N atomic ratio and $\delta^{13}C$ isotopic composition. Prior to the combustion, the mineralogy and the TOC content of two of the samples were determined on their powders by XRD (Bruker AXS D4 Endeavor X-ray diffractometer) and Flash Elemental Analyzer 1112 (Thermo) respectively. The $\delta^{13}C_{organic}$ value was determined by Gas Ratio Isotope Ration Mass Spectrometry, following flash combustion, after cleaning the samples from any carbonate remains by acid digestion. The porosity and permeability were determined on the bulk shale after crushing.

Shales are highly friable and fissile. It is very difficult to get undamaged samples for study but here, we had access to relatively intact drill core samples. For step combustion, the samples were extracted from the central portion of the drill cores to minimize superficial effects of core retrieval and handling related contamination. They were then crushed to mm-sized fragments using agate mortar and pestle, easily achievable as they split along the fissile planes. Between 5 and 10 mg of samples were combusted from 200 to 1400°C (± 10°C), in incremental steps of 100–200°C each, using 2 torr of O_2, introduced to the system from CuO under ultra-high vacuum conditions. The total number of steps varied between nine and 10 and the time of combustion was 30 min for each step. A fully automated mass spectrometric complex, Finesse, was used for carbon and nitrogen analyses (Verchovsky, 2017). The combustion system used was all metal with a CuO finger to clean up the nitrogen fraction before introducing the gas to the mass spectrometer. The CO_2 was trapped using a cold finger.

Simultaneous thermal analysis using a NETZSCH STA 449 C was used to investigate mass changes [thermogravimetry (TG); differential TG (DTG)] and energy flows [differential scanning calorimetry (DSC)] as a function of temperature, to investigate the combustion experiments. STA analysis was conducted on two samples using ∼200 mg of bulk, crushed powder in an 85 μL alumina crucible (and an identical reference crucible) with an air purge gas flow rate of 100 mL/min, equilibration at 40°C for 10 min, followed by a heating rate of 10°C/min up to 1400°C.

SAMPLES AND GEOLOGICAL HISTORY

The samples belong to the Haynesville-Bossier Formation in northwestern Louisiana, eastern Texas, deposited during the Late Jurassic (156 to 145.5 Ma) in a marine environment. The organic rich shale is related to the tectonically formed East Texas Basin (ETB), about 125 to 150 km long and 50 km wide, considered a sub-basin of the larger basin of the Gulf of Mexico (Jackson and Laubach, 1988; Salvador, 1991). It was formed and developed during the Triassic through the Jurassic related to breakup, rifting and extension of Pangea with the opening of the Gulf of Mexico Province (Mainali, 2011). During the Jurassic, a possible elevated southern margin restricted circulation resulting in the deposition of anhydrite and salt, but eventually transited to open marine condition with progressive subsidence. In general, the Haynesville is significantly more calcareous and OC rich than the overlying Bossier, the later having higher clay content. The samples for this study belong to Bossier and retrieved from different depth of two cores which are in close proximity, separated by only ∼8 km between them. Because of the high temperature gradient of ∼ 60°C/km during the Jurassic, the Haynesville-Bossier shale was exposed to temperature of 150–200°C during the last ∼ 100 Myrs (Nunn, 2012).

RESULTS

The mineralogy, porosity and permeability of two of the samples, each from a different core, are listed in **Table 1** along with their TOC content. They have comparable TOC (1.2–1.5 wt%) and mainly consist of carbonate, clay, and quartz (>80%). In terms of content between carbonate and clay minerals there is a difference of < 15% between the samples. Sample S-2(1) has a higher carbonate content than S-2(3) (32 vs. 14%) but a lower clay content (34 vs. 46%). The carbonates are mostly calcite, with some dolomite present as well. Illite is the dominant clay mineral with some kaolinite, chlorite and mixed illite/smectite layer, although quantification is not possible. Other minerals present include K-feldspar, plagioclase, pyrite, and apatite. Both the samples have comparable porosity (9 to 11% of bulk volume) while the permeability of S-2(1) ($\sim 10^{-4}$ md) is higher by an order of magnitude than S-2(3). The $\delta^{13}C_{organic}$ (denoting source of organic matter) of the samples are also comparable (**Table 2**). High T_{max} of > 400°C determined by rock eval pyrolysis on the samples indicates that they are thermally over matured.

In **Tables 2**, **3**, the carbon and nitrogen concentration and isotopic ratios along with elemental C/N values are listed for bulk values and individual combustion steps of each sample respectively. There are some differences in the carbon content when compared to XRD measurements (**Table 1**) that can be related to shale heterogeneity, also as the two methods involved

TABLE 1 | XRD mineral compositions combined with TOC and normalized to 100%.

Sample	Clay	Carbonate	Quartz	[Y]Others	TOC	Total	*Porosity	#Permeability
			Weight%				%	md
S-2 (1)	34	32	20	14	1.5	100	11.2 ± 1.4	$(3.4 \pm 3.5) \times 10^{-4}$
S-2 (3)	46	14	25	15	1.2	100	8.9 ± 0.7	$(1.6 \pm 0.3) \times 10^{-5}$

[Y]*Others include K-feldspar, plagioclase, pyrite, and apatite.* **Correspond to measured dry helium porosity and* #*press decay permeability of the samples.*

TABLE 2 | Bulk composition of samples in terms of carbon (C) and nitrogen (N) concentration, $\delta^{13}C$ (bulk and organic), and atomic C/N ratios.

Sample	Depth (m)	*C (wt%)	*δ^{13}Cbulk (‰)	δ^{13}Corganic (‰)	N (ppm)	C/N
S-2 (1)	3592.2	3.0	-19.7 ± 0.4	-26.8 ± 0.1	1030	29 ± 3
S-2 (3)	3495	2.1	-18.7 ± 0.1	-27.3 ± 0.1	1396	15 ± 2
S-3 (3)	3495.3	2.2	-16.6 ± 1.2	-27.0 ± 0.1	1320	17 ± 2

**From Basu et al. (2018).*

analyses of different weight of samples. But, the release profiles of all the three samples for step combustion are comparable. The peak nitrogen release occurs at 500–600°C, at a slightly lower temperature as compared to the peak carbon release at 600–700°C. The total carbon content of the samples is between 2 and 3 wt.% while the nitrogen concentration varies between 1000 and 1400 ppm. Their $\delta^{13}C_{organic}$ (measured independently) are $\sim -27‰$ and comparable. Given marine carbonates have $\delta^{13}C$ (up to $+4‰$) with a considerable range when affected by diagenesis (Murata et al., 1969), the $\delta^{13}C$ of -20 to $-16‰$ for the three bulk shales from this study, indicates mixing between OC and inorganic carbon, the later contributed by the carbonates. The peak release of carbon is coincident with elevated $\delta^{13}C$ suggestive of breakdown of the carbonate minerals. The peak release of nitrogen for S-2(3) and S-3(3) are coincident with low C/N ratios suggestive of contribution from clay minerals and/or associated organic matter. The nitrogen release profile of S-2(1) is more prolonged than the other two samples. The C/N of the samples are in the range of 15–30. Instrumental blank corrections for both carbon and nitrogen were below significance.

For STA, five characteristic regions for shales in the studied interval from 50 to 1400°C could be identified (**Appendix 2**). At 50 to 150°C, there is mainly loss of free water/moisture physisorbed on the surfaces of particles, and clay-bound fluids resulting in a slight weight loss [0.69 wt.% for S-2(1) and 0.79 wt.% for S-2(3)] and a slight visible endothermic process. At the second temperature region of 300–650°C, there is a mass loss [6.12 wt.% for S-2(1); 3.16 wt.% for S-2(3)] attributed to decomposition of organic matter (300–600°C), an exothermic process shown on DSC curve, with decomposition of clay, e.g., degradation of kaolinite/illite (500–550°C) and chlorite (580–625°C). The complex peak in this temperature range [mainly for S-2(3)] with a shoulder at the lower temperature corresponding to the oxidation reaction of light hydrocarbons, while the main peak corresponds to the oxidation of heavy hydrocarbons and fixed carbon (Sun et al., 2015). Also, presence of any pyrite, might influence the TGA curve in this temperature region due to oxidation of that mineral at around 500°C (Zhang et al., 2014). The decomposition of carbonates was observed in the DTG curve from ∼625–850°C (dolomite 625–720°C and calcite 780–840°C) with mass losses of 4.1 wt.% for S-2(1) and 3.5 wt.% for S-2(3). At 850–1150°C, the mass losses of 1.5 wt.% for S-2(1) and 2.6 wt.% for S-2(3) can be attributed to decomposition and transformation of more stable mineral phases such as quartz, silicate and iron-bearing phases (Hajpal and Torok, 2004). At the highest temperature of 1150–1400°C, the mass loss of 0.7 wt.% for S-2(1) and 0.6 wt.% for S-2(3) with a broad endothermic region can indicate decomposition/transformation and or melting of the residual sample.

DISCUSSION

Source of OM

The organic matter may be present in different forms from multiple sources (e.g., marine and continental), that may have different thermal maturity and stability. Marine organic matter is constituted of phytoplankton debris or detritus with proteins/amino acids, carbohydrates, and lipids as the main chemical components (Burdige, 2007). On the other hand, continental organic matter is composed of terrestrial biomass including plant residue and soil organic matter. Since continental derived organic matter consists of already altered and degraded remains of the living terrestrial biomass (e.g., soil humus), it is less susceptible to further degradation and alteration as compared to marine organic matter. The organic matter for the three samples in this study is predominantly derived from continental source with any marine contribution being minor, as seen previously from C/N and $\delta^{13}C$ in shale retrieved from various depth of the studied cores (Basu et al., 2018). This is corroborated by the measured $\delta^{13}C_{organic}$ ratio of $\sim -27‰$ in all the three samples (**Table 2**), in agreement with expected $\delta^{13}C$ of $-27‰$ for land plant organic matter, as to $\sim -20‰$ in marine algal organic matter (Meyers, 2014).

Multiple OC Components Based on Step Combustion Release Profile

The peak release of nitrogen (∼70% of the total) in S-2(3) and S-3(3) corresponds to 500–600°C indicating the breakdown of organic matter and some clay minerals in this temperature

TABLE 3 | Individual step release of carbon (C) and nitrogen (N) from shale during combustion with corresponding $\delta^{13}C$ and C/N ratios.

Temperature (°C)	Fractional release (%)		$\delta^{13}C$ (‰)	C/N
	C	N		
S-2(1)				
200		0.6		
400	6.6	18.3	−23.6 ± 0.1	11 ± 1
500	14.1	22.5	−23.7 ± 0.1	19 ± 2
600	36.2	24.8	−22.2 ± 0.1	42 ± 4
700	37.7	17.3	−14.3 ± 0.1	64 ± 6
800	3.3	7.9	−24.8 ± 0.1	12 ± 1
900	1.2	5.0	−24.9 ± 0.2	7 ± 0.7
1000	0.7	2.3	−24.4 ± 0.2	9 ± 0.8
1200	0.1	1.2	−23.6 ± 0.1	3 ± 0.1
S-2(3)				
200	1.4	0.3	−28.8 ± 0.1	64 ± 6
400	4.5	7.5	−16.4 ± 0.1	9 ± 0.9
500	8.7	40.2	−17.2 ± 0.2	3 ± 0.1
600	27.0	23.5	−19.2 ± 0.1	18 ± 2
700	30.1	10.9	−12.1 ± 0.2	43 ± 4
800	7.4	6.1	−23.8 ± 0.3	19 ± 2
900	3.7	4.4	−30.0 ± 0.1	13 ± 1
1000	3.2	2.9	−25.8 ± 0.1	17 ± 2
1200	10.9	4.2	−25.1 ± 0.1	40 ± 4
1400	3.0	0.3	−25.2 ± 0.1	64 ± 6
S-3(3)				
200	0.7	0.1	−30.9 ± 0.2	130 ± 13
400	4.5	6.5	−23.1 ± 0.2	12 ± 1
500	14.7	45.5	−4.8 ± 1.2	5 ± 0.1
600	31.9	22.1	−18.0 ± 0.6	24 ± 2
700	27.8	12.1	−13.4 ± 0.3	39 ± 4
800	5.0	5.8	−24.6 ± 0.2	15 ± 1
900	4.5	3.8	−26 ± 0.3	20 ± 2
1000	2.4	1.9	−25.5 ± 0.1	21 ± 2
1200	7.9	2.1	−26 ± 0.2	63 ± 6
1400	0.5		−24.4 ± 0.1	

range, also suggested from STA experiments. For S-2(1), the nitrogen release is much more prolonged from 400 to 700°C. While all other attributes such as TOC and nitrogen content are comparable, S-2(1) has a notably 18% higher carbonate content. The prolonged release can be related to physical protection of the organic matter by the carbonate minerals in S-2(1). But in all the three samples, peak release of carbon (>55%) occurred between 600 and 700°C with elevated $\delta^{13}C$, corresponding to the breakdown of carbonate minerals, as also seen from STA experiments. Alternatively, the prolonged release can be an effect of fabric/texture of the sample, which is beyond the scope of this study. It is possible, that in S-2(1), the mineral matrix has specific arrangement of its constituents (e.g., alternation of organic and clay nanolayers) (Salmon et al., 2000), aiding in physical protection of the organic matter and preventing its breakdown. This can only be confirmed from detailed study of the nano-scale textural arrangement of the shales.

Based on the carbon and nitrogen release profiles and the associated $\delta^{13}C$ and N/C ratios, up to five different components can be identified associated with different release temperature as described in **Table 4**.

<400°C

A very small fraction of total carbon (<1.5% of the total) is released at low temperature of 200°C for samples S-2(3) and S-3(3), also accompanied by very low nitrogen content (<0.5%) and with depleted $\delta^{13}C$ of −30 to −28‰. In agreement with observations from STA experiments, this component can be attributed to free phases that can accumulate at the mouth of pore spaces or along mineral edges, with least preservation protection. The high C/N and extremely depleted $\delta^{13}C$ is suggestive of adsorbed thermogenic, methane in these two samples (Golding et al., 2013). The possibility of this adsorbed component to be the result of depressurization during core retrieval cannot be completely ruled out. In S-2(1), a comparable, carbon component at an early temperature step is lacking although a small fractional nitrogen release is observed. This nitrogen dominated component is formed during decomposition of organic matter, with degraded matter being preferentially adsorbed on charged clay mineral surfaces as exchangeable nitrogen (Scholten, 1991). Interaction of organic matter by physisorption with silicate mineral matrix has been identified during chemical extraction of mineral matrices in shale using acid/ether extracts (Jeong and Kobylinski, 1983).

Such a low temperature component of the organic matter, will be unstable and mobile, and easily lost from the shale during geological processes. This readily mobile component is denoted as C-1 (**Figures 1–3**) and contributes toward a very small fraction of the total OC present.

400–800°C

This temperature range corresponds to the breakdown of clay and carbonate minerals and release of associated organic matter that may be adsorbed on the mineral surfaces, along with heavy hydrocarbons that may be present. It constitutes the bulk of total carbon released, contributed from the breakdown of carbonate minerals such as calcite and dolomite. Based on TOC and bulk carbon concentration, this temperature range also accounts for > 60% of the TOC in the shales (assuming all carbon that is released at < 400°C and > 800°C to be OC). The peak release of nitrogen indicating breakdown of clay minerals (500–600°C) occurs at a slightly lower temperature as compared to carbon corresponding to the breakdown of the carbonate minerals (600–700°C). It implies that clay-associated OC [denoted as C-2(a); **Figures 1–3**], can be relatively less stable and more mobile than the carbonate associated OC [denoted as C-2(b); **Figures 1–3**]. While C-2 can be physically/chemically adsorbed on clay surfaces, they are more likely to be biomineralized with the carbonates. But given the overlap as to the breakdown of the clay and carbonate phases, any differences between relative stability of these two components will be minor.

The instability of clay minerals in shale is related to their hydrophyllic and charged nature, particularly for expandable clay such as smectite where it can result in swelling. However, whether

TABLE 4 | OC components present in a shale as identified based on their variable release temperature during step heating.

OC component	Release temperature (°C)	Associated mineral	Mode of occurrence	Expected reaction to chemical treatment	Level of stability
C-1	~200	Not specific; dispersed along mineral edges and mouth of pore spaces.	Accumulates	Extractable by organic solvent	Least stable (highly mobile) ~PMOC
C-2(a)	400–800	Clay	Physically adsorbed and chemically bonded as organomineral nanocomposites. Occurs on both internal and external mineral surfaces as well as interlamellar spaces.	Extractable by either organic solvent or wet chemical oxidation	PMOC + CMOC + SOC
C-2(b)	400–800	Carbonate	Biominerals and occlusions	Extractable by wet chemical oxidation	SOC
C-3(a)	1000–1200	Silicate	Biominerals and occlusions	Not easily extractable by wet chemical oxidation	Very stable and immobile VSOC
C-3(b)	~1400	Not specific; dispersed in the shale matrix	Graphitized	Not extractable by wet chemical oxidation	Extremely stable and least mobile ExSOC

Their associated mineral phases and possible mode of occurrence and extractability by chemical treatment are given. PMOC, physically mobile OC; CMOC, chemically mobile OC; SOC, stable OC; VSOC, very stable OC; ExSOC, extremely stable OC (modified after Zhu et al., 2016).

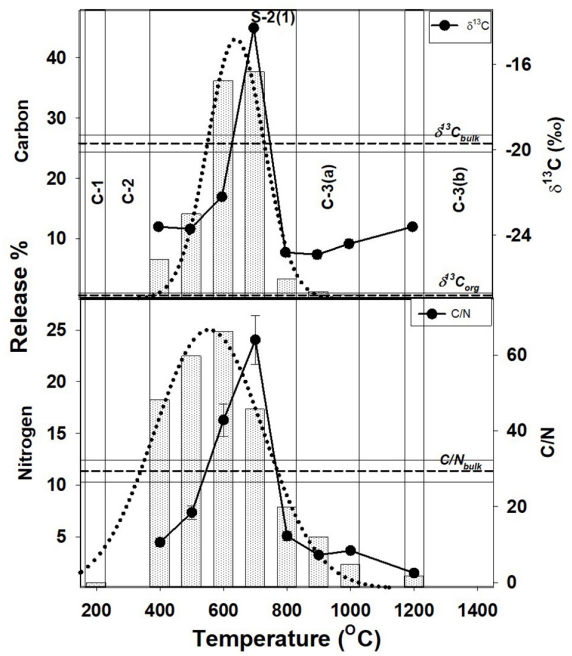

FIGURE 1 | Step combustion temperature vs. carbon and nitrogen release percent for S-2(1). The $\delta^{13}C$ and C/N for each temperature step are shown along with the bulk C/N and $\delta^{13}C$ (C/N_{bulk}, $\delta^{13}C_{bulk}$), and, organic $\delta^{13}C$ ($\delta^{13}C_{organic}$) ratios. The different OC components, C-1, C-2, C-3(a) and C-3(b), released at different temperature due to differences in their stability resulting from their variable mode of association with the minerals present, are also shown.

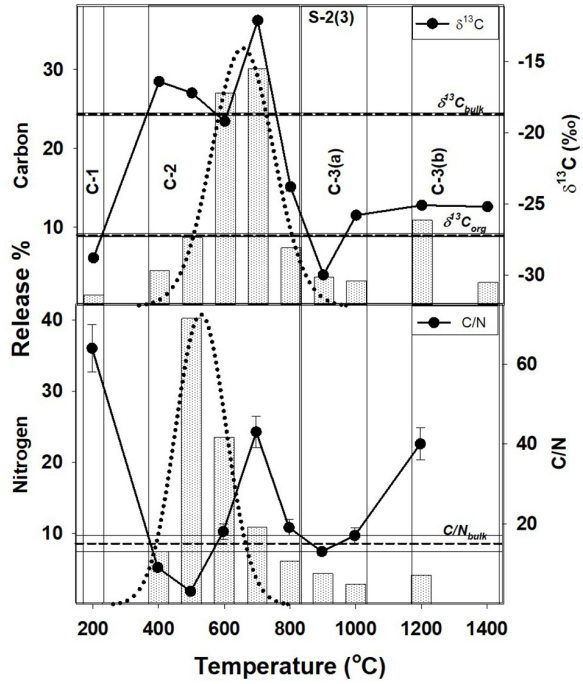

FIGURE 2 | Step combustion temperature vs. carbon and nitrogen release percent for S-2(3). The isotopic and elemental ratios for each temperature step are shown along with the bulk values and the corresponding OC components [C-1, C-2, C-3(a), and C-3(b)]. For further details, refer to text and **Figure 1**.

such swelling related to osmosis by the action of an external fluid can occur significantly in a compacted, impermeable shale is debatable, although internal microfractures can be efficient fluid conduits (Santarelli and Carminati, 1995; Wilson and Wilson, 2014). In addition, some water may be present in intra-aggregate pore spaces in smectitic clay since deposition and through burial, compression and lithification, but this is a bound state and not free (Touret et al., 1990). Based on modeling, it has been

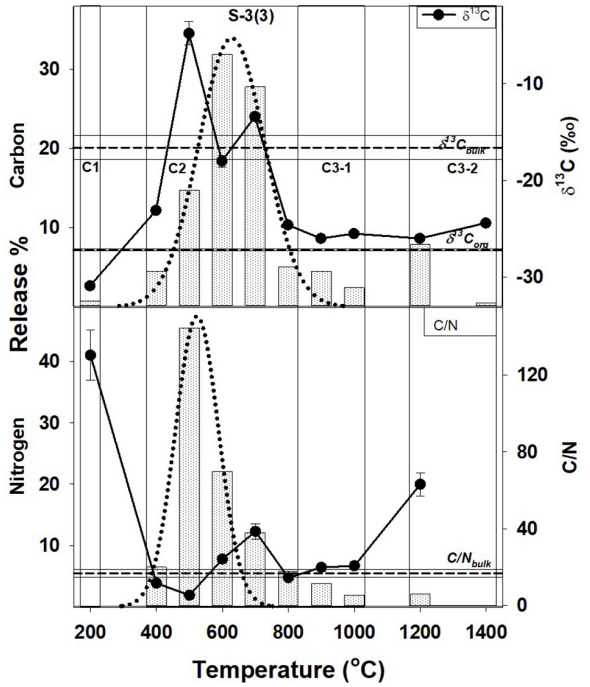

FIGURE 3 | Step combustion temperature vs. carbon and nitrogen release percent for S-3(3). The isotopic and elemental ratios for each temperature step are shown along with the bulk values and the corresponding OC components [C-1, C-2, C-3(a), and C-3(b)]. For further details, refer to text and **Figure 1**.

observed that interlamellar water in smectites is stable up to at least 180°C corresponding to a depth of 6 km without affecting the mineral stability (Odriozola and Guevara-Rodríguez, 2004). This is in agreement with observation from the step combustion experiment of this study, where clay mineral instability is only initiated at temperature > 200°C. A recent study has shown that the OC enrichment is strongly correlated to the high surface area clay minerals where, it occurs as intercalation with phyllosilicate minerals as organomineral nanocomposites that persists through a range of burial depth up to the oil window (Kennedy et al., 2014). With illitization, the OC and clays organize themselves into nano-scale aggregates without any net loss, although there might be significant decrease in the total mineral surface area. Together with results from this study, it is clear that the occurrence of high surface area detrital clay minerals helps in the preservation of OC as nanocomposites and aggregates not only during burial but also at higher temperature during subduction.

Carbonate minerals are not susceptible to breakdown during interaction and reaction with the formation water that is trapped in the pore spaces. The formation water is expected to be saline and already saturated with the minerals in the host rock (Kaszuba et al., 2013). So although the role of carbonate minerals for stabilizing OC is less significant as compared to the clay minerals, it is still possible to trap OC within the stable structure of the carbonate minerals as formanifera, corals and cocolithospores augmenting its stability (Ingalls et al., 2003, 2004). Interaction of organic matter with the carbonate matrix may also be in the form of chemical bonding (Jeong and Kobylinski, 1983). Interaction of clay minerals and carbonate with OC till their breakdown at 400–800°C (clay) and 500–800°C (carbonate), are important in the preservation of carbon in shale (**Figures 1–3**). This is in agreement with carbon retention in sediments at temperature of up to 600°C in intact subducting slabs in absence of infiltrating fluids (Cook-Kollars et al., 2014; Collins et al., 2015).

>800°C

The OC at higher temperature steps is contemporaneously released with decomposition and transformation of stable mineral phases such as quartz, K-feldspar and other silicates, as indicated by STA analyses. This component is marked as C-3(a) and is distinct from C-3(b) (**Figures 1–3**), the later released at temperature exceeding 1000°C. Like calcite, silicates can also be important for stabilizing OC in biominerals (Carter and Mitterer, 1978; Maita et al., 1982) accounting for the release of C-3(a) at temperature corresponding to the breakdown of the silicate minerals. Organic matter can also be contained and protected in pore spaces surrounded by silicate minerals (Ma et al., 2017), as an occlusion in a mineral matrix.

C-3(b), observed in S-2(3), and S-3(3) represents graphitized carbon marked by high C/N and slightly enriched $\delta^{13}C$ (as compared to $\delta^{13}C_{organic}$). An enrichment of $\delta^{13}C$ during graphitization of carbonaceous matter occurs as ^{12}C-^{13}C bonds in C-complexes are broken with increasing thermal stress (Fomina et al., 2019). Although C-3(b) is a very small fraction of the total OC present in shale, its survival during combustion at temperature > 1000°C, imply that it can be preserved even in the hottest subduction zones. Transfer of carbon to the deep Earth locked as graphite at temperature of up to 1200°C with negligible fluid flux, correspond to depths of ∼80–250 km depending on the geothermal gradient (Stern, 2002; Galvez et al., 2013; Zhang et al., 2018). However, given the low density of graphite (2.3 gm/cc) as compared to that of mantle peridotite (3.1–3.4 gm/cc), it can seggregate as a refractory phase in the shallow mantle wedge with restricted deep subduction, while the associated metasediments and carbonates from the slab can form CO_2-rich melt (Kelemen and Manning, 2015). Mantle graphite is indeed known from much shallower depths than diamonds, and also can be related to subduction (Kennedy and Kennedy, 1976; Schulze et al., 1997).

There is a small possibility that this high temperature component is related to highly stable mineral phases like Fe-Ti-Al oxides formed by recrystallization and transformation during the combustion experiments in this study. Such a phase formed can trap OC as occluded or coated phases. Formation of such a mineral phase during these experiments is unlikely as it is not consistently observed in all the three samples [not observed for sample S-2(1) at 1400°C].

The different components released at different temperature during combustion of shungites, a unique rock bearing 1 to 100% amorphous carbon, has been related to the variable oxidation temperature of different organic matter type having distinct C/N and, carbon and nitrogen isotopic

composition (Verchovsky et al., 2018). In our study, given the consistent $\delta^{13}C_{organic}$ of – 27‰ in all the three samples indicating a continental source, and their $\delta^{13}C_{bulk}$ values explainable by mixing between OC and carbonate components, such a possibility is unlikely. This is supported by C/N and $\delta^{13}C$ mixing relationship observed in a previous study (Basu et al., 2018). It is possible that in the shungites, the observed differential release pattern of nitrogen (with accompanying carbon) is a consequence of how the components are sited in their different forms. For example, they can be present as exchangeable or fixed nitrogen or, hosted in the core of the carbonaceous matrix encapsulated from the influence of any hot, infiltrating fluids (Scholten, 1991; Boudou et al., 2008).

OC Components and Their Host Sites

Organic matter in shale can be present as adsorbed component, both on internal and external surfaces of minerals or, accumulated freely at the mouth or edge of the pore spaces and, the interlayer spaces of the clay minerals (Zhu et al., 2016). The associated carbon, occurring as freely accumulated OC along with physically adsorbed OC on external clay surfaces, can be easily extracted by organic solvent and referred to as the physically mobile OC (PmOC). Chemically bonded OC (CmOC) present in the internal surfaces of the minerals can only be removed by wet chemical oxidation by breaking the chemical bonds. But the most stable OC (SOC), occurs in the interlayer spacing of clay minerals, black carbon and occluded in carbonates and is not affected by wet chemical oxidation. Based on treatment with chemical reagents, OC components have the following sequence of mobility, PmOC > CmOC > SOC, which corresponds to a reverse trend in their stability (Zhu et al., 2016). The OC component can be sorbed to the surfaces interacting variably, sometimes via multiple points that enhances its overall stability (Keil and Mayer, 2014).

In this study, based on step combustion experiments and temperature release up to five components can be identified. In an order of increasing release temperature reflecting increasing stability and decreasing mobility from their host sites in a shale, they are C-1 < C-2(a) < C-2(b) < C-3(a) < C-3(b) (**Table 4**). C-1 occurs as a free component while C-2(a) is associated with clay minerals and both are equivalent to PmOC. C-2(a) corresponds to the physically adsorbed component on the surfaces of clay minerals. C-2(a) also includes the more retentive, chemically adsorbed component present in the internal surfaces of the clay minerals or, in their interlamellar spaces and comparable to CmOC and SOC respectively. Consequently, C-2(a) is released over a range of temperature in our experiments from 400 to 800°C. Closely associated with C-2(a), must be the OC occurring as biomineral or occluded phases associated with the carbonate minerals and denoted as C-2(b), which correspond to SOC. The C-3(a) occurs as biomineral or as occluded phase with silicate minerals, not distinguished by chemical reagents. Based on this study, we denote this component as very stable OC (VSOC). The graphitized OC also identified as SOC by Zhu et al. (2016), is categorized in this study as extremely stable OC (ExSOC) and is the most stable of all OC components in the shale.

CONCLUSION

Stepwise combustion of three shales from the Jurassic Haynesville-Bossier Formation suggests that the OC present in them occurs as different components. As the organic matter from the three samples are identical in terms of $\delta^{13}C_{organic}$, TOC content and thermal maturity, any selective degradation related to its type, should be minimum, although cannot be ruled out completely. Rather, the different components are released at different temperature steps due to differences in their stability, as related to their association with various mineral phases such as clay minerals, carbonate, and silicates. This highlights the significance of organic-mineral interaction in the preservation of OC components. The OC is hosted differently with these mineral phases sometimes sorbed as small molecules to the external surface or chemically sorbed to the internal surfaces of the clay minerals. It may be biomineralized or occluded by carbonate and silicate while a very small fraction can occur as free accumulates or in the graphitized form. In absence of any externally infiltrating fluid in a closed system, mineral associated OC is well-preserved till the breakdown of the shale constituent minerals such as clay and carbonate. This corresponds to peak release of 500–600°C for the phyllosilicate clay minerals and 600–700°C for the carbonate, indicating depth of ∼80 to 100 km, depending on the thermal regime of the subduction zone (Syracuse et al., 2010).

The OC components present in a shale is released at different temperature during step combustion in order of their increasing stability and decreasing mobility from their host sites. In conjunction with results from a previous study correlating the occurrence of organic matter and chemical stability (Zhu et al., 2016), the following components can be identified:

C-1 – Released at 200°C, occurs as free accumulates at the mouth of the pore spaces or edge of minerals in a shale. It is likely to be extracted using organic solvent and, is prone to be lost from the shale during diagenesis. It constitutes a very small fraction of the total OC.

C-2(a) – Released predominantly at 400–700°C, it is the OC component that is associated with clay minerals. It can be physically adsorbed on the external mineral surfaces and can be extracted using organic solvent. A more stable form can be chemically adsorbed in the internal surfaces of the clay minerals forming intercalations as organomineral nanocomposites, and can only be released by breaking the chemical bonds by wet chemical oxidation. C-2(a) can occur in the interlamellar spaces making them highly stable that would be non-extractable by chemical oxidation. A large fraction of the total OC in shale occurs as C-2(a).

C-2(b) – Released predominantly at 500–800°C, it refers to the OC component that is associated with the carbonate minerals, either occluded or in the biomineralized form. It should be extractable by wet chemical oxidation.

C-3(a) – Released at 800–1000°C, this OC component is associated with the silicate minerals in the biomineralized form or as occlusions. It occurs as a very stable form and is

unlikely to be extractable by wet chemical oxidation as easily as C-2(a) or C-2(b).

C-3(b) – Released at 1200–1400°C, this corresponds to the graphitized OC that should be non-reactive to wet chemical oxidation. It is a small fraction of the total OC but is highly stable in the shale.

Except C-1, all other components are retained till high temperature in the shale suggesting that they can survive during geological processes such as burial diagenesis and subduction. C-3(b), if subducted, can remain as a refractory phases in the shallow mantle without being oxidized.

Future studies should consider how shale fabric (relationship between the different minerals and the resulting pore spaces within the volume of the shale), texture (size distribution of constituent particles in terms of clay, silt and sand sized particles) and structure (bedding planes, fissility, sedimentary laminations) influence the interaction between minerals and organic matter affecting the stability/mobility of the OC components present.

DATA AVAILABILITY STATEMENT

All datasets generated for this study are included in the article/**Supplementary Material**.

AUTHOR CONTRIBUTIONS

SB wrote and edited the manuscript, and conducted the combustion experiments, and XRD and TOC measurements. AV provided instrumental guidance, performed the combustion experiments, and edited the manuscript. AB performed the STA experiments and edited the manuscript. AJ edited the manuscript and provided input for the overall work, collaborating with SB. A-LJ performed the organic carbon isotopic measurements and edited the manuscript.

FUNDING

Funding for this work was provided to SB by an industry consortium constituted by BG Group (now Shell), who also provided the specimen used under award 159877.

ACKNOWLEDGMENTS

The authors thank Dr. S. Mikhail for his editorial handling, and Dr. Alberto Vitale Brovarone and Dr. Vadim Reutsky for their insightful comments and constructive review that greatly helped to improve the quality of the manuscript.

SUPPLEMENTARY MATERIAL

The Supplementary Material for this article can be found online at: https://www.frontiersin.org/articles/10.3389/feart.2019.00297/full#supplementary-material

REFERENCES

Ague, J. J., and Nicolescu, S. (2014). Slab melting as a barrier to deep carbon subduction. *Nat. Geosci.* 7, 355–360. doi: 10.1038/NGEO2143

Aiuppa, A., Fischer, T. P., Plank, T., and Bani, P. (2019). CO2 flux emissions from the Earth's most actively degassing volcanoes, 2005-2015. *Sci. Rep.* 9:5442. doi: 10.1038/s41598-019-41901-y

Alt, J. C., Teagle, D. A. H., and Damon, A. H. (1999). The uptake of carbon during alteration of ocean crust. *Geochim. Cosmochim. Acta* 63, 1527–1535. doi: 10.1016/S0016-7037(99)00123-4

Barry, P. H., de Moor, J. M., Giovannelli, D., Schrenk, M., Hummer, D. R., Lopez, T., et al. (2019). Forearc carbon sink reduces long-term volatile recycling into the mantle. *Nature* 568, 487–492. doi: 10.1038/s41586-019-1131-5

Basu, S., Ahmed, J., Jones, A. P., and Verchovsky, A. B. (2018). Characterisation of carbón components and their isotopic composition in gas shales. *Energy Proc.* 146, 47–52. doi: 10.1016/j.egypro.2018.07.007

Berner, R. A. (2003). The long-term carbon cycle, fossil fuels and atmospheric composition. *Nature* 426, 323–326. doi: 10.1038/nature02131

Blatt, H., and Jones, R. (1975). Proportions of exposed igneous, metamorphic, and sedimentary rocks. *GSA Bull.* 86, 1085–1088.

Boudou, J.-P., Schimmelmann, A., Ader, M., Mastalerz, M., Sebilo, M., and Gengembre, L. (2008). Organic nitrogen chemistry during low-grade metamorphism. *Geochim. Cosmochim. Acta* 72, 1199–1221. doi: 10.1016/j.gca.2007.12.004

Burdige, D. J. (2007). Preservation of organic matter in marine sediments: controls, mechanisms, and an imbalance in sediment organic carbon budgets? *Chem. Rev.* 107, 467–485. doi: 10.1021/cr050347q

Carter, P. W., and Mitterer, R. M. (1978). Amino acid composition of organic matter associated with carbonate and non-carbonate sediments. *Geochim. Cosmochim Acta* 42, 1231–1238. doi: 10.1016/0016-7037(78)90116-3

Chiodini, G., Granieri, D., Avino, R., Caliro, S., Costa, A., Minopoli, G., et al. (2010). Non-volcanic CO2 earth degassing: case of mefite d'Ansanto (southern Apennines), Italy. *Geophys. Res. Lett.* 37:L11303. doi: 10.1029/2010GL042858

Clift, P. D. (2017). A revised budget for Cenozoic sedimentary carbon subduction. *Rev. Geophys.* 55, 97–125. doi: 10.1002/2016RG000531

Collins, N. C., Bebout, G. E., Angiboust, S., Agard, P., Scambelluri, M., Crispini, L., et al. (2015). Subduction zone metamorphic pathway for deep carbon cycling: II. Evidence from HP/UHP metabasaltic rocks and ophicarbonates. *Chem. Geol.* 412, 132–150. doi: 10.1016/j.chemgeo.2015.06.012

Coogan, L. A., Parrish, R. R., and Roberts, N. M. W. (2016). Early hydrothermal carbon uptake by the upper oceanic crust: insight from in situ U-Pb dating. *Geology* 44, 147–150. doi: 10.1130/G37212.1

Cook-Kollars, J., Bebout, G. E., Collins, N. C., Angiboust, S., and Agard, P. (2014). Subduction zone metamorphic pathway for deep carbon cycling: I. Evidence from HP/UHP metasedimentary rocks, Italian Alps. *Chem. Geol.* 386, 31–48. doi: 10.1016/j.chemgeo.2014.07.013

Dayal, A. M. (2017). "Deposition and Diagenesis," in *Shale Gas: Exploration and Environmental and Economic Impacts*, eds A. M. Dayal, and D. Mani, (Amsterdam: Elsevier Inc.), 13–23. doi: 10.1016/B978-0-12-809573-7.00002-0

Di-Giovanni, C., Disnar, J.-R., and Macaire, J.-J. (2002). Estimation of the annual organic carbon yield related to carbonated rocks chemical weathering: implications for the global organic carbon cycle understanding. *Glob. Planet. Change* 32, 195–210. doi: 10.1016/S0921-8181(01)00141-2

Duncan, M. S., and Dasgupta, R. (2017). Rise of Earth's atmospheric oxygen controlled by efficient subduction of organic carbon. *Nat. Geosci.* 10, 387–392. doi: 10.1038/NGEO2939

Etiope, G., and Sherwood-Lollar, B. (2013). Abiotic methane on Earth. *Rev. Geophys.* 51, 276–299. doi: 10.1002/rog.20011

Evans, K. (2011). Metamorphic carbon fluxes: how much and how fast? *Geology* 39, 95–96. doi: 10.1130/focus012011.1

Fomina, E., Kozlov, E., Lokhov, K., Lokhova, O., and Bocharov, V. (2019). Carbon sources and the graphitization of carbonaceous matter in precambrian rocks of the keivy terrane (Kola Peninsula, Russia). *Minerals* 9:94. doi: 10.3390/min9020094

Galvez, M. E., Beyssac, O., Martinez, I., Benzerara, K., Chaduteau, C., Malvoisin, B., et al. (2013). Graphite formation by carbonate reduction during subduction. *Nat. Geosci.* 6, 473–477. doi: 10.1038/NGEO1827

Golding, S. D., Boreham, C. J., and Esterle, J. (2013). Stable isotope geochemistry of coal bed and shale gas and related production waters: a review. *Int. J. Coal Geol.* 120, 24–40. doi: 10.1016/j.coal.2013.09.001

Hajpal, M., and Torok, A. (2004). Mineralogical and colour changes of quartz sandstones by heat. *Environ. Geol.* 46, 311–322. doi: 10.1007/s00254-004-1034-z

Henry, D. G., Jarvis, I., Gillmore, G., and Stephenson, M. (2019). Raman spectroscopy as a tool to determine the thermal maturity of organic matter: application to sedimentary, metamorphic and structural geology. *Earth Sci. Rev.* (in press) . doi: 10.1016/j.earscirev.2019.102936

Huang, F., Daniel, I., Cardon, H., Montagnac, G., and Sverjensky, D. A. (2017). Immiscible hydrocarbon fluids in the deep carbon cycle. *Nat. Commun.* 8:15798. doi: 10.1038/ncomms15798

Ingalls, A. E., Aller, R. C., Lee, C., and Wakeham, S. G. (2004). Organic matter diagenesis in shallow water carbonate sediments. *Geochim. Cosmochim. Acta* 68, 4363–4379. doi: 10.1016/j.gca.2004.01.002

Ingalls, A. E., Lee, C., and Druffel, E. R. M. (2003). Preservation of organic matter in mound-forming coral skeletons. *Geochim. Cosmochim Acta* 67, 2827–2841. doi: 10.1016/S0016-7037(03)00079-6

Jackson, M. L. W., and Laubach, S. E. (1988). Cretaceous and tertiary compressional tectonics as the cause of the Sabine Arch, East Texas and Northwest Louisiana. *Gulf Coast Assoc. Geol. Soc. Trans.* 38, 245–256.

Jarrard, R. D. (2003). Subduction fluxes of water, carbon dioxide, chlorine and potassium. *Geochem. Geophys. Geosyst.* 4:8905. doi: 10.1029/2002GC000392

Jeong, K. M., and Kobylinski, T. P. (1983). Organic-Mineral matter interactions in green river oil shale. *Geochem. Chem. Oil Shales* 230, 493–512. doi: 10.1021/bk-1983-0230.ch028

Kaszuba, J., Yardley, B., and Andreani, M. (2013). Experimental perspectives of mineral dissolution and precipitation due to carbon dioxide-water-rock interactions. *Rev. Miner. Geochem.* 77, 153–188. doi: 10.2138/rmg.2013.77.5

Keil, R. G., and Mayer, L. M. (2014). Mineral matrices and organic matter. *Treatise Geochem.* 2014, 337–359. doi: 10.1016/B978-0-08-095975-7.01024-X

Kelemen, P. B., and Manning, C. E. (2015). Reevaluating carbon fluxes in subduction zones, what goes down, mostly comes up. *Proc. Natl. Acad. Sci. U.S.A.* 112, E3997–E4006. doi: 10.1073/pnas.1507889112

Kennedy, C. S., and Kennedy, G. C. (1976). The equilibrium boundary between graphite and diamond. *J. Geophys. Res.* 81, 2467–2470. doi: 10.1029/JB081i014p02467

Kennedy, M. J., Löhr, S. C., Fraser, S. A., and Baruch, E. T. (2014). Direct evidence for organic carbon preservation as clay-organic nanocomposites in a Devonian black shale; from deposition to diagenesis. *Earth Planet. Sci. Lett.* 388, 59–70. doi: 10.1016/j.epsl.2013.11.044

Li, Y. (2017). Immiscible C-H-O fluids formed at subduction zone conditions. *Geochem. Perspect. Lett.* 3, 12–21. doi: 10.7185/geochemlet.1702

Ma, L., Taylor, K. G., Dowey, P. J., Courtois, L., Gholinia, A., and Lee, P. D. (2017). Multi-scale 3D characterisation of porosity and organic matter in shales with variable TOC content and thermal maturity: examples from the lublin and baltic basins, Poland and Lithuania. *Int. J. Coal Geol.* 180, 100–112. doi: 10.1016/j.coal.2017.08.002

Mainali, P. (2011). *Chemostratigraphy and the Paleoceanography of the Bossier-Haynesville Formation, East Texas Basin, TX and LA, USA*. Master's thesis, University of Texas, Arlington.

Maita, Y., Montani, S., and Ishii, J. (1982). Early diagenesis of amino acids in Okhotsk Sea sediments. *Deep Sea Res. Part A Oceanogr. Res. Pap.* 29, 485–498. doi: 10.1016/0198-0149(82)90072-3

Meyers, P. A. (2014). Why are the δ13Corg values in Phanerozoic black shales more negative than in modern marine organic matter? *Geochem. Geophys. Geosyst.* 15, 3085–3106. doi: 10.1002/2014GC005305

Murata, K. J., Friedman, I., and Madsen, B. M. (1969). Isotopic composition of diagenetic carbonates in marine Miocene formations of California and Oregon. *U.S. Geol. Survey Prof. Pap.* 614-B, 1–24. doi: 10.3133/pp614B

Nunn, J. A. (2012). Burial and thermal history of the Haynesville Shale: implications for overpressure, gas generation, and natural hydrofracture. *GCAGS J.* 1, 81–96.

Odriozola, G., and Guevara-Rodríguez, F. de, J. (2004). Na-montmorillonite hydrates under basin conditions: hybrid monte carlo and molecular dynamics simulations. *Langmuir* 20, 2010–2016. doi: 10.1021/la035784j

Petsch, S. T., Edwards, K. J., and Eglinton, T. I. (2005). Microbial transformations of organic matter in black shales and implications for global biogeochemical cycles. *Palaeogeogr. Palaeoclimatol. Palaeoecol.* 219, 157–170. doi: 10.1016/j.palaeo.2004.10.019

Saikkonen, R. J., and Rautiainen, I. A. (1990). Determination of total and non-carbonate carbon in rock samples by a method using infrared absorption. *Bull. Geol. Soc. Finland* 62, 149–156. doi: 10.17741/bgsf/62.2.005

Salmon, V., Derenne, S., Lallier-Vergès, E., Largeau, C., and Beaudoin, B. (2000). Protection of organic matter by mineral matrix in a Cenomanian black shale. *Organ. Geochem.* 31, 463–474. doi: 10.1016/S0146-6380(00)00013-19

Salvador, A. (1991). "Origin and development of the Gulf of Mexico basin," in *The Gulf of Mexico Basin. The Geology of North America*, ed. A. Salvador, (Boulder, CO: Geological Society of America), doi: 10.1130/DNAG-GNA-J.389

Santarelli, F. J., and Carminati, S. (1995). Do shales swell? A critical review of available evidence. *Soc. Pet. Eng. Pap. SPE* 29421, 741–756. doi: 10.2118/29421-MS

Scholten, S. O. (1991). *The Distribution of Nitrogen Isotopes in Sediments*. Dissertation, Faculteit Aardwetenschappen, Utrecht University Repository, Utrecht.

Schulze, D. J., Valley, J. W., Viljoen, K. S., Stiefenhofer, J., and Spicuzza, M. (1997). Carbon isotope composition of graphite in mantle eclogites. *J. Geol.* 105, 379–386. doi: 10.1086/515933

Schwarzenbach, E. M., Caddick, M. J., Petroff, M., Gill, B. C., Cooperdock, E. H. G., and Barnes, J. D. (2018). Sulphur and carbon cycling in the subduction zone mélange. *Sci. Rep.* 8:15517. doi: 10.1038/s41598-018-33610-9

Smith, J. G. (2003). Aspects of the Loss-on-ignition (loi) technique in the context of clay-rich, glaciolacustrine sediments. *Geografiska Ann. Ser. A Phys. Geogr.* 85, 91–97. doi: 10.1111/1468-0459.00191

Stern, R. J. (2002). Subduction Zones. *Rev. Geophys.* 40, 3–1. doi: 10.1029/2001RG000108

Sun, Y.-H., Bai, F.-T., Lü, X.-S., Li, Q., Liu, Y.-M., Guo, M.-Y., et al. (2015). A novel energy-efficient pyrolysis process: self-pyrolysis of oil shale triggered by topochemical heat in a horizontal fixed bed. *Sci. Rep.* 5:8290. doi: 10.1038/srep08290

Syracuse, E. M., van Keken, P. E., and Abers, G. A. (2010). The global range of subduction zone thermal models. *Phys. Earth Planet. Inter.* 183, 73–90. doi: 10.1016/j.pepi.2010.02.004

Thomson, A. R., Walter, M. J., Kohn, S. C., and Brooker, R. A. (2016). Slab melting as a barrier to deep carbon subduction. *Nature* 529, 76–79. doi: 10.1038/nature16174

Touret, O., Pons, C. H., Tessier, D., and Tardy, Y. (1990). Etude de la repartition de l'eau dans des argiles saturees Mg2+ aux fortes teneurs en eau. *Clay Miner.* 25, 217–233. doi: 10.1180/claymin.1990.025.2.07

Tsuno, K., and Dasgupta, R. (2011). Melting phase relation of nominally anhydrous, carbonated pelitic-eclogite at 2.5–3.0 GPa and deep cycling of sedimentary carbon. *Contrib. Mineral. Petrol.* 161, 743–763. doi: 10.1007/s00410-010-0560-9

Tsuno, K., Dasgupta, R., Danielson, L., and Righter, K. (2012). Flux of carbonate melt from deeply subducted pelitic sediments: geophysical and geochemical implications for the source of Central American volcanic arc. *Geophys. Res. Lett.* 39:L16307. doi: 10.1029/2012GL052606

Verchovsky, A. B. (2017). Origin of isotopically light nitrogen in meteorites. *Geochem. Int.* 55, 957–970. doi: 10.1134/S0016702917110106

Verchovsky, A. B., Gol'tsyn, N. A., Prasolov, E. M., and Lokhov, K. I. (2018). Nitrogen isotopic composition of shungite from the onega structure, Russia, and the origin of the organic matter. *Geochem. Int.* 56, 1341–1353. doi: 10.1134/S0016702918130086

Vitale Brovarone, A., Isabelle, M., Elmaleh, A., Compagnoni, R., Chaduteau, C., Ferraris, C., et al. (2017). Massive production of abiotic methane during subduction evidenced in metamorphosed ophicarbonates from the Italian Alps. *Nat. Commun.* 8:14134. doi: 10.1038/ncomms14134

Voyer, M. L., Hauri, E. H., Cottrell, E., Kelley, K. A., Salters, V. J. M., Langmuir, C. H., et al. (2019). Carbon fluxes and primary magma CO2 contents along the global mid-ocean ridge system. *Geochem. Geophys. Geosyst.* 20, 1387–1424. doi: 10.1029/2018GC007630

Wallmann, K., and Aloisi, G. (2012). "The global carbon cycle: geological processes," in *Fundamentals of Geobiology*, eds A. H. Knoll, D. E. Canfield, and K. O. Konhauser, (Hoboken, NJ: Blackwell Publishing Ltd.), 20–34.

Wilson, M. J., and Wilson, L. (2014). Clay mineralogy and shale instability: an alternative conceptual analysis. *Clay Miner.* 49, 127–145. doi: 10.1180/claymin.2014.049.2.01

Wright, M. C., Court, R. W., Kafantaris, F.-C. A., Spathopoulos, F., and Sephton, M. A. (2015). A new rapid method for shale oil and shale gas assessment. *Fuel* 153, 231–239. doi: 10.1016/j.fuel.2015.02.089

Yang, J., Hatcherian, J., Hackley, P. C., and Pomerantz, A. E. (2017). Nanoscale geochemical and geomechanical characterization of organic matter in shale. *Nat. Commun.* 8:2179. doi: 10.1038/s41467-017-02254-0

Zeng, X., Cai, J., Dong, Z., Bian, L., and Li, Y. (2018). Relationship between mineral and organic matter in shales: the case of shahejie formation, Dongying Sag, China. *Minerals* 8:222. doi: 10.3390/min8060222

Zhang, S., Ague, J. J., and Vitale Brovarone, A. (2018). Degassing of organic carbon during regional metamorphism of pelites, Wepawaug Schist, Connecticut, USA. *Chem. Geol.* 490, 30–44. doi: 10.1016/j.chemgeo.2018.05.003

Zhang, Y., Ge, X., Nakano, J., Liu, L., Wang, X., and Zhang, Z. (2014). Pyrite transformation and sulfur dioxide release during calcination of coal gangue. *RSC Adv.* 4, 42506–42513. doi: 10.1039/C4RA06954D

Zhu, X., Cai, J., Liu, W., and Lu, X. (2016). Occurrence of stable and mobile organic matter in the clay-sized fraction of shale: significance for petroleum geology and carbon cycle. *Int. J. Coal Geol.* 160-161, 1–10. doi: 10.1016/j.coal.2016.03.011

Conflict of Interest: The authors declare that the research was conducted in the absence of any commercial or financial relationships that could be construed as a potential conflict of interest.

frontiers in Earth Science

ORIGINAL RESEARCH
published: 13 December 2019
doi: 10.3389/feart.2019.00332

Tectonic Controls on Carbon and Serpentinite Storage in Subducted Upper Oceanic Lithosphere for the Past 320 Ma

Andrew S. Merdith[1], Suzanne E. Atkins[1,2] and Michael G. Tetley[1]*

[1] CNRS, UMR 5276 LGL-TPE, F-69622, University of Lyon, Université Lyon 1, Ens de Lyon, Lyon, France, [2] Département de Géosciences, École Normal Supérieure, Paris, France

The subduction of upper oceanic lithosphere acts as a primary driver of Earth's deep carbon and water cycles, providing a key transportation mechanism between surface systems and the deep Earth. Carbon and water are stored and transported in altered oceanic lithosphere. In this study, we present mass estimates of the subducted carbon and serpentinite flux from 320 to 0 Ma. Flux estimates are calculated using a full-plate tectonic reconstruction to build a descriptive model of oceanic lithosphere at points along mid-ocean ridges. These points then track the kinematic evolution of the lithosphere until subduction. To address uncertainties of modeled spreading rates in synthetic ocean basins, we consider the preserved recent (83–0 Ma) spreading history of the Pacific Ocean to be representative of the Panthalassa Ocean. This analysis suggests present-day subducting upper oceanic lithosphere contains 10–39 Mt/a of carbon and 900–3500 Mt/a of serpentinite (∼150–450 Mt/a of water). The highest rates of carbon delivery to trenches (20–100 Mt/a) occurred during the Early Cretaceous, as upper oceanic lithosphere subducted during this period formed in times of warm bottom water and the Cretaceous period experienced high seafloor production and consumption rates. Additionally, there are several episodes of high serpentinite delivery to trenches over the last 100 Ma, driven by extensive serpentinization of mantle peridotites exposed at slow spreading ridges. We propose variations in subduction regimes act as the principal control on the subduction of carbon stored in upper oceanic lithosphere, as since 320 Ma the volume of stored carbon across all ocean basins varies by less than an order of magnitude. For pre-Pangea times (<300 Ma), this suggests estimates of seafloor consumption represent a reasonable first-order approximation of carbon delivery. Serpentinite and associated water flux at subduction zones appear to be primarily controlled by the spreading regime at mid-ocean ridges. This is apparent during times of supercontinent breakup where slow spreading ridges produce highly serpentinized crust, and is observed in the present-day Atlantic, Arctic and Indian oceans, where our model suggests upper oceanic lithosphere is up to ∼100 times more enriched in serpentinite than the Panthalassa and Pacific oceans.

Keywords: deep carbon cycle, serpentinite, subduction flux, water and carbon storage, oceanic crust, tectonics

OPEN ACCESS

Edited by:
Dan J. Bower,
University of Bern, Switzerland

Reviewed by:
Meng Tian,
University of Bern, Switzerland
Grace Shephard,
University of Oslo, Norway

****Correspondence:***
Andrew S. Merdith
andrew.merdith@univ-lyon1.fr

Specialty section:
This article was submitted to Structural Geology and Tectonics, a section of the journal Frontiers in Earth Science

Received: *19 June 2019*
Accepted: *29 November 2019*
Published: *13 December 2019*

Citation:
Merdith AS, Atkins SE and Tetley MG (2019) Tectonic Controls on Carbon and Serpentinite Storage in Subducted Upper Oceanic Lithosphere for the Past 320 Ma. Front. Earth Sci. 7:332. doi: 10.3389/feart.2019.00332

INTRODUCTION

The cycling of oceanic lithosphere from creation at mid-ocean ridges to destruction at subduction zones is the surface expression of the dynamic relationship between Earth's tectonic plates and the convecting mantle over geological timescales (Conrad and Lithgow-Bertelloni, 2002, 2004; Becker, 2006; Seton et al., 2012). Whilst primarily a cycle of rocky material, the oceanic lithosphere also carries a significant mass of volatiles including carbon and water (Jarrard, 2003). These volatiles are sequestered and stored by alteration of the lithosphere through exposure to seawater (Janecky and Seyfried, 1986; Alt and Teagle, 1999), and are either released into melt or enter storage in the mantle during subduction. As a result, the cycling of oceanic lithosphere is a driver of the deep carbon (Dasgupta and Hirschmann, 2010) and water cycles (van Keken et al., 2011), which in turn carry important implications for climate stability (Kasting, 1989), and the rheology of the mantle (Hirth and Kohlstedt, 1996).

Alteration of the upper oceanic lithosphere by contact with seawater occurs globally in all ocean basins. The manner of the alteration depends on the lithological properties of the oceanic crust. New oceanic crust is continuously formed at mid-ocean ridges by magmatic processes, and the upper layers of volcanic crust cool rapidly when exposed to seawater, either directly or indirectly as it percolates through the rock. Alteration in these cases is most concentrated in the upper few hundred meters of the volcanic portions of the crust. However, at slow spreading ridges (full spreading rate < 40 mm/a), the geotherm is insufficient to induce extensive melt and asymmetric, tectonic exhumation of the upper lithospheric mantle occurs with little or no volcanic material (Tucholke and Lin, 1994). This exposes mantle peridotite, rather than basalt, to seawater (Cannat, 1993), resulting in extensive serpentinization of large areas of the peridotitic upper oceanic lithosphere (Früh-Green et al., 2004; Sauter et al., 2013).

The carbon sequestered in oceanic lithosphere comes from several sources, changing through the lifetime of the rock. The initial source is mantle carbon which is degassed at mid-ocean ridges directly into the water column (Dasgupta, 2013) or stored in carbon minerals at the base of the lithosphere (Keller et al., 2017). Freshly formed upper-oceanic lithosphere sequesters carbon in the form of carbonate through precipitation within the volcanic suites of oceanic crust during alteration (Alt and Teagle, 1999; Gillis and Coogan, 2011) or serpentinized peridotite (Alt et al., 2013). As the newly formed crust moves away from the mid-ocean ridge, sediment is deposited. After the Late-Cretaceous (Dutkiewicz et al., 2019), these sediments function as a major sink of both inorganic and organic carbon (Jarrard, 2003; Clift, 2017). Once subducted, carbon stored in sediments and crust can either be released into the lithosphere and atmosphere through melting and/or volcanic outgassing, or recycled back into the mantle (Zhang and Zindler, 1993; Sleep and Zahnle, 2001) as part of the deep carbon cycle (Dasgupta and Hirschmann, 2010). In particular, the metasomatism of oceanic crust occurring within subduction zones stores carbon in blueschists and greenschists (Bebout and Barton, 1989; Kelemen and Manning, 2015), and calcite has been identified as a major storage of carbon in the forearc (Barry et al., 2019).

The alteration of oceanic lithosphere also results in chemically bound water being stored in altered basalts and peridotites, within clay minerals and rocks such as serpentinite (Thompson, 1992). Serpentinite can store up to 13 wt% water, whilst estimates for altered basalts range between 2.7 and 5.7% (Staudigel et al., 1996; Jarrard, 2003; Gerya et al., 2006). Stored water is either dehydrated during subduction or, if subduction is cold and fast, can be returned to the mantle as "return flow" (van Keken et al., 2011). Quantifying the mass of water in oceanic lithosphere as it enters subduction zones is important for understanding and constraining depth-dependent metamorphic processes in the upper mantle and estimating rates of return flow, each having significant implications for viscosity variations deeper in the mantle (Hirth and Kohlstedt, 1996), long term sea level change (Karlsen et al., 2019) and post-seismic deformation (Muto et al., 2016).

Bottom-up approaches, which start from geophysical and geochemical first principles, have been used to calculate how much carbon or water any piece of oceanic crust can store to estimate global storage capacity in the oceanic lithosphere at present day (Staudigel et al., 1996; Jarrard, 2003; Dasgupta and Hirschmann, 2010; Alt et al., 2013; Bodnar et al., 2013; Kelemen and Manning, 2015). A number of studies explore the present-day behavior of chemically bound water in subducted slabs (Hacker, 2008; van Keken et al., 2011), requiring estimates of volatile supply to subduction zones. These studies use concentrations from Jarrard (2003) who estimated the weight percent (wt%) of water stored in different layers of oceanic crust entering subduction zones at the present day, using crustal age together with dredge and core data adjacent to trenches. We also use Jarrard (2003) as reference data for material formed at fast-spreading ridges. However, Jarrard (2003) did not consider the distribution of strongly serpentinitic lithosphere formed at slow spreading ridges entering subduction zones (Kerrick, 2002). The flux of these volatiles at a subduction zone is expected to vary through time because of the time-dependence of both the volume and alteration of oceanic lithosphere. Müller and Dutkiewicz (2018) estimate carbon storage based on carbon stored in altered crust using a plate reconstruction to trace parcels of seafloor through time. However, in addition to altered basalts, there is a significant amount of carbon stored in other components of oceanic crust including sheeted dykes and gabbros which were not explicitly considered in their study ($\sim$0.145 wt% ($\sim$1200 m thick) and 0.01 wt% ($\sim$5000 m thick), respectively) (Alt and Teagle, 1999; Jarrard, 2003; Alt et al., 2013; Kelemen and Manning, 2015). In this study, we follow a similar approach to Müller and Dutkiewicz (2018), extending the analysis to the full crustal suite including serpentinized peridotite, allowing us to calculate estimates of water delivery in serpentinites and the upper 300 m of altered basalts to trenches.

In constructing bottom-up approaches to model volatile storage in oceanic lithosphere, we must consider a range of dependent and independent variables and the observational and analytical data that best constrain them (Crameri et al., 2019). Calculating estimates of carbon storage requires data

constraining the: (i) thicknesses of each volcanic layer, (ii) proportion of peridotite exhumed into the upper oceanic lithosphere, (iii) degree of serpentinization, (iv) degree of basalt alteration, (v) bottom water temperature, and (vi) spreading rate. Consequently, uncertainties associated with each type of constraining data must be included and addressed in the construction of first-order subduction flux models. Quantification of these constraints is difficult even for times with a well-preserved seafloor spreading record, presenting a significant challenge for the Palaeozoic and Mesozoic where a complete geological or geophysical classification of the oceanic lithosphere does not exist. The bulk of observations come from a limited number of sampling sites adjacent to mid-ocean ridges, drill cores on continent-ocean boundaries, and dredge samples (Constantin et al., 1995; Früh-Green et al., 1996; Minshull et al., 2006; Shilobreeva et al., 2011). As a result of these limitations, few time-dependent studies have been completed that are able to both quantitatively estimate the storage of carbon or water in serpentinite at mid-ocean ridges and track ocean basin evolution to estimate the subduction flux of these elements and minerals through time.

The structure, composition, and potential volatile storage capacity of the oceanic lithosphere can be inferred as a function of the spreading rate of the ridge at which it formed. As the spreading rate varies both spatially and temporally (Müller et al., 2008; Crameri et al., 2019), the subduction of carbonates and water-rich serpentinites must also be allowed to vary spatially and temporally in any subduction flux model. The time-dependent storage capacity of oceanic lithosphere presents the second major challenge in a bottom-up approach. To do this, we use full-plate tectonic reconstructions built using a synthesis of geological, geophysical and geochemical data to constrain the locations and nature of plate boundaries in a self-consistent, evolving network (Seton et al., 2012). For the Cenozoic and Mesozoic, where oceanic lithosphere is preserved, isochrons and fracture zones are used to reconstruct ocean basins, and constrain the relative motion of plates. For times older than 200 Ma, where very little lithosphere from that period remains at present day (<30%) (Torsvik et al., 2010; Domeier and Torsvik, 2017), greater importance is placed on jointly interpreting continental palaeomagnetic and geological data in order to approximate the azimuth, and magnitude of plate motion. For example, plate models spanning the Mesozoic and Cenozoic provide a geological constraint on both the length of spreading systems and the rate at which they evolve (Müller et al., 2008, 2016). In comparison, plate reconstructions spanning the Palaeozoic (Domeier and Torsvik, 2014; Domeier, 2016, 2018; Young et al., 2019) and earlier times (Merdith et al., 2017) provide minimum ridge-length estimates requiring artificial spreading and convergence rates, making them a useful, but incomplete tool for extending analyses to pre-Pangea times. This is because spreading rates are tied to both the proportion of exhumed mantle lithosphere and the resulting composition of the upper oceanic lithosphere (Tucholke and Lin, 1994; Reston and McDermott, 2011), and seafloor production rates. Consequently, addressing the inherent uncertainty of pre-Pangea spreading rates is critical to constrain the storage of volatiles and the volume of oceanic lithosphere delivered to subduction zones.

Here, we build a bottom-up estimate of carbonate storage in the complete upper oceanic lithosphere including volcanics and altered peridotites, and an estimate of model uncertainty. Our approach ties the storage and the resulting availability of carbon in upper oceanic lithosphere directly to seafloor production rates and a defined volume of rock. We use a suite of descriptive system components identified and defined using present-day observations and data compilations (e.g., Kelemen and Manning, 2015) to estimate the volume of carbon stored in upper oceanic lithosphere. The time-dependence of our model is constrained by a recent full-plate reconstruction extending back to 410 Ma (Matthews et al., 2016), providing an integrated interpretation of the global evolution of tectonic plates on Earth's surface. We test the sensitivity of our results to the effects of uncertainties in the geochemical data and plate reconstruction, providing a method to address uncertainty.

METHODOLOGY

Spreading Rate

To track the time-dependent evolution of tectonic plates and their boundaries, we use the plate reconstruction model of Matthews et al. (2016) spanning from 410 to 0 Ma and corrected for the model errata identified and explained in Torsvik et al. (2019). This plate model is a synthesis of the Domeier and Torsvik (2014) model for the late Palaeozoic (410–250 Ma) and the Müller et al. (2016) model for the Mesozoic and Cenozoic (230–0 Ma). We use the *Python* programing language[1] with the *GPlates* software and python API *pyGPlates*[2] to interrogate the reconstruction of Matthews et al. (2016) and build a time-dependent database of mid-ocean ridges, spreading segment lengths and spreading rates.

Since the breakup of Pangea, the strongest constraint for the reconstruction of past plate motion including spreading rates is provided by the preserved oceanic lithosphere (Hellinger, 1981; Lithgow-Bertelloni and Richards, 1998). Consequently, the estimated uncertainty of a plate reconstruction model can be related to the amount of lithosphere that is preserved at a given time (Torsvik et al., 2010). In order to accommodate this unavoidable uncertainty in the Palaeozoic and Early Mesozoic where little oceanic lithosphere remains preserved, we broadly distinguish ocean basins as either "internal" or "external" (Murphy and Nance, 2003), adopting a different approach for each type.

Internal oceans, such as the Atlantic and Indian Oceans, are defined as occurring typically on overriding plates formed during supercontinent breakup and initially contain a large component of continental lithosphere that decreases gradually over time as the ocean expands. External oceans, such as the Panthalassa and Pacific Oceans, are defined as remaining stable through at least a single supercontinent cycle (Merdith et al., 2019), are ringed by

[1] www.python.org

[2] www.gplates.org

subduction (Collins, 2003; Domeier and Torsvik, 2014), and are composed almost entirely of oceanic lithosphere. In our analysis we classify the Panthalassa and Pacific Oceans as the only external oceans, whilst all other basins in the plate model are considered internal oceans (e.g., **Figures 1A–F**). For external oceans earlier than 160 Ma (rounding down to the nearest 10 Ma from the age of the earliest magnetic lineations of seafloor spreading preserved in the Pacific Ocean (e.g., Müller et al., 2016), we treat spreading rate as a free parameter in our calculations and compare these results to those produced by explicitly using the spreading rate taken from the plate model. We use this method to assess the validity of synthetic ocean plates (i.e., ocean plates presumed to have existed, but of which no evidence remains *in situ*), and to explore the sensitivity of our results to variations of spreading rate.

The Pacific Ocean is the only large, stable, external ocean that is well-constrained in plate models for the last ∼83 Ma

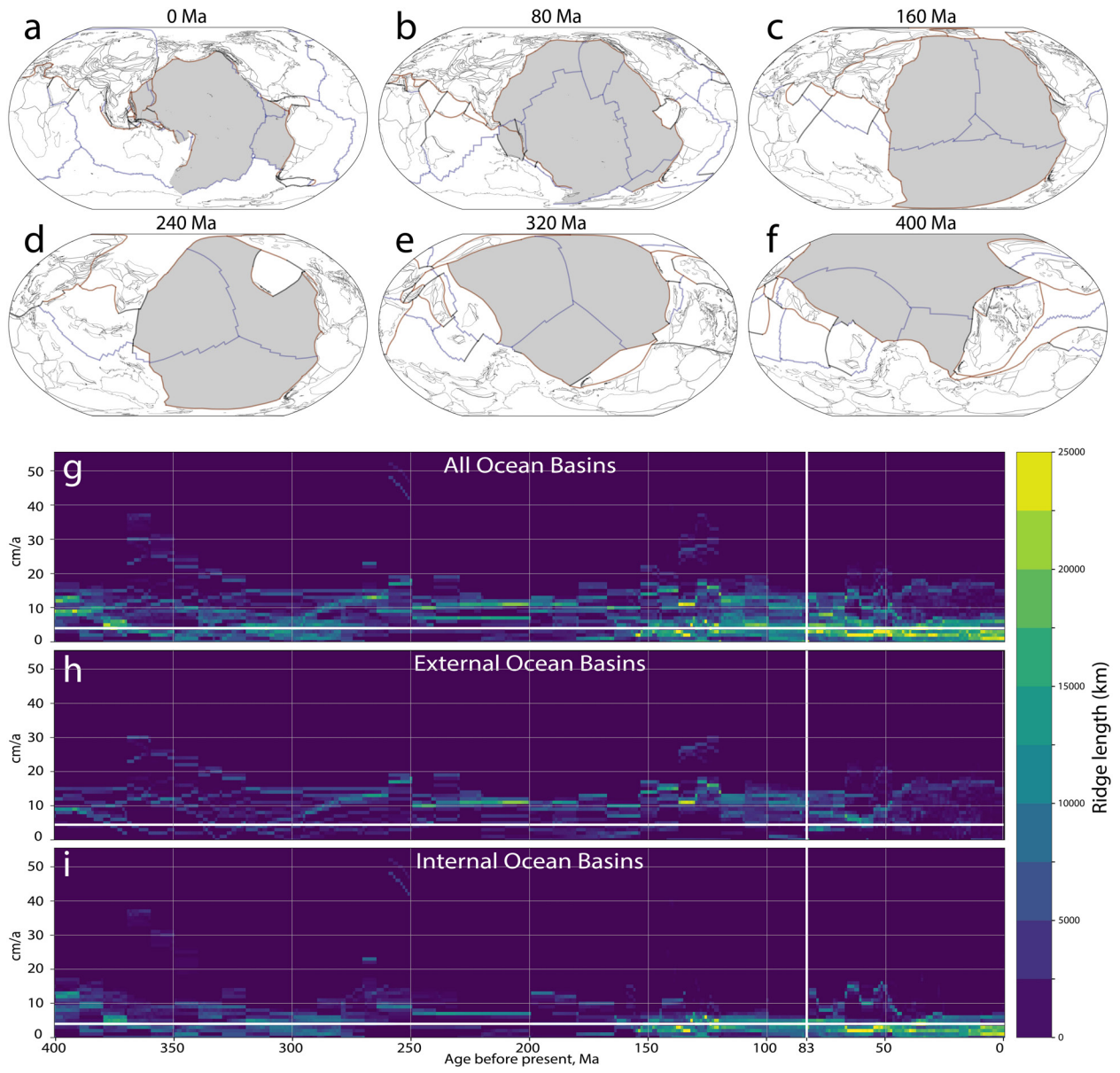

FIGURE 1 | Evolution of the Pacific Ocean used in our analysis. **(A–F)** Snapshots of the Pacific and Panthalassa Oceans and associated basins used to extract spreading rate distributions (dark gray). All plates constituting the Pacific basin during the last 83 Ma were identified using the model of Matthews et al. (2016). Mid-ocean ridges in blue, subduction zones in brown, and connecting plate boundaries in gray. Tectonic plates highlighted in dark gray are what we considered "external" ocean basins, while internal ocean basins are the remainder. **(G–I)** show the distribution of full ridge spreading rates sampled at spreading segments in cm/a with **(G)** all ocean basins, **(H)** external ocean basins, and **(I)** internal ocean basins. The bold vertical white line shows the 83 Ma cut off, where we use the external ocean distribution as an archetype for pre-160 Ma external ocean basins. The horizontal white lines are at 4 cm/a, where in our model we separate amagmatic and magmatic crustal forming processes at ridges.

(Wright et al., 2016). For this study, we assume that other large external oceans that have existed through time behave in a similar way, thereby assuming the tectonic mechanisms acting at present-day in the Pacific are representative of external oceans for the last 400 Ma (**Figure 1G**). We extract Pacific spreading rates for the last 83 Ma at a temporal resolution of 1 Ma and an along-ridge strike spatial resolution of 1 km (**Figure 1H**) to produce representative external ocean spreading rate distributions. For external oceans younger than 160 Ma, we use the spreading rate as modeled by the plate model, whilst for times earlier than 160 Ma we use the Pacific data to provide representative distributions (**Figure 1H**) of spreading rates for large, stable, and external ocean basins in deeper time (**Figures 1D–F**). Each ridge segment at each timestep in an external, pre-160 Ma ocean uses a spreading rate randomly drawn from the observed distribution of Pacific data. For internal oceans we use the explicit spreading rates from the plate model, as in the absence of preserved oceanic lithosphere, the geological and palaeomagnetic data used to construct the plate model provide a first-order constraint on times and rates for rift, drift and collision (**Figure 1I**). As part of the evaluation of our methodology, we compare the results of our preferred approach using Pacific-Ocean derived spreading rates (POSR) with results produced when using plate-model spreading rates directly (PMSR) (section "Plate Model vs. Pacific Ocean Spreading Rates").

Properties of Upper Oceanic Lithosphere

The carbon storage capacity of oceanic lithosphere is determined by its relative proportion of peridotitic and volcanic suites. The relative proportions of volcanic and peridotitic suites result from melt supply at ridges and can be broadly linked to spreading rates (Cannat, 1993; Tucholke and Lin, 1994), and the transition from amagmatic or low melt percentage to magmatic spreading (Dick et al., 2003). At high spreading rates, ocean crust is formed by magmatic processes. When the spreading rate is slow enough that the thermal profile of the ridge is too cool to support a magma chamber or to trigger a melt product that can be incorporated into the oceanic crust, mantle peridotite is exposed to seawater (Sleep and Barth, 1997). In these cases the lithospheric mantle is tectonically exhumed into the rock column by asymmetric detachment faulting (Tucholke et al., 2008; Carbotte et al., 2016), exposing mantle peridotites and ultramafics to seawater where serpentinization can occur (Cannat et al., 2010; **Figure 2A**). We begin our analysis at the initiation of seafloor spreading, neglecting transitional crust that is exposed during continental rifting, although this can also be variably serpentinized (e.g., Zastrozhnov et al., 2018). By estimating the proportion of peridotite present, we also estimate the proportion of the magmatic component. We divide the total thickness of the magmatic suite into sub-components: upper volcanics (basalt), lower volcanics, transition layer, sheeted dykes, and gabbros, after Alt and Teagle (1999) and Jarrard (2003) (**Figure 2B**). Each subdivision has a specific distribution of carbon associated with it, which we randomly sample and re-combine to estimate the cumulative total amount of carbon present.

The exhumation rate of mantle lithosphere acts as a control on the degree of bulk rock serpentinization over million-year timescales. However, there is little geological data constraining the degree of serpentinization at ridge systems, compounded by the fact that many recovered samples are described only qualitatively. Dredged material from ridges spreading at less than 40 mm/a have returned variably serpentinized samples ranging from 20% to 100% (Dick, 1989; Sauter et al., 2013). As spreading rate increases and magmatic oceanic crust is produced, serpentinization is considered to be a negligible component of the crustal profile, though dredges at fast spreading ridges have returned fully serpentinized samples (Constantin et al., 1995). Cannat et al. (2010) used seismic data from Canales et al. (2000) to build bulk rock estimates of serpentinization at ridges spreading at less than 40 mm/a. They estimate that approximately the first kilometer of crustal profile is highly serpentinized (80–100%) as a result of extensive fracturing during exhumation. At this depth, there is an inflexion in the degree of serpentinization, with a linear decrease between a depth of 3.2 and 4 km to 0% (**Figure 2C**). To account for the variation and uncertainty within the seismic data, we parameterize the relationship between depth and serpentinization using the initial degree of serpentinization at the surface of the lithosphere (*dsSurf*), the depth of the inflection point (*dInflex*) and the depth to serpentinized mantle (*dBot*) (e.g., **Figure 2C**). *dInflex* and *dBot* are taken from Cannat et al. (2010) (e.g., **Table 1**). To reflect the greater uncertainty related to the initial degree of serpentinization, we employ a negative correlative relationship between *dsSurf* and spreading rate, such that the slower the spreading ridge, the higher the degree of serpentinization (**Figure 2D**). Slow ridges exhibit high variability in the degree of serpentinization, especially as they approach spreading rates of 40 mm/a (e.g., Dick et al., 2003) and have a broader range of *dsSurf* (**Figure 2D**).

Bottom Water Temperature

Carbonate precipitation in the upper 300 m of basaltic oceanic crust is a function both of age and bottom water temperature (Gillis and Coogan, 2011; Coogan et al., 2016). Warmer bottom water results in a higher carbonate precipitation rate, and greater progressive uptake of carbonate over the life of oceanic crust, with ∼80% of carbonate being sequestered within 20 Ma of crustal formation (Coogan et al., 2016). Young (<5 Ma) oceanic crust is therefore less enriched in carbonate relative to older oceanic crust (>20 Ma), although this is moderated by the evolution of bottom water temperature (Alt and Teagle, 1999; Gillis and Coogan, 2011). Müller and Dutkiewicz (2018) used these observations with a bottom water temperature curve from 400 to 0 Ma to derive a log-weighted relationship between seafloor age, water temperature and wt% of precipitated carbonate (**Figure 3A**). We apply a similar relationship as a weighting factor in our calculation of carbon storage for the upper volcanic layers only. For each segment of oceanic crust, we calculate the integrated average bottom water temperature for the first 20 Ma from this curve (e.g., **Figure 3B**) and scale the mean wt% of carbon accordingly. The pre-scaled mean wt% carbon is drawn randomly from the distribution defined by Kelemen and Manning (2015).

The mean carbon wt% from Kelemen and Manning (2015) was calculated from all recovered oceanic basalt samples and used to calculate storage capacity only at present-day. From this,

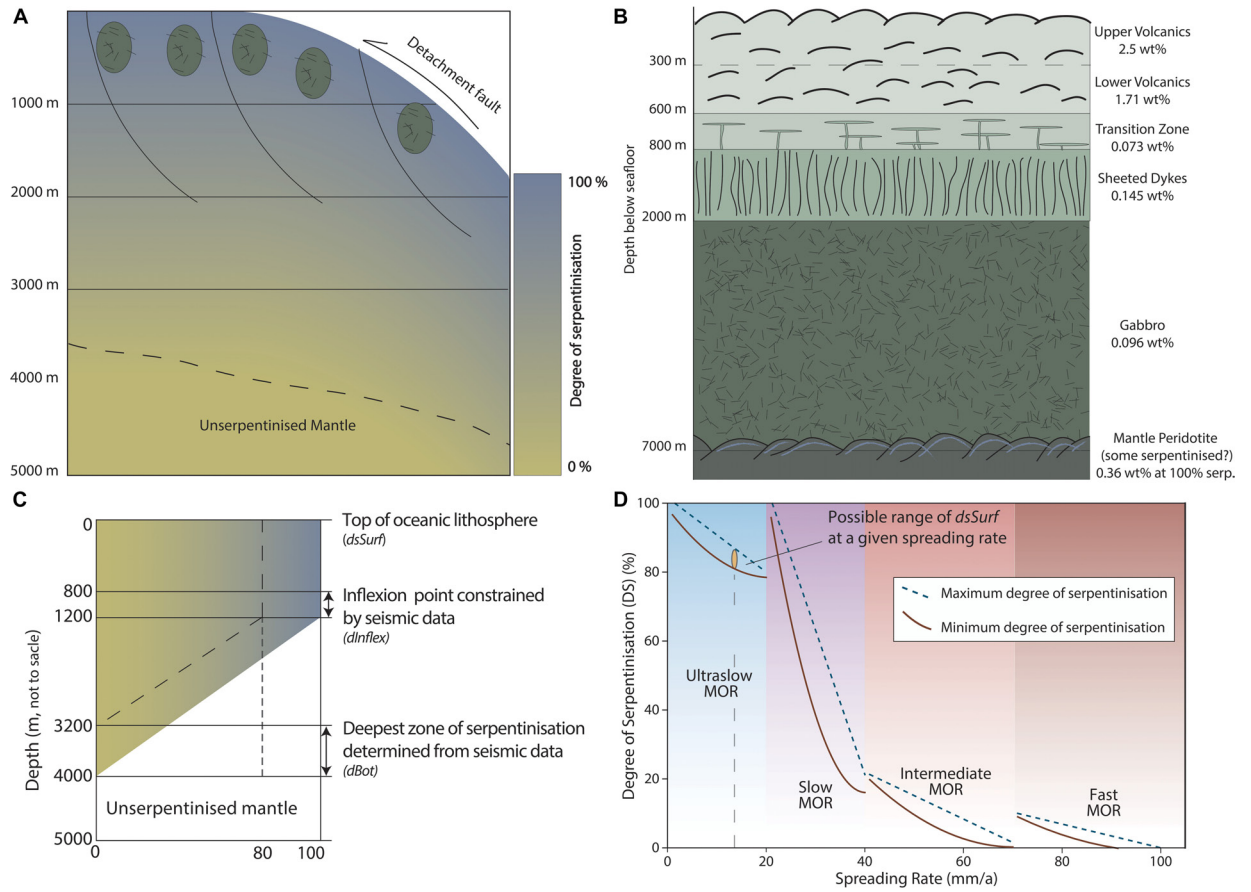

FIGURE 2 | Schematic cross sections of upper oceanic lithosphere produced at **(A)** slow spreading ridges (full spreading rate < 40 mm/a) where tectonic exhumation of the lithospheric mantle occurs, and **(B)** fast spreading ridges (full spreading rate > 40 mm/a) where the typical column of oceanic crust consisting of basalts, dykes, and gabbros is formed. At these slow ridges **(A)**, the mantle lithosphere is exposed to seawater, and undergoes serpentinization to a depth of ~3200–4000 m. Weight percentages of carbonate for each layer are taken from Kelemen and Manning (2015). **(C)** Parameterization of the seismic relationship from Cannat et al. (2010) to estimate the depth of serpentinization and the overall degree of serpentinization of a system. **(D)** Initialization and inverse correlative relationship of degree of serpentinization and spreading rate that we employ in this model.

we prescribe a weighting of unity to bottom water temperature coinciding with the 15–20°C threshold identified by Müller and Dutkiewicz (2018), then scale each 5°C temperature bracket accordingly from factor 0.4 at 0–5°C to factor 1.2 at 20–25°C. This processing step is included as the relationship presented by Müller and Dutkiewicz (2018) was established using the same samples as Kelemen and Manning (2015). This results in scaling the values of carbon wt% in the upper volcanic layer drawn from the Kelemen and Manning (2015) data to better reflect the temporal history of ocean bottom water temperature. Thus, oceanic crust produced in cooler water (e.g., Miocene to present and the late Carboniferous) will have carbonate storage capacity scaled down, whilst oceanic crust produced during the Triassic, when bottom water was warmer, will be more enriched in carbonate (**Figure 3A**).

Subduction Zone Calculation

To calculate subduction flux we follow the methodology set out by Dutkiewicz et al. (2019). This approach tessellates subduction zones in a given *GPlates* plate reconstruction along the great circle of each straight-line segment of the polyline representing the subduction zone. Subduction polarity is accounted for to ensure that only raster cells located on the downgoing plate are used to calculate subduction flux. The thickness of carbon or serpentinite along the subduction segment is found from a raster of values. Convergence rates are extracted for each tessellated subduction segment, and volume is calculated by multiplying thickness with tessellation width and the local convergence rate.

Bringing It All Together

The distribution and storage of both carbon and serpentinite in upper oceanic lithosphere is a function of mid-ocean ridge processes that have occurred continuously for at least the last 200 Ma (Alt and Teagle, 1999; Cannat et al., 2010). Our approach brings the previously described components together to calculate the volume of carbonate and serpentinite at each time

TABLE 1 | Parameter description, dependencies, and references.

Parameter	Dependency	Calculation	Source
Spreading rate (mm/a)	Age	<160 Ma, from plate model >160 Ma and within Panthalassa Ocean Basin (e.g., **Figure 2**), sampled from Pacific distribution for 0–83 Ma >160 Ma and outside Panthalassa Ocean, from plate model	Matthews et al. (2016)
Bottom water temperature (°C)	Age	**Figure 3A**	Müller and Dutkiewicz (2018)
Peridotite (%)	Spreading rate	Sampled from truncated normal distributions, range and standard deviation given <20 mm/a, 70–90, 6 20–40 mm/a, 12.5–70, 19.6 40–70 mm/a, 5–15, 2.87 70 mm/a, 0–10, 2.87	Constantin et al. (1995); Carlson (2001); Sauter et al. (2013)
Upper oceanic lithosphere thickness (km)	Spreading rate	<40 mm/a, 3–4, 0.4 >40 mm/a, 7 ± 1	Bown and White (1994); Muller et al. (1999); Cannat et al. (2003); Meyzen et al. (2003); Michael et al. (2003); Minshull et al. (2006);
Degree of serpentinization (%)	Spreading rate	0–20 mm/a, 80–100% 20–40 mm/a, 20–100% >40 mm/a, 0–20%	Constantin et al. (1995); Cannat et al. (2010)
Thickness of the serpentinite layer	Peridotite %, degree of serpentinization (%), volcanic, gabbro, and dyke and transition thicknesses	<40 mm/a, degree of serpentinization multiplied by peridotite proportion and upper oceanic lithospheric thickness >40 mm/a, sampled from truncated normal distributions with ranges dependent on spreading rate, multiplied by rock thicknesses, and peridotite %	
Upper volcanic layer thickness (km)	Spreading rate	<40 mm/a, 0 >40 mm/a, sampled from normal distribution 0.24–0.360	From Kelemen and Manning (2015), adopted from Alt and Teagle (1999) and Shilobreeva et al. (2011)
Lower volcanic layer thickness (km)	Spreading rate	<40 mm/a, 0 >40 mm/a, sampled from normal distribution 0.24–0.360	From Kelemen and Manning (2015), adopted from Alt and Teagle (1999) and Shilobreeva et al. (2011)
Transition thickness (km)	Spreading rate	<40 mm/a, 0 >40 mm/a, sampled from normal distribution 0.16–0.240	From Kelemen and Manning (2015), adopted from Alt and Teagle (1999) and Shilobreeva et al. (2011)
Sheeted dykes thickness (km)	Spreading rate	<40 mm/a, 0 >40 mm/a, sampled from normal distribution 0.96–1.48	From Kelemen and Manning (2015), adopted from Alt and Teagle (1999) and Shilobreeva et al. (2011)
Gabbros thickness (km)	Peridotite %, thickness of the serpentinized layer	<40 mm/a, linear dependence on inputs >40 mm/a, sampled from normal distribution 4.0–6.0	From Kelemen and Manning (2015), adopted from Alt and Teagle (1999) and Shilobreeva et al. (2011)
Upper volcanics CO_2 (wt %)	Spreading rate, bottom water temperature	<40 mm/a, 0 >40 mm/a and <5°, uniform 0.2–0.6 >40 mm/a and 5–10°, uniform 0.6–1.2 >40 mm/a and 10–15°, uniform 1.2–2 >40 mm/a and 15–20°, uniform 2.0–3.0 >40 mm/a and >20°, uniform 3.0–4.2	Kelemen and Manning (2015)
Lower volcanics CO_2 (wt %)	Spreading rate, bottom water temperature	<40 mm/a, 0 >40 mm/a and <5°, sampled from uniform distribution 0.00–0.01 >40 mm/a and 5–10°, uniform 0.00–0.02 >40 mm/a and 10–15°, uniform 0.00–0.03 >40 mm/a and 15–20°, uniform 0.00–0.05 >40 mm/a and >20°, uniform 0.00–0.06	Kelemen and Manning (2015)
Transition CO_2 (wt %)	Spreading rate	<40 mm/a, 0 >40 mm/a, uniform distribution 0.00–0.02	Kelemen and Manning (2015)
Sheeted dykes CO_2 (wt %)	Spreading rate	<40 mm/a, 0 >40 mm/a, uniform distribution 0.00–0.04	Kelemen and Manning (2015)
Gabbro CO_2 (wt %)		Sampled from normal distribution, mean 0.096, std. 0.05	Kelemen and Manning (2015)
Serpentinite CO_2 (wt %)	Spreading rate	<40 mm/a, sampled from uniform distribution 0.32–0.36 for the upper 1 km, then linearly decreasing to 0.00 at max depth >40 mm/a, 0.32	Kelemen and Manning (2015)
Total CO_2	Thickness of serpentinized layer, maximum carbon, peridotite %, spreading rate, and CO_2 of all rock layers	Linear combination of parameters	

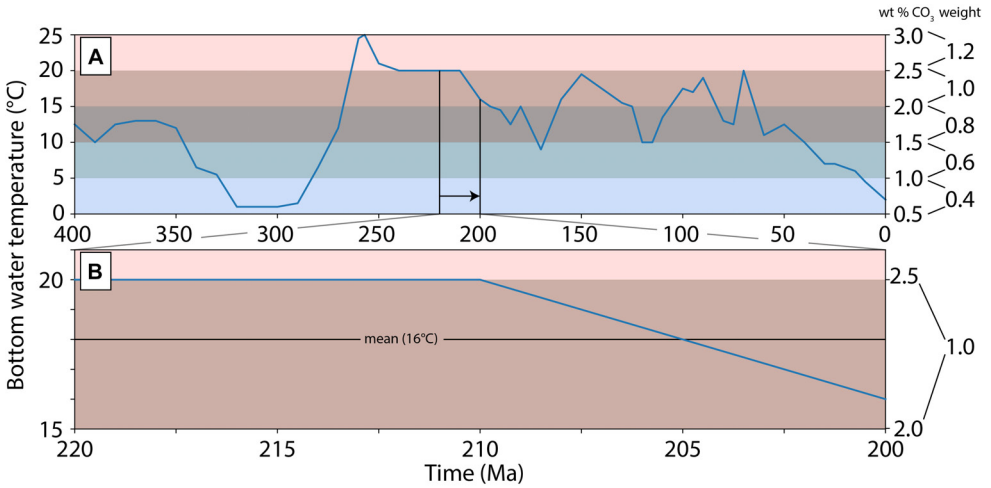

FIGURE 3 | (A) Bottom water temperature curve from 400 to 0 Ma with a resolution of 10 Ma after Müller and Dutkiewicz (2018). Wt% carbonate and the applied weighting factor prescribed in 5°C bands. The bands are represented by the horizontal colored bars. **(B)** Calculated mean water temperature using a moving 20 Ma window to scale carbonate wt%. At each time step we perform **(B)** to determine the average bottom water temperature of a parcel of fresh oceanic crust.

step along mid-ocean ridge segments where upper oceanic lithosphere crystallizes.

We distinguish crust forming at mid-ocean ridges prior to 160 Ma from younger times as only 20% of seafloor older than 160 Ma is preserved at the present day (Torsvik et al., 2010; Torsvik and Cocks, 2016; Domeier and Torsvik, 2017). Ocean crust that formed more recently than 160 Ma store the thickness of carbonate as a sum of the constituent layers of upper oceanic lithosphere. In calculating the amount of carbon stored we first establish two variables: (i) the total thickness of the crustal column, and (ii) the proportion of peridotite, which also implicitly provides us with an estimated magmatic proportion of the crust. Both of these components are drawn randomly from normal distributions for thickness and peridotite proportion, as observed at the present day (**Table 1**). At intermediate and fast spreading ridges where magmatic spreading dominates, we subdivide the resulting volcanic component into sublayers, each with their own specific thicknesses (Alt and Teagle, 1999). Each sublayer is then assigned a wt% of carbonate (Kelemen and Manning, 2015), with values drawn randomly from a uniform distribution (**Table 1**). Small portions of peridotite may be exposed at the base of the crust and undergo minor serpentinization. These observations of serpentinized peridotite are also included in our calculation, but given the scarcity of peridotite (<10%) and low degree of serpentinization (<10%), they typically make up less than 1% of the total rock volume available for carbon storage at intermediate and fast spreading ridges. At slow and ultraslow ridges where amagmatic spreading dominates, lenses of gabbros are included within the exhumed peridotite and are considered to be the only volcanic component present in our model. Gabbros are treated in the same way as at fast ridges, where a wt% of carbon present is drawn at random from the distribution defined in Kelemen and Manning (2015). The carbon stored in the serpentinized peridotite component of these ridges ranges between 0.32 and 0.36 wt% at 100% serpentinization, decreasing linearly to 0 wt% at 0% serpentinization. We apply this to the serpentinization model described above (section "Properties of Upper Oceanic Lithosphere"), such that the carbon wt% remains constant to *dInflex*, before then decreasing linearly to 0 wt% at *dBot*.

For upper oceanic lithosphere forming prior to 160 Ma and located within the Panthalassa Ocean, we follow the same procedure as above for crust younger than 160 Ma with one exception. For these ridge segments we randomly sample the distribution of Pacific Ocean spreading rate (e.g., **Figure 1H**). The spreading rate from this distribution is then used in our calculation to characterize the lithosphere (magmatic vs. amagmatic) and calculate an estimated cumulative thickness of carbon storage and serpentinite formation. We multiply the thickness in these cases by the sampled spreading rate. This approach records the cumulative vertical area of carbon and serpentinite storage between two hypothetical isochrons perpendicular to the spreading direction instead of cumulative thickness of a crustal profile. When these portions of lithosphere reach a subduction zone, we multiply them only by the length of subduction. Internal oceans prior to 160 Ma use the spreading rate taken directly from the plate model, as their spreading histories are constrained by a combination of geological and palaeomagnetic data.

Our analysis begins at 400 Ma and progresses toward 0 Ma. At t = 400 Ma (i.e., start time) we tessellate each ridge segment at a resolution of 2 arc degrees along the segment's great circle to ensure sufficient coverage. At these points (mid-points of each tessellated segment), we perform our calculation for carbon storage and serpentinite formation, resulting in each point being associated with a latitude, longitude and a z-value (which consists of the thickness of carbon, serpentinite, and the crustal composition, e.g., thickness of different layers, proportion of peridotite). We also determine the average bottom water temperature for the next 20 Ma at each timestep, and apply a

modifier to the wt% of carbonate in the upper volcanic layer (section "Bottom Water Temperature"). Using stage rotations from the plate model we rotate these points forward in time in 1 Ma increments, preserving the z-values that were calculated at the ridge segment. At each time step (i.e., t = 399 Ma), we repeat the calculation (carbon and serpentinite storage and formation) for the next set of points at the mid-ocean ridge, representing newly formed crust. We then rotate these new, ridge segment points, along with any current points from previous timesteps, forward in time using the plate model. At each timestep we perform a subduction test after Williams (2019)[3] (see the section "Method and Code"). This process is repeated until the analysis end time is reached.

Table 1 details which parameter values are chosen by random sampling, the distributions from which they are drawn, and the dependency of each parameter on other randomly sampled parameters. The Pearson correlation coefficient of each parameter is presented in **Figure 4**. Peridotite percent is negatively correlated with the thickness of other rock types, as these are a function of volcanic percentage which constitutes the non-peridotite component of the rock column.

To facilitate community efforts and future developments, we provide interactive *Project Jupyter* notebooks[4] and associated metadata of our methodology with this publication (**Supplementary Material 7**).

RESULTS

Model Uncertainty

Our approach to estimate carbon flux in subduction zones requires the characterization of upper oceanic lithosphere through time, from which we can extract the total thicknesses of carbon and serpentinite stored and formed in the lithospheric profile. From this, area and volume become a function of spreading/convergence rate and ridge/subduction length, respectively. Carbon storage in oceanic crust is dominated by the upper volcanic layer (top ∼300 m of crust), although

[3]https://github.com/siwill22/agegrid-0.1

[4]www.jupyter.org

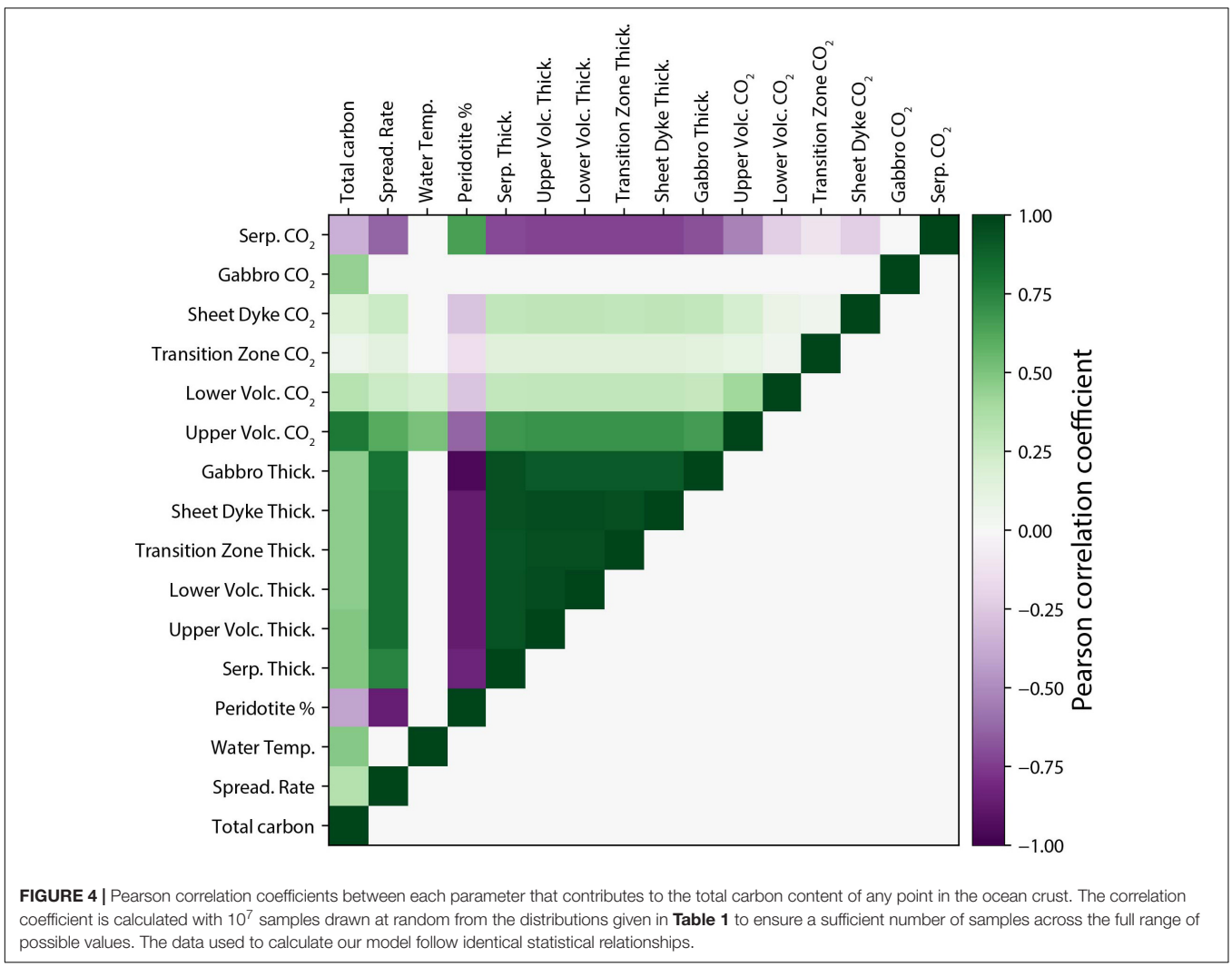

FIGURE 4 | Pearson correlation coefficients between each parameter that contributes to the total carbon content of any point in the ocean crust. The correlation coefficient is calculated with 10^7 samples drawn at random from the distributions given in **Table 1** to ensure a sufficient number of samples across the full range of possible values. The data used to calculate our model follow identical statistical relationships.

both the sheeted dyke complexes and gabbros contribute a significant proportion (∼40% of the total), as they have a greater proportional thickness in the oceanic crust column (**Figures 5A,B**, see **Supplementary Material 1**, **2** for tables of results). This translates to a cumulative transport point thickness of roughly 3–4 m of carbon in oceanic crust formed at a fast spreading ridge assuming a bottom water temperature of 12°C. Oceanic lithosphere exhumed at slow ridges also sequesters carbon at a similar order of magnitude to fast ridges (thickness of ∼1.5 m). This carbon is predominantly stored in altered peridotite (thickness of ∼1.15 m), though gabbroic lenses which are also formed at slow ridges contribute a similar amount of carbon (thickness of ∼0.3 m) (**Figures 5C,D**). Colder bottom water, such as at present day, scale down the amount of carbon stored, while warmer water during the Triassic and Jurassic acts to scale the values up. Consequently, ocean crust forming since the Cretaceous is only 25–50% as enriched with carbonate as that formed during the Triassic and Jurassic. Serpentinite itself is almost entirely found at slow and ultraslow spreading ridges, where it forms ∼33% of the rock column, with remnant gabbroic lenses and unaltered peridotite forming the other components (in our model each occupies a similar thickness of 1000–1300 m) (**Figure 5D**). At fast ridges, the thickness of serpentinite is two orders of magnitude lower (73 ± 60 m), making up less than 1% of the total column and the corresponding storage of carbonate in serpentinite here is almost completely negligible (thickness of ∼0.06 m) (**Figure 5A**).

We present the conditional probability of the total carbon content in any crustal segment, given a known spreading rate, including all possible variations of every parameter (**Figure 6**). This shows both the full distribution of possible carbon content at any spreading rate and how any error or uncertainty impacts the total carbon content. The possible range of carbon storage is much greater at higher spreading rates because of larger variations in volcanic structure. There are clear changes in the distribution of carbon content at spreading rates of 20 and 40 mm/a (**Table 1**). These points are where the uncertainty in spreading rate will have the largest effect, tipping the lithosphere into a different carbon-storage regime. Away from these points, even relatively large uncertainties in spreading rate will have minimal effect on the distribution of possible carbon content. This range of possible values is sampled according to the modeled spreading rates to produce the distributions shown in **Figures 5**, **6**. These give an estimate of the uncertainty of our results, including all of the uncertainties in the geochemical data. The wide range of possible values does not obscure the large-scale patterns seen in our model, which are caused by variations in spreading and subduction rates.

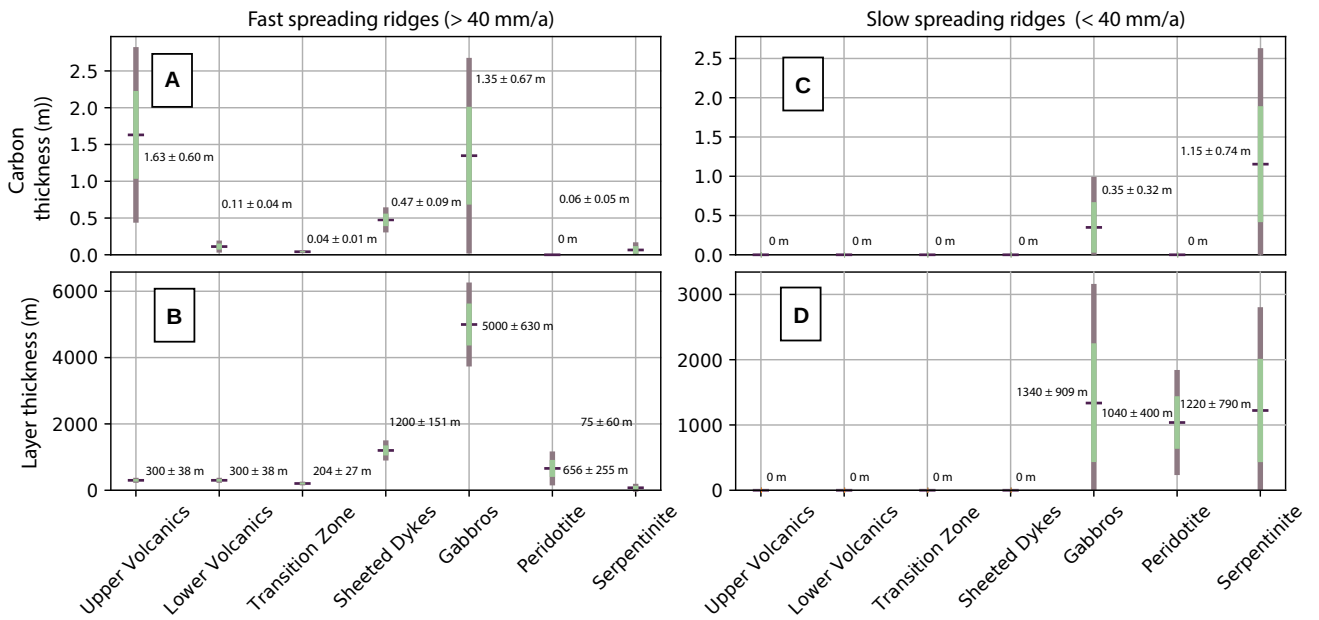

FIGURE 5 | Summary of predicted crustal and carbon storage thicknesses at fast and slow spreading ridges from our model and the carbonate values from Kelemen and Manning (2015). A spreading rate drawn randomly from the present-day distribution of global spreading rates preserved in ocean basins (37 ± 27 mm/a) is used to initiate the calculation. Using this spreading rate, we determine the thickness of the different oceanic crust components and their corresponding carbon thickness. To ensure components are adequately sampled, this process was repeated 10000 times. The average bottom water temperature of the last 400 Ma, 12°C (Müller and Dutkiewicz, 2018), was used in the calculation, meaning the thicknesses are ∼60% of expected thicknesses assuming warm bottom water (∼20°C). Purple shows the maximum range of values, with one standard deviation highlighted in green. Text in the panels describes the mean and one standard deviation. **(A)** Range of possible carbon thicknesses for each lithological unit in crust produced at fast spreading ridges. **(B)** Range of possible thicknesses of each lithological unit in crust produced at fast spreading ridges. **(C)** Range of possible carbon thicknesses for each lithological unit in crust produced at slow spreading ridges. **(D)** Range of possible thicknesses of each lithological unit in crust produced at slow spreading ridges.

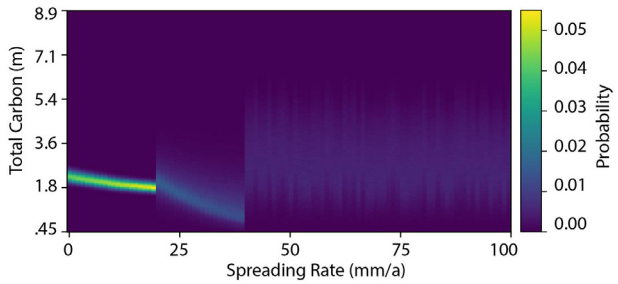

FIGURE 6 | Conditional probability of the value of total carbon sequestered in ocean crust as a function of the spreading rate of the ridge at which it formed, with the ranges determined by all the variation in parameters listed in **Table 1**.

Results

We present our results initially as distributions using the Pacific Ocean spreading rate (POSR) data, with a comparison between the POSR and plate model spreading rate (PMSR) following this section. The results for carbon storage and flux in ocean basins have temporal and spatial variability (e.g., **Figures 7A,B**, **8**). Our model suggests that at present-day between 20 and 60 Mt of carbon are sequestered at mid-ocean ridges (**Figure 7A**) and between 20 and 40 Mt of carbon are entering subduction zones (**Figure 7B**). Levels of carbon sequestration at mid-ocean ridges peak during the Early Cretaceous (250–300 Mt/a at ca. 150–130 Ma, **Figure 7A**) and just prior to the Carboniferous-Permian boundary (250–350 Mt/a at ca. 255–250 Ma). These results show that between these two peaks (during the Permian–Jurassic), carbon sequestration was at a slightly higher level than over the last 50 Ma, about 1.3 times present-day values. The mass of subducted carbon exhibits a similar but less pronounced pattern, with our estimates suggesting between 15 and 60 Mt/a of carbon being subducted during the Carboniferous, before decreasing to 15–40 Mt/a until the Cretaceous (**Figure 7B**). By 150 Ma our results suggest greater than 65 Mt/a of carbon were being subducted, remaining at a similar level for most of the Cretaceous before decreasing from ca. 75 Ma toward present-day (**Figure 7B**).

The Pacific and Panthalassa Oceans are the two ocean basins with the highest carbon storage, irrespective of bottom water temperature (**Figure 8**). During times of warm bottom water (250–200 Ma) carbon storage in the Pacific and Panthalassa oceans reaches approximately 7 m at maximum (∼0.1 wt% of seafloor production, e.g., **Figures 8E,F**), although during times of cool bottom water (300 Ma and present-day) the thickness is between 1 and 2.5 m (∼0.05 wt% of seafloor production, e.g., **Figures 8A,G**). The maximum amount of sequestered carbon during the Triassic is matched only during the breakup of Pangea (ca. 150–100 Ma), when the water temperature was lower but global mid-ocean ridge length much longer (Müller and Dutkiewicz, 2018; **Figure 7A**), resulting in a higher availability of fresh basalt for alteration.

Serpentinite mass exhibits a different trend, with both storage and subduction masses showing a much stronger temporal and spatial variability than carbon (**Figures 7C,D**, **9**). The Carboniferous is marked by higher production of serpentinite, between 500 and 2000 Mt/a (**Figures 7C**, **9G**). This drops rapidly at ca. 275 Ma to between 250 and 500 Mt/a, before slowly increasing from ca. 200 Ma to present-day to values between 700 and 2200 Mt/a (**Figure 7C**). The largest mass of serpentine produced is at ca. 60 Ma (**Figure 7C**). Significant spikes in the amount of serpentinite being subducted begin from ca. 120 Ma (**Figure 7D**), with some areas of the Pacific Ocean producing small pockets of serpentinite from ca. 200 Ma that reach the Andean and New Zealand margins during the Cretaceous (**Figures 9C,D**).

The production of serpentinites for pre-Jurassic times is principally controlled by the evolution of the Meso-Tethys Ocean

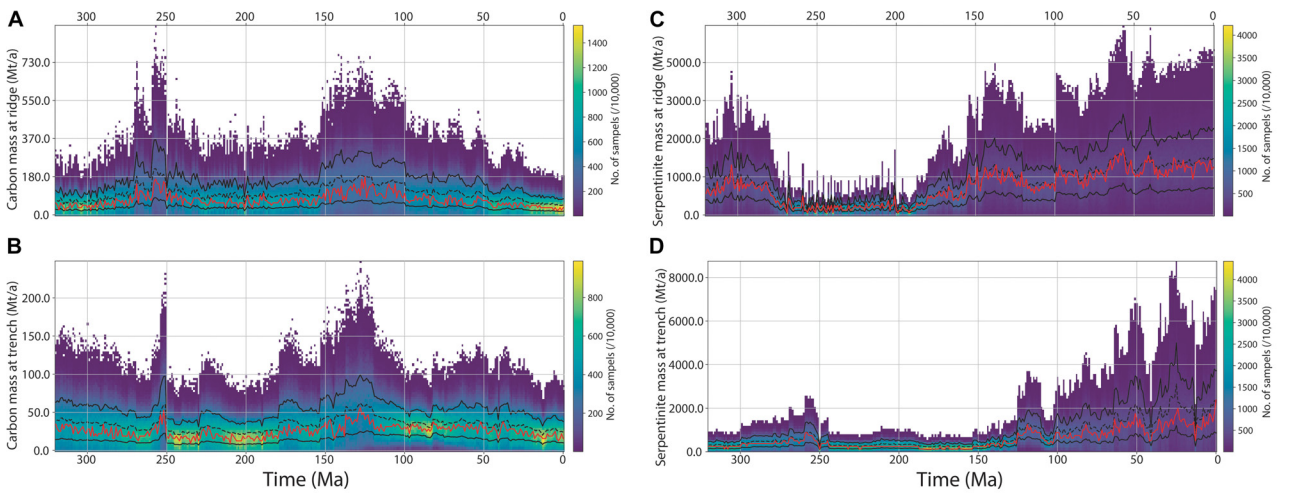

FIGURE 7 | Distributions (10000 samples) of **(A)** mass of carbon sequestrated at mid-ocean ridges, **(B)** mass of carbon entering a subduction zone, **(C)** mass of serpentinite formation at mid-ocean ridges, and **(D)** mass of serpentinite entering a subduction zone. Red line is mode of samples, dashed black line is mean (∼, to mode for **C**), and solid black lines show 1 standard deviation from the mean. The carbon distribution is skewed to the right.

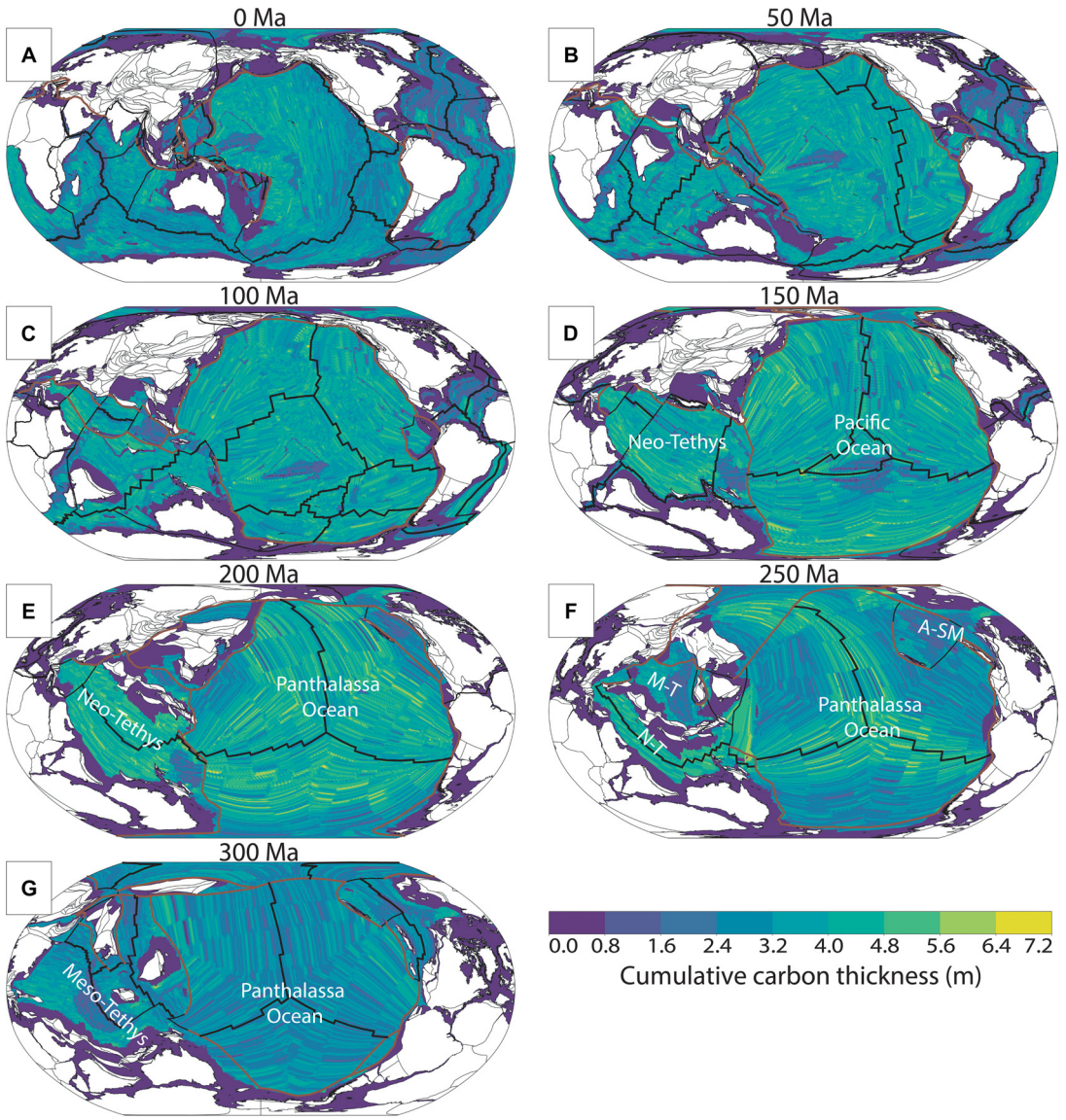

FIGURE 8 | (A–G) Cumulative thickness of carbon sequestered adjacent to mid-ocean ridges and transported in the upper oceanic lithosphere through ocean basins toward subduction zones since 300 Ma in 50 Ma intervals (see **Supplementary Material 3** for 1 Ma grids and rasters and **Supplementary Material 5** for an animation). Thicknesses calculated prior to 160 Ma are converted from vertical area to point thickness. A-SM, Alexander-Stoney Mountain ocean basin; M-T, Meso-Tethys Ocean; N-T, Neo-Tethys Ocean. Purple areas represent lithosphere not covered by our analysis or the plate model, such as submerged continental lithosphere or lithosphere trapped between a continent and a subduction zone (principally in the Palaeozoic), which would represent earlier (pre-400 Ma) oceanic crust. Black lines are mid-ocean ridges, brown lines are subduction zones.

and the Alexander-Slide Mountain ocean basin that opened on the northwestern margin of Laurentia (Matthews et al., 2016; **Figures 9E–G**). This is because their modeled spreading rates are low enough (<40 mm/a) that our methodology treats them as exposing large amounts of peridotite that is serpentinized. Hence, the opening and closure of these oceans result in the only significant disparity in serpentinite subduction prior to the Jurassic at ca. 180 Ma as the Panthalassa Ocean makes up the rest of the globe's ocean basins. The majority of serpentinite produced in the last 320 Ma currently resides in the Atlantic, Indian and Arctic oceans, whereas the Pacific and Panthalassa oceans are relatively barren (**Figure 9A**). Consequently, for more recent times small onsets of subduction in the Atlantic and Indian oceans act as principal drivers for the subsequent peaks from 100 Ma to present.

Plate Model vs. Pacific Ocean Spreading Rates

In this study, we compare our results which use the geologically recent (83–0 Ma) Pacific Ocean spreading rates (POSRs) as a proxy for the Panthalassa Ocean between 400 and

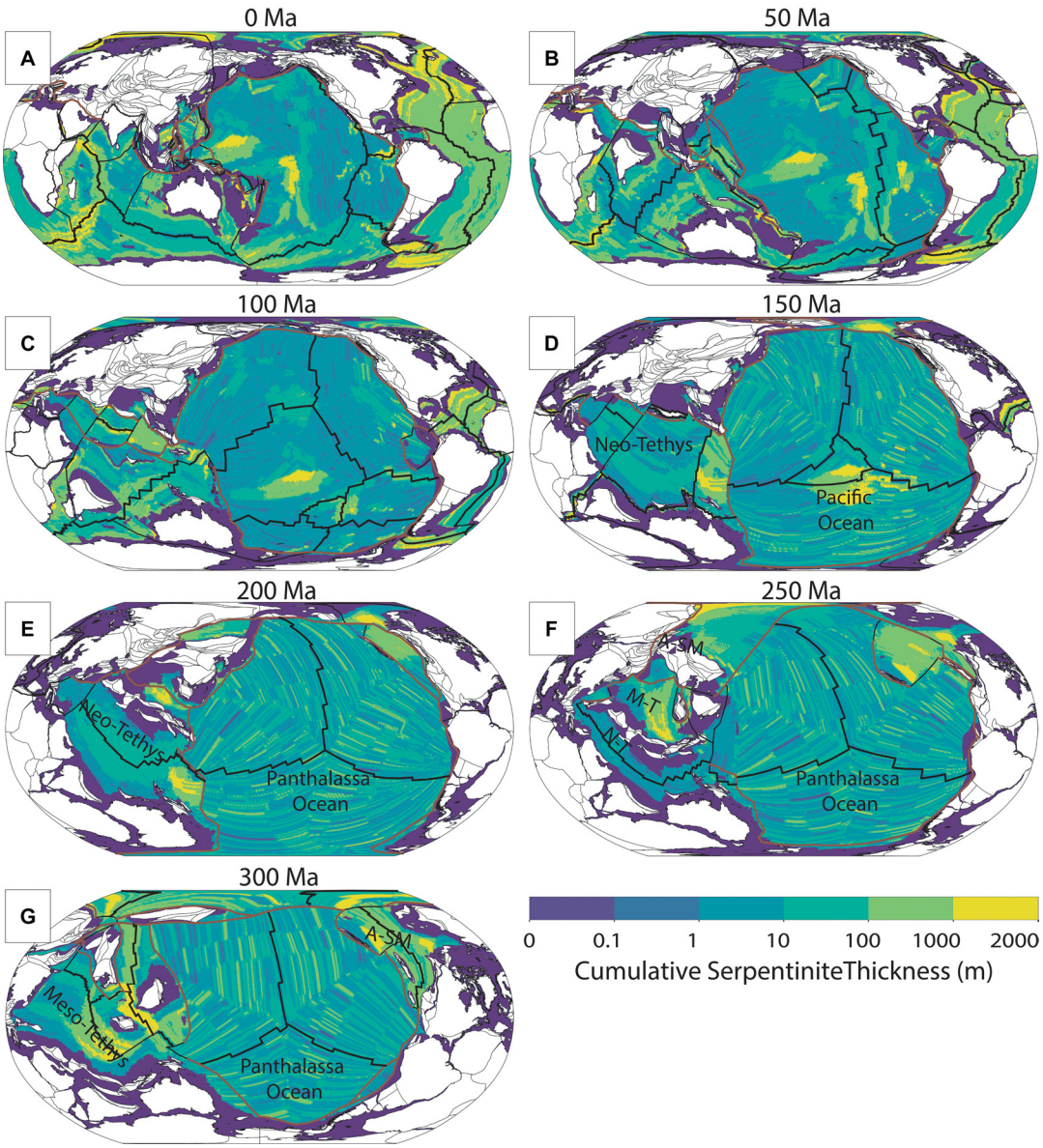

FIGURE 9 | (A–G) Cumulative thickness of serpentinite formed near mid-ocean ridges and transported in the upper oceanic lithosphere through ocean basins toward subduction zones since 300 Ma in 50 Ma intervals (see **Supplementary Material 4** for 1 Ma grids and rasters, and **Supplementary Material 6** for an animation). Thicknesses calculated prior to 160 Ma are converted from vertical area to point thickness. Since Pangea breakup, our model suggests extensive serpentinite formation in the Arctic, Atlantic, and Indian oceans. A-SM, Alexander-Stoney Mountain ocean basin; M-T, Meso-Tethys Ocean; N-T, Neo-Tethys Ocean. Purple areas represent lithosphere not covered by our analysis or the plate model, such as submerged continental lithosphere or lithosphere trapped between a continent and a subduction zone (principally in the Palaeozoic), which would represent earlier (pre-400 Ma) oceanic crust. Black lines are mid-ocean ridges, brown lines are subduction zones.

160 Ma, with a calculation that directly incorporated the PMSR from the reconstruction of Matthews et al. (2016) (**Figure 10**). To the first-order, there is little difference between both approaches, suggesting that for analysis of ocean basin lithosphere properties and dynamics existing plate models of the Palaeozoic produce reasonable estimates of carbon and serpentinite storage. However, there are some specific times where the approaches deviate as a consequence of how spreading rate is modeled in both approaches.

The sequestration and delivery of carbon from ridges to trenches is reasonably similar across both models (**Figures 10A,B**). In the POSR model, carbon sequestration displays a series of spikes occurring between 220 and 160 Ma. These are likely a consequence of passing a new spreading rate in at each timestep, resulting in a more pronounced temporal variation (**Figure 10A**). Key deviations of sequestration occur between 270 and 230 Ma, where the PMSR model suggests more carbon was being stored than the POSR model. In particular,

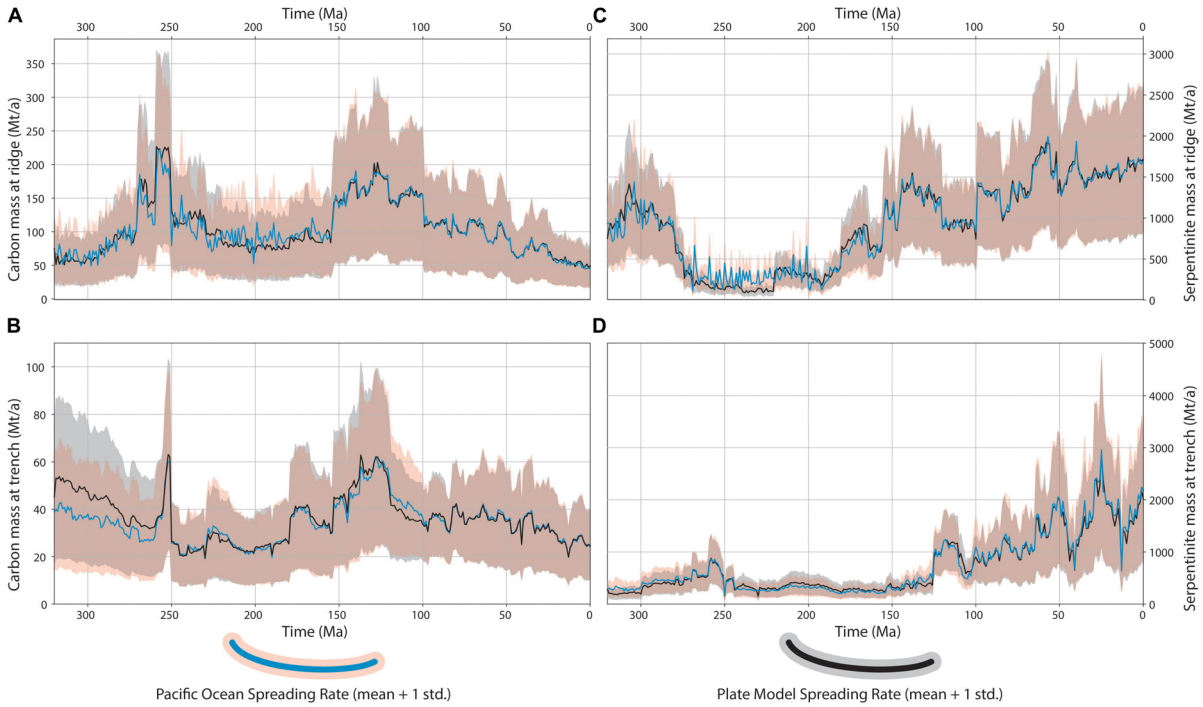

FIGURE 10 | Comparison of two approaches used in this analysis, POSR (red shaded area and blue line are one standard deviation and mean, respectively), and PMSR (gray shaded area and black line are one standard deviation and mean, respectively). **(A)** Carbon sequestration at ridges in altered ocean lithosphere, **(B)** carbon mass in altered ocean lithosphere at trenches, **(C)** serpentinite mass from altered mantle peridotite at ridges, and **(D)** serpentinite mass in altered mantle peridotite at trench.

we highlight the peak of carbon sequestration suggested in the PMSR between 255 and 250 Ma, which is not reflected in the POSR results (**Figure 10A**). This is important because this time coincides with the P-T mass extinction event and an incredibly pronounced change in carbon capture occurring just prior (350 Mt/a to 200 Mt/a) to the event could potentially provide key insights into palaeoclimate drivers during this period. However, the comparison of our two approaches suggests that the extent of carbon capture at this time may be a consequence of artificially high spreading rates for Panthalassa. Between 320 and 260 Ma, the PMSRs suggesting an extra ∼25–30% of carbon was being delivered to trenches compared to the POSR results (PMSR upper bound of ∼85 Mt/a vs. ∼65 Mt/a for POSR) (**Figure 10B**). This is a direct function of a distribution of faster spreading rates in the plate model between 400 and 320 Ma (e.g., **Figure 1H**) compared to the distribution of slower spreading rates that are used in the POSR calculation. Unlike the sequestration estimates, the peak at ca. 255–250 Ma in carbon delivery at trenches is reflected in both POSR and PMSR results (**Figure 10B**).

Mass estimates of serpentinite between POSR and PMSR at ridges and trenches are also broadly similar, but with some key times of deviation. Formation of serpentinite at ridges deviates most strongly between 270 and 220 Ma, with the POSR model suggesting 3 times as much serpentinite could have formed at ridges (300 Mt/a vs. 100 Mt/a). This deviation is the most statistically significant across the entire evaluation, with the mean of each approach being separated by their standard deviation. This is due to the modeled Panthalassa spreading rates being consistently above 40 mm/a, with modal spreading rate between 100 and 150 mm/a (**Figure 1H**) from 250 to 220 Ma. As with carbon sequestration, the high variation of values during this time is most likely a function of passing in a unique spreading rate at each timestep. The delivery of serpentinite to trenches displays very little difference between the models. The POSR results suggest slightly more serpentinite is being delivered between 320 and 260 Ma, and also between 140 and 120 Ma. The earlier of these two deviations is barely statistically significant, with the mean of POSR result falling outside the deviation band of the PMSR result. The latter deviation is the result of the aforementioned spreading rate differences between 250 and 220 Ma.

INTERPRETATION AND COMPARISON OF RESULTS

The results of this study, which estimate the mass of subducted carbon sequestered in upper oceanic lithosphere, can be linked directly to seafloor production rates. This is in contrast to previous estimates of subducted carbon that typically rely only on the volume of rock entering subduction zones (Dasgupta and Hirschmann, 2010; Kelemen and Manning, 2015). Additionally, as most estimates are only given for present-day and do

not include a time-dependent component, it is difficult to directly compare the results of this study against studies applying alternative approaches. At present day, Kelemen and Manning (2015) (hereby referred to as KM15) and Dasgupta and Hirschmann (2010) (hereby referred to as DH10) suggest a carbon flux at subduction zones of between 22 and 29 Mt/a and 12 and 61 Mt/a, respectively (**Figures 11B,C**). Our estimates, and those of Müller and Dutkiewicz (2018) (hereby referred to as MD18), suggest between 10–39 Mt/a and 15–25 Mt/a at present day, respectively: each within a similar range to those of KM15. The slightly reduced lower-range estimates of both our result and that of MD18 relative to KM15 and DH10 are likely due to two factors. First, both the results of this study and MD18 include the effect of bottom water temperature on carbon storage, which given the cooler waters since the Cretaceous (Lear et al., 2000), result in slightly lower estimates at present-day (carbon crustal mean of 0.11 wt% instead of 0.196 wt% in KM15). Secondly, the estimated subduction zone length at present day differs between KM15 and both MD18 and our study (45000 km vs. 55000 km, respectively). None-the-less, the range estimated by

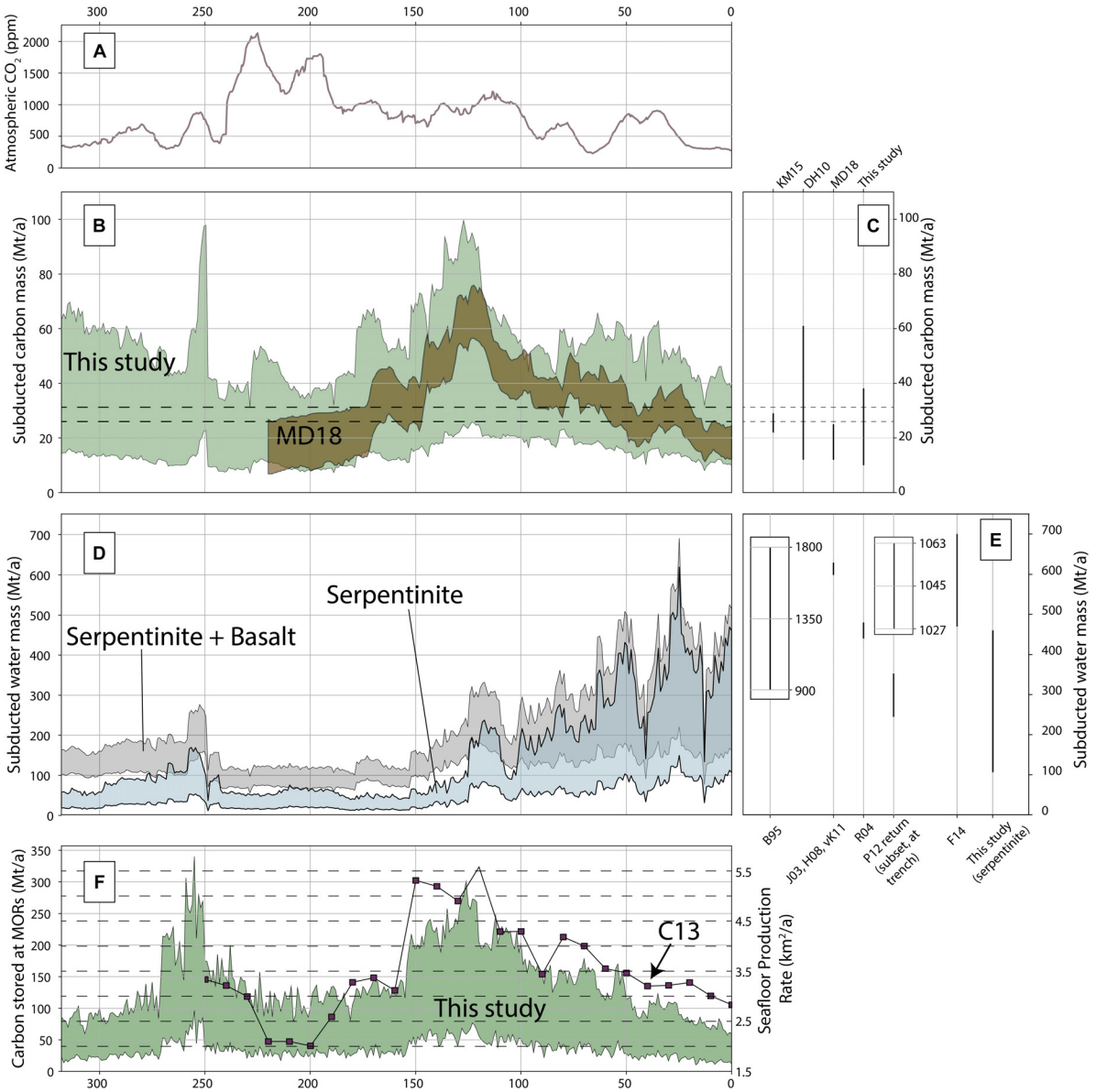

FIGURE 11 | (A) Atmospheric CO_2 after Foster et al. (2017). **(B)** Mass of carbon entering subduction zones according to our results (green) and Müller and Dutkiewicz (2018) (bronze, MD18). **(C)** Present-day estimates from other studies. KM15, Kelemen and Manning (2015); DH10, Dasgupta and Hirschmann (2010); MD18, Müller and Dutkiewicz (2018). **(D)** Mass of water stored in serpentinite and the upper volcanic layer entering subduction zones. **(E)** present-day estimates of water storage in oceanic crust; B95, Bebout (1995); J03, Jarrard (2003); R04, Rüpke et al. (2004); H08, Hacker (2008); vK11, van Keken et al. (2011); P12, return flow from Parai and Mukhopadhyay (2012) (inset is delivery to trench), and F14, Faccenda (2014). **(F)** Seafloor production rates after Coltice et al. (2013) for the past 250 Ma (purple squares, C13) and our estimates of carbon stored in upper oceanic lithosphere at mid-ocean ridges (green band).

KM15 encompasses our mean (∼28 Mt/a) and lies just above the modal distribution at present-day (15–18 Mt/a, **Figure 7B**).

Estimates of time-varying carbon subduction flux in this study can be evaluated in two ways: either through a direct comparison with the MD18 curve, or by evaluating the misfit between our results and present-day estimates (**Figures 11B,C**). Although our calculated mean is broadly similar to that of MD18, it has a larger standard deviation (14 Mt/a). This is to be expected as our calculation explicitly includes carbon stored in individual layers of oceanic crust and we explored the effect of varying thicknesses and carbon content of these layers. Importantly, our results show a peak in the early-mid Cretaceous at ca. 140–120 Ma (20–80 Mt/a) consistent with MD18 as a consequence of enriched Triassic and Jurassic ocean crust being subducted. As a proportional relationship exists between carbon stored in the upper 300 m of oceanic crust and carbon stored in the entire column at all fast ridges due to a fixed ratio of carbon wt% and layer thickness, we interpret times of trend deviation from MD18 to be the result of serpentinite subduction at the expense of upper volcanic subduction.

For the majority of our calculated history of carbon flux, the values, including uncertainties, lie inside the range proposed for present day by DH10 (**Figures 11B,C**). During times when the upper estimate of our range deviates from their present-day estimate (e.g., 250 Ma, 150–100 Ma), our results suggest the mass of carbon being subducted was up to 80 Mt/a. The lowest estimate (∼10 Mt/a at ∼200 Ma) of our range is slightly less than the minimum present-day range suggested by DH10, suggesting a value between 10 and 15 Mt/a could be considered as a minimum mass of carbon delivery to trenches at any one time. The narrower distribution of KM15 further highlights the deviation in all three of these time periods.

The decrease between 250 and 230 Ma in the mass of subducted carbon in our model is likely a result of two factors (**Figure 11B**). First, cold bottom water temperature between 320 and 270 Ma (∼1–8°C) gives a 40–60% relative reduction of carbonate in our model, and secondly, as Pangea was fully formed during this time, there were only two major ocean basins (Panthalassa and the Meso-Tethys) serving to limit the number of active spreading ridges. We ascribe a similar scenario to the peak of carbon subduction in the Late Jurassic and Early Cretaceous, consistent with MD18. During this period oceanic crust that formed during the Triassic and Jurassic in warm bottom water temperatures begins to be subducted, and there is an increase in mid-ocean ridge and subduction length as a result of the breakup of Pangea, resulting in more consumption of oceanic crust (**Figures 8D**, **9D**; Coltice et al., 2013; Van Der Meer et al., 2014; Müller et al., 2016).

Although displaying temporal variation, uncertainty associated with the calculated tectonic parameters is sufficient to identify a small band of carbon subduction that could be considered constant for the last 320 Ma (26–31 Mt/a) (dashed lines, **Figure 11B**). This band shows a small amount of overlap with the estimates of KM15, suggesting it could be a useful starting value for any study using arc flux of carbon for pre-Pangea times (see also section "Water Storage and Delivery").

Estimates of serpentinite mass at trenches are much more difficult to directly compare with other studies than carbon estimates. This is because other studies have not estimated the time sensitive delivery of serpentinite to subduction zones, and also due to geographic uncertainties associated with the location of off-axis serpentinized oceanic lithosphere at present-day. These two factors mean there is little available data to evaluate our model against. To address this, as our approach traces serpentinite from ridge to trench, we compare our results to bulk rock properties at ridges from previous studies, assuming the evolution of ocean basins moves bodies of serpentinite away from ridges over time. Worman et al. (2016) developed mechanistic models to calculate hydrogen production from serpentinization at mid-ocean ridges, with their preferred model suggesting that at slow and ultraslow ridges the thickness of "serpentinizing peridotite' ranges between 0.7 and 2.8 km. This estimate is approximately congruent with the proportion of peridotite exhumed at slow ridges in our model. Worman et al. (2016) do not estimate the total volume of serpentinized peridotite, though their preferred result (∼0.35–1.4 km of serpentinite), which assumes the serpentinization reaction is 50% complete, is similar to our results, not accounting for volume or density changes. A study by Cannat et al. (2010) also estimated bulk rock serpentinization of off-axis ultramafics, however, as we use these data to guide the inputs to our model, this study cannot be used to benchmark our results. Additionally, as both Worman et al. (2016) and Cannat et al. (2010) only analyzed bulk rock at present-day ridges, their results do not present a time-sensitive analysis nor convey the spatial distribution in ocean basins.

Our model shows a clear bimodal distribution of serpentinite in ocean basins as a function of the spreading history of any single basin (**Figure 9**). Basins where ridges spread less than 20 mm/a tend to produce a cumulative serpentinite thickness of ∼800–1500 m, whilst spreading rates between 20 and 40 mm/a produce more varied serpentinitic thicknesses of ∼100–1000 m (**Figure 9**). The Atlantic Ocean (in particular the north Atlantic), the Arctic Ocean, the Labrador Sea and the southwest Indian Ocean all are enriched in serpentinite relative to the bulk Pacific and Panthalassa Oceans (**Figure 9A**). The evolution of the Indian Ocean is particularly noteworthy in this regard, as our model suggests it contained very little serpentinite early in its existence (**Figures 9B,C**) as a consequence of the rapid velocity of the Indian plate. Once Greater India collided with Asia, the spreading system slowed considerably and our model suggests extensive peridotite emplacement and serpentinite production around the southwest Indian Ridge (**Figure 9A**). This has been suggested previously by Sauter et al. (2013), who argue detachment faulting at the SW Indian ridge has accommodated 100% of plate divergence for the past 11 Ma. The peridotite exposed from these detachment faults is highly serpentinized, with dredges producing samples of up to 80–100% serpentinization (Sauter et al., 2013) and a single borehole suggesting a body of serpentinite up to 3 km thick (Muller et al., 1997). Prior to Pangea breakup (320–200 Ma), our model suggests that the majority of serpentinite was preserved in marginal basins (e.g., Alexander-Stoney Mountain basin, Annamia-South China basin) or smaller internal oceans (e.g., Meso Tethys) (**Figures 9E–G**). These predictions are incredibly difficult to ground truth, and are sensitive to the plate model used (see section "Plate Model and Associated Uncertainty"), however, have the potential to inform

future research such as the investigation of arc flare ups (Lee and Lackey, 2015; Cashman et al., 2017).

DISCUSSION

Plate Model and Associated Uncertainty

Although they are excellent tools for reconstructing first-order paleogeographic configurations through time, plate models such as Matthews et al. (2016) contain a number of quantitative and qualitative uncertainties that must be taken into consideration when used to construct geological or geodynamic models. Plate models of this type comprise three underlying models: an absolute plate motion (APM) model, constraining global motions to a fixed reference frame; a relative plate motion (RPM) model, constraining the relative motion of adjacent features; and a plate circuit (PC) model which acts as the "connective tissue" tying RPM features to the APM (Müller et al., 2016). Reconstruction kinematics are highly sensitive to the choices of APM, RPM and PC, as each introduce independent uncertainties, with resulting plate models prone to unphysical geodynamic behavior rendering all analyses using these data as plate model specific (Tetley et al., 2019). Additionally, the requirement for the inclusion of synthetic plates and associated boundaries for times older than ∼160 Ma (as explored in this study, e.g., Panthalassa Ocean), introduces significant kinematic uncertainty which is difficult to quantify due to the APM, RPM, and PC dependency described above (Torsvik et al., 2010; Müller et al., 2016; Torsvik and Cocks, 2016; Tetley et al., in press, 2019). Therefore, the significance of our comparison between the POSR and PMSR methodologies shows that, at least for the Palaeozoic, results derived from the synthetic components of the plate model can be used to identify times of interest or a first-order trend for further investigation.

An unaddressed uncertainty in plate reconstruction models that affects our results are temporal changes in spreading rates that occur within internal oceans. Although the distribution of spreading rates for both internal and external oceans shows little variation (**Figures 1H,I**), pre-Pangea plate models are constructed using palaeomagnetic and geological data that typically have a coarser temporal resolution than data preserved in the present-day ocean basins (e.g., magnetic lineations). Consequently, this necessitates interpolation to equally sample ocean basins through time, which implicitly assumes a linear spreading rate between data points. This approach is most effective in cases where highly detailed apparent polar wander paths (APWPs) able to capture changes in velocity are available for a given block (e.g., Domeier, 2018), and most sensitive to cases where spreading rates are interpolated between rift-drift transition and continent-continent collision. In either case, the ability of the geological record to distinguish subtle changes in spreading rate is highly limited, making alternative periods of fast, and slow spreading in any internal ocean equally likely. These subtle variations have minimal impact on our estimates of carbon delivery, however, they would affect estimates of serpentinization. We consider the risk of this to be minimal in our models, but acknowledge a uniformitarian approach does not preclude this. For example, Brune et al. (2016) show that final continental breakup is marked by a rapid increase in divergence rate, which relaxes within ∼10 Ma to a slower drift speed. Analysis of the Atlantic and Indian Oceans at present-day reveal a series of variations in spreading rate and orientation (Müller et al., 2016) occurring, at a minimum, on a 10–20 Ma timescale. Excluding the Indian ocean, most changes in spreading rates are of less than 30 mm/a, and typically closer to values of 5–10 mm/a. The variation in timescale is approximately equivalent to the temporal spacing of smoothed APWPs (e.g., Torsvik et al., 2012), suggesting that for the evolution of internal oceans constrained by well-constructed APWPs, the modeled spreading rates are reliable.

Dynamic Drivers of Carbon and Serpentinite in Ocean Basins

An important question motivating this work is how the broader-scale plate tectonic system drives and controls variation in the carbon and serpentinization cycle. We observe notable differences in the trends of carbon and serpentinite subduction flux curves within our results. As both curves were derived using the same plate boundaries (Matthews et al., 2016), this suggests that carbon and serpentinite sequestration and subduction are controlled by more than plate boundary geometry alone. The storage capacity of carbon in the upper oceanic lithosphere is dependent on the combination of mid-ocean ridge length and bottom water temperature, rather than variations in mid-ocean ridge spreading rate, as although the storage method is different, crust from fast and slow ridges can store similar total amounts of carbon (Kelemen and Manning, 2015). Therefore, as seafloor production rates control the amount of carbon sequestered, we suggest that the total volume of carbon entering a subduction zone is a function not of the geodynamic nature of mid-ocean ridges, but rather the global abundance of subduction at any given time on Earth. The temporal variability of carbon entering a trench is therefore relatively insensitive to mid-ocean ridge dynamics or the evolution of ocean basins, instead appearing most strongly related to the volume of oceanic crust being subducted (e.g., **Figures 7B**, **12A**). A consequence of this is that total volumes of carbon sequestration in ocean basins remain relatively constant through time (**Figures 12B,C**). This has important implications for estimating time-dependent carbon flux at arcs, as evidence of arcs are more readily preserved in the geological record than evidence of rifts or ridges (Cao et al., 2017; Merdith et al., 2019). This suggests first-order estimates of carbon flux at arcs could be made for the Neoproterozoic and Palaeozoic using only calculations of plate boundary length and convergence rate, analogous to arguments made for episodic zircon age spectra (Domeier et al., 2018). This formulation could provide important constraints for modeling of palaeoclimate and biogeochemical processes during these times (Lenton et al., 2018; Mills et al., 2019).

Serpentinites, by comparison, appear concentrated only in specific ocean basins (**Figure 9**), with their subsequent delivery to trenches not as spatio-temporally consistent as that of carbon. We propose that the subduction flux of serpentinite (and the associated water storage) is not principally controlled

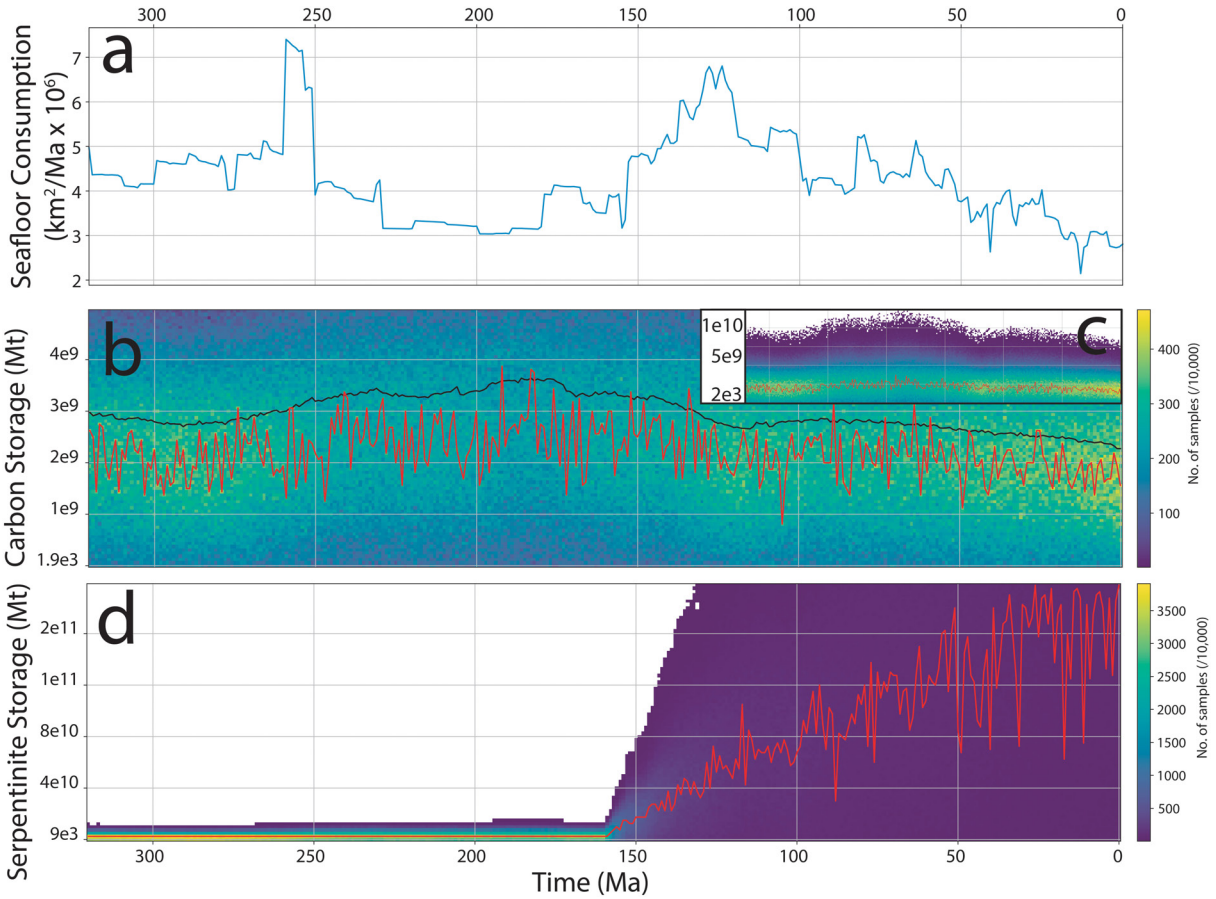

FIGURE 12 | (A) Seafloor consumption rates from Matthews et al. (2016) (using PMSR). **(B)** Binned distribution of total sequestered carbon in ocean basins (black line is the mean, red line is the mode) using POSR. **(C)** Full distribution of **(B)**. **(D)** Binned distribution of total serpentinite in ocean basins (red line is the mode) using POSR. Due to the interpolation and gridding of our data, together with inconsistencies in the plate model, our measure of total storage slightly over-estimates the actual result and is to be interpreted as a maximum. See **Supplementary Material 1**, **2** for table of results and **Supplementary Material 3**, **5** for grids in 1 Ma timesteps.

by subduction, but instead by variations in spreading rate, as spreading rate provides a first-order control on the volume of exhumed mantle within an ocean basin. Internal oceans, defined as oceans occurring on overriding plates as a result of supercontinent breakup, are thought to evolve more slowly as the main driver of plate motion (subduction) is not acting upon them. This implies that during the closure of one or more internal oceans, the flux of serpentinite and water being subducted will be significantly higher than during supercontinent breakup, or during periods of drift when few internal oceans are actively closing, as characterized by global plate configurations over the last 300 Ma (Cogné and Humler, 2008). Furthermore, if we consider that oceanic lithosphere is completely recycled every ∼200 Ma, it would suggest that the periodicity of serpentinite (and water) storage and subduction is related to the supercontinent cycle. In this case, the stage of supercontinent assembly (such as during the amalgamation of Gondwana or Pangea, or the future closure of the Atlantic Ocean) would be marked by extensive delivery of serpentinite (**Figure 12D**) and water into continental arcs, which may affect accretionary dynamics during subsequent continental collision (Menant et al., 2019).

Water Storage and Delivery

In this study, we provide a bottom-up mass estimate of water bound in both serpentinite and the volcanic layers of oceanic crust at trenches. Lithospheric flexure of oceanic crust adjacent to trenches is also thought to contribute to mantle serpentinization (Ranero et al., 2003; Grevemeyer et al., 2018; Scambelluri et al., 2019). However, it is poorly constrained (Faccenda, 2014) and subsequently not considered in this study. Whilst quantitative estimates of serpentinite delivery from ridge to trench do not exist in alternative studies, there are a number of investigations into the mass of water entering subduction zones (Iwamori, 1998), which we use to evaluate our results. As estimates of hydrated oceanic crust have been provided in numerous previous studies (Rüpke et al., 2004; Hacker, 2008; van Keken et al., 2011), we focus our contribution on analyzing the time-sensitive delivery of water stored in serpentinite to subduction zones. Our estimates of water mass in serpentinite at subduction can be used alongside

estimates of oceanic crust as a first-order approximation to constrain thermodynamic models investigating water content in the mantle wedge.

Estimates of subducted water mass stored within oceanic crust typically range between 400 and 1800 Mt/a (Bebout, 1995; Schmidt and Poli, 1998, 2003), with more recent studies suggesting a lower range between 400 and 600 Mt/a (Jarrard, 2003; Rüpke et al., 2004; Hacker, 2008; van Keken et al., 2011; Faccenda, 2014; **Figures 11D,E**). Notably, the upper extents of estimates from early studies (prior to accounting for dehydration) are up to an order of magnitude higher than our estimates of water stored in serpentinite (100–450 Mt/a). Our estimates are slightly lower than those of Jarrard (2003) (hereby referred to as J03), who suggested a delivery of 600 Mt/a in oceanic crust, representing a geologically complete estimate of water delivery to trenches. If our analysis included only water stored in upper volcanic layers (2.7 wt% in our analysis, black shaded area in **Figure 11D**), our estimates would approach parity with J03, though we do not include water stored in the entire crustal profile or pore water. Consequently, the sum of our serpentinitic component (100–450 Mt/a) and J03's estimate of ocean crust storage (∼600 Mt/a) may reflect a more complete picture of water delivery to trenches (at present-day), with a total almost doubling the global water budget (Jarrard, 2003) at trenches before accounting for additional serpentinization of the mantle occurring due to trench flexure.

The combined estimate of water in upper oceanic lithosphere (∼700–1100 Mt/a) is similar to the range suggested by Faccenda (2014) (hereby, F14) (**Figure 11E**) for oceanic crust, and that of Parai and Mukhopadhyay (2012) (hereby, PM12). PM12 applied a Monte Carlo approach to model the mantle deep water cycle, with results suggesting a steady state estimate of water entering the trench between ∼1020 and 1070 Mt/a, with a return flow consisting of about 30% (280–380 Mt/a). Additionally, PM12 found subduction scenarios with large water flux (>1400 Mt/a) were unlikely to reproduce expected sea level changes throughout the Phanerozoic. The addition of substantial mantle hydration during flexure to the combined estimate, such as that suggested in F14 of ∼1000 Mt/a, would greatly exceed the upper limit of PM12. However, as noted in both F14 and this study, there is large spatial (and temporal) variability of both serpentine in ocean basins and the degree of trench flexure, making it difficult to infer a "static" present-day value. In our model there is little serpentinite being subducted around the Pacific. Comparably, the eventual closure of the Atlantic and/or Indian Ocean would likely greatly increase the delivery of water to trenches.

We can also consider the predicted water content contained within the total mass of serpentinite in all ocean basins through time (**Figure 12D**). Our present-day estimate of serpentinite within all ocean basins suggests $\sim 4.3 \bullet 10^{19}$ kg of water is stored in mantle peridotite altered at mid-ocean ridges (using the mean value of $3.1 \bullet 10^{11}$ Mt and 13.5 wt% water). This is approximately one-third of the amount estimated to be stored in oceanic crust by Bodnar et al. (2013). Considering that ridges with significant peridotite exhumation are unlikely to produce basaltic crust during this time, the ratio of volcanic to peroditic crust could be higher. This high amount of potential water storage is significant as the distribution of serpentinite has clear temporal variation, potentially making this an under-explored component for constraining sea level (Rüpke et al., 2004; Parai and Mukhopadhyay, 2012; Karlsen et al., 2019).

Relationship With Atmospheric Carbon Dioxide

One of the key motivations for estimating the mass of carbon entering subduction zones is the potential to provide constraints on the delivery of CO_2 from the crust to the atmosphere via volcanic outgassing. However, this is a non-trivial problem as the fate of carbon stored in subducted oceanic lithosphere is poorly understood. Specifically, the proportion of carbon that: (i) remains in the slab and is subsequently recycled into the mantle, (ii) is mobilized but trapped in the arc wedge and subsequently incorporated into continental lithosphere, and (iii) is expelled by a volcano into the atmosphere, is collectively poorly constrained and thought to vary depending on a range of tectonic, petrological, geochemical and geodynamic variables (Dasgupta and Hirschmann, 2010; Kelemen and Manning, 2015). Kelemen and Manning (2015) estimated that between ∼30 and 100% of subducted carbon is recycled into the overriding plate, where it is then either incorporated into carbon bearing minerals or is degassed as CO_2, with the remaining carbon being transported into the mantle. We assume decarbonation of the slab and either degassing by volcanoes or sequestration in the wedge occurs on sub-1 Ma timescales (Van Der Meer et al., 2014), as CO_2 rich fluids from the slab are released early in the dehydration process (John et al., 2012). However, this suggests there is little lag time between subduction and outgassing on tectonic scales, and does not provide any clear way for estimating the proportion of carbon being delivered to the atmosphere. A proxy that could be used to evaluate our estimates are atmospheric CO_2 records, themselves the summation of multiple other sources of carbon such as degassing from ridges (Kerrick, 2001) and continental rifts (Brune et al., 2017). As a result of this, we expect some level of mismatch between our estimates and those of atmospheric CO_2 through time.

Some similarity exists between our results of carbon delivery to trenches and estimates of time-dependent atmospheric CO_2 (Foster et al., 2017), particularly during the late Permian and Early Triassic (**Figures 11A,B**). The peak at ∼75 Ma in our estimates of subducted carbon also appears to correlate with a CO_2 peak at this time, though the progression in our results after this peak (toward 50 Ma) deviates from the CO_2 curve. Here (∼70–55 Ma) our results show an increase in carbon delivery to trenches while atmospheric CO_2 drops, until the Cenozoic rifting period initiates (Brune et al., 2017). The more recent evolution of subducted carbon and atmospheric CO_2 also show similarities, with a local maxima occurring in the late Eocene (∼40 Ma), before both curves decrease toward present-day values (**Figures 11A,B**). Significant deviations occur in the Carboniferous to early Permian, the Triassic-Jurassic boundary and during the Early Cretaceous (**Figures 11A,B**). In the first of these deviations our results show declining carbon delivery while CO_2 increases; in the second, atmospheric CO_2 peaks while our

estimates remain constant; and in the Early Cretaceous we have a broad peak of carbon delivery to trenches while atmospheric CO_2 remains constant. Deviations where our estimates of carbon delivery to trenches increase while atmospheric CO_2 either remains constant or decreases are most likely a consequence of other crustal, tectonic or biological factors at play that were not considered in this study. Conversely, deviations when atmospheric CO_2 peak while carbon delivery remains constant may be accounted for through either rift or ridge degassing. In this case, the first and third deviation are somewhat enigmatic in comparison to our results, suggesting either the amount of carbon degassed from subduction zones changes over time in a manner not related to the tectonic parameters (i.e., the length and convergence rate), or there is a co-dependence between tectonic sources and sinks of carbon (e.g., rifts, ridges, and arcs) that operate on different timescales. This would suggest that subduction zones and arc-degassing can not solely account for atmospheric CO_2 variations.

Although we do not explicitly measure seafloor production rates, we can estimate them as carbon storage in the upper oceanic lithosphere is broadly proportionally related to spreading rate (**Figure 11F**), as the thickness of oceanic crust is approximately constant. Our estimates are similar to both those of Coltice et al. (2013) (**Figure 11F**, black line with purple boxes), and the combined spreading rate and ridge length predictions of MD18 (Müller and Dutkiewicz (2018) their Figures 2B,C). Following this, assuming that carbon degassing is approximately linearly proportional to seafloor production rates (e.g., Kerrick (2001), though we note that CO_2 content of magmas are not constant across the globe), the relative shape of any carbon degassing curve should follow the seafloor production rate curve, providing a first-order estimate of degassing from mid-ocean ridge systems. Applying this approach, the atmospheric CO_2 curve (**Figure 11A**) shows some correlation with seafloor production rates (**Figure 11F**, using carbon storage at mid-ocean ridges as a proxy), and is most strongly demonstrated by peaks in the latest Carboniferous and early Eocene (∼55–50 Ma). Inversely, and perhaps more interestingly, are times of strong deviation between the curves in **Figures 11A,B,F** in particular the aforementioned peak of atmospheric CO_2 in the Triassic-Jurassic (**Figure 11A**) that do not appear to be correlated with the amount of carbon being subducted (**Figure 11B**), carbon sequestration or seafloor production rates (**Figure 11F**). The exact cause of this is unclear from our analysis, however, rift degassing may be one potential contributor, as it can deliver a similar volume of carbon directly into the atmosphere as that from mid-ocean ridges or subduction zones over geological time (Brune et al., 2017).

CONCLUSION

The long-term evolution of carbon and water on Earth is in part controlled by the continual recycling of oceanic lithosphere between mid-ocean ridges and subduction zones. Here we present a general method for the geological characterization of ocean basins constrained by full-plate tectonic reconstruction models explicitly mapping the location and geometry of mid-ocean ridges and subduction zones. We calculate the amount of carbonate and serpentinite preserved in both the oceanic crust and exhumed mantle lithosphere at a given mid-ocean ridge, then trace those masses through time to calculate the subduction flux of each. We find carbon storage is approximately uniform throughout geological time, and propose variation in observed subduction flux is controlled by subduction dynamics and not mid-ocean ridge dynamics. We find present-day rates of carbon subduction in upper oceanic lithosphere to be at the lowest levels for the past 200 Ma (15–39 Mt/a). Additionally, our results suggest the amount of serpentinite (and volume of water stored within it) being subducted at present-day is higher than between the Carboniferous to Cretaceous. We infer this is because the primary tectonic control on the mass of serpentinite delivered to a trench is the geodynamic nature of mid-ocean ridges, as only slow and ultraslow spreading ridges result in the exhumation of the lithospheric mantle such that it is in contact with ocean water, allowing extensive serpentinization to occur. Our results predict that much of the serpentinite formed in the past 320 Ma remains preserved in ocean basins located within the Atlantic, Indian and Arctic oceans. This suggests the closure of internal oceans, such as during the assembly of a supercontinent, result in increased subduction of water relative to times of supercontinent breakup or drift (e.g., the past 300 Ma).

DATA AVAILABILITY STATEMENT

All datasets generated for this study are included in the article/**Supplementary Material**.

AUTHOR CONTRIBUTIONS

AM, SA, and MT conceived of the study together. AM designed and carried out the analysis, and wrote the manuscript with contributions and input from SA and MT. SA characterized the Pacific-Ocean spreading rate to pass into pre-Pangea times. All authors contributed to the discussion.

FUNDING

AM was supported by the Deep Energy Community of the Deep Carbon Observatory. SA was supported by the AUGURY European Research Council Project 617588, the European Union Horizon 2020 Research and Innovation Programme under grant agreement TRANSCALE 716542, and EU H2020 Marie Skłodowska-Curie Individual Fellowship TEMPO Project 838535. MT was supported by the AUGURY European Research Council Project 617588. This is a contribution to IGCP 648.

ACKNOWLEDGMENTS

We thank the editor and reviewers for their constructive criticism which helped to improve the manuscript. All authors

appreciate discussion and advice from I. Daniel, M. Andreani, and N. Coltice.

SUPPLEMENTARY MATERIAL

The Supplementary Material for this article can be found online at: https://figshare.com/articles/Supp_material_Merdithetal_Frontiers_zip/11323463/1

MATERIAL S1 | Carbon table of results.

MATERIAL S2 | Serpentinite table of results.

MATERIAL S3 | Carbon grids and rasters.

MATERIAL S4 | Serpentinite grids and raster.

MATERIAL S5 | Carbon animation.

MATERIAL S6 | Serpentinite animation.

MATERIAL S7 | *Jupyter* notebooks.

REFERENCES

Alt, J. C., Schwarzenbach, E. M., Früh-Green, G. L., Shanks, W. C., Bernasconi, S. M., Garrido, C. J., et al. (2013). The role of serpentinites in cycling of carbon and sulfur: seafloor serpentinization and subduction metamorphism. *Lithos* 178, 40–54. doi: 10.1016/j.lithos.2012.12.006

Alt, J. C., and Teagle, D. A. H. (1999). The uptake of carbon during alteration of ocean crust. *Geochim. Cosmochim. Acta* 63, 1527–1535. doi: 10.1016/S0016-7037(99)00123-124

Barry, P. H., de Moor, J. M., Giovannelli, D., Schrenk, M., Hummer, D. R., Lopez, T., et al. (2019). Forearc carbon sink reduces long-term volatile recycling into the mantle. *Nature* 568, 487–492. doi: 10.1038/s41586-019-1131-1135

Bebout, G. E. (1995). The impact of subduction-zone metamorphism on mantle-ocean chemical cycling. *Chem. Geol.* 126, 191–218. doi: 10.1016/0009-2541(95)00118-115

Bebout, G. E., and Barton, M. D. (1989). Fluid flow and metasomatism in a subduction zone hydrothermal system: catalina schist terrane. California. *Geology* 17:976. doi: 10.1130/0091-7613(1989)017<0976:ffamia>2.3.co;2

Becker, T. W. (2006). On the effect of temperature and strain-rate dependent viscosity on global mantle flow, net rotation, and plate-driving forces. *Geophys. J. Int.* 167, 943–957. doi: 10.1111/j.1365-246X.2006.03172.x

Bodnar, R. J., Azbej, T., Becker, S. P., Cannatelli, C., Fall, A., and Severs, M. J. (2013). Whole Earth geohydrologic cycle, from the clouds to the core: the distribution of water in the dynamic Earth system. *Geol. Soc. Am. Spec. Pap.* 500, 431–461.

Bown, J. W., and White, R. S. (1994). Variation with spreading rate of oceanic crustal thickness and geochemistry. *Earth Planet. Sci. Lett.* 121, 435–449. doi: 10.1016/0012-821X(94)90082-90085

Brune, S., Williams, S. E., Butterworth, N. P., and Müller, R. D. (2016). Abrupt plate accelerations shape rifted continental margins. *Nature* 536, 201–204. doi: 10.1038/nature18319

Brune, S., Williams, S. E., and Müller, R. D. (2017). Potential links between continental rifting, CO2 degassing and climate change through time. *Nat. Geosci.* 10, 941–946. doi: 10.1038/s41561-017-0003-6

Canales, J. P., Collins, J. A., Escartín, J., and Detrick, R. S. (2000). Seismic structure across the rift valley of the Mid-Atlantic Ridge at 23 20'(MARK area): implications for crustal accretion processes at slow spreading ridges. *J. Geophys. Res.* 105, 28411–28425. doi: 10.1029/2000JB900301

Cannat, M. (1993). Emplacement of mantle rocks in the seafloor at mid-ocean ridge. *J. Geophys. Res.: Solid Earth* 4163:4172.

Cannat, M., Fontaine, F., and Escartín, J. (2010). "Serpentinization and associated hydrogen and methane fluxes at slow spreading ridges," in *Diversity of Hydrothermal Systems on Slow Spreading Ocean Ridges Geophysical Monograph Series*, eds P. A. Rona, C. W. Devey, J. Dyment, and B. J. Murton, (Washington, DC: American Geophysical Union), 241–264. doi: 10.1029/2008gm000760

Cannat, M., Rommevaux-Jestin, C., and Fujimoto, H. (2003). Melt supply variations to a magma-poor ultra-slow spreading ridge (Southwest Indian Ridge 61° to 69° E). *Geochem. Geophys. Geosyst.* 4, 1–21. doi: 10.1029/2002GC000480

Cao, W., Lee, C.-T. A., and Lackey, J. S. (2017). Episodic nature of continental arc activity since 750 Ma: a global compilation. *Earth Planet. Sci. Lett.* 461, 85–95. doi: 10.1016/j.epsl.2016.12.044

Carbotte, S. M., Smith, D. K., Cannat, M., and Klein, E. M. (2016). Tectonic and magmatic segmentation of the global ocean ridge system: a synthesis of observations. *Geol. Soc. Lon. Spec. Publ.* 420, 249–295. doi: 10.1144/SP420.5

Carlson, R. L. (2001). The abundance of ultramafic rocks in atlantic ocean crust. *Geophys. J. Int.* 144, 37–48. doi: 10.1046/j.0956-540x.2000.01280.x

Cashman, K. V., Sparks, R. S. J., and Blundy, J. D. (2017). Vertically extensive and unstable magmatic systems: a unified view of igneous processes. *Science* 355:eaag3055. doi: 10.1126/science.aag3055

Clift, P. D. (2017). A revised budget for cenozoic sedimentary carbon subduction: cenozoic carbon subduction. *Rev. Geophys.* 55, 97–125. doi: 10.1002/2016RG000531

Cogné, J.-P., and Humler, E. (2008). Global scale patterns of continental fragmentation: wilson's cycles as a constraint for long-term sea-level changes. *Earth Planet. Sci. Lett.* 273, 251–259. doi: 10.1016/j.epsl.2008.06.030

Collins, W. J. (2003). Slab pull, mantle convection, and Pangaean assembly and dispersal. Earth Planet. *Sci. Lett.* 205, 225–237. doi: 10.1016/s0012-821x(02)01043-9

Coltice, N., Seton, M., Rolf, T., Müller, R. D., and Tackley, P. J. (2013). Convergence of tectonic reconstructions and mantle convection models for significant fluctuations in seafloor spreading. *Earth Planet. Sci. Lett.* 383, 92–100. doi: 10.1016/j.epsl.2013.09.032

Conrad, C. P., and Lithgow-Bertelloni, C. (2002). How mantle slabs drive plate tectonics. *Science* 298, 207–209. doi: 10.1126/science.1074161

Conrad, C. P., and Lithgow-Bertelloni, C. (2004). The temporal evolution of plate driving forces: Importance of "slab suction" versus "slab pull" during the Cenozoic. *J. Geophys. Res.* 109:B10407. doi: 10.1029/2004JB002991

Constantin, M., Hékinian, R., Ackermand, D., and Stoffers, P. (1995). "Mafic and ultramafic intrusions into upper mantle peridotites from fast spreading centers of the easter microplate (South East Pacific)," in *Mantle and Lower Crust Exposed in Oceanic Ridges and in Ophiolites*, eds R. L. M. Vissers, and A. Nicolas, (Netherlands: Springer), 71–120. doi: 10.1007/978-94-015-8585-9_4

Coogan, L. A., Parrish, R. R., and Roberts, N. M. W. (2016). Early hydrothermal carbon uptake by the upper oceanic crust: Insight from in situ U-Pb dating. *Geology* 44, 147–150. doi: 10.1130/G37212.1

Crameri, F., Conrad, C. P., Montési, L., and Lithgow-Bertelloni, C. R. (2019). The dynamic life of an oceanic plate. *Tectonophysics* 760, 107–135. doi: 10.1016/j.tecto.2018.03.016

Dasgupta, R. (2013). Ingassing, storage, and outgassing of terrestrial carbon through geologic time. *Rev. Mineral. Geochem.* 75, 183–229. doi: 10.2138/rmg.2013.75.7

Dasgupta, R., and Hirschmann, M. M. (2010). The deep carbon cycle and melting in Earth's interior. *Earth Planet. Sci. Lett.* 298, 1–13. doi: 10.1016/j.epsl.2010.06.039

Dick, H. J. B. (1989). Abyssal peridotites, very slow spreading ridges and ocean ridge magmatism. *Geol. Soci. Lon., Spec. Publ.* 42, 71–105. doi: 10.1144/GSL.SP.1989.042.01.06

Dick, H. J. B., Lin, J., and Schouten, H. (2003). An ultraslow-spreading class of ocean ridge. *Nature* 426, 405–412. doi: 10.1038/nature02128

Domeier, M. (2016). A plate tectonic scenario for the Iapetus and Rheic oceans. *Gondwana Res.* 36, 275–295. doi: 10.1016/j.gr.2015.08.003

Domeier, M. (2018). Early Paleozoic tectonics of Asia: towards a full-plate model. *Geosci. Front.* 9, 789–862. doi: 10.1016/j.gsf.2017.11.012

Domeier, M., Magni, V., Hounslow, M. W., and Torsvik, T. H. (2018). Episodic zircon age spectra mimic fluctuations in subduction. *Sci. Rep.* 8:17471. doi: 10.1038/s41598-018-35040-z

Domeier, M., and Torsvik, T. H. (2014). Plate tectonics in the late Paleozoic. *Geosci. Front.* 5, 303–350. doi: 10.1016/j.gsf.2014.01.002

Domeier, M., and Torsvik, T. H. (2017). Full-plate modelling in pre-Jurassic time. *Geol. Mag.* 156, 261–280. doi: 10.1017/S0016756817001005

Dutkiewicz, A., Dietmar Müller, R., Cannon, J., Vaughan, S., and Zahirovic, S. (2019). Sequestration and subduction of deep-sea carbonate in the global ocean since the Early Cretaceous. *Geology* 47, 91–94. doi: 10.1130/G45424.1

Faccenda, M. (2014). Water in the slab: a trilogy. *Tectonophysics* 614, 1–30. doi: 10.1016/j.tecto.2013.12.020

Foster, G. L., Royer, D. L., and Lunt, D. J. (2017). Future climate forcing potentially without precedent in the last 420 million years. *Nat. Commun.* 8:14845. doi: 10.1038/ncomms14845

Früh-Green, G. L., Connolly, J. A. D., Plas, A., Kelley, D. S., and Grobéty, B. (2004). "Serpentinization of oceanic peridotites: Implications for geochemical cycles and biological activity," in *The Subseafloor Biosphere at Mid-Ocean Ridges Geophysical Monograph Series*, eds W. S. D. Wilcock, E. F. DeLong, D. S. Kelley, J. A. Baross, and S. Craig Cary, (Washington, DC: American Geophysical Union), 119–136. doi: 10.1029/144gm08

Früh-Green, G. L., Plas, A., and Lécuyer, C. (1996). 14. Petrologic and stable isotope constraints on hydrothermal alteration and serpentinization of the EPR shallow mantle at hess deep (site 895). *Proc. Ocean Drill. Prog. Sci. Results* 147, 255–291.

Gerya, T. V., Connolly, J. A. D., Yuen, D. A., Gorczyk, W., and Capel, A. M. (2006). Seismic implications of mantle wedge plumes. *Phys. Earth Planet. Inter.* 156, 59–74. doi: 10.1016/j.pepi.2006.02.005

Gillis, K. M., and Coogan, L. A. (2011). Secular variation in carbon uptake into the ocean crust. *Earth Planet. Sci. Lett.* 302, 385–392. doi: 10.1016/j.epsl.2010.12.030

Grevemeyer, I., Ranero, C. R., and Ivandic, M. (2018). Structure of oceanic crust and serpentinization at subduction trenches. *Geosphere.* 14, 395–418. doi: 10.1130/ges01537.1

Hacker, B. R. (2008). H2O subduction beyond arcs. *Geochem. Geophys. Geosyst.* 9:Q03001. doi: 10.1029/2007GC001707

Hellinger, S. J. (1981). The uncertainties of finite rotations in plate tectonics. *J. Geophys. Res.* 86, 9312–9318. doi: 10.1029/JB086iB10p09312

Hirth, G., and Kohlstedt, D. L. (1996). Water in the oceanic upper mantle: implications for rheology, melt extraction and the evolution of the lithosphere. *Earth Planet. Sci. Lett.* 144, 93–108. doi: 10.1016/0012-821X(96)00154-159

Iwamori, H. (1998). Transportation of H2O and melting in subduction zones. *Earth Planet. Sci. Lett.* 160, 65–80. doi: 10.1016/S0012-821X(98)00080-86

Janecky, D. R., and Seyfried, W. E. (1986). Hydrothermal serpentinization of peridotite within the oceanic crust: experimental investigations of mineralogy and major element chemistry. *Geochim. Cosmochim. Acta* 50, 1357–1378. doi: 10.1016/0016-7037(86)90311-X

Jarrard, R. D. (2003). Subduction fluxes of water, carbon dioxide, chlorine, and potassium. *Geochem. Geophys. Geosyst.* 4:8905. doi: 10.1029/2002GC000392

John, T., Gussone, N., Podladchikov, Y. Y., Bebout, G. E., Dohmen, R., Halama, R., et al. (2012). Volcanic arcs fed by rapid pulsed fluid flow through subducting slabs. *Nat. Geosci.* 5:489. doi: 10.1038/ngeo1482

Karlsen, K. S., Conrad, C. P., and Magni, V. (2019). Deep water cycling and sea level change since the breakup of pangea. *Geochem. Geophys. Geosyst.* 20, 2919–2935. doi: 10.1029/2019GC008232

Kasting, J. F. (1989). Long-term stability of the Earth's climate. *Glob. Planet. Change* 75, 83–95.

Kelemen, P. B., and Manning, C. E. (2015). Reevaluating carbon fluxes in subduction zones, what goes down, mostly comes up. *Proc. Natl. Acad. Sci. U.S.A.* 112, E3997–E4006. doi: 10.1073/pnas.1507889112

Keller, T., Katz, R. F., and Hirschmann, M. M. (2017). Volatiles beneath mid-ocean ridges: deep melting, channelised transport, focusing, and metasomatism. *Earth Planet. Sci. Lett.* 464, 55–68. doi: 10.1016/j.epsl.2017.02.006

Kerrick, D. (2002). Geology. Serpentinite seduction. *Science* 298, 1344–1345. doi: 10.1126/science.298.5597.1344

Kerrick, D. M. (2001). Present and past nonanthropogenic CO2 degassing from the solid Earth. *Rev. Geophys.* 39, 565–585. doi: 10.1029/2001RG000105

Lear, C. H., Elderfield, H., and Wilson, P. A. (2000). Cenozoic deep-Sea temperatures and global ice volumes from Mg/Ca in benthic foraminiferal calcite. *Science* 287, 269–272. doi: 10.1126/science.287.5451.269

Lee, C.-T. A., and Lackey, J. S. (2015). Global continental arc flare-ups and their relation to long-term greenhouse conditions. *Elements* 11, 125–130. doi: 10.2113/gselements.11.2.125

Lenton, T. M., Daines, S. J., and Mills, B. J. W. (2018). COPSE reloaded: an improved model of biogeochemical cycling over Phanerozoic time. *Earth-Sci. Rev.* 178, 1–28. doi: 10.1016/j.earscirev.2017.12.004

Lithgow-Bertelloni, C., and Richards, M. A. (1998). The dynamics of cenozoic and mesozoic plate motions. *Rev. Geophys.* 36, 27–78. doi: 10.1029/97RG02282

Matthews, K. J., Maloney, K. T., Zahirovic, S., Williams, S. E., Seton, M., and Müller, R. D. (2016). Global plate boundary evolution and kinematics since the late Paleozoic. *Glob. Planet. Chang.* 146, 226–250. doi: 10.1016/j.gloplacha.2016.10.002

Menant, A., Angiboust, S., and Gerya, T. (2019). Stress-driven fluid flow controls long-term megathrust strength and deep accretionary dynamics. *Sci. Rep.* 9:9714. doi: 10.1038/s41598-019-46191-y

Merdith, A. S., Collins, A. S., Williams, S. E., Pisarevsky, S., Foden, J. D., Archibald, D. B., et al. (2017). A full-plate global reconstruction of the Neoproterozoic. *Gondwana Res.* 50, 84–134. doi: 10.1016/j.gr.2017.04.001

Merdith, A. S., Williams, S. E., Brune, S., Collins, A. S., and Müller, R. D. (2019). Rift and plate boundary evolution across two supercontinent cycles. *Glob. Planet. Chang.* 173, 1–14. doi: 10.1016/j.gloplacha.2018.11.006

Meyzen, C. M., Toplis, M. J., Humler, E., Ludden, J. N., and Mével, C. (2003). A discontinuity in mantle composition beneath the southwest Indian ridge. *Nature* 421:731. doi: 10.1038/nature01424

Michael, P. J., Langmuir, C. H., Dick, H. J. B., Snow, J. E., Goldstein, S. L., Graham, D. W., et al. (2003). Magmatic and amagmatic seafloor generation at the ultraslow-spreading Gakkel ridge. *Arctic Ocean. Nat.* 423:956. doi: 10.1038/nature01704

Mills, B. J. W., Krause, A. J., Scotese, C. R., Hill, D. J., Shields, G. A., and Lenton, T. M. (2019). Modelling the long-term carbon cycle, atmospheric CO2, and Earth surface temperature from late Neoproterozoic to present day. *Gondwana Res.* 67, 172–186. doi: 10.1016/j.gr.2018.12.001

Minshull, T. A., Muller, M. R., and White, R. S. (2006). Crustal structure of the Southwest Indian Ridge at 66 E: seismic constraints. *Geophys. J. Int.* 166, 135–147. doi: 10.1111/j.1365-246x.2006.03001.x

Muller, M. R., Minshull, T. A., and White, R. S. (1999). Segmentation and melt supply at the Southwest Indian Ridge. *Geology* 27, 867–870.

Muller, M. R., Robinson, C. J., Minshull, T. A., White, R. S., and Bickle, M. J. (1997). Thin crust beneath ocean drilling program borehole 735B at the Southwest Indian Ridge? *Earth Planet. Sci. Lett.* 148, 93–107. doi: 10.1016/S0012-821X(97)00030-37

Müller, R. D., and Dutkiewicz, A. (2018). Oceanic crustal carbon cycle drives 26-million-year atmospheric carbon dioxide periodicities. *Sci. Adv.* 4:eaaq0500. doi: 10.1126/sciadv.aaq0500

Müller, R. D., Sdrolias, M., Gaina, C., and Roest, W. R. (2008). Age, spreading rates, and spreading asymmetry of the world's ocean crust. *Geochem. Geophys. Geosyst.* 9:Q0400. doi: 10.1029/2007GC001743

Müller, R. D., Seton, M., Zahirovic, S., Williams, S. E., Matthews, K. J., Wright, N. M., et al. (2016). Ocean basin evolution and global-scale plate reorganization events since pangea breakup. *Annu. Rev. Earth Planet. Sci.* 44, 107–138. doi: 10.1146/annurev-earth-060115-12211

Murphy, B. J., and Nance, D. R. (2003). Do supercontinents introvert or extrovert?: Sm-Nd isotope evidence. *Geology* 31, 873–876. doi: 10.1130/G19668.1

Muto, J., Shibazaki, B., Iinuma, T., and Ito, Y. (2016). Heterogeneous rheology controlled postseismic deformation of the 2011 Tohoku−Oki earthquake. *Geophysical.* 43, 4971–4978. doi: 10.1002/2016GL068113

Parai, R., and Mukhopadhyay, S. (2012). How large is the subducted water flux? New constraints on mantle regassing rates. *Earth Planet. Sci. Lett.* 31, 396–406. doi: 10.1016/j.epsl.2011.11.024

Ranero, C. R., Morgan, J. P., McIntosh, K., and Reichert, C. (2003). Bending-related faulting and mantle serpentinization at the Middle America trench. *Nature* 425, 367–373. doi: 10.1038/nature01961

Reston, T. J., and McDermott, K. G. (2011). Successive detachment faults and mantle unroofing at magma-poor rifted margins. *Geology* 39, 1071–1074. doi: 10.1130/G32428.1

Rüpke, L. H., Morgan, J. P., Hort, M., and Connolly, J. A. D. (2004). Serpentine and the subduction zone water cycle. *Earth Planet. Sci. Lett.* 223, 17–34. doi: 10.1016/j.epsl.2004.04.018

Sauter, D., Cannat, M., Rouméjon, S., Andreani, M., Birot, D., Bronner, A., et al. (2013). Continuous exhumation of mantle-derived rocks at the Southwest

Indian Ridge for 11 million years. *Nat. Geosci.* 6:314. doi: 10.1038/ngeo1771

Scambelluri, M., Cannaò, E., and Gilio, M. (2019). The water and fluid-mobile element cycles during serpentinite subduction. *A review. Eur. J. Mineral.* 31, 405–428. doi: 10.1127/ejm/2019/0031-2842

Schmidt, M. W., and Poli, S. (1998). Experimentally based water budgets for dehydrating slabs and consequences for arc magma generation. *Earth Planet. Sci. Lett.* 163, 361–379. doi: 10.1016/S0012-821X(98)00142-143

Schmidt, M. W., and Poli, S. (2003). Generation of Mobile Components during Subduction of Oceanic Crust. *Treatise Geochem.* 3:659. doi: 10.1016/B0-08-043751-6/03034-3036

Seton, M., Müller, R. D., Zahirovic, S., Gaina, C., Torsvik, T., Shephard, G., et al. (2012). Global continental and ocean basin reconstructions since 200Ma. *EarthSci. Rev.* 113, 212–270. doi: 10.1016/j.earscirev.2012.03.002

Shilobreeva, S., Martinez, I., Busigny, V., Agrinier, P., and Laverne, C. (2011). Insights into C and H storage in the altered oceanic crust: results from ODP/IODP Hole 1256D. *Geochim. Cosmochim. Acta* 75, 2237–2255. doi: 10.1016/j.gca.2010.11.027

Sleep, N. H., and Barth, G. A. (1997). The nature of oceanic lower crust and shallow mantle emplaced at low spreading rates. *Tectonophysics* 279, 181–191. doi: 10.1016/s0040-1951(97)00121-122

Sleep, N. H., and Zahnle, K. (2001). Carbon dioxide cycling and implications for climate on ancient Earth. *J. Geophys. Res.* 106, 1373–1399. doi: 10.1029/2000JE001247

Staudigel, H., Plank, T., White, B., and Schmincke, H.-U. (1996). "Geochemical fluxes during seafloor alteration of the basaltic upper oceanic crust: DSDP Sites 417 and 418: Bebout/Subduction top to bottom," in *Subduction Top to Bottom Geophysical Monograph Series*, eds G. E. Bebout, D. W. Scholl, S. H. Kirby, and J. P. Platt, (Washington, D. C: American Geophysical Union), 19–38. doi: 10.1029/gm096p0019

Tetley, M. G., Li, Z.-X., Matthews, K. J., Williams, S. E., and Müller, R. D. (in press). Decoding earth's plate tectonic history using sparse geochemical data. *Geosci. Front.* doi: 10.1016/j.gsf.2019.05.002

Tetley, M. G., Williams, S. E., Gurnis, M., Flament, N., and Müller, R. D. (2019). Constraining absolute plate motions since the Triassic. *J. Geophys. Res.* 124, 7231–7258. doi: 10.1029/2019JB017442

Thompson, A. B. (1992). Water in the Earth's upper mantle. *Nature* 358, 295–302. doi: 10.1038/358295a0

Torsvik, T. H., and Cocks, L. R. M. (2016). *Earth History and Palaeogeography*. Cambridge: Cambridge University Press.

Torsvik, T. H., Steinberger, B., Gurnis, M., and Gaina, C. (2010). Plate tectonics and net lithosphere rotation over the past 150My. *Earth Planet. Sci. Lett.* 291, 106–112. doi: 10.1016/j.epsl.2009.12.055

Torsvik, T. H., Steinberger, B., Shephard, G. E., Doubrovine, P. V., Gaina, C., Domeier, M., et al. (2019). Pacific–panthalassic reconstructions: overview, errata and the way forward. *Geochem. Geophys. Geosyst.* 20, 3659-3689. doi: 10.1029/2019GC008402

Torsvik, T. H., Van der Voo, R., Preeden, U., Mac Niocaill, C., Steinberger, B., Doubrovine, P. V., et al. (2012). Phanerozoic polar wander, palaeogeography and dynamics. *Earth-Sci. Rev.* 114, 325–368. doi: 10.1016/j.earscirev.2012.06.007

Tucholke, B. E., Behn, M. D., Roger Buck, W., and Lin, J. (2008). Role of melt supply in oceanic detachment faulting and formation of megamullions. *Geology* 36, 455–458. doi: 10.1130/G24639A.1

Tucholke, B. E., and Lin, J. (1994). A geological model for the structure of ridge segments in slow spreading ocean crust. *J. Geophys. Res.* 99, 11937–11958. doi: 10.1029/94JB00338

Van Der Meer, D. G., Zeebe, R. E., van Hinsbergen, D. J. J., Sluijs, A., Spakman, W., and Torsvik, T. H. (2014). Plate tectonic controls on atmospheric CO2 levels since the Triassic. *Proc. Natl. Acad. Sci. U.S.A.* 111, 4380–4385. doi: 10.1073/pnas.1315657111

van Keken, P. E., Hacker, B. R., Syracuse, E. M., and Abers, G. A. (2011). Subduction factory: 4. Depth-dependent flux of *H*2O from subducting slabs worldwide. . *J. Geophys. Res* 116, B01401. doi: 10.1029/2010JB007922

Williams, S. E. (2019). *Siwill22/Agegrid-0.1 v1-alpha (Version v1-alpha)*.

Worman, S. L., Pratson, L. F., Karson, J. A., and Klein, E. M. (2016). Global rate and distribution of H2 gas produced by serpentinization within oceanic lithosphere: H2 formation in ocean lithosphere. *Geophys. Res. Lett.* 43, 6435–6443. doi: 10.1002/2016GL069066

Wright, N. M., Seton, M., Williams, S. E., and Müller, R. D. (2016). The Late Cretaceous to recent tectonic history of the Pacific Ocean basin. *Earth-Sci. Rev.* 154, 138–173. doi: 10.1016/j.earscirev.2015.11.015

Young, A., Flament, N., Maloney, K., Williams, S., Matthews, K., Zahirovic, S., et al. (2019). Global kinematics of tectonic plates and subduction zones since the late Paleozoic Era. *Geosci. Front.* 10, 989–1013. doi: 10.1016/j.gsf.2018.05.011

Zastrozhnov, D., Gernigon, L., Gogin, I., Abdelmalak, M. M., Planke, S., Faleide, J. I., et al. (2018). Cretaceous-paleocene evolution and crustal structure of the northern vøring margin (Offshore Mid-Norway): results from integrated geological and geophysical study. *Tectonics* 37, 497–528. doi: 10.1002/2017TC004655

Zhang, Y., and Zindler, A. (1993). Distribution and evolution of carbon and nitrogen in Earth. *Earth Planet. Sci. Lett.* 117, 331–345. doi: 10.1016/0012-821X(93)90088-Q

Conflict of Interest: The authors declare that the research was conducted in the absence of any commercial or financial relationships that could be construed as a potential conflict of interest.

frontiers in Earth Science

ORIGINAL RESEARCH
published: 16 June 2020
doi: 10.3389/feart.2020.00209

A Review of H_2, CH_4, and Hydrocarbon Formation in Experimental Serpentinization Using Network Analysis

Samuel Barbier[1,2†], Fang Huang[3,4†], Muriel Andreani[1], Renbiao Tao[1], Jihua Hao[1], Ahmed Eleish[3], Anirudh Prabhu[3], Osama Minhas[3], Kathleen Fontaine[3], Peter Fox[3] and Isabelle Daniel[1]*

[1] Univ Lyon, Univ Lyon 1, ENSL, CNRS, Laboratoire de Géologie de Lyon UMR 5276, Villeurbanne, France, [2] Total CSTJF, Pau, France, [3] Tetherless World Constellation, Rensselaer Polytechnic Institute, Troy, NY, United States, [4] CSIRO Mineral Resources, Kensington, WA, Australia

The origin of methane and light hydrocarbons (HCs) in natural fluids from serpentinization has commonly been attributed to the abiotic reduction of oxidized carbon by H_2 through Fischer-Tropsch-type (FTT) reactions. Multiple experimental serpentinization studies attempted to identify the parameters that control the abiotic production of H_2, CH_4, and light HC. H_2 is systematically and significantly formed in experiments, indicating that its production during serpentinization is well established. However, the large variance in concentration (eight orders of magnitude) is difficult to address because of the large number of parameters that vary from one experiment to another. CH_4 and light HC production is much lower and also highly variable, leading to a vivid debate on potential role of metal catalysts and organic contamination. We have built a dataset that includes experimental setups, conditions, reactants, and products from 30 peer-reviewed articles reporting on experimental serpentinization and performed dimensionality reduction and network analysis to achieve an unbiased reading of the literature and fuel the debate. Our analysis distinguishes four experimental communities that highlights usual experimental protocols and the conditions tested so far. As expected, H_2 production is mainly controlled by T and P though a strong variability remains within a given P-T range. Accessory metal-bearing phases seem to favor H_2 production, while their role as catalyst or reactant is hampered by the lack of mineralogical characterization. CH_4 and light HC concentrations are highly variable, uncorrelated to each other, and much lower than concentrations of potential reactants (H_2, initial carbon). Accessory phases proposed as FTT catalysts do not enhance CH_4 production, confirming the inefficiency of this reaction. CH_4 only displays a positive correlation with temperature suggesting a kinetic/thermal control on its forming reaction. The carbon budget of some experiments indicates contamination in agreement with available labeled ^{13}C studies. Salts in initial solutions are possible sources of organic contaminants. Natural systems certainly exploit longer reaction time or other reactional paths to form the observed CH_4 and HC. The reducing potential of serpentinization can also produce intermediate metastable carbon phases in liquid or solid as observed in natural samples that should be targeted in future experiments.

Keywords: experimental serpentinization, hydrothermal, abiotic hydrogen, methane, data and network analysis

OPEN ACCESS

Edited by:
Sung Keun Lee,
Seoul National University,
South Korea

Reviewed by:
Charles Le Losq,
UMR 7154 Institut de Physique du Globe de Paris, France
Fabrice Brunet,
UMR 5275 Institut des Sciences de la Terre (ISTERRE), France

****Correspondence:***
Fang Huang
f.huang@csiro.au

† These authors share first authorship

Specialty section:
This article was submitted to Earth and Planetary Materials, a section of the journal Frontiers in Earth Science

Received: *02 August 2019*
Accepted: *19 May 2020*
Published: *16 June 2020*

Citation:
Barbier S, Huang F, Andreani M, Tao R, Hao J, Eleish A, Prabhu A, Minhas O, Fontaine K, Fox P and Daniel I (2020) A Review of H_2, CH_4, and Hydrocarbon Formation in Experimental Serpentinization Using Network Analysis. Front. Earth Sci. 8:209. doi: 10.3389/feart.2020.00209

INTRODUCTION

The discovery of widespread, natural H_2 seepages has a high potential for C-free energy. In natural environments, H_2 is often accompanied by CH_4 and organic compounds, of which the biotic or abiotic origin is still under discussion (Charlou et al., 2002; Proskurowski et al., 2006, 2008; Konn et al., 2009; Etiope and Sherwood Lollar, 2013; Monnin et al., 2014; Vitale Brovarone et al., 2017; Wang et al., 2018; Young, 2019). In most cases, H_2, CH_4, and the organic compounds are first or second order products of serpentinization reactions, which are the hydrothermal alteration of ultramafic rocks. As illustrated in **Figure 1**, various proportions of H_2 and CH_4 are detected in fluids from different serpentinizing systems over a wide range of pressure (P), temperature (T), and pH conditions, such as mid-oceanic ridges (Charlou et al., 2002; Proskurowski et al., 2006, 2008; Konn et al., 2009; Fouquet et al., 2013), or ophiolites (Chavagnac et al., 2013; Monnin et al., 2014; Etiope et al., 2018). These abiotic moieties have attracted much attention since they could serve as an energy source to sustain deep life and potentially contributed to its origin on Earth and elsewhere in the solar system (Sleep et al., 2004; Schulte et al., 2006; Oze and Sharma, 2007; Ehlmann et al., 2010; Russell et al., 2010; Hellevang et al., 2011; Zahnle et al., 2011; Glein et al., 2015; Holm et al., 2015; Brazil, 2017; Etiope et al., 2018; Ménez et al., 2018).

H_2 production during serpentinization results from the oxidation of the ferrous component of ferromagnesian minerals (e.g., olivine, pyroxenes) coupled to the reduction of water (Thayer, 1966). In turn, H_2 can reduce oxidized forms of carbon into CH_4 and light hydrocarbons (HCs) via a Sabatier or Fischer-Tropsch-type (FTT) reaction (Szatmari, 1989). Industrial reactions use CO as the carbon source under gaseous conditions with metal catalysts to overcome kinetics hindrance, either Ru- or Rh-based and Ni-based for Sabatier and FTT reactions, respectively. However, the main source of oxidized carbon in natural systems is CO_2, bi-carbonate, or carbonate ions depending on the pH, rather than CO, and reactions are likely to occur under aqueous conditions (McCollom, 2013). Consequently, the common use of Sabatier-type (R1) and FTT (R2) reactions among the geoscience community are:

$$4\,H_2 + CO_2 = CH_4 + 2\,H_2O \quad (R1)$$

$$(3n+1)\,H_2 + n\,CO_2 = C_nH_{2n+2} + 2n\,H_2O \quad (R2)$$

The increased interest for these natural reactions over the last decades has led to a large number of thermodynamic modeling and experimental studies of serpentinization. Thermodynamic models using crustal conditions predict that H_2 concentration at equilibrium with serpentinized peridotite increases with T and can reach hundreds of mM at optimum conditions (~300°C) (Klein et al., 2009, 2013). This is close to the concentration expected near a reaction front, but an order of magnitude higher than those measured at oceanic vents (Andreani et al., 2013; Fouquet et al., 2013). CH_4 is favored relative to CO_2 with decreasing temperature and increasing H_2 concentration, and should be the dominant C-bearing component in hydrothermal fluids released from serpentinization at temperatures below 400°C (Shock, 1992, Zolotov and Shock, 1999, 2000; McCollom, 2013), similar to observations in natural fluids (**Figure 1**). In experiments, the system tends toward equilibrium with time, but it is affected by kinetic effects that are related to a series of crucial parameters such as T, P, grain size, time, or fluid composition. **Figure 2** shows a compilation of the H_2 and CH_4 concentrations produced during experimental serpentinization from the original dataset (Huang et al., unpublished). These concentrations agree with our understanding of serpentinization kinetics, displaying a higher H_2 concentration in higher T experiments (>200°C) than in low T ones (<100°C) (**Figure 2A**), and also overlap with natural concentrations. Nevertheless, a detailed examination of **Figure 2A** reveals some discrepancies between results for ranges of T that are not easily attributable to parameters that affect kinetics, and questions the optimum conditions for H_2 production. The situation appears much more complex and controversial when it comes to CH_4 and HC production (**Figure 2B**). Although some experimental concentrations agree well with measurements for high-temperature (HT) fluids, the experimental trend displays an increase of CH_4 as a function of T, which is opposite to the decrease expected from thermodynamic models. Moreover, experiments using ^{13}C labeled sources, $^{13}CO_2$, $H^{13}COOH$, $NaH^{13}CO_3$, resulted in virtually no $^{13}CH_4$ production (roughly two orders of magnitude below $^{12}CH_4$) raising the issue of potential contamination by ubiquitous organic carbon in most experiments (McCollom and Seewald, 2001; McCollom, 2003, 2016; Foustoukos and Seyfried, 2004; Fu et al., 2007; Ji et al., 2008; McCollom et al., 2010; Lazar et al., 2012, 2015; Grozeva et al., 2017). These experiments have fueled questions about whether the abiotic synthesis of CH_4 during serpentinization reactions actually occurs.

In order to feed the debate and achieve an unbiased reading of the available literature, we have built a comprehensive dataset of the experimental results of serpentinization available in the literature (Huang et al., unpublished), and, after dimensionality reduction, applied machine learning tools, a yet underused approach in geosciences. This approach provides an overview of the different conditions and protocols used so far, including the wide variety of experimental parameters that cannot be easily handled on regular plot (e.g., **Figure 2**). Finally, we discuss the variability of H_2 and CH_4 concentrations along with the consistency of the global dataset.

DATA AND METHODS

Data Description

A large number of experiments have been conducted to study serpentinization, aiming at understand the abiotic production of H_2, CH_4, and other HCs during water–rock interactions (Berndt et al., 1996; Horita and Berndt, 1999; McCollom and Seewald, 2001, 2003; Allen and Seyfried, 2003; Foustoukos and Seyfried, 2004; Seewald et al., 2006; Fu et al., 2007, 2008; Seyfried et al., 2007; Ji et al., 2008; Dufaud et al., 2009; Jones et al., 2010; McCollom et al., 2010, 2016; Marcaillou et al., 2011; Neubeck et al., 2011, 2014; Lafay et al., 2012; Lazar et al., 2012, 2015; Klein and McCollom, 2013; Okland et al., 2014; Huang et al., 2015, 2016; Klein et al., 2015; McCollom, 2016; McCollom and Donaldson, 2016; Grozeva et al., 2017; Miller et al., 2017).

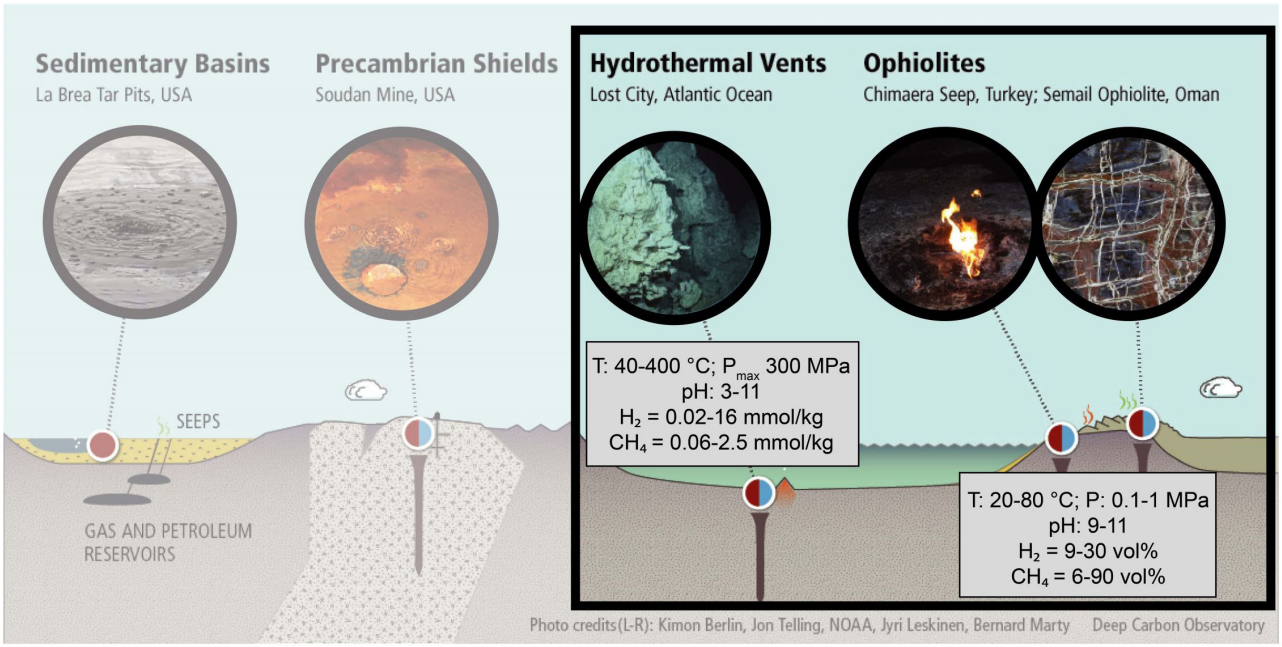

FIGURE 1 | Geologic settings of intense H_2 and CH_4 degassing on Earth. The red and blue colors reflect the biotic and abiotic contributions, respectively, of which the relative fluxes are still under debate. The biotic production includes present-day microbial activity and thermogenic breakdown of organic matter from biological origin. The abiotic production results from radiolysis in Precambrian shields and serpentinization reactions at mid-ocean ridges or in ophiolites. Serpentinization settings are highlighted. (Credit: Josh Wood, modified with permission).

The most extensive dataset compiled so far is described in a companion data paper (Huang et al., unpublished). This dataset includes serpentinization experiments in which minerals are initially introduced as reactants, as well as experiments run without solid reactants. The latter correspond either to blank experiments—designed to evaluate unavoidable contaminations (e.g., background carbon or H_2 production)—or to relevant systems in which H_2 levels would not be limited by mineral dissolution and could reach higher values, such as experiments with formate as a source of H_2 and C.

The database (Huang et al., unpublished) indicates that the scientific community is mainly focused on two geological settings: ophiolites, characterized by low pressure (LP) and low temperature (LT) conditions (ambient or vapor saturation pressure, T < 100°C) and oceanic hydrothermal environments characterized by medium pressure (MP) to high pressure (HP) and HT conditions (30–300 MPa; 200–500°C). The highest pressures tested, at 350 MPa, are also relevant to shallow subduction environments where serpentinization occurs in the mantle wedge or fractured subducting lithosphere. There is a clear lack of data between 100 and 200°C, and between 50 and 300 MPa (**Figure 3** and **Supplementary Figure S1**).

Various types of reactors were used to cover this large range of P-T conditions. For instance, gold cells in autoclave are common for experiments at HT (200–500°C) and HP (300 MPa) conditions (Huang et al., 2015, 2016; Lazar et al., 2015) while Parr type autoclaves, with or without flexible cells made of gold or titanium, are better suited for experiments at HT (200–500°C) and MP (30–50 MPa) conditions (Berndt et al., 1996; Horita and Berndt, 1999; McCollom and Seewald, 2001, 2003; Allen and Seyfried, 2003; Foustoukos and Seyfried, 2004; Seewald et al., 2006; Fu et al., 2007, 2008; Seyfried et al., 2007; Ji et al., 2008; Dufaud et al., 2009; Jones et al., 2010; McCollom et al., 2010, 2016; Marcaillou et al., 2011; Lafay et al., 2012; Lazar et al., 2012; Klein and McCollom, 2013; Klein et al., 2015; McCollom, 2016; Grozeva et al., 2017). Comparably, borosilicate glass bottles were preferred for LT and LP experimental conditions (Neubeck et al., 2011, 2014; Okland et al., 2014; McCollom and Donaldson, 2016; Miller et al., 2017). **Figure 3** is a swarm plot showing the number of data points in green of a given value for a series of selected parameters. The gray box represents the 25–75th percentile and the gray line is the median value. The gray lines outside the box represent the minimum and maximum values, with the exception of outliers. P, T, and initial/final pH of the fluid follow a bimodal distribution that mimics the natural conditions illustrated in **Figure 1**. Addition of NaCl or $NaHCO_3$ salts, presence of catalyst, and gold capsules are the most frequent features in the dataset, used in more than 50% of experiments. This indicates that inorganic carbon in experiments is most often introduced as $NaHCO_3$ salt, and that the most classical reactors are made of gold. Other dataset features are highly variable, for example, all experiments have their own starting materials (e.g., mineral assemblages, fluid compositions), sample volumes that range from 0.05 to 180 mL, and experimental run durations from hours to a year.

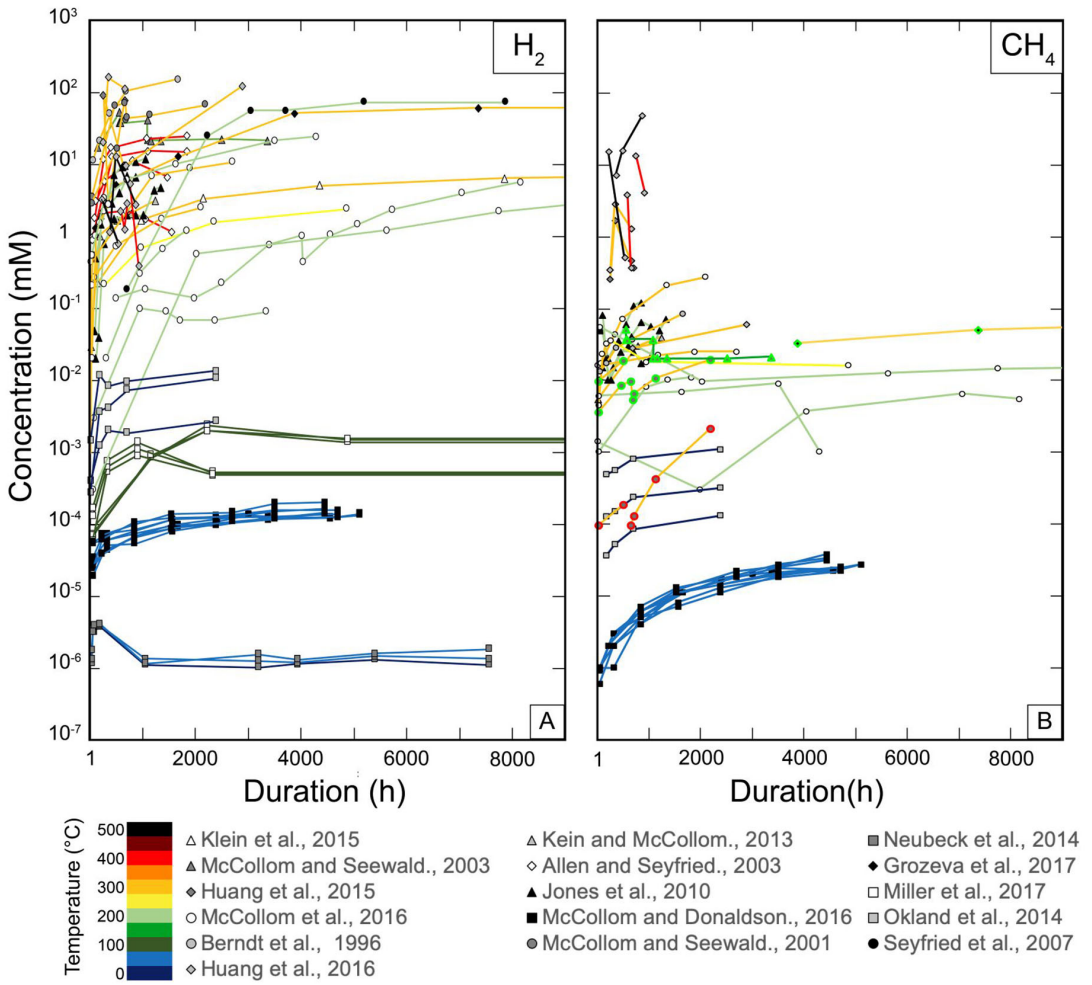

FIGURE 2 | Summary of H_2 **(A)** and CH_4 **(B)** concentrations produced as a function of time and temperature during serpentinization experiments, in which duration can reach ca. 11 months. Concentrations span over eight orders of magnitude from nanomoles to hundreds of millimoles.

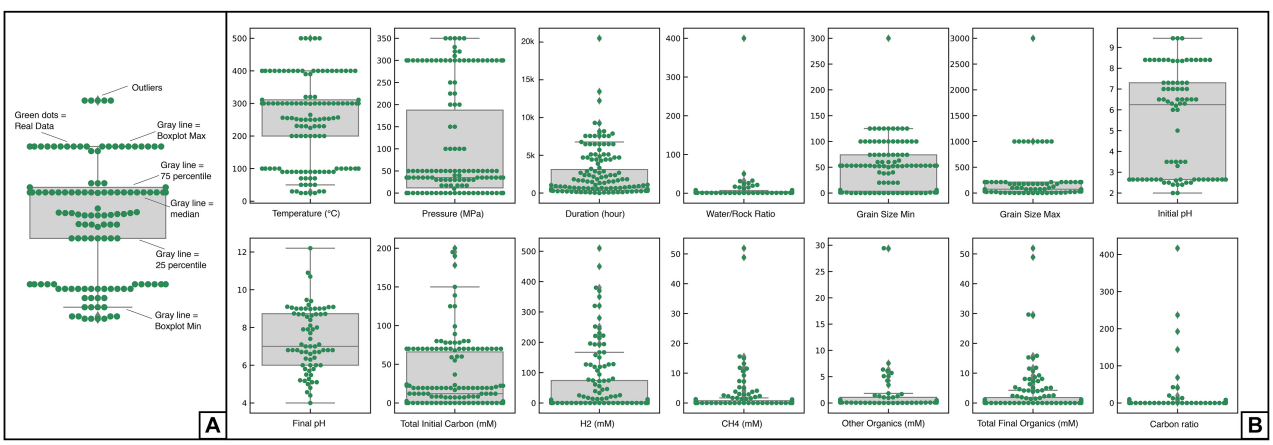

FIGURE 3 | (A) Presentation of the general attributes of a swarm plot that helps to visualize the distribution of a selected data feature (green dots), e.g., temperature, H_2, CH_4, and related boxplots. **(B)** Swarm plots of the distribution of data according to experimental parameters and results analyzed in this contribution. The *x*-axis indicates the parameter, and values are plotted against the *y*-axis.

TABLE 1 | Description of the working dataset modified from Huang et al. (unpublished) organized in three major sections: article's information (green), experimental conditions (blue), and results (yellow).

Article's informations		Experimental conditions														Results	
Title of the Publication	Authors et al XXXX	Number of individual experiments	Temperature / Pressure	Duration at each analyses	Solids composition	Initial knows catalyst (s)	Solution composition	Is blank	Grainsize	Initial pH	Mass solids and liquid	W/R ratio	Total initial carbon	Reactor composition	Intermediate sampling	Final pH	Gases and liquids formations
Title	Author et al., XXXX	N°	(°C / Mpa)	(Hours)	Olivine only, Olivine free, Olivine and other, Peridotite, No solids (1 (yes) or 0 (no))	Presence of catalyst(s), Spinel, Chromite, Magnetite, Ni-bearing, Fe-bearing (1 (yes) or 0 (no))	Water, NaCl, NaHCO3, HCOOH, other salts,… (mol-mmol/kg)	(1 (yes) or 0 (no))	*min and max (μm)*	X (num)	X (g)	X (num)	X (mol-mmol/kg)	Gold, Titanium,, Plastic and glass,…. 1 (yes) or 0 (no)	(1 (Yes) or 0 (No))	X (num)	H2, CH4, Other organics, total final organics, C conversion (mol-mmol/kg)

Sub sections and summary of contents are also displayed with examples of value, unit when appropriate, character (0 or 1).

The complete dataset (Huang et al., unpublished) includes more than 100 parameters. Each column represents a feature, such as an experimental parameter, reactant, or product, and each row is a measurement. Some of the 100 features of the complete dataset are too sparse to allow running data analysis algorithms directly. Hence, in the present study, we performed dimensionality reduction by removing the less variable parameters and combined some features to increase data density within 37 features in a working dataset (**Table 1**). Hereafter, we will refer to the header of the column that is an explicit shortcut for its content. For example, the "Other_organics" feature sums all organic products except CH_4; the "Fe_bearing" feature combines all Fe-bearing solids (synthetic or natural) added to the system (e.g., FeO, hematite, sulfides) except olivine and magnetite, which are considered as independent parameters. Some experiments include multiple samplings as a function of time and had more than one measurement (as shown in **Figure 2**); in these cases, only the final measurements were kept for the analysis in order to prevent overweighting those experiments in the analysis. Hence, the final working dataset includes 158 measurements in total, which result from experimental runs with different durations.

Pearson Correlation Coefficient Matrix

The Pearson correlation coefficient is a value between -1 and 1 that indicates the extent of linear correlation between two variables. A coefficient of -1 or 1 means the two variables are in perfect negative or positive correlation respectively, with 0 indicating no correlation. Details of how the coefficient is calculated can be found in Pearson (1895) and Lee Rodgers and Alan Nice Wander (1988). The pairwise Pearson correlation coefficient matrix for our final dataset is calculated and displayed in **Figure 4**.

It is worth noting that some parameters are dependent and led to some of the strongest correlation, e.g., between "CH_4," "Other_organics," and "Total_final_organics," the latter being the sum of the formers. Another example is "Spinel," which correlates with "Peridotite" and "Presence_catalyst" because peridotite is partly composed of spinel and spinel is a common catalyst of some reactions. Conversely, "Magnetite," which was separated from the "Fe-bearing" and "Spinel" lists, does not correlate with "Fe-bearing" and "Spinel."

The experimental protocol also induced some strong correlations. For instance, temperature is strongly positively correlated with the parameter, "With_Gold," and negatively correlated with the parameter, "With_Plastics+Glass," classically used for HT and LT experiments, respectively. Similarly, the use of formate, "HCOOH," as a source of carbon and H_2 is strongly correlated to the highest levels of initial carbon, "Total_Initial_C_mM," which are used in the gold reactors ("With_Gold") predominantly in experiments that did not include mineral phases ("No_solid").

The black box (**Figure 4**) highlights the correlations of interest, i.e., between all parameters, H_2, and carbon products. It shows the lack of strong correlations that prevent the interpretation of the database using conventional wisdom. These relationships are presented and discussed in Section "Results and Discussion," with the help of network analysis.

Network Analysis

Network analysis is a collection of analytical and visualization methods that have been employed to study complex systems in various fields of science and technology. For example, in biology, it has been applied to the study of ecosystem diversity (Banda-R et al., 2016), proteomics and protein–protein interactions (Amitai et al., 2004; Harel et al., 2015), evolution (Vilhena et al., 2013), and mass extinction events in Earth's history (Muscente et al., 2018, 2019). In urban planning, networks have been used to model power grids (Pagani and Aiello, 2013), roads (Dong and Pentland, 2009), and water supply systems (Geem, 2006) as well as communications infrastructure (Hansen and Smith, 2014). Networks of people have also featured prominently in the study of social media, the spread of infectious diseases, the structure of criminal organizations, and connections among research collaborators (Otte and Rousseau, 2002; Abraham et al., 2010; Eslick, 2012; Scott and Carrington, 2015).

The power of network analysis arises mainly from its capability of representing and visualizing large sets of highly dimensional data and exposing the complex relationships amongst them. Entities are represented by nodes (vertices) and are connected by edges (links) that illustrate the relationship

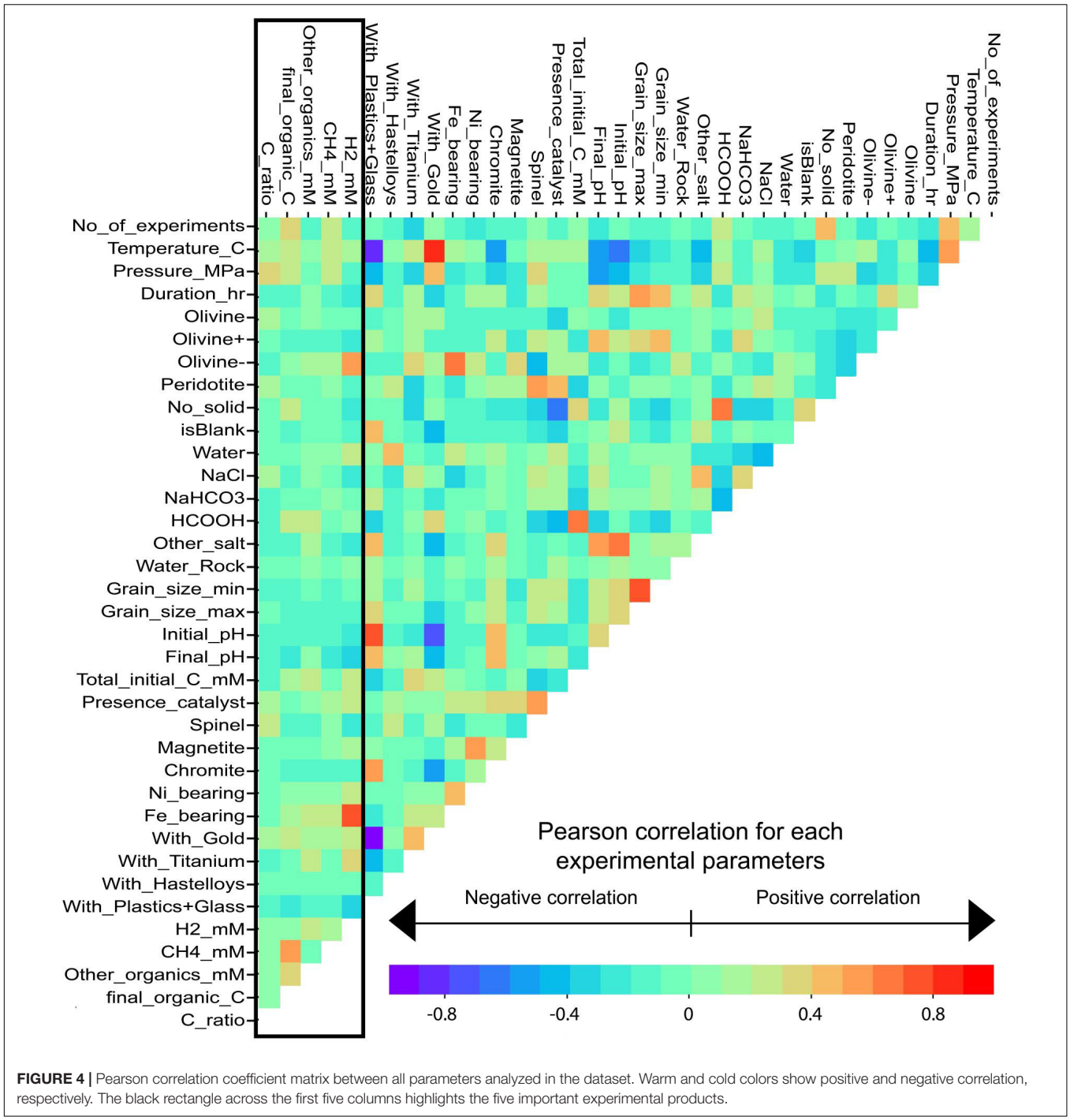

FIGURE 4 | Pearson correlation coefficient matrix between all parameters analyzed in the dataset. Warm and cold colors show positive and negative correlation, respectively. The black rectangle across the first five columns highlights the five important experimental products.

between entities. The visual attributes of the nodes such as shape, color, or radius, and of edges such as weight (line thickness), can be mapped to values resulting in a dynamic and more expressive network diagram. Visual inspection of the diagram with some perturbation of the parameters is a powerful tool for revealing potentially unseen patterns and characteristics in the data. A number of quantitative analytical techniques can be applied to the network in order to study and quantify the significance of these patterns and behaviors.

In this methodology, the nodes refer to each experiment within the dataset, and edges represent the similarity between different experiments. Therefore, nodes that cluster together have short edges, and represent similar experiments. At the end of the analysis, a cluster of nodes then becomes a community of similar experiments. The

method to calculate similarity scores is explained in the following section.

Cosine Similarity Matrix

The network is built from a pre-calculated cosine similarity matrix (Janbandhu and Karhade, 2015). Each experimental measurement can be treated as a 35-dimension numeric vector (37 experimental features minus two article information features), and the pairwise cosine similarity score is calculated between each vector. The cosine similarity scores between two experimental features represent the combined effect of all parameters and vary between −1 and 1.

In the working dataset, 0 stands for no and 1 for yes, for categorical values. Numerical values such as temperature, pressure, or durations were normalized between 0 and 1 to avoid biases due to different value ranges. We then used the similarity scores as the edge weights of the networks. Since we consider just serpentinization experiments, many studies have some parameters in common, which results in a fully connected network with varying edge weights. Even though a fully connected network contains abundant information and potential insights, we choose to optimize the efficiency of the community detection algorithms by choosing a threshold to eliminate edges with low importance. For this purpose, we ran experiments by eliminating edges with low similarity scores and testing their effects on the results of the community detection algorithms.

Fruchterman–Reingold Force-Directed Networks

The Fruchterman–Reingold force-directed graph algorithm (Fruchterman and Reingold, 1991) simulates attractive and repulsive forces between the nodes, similar to those of molecular or planetary simulations, while attempting to find a minimum energy state for the network layout. It is based on two general principles: (1) nodes connected by an edge should be drawn near each other and (2) nodes should not overlap. To compute the layout, the method iteratively adds nodes to the diagram while recalculating the attractive and repulsive forces and displacing existing nodes accordingly. As such, we do not control the lengths of the edges or the final positions of the nodes, which are determined when the system reaches equilibrium. In this study, we use a python package called *Networkx* (v. 2.3) (Hagberg et al., 2008) to build the network. The 3D network structure is fixed by this algorithm, but its 2D projection can change at different angles randomly, meaning that every time when we run the code, the 2D project will change. For any algorithm involving randomization, a seed can be used to make the algorithm produce consistent results. We tested a set of seeds from 0 to 200 and found that seed 103 gives the clearest and most informative layout for our data. If the reader wants to reproduce our results, please use the same seed number as ours.

Louvain Community Detection Algorithm

The Louvain community detection algorithm (Blondel et al., 2008) attempts to find community structure in a network through multi-level modularity optimization. Initially, each node is assigned to its own community. At each step, nodes are reassigned to the communities with which they achieve the highest contribution to modularity. When no more nodes can be reassigned, the process is applied again to the merged communities and is stopped when there is only a single vertex remaining or modularity cannot be further improved. The algorithm in this paper is implemented using a package called *python-louvain*[1].

RESULTS AND DISCUSSION

Detection of Four Communities of Experiments: A Snapshot of the Literature

The Pearson similarity matrix (**Figure 4**) built from our dataset revealed no clear trend between experimental parameters and reaction products. It mostly identifies a couple of strong and inevitable correlations between some experimental parameters, such as the use of gold cells for HT experiments (see section "Pearson Correlation Coefficient Matrix"). However, it confirmed that (despite some trends on the kinetic curves that could already be drawn using the complete database; **Figure 2**), data discrepancies cannot be easily interpreted using conventional wisdom. We used the parameters reported from each experiment in our dataset to build a cosine similarity matrix, and then constructed a network (see section "Data and Methods") with a layout defined by Fruchterman–Reingold force-directed graph algorithm. Four communities were detected using the Louvain community detection algorithm, as colored distinctively in **Figure 5A**, and plotted individually in **Figure 5B**. These experimental communities present overall similarity among different experiments when taking into account all experimental features, including starting materials, reactants, reactors, fluids, reaction products, and potential catalysts. Hence, they provide a full "picture" of the available literature, i.e., the conditions that have been explored to date and the degree of similarity or dissimilarity of the results. For ease of comparison, the network diagrams presented in **Figure 5** follow the same color chart and layout throughout the manuscript.

The cosine similarity threshold and the initial node have been tested before ending up with these four experimental communities. **Supplementary Figure S2** shows that by successively removing the weakest 10, 30, 50, and 70% of the edge connections, the communities detected by Louvain algorithm are quite similar. We therefore infer that these communities are robust and represent real trends in the data. The number of communities detected is always four, and communities 0, 1, and 3 virtually stayed the same. When we remove the weakest 70 % of edge connections, nodes 143, 144, and 145 in community 3 moved into community 2.

Our analysis enabled us to find the optimum threshold (0.39) where the community detection algorithms produce very similar results to the densely connected networks, while increasing the efficiency of the network. This approach assisted in identifying the important edges in the network structure. Depending on

[1]https://python-louvain.readthedocs.io/en/latest/

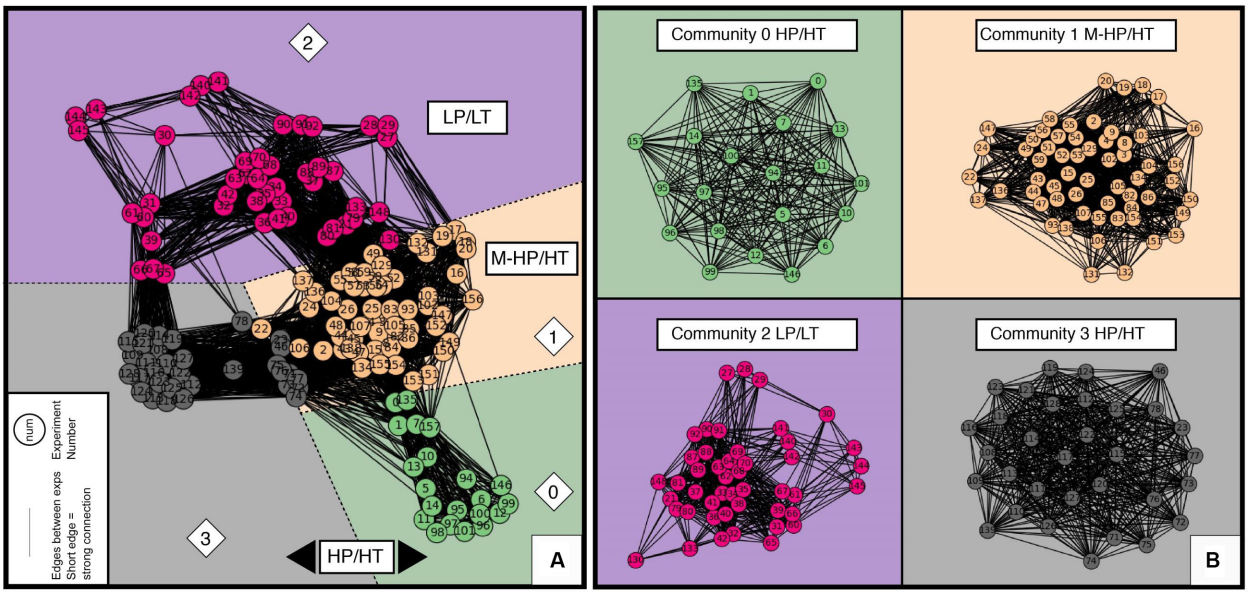

FIGURE 5 | Networks built with the cosine similarity matrix calculated from the dataset, with the four detected communities that are a snapshot of the conditions tested so far and their usual experimental protocols (community 0: HP/HT using HCOOH as a source of C and H_2, community 1: M-HP/HT, community 2: LP/LT, community 3: HP/HT with C_ratio > 1) (see **Figures 6**, **7**). **(A)** The full network. Each filled circle (node) represents an experiment, which number is included and allows to back track the corresponding experiment in the database. The shorter the link (edge) between two circles, the higher the correlation between the experiments. **(B)** The four separate community networks. Communities have been arbitrarily color coded as a guide for the eyes, which remained the same in all figures—green, brown, purple, and gray, for communities 0, 1, 2, and 3, respectively.

the initial node chosen by the algorithm, the number of detected communities was dominantly four but could increase to five occasionally. The initial node is chosen randomly by the algorithm, and the random state can be set with a random seed. As explained in Section ""Fruchterman–Reingold Force-Directed Networks," if you want to reproduce the layout of our plots, please use a seed of 29. As the random seed varied, community 0 always remained the same, but a few nodes on the edges of communities 1 and 2 (e.g., node 143, 144.), and 1 and 3 (e.g., node 22, 46, 106) would change.

In order to identify the main features that control the separation into the four communities identified with Louvain algorithm, we colored the nodes of the network as a function of the value of each experimental parameter. For parameters with binary values, white and lemon colors were used for 0 and 1, respectively. Red stands for unreported values. Selected plots are displayed in **Figure 6**; others are available in **Supplementary Figure S3**. This data analysis highlights the primary control of temperature (T) and pressure (P) on the experimental communities (**Figures 6A,B**), akin to natural end-member conditions (**Figure 1**). Community 2 clearly corresponds to LP/LT experiments at ambient P and T below 100°C, while the other communities encompass experiments run at higher P and T. Community 1 differs from communities 0 and 3 because of pressure and covers MP range between 10 and 100 MPa. Community 3 differs from community 0 and others because it contains experiments that exclusively used the decomposition of formic acid HCOOH as a source of H_2 and CO_2 and buffered the initial pH to the lowest values reported in the literature (**Figures 6C,D**). Community 3 also lacks information on the water-to-rock ratio since neither a solid phase (**Figure 6E** and **Supplementary Figure S3A**), nor NaCl was added to the fluid (**Supplementary Figure S3B**), distinguishing it from almost all other experiments. It is worth noting that except for experiments performed with HCOOH, initial pH values are rarely reported in experiments within communities 0 and 1, and are most likely close to neutral or slightly alkaline considering the presence of NaCl with or without $NaHCO_3$, respectively. Visualization of community 2 shows that LP/LT experiments have also been run at neutral to basic conditions to mimic outflow fluid composition in ophiolitic settings. Hence, experimental results of community 3 cannot be directly compared to the others and will be plotted in the following graphs for informative purposes only. Detailed examination of the communities' characteristics highlights the lack of experiments under initial acidic conditions that are supposed to be the most favorable for olivine dissolution (Oelkers, 1999; Kaszuba et al., 2013). This might be due to the fact that natural serpentinizing systems are not expected to be acidic at a temperature of or below 300°C. However, reaction with acidic HT hydrothermal fluids such as those escaping from peridotite-hosted hydrothermal vents at slow-spreading ridges can occur (Fouquet et al., 2013). Finally, analysis of the communities shows that the initial fluid composition is a feature that has never been explored so far, especially in HT experiments.

When looking at individual communities (**Figure 5B** and **Supplementary Figure S4**), experiments are also well grouped into clusters of LP/LT, MP/HT, and HP/HT conditions, even if P and T only partially characterize the communities. Communities

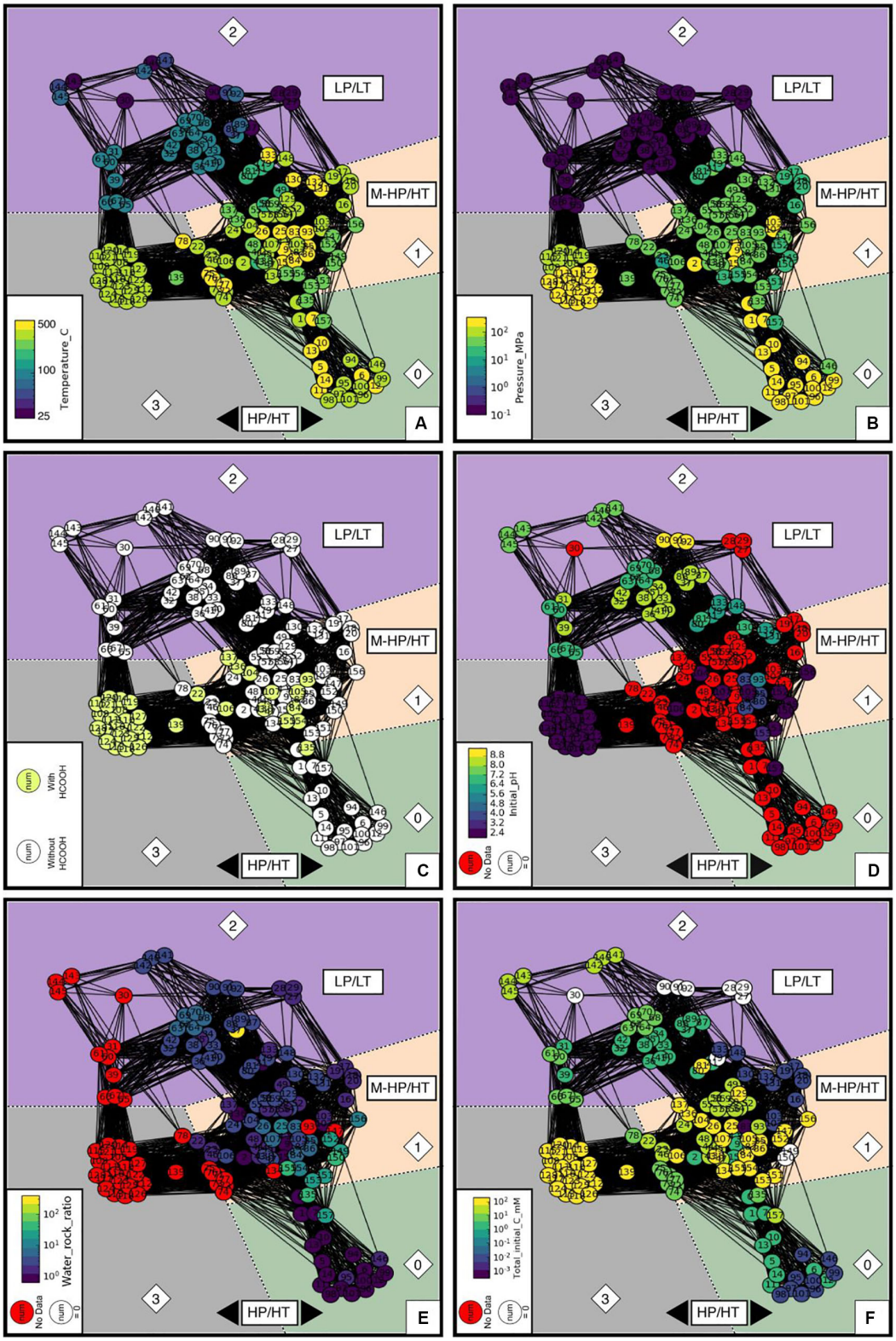

FIGURE 6 | Values of the parameters that dominantly control the distribution of the data in four different communities of experiments: **(A)** temperature in °C; **(B)** pressure in MPa; **(C)** presence or absence of formic acid in the starting aqueous solution, with or without HCOOH; **(D)** pH of the starting aqueous solution (Initial_pH); **(E)** relative amount of water and rock (Water_rock_ratio); and **(F)** the total initial carbon concentration in the starting aqueous solution by adding up all carbon species (Total_initial_carbon_mM). All red filled circles indicate that the value of the parameter is missing in the original article that presents the experiment.

1 and 3 contain the highest number of nodes while community 0 is the smallest one, illustrating the limited number of experiments run at the pressure of hundreds of MPa. Communities 0, 1, and 3 form round layouts, whereas the layout of community 2 is irregular. Considering the layouts are defined by the force directed algorithm, this analysis indicates that the diversity of experimental parameters, notably fluid composition, is generally much larger in LP/LT experiments (community 2) than in others. For example, this is visible when looking at the variety of initial pH values, "other_salts" (e.g., $MgCl_2$, $CaCl_2$), or water-rock ratio tested under ambient pressure and temperature below 100°C (LP/LT).

H_2, CH_4, and Hydrocarbon Production

Figure 7 shows the distribution of the concentrations of gaseous H_2, CH_4, and other organics together with the carbon ratio ("C_ratio") among the four communities. The C_ratio is the ratio between the carbon initially introduced in the system and the final measured one, according to the available information. This cannot take into account the potential carbon contamination of reactants that has never been quantified by the authors of the publications analyzed in the database. The distribution of H_2 concentrations across communities is bimodal, spans eight orders of magnitude, and correlates with temperature (LT versus HT) but not pressure (**Figure 7A**) with the exception of community 3, whose experimental production of H_2 was not reported. CH_4 concentration spans five orders of magnitude and correlates with both T and P (**Figure 7B**); production is lower at LP/LT (community 2) than at HT (communities 1 and 3), and the highest concentrations are clustered in community 0 at HP. Community 0 is also characterized by "C_ratio" values higher than one (**Figure 7D**), which are unrealistic and necessitate that an unidentified source of carbon was present in the system, hence indicating contamination issues with the samples. It may also be responsible for the occurrence of other organic products ("Other_organics"), which systematically occur in community 0 (**Figure 7C**) and are occasionally observed in the others. Therefore, we will not discuss the results of community 0 further.

Figure 8 further illustrates the evolution of H_2 and CH_4 concentration as a function of P and T together with values from ^{13}C-labeled and blank experiments. As our dataset only considers the last sampling point of each experimental set (see section "Data Description"), the experimental duration varies from one data point to another. Hence, we also plot H_2 and CH_4 concentration as a function of duration (**Figure 8C**) to check whether the variability observed at a given P or T does not simply result from experimental duration (reaction kinetics). **Figure 8** confirms the overall trends depicted on **Figure 2** (regular kinetic curves using the non-reduced database) for both H_2 and CH_4 distribution and better highlights the strong variability of concentrations for given P-T conditions. The lack of consistency of the whole database is confirmed by the absence of correlation between gas concentrations and duration when observing all final experimental points from different experiments (**Figures 8C,F**). It is worth noting that blank experiments are frequently reported at LP/LT, while none are available at higher T to establish background levels of H_2 and CH_4 under those conditions. Experiments starting with ^{13}C labeled sources have been used instead to test carbon contamination issue in a limited number of experiments (triangle symbols in **Figure 8**), but background levels of H_2 remain unknown to date.

The evolution of H_2 concentration as a function of P and T (**Figures 8A,B**) also highlights two regimes of reaction, at LP/LT below 100°C in the MPa range, and at MP–HP/HT above 200°C. In the LP/LT regime (community 2), H_2 concentration is low, between 10^{-1} and 10^{-3} mM, and blanks indicate that concentrations below micromolar are not significant. In the MP–HP/HT regime (communities 0, 1, and 3), H_2 concentrations can almost reach molar concentrations. HCOOH-bearing experiments (community 3) always have the highest values reported. This is expected because in these cases H_2 comes from the decomposition of HCOOH that was introduced at high concentration (10–100 mM) in the starting fluid. In the other groups where H_2 results from redox reaction with iron-bearing phases, H_2 concentration is highly variable and no sweet spot for H_2 production could be identified, hence preventing the description of a trend with either T or P (**Figure 7**). This does not correlate with serpentinization kinetics deduced from solid phase transformation (olivine-to-serpentine transformation, Martin and Fyfe, 1970; Malvoisin et al., 2012; McCollom et al., 2016). Indeed, serpentinization kinetics classically display a bell curve with a maximum at ∼250–300°C that is not observed in the current H_2 dataset. H_2 concentrations are neither correlated to duration nor to grain size (**Figure 4**). Available data on initial pH (**Figure 6D**) are too scarce to be conclusive. Rather, **Figure 4** shows that H_2 concentrations display strong positive correlation with "Olivine-" (i.e., olivine-free run) and "Fe_bearing" features, which are highly correlated to each other as well. This suggests that the highest levels of H_2 are reached with a source of Fe (0 or II) other than olivine, i.e., derived from Fe-bearing species such as Fe-bearing salts, oxides, or alloys. Olivine, whose iron content is lower and whose release in the fluid is controlled by dissolution kinetics, appears less efficient at producing H_2 than the other iron-rich compounds. However, this does not explain the variability among serpentinization experiments [i.e., the olivine-bearing experiments ("Olivine" and "Olivine+") that dominate the database (e.g., **Figure 2**)]. It is worth noting that H_2 also positively correlates with the presence of catalysts "Presence_catalyst" (**Figure 4**), whose occurrence is widely distributed among all communities (**Figures 10A–D**) suggesting either a catalytic or a reactive role of these phases on the production of H_2 (see section "Effect of Accessory Solid Phases" for details).

In order to produce abiotic methane, assuming that it forms by an FTT reaction, an oxidized form of carbon is often added to the starting fluid. The CH_4 concentration is then measured (**Figure 2B**) at the end of experiments. The evolution of CH_4 evolution as a function of P and T (**Figures 8D,E**) first shows that CH_4 concentrations are one to two orders of magnitude below those of H_2 (**Figure 9A**). **Figures 9B–D** show that CH_4 concentrations are also well below the concentrations of the oxidized carbon sources deliberately introduced in experiments, except for community 0 which was removed from

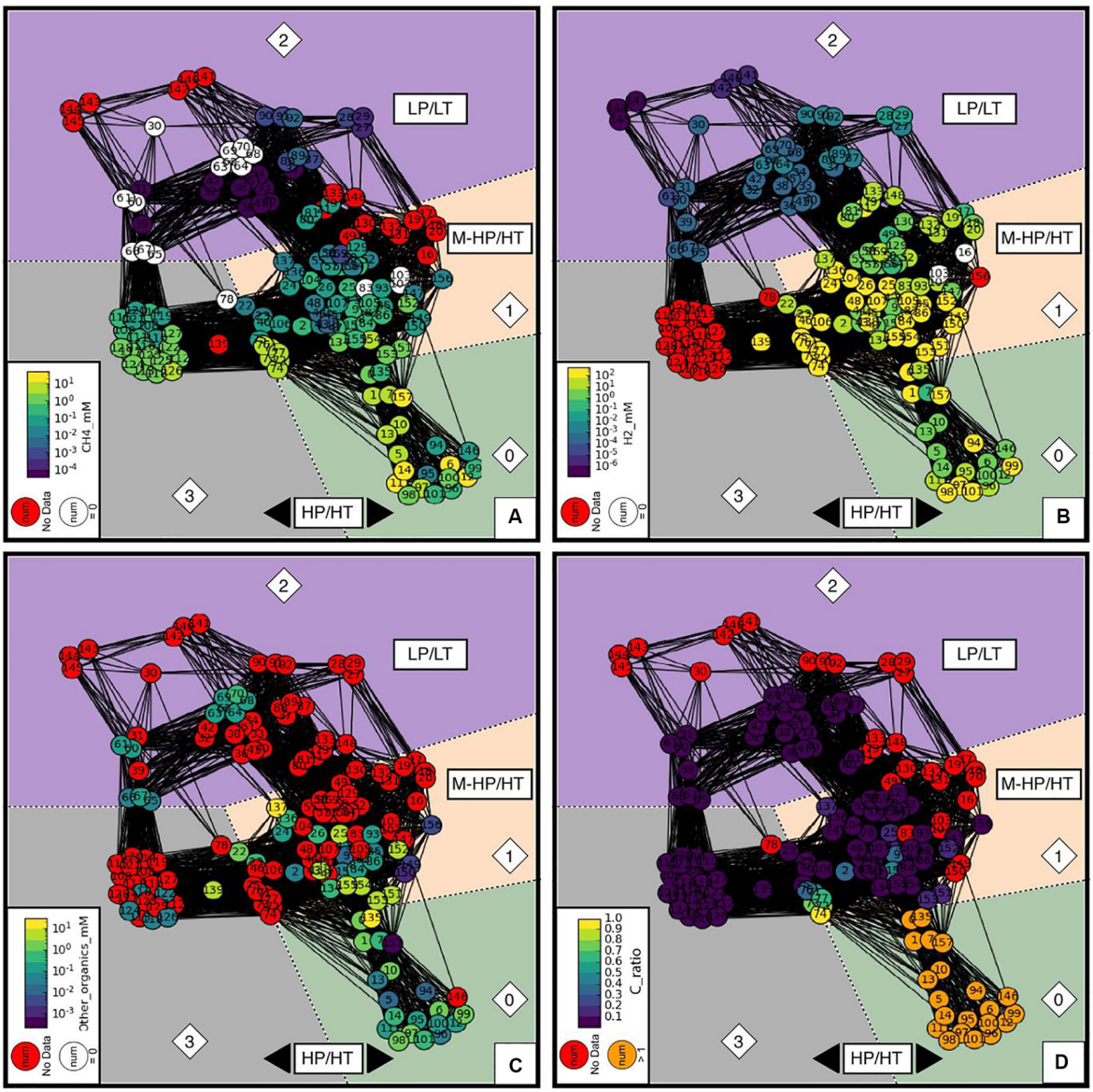

FIGURE 7 | Networks of concentrations of: **(A)** CH_4, **(B)** H_2, and **(C)** other organic species. The heatmap color from cold to warm corresponds to low to high concentrations. Red nodes refer to experiments that did not report relevant concentrations. Experiments labeled in white have concentrations below detection limits, which are set to 0 in the database. **(D)** C_ratio - total final carbon divided by total initial carbon. Theoretically, C_ratio should be between 0 and 1. Dark purple nodes are experiments that did not include or report initial carbon concentrations (set to 0 by convention). Red nodes refer again to final carbon concentrations not reported in the original literature. The orange nodes, mainly in community 0, are experiments reports more final carbon than initial carbon, i.e., C_ratio higher than 1. This suggests that those experiments might have undocumented contamination issues.

discussion because of an unrealistic "C_ratio" (**Figure 7D**). First, this indicates that the low CH_4 concentrations do not result from limited reactant availability for reaction R1. Second, it suggests that CH_4 formation by reduction of oxidized carbon forms, if possible, is not efficient and far from equilibrium. Only LP/LT experiments displaying the lowest values of methane concentration achieve values close to expected CH_4 concentrations (**Figure 9A**). These low methane concentrations, near micromolar level, are still above those of blank experiments run at similar conditions. At high T, ^{13}C-labeled experiments report undetectable to micromolar levels of $^{13}CH_4$, whether catalysts are present or not (see section "Effect of Accessory Solid Phases"). These concentrations are well below the CH_4 concentration measured in all other experiments (**Figures 8D–F**, **9B–D**). Assuming that the use of a heavy carbon source in ^{13}C-labeled experiments does not have a kinetic effect on carbon reduction reactions, these results indicate that abiotic CH_4 has never been formed at a significant level during serpentinization experiments. As such a strong statement rules out most of—if not all of—the available literature we further investigated the present

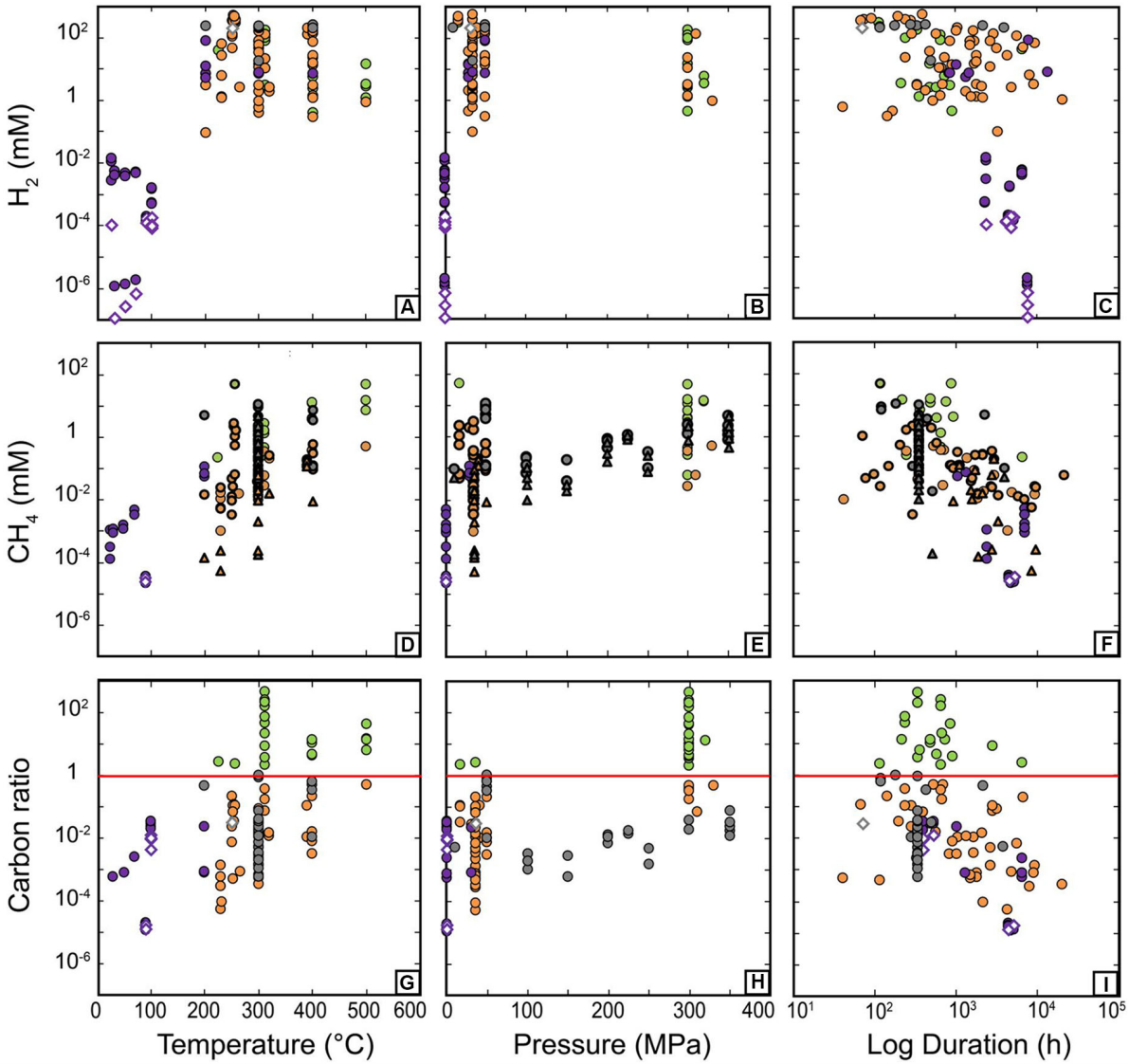

FIGURE 8 | Concentrations of H_2 **(A–C)**, CH_4 **(D–F)**, and carbon conversion **(G–I)** displayed as a function of temperature **(A,D,G)**, pressure **(B,E,H)**, and experiment duration **(C,F,I)**. Diamond symbols correspond to "blank experiments" run without minerals in the experimental load. Thick triangle symbols in **(D–F)** highlight $^{13}CH_4$ concentration while thick circles show the corresponding total CH_4 also including $^{12}CH_4$. In **(G,H)**, the red line corresponds to a carbon ratio value of 1, beyond which is suspected to be contaminated. Color coding consistent with **Figure 5**.

database to discuss this hypothesis (see section "Contamination Issues") and investigated the consistency of the available data for actual CH_4 production by an FFT process.

The dataset shows that CH_4 concentrations display a logarithmic increase with T between ambient T and 500°C (**Figure 8D**) and they do not show any dependence on pressure above 30 MPa. The increase of CH_4 concentration with T is also well highlighted by the ^{13}C-labeled experiments, despite much lower $^{13}CH_4$ concentrations. The strong variability of CH_4 concentrations among experiments from the largest community (community 1) precludes any further correlation between CH_4 and pressure. **Figure 8F** highlights that duration does not account for the variability of CH_4 concentrations in experiments at given P-T conditions. The same holds for "grain_size," which is uncorrelated with CH_4 concentrations (**Figure 4**).

McCollom et al. (2010) suggested that the nature of initial carbon source may affect the system reactivity, and they showed that dissolved CO and HCOOH carbon sources are more effective at abiotic organic synthesis than CO_2. We test this hypothesis by comparing the CH_4 concentrations reached for the different types of carbon source ((bi-)carbonate salts, HCOOH, or CO_2) (**Figures 9B–D**). This selection of carbon sources is not the choice of the authors, it simply reflects the C-sources reported in the publications. HCOOH-bearing experiments (mainly community 3—all run at similar T conditions), in which high amounts of HCOOH have been added (10–100 mM), produced the highest

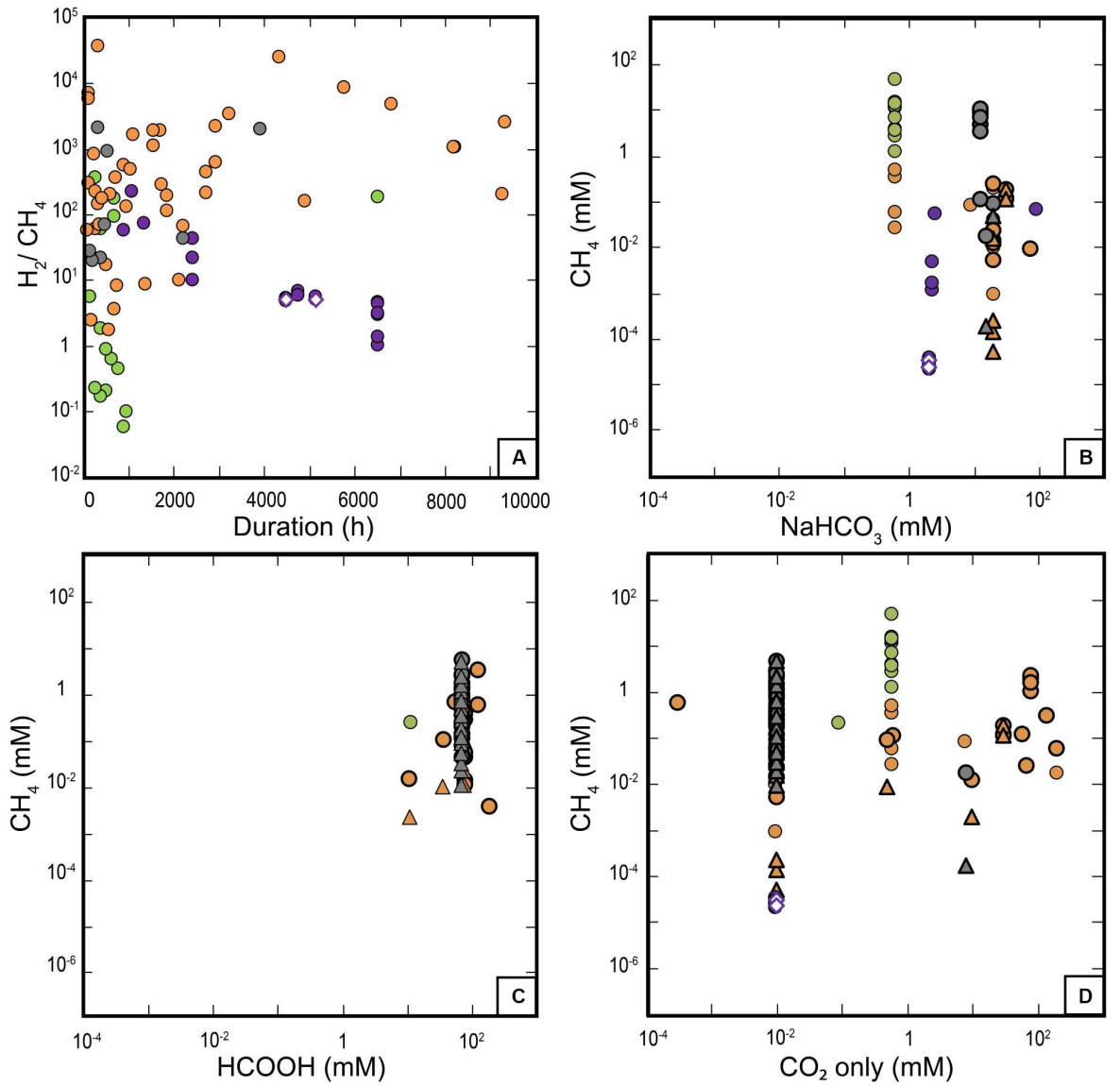

FIGURE 9 | (A) H_2/CH_4 ratio as a function of time. CH_4 concentration as a function of the initial carbon sources in experiments (bi-)carbonate salts **(B)**, HCOOH **(C)**, and CO_2 **(D)**. Thick triangles and circles correspond to labeled $^{13}CH_4$ and total methane, respectively. Color coding consistent with **Figure 5**.

CH_4 concentrations (∼10 mM) at HP (**Figures 8D,E**, **9C**), excluding data from community 0 because of contamination issues. Such experiments, in which olivine is mostly absent and HCOOH decomposes to H_2, CO_2 (±CO) at HT, are reported here for comparison but are not representative of the actual serpentinization process investigated so far in experiments. Experiments of community 2 at LP/LT have only used $NaHCO_3$ at one concentration and show variable CH_4 production. It appears that the most comprehensive dataset for this discussion is provided by the experiments in community 1 at MP–HP/HT. In community 1, CH_4 concentrations display an overall correlation with CO_2 content, which is also evidenced in ^{13}C-labeled experiments for lower CH_4 concentrations. Such a correlation is not observed with initial $NaHCO_3$ concentrations whose variation range is too limited. This precludes the comparison between the reactivity of carbonate/bicarbonate ions versus CO_2.

The above observations show that despite considerable efforts, the available experimental dataset remains incomplete and limits the analysis. Nevertheless, results deeply question the potential of these carbon sources to efficiently react with the H_2 derived from serpentinization, and suggest a strong inhibition of R1 under those conditions, even with high reactant concentrations. In addition, the increase of CH_4 as a function of T (**Figure 8D**) does not follow thermodynamic predictions and rather indicates a kinetic or a thermal control of experimental CH_4 production, whatever the reaction is. The only plausible trajectory toward equilibrium is observed for LP/LT experiments (community 2, **Figure 9A**) and may be related to the presence of a gaseous

phase in most of these experiments run into incubation flasks, i.e., in conditions closer to those ideal for reactions R1 and R2. The potential importance of a gaseous phase that could be mandatory for CH_4 production was already raised by some authors and deserves further investigation (Etiope et al., 2011; McCollom, 2013).

Data on the production of organic products other than methane are very sparse and were combined in the dataset into a feature called "Other_organics" (**Figure 7C**) that dominantly includes small organic molecules (<0.1 mM) measured in either the liquid phase at LP/LT (organic acids, community 2) or the gas phase at MP/HT (HCs, communities 1 and 3). These sparse data do not show any obvious correlation with CH_4, as possibly expected from reaction R2 (**Figures 4**, **7C**). **Figure 4** rather points to a positive correlation between "Other_organics" and "Total_inital_C" that is potentially true for the whole P-T range since "Other_organics" (mainly in the form of organic acids) were also detected at LP/LT conditions in the aqueous phase while CH_4 was not.

Effect of Accessory Solid Phases

Metal-bearing catalysts are critical to the industrial production of H_2 or CH_4 in gaseous phase. Notably they are critical for (R1) and (R2) to overcome the first step of CO_2 reduction to CO by the water-gas shift reaction. The lack of data on CO occurrence and concentration in hydrothermal experiments focusing on serpentinization does not allow either decomposing reaction mechanisms or discussing the potential role of CO as an intermediate phase, which has been examined by a previous experimental study (Seewald et al., 2006). In addition, under aqueous conditions, the catalytic phases can be more reactive and propitious to alteration and consequently act either as real catalysts (do not react but accelerate the reaction) or as reactants whose transformation directly produces H_2 (e.g., alloy) or facilitates olivine dissolution, such as aluminum (Andreani et al., 2013). Addition of any material in a reactor also induces potential introduction of carbon contamination that could contribute to gas production.

To distinguish the role of potential catalysts, an in-depth characterization of the solid surfaces before and after experiment is mandatory. Unfortunately, this step has not been done in the large majority of experiments, hence preventing any inference. This also precludes the potential identification of precipitated carbonaceous phases among solids (Milesi et al., 2015; Andreani and Ménez, 2019). Here we take advantage of the dataset to discuss potential correlation between the concentration of reaction products such as H_2, CH_4, or the other organics, and the presence or absence of potential catalysts in experiments for guiding future studies. The list of potential catalysts includes those introduced in the experiments as solids, natural or synthetic, such as Cr-spinel, magnetite, chromite, Ni- or Fe-bearing minerals or alloys. It also includes those produced by the serpentinization reaction such as magnetite or spinel, that have a recognized significant effect on the reaction. For example, spinel has been shown to improve H_2 production at LP/LT (Mayhew et al., 2013). We also do not underestimate the potential catalytic role of the constitutive materials of the reactor vessels commonly made of Au, Ti of Hastelloy^{TM} (a Ni/Fe-bearing alloy), whose catalytic properties have been demonstrated for some other reactions notably in aqueous systems, for example, CO_2 reduction to CO (Chen et al., 2012), reforming reactions (Van Haasterecht et al., 2014), H_2 production (Michiels et al., 2018; Fowler et al., 2019), and HCOOH dehydrogenation (Brunet and Lanson, 2019). Despite such evidence, especially for Au and Ti which are the most used for studying serpentinization reactions, reactor vessels are classically considered as inert for geochemical experiments dedicated at understanding the potential of serpentinization to produce abiotic H_2, CH_4, and light HC.

In the previous section, we highlighted the positive correlations between H_2 and the presence of potential metal catalysts ("Presence_catalysts"). A more detailed examination of **Figure 4** shows a positive correlation between H_2 production and the following catalysts, in decreasing order: "Fe-bearing" > "Titanium" > "Au" ∼ "Ni-bearing" > "magnetite." "Chromite" and "Hastelloy" have no correlation and "Spinel" a potentially negative one with H_2. The case of titanium reactors is well known as Ti-reactors have to be pre-oxidized prior to hydrothermal experiments in order to avoid H_2 production from Ti oxidation (Seewald et al., 2006) and we reasonably assume that this step was run before experiments. Hastelloy, gold, or Ti do not have any recognized catalytic properties for H_2 production or CH_4 formation, and the strong correlation between H_2 concentrations and gold or titanium could also well be due to the fact that H_2 production is intrinsically more efficient at MP-HP/HT in hydrothermal reactors that are systematically made of gold and titanium. Hence, it is not yet possible to disentangle between P-T and catalytic effects here. **Figure 10** shows the concentrations of H_2 as a function of experimental duration for experiments run with the catalysts usually considered as the most optimal, i.e., omitting reactor metals and spinel, the latter displaying a slight negative correlation with H_2. **Figure 10** fits well with the ordering of potential catalysts previously identified on **Figure 4** ("Fe-bearing" > "Ni-bearing" > "magnetite"). Irrespective of the run duration or the community, the addition of "Fe-bearing" phases that encompass both Fe(II) and Fe(III) compounds appears to be the most efficient and leads to the highest production of H_2 (**Figure 10A**). A strong contribution of Fe(II) oxidation is expected in most cases but there may be underappreciated effects of Fe(III)-bearing phases yet to be explored in future works. H_2 synthesis is also clearly enhanced by the presence of Ni-bearing phases at MP/HT conditions (community 1) while magnetite seems to be efficient for both LP/LT (community 2) and MP/HT conditions (community 1). As for "Fe-bearing" phases, oxidation of Fe(II) in magnetite and of Ni or reduced sulfur in Ni-bearing phases such as alloys or sulfides may intrinsically produce more H_2 without a true catalytic effect occurring. Indeed, moderate amounts of Ni metal particles have recently been identified as catalysts of FeO oxidation under hydrothermal conditions (Michiels et al., 2018) and this effect may be extrapolated to Fe-bearing minerals such as olivine (Brunet, 2019). Conversely, H_2 concentrations in spinel-bearing experiments cover the whole range of concentrations despite run duration or P-T conditions

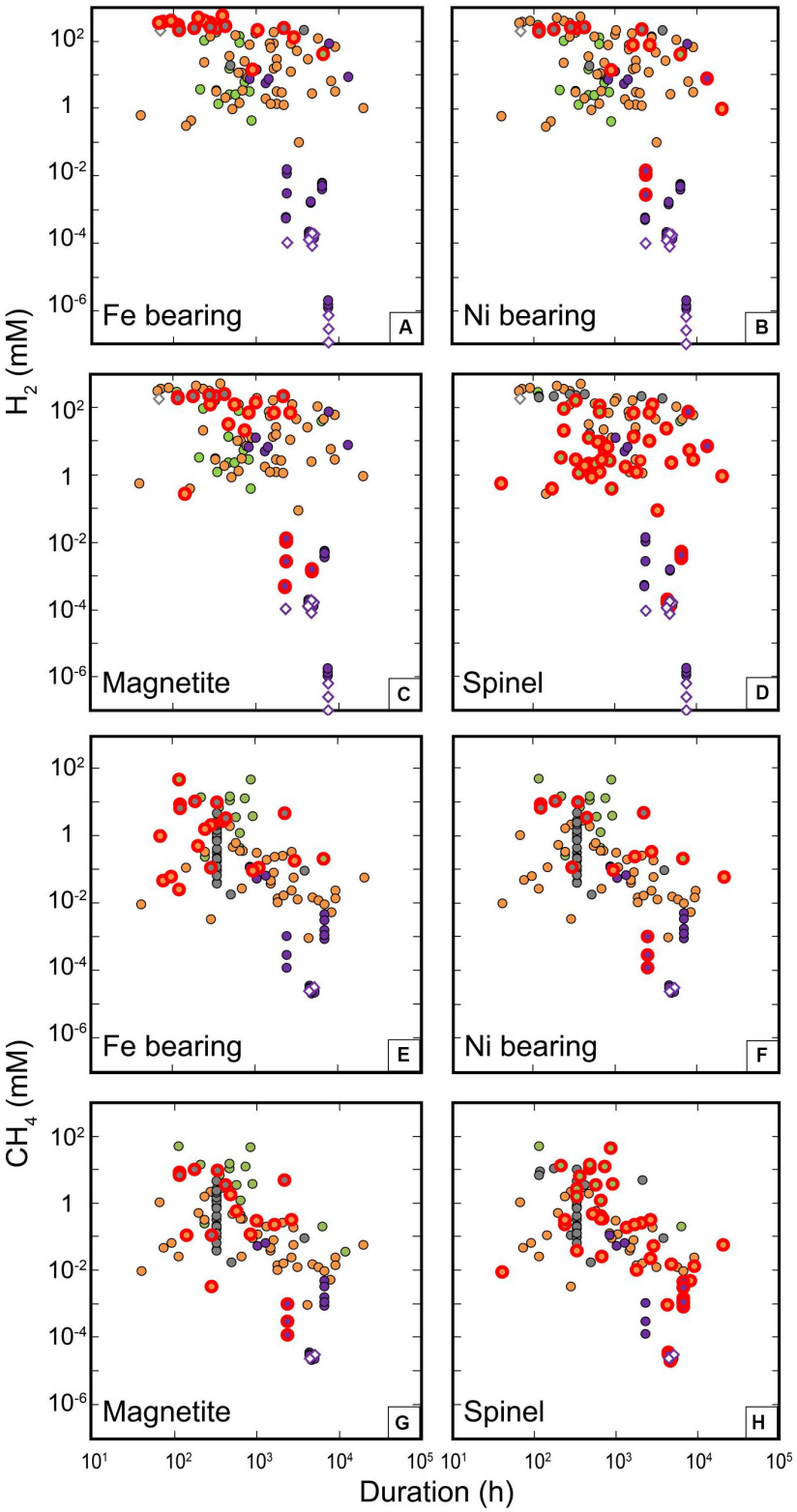

FIGURE 10 | Potential catalytic effects on the formation of H_2 and CH_4. Concentrations of H_2 **(A–D)** and CH_4 **(E–H)** are plotted against run durations. Diamond symbols correspond to experiments without initial mineral phases, and red thick circles highlight the experiments with relevant catalyst reactants. **(A)** "Fe-bearing" ones include metallic iron, hematite, Ni-Fe alloys, FeS, FeO except magnetite; **(B)** "Ni-bearing" ones include NiS, Ni-Fe alloys; **(C)** "Magnetite" corresponds to experiments with magnetite; **(D)** "Spinel" corresponds to experiments with spinel or spinel-bearing peridotite. Color coding consistent with **Figure 5**.

(all communities) and always lie below the maximum values observed, which explains the negative correlation observed in **Figure 4**. Hence, spinel does not appear as a good candidate for catalyzing H_2 production under those conditions. The effect on H_2 production of those different phases often introduced in experiments contributes to the variability of concentrations observed for similar thermodynamic conditions, whatever the mechanisms behind.

The correlation between the presence of potential catalysts "Presence_catalysts" and CH_4 concentration is much lower than for H_2, and simply zero with "other organics" (**Figure 4**). Potential effects of the different catalyst candidates appear in the following decreasing order for CH_4: "Fe-bearing" > "Au" > "Ni-bearing" ∼ "Magnetite" ∼ "spinel," while "Ti," "Hastelloy," or "Chromite" have no correlation with CH_4 concentration (**Figure 4**). As for H_2, we will not consider metals constitutive of reactors any further and rather focus on the effects of "Fe-bearing," "Ni-bearing," "Magnetite," and "Spinel" (**Figure 10**). Spinel correlates more positively with the "Carbon _ratio" (**Figure 4**) than with CH_4 and is not explained by any correlations with "Other_organics" or "Total_final_carbon." This is probably due to the fact that the highest values of "Carbon_ratio" are obtained in the experiments of community 0. These experiments were run with spinel-bearing peridotites as reactants and produced such a large amount of methane at HT that they reached an unrealistic carbon ratio beyond 1, indicative of contamination as aforementioned. Contrary to H_2 catalysis, the weak correlations noticed in **Figure 4** are hardly visible in **Figure 10** for CH_4 that does seem affected by any of the selected potential catalytic phases, whatever the community. This questions some previous results that have highlighted the potential role of similar catalysts to explain the high CH_4 concentration obtained in their experiments. Our analysis of the dataset compiled from the literature is again in better agreement with the results of ^{13}C-labeled experiments that did not detect any significant $^{13}CH_4$ production despite the presence of potential catalytic phases (McCollom et al., 2010; Grozeva et al., 2017).

Contamination Issues

The previous sections have shown that H_2 is systematically and significantly formed in experiments, indicating that its production during serpentinization is well established. This is apparent even at LP/LT, despite the general lack of blank experiments required to estimate background levels at these conditions. Catalytic effects and reactive Fe-bearing phases other than olivine contribute to the observed variability of H_2 concentrations for given P-T conditions.

This is much more different for CH_4 and HC production. In line with the results of the ^{13}C-labeled and blank experiments, this in-depth analysis of the experimental dataset reinforces the hypothesis that CH_4 and other organic products in serpentinization experiments are either not produced by FTT reactions, or are produced only at very low levels, much lower than those reported in virtually all experiments (**Figures 8**, **9**). The amount of CH_4 possibly produced by R1 seems to be sensitive to the initial CO_2 content (**Figure 9D**), but uncorrelated to the production of other organic products. In addition, no obvious catalytic effects have been identified (**Figure 10**), confirming that FTT reactions are not efficient under aqueous conditions with the catalysts tested so far, which are abundant in natural systems. These observations call for potential contamination issues in most CH_4-bearing experiments. Various organic contaminants can indeed be brought to the system via reactants, carried by minerals surfaces (Tingle et al., 1990), organic particles among solid reactants (e.g., pollen: Berndt et al., 1996), fluid inclusions, or derived from chemicals with complex manufacturing process (e.g., purification and storage of lab salts). It results in an underappreciated amount and variety of additional organic compounds in the reactive system. Since the carbon-load of each ingredient used in experiments described in the literature has never really been characterized, it is unfortunately difficult to propose specific reactions. Moreover, such minute amounts of organics can decompose with T or evolve toward more reduced compounds, producing an even larger variety of compounds, potentially including CH_4 and HC. This could fit with the sensitivity of CH_4 concentration to T. The positive correlation of "Other_Organics" with the "Initial_C_content" that is dominantly brought by chemicals, also suggests that salts can be an important source of contamination. This contamination source should be characterized when running future experiments, especially at MP-HP/HT where blanks are systematically missing.

These contamination issues also highlight the need to investigate both the aqueous and gaseous phases when investigating understanding carbon processes under hydrothermal conditions. This is to better characterize organic contaminants and possibly identify unexpected products other than CH_4 and HC that do not efficiently form during serpentinization. Such data are very limited to date and virtually missing at MP–HP/HT for which liquid sampling and analysis is more challenging. Similarly, the content and forms of carbon in solid products have never been reported in the literature while the limited formation of CH_4 suggests other reaction path, possibly involving minerals, new C-bearing reactants, and metastable organic products, whether soluble or not (Andreani and Ménez, 2019).

CONCLUSION

We built a comprehensive dataset on H_2, CH_4, and HC concentrations measured during abiotic experimental serpentinization as they are reported in the available literature, without any *a priori* on whether or not those gases are actually produced by the reaction or (partly) result from an interfering process such as contamination. We reduced the dimensionality of the dataset compiling some features who are too sparse in larger ones to obtain representable parameters. We notably had to select the final points only in multi-sampling experiments, to prevent overweighting them. We then performed analysis and visualization using statistical methods and unsupervised clustering network analysis. This approach allowed us to discuss the role of numerous parameters on the observed highly variable concentrations of H_2 and CH_4. The Pearson correlation

covariance indicated pairwise correlations among all parameters, and network analysis helped classify experiments into four main communities that correspond to (1) the P-T conditions of experiments and (2) experimental practices. These communities offer an overview of the conditions tested so far for serpentinization experiments and enable us to identify the data that can be reasonably compared to each other. Two communities correspond to serpentinization reaction at LP/LT (community 2) and MP-HP/HT (community 1), while one community corresponds to HCOOH-bearing experiments (community 3) in which no solid is involved, and a last one (community 0) is characterized by an unreasonable final carbon content exceeding the one initially introduced, clearly indicating contamination.

Two main regimes of H_2, CH_4, and HC production are distinguished, leading to low concentrations at LP/LT and high concentrations at MP-HP/HT, as depicted by the comparison to regular kinetic curves. However, neither P-T conditions nor grain size explains the remaining variability of H_2, CH_4, or HC concentrations that span eight, five, and four orders of magnitude, respectively. These H_2 variations could be explained by the sensitivity of H_2 production to accessory phases classically introduced in experiments for their potential catalytic effects on CO_2 reduction. The most efficient phases are Fe- and Ni-bearing phases that can enhance H_2 production via either catalytic or reactive effect (metal oxidation), both of which have yet to be assessed by an in-depth characterization of solids phases in such experiments. CH_4 concentration are always one to two orders of magnitude lower than those of H_2 and of oxidized carbon sources, therefore indicating inefficient reduction reactions which are not limited by reactants. The only clear trend is the increase of CH_4 as a log function of T, which is opposite to predictions made by thermodynamic models (Shock, 1992) and rather suggests a kinetic control, whatever the reaction is: carbon reduction reaction or thermal degradation/evolution of organic contaminants. Dataset analysis also shows that among the reactants of the classical FTT reaction, i.e., H_2 and inorganic carbon sources [CO_2 or (bi-)carbonates ions], CO_2 is slightly correlated to CH_4 concentration but represent very low conversion yield (<1%), and no correlation is observed between CH_4 and HC concentrations. No potential catalyst could be identified for CH_4 formation under hydrothermal conditions for all conditions tested so far, in agreement with the limited number of ^{13}C-labeled experiments. Only LP/LT experiments tend to a H_2/CH_4 ratio close to equilibrium for an FTT reaction, indicating that experiments run at higher P-T conditions (P > ambient P or Psat; T > 100°C) were far from equilibrium or unrelated to FTT reactions. In addition to an unquantified contamination from solids (on surfaces or in inclusions), dataset analysis suggests a contamination contribution of C-bearing salts to CH_4 and HC production in most experiments.

This study shows that the available dataset on H_2 and CH_4 production during serpentinization is incomplete and not internally consistent despite a general increase with P and T. The lack of blank experiments at HT precludes the evaluation background levels of H_2, while available ^{13}C-labeled experiments rule out most available results from the dataset at HT conditions (200–500°C). Our analysis of the data agrees with the latter hypothesis and suggests that the strong variability of H_2 and CH_4 could result from the effect of accessory phases for H_2 production, and from the unquantified effect of different sources of contaminants whose decomposition or evolution with increasing reducing conditions is most sensitive to T and produces CH_4 and HC at higher T. Recent hypotheses propose on a deep source of methane formed by CO_2 reduction in fluid inclusions over millions of years (McDermott et al., 2015; Grozeva et al., 2020), overriding kinetic barriers. Whether ophiolitic settings have the current capacity for releasing such a deep CH_4 reservoir remains an open question and the experimental dataset at LP/LT is still too limited to conclude on the efficiency of olivine alteration. In any case, abiotic reactions other than FTT ones certainly exploit the reduction potential of the current serpentinization in natural systems under shorter time scale and they remain to be identified. Future experimental work should consider this possibility while systematically exploring the organic content in liquids and solids, the reactivity and surfaces of accessory phases, and the variability of the isotopic signal of biotic and abiotic methane.

DATA AVAILABILITY STATEMENT

All datasets and scripts generated and used in this study are available at: https://github.com/bronzitte/Network_analysis_abiotic_methane.git.

AUTHOR CONTRIBUTIONS

SB, FH, MA, PF, and ID contributed to conception and design of the study. SB, MA, RT, JH, and ID collected the data. FH, AE, AP, OM, and PF cleaned data and performed the analysis. SB, FH, MA, and ID wrote the manuscript with inputs from all authors.

FUNDING

This research was supported by the AP Sloan Foundation through the Deep Carbon Observatory's Deep Energy Community and Data Science team (partly award G-2018-11204). SB also thanks TOTAL EP R&D Project MAFOOT for financial support. It is partially funded by the French National Research Agency through the PREBIOM project #ANR-15-CE31-0010.

ACKNOWLEDGMENTS

We are grateful to the authors of the 30 publications used for this analysis. We are indebted to Andrew Merdith for improving the English writing of this contribution. We also want to thank the two reviewers for their fruitful comments that considerably improved the manuscript.

SUPPLEMENTARY MATERIAL

The Supplementary Material for this article can be found online at: https://www.frontiersin.org/articles/10.3389/feart.2020.00209/full#supplementary-material

FIGURE S1 | (A) Temperature and pressure distribution of serpentinization experiments reported in literature. Diamonds and filled circles represent mineral free and bearing experiments, respectively. Individual networks representation of temperature **(B)** and pressure **(C)** of experiments. The heatmap color from cold to warm illustrates low to high values. Four communities of experiments explained **Figure 5** captions.

FIGURE S2 | Sensitivity test results on the cosine similarity threshold. The number of communities detected by Louvain algorithm is shown in the figure after removing the weakest 10, 30, 50, and 70 % of the edge connections. Results show that the number of communities detected is always four, and communities 0, 1, and 3 almost stayed the same. The algorithm is pretty robust. Therefore, we did the analysis by removing 70% of the weakest edges.

FIGURE S3 | (A) Full networks representation of experiments with or without solid reactants—white means with solids and yellow means fluid only. Experiments with or without a specific solid reactant—white means without and yellow means with: **(B)** sodium bicarbonate; **(C)** NaCl; **(D)** other salts, including KCl, $CaCl_2$, $MgCl_2$, NH_4Cl, K_2HPO_4, KNO_3, $Ca(OH)_2$, $CaSO_4.H_2O$, $Mg(SO_4)_2 \cdot 7H_2O$.

FIGURE S4 | In addition to **Figure 7**, it shows the distribution of the concentration of **(A)** H_2, **(B)** CH_4, **(C)** total other organics in mM, and **(D)** carbon ratio, across the experiments represented in individual community networks. Color coding consistent with **Figure 7**.

REFERENCES

Abraham, A., Hassanien, A.-E., and Snasel, V. (2010). *Computational Social Network Analysis: Trends, Tools and Research Advances (Computer Communications and Networks)*. Berlin: Springer Science & Business Media.

Allen, D. E., and Seyfried, W. E. (2003). Compositional controls on vent fluids from ultramafic-hosted hydrothermal systems at mid-ocean ridges: an experimental study at 4 00°C, 500 bars. *Geochim. Cosmochim. Acta* 67, 1531–1542. doi: 10.1016/S0016-7037(02)01173-0

Amitai, G., Shemesh, A., Sitbon, E., Shklar, M., Netanely, D., Venger, I., et al. (2004). Network analysis of protein structures identifies functional residues. *J. Mol. Biol.* 344, 1135–1146. doi: 10.1016/j.jmb.2004.10.055

Andreani, M., Daniel, I., and Pollet-Villard, M. (2013). Aluminum speeds up the hydrothermal alteration of olivine. *Am. Mineral.* 98, 1738–1744. doi: 10.2138/am.2013.4469

Andreani, M., and Ménez, B. (2019). "New perspectives on abiotic organic synthesis and processing during hydrothermal alteration of the oceanic lithosphere," in *Deep Carbon*, eds B. Orcutt, I. Daniel, and R. Dasgupta, (Cambridge: Cambridge University Press), 447–479. doi: 10.1017/9781108677950.015

Banda-R, K., Delgado-Salinas, A., Dexter, K. G., Linares-Palomino, R., Oliveira-Filho, A., Prado, D. E., et al. (2016). Plant diversity patterns in neotropical dry forests and their conservation implications. *Science* 353, 1383–1387.

Berndt, M. E., Allen, D. E., and Seyfried, W. E. (1996). Reduction of CO2 during serpentinization of olivine at 300°C and 500 bar. *Geology* 24, 351–354. doi: 10.1130/0091-76131996024

Blondel, V. D., Guillaume, J. L., Lambiotte, R., and Lefebvre, E. (2008). Fast unfolding of communities in large networks. *J. Stat. Mech. Theory Exp.* 2008:10008. doi: 10.1088/1742-5468/2008/10/P10008

Brazil, R. (2017). Hydrothermal vents and the oriqins of life. *Chem. World* 14, 48–53.

Brunet, F. (2019). Hydrothermal production of H2 and magnetite from steel slags: a geo-inspired approach based on olivine serpentinization. *Front. Earth Sci.* 7:17. doi: 10.3389/feart.2019.00017

Brunet, F., and Lanson, M. (2019). Effect of gold and magnetite on the decomposition kinetics of formic acid at 200° C under hydrothermal conditions. *Chem. Geol.* 507, 1–8.

Charlou, J. L., Donval, J. P., Fouquet, Y., Jean-Baptiste, P., and Holm, N. (2002). Geochemistry of high H2 and CH4 vent fluids issuing from ultramafic rocks at the Rainbow hydrothermal field (36°14'N,MAR). *Chem. Geol.* 191, 345–359. doi: 10.1016/S0009-2541(02)00134-1

Chavagnac, V., Monnin, C., Ceuleneer, G., Boulart, C., and Hoareau, G. (2013). Characterization of hyperalkaline fluids produced by low-temperature serpentinization of mantle peridotites in the Oman and Ligurian ophiolites. *Geochem. Geophys. Geosyst.* 14, 2496–2522. doi: 10.1002/ggge.20147

Chen, Y., Li, C. W., and Kanan, M. W. (2012). Aqueous CO2 reduction at very low overpotential on oxide-derived Au nanoparticles. *J. Am. Chem. Soc.* 134, 19969–19972.

Dong, W., and Pentland, A. (2009). "A network analysis of road traffic with vehicle tracking data," in *AAAI Spring Symposium – Technical Report*, (Menlo Park, CA: Association for the Advancement of Artificial Intelligence), 7–12.

Dufaud, F., Martinez, I., and Shilobreeva, S. (2009). Experimental study of Mg-rich silicates carbonation at 400 and 500 °C and 1 kbar. *Chem. Geol.* 265, 79–87. doi: 10.1016/j.chemgeo.2009.01.026

Ehlmann, B. L., Mustard, J. F., and Murchie, S. L. (2010). Geologic setting of serpentine deposits on Mars. *Geophys. Res. Lett.* 37:L06201. doi: 10.1029/2010gl042596

Eslick, V. G. (2012). *Book Review: Understanding Social Networks: Theories, Concepts, and Findings*. Oxford: Oxford University Press, doi: 10.1177/136078041201700402

Etiope, G., Ifandi, E., Nazzari, M., Procesi, M., Tsikouras, B., Ventura, G., et al. (2018). Widespread abiotic methane in chromitites. *Sci. Rep.* 8:8728. doi: 10.1038/s41598-018-27082-0

Etiope, G., Schoell, M., and Hosgörmez, H. (2011). Abiotic methane flux from the Chimaera seep and Tekirova ophiolites (Turkey): understanding gas exhalation from low temperature serpentinization and implications for Mars. *Earth Planet. Sci. Lett.* 310, 96–104. doi: 10.1016/j.epsl.2011.08.001

Etiope, G., and Sherwood Lollar, B. (2013). Abiotic methane on earth. *Rev. Geophys.* 51, 276–299. doi: 10.1002/rog.20011

Fouquet, Y., Cambon, P., Etoubleau, J., Charlou, J. L., Ondréas, H., Barriga, F. J. A. S., et al. (2013). Geodiversity of hydrothermal processes along the mid-atlantic ridge and ultramafic-hosted mineralization: a new type of oceanic Cu-Zn-Co-Au volcanogenic massive sulfide deposit. *Geophys. Monogr. Ser.* 188, 321–367. doi: 10.1029/2008GM000746

Foustoukos, D. I., and Seyfried, W. E. (2004). Hydrocarbons in hydrothermal vent fluids: the role of chromium-bearing catalysts. *Science* 304, 1002–1005. doi: 10.1126/science.1096033

Fowler, A. P. G., Scheuermann, P., Tan, C., and Seyfried, W. Jr. (2019). Titanium reactors for redox-sensitive hydrothermal experiments: an assessment of dissolved salt on H2 activity-concentration relations. *Chem. Geol.* 515, 87–93.

Fruchterman, T. M. J., and Reingold, E. M. (1991). Graph drawing by force−directed placement. *Softw. Pract. Exp.* 21, 1129–1164. doi: 10.1002/spe.4380211102

Fu, Q., Foustoukos, D. I., and Seyfried, W. E. (2008). Mineral catalyzed organic synthesis in hydrothermal systems: an experimental study using time-of-flight secondary ion mass spectrometry. *Geophys. Res. Lett.* 35:L033389. doi: 10.1029/2008GL033389

Fu, Q., Sherwood Lollar, B., Horita, J., Lacrampe-Couloume, G., and Seyfried, W. E. (2007). Abiotic formation of hydrocarbons under hydrothermal conditions: constraints from chemical and isotope data. *Geochim. Cosmochim. Acta* 71, 1982–1998. doi: 10.1016/j.gca.2007.01.022

Geem, Z. W. (2006). Optimal cost design of water distribution networks using harmony search. *Eng. Optim.* 38, 259–280. doi: 10.1080/03052150500467430

Glein, C. R., Baross, J. A., and Waite, J. H. Jr. (2015). The pH of Enceladus' ocean. *Geochim. Cosmochim. Acta* 162, 202–219.

Grozeva, N. G., Klein, F., Seewald, J. S., and Sylva, S. P. (2017). Experimental study of carbonate formation in oceanic peridotite. *Geochim. Cosmochim. Acta* 199, 264–286. doi: 10.1016/j.gca.2016.10.052

Grozeva, N. G., Klein, F., Seewald, J. S., and Sylva, S. P. (2020). Chemical and isotopic analyses of hydrocarbon-bearing fluid inclusions in olivine-rich rocks. *Philos. Trans. A Math. Phys. Eng. Sci.* 378:20180431. doi: 10.1098/rsta.2018.0431

Hagberg, A. A., Schult, D. A., and Swart, P. J. (2008). *Exploring Network Structure, Dynamics, and Function using NetworkX*. Los Alamos, NM: Los Alamos National Lab (LANL).

Hansen, D. L., and Smith, M. A. (2014). *Social Network Analysis in HCI*. Hoboken, NJ: John Wiley & Sons, doi: 10.1007/978-1-4939-0378-8_17

Harel, A., Karkar, S., Cheng, S., Falkowski, P. G., and Bhattacharya, D. (2015). Deciphering primordial cyanobacterial genome functions from protein network analysis. *Curr. Biol.* 25, 628–634. doi: 10.1016/j.cub.2014.12.061

Hellevang, H., Huang, S., and Thorseth, I. H. (2011). The potential for low-temperature abiotic hydrogen generation and a hydrogen-driven deep biosphere. *Astrobiology* 11, 711–724. doi: 10.1089/ast.2010.0559

Holm, N. G., Oze, C., Mousis, O., Waite, J. H., and Guilbert-Lepoutre, A. (2015). Serpentinization and the formation of H2 and CH4 on celestial bodies (Planets, Moons, Comets). *Astrobiology* 15, 587–600. doi: 10.1089/ast.2014.1188

Horita, J., and Berndt, M. E. (1999). Abiogenic methane formation and isotopic fractionation under hydrothermal conditions. *Science* 285, 1055–1057. doi: 10.1126/science.285.5430.1055

Huang, R., Sun, W., Liu, J., Ding, X., Peng, S., and Zhan, W. (2016). The H2/CH4 ratio during serpentinization cannot reliably identify biological signatures. *Sci. Rep.* 6:33821. doi: 10.1038/srep33821

Huang, R. F., Sun, W. D., Ding, X., Liu, J. Z., and Peng, S. B. (2015). Olivine versus peridotite during serpentinization: gas formation. *Sci. China Earth Sci.* 58, 2165–2174. doi: 10.1007/s11430-015-5222-3

Janbandhu, M. R., and Karhade, M. (2015). Introduction to information retrieval systems. *Int. J. Recent Innov. Trends Comput. Commun.* 3, 2051–2054. doi: 10.17762/ijritcc2321-8169.150462

Ji, F., Zhou, H., and Yang, Q. (2008). The abiotic formation of hydrocarbons from dissolved CO2 under hydrothermal conditions with cobalt-bearing magnetite. *Orig. Life Evol. Biosph.* 38, 117–125. doi: 10.1007/s11084-008-9124-7

Jones, L. C., Rosenbauer, R., Goldsmith, J. I., and Oze, C. (2010). Carbonate control of H2 and CH4 production in serpentinization systems at elevated P-Ts. *Geophys. Res. Lett.* 37:L043769. doi: 10.1029/2010GL043769

Kaszuba, J., Yardley, B., and Andreani, M. (2013). Experimental perspectives of mineral dissolution and precipitation due to carbon dioxide-water-rock interactions. *Rev. Mineral. Geochem.* 77, 153–188. doi: 10.2138/rmg.2013.77.5

Klein, F., Bach, W., Jöns, N., McCollom, T., Moskowitz, B., and Berquó, T. (2009). Iron partitioning and hydrogen generation during serpentinization of abyssal peridotites from 15°N on the mid-atlantic ridge. *Geochim. Cosmochim. Acta* 73, 6868–6893. doi: 10.1016/j.gca.2009.08.021

Klein, F., Bach, W., and McCollom, T. M. (2013). Compositional controls on hydrogen generation during serpentinization of ultramafic rocks. *Lithos* 178, 55–69. doi: 10.1016/j.lithos.2013.03.008

Klein, F., Grozeva, N. G., Seewald, J. S., McCollom, T. M., Humphris, S. E., Moskowitz, B., et al. (2015). Fluids in the crust. Experimental constraints on fluid-rock reactions during incipient serpentinization of harzburgite. *Am. Mineral.* 100, 991–1002. doi: 10.2138/am-2015-5112

Klein, F., and McCollom, T. M. (2013). From serpentinization to carbonation: new insights from a CO2 injection experiment. *Earth Planet. Sci. Lett.* 379, 137–145. doi: 10.1016/j.epsl.2013.08.017

Konn, C., Charlou, J. L., Donval, J. P., Holm, N. G., Dehairs, F., and Bouillon, S. (2009). Hydrocarbons and oxidized organic compounds in hydrothermal fluids from Rainbow and Lost City ultramafic-hosted vents. *Chem. Geol.* 258, 299–314. doi: 10.1016/j.chemgeo.2008.10.034

Lafay, R., Montes-Hernandez, G., Janots, E., Chiriac, R., Findling, N., and Toche, F. (2012). Mineral replacement rate of olivine by chrysotile and brucite under high alkaline conditions. *J. Cryst. Growth* 347, 62–72. doi: 10.1016/j.jcrysgro.2012.02.040

Lazar, C., Cody, G. D., and Davis, J. M. (2015). A kinetic pressure effect on the experimental abiotic reduction of aqueous CO 2 to methane from 1 to 3.5kbar at 300°C. *Geochim. Cosmochim. Acta* 151, 34–48. doi: 10.1016/j.gca.2014.11.010

Lazar, C., McCollom, T. M., and Manning, C. E. (2012). Abiogenic methanogenesis during experimental komatiite serpentinization: implications for the evolution of the early Precambrian atmosphere. *Chem. Geol.* 326–327, 102–112. doi: 10.1016/j.chemgeo.2012.07.019

Lee Rodgers, J., and Alan Nice Wander, W. (1988). Thirteen ways to look at the correlation coefficient. *Am. Stat.* 42, 59–66. doi: 10.1080/00031305.1988.10475524

Malvoisin, B., Brunet, F., Carlut, J., Rouméjon, S., and Cannat, M. (2012). Serpentinization of oceanic peridotites: 2. Kinetics and processes of San Carlos olivine hydrothermal alteration. *J. Geophys. Res. Solid Earth* 117:B04102. doi: 10.1029/2011JB008842

Marcaillou, C., Muñoz, M., Vidal, O., Parra, T., and Harfouche, M. (2011). Mineralogical evidence for H2 degassing during serpentinization at 300°C/300bar. *Earth Planet. Sci. Lett.* 303, 281–290. doi: 10.1016/j.epsl.2011.01.006

Martin, B., and Fyfe, W. S. (1970). Some experimental and theoretical observations on the kinetics of hydration reactions with particular reference to serpentinization. *Chem. Geol.* 6, 185–202. doi: 10.1016/0009-2541(70)90018-5

Mayhew, L. E., Ellison, E. T., McCollom, T. M., Trainor, T. P., and Templeton, A. S. (2013). Hydrogen generation from low-temperature water-rock reactions. *Nat. Geosci.* 6, 478–484. doi: 10.1038/ngeo1825

McCollom, T. M. (2003). Formation of meteorite hydrocarbons from thermal decomposition of siderite (FeCO3). *Geochim. Cosmochim. Acta* 67, 311–317. doi: 10.1016/S0016-7037(02)00945-6

McCollom, T. M. (2013). Laboratory simulations of abiotic hydrocarbon formation in earth's deep subsurface. *Rev. Mineral. Geochemistry* 75, 467–494. doi: 10.2138/rmg.2013.75.15

McCollom, T. M. (2016). Abiotic methane formation during experimental serpentinization of olivine. *Proc. Natl. Acad. Sci. U.S.A.* 113, 13965–13970. doi: 10.1073/pnas.1611843113

McCollom, T. M., and Donaldson, C. (2016). Generation of hydrogen and methane during experimental low-temperature reaction of ultramafic rocks with water. *Astrobiology* 16, 389–406. doi: 10.1089/ast.2015.1382

McCollom, T. M., Klein, F., Robbins, M., Moskowitz, B., Berquó, T. S., Jöns, N., et al. (2016). Temperature trends for reaction rates, hydrogen generation, and partitioning of iron during experimental serpentinization of olivine. *Geochim. Cosmochim. Acta* 181, 175–200. doi: 10.1016/j.gca.2016.03.002

McCollom, T. M., Lollar, B. S., Lacrampe-Couloume, G., and Seewald, J. S. (2010). The influence of carbon source on abiotic organic synthesis and carbon isotope fractionation under hydrothermal conditions. *Geochim. Cosmochim. Acta* 74, 2717–2740. doi: 10.1016/j.gca.2010.02.008

McCollom, T. M., and Seewald, J. S. (2001). A reassessment of the potential for reduction of dissolved CO2 to hydrocarbons during serpentinization of olivine. *Geochim. Cosmochim. Acta* 65, 3769–3778. doi: 10.1016/S0016-7037(01)00655-X

McCollom, T. M., and Seewald, J. S. (2003). Experimental constraints on the hydrothermal reactivity of organic acids and acid anions: I. Formic acid and formate. *Geochim. Cosmochim. Acta* 67, 3625–3644. doi: 10.1016/S0016-7037(03)00136-4

McDermott, J. M., Seewald, J. S., German, C. R., and Sylva, S. P. (2015). Pathways for abiotic organic synthesis at submarine hydrothermal fields. *Proc. Natl. Acad. Sci. U.S.A.* 112, 7668–7672. doi: 10.1073/pnas.1506295112

Ménez, B., Pisapia, C., Andreani, M., Jamme, F., Vanbellingen, Q. P., Brunelle, A., et al. (2018). Abiotic synthesis of amino acids in the recesses of the oceanic lithosphere. *Nature* 564, 59–63. doi: 10.1038/s41586-018-0684-z

Michiels, K., Haesen, A., Meynen, V., and Spooren, J. (2018). Applicability of fine industrial metallic iron-rich waste powders for hydrothermal production of hydrogen gas: the influence of non-ferrous contaminants. *J. Clean. Prod.* 195, 674–686.

Milesi, V., Guyot, F., Brunet, F., Richard, L., Recham, N., Benedetti, M., et al. (2015). Formation of CO2, H2 and condensed carbon from siderite dissolution in the 200–300 C range and at 50 MPa. *Geochim. Cosmochim. Acta* 154, 201–211.

Miller, H. M., Mayhew, L. E., Ellison, E. T., Kelemen, P., Kubo, M., and Templeton, A. S. (2017). Low temperature hydrogen production during experimental hydration of partially-serpentinized dunite. *Geochim. Cosmochim. Acta* 209, 161–183. doi: 10.1016/j.gca.2017.04.022

Monnin, C., Chavagnac, V., Boulart, C., Ménez, B., Gérard, M., Gérard, E., et al. (2014). Fluid chemistry of the low temperature hyperalkaline hydrothermal system of Prony bay (New Caledonia). *Biogeosciences* 11, 5687–5706. doi: 10.5194/bg-11-5687-2014

Muscente, A. D., Bykova, N., Boag, T. H., Buatois, L. A., Mángano, M. G., Eleish, A., et al. (2019). Ediacaran biozones identified with network analysis provide evidence for pulsed extinctions of early complex life. *Nat. Commun.* 10:911. doi: 10.1038/s41467-019-08837-3

Muscente, A. D., Prabhu, A., Zhong, H., Eleish, A., Meyer, M. B., Fox, P., et al. (2018). Quantifying ecological impacts of mass extinctions with network analysis of fossil communities. *Proc. Natl. Acad. Sci. U.S.A.* 115, 5217–5222. doi: 10.1073/pnas.1719976115

Neubeck, A., Duc, N. T., Bastviken, D., Crill, P., and Holm, N. G. (2011). Formation of H2and CH4by weathering of olivine at temperatures between 30 and 70°C. *Geochem. Trans.* 12:6. doi: 10.1186/1467-4866-12-6

Neubeck, A., Duc, N. T., Hellevang, H., Oze, C., Bastviken, D., Bacsik, Z., et al. (2014). Olivine alteration and H2 production in carbonate-rich, low temperature aqueous environments. *Planet. Space Sci.* 96, 51–61. doi: 10.1016/j.pss.2014.02.014

Oelkers, E. H. (1999). "A comparison of forsterite and enstatite dissolution rates and mechanisms," in *Growth, Dissolution and Pattern Formation in Geosystems*, eds B. Jamtveit, P. Meakin, and P. Meakin, (Berlin: Springer), 253–267. doi: 10.1007/978-94-015-9179-9_12

Okland, I., Huang, S., Thorseth, I. H., and Pedersen, R. B. (2014). Formation of H2, CH4 and N-species during low-temperature experimental alteration of ultramafic rocks. *Chem. Geol.* 387, 22–34. doi: 10.1016/j.chemgeo.2014.08.003

Otte, E., and Rousseau, R. (2002). Social network analysis: a powerful strategy, also for the information sciences. *J. Inf. Sci.* 28, 441–453. doi: 10.1177/016555150202800601

Oze, C., and Sharma, M. (2007). Serpentinization and the inorganic synthesis of H2 in planetary surfaces. *Icarus* 186, 557–561. doi: 10.1016/j.icarus.2006.09.012

Pagani, G. A., and Aiello, M. (2013). The power grid as a complex network: a survey. *Phys. A Stat. Mech. Appl.* 392, 2688–2700. doi: 10.1016/j.physa.2013.01.023

Pearson, K. (1895). VII. Note on regression and inheritance in the case of two parents. *Proc. R. Soc. London* 58, 240–242. doi: 10.1098/rspl.1895.0041

Proskurowski, G., Lilley, M. D., Kelley, D. S., and Olson, E. J. (2006). Low temperature volatile production at the Lost City Hydrothermal Field, evidence from a hydrogen stable isotope geothermometer. *Chem. Geol.* 229, 331–343. doi: 10.1016/j.chemgeo.2005.11.005

Proskurowski, G., Lilley, M. D., Seewald, J. S., Früh-Green, G. L., Olson, E. J., Lupton, J. E., et al. (2008). Abiogenic hydrocarbon production at lost city hydrothermal field. *Science* 319, 604–607. doi: 10.1126/science.1151194

Russell, M. J., Hall, A. J., and Martin, W. (2010). Serpentinization as a source of energy at the origin of life. *Geobiology* 8, 355–371. doi: 10.1111/j.1472-4669.2010.00249.x

Schulte, M., Blake, D., Hoehler, T., and McCollom, T. (2006). Serpentinization and its implications for life on the early Earth and Mars. *Astrobiology* 6, 364–376. doi: 10.1089/ast.2006.6.364

Scott, J., and Carrington, P. (2015). *The SAGE Handbook of Social Network Analysis*. Thousand Oaks, CA: SAGE publications, doi: 10.4135/9781446294413

Seewald, J. S., Zolotov, M. Y., and McCollom, T. (2006). Experimental investigation of single carbon compounds under hydrothermal conditions. *Geochim. Cosmochim. Acta* 70, 446–460. doi: 10.1016/j.gca.2005.09.002

Seyfried, W. E., Foustoukos, D. I., and Fu, Q. (2007). Redox evolution and mass transfer during serpentinization: an experimental and theoretical study at 200°C, 500 bar with implications for ultramafic-hosted hydrothermal systems at Mid-Ocean Ridges. *Geochim. Cosmochim. Acta* 71, 3872–3886. doi: 10.1016/j.gca.2007.05.015

Shock, E. L. (1992). "Chapter 5 chemical environments of submarine hydrothermal systems," in *Origins of Life and Evolution of the Biosphere*, ed. A. W. Schwartz, (Berlin: Springer), 67–107. doi: 10.1007/BF01808019

Sleep, N. H., Meibom, A., Fridriksson, T., Coleman, R. G., and Bird, D. K. (2004). H 2 -rich fluids from serpentinization: geochemical and biotic implications. *Proc. Natl. Acad. Sci. U.S.A.* 101, 12818–12823. doi: 10.1073/pnas.0405289101

Szatmari, P. (1989). Petroleum formation by Fischer-Tropsch synthesis in plate teconics. *Am. Assoc. Pet. Geol. Bull.* 73, 989–998. doi: 10.1306/44b4a2cb-170a-11d7-8645000102c1865d

Thayer, T. P. (1966). Serpentinization considered as a constant-volume metasomatic process. *Am. Mineral. J. Earth Planet. Mater.* 51, 685–710.

Tingle, T. N., Hochella, M. F. Jr., Becker, C. H., and Malhotra, R. (1990). Organic compounds on crack surfaces in olivine from San Carlos, Arizona and Hualalai Volcano, Hawaii. *Geochim. Cosmochim. Acta* 54, 477–485.

Van Haasterecht, T., Ludding, C. C. I., De Jong, K. P., and Bitter, J. H. (2014). Toward stable nickel catalysts for aqueous phase reforming of biomass-derived feedstock under reducing and alkaline conditions. *J. Catal.* 319, 27–35.

Vilhena, D. A., Harris, E. B., Bergstrom, C. T., Maliska, M. E., Ward, P. D., Sidor, C. A., et al. (2013). Bivalve network reveals latitudinal selectivity gradient at the end-Cretaceous mass extinction. *Sci. Rep.* 3:1790. doi: 10.1038/srep01790

Vitale Brovarone, A., Martinez, I., Elmaleh, A., Compagnoni, R., Chaduteau, C., Ferraris, C., et al. (2017). Massive production of abiotic methane during subduction evidenced in metamorphosed ophicarbonates from the Italian Alps. *Nat. Commun.* 8:14134. doi: 10.1038/ncomms14134

Wang, D. T., Reeves, E. P., McDermott, J. M., Seewald, J. S., and Ono, S. (2018). Clumped isotopologue constraints on the origin of methane at seafloor hot springs. *Geochim. Cosmochim. Acta* 223, 141–158. doi: 10.1016/j.gca.2017.11.030

Young, E. D. (2019). "A two-dimensional perspective on CH4 isotope clumping," in *Deep Carbon*, eds B. N. Orcutt, I. Daniel, and R. Dasgupta, (Cambridge: Cambridge University Press), 388–414. doi: 10.1017/9781108677950.013

Zahnle, K., Freedman, R. S., and Catling, D. C. (2011). Is there methane on Mars? *Icarus* 212, 493–503. doi: 10.1016/j.icarus.2010.11.027

Zolotov, M., and Shock, E. (1999). Abiotic synthesis of polycyclic aromatic hydrocarbons on Mars. *J. Geophys. Res. E Planets* 104, 14033–14049. doi: 10.1029/1998JE000627

Zolotov, M. Y., and Shock, E. L. (2000). Abiotic origin for hydrocarbons in the Allan Hills 84001 martian meteorite through cooling of magmatic and impact-generated gases. *Meteorit. Planet. Sci.* 35, 629–638. doi: 10.1111/j.1945-5100.2000.tb01443.x

Conflict of Interest: The authors declare that the research was conducted in the absence of any commercial or financial relationships that could be construed as a potential conflict of interest.

frontiers in Earth Science

REVIEW
published: 27 August 2020
doi: 10.3389/feart.2020.00208

Exploring Carbon Mineral Systems: Recent Advances in C Mineral Evolution, Mineral Ecology, and Network Analysis

Shaunna M. Morrison[1], Joy Buongiorno[1], Robert T. Downs[2], Ahmed Eleish[3], Peter Fox[3], Donato Giovannelli[4,5,6,7]*, Joshua J. Golden[2], Daniel R. Hummer[8], Grethe Hystad[9], Louise H. Kellogg[10], Oliver Kreylos[10], Sergey V. Krivovichev[11], Chao Liu[1], Andrew Merdith[12], Anirudh Prabhu[3], Jolyon Ralph[13], Simone E. Runyon[14], Sabin Zahirovic[12] and Robert M. Hazen[1]*

[1] Earth and Planets Laboratory, Carnegie Institution for Science, Washington, DC, United States, [2] Department of Geosciences, The University of Arizona, Tucson, AZ, United States, [3] Department of Earth and Environmental Sciences, Tetherless World Constellation, Rensselaer Polytechnic Institute, Troy, NY, United States, [4] Department of Biology, University of Naples Federico II, Naples, Italy, [5] Institute for Biological Resources and Marine Biotechnology, National Research Council of Italy, Ancona, Italy, [6] Department of Marine and Coastal Sciences, Rutgers The State University of New Jersey, New Brunswick, NJ, United States, [7] Earth-Life Science Institute, Tokyo Institute of Technology, Tokyo, Japan, [8] School of Earth Systems and Sustainability, Southern Illinois University, Carbondale, IL, United States, [9] Department of Mathematics, Statistics and Computer Science, Purdue University Northwest, Hammond, IN, United States, [10] Department of Earth and Planetary Sciences, University of California, Davis, Davis, CA, United States, [11] Kola Science Centre of the Russian Academy of Sciences, Apatity, Russia, [12] EarthByte Group, School of Geosciences, The University of Sydney, Sydney, NSW, Australia, [13] Mindat.org, Mitcham, United Kingdom, [14] Department of Geology and Geophysics, University of Wyoming, Laramie, WY, United States*

OPEN ACCESS

Edited by:
Carmen Sanchez-Valle, University of Münster, Germany

Reviewed by:
Siobhan A. Wilson, University of Alberta, Canada
Fabrice Brunet, UMR 5275 Institut des Sciences de la Terre (ISTERRE), France

***Correspondence:**
Shaunna M. Morrison
smorrison@carnegiescience.edu
Donato Giovannelli
donato.giovannelli@gmail.com

Specialty section:
This article was submitted to Earth and Planetary Materials, a section of the journal Frontiers in Earth Science

Received: *30 June 2019*
Accepted: *19 May 2020*
Published: *27 August 2020*

Citation:
Morrison SM, Buongiorno J, Downs RT, Eleish A, Fox P, Giovannelli D, Golden JJ, Hummer DR, Hystad G, Kellogg LH, Kreylos O, Krivovichev SV, Liu C, Merdith A, Prabhu A, Ralph J, Runyon SE, Zahirovic S and Hazen RM (2020) Exploring Carbon Mineral Systems: Recent Advances in C Mineral Evolution, Mineral Ecology, and Network Analysis. Front. Earth Sci. 8:208. doi: 10.3389/feart.2020.00208

Large and growing data resources on the spatial and temporal diversity and distribution of the more than 400 carbon-bearing mineral species reveal patterns of mineral evolution and ecology. Recent advances in analytical and visualization techniques leverage these data and are propelling mineralogy from a largely descriptive field into one of prediction within complex, integrated, multidimensional systems. These discoveries include: (1) systematic changes in the character of carbon minerals and their networks of coexisting species through deep time; (2) improved statistical predictions of the number and types of carbon minerals that occur on Earth but are yet to be discovered and described; and (3) a range of proposed and ongoing studies related to the quantification of network structures and trends, relation of mineral "natural kinds" to their genetic environments, prediction of the location of mineral species across the globe, examination of the tectonic drivers of mineralization through deep time, quantification of preservational and sampling bias in the mineralogical record, and characterization of feedback relationships between minerals and geochemical environments with microbial populations. These aspects of Earth's carbon mineralogy underscore the complex co-evolution of the geosphere and biosphere and highlight the possibility for scientific discovery in Earth and planetary systems.

Keywords: carbon, mineral evolution, mineral ecology, network analysis, carbon minerals

INTRODUCTION

Minerals, including carbon-bearing phases, are the oldest available materials from the ancient history of our planet and other bodies in our solar system – they record information about their genetic environments and any subsequent weathering and alteration they underwent, offering a glimpse of ancient environments through deep time. In this work, we describe some of the important carbon mineral data resources, outline a number of new advances in data-driven discovery in carbon and other mineral systems, including new insights from mineral network visualizations and statistical modeling. We also preview upcoming studies and directions of research related to the diversity and distribution of mineral species, statistical modeling of complex, multidimensional data objects and their underlying trends, tectonic drivers of mineralization, characterization of relationships between microbial populations, their expressed protein functions and the geochemical environment, quantification of preservational and sampling bias present in the mineralogical record, and a number of predictive algorithms including those which predict formational environments of minerals as well as the location of previously unknown mineral localities.

Carbon minerals are particularly compelling for multi-dimensional analysis due to their diverse range of bonding behaviors, paragenetic modes, mineral properties, and ages. Carbon minerals are some of the first condensed phases formed in a solar system and among the hardest materials known, yet carbon minerals are also some of the latest occurring and most ephemeral crystalline phases. Carbon has the ability to behave as a cation, anion, or neutral atom, allowing bonding with itself and 80+ other elements, with a variety of bonding coordination numbers including 2, 3, and 4, and valance states of −4, +2, and +4 (Hazen et al., 2013a). Many of the first crystals formed in our cooling solar system were refractory carbon-bearing phases, including diamond (C) (Lewis et al., 1987), graphite (C) (Amari et al., 1990), and moissanite (*SiC*) (Zinner et al., 1987). Carbon and its mineral phases are intrinsically linked to organic and biological processes – biomineralization is responsible for a significant portion of rhombohedral carbonates on Earth's surface and organic minerals make up nearly 15% of the 411 known carbon mineral species (as of June 2019; rruff.info/ima). Carbon's widely varying character offers a fascinating opportunity to employ rapidly developing advanced analytics and visualization techniques to characterize its complex, multivariate systems and answer previously inaccessible questions at the interface of Earth, planetary, and life sciences.

MINERAL DATA RESOURCES

The International Mineralogical Association List of Mineral Species

The International Mineralogical Association (IMA) list of mineral species (RRUFF.info/IMA) is part of the RRUFF Project (Lafuente et al., 2015) – a mineral library and series of databases with the goal of providing robust, diverse mineralogical data, including high-quality chemical, spectral, and diffraction data, the IMA list of approved mineral species, the American Mineralogist Crystal Structure Database (AMCSD; RRUFF.geo.arizona.edu/AMS/amcsd.php), mineral locality age information (see "Mineral Evolution Database" section below), and other mineral properties (see "Mineral Properties Database" section below). The IMA list allows users to search the over 5400 (as of June 2019) mineral species by name, chemical composition, unit-cell parameters and crystallography, crystal structure group, paragenetic mode, and the availability of ancillary data including crystal structure files in the AMCSD or direct RRUFF Project analyses. This database also provides useful information about each mineral species, including composition, oldest known age, crystal structure group, and unit-cell parameters along with corresponding compositions, all of which can be downloaded in a number of machine-readable file formats. Lastly, this page offers links to a number of related informational pages and websites, including the Handbook of Mineralogy (Anthony et al., 2003), measured data in RRUFF Project databases, crystal structure files in the AMCSD, mineral locality information at Mindat.org (see "Mindat.org" section below), and age and locality data in the Mineral Evolution Database (MED).

The Mineral Evolution Database (MED)

The Mineral Evolution Database (MED; RRUFF.info/Evolution; Golden et al., 2016; Prabhu et al., 2020) was created to support mineral evolution and ecology studies – studies that examine and characterize spatial and temporal mineral diversity and distribution in relation to geologic, biologic, and planetary processes (Hazen et al., 2008, 2011, 2013c,b, 2014, 2015a,b, 2016, 2017a,b, 2019b; Hazen and Ferry, 2010; McMillan et al., 2010; Golden et al., 2013; Hazen, 2013, 2018, 2019; Grew and Hazen, 2014; Zalasiewicz et al., 2014; Grew et al., 2015; Hystad et al., 2015b,a, 2019a; Liu et al., 2017a,b, 2018b; Ma et al., 2017; Morrison et al., 2017b; Glikson and Pirajno, 2018). The MED contains mineral locality and age information extracted from primary literature and the mineral-locality database, Mindat.org. As of 14 June 2019, 15,906 unique ages for 6,253 directly dated mineral localities, documenting 810,907 mineral-locality pairs and 194,090 mineral-locality-age triples are available in the MED. Specific to the known 411 carbon-bearing phases, there are 8,635 dated carbon mineral localities, 94,677 carbon mineral-locality pairs, and 20,773 dated carbon mineral-locality pairs available in the MED, as of June 2019. These data have been assembled and documented to maximize the accuracy and transparency of age associations, which include data on specific mineral formations, mineralization events, element concentrations, and/or deposit formations. The MED interface allows many sorting and displaying options, including sorting by age or locality name, as well as displaying all of the queried minerals at a given locality or displaying a line of data for each mineral-locality pair. These data are available for download directly from the MED (RRUFF.info/Evolution) with various file format options.

The Mineral Properties Database (MPD)

The Mineral Properties Database (MPD; Morrison et al., 2017b; Prabhu et al., 2019a) was created with the goal of better understanding the multidimensional, multivariate trends amongst mineral species and their relationships to geologic materials, preservational and sampling biases, and geologic, biologic, and planetary processes. At present, this database contains dozens of parameters, including age, color, redox state, structural complexity (Krivovichev, 2012, 2013, 2016, 2018; Hazen et al., 2013b; Grew et al., 2016; Krivovichev et al., 2017, 2018) and method of discovery associated with copper, uranium, and carbon minerals. Ongoing efforts are in place to expand to minerals of each element of the periodic table. These data, coupled with those of the MED, offer the opportunity to study changes in redox conditions through deep time and are the basis for mineral network analysis studies (Morrison et al., 2017b; Perry et al., 2018; Hazen, 2019; Hazen et al., 2019b). This database will be publicly available through the RRUFF Project on the Open Data Repository platform (ODR; opendatarepository.org). The ODR interface will maximize the flexibility with which users view, explore, subset, and download data of interest.

Mindat.org

Hudson Institute of Mineralogy's Mindat.org is an interactive mineral occurrence database with a wealth of information on mineral localities around the globe, as well as Apollo Lunar samples and meteorites. At present, mindat houses nearly 300,000 mineral localities, with >1.2 million mineral-locality pairs and nearly one million mineral photographs. A large majority of the mineral occurrence information available on Mindat.org is from published literature, but users can also add localities, mineral-locality pairs, photographs, and references. The MED directly interfaces with mindat, harnessing and incorporating the huge amount of mineral locality data held in mindat. It has been an important resource for scientific research and discovery – many studies on the diversity and distribution of minerals on Earth's surface have relied in part on mindat mineral locality information (Hazen et al., 2008, 2011, 2013c,b, 2014, 2015a,b, 2016, 2017a,b, 2019b; Hazen and Ferry, 2010; McMillan et al., 2010; Golden et al., 2013; Hazen, 2013, 2018, 2019; Grew and Hazen, 2014; Grew et al., 2015; Hystad et al., 2015a,b, 2019a; Liu et al., 2017a,b, 2018b; Ma et al., 2017; Morrison et al., 2017b). These studies include those of Carbon Mineral Ecology detailed below.

Global Earth Mineral Inventory (GEMI)

The Global Earth Mineral Inventory (GEMI[1]) is a Deep Carbon Observatory (DCO) data legacy project born out of the diverse data types collected in conjunction with the DCO's broad range of scientific driving questions (Prabhu et al., 2019a, 2020). Specifically, Prabhu et al. (2019a, 2020) aimed to support and facilitate scientific discovery by merging and integrating DCO data products, such as the MPD and MED, into a digestible, accessible, and user-friendly format for exploration, statistical analysis, and visualization. Therefore, GEMI is a faceted, searchable knowledge graph or network in which each node represents a feature of the MED and MPD – allowing users to explore, query, and extract the specific subset of data or combinations of data necessary for their research goal.

[1]https://dx.deepcarbon.net/11121/6200-6954-6634-8243-CC

CARBON MINERAL ECOLOGY

Statistical approaches are particularly useful in characterizing surface and near-surface environments where biology and reaction kinetics play a major role in mineral formation and stability, as opposed to the dominance of thermodynamics in the subsurface. Mineral ecological studies employ the MED and Mindat.org to examine and characterize the spatial diversity and distribution of mineral species on planetary bodies (Hazen et al., 2015b,a, 2016, 2017b; Hystad et al., 2015a,b; Grew et al., 2017; Liu et al., 2017a, 2018a). "Mineral species" in this case are those recognized by the IMA Commission on New Minerals, Nomenclature and Classification (CNMNC), which often does not account for subtle variations in chemistry or formational processes (see section "Natural Kind Clustering"). Previous studies have found that minerals on Earth's surface follow a distinct trend, a "Large Number of Rare Events" (LNRE) frequency distribution in which most mineral species are rare, occurring at fewer than five geologic localities, and only a few species are very common (Hazen et al., 2015b; Hystad et al., 2015a,b).

The discovery of an LNRE frequency distribution across all mineral systems on Earth enabled the modeling of accumulation curves and, thereby, the prediction of the number of missing or previously unknown mineral species that occur on Earth but have yet to be discovered. Carbon minerals are no exception to the LNRE trend and Hazen et al. (2016) explored their ecology – discovering that in addition to the 400 known carbon mineral species, there were likely at least 145 more species awaiting discovery. Hazen et al. (2016) delved into the likely candidates of missing species, generating accumulation curves for carbon minerals with and without oxygen, hydrogen, calcium, and sodium. They predicted that, of the 145 as-yet undiscovered carbon minerals, 129 would contain oxygen, 118 would contain hydrogen, 52 would contain calcium, and 63 would contain sodium. This study led to the Carbon Mineral Challenge (mineralchallenge.net) – a DCO initiative to engage scientists and collectors in finding and identifying the missing carbon phases. As of June 2019, the Carbon Mineral Challenge boasts 30 new mineral species approved by IMA, a number of which were predicted in Hazen et al. (2016).

At the time of the initial mineral ecology studies, it was understood that the models and the predictions based upon them were to be treated as lower limits of the estimate of missing mineral species. This is due, in part, to sampling bias toward well-crystallized, colorful, or economically valuable specimens. An additional constraint is the advent of new, unforeseen technology that can identify and distinguish minerals at increasingly finer scales. While it is difficult to predict the next technological advance, we can attempt to develop better models to make predictions on our existing data. With this in mind, Hystad

et al. (2019a) developed a new Bayesian technique for modeling mineral frequency distribution and predicting the number of undiscovered mineral species on Earth's surface. Hystad et al. (2019a) updated the prediction of the number of missing mineral species on Earth from the previous minimum estimate of 6394 (Hystad et al., 2015a,b) to an increased estimate of 9308 with 95% posterior interval (8650, 10,070). Note that this new, higher value is still a low estimate due to the unknowns of future technology.

Here, we apply the Poisson lognormal model of Hystad et al. (2019a) to the currently known 411 carbon mineral species and their 50,095 localities (with 94,677 mineral-locality pairs, 22% of which have associated ages, as of June 2019). **Figure 1A** illustrates the carbon mineral frequency distribution with a Poisson lognormal LNRE model overlaid in blue. The frequency distribution is used to generate an accumulation curve (**Figure 1B**), which models the expected number of carbon minerals species as a function of the number of localities characterized, and therefore predict the expected number of carbon mineral species currently present on Earth's surface, many of which remain undiscovered. The new estimate of carbon mineral diversity on Earth is 993 with a 95% posterior interval of (759, 1268), up from the former prediction of 548 carbon mineral species (Hazen et al., 2016). Note again that, as with the above, this prediction should be considered a lower estimate given the unknowns associated with future technological advances and their impacts on mineral discovery.

CARBON MINERAL NETWORK ANALYSIS AND VISUALIZATION

Network Analysis

Network analysis, a subfield of graph theory (Otte and Rousseau, 2002; Clauset et al., 2004; Newman, 2006; Kolaczyk, 2009a; Abraham et al., 2010; Newman and Mark, 2010), is particularly useful for visualizing many variables in a multidimensional system in a digestible and meaningful way, particularly when the questions rely on the interrelationships of many entities and their properties, as is the case in mineralogical systems in the context of Earth and planetary processes. Networks are composed of nodes (or vertices) representing entities and edges (or links) between the nodes symbolizing a relationship between two connected nodes. Nodes can be sized, shaped, colored, etc. according to any variables of interest. Likewise, edges can be directed, colored, texturized, or their thickness can be adjusted to represent any parameter of choice and the length of edges can be scaled in proportion to the strength of the connecting variable. With all of these options, it is possible to display upward of eight variables within one network. Network renderings are projections from N-1 dimensional space (where N is the number of different mineral species) into two or three dimensions, although the multidimensionality is preserved in the original data object and therefore in any statistical metrics derived from the network data. Network metrics fall into two categories, the first of which are "local" metrics that describe the role and significance of individual nodes in a network. Local metrics include degree, which is the number of links connected to a given node, and betweenness, a measure of the number of geodesic (shortest) paths that pass through a given node. The second type of metrics are "global" and are used to evaluate overall trends within a network and allow for comparison of different networks, such as networks of minerals of different elements, from different environments or

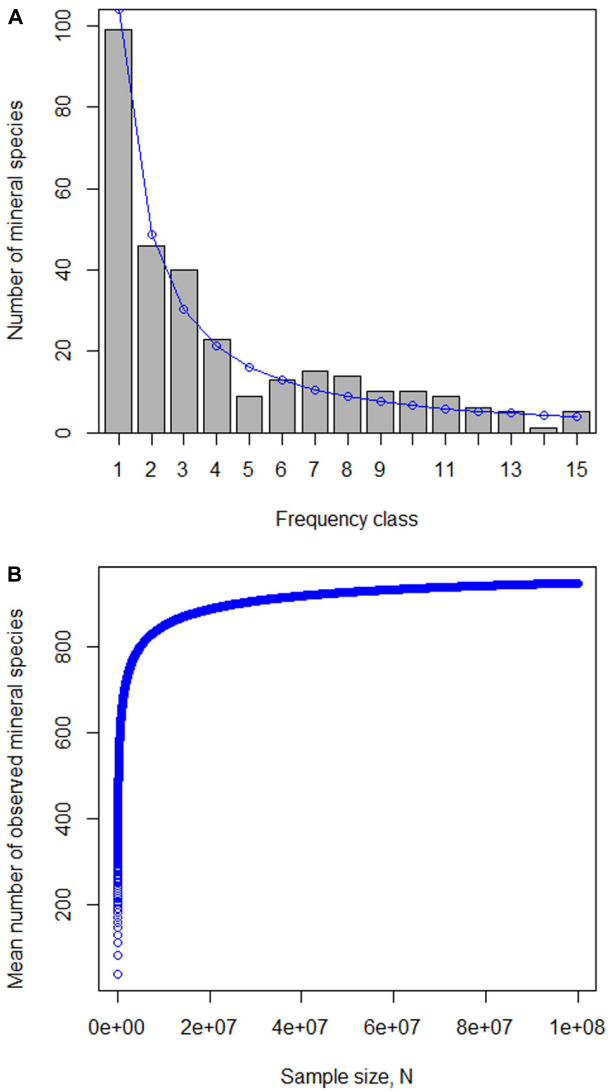

FIGURE 1 | (A,B) Carbon mineral frequency distribution and corresponding accumulation curve. **(A)** The frequency distribution of carbon minerals on Earth's surface. The *x*-axis, "frequency class," is the number of minerals that occur at a locality. The *y*-axis is the number of mineral species that occur at exactly the corresponding frequency class (i.e., nearly 100 carbon mineral species occur at exactly one locality). The blue line represents the Poisson lognormal LNRE model. **(B)** Accumulation curve for the mean number of carbon mineral species versus the number of localities sampled, N, based on the Poisson lognormal LNRE model. Today, there are 411 known carbon mineral species based on N = 92,466 sampled localities. As N approaches infinity, the median number of predicted carbon mineral species is 993 with a 95% posterior interval of (759, 1268).

planetary bodies, or a series of networks over a time interval. Global metrics include density, which is the number of links divided by the number of possible links (i.e., a measure of the interconnectedness of a network), and centralization, a measure of how central a network's "most central" node is relative to how central all the other nodes are (i.e., indicating whether or not there are many highly interconnected nodes or if there are a few key "broker" nodes). Additionally, there are a number of network modularity and community detection algorithms, which allows users to determine if there are distinct groups within their network and what nodes belong to those groups. With further exploration, users can determine what characteristics are shared within each group and/or between groups. Furthermore, random forest or decision tree algorithms can offer insight into the relative importance or weight of each characteristic to the network partitioning.

Mineral Network Analysis

Mineral network analysis, which is a powerful approach to exploring complex multidimensional and multivariate systems, facilitates a holistic, integrated, higher-dimensional understanding of Earth and planetary systems (Morrison et al., 2017b; Hazen et al., 2019a,b). The renderings of Fruchterman-Reingold force-directed (Fruchterman and Reingold, 1991; Csardi and Nepusz, 2006) mineral coexistence networks herein are of two types: unipartite and bipartite. Interactive, manipulatable versions of these networks, including node labels, can be found at https://dtdi.carnegiescience.edu/node/4557.

Unipartite Mineral Networks

In the unipartite networks (**Figures 2–4**), each node represents a mineral species; the nodes are sized according to the frequency of occurrence of each species and colored according to chemistry, paragenetic mode, or structural complexity; the edges represent co-occurrence (which may or may not correspond to an equilibrium assemblage) of two mineral species at a locality on Earth's surface and their length is scaled inversely proportional to their frequency of co-occurrence (i.e., when two species occur together more frequently, they are closer together in the graph). Note that while the nodes of **Figures 2–4** are colored according to various parameters (e.g., composition, paragenetic mode), those parameters were not coded into the network layout – meaning that the network topology and any trends are strictly a function of mineral co-occurrence. A number of interesting trends can be observed in the topologies of unipartite mineral co-occurrence networks. Firstly, the copper (Cu) networks show a high density and low centralization; in the Cu network colored by chemistry (**Figure 2A**), there is strong chemical segregation in which sulfides (red nodes) cluster together, as do sulfates (yellow nodes), and Cu mineral containing oxygen and no sulfur (blue nodes) (Morrison et al., 2017b; Hazen et al., 2019a,b). This chemical segregation results in chemical trend lines throughout the graph, including sulfur fugacity, fS_2, increasing from bottom (oxides) of the graph to top (through sulfates and into sulfides) and oxygen fugacity, fO_2, increasing from the top left (sulfides) to the bottom (sulfates and oxides). For any variable that exhibits an embedded trendline, that trend can be used to predict the value of said variable for any node in which the value is unknown. In the case of chemical variables in mineral networks representing equilibrium assemblages, this could allow for the extraction of thermochemical parameters. Secondly, **Figure 2B** renders the Cu network with nodes colored by crystal structural complexity (Hazen et al., 2013b; Krivovichev, 2013, 2016, 2018; Krivovichev et al., 2017, 2018). Structural complexity is a mathematical measure for evaluating the symmetry and chemical complexity

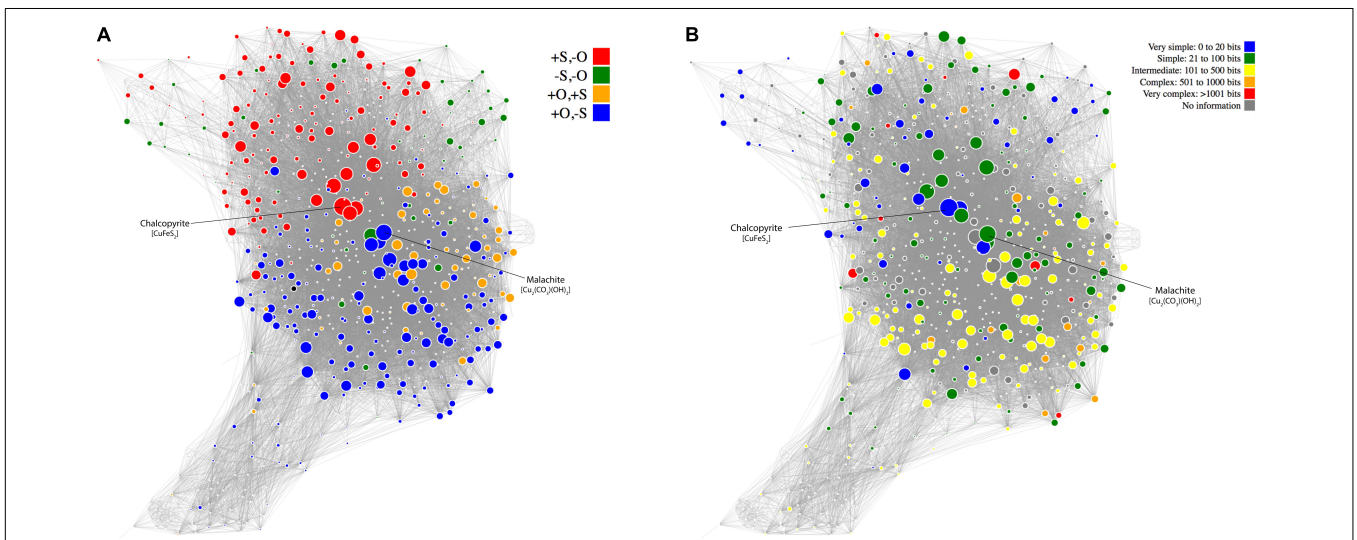

FIGURE 2 | (A,B) Copper mineral networks. Force directed, unipartite, copper (Cu) mineral network renderings. Nodes represent Cu mineral species, sized according to their frequency of occurrence. Edges represent co-occurrence of mineral species at localities on Earth's surface; edge length is scaled inversely proportional to frequency of co-occurrence. **(A)** Nodes are colored according to chemical composition, specifically the presence or absence of sulfur and oxygen. **(B)** Nodes are colored according to crystal structural complexity (i.e., the bits of information contained in each crystal structure; Krivovichev, 2013).

of a mineral's crystal structure and IMA-approved ideal chemical formula, and converting that complexity into information, measured in bits. Krivovichev et al. (2018) hypothesize crystal structure complexity exhibited by minerals has increased through deep time, with the simplest structures existing at the earliest stages of mineral evolution and becoming increasingly complex moving into modern day. In this network, there is segregation resulting in a trendline from the simplest crystal structures to moderately complex structures. The most complex structures are few and scattered throughout the network, an unexpected trend that begs further investigation alongside whether or not age of first occurrence plays a role in the structural complexity trends observed in network **Figure 2B**. Thirdly, the chromium (Cr) network (**Figure 3**) has a very low density and high centralization, with the mineral phase chromite having the highest centrality (Morrison et al., 2017b; Hazen et al., 2019a,b). The most notable feature of the Cr co-occurrence network is its strong clustering by paragenetic mode, indicating that formational environment and mode is the strongest driver for Cr mineral co-occurrence. Lastly, **Figure 4** illustrates the changes in carbon mineral co-occurrence through deep time. The earliest known carbon minerals are few and form a dense, highly interconnected network with low centralization. Through time into modern day, the density decreases slightly while the centralization becomes significantly more pronounced, forming two lobes of carbon mineral populations connected by a few key nodes of high centrality beginning as early as 799 Ma and becoming very distinct at 251 Ma, contemporaneous with the end-Permian mass extinction. These two lobes comprise different populations of carbon mineral chemistry, with the left lobe containing a much higher proportion of organic carbon minerals and hydrous phases containing transition elements, lanthanides, and/or actinides, and the right lobe having a higher frequency of anhydrous phases lacking transition elements, lanthanides, or actinides. This unexpected trend and its underlying geologic or biologic implications are the subject of further study.

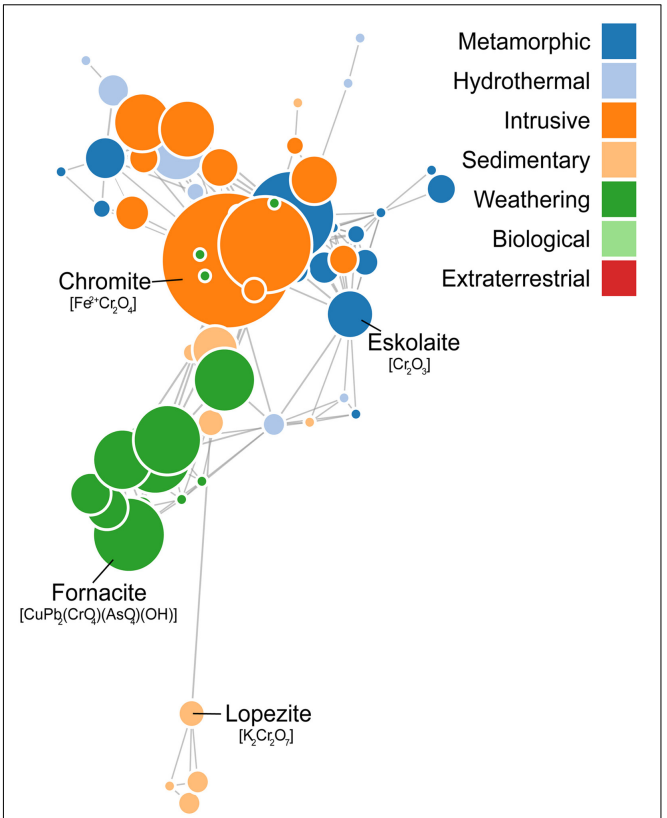

FIGURE 3 | Unipartite chromium mineral network. Force directed, unipartite, chromium (Cr) mineral network rendering. Nodes represent Cr mineral species, sized according to their frequency of occurrence and colored according to their paragenetic mode. Edges represent co-occurrence of mineral species at localities on Earth's surface; edge length is scaled inversely proportional to frequency of co-occurrence.

Bipartite Mineral Network

In the bipartite network rendering (**Figure 5**), the set of colored nodes represent carbon mineral species, sized by their frequency of occurrence and colored according to the age of the oldest known occurrence (Hazen, 2019; Hazen et al., 2019a). The other set of nodes in black represent the localities at which the carbon minerals occur, sized proportionally to their carbon mineral diversity (i.e., the number of mineral species found at a locality). The edges between nodes signifying that a mineral occurs at a locality. Mineral bipartite diagrams illustrate many relationships between carbon minerals and their locations on Earth's surface. The first surprising feature of the network is the "U-shaped" (or "vase shaped" in 3D, see "Advanced Mineral Network Visualizations" section below) locality node distribution. This topology provides a striking visual representation of mineral ecology, specifically the LNRE frequency distribution in which there are a few very common species (such as calcite and aragonite), but most species are rare. In the network graph, the most common minerals fall at the bottom of the locality "U," the frequency of occurrence quickly falls off moving up and out of the locality "U," ultimately radiating outward and around the locality nodes where the majority of carbon minerals lie, most of which have small radii (i.e., they occur at very few localities). Another related feature clearly visible in the rendering is that rare mineral species tend to occur at localities rich in other rare species, as opposed to localities dominated by the more common species. This is visible at the individual node level, but also in the overall topology of the network: the mineral diversity of the localities, and therefore the size of the locality nodes, decreases from top to the bottom, as the network trends from more rare mineral species into more common mineral species. This trend gives researchers exploration targets to look for new, rare mineral species: at localities already known to host other rare mineral species. This qualitative observation can be parlayed into a quantitative method, specifically affinity analysis (see "Affinity Analysis" in the future directions section below) for predicting new locations of existing mineral species, predicting which minerals are likely to occur but have not been reported at a given locality, and possibly make predictions on the most likely

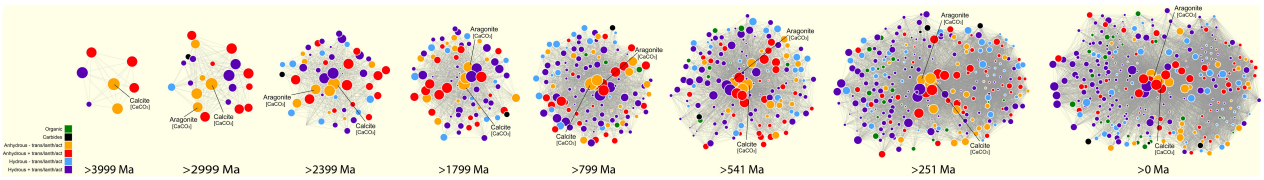

FIGURE 4 | Evolving unipartite carbon mineral networks. Force directed, unipartite, carbon mineral network renderings. Nodes represent carbon mineral species, sized according to their frequency of occurrence and colored according to composition. Edges represent co-occurrence of mineral species at localities; edge length is scaled inversely proportional to frequency of co-occurrence. Each network represents a cumulative time bin in order to illustrate the changes in carbon mineralogy on Earth's surface through deep time.

locations for finding new mineral species. Additionally, an embedded timeline can be observed in the carbon mineral-locality network topology. The nodes of **Figure 5** are colored according to the age of first occurrence; however, their ages were not coded into the network layout – meaning that the network topology is strictly a function of mineral-locality occurrence. Despite the lack of age information encoded in the topological layout, the oldest known minerals occur at the bottom of the locality "U" and radiate up and outward as the minerals become younger, with the youngest minerals skirting around the outside of the locality "U". Observing trendlines in any network system can lead to predicting missing values, but age, in particular, offers the opportunity to pin other parameters, such as chemistry, structural complexity, bioavailability, etc. to a timeline and therefore relate these parameters to geologic, biologic, or planetary events throughout deep time.

Advanced Mineral Network Visualizations

Network renderings are projections from multidimensional space into two dimensions and, inherently, some information is lost. Therefore, it is important to explore variations in visualization techniques that will allow the user to maximize the accuracy and amount of information rendered. With this in mind, we are developing 3D networks and also exploring virtual reality (VR) techniques for visualization and network manipulation. VR offers two primary benefits for visual analytics: (1) the ability to employ true 3D layouts that are not projected to 2D displays and offer additional insight especially for very dense networks, and (2) direct natural interaction, and observation of a network's response to such, creates an additional dimension for analysis not captured in static or non-interactive visualizations. At the following link, a video demonstration of an early VR visualization prototype of the bipartite carbon mineral-locality network in **Figure 5** can be viewed[2]. The locality "U-shape" observed in the 2D version becomes a "vase" shape in 3D, with the most common, oldest carbon minerals at the base of the locality vase and the youngest, rarest carbon minerals radiate out of the top of the locality vase and down the sides. This and other networks can also be explored in an immersive fashion with VR.

[2]https://www.youtube.com/watch?v=5GDnpqpOokU

ORGANIC CARBON MINERALOGY IN EARLY EARTH ENVIRONMENTS AND PLANETARY SYSTEMS

Currently, there are more than 50 organic mineral species approved by the IMA (Skinner, 2005; Perry et al., 2007; Echigo and Kimata, 2010; Hazen et al., 2013a; Piro and Baran, 2018), most of which form through alteration of biological materials (Oftedal, 1922; Rost, 1942; Nasdala and Pekov, 1993; Perry et al., 2007; Chesnokov et al., 2008; Witzke et al., 2015; Pekov et al., 2016; Hummer et al., 2017). Recent discoveries and new studies of organic minerals (Pekov et al., 2016; Bojar et al., 2017; Hummer et al., 2017; Mills et al., 2017) and minerals with metal-organic framework structures that contain metal centers bonded via molecular linkers into porous assemblies of different dimensionalities (Huskić et al., 2016) led to the formulation of novel geomimetic approaches in the design and synthesis of metal-organic frameworks (Huskić and Friščić, 2018; Huskiæ and Frišèiæ, 2019; Li et al., 2019). Most organic minerals observed on Earth today are oxalates and carboxylates of low nutrient value to microbes (Benner et al., 2010) and are therefore able to persist on a planet teeming with life. The presence of life limits the long-term survival of other organic crystals on modern Earth, but such crystals, including co-crystals, could have existed on early Earth and may currently exist on other planetary bodies (Hazen, 2018; Maynard-Casely et al., 2018; Morrison et al., 2018). Organic molecules can be created by abiotic processes (Glasby, 2006; Fu et al., 2007; Kolesnikov et al., 2009; McCollom, 2013; Sephton and Hazen, 2013; Huang et al., 2017). They have been shown to exist in many planetary settings, including meteorites (Cooper et al., 2001; Sephton, 2002; Pizzarello et al., 2006; Burton et al., 2012; Sephton and Hazen, 2013; Kebukawa and Cody, 2015; Cooper and Rios, 2016; Koga and Naraoka, 2017), comets (Kimura and Kitadai, 2015), and have been detected or are hypothesized to exist on many other planetary bodies in our solar system, including Mars, Titan, Enceladus, Callisto, and Ganymede (McCord et al., 1997; Formisano et al., 2004; Cable et al., 2012, 2018; Kimura and Kitadai, 2015; Webster et al., 2015, 2018; Zolensky et al., 2015; Hand, 2018; Maynard-Casely et al., 2018). On bodies with low temperatures there is also the possibility of clathrates containing and protecting organic molecules (Kvenvolden, 1995; Buffett, 2000; Shin et al., 2012; Hazen et al., 2013c; Maynard-Casely et al., 2018). Therefore, the

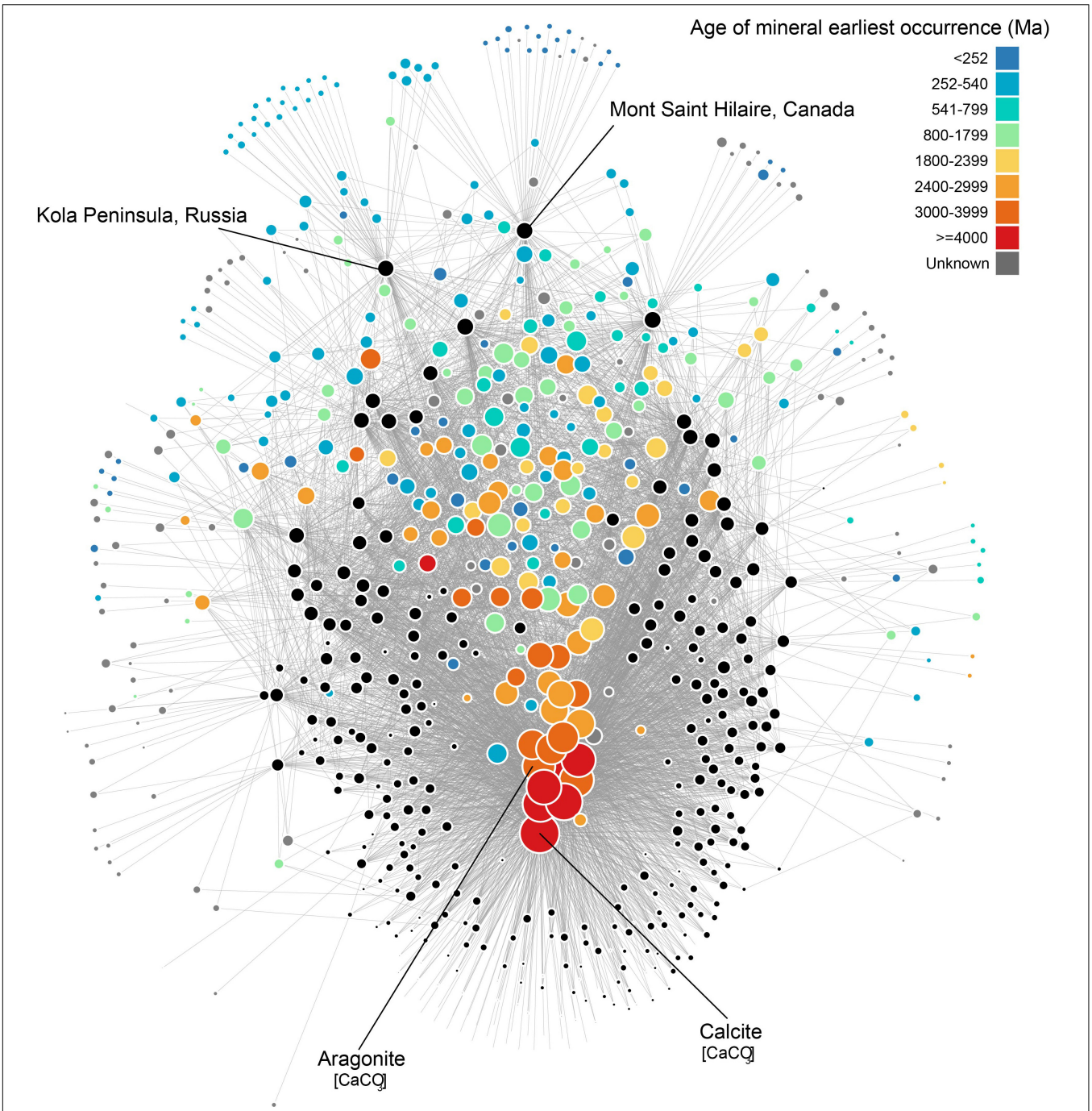

FIGURE 5 | Bipartite carbon mineral-locality network. Force directed, bipartite, carbon mineral-locality network rendering. Colored nodes represent carbon mineral species, sized according to their frequency of occurrence and colored according to age of first occurrence. Black nodes represent carbon mineral localities on Earth and are sized according to mineral diversity (i.e., the number of mineral species found at a locality). Edges represent the occurrence of a mineral species at a locality.

earliest, prebiotic minerals on Earth's surface, many of which may currently be present on other planetary bodies, were likely organic crystalline compounds, such as amino acids, nucleobases, hydrocarbons, co-crystals, clathrates, and other species that have since been consumed by cellular life here on Earth (Hazen, 2018; Morrison et al., 2018).

CURRENT AND FUTURE DIRECTIONS

Network Structure Quantification

Many trends associated with geologic or planetary processes have been recognized in the topologies of mineral networks and a multitude of unrecognized trends also exist within

mineral network topologies and/or data objects. Therefore, it is imperative to develop statistical methods for quantifying mineral network structures and relating these structures to their underlying geologic, biologic, or planetary drivers (Hystad et al., 2019b). Such methods will allow for the systematic study of network features, such as degree distribution, distribution of shared partners, centrality, clustering, connected subgraphs, and cliques, and will employ an exponential random graph model (ERGM) (Frank and Strauss, 1986; Snjiders, 2002; Hunter and Handcock, 2006; Snijders et al., 2006; Hunter, 2007; Pattison et al., 2007; Lusher et al., 2012). The models will determine whether or not the substructures within a network occur more often than would be expected by chance. They will also determine which attributes are most significant to mineral co-occurrence, or any other relationship of interest, including, for example, whether or not minerals of the same paragenetic mode tend to be found at the same location or if there is a more influential parameter. The ERGM model will be expanded to include multilevel networks (Wang et al., 2013), such as one of mineral species, their localities, and their chemical compositions. The multilevel approach will provide a means to model the complex dependence structures and interactions amongst the many network parameters. Additionally, we will employ a latent network model, which models unobserved factors that underlie the expression of network structures by incorporating latent variables (Kolaczyk, 2009b; Kolaczyk and Csárdi, 2014).

Natural Kind Clustering

Physical and chemical attributes of minerals are the direct product of and, as a result, encode their formational conditions and any subsequent weathering and alteration. Therefore, multivariate correlation of these attributes will allow for association of minerals to their paragenetic modes, resulting in a number of distinct "natural kinds" within a mineral species (Hazen, 2019). For example, diamond may have many "natural kinds," including stellar vapor-deposited diamonds (Hazen et al., 2008; Ott, 2009; Hazen and Morrison, 2019), Type I (Davies, 1984; Shirey et al., 2013; Sverjensky and Huang, 2015), Type II (Smith et al., 2016), and carbonado (Heaney et al., 2005; Garai et al., 2006). Cluster analysis and classification algorithms will allow characterization and designation of various natural kinds of each mineral species and thereby relate the wealth of information contained within mineral samples to their geologic, biologic, and/or planetary origins. Designation of the natural kinds of minerals within the earliest environments of our universe is given in Hazen and Morrison (2019) and Morrison and Hazen (2020), preliminary work is underway to classify the natural kinds of many mineral species, with a particular focus on carbon-bearing phases, including diamond, calcite, and aragonite (Boujibar et al., 2019; Zhang et al., 2019).

Affinity Analysis

The mineral co-occurrence information stored in the MED and Mindat.org provide the means to make predictions on the most likely locations to find certain mineral species, geologic settings, deposits, and/or planetary environments, as well as a probabilistic list of minerals likely to occur at any given locality (Prabhu et al., 2019b; Morrison et al., 2020). Affinity analysis is a machine learning method that discovers relationships between various entities in a dataset. This method analyzes co-occurrence data and identifies strong rules based on associations between entities. This method was first introduced by Agrawal and Srikant (1994), and they present two algorithms to create association rules (i.e., the *Apriori* and AprioriTid algorithms). *Apriori* uses a bottom-up approach where subsets of entities that frequently co-occur are generated as candidates for testing against the data. The number of occurrences of the candidates are then compiled and patterns observed from the occurrence of these candidates are used to generate rules. For example, consider the following small carbon mineral dataset:

{malachite, calcite, azurite}
{malachite, azurite}
{malachite, calcite, azurite, dolomite}
{malachite, calcite}

Let us assume these data represents the co-occurrence of carbon minerals. If we generate candidates of size 2 and 3, then most commonly occurring sets of minerals are:

Candidates	Occurrences (Support)
{malachite, calcite}	3
{malachite, azurite}	3
{malachite, calcite, azurite}	2
{malachite, calcite, dolomite}	1
{malachite, azurite, dolomite}	1

Based on the occurrence of candidates, we can create the following rules:

- 75% of the sets with malachite also contain calcite.
- 75% of the sets with malachite also contain azurite.
- 50% of the sets with malachite and calcite also contain azurite.
- 25% of the sets with malachite and calcite also contain dolomite.
- 25% of the sets with malachite and azurite also contain dolomite.

Such association rules can be used to predict the probability of occurrence for certain minerals or mineral assemblages, given the currently known mineralogy of a locality. Therefore, this method allows for prediction of the most probable locations on Earth or other planetary bodies to find mineral species or mineral assemblages of interest, as well as certain geologic settings, deposits, or environments. Likewise, this method can assess the probability of finding any mineral species at a locality in question. In a preliminary case study on Mindat.org mineral occurrence data, pair-wise correlations (i.e., candidates of size 2) were used to predict a likely locality of the mineral species wulfenite. The model predicted the Surprise Mine, Cookes Peak District, Luna County, NM, United States as a very likely new

location of wulfenite (locality[3]). Erin Delventhal, a member of the Mindat.org management team, validated this prediction by going to Cookes Peak and positively identifying an occurrence of wulfenite (image of collected sample[4]). These preliminary results highlight the promise of discovery with affinity analysis in mineral systems.

GPlates Plate Tectonic Reconstructions

GPlates is an open-source and cross-platform plate reconstruction software that enables users to incorporate any vector or raster data into digital community plate motion models (Merdith et al., 2017; Müller et al., 2018; Young et al., 2019). Incorporation of mineralogical data into plate tectonic reconstructions (**Figure 6**) will illuminate tectonic drivers and feedbacks of mineralization through deep time, such as identifying tectonic settings that preferentially generate or focus particular mineral species. We will begin to answer questions related to subduction conditions (i.e., depth of mantle wedge interaction and estimation of slab angle, rate of subduction, devolatilization of the subducting slab, etc.) of subduction-related mineralization, characterize mineralization associated with mantle plume and hydrothermal settings, collisional regimes, and identify mineralization clearly not controlled by tectonic influences. A video of a preliminary reconstruction model of carbon mineralization through deep time (from modern day to 1.0 Ga) can be found at https://4d.carnegiescience.edu/explore-our-science.

Quantifying Preservational Bias

Preservational and sampling bias is inherent to geologic materials, the magnitude of which is not uniform through time or across a system and, therefore, can be very difficult to quantify. Recent data-driven studies of mineralization associated with the Rodinian assembly (Liu et al., 2017b, 2018b) have examined the differences in the mineralogy and geochemistry of igneous rocks associated with the assembly of the Rodinian supercontinent, as igneous rocks of Rodinian age tend to have different geochemical signatures than those from other supercontinents. The question remains: how much of the trend is related to conditions and processes during assembly and how much is related to preservational and sampling bias? This is evident in **Figure 6** where major increases in carbon mineralization is associated with the younger mega-continent of Gondwana and supercontinent of Pangea, while the signal related to Nuna and Rodinia assembly is more subdued in the cumulative frequency plot. This question must also be asked of many other formational environments, including those relevant to carbon mineralization (e.g., carbonate platforms, carbonatites). Ongoing and future studies will attempt to quantify preservational bias in the mineralogical record by examining factors that contribute to preservation, such as mineral characteristics (e.g., solubility, hardness), common tectonic settings of mineral formation, etc. It is also important to consider human factors that govern sampling, including economic significance of the material, physical characteristics (e.g., color, crystal habit, size, luster), and scientific importance, and may result in sampling bias within datasets. These data will be used to develop statistical models for prediction of the amount of erosional loss through deep time.

[3]https://www.Mindat.org/loc-300363.html

[4]https://www.mindat.org/photo-930500.html

Microbial Populations and Mineral Systems

An underlying driving principle of studying Earth's mineralogy through deep time is to gain insight into the co-evolution of the geosphere and biosphere. Mineral evolution studies characterize Earth's mineralogy during the time of life's emergence and throughout its evolution, but how do we garner an understanding of direct influence and feedback systems between Earth materials (e.g., the "geochemical environment") and microbial populations? Given the dearth of ancient microbial samples, we can examine modern day equivalents, particularly in geochemical environments most likely to be analogous to ancient environments (e.g., hydrothermal vents, hot springs). Therefore, a study is underway to employ advanced analytics and visualization, including network analysis, to characterize the complex, multidimensional, multivariate relationships between the metagenomes of extant microbial populations and their geochemical environments (Morrison et al., 2017a; Buongiorno et al., 2019a,b, 2020; Giovannelli et al., 2019). **Figures 7A,B** illustrate a preliminary look at bipartite networks of sampling site locations and their metagenomes (A) and mineralogy (B). A multilevel network approach (see "Network Structure Quantification" section above) and transfer learning techniques will be used to relate location, metagenomic data, and mineralogy (**Figures 7A,B**), as well as aqueous geochemistry, temperature, pressure, pH, salinity, and more, and to generate models quantifying the complex relationships therein. These studies are examining trends in metagenomic and geochemical parameters across a single arc system (Barry et al., 2019a,b), across multiple systems such as volcanic arcs, mid-oceanic ridges, and hot spots, and across disparate systems around our planet, as depicted in **Figures 7A,B** (e.g., including settings like acid-mine drainage, permafrost, and hot springs). Targeting closely related systems, such as a single volcanic arc or all hotspot related hot spring systems, allows tight correlation of changes in geochemical conditions with changes in microbial communities due to the fact that there is less variance in the environmental parameters. Whereas a more global comparison allows for examination of all possible environmental and microbial variables. Preliminary results show distinct, complex trends in geochemical parameters related to changes in protein functions of microbial populations.

DISCUSSION

Motivated by understanding Earth's mineral diversity and distribution through deep time, bioavailability of redox sensitive elements during the emergence and evolution of life, biosignatures at mineralogical and planetary scales, and underlying geologic and biologic drivers of mineralization, we have made many discoveries in carbon science, including: (1) Earth's mineralogy is a function of the physical, chemical, and biological processes that are different at each stage of planetary evolution. (2) Earth's mineral diversity and spatial distribution

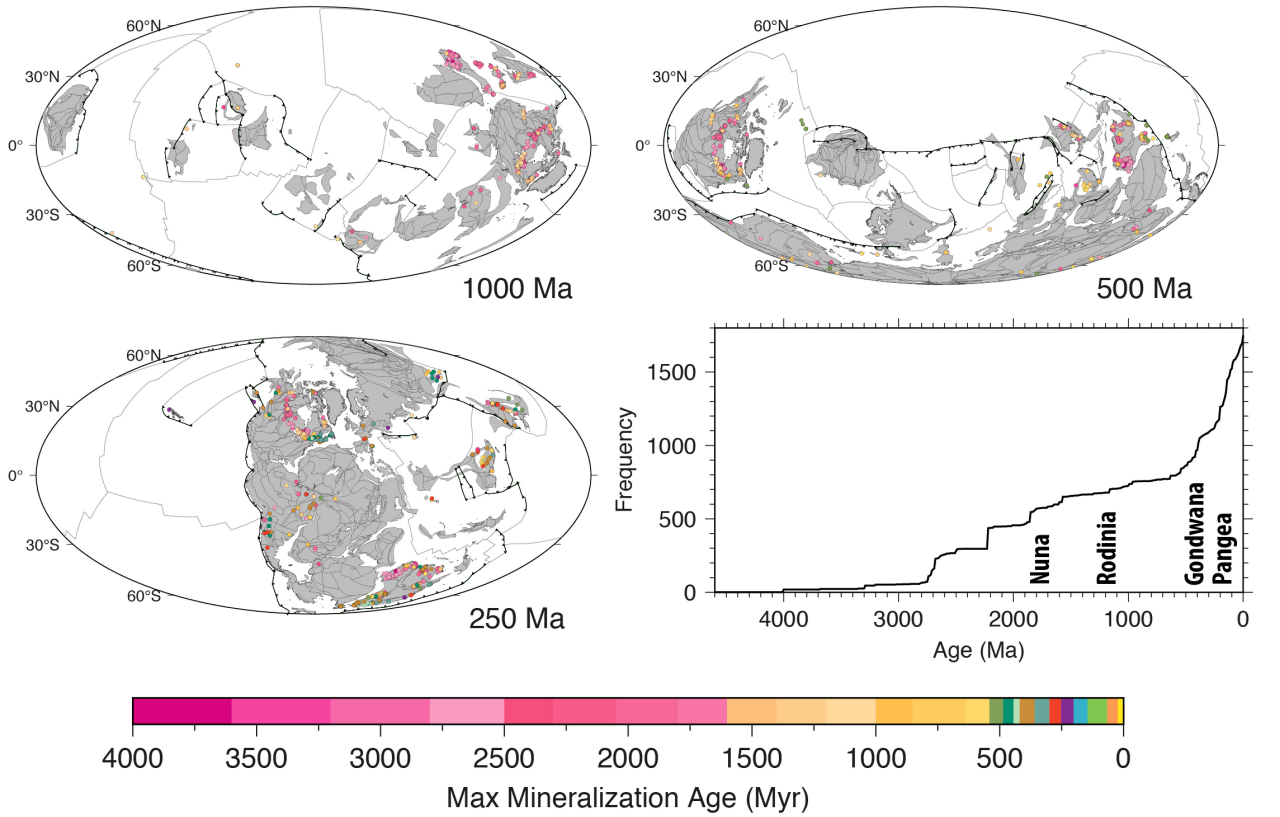

FIGURE 6 | GPlates plate tectonic reconstruction snapshots with carbon mineral occurrences, and a cumulative frequency plot highlighting that some increases in carbon mineral occurrences are contemporaneous with changes in the supercontinent cycle. Full video (modern day to 1.0 Ga) available at https://4d.carnegiescience.edu/explore-our-science.

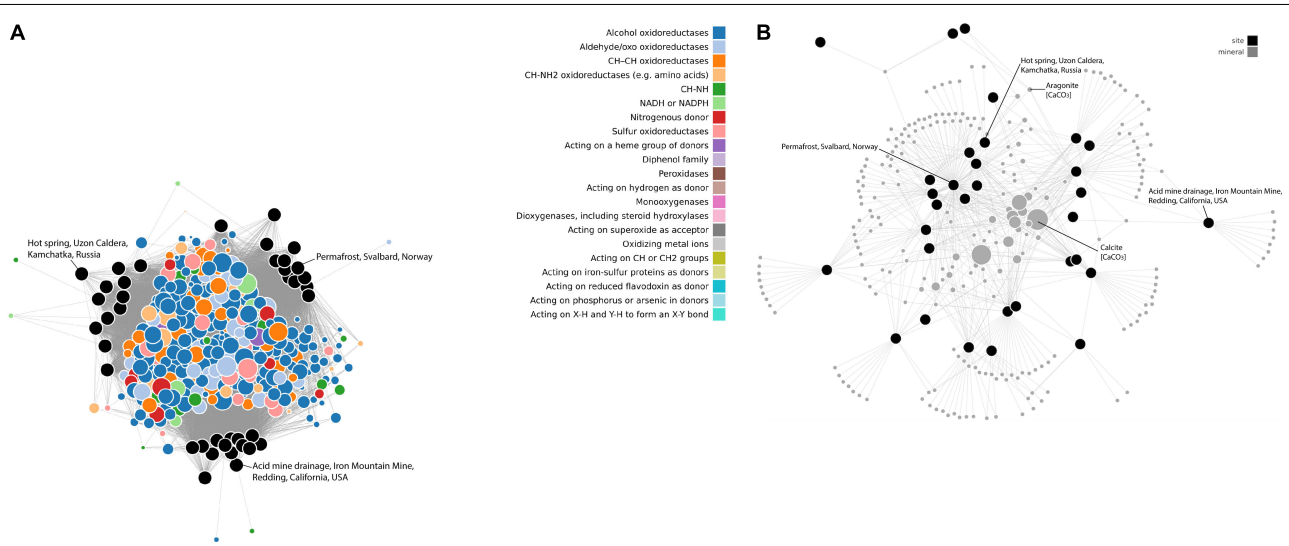

FIGURE 7 | (A,B) Bipartite microbial population-locality and mineral-locality networks. Force-directed, bipartite networks of a preliminary analysis of interaction between metagenomes and mineralogy of the same sampling sites. **(A)** Metalloprotein oxidoreductases (colored nodes; enzyme commission EC1 class) and the sites where they were found (black nodes). Enzyme nodes sized according to their counts and colored by their subclass. **(B)** Bipartite network of the mineral diversity at the same sites. Mineral nodes in gray, sized according to their mineral diversity; site nodes in black.

follows an LNRE trend, a trend that is visually represented in the topology of mineral-locality bipartite network renderings and is likely a planetary-scale biosignature. (3) Predication of as-yet undiscovered mineral species, which spurred the Carbon Mineral Challenge – an initiative that has reported 30 new carbon minerals species in less than 3 years. (4) Recognition of embedded trend lines in network topologies, such as those of chemical composition, crystal structural complexity, time, and paragenetic mode. In addition, this work has developed new tools for visualization of mineral systems, including mineral networks, as well as 3D and VR platforms thereof. Furthermore, we are exploring and are on the brink of discoveries related to (1) quantifying mineral network structures and their underlying geologic, biologic, and planetary drivers, (2) predicting mineral paragenetic mode on Earth and other planetary bodies through natural kind clustering, (3) predicting the new locations of mineral occurrence and missing minerals at specified locations on Earth's surface via affinity analysis, (4) investigating the tectonic drivers of mineralization through deep time through integration with paleotectonic reconstructions, (5) understanding the complex feedback systems controlling the relationships between mineralogy and the geochemical environment with microbial populations and their enzymatic functions, and (6) quantifying preservational and sampling bias in the mineralogical record. These recent discoveries and new research directions show great promise for further unraveling the complexities surrounding carbon mineral formation, the deep carbon cycle, and life's coevolution with Earth materials and processes.

AUTHOR CONTRIBUTIONS

The individuals listed with the following projects or databases provided discussion, performed analyses, and/or collected/curated data. JG, RH, RD, and SM: the International Mineralogical Association list of mineral species (RRUFF.info/IMA). CL, DH, JG, JR, RH, RD, SR, and SM: the Mineral Evolution Database (MED). AE, AP, JR, RH, RD, SM, and SK: the Mineral Properties Database (MPD). JR: Mindat.org. AE, AP, JG, JR, PF, RH, RD, SM, and SK: Global Earth Mineral Inventory (GEMI). AE, CL, DH, GH, JG, JR, RH, RD, and SM: Mineral ecology. AE, AP, CL, DH, GH, JG, JR, LK, OK, PF, RH, RD, and SM: network analysis. DH, RH, SM, and SK: organic carbon mineralogy. AE, AP, CL, PF, RH, and SM: natural kind clustering. AE, AP, JG, JR, PF, RH, and SM: affinity analysis. AM, CL, JG, RH, SM, and SZ: GPlates plate tectonic reconstructions. AE, AP, DG, JB, PF, RH, and SM: microbial populations and mineral systems. CL, JR, RH, and SR: quantifying preservational bias.

FUNDING

This publication is a contribution to the Deep Carbon Observatory. Studies of mineral evolution, mineral ecology, and data-driven discovery in mineral systems are supported by the Deep Carbon Observatory, the Alfred P. Sloan Foundation, the W. M. Keck Foundation, the John Templeton Foundation, the NASA Astrobiology Institute (80NSSC18M0093), a private foundation, and the Carnegie Institution for Science. SK thanks Russian Science Foundation for financial support (grant 19-17-00038). SZ was supported by Alfred P. Sloan grants G-2017-9997 and G-2018-11296 through the Deep Carbon Observatory, and Australian Research Council grant IH130200012. Any opinions, findings, or recommendations expressed herein are those of the authors and do not necessarily reflect the views of the funding agencies or affiliated organizations.

ACKNOWLEDGMENTS

The authors thank the reviewers of this manuscript for their insightful and constructive feedback. A special thanks goes to Erin Delventhal for her field work to identify a previously unreported wulfenite locality.

SUPPLEMENTARY MATERIAL

The Supplementary Material for this article can be found online at: https://www.frontiersin.org/articles/10.3389/feart.2020.00208/full#supplementary-material

REFERENCES

Abraham, A., Hassanien, A.-E., and Snasel, V. (2010). *Computational Social Network Analysis: Trends, Tools and Research Advances*, eds A. Abraham, A. E. Hassanien, and V. Snasel (New York, NY: Springer).

Agrawal, R., and Srikant, R. (1994). "Fast algorithms for mining association rules," in *Proceedings of the 20th International Conference on Very Large Data Bases*, San Jose, CA, 487–499.

Amari, S., Anders, E., Virag, A., and Zinner, E. (1990). Interstellar graphite in meteorites. *Nature* 345, 238–240. doi: 10.1038/345238a0

Anthony, J. W., Bideaux, R. A., Bladh, K. W., and Nichols, M. C. (2003). *Handbook of Mineralogy*. Chantilly, VA: Mineralogical Society of America.

Barry, P. H., de Moor, J. M., Giovannelli, D., Schrenk, M., Hummer, D. R., Lopez, T., et al. (2019a). Forearc carbon sink reduces long-term volatile recycling into the mantle. *Nature* 568, 487–492. doi: 10.1038/s41586-019-1131-5

Barry, P. H., Nakagawa, M., Giovannelli, D., Maarten de Moor, J., Schrenk, M., Seltzer, A. M., et al. (2019b). Helium, inorganic and organic carbon isotopes of fluids and gases across the Costa Rica convergent margin. *Sci. Data* 6:284. doi: 10.1038/s41597-019-0302-4

Benner, S. A., Kim, H.-J., Kim, M.-J., and Ricardo, A. (2010). Planetary organic chemistry and the origins of biomolecules. *Cold Spring Harb. Perspect. Biol.* 2:a003467. doi: 10.1101/cshperspect.a003467

Bojar, H.-P., Walter, F., and Baumgartner, J. (2017). Joanneumite, $Cu(C_3N_3O_3H_2)_2(NH_3)_2$, a new mineral from Pabellón de Pica, Chile and the crystal structure of its synthetic analogue. *Mineral. Mag.* 81, 155–166. doi: 10.1180/minmag.2016.080.078

Boujibar, A., Zhang, S., Howell, S., Prabhu, A., Narkar, S., Hystad, G., et al. (2019). Natural kind clustering of presolar silicon carbides and its astrophysical implications. *AGUFM* 2019:V11C-02.

Buffett, B. A. (2000). Clathrate hydrates. *Annu. Rev. Earth Planet. Sci.* 28, 477–507.

Buongiorno, J., Fullerton, K., Rogers, T., Giovannelli, D., DeMoor, M., Barry, P., et al. (2019a). "Interactions between microbial communities and their geologic environment at the Costa Rica active margin," in *Proceedings of the Goldschmidt Annual Meeting*, Barcelona.

Buongiorno, J., Giovannelli, D., DeMoor, M., Barry, P., Shrenk, M., Lloyd, K., et al. (2020). "An integrated machine learning approach reveals geochemical controls on microbial electron-transfer protein abundance," in *Proceedings of the Goldschmidt Annual Meeting (Virtual)*.

Buongiorno, J., Herbert, L. C., Wehrmann, L. M., Michaud, A., Laufer, K., Røy, H., et al. (2019b). Complex microbial communities drive iron and sulfur cycling in Arctic fjord sediments. *Appl. Environ. Microbiol.* 85:e00949-19. doi: 10.1128/AEM.00949-19

Burton, A. S., Stern, J. C., Elsila, J. E., Glavin, D. P., and Dworkin, J. P. (2012). Understanding prebiotic chemistry through the analysis of extraterrestrial amino acids and nucleobases in meteorites. *Chem. Soc. Rev.* 41, 5459–5472.

Cable, M. L., Hörst, S. M., Hodyss, R., Beauchamp, P. M., Smith, M. A., and Willis, P. A. (2012). Titan tholins: simulating titan organic chemistry in the cassini-huygens era. *Chem. Rev.* 112, 1882–1909. doi: 10.1021/cr200221x

Cable, M. L., Vu, T. H., Maynard-Casely, H. E., Choukroun, M., and Hodyss, R. (2018). The acetylene-ammonia co-crystal on titan. *ACS Earth Sp. Chem.* 2, 366–375. doi: 10.1021/acsearthspacechem.7b00135

Chesnokov, B. V., Shcherbakova, Y. P., and Nishanbayev, T. P. (2008). *Minerals from Burned Dumps of Chelyabinsk Coal Basin*. Miass: Russian Academy of Sciences, 139.

Clauset, A., Newman, M. E. J., and Moore, C. (2004). Finding community structure in very large networks. *Phys. Rev. E.* 70:066111. doi: 10.1103/PhysRevE.70.066111

Cooper, G., Kimmich, N., Belisle, W., Sarinana, J., Brabham, K., and Garrel, L. (2001). Carbonaceous meteorites as a source of sugar-related organic compounds for the early earth. *Nature* 414, 879–883. doi: 10.1038/414879a

Cooper, G., and Rios, A. C. (2016). Enantiomer excesses of rare and common sugar derivatives in carbonaceous meteorites. *Proc. Natl. Acad. Sci. U.S.A.* 113, E3322–E3331.

Csardi, G., and Nepusz, T. (2006). *The Igraph Software Package for Complex Network Research. InterJournal Complex Systems 1695*. Available online at: http://igraph.sf.net (accessed March 8, 2012).

Davies, G. (1984). *Diamond*. Bristol: Adam Hilger Ltd.

Echigo, T., and Kimata, M. (2010). CRYSTAL CHEMISTRY AND GENESIS OF ORGANIC MINERALS: A REVIEW OF OXALATE AND POLYCYCLIC AROMATIC HYDROCARBON MINERALS. *Can. Mineral.* 48, 1329–1357. doi: 10.3749/canmin.48.5.1329

Formisano, V., Atreya, S., Encrenaz, T., Ignatiev, N., and Giuranna, M. (2004). Detection of methane in the atmosphere of mars. *Science* 306, 1758–1761. doi: 10.1126/science.1101732

Frank, O., and Strauss, D. (1986). Markov graphs. *J. Am. Stat. Assoc.* 81, 832–842. doi: 10.1080/01621459.1986.10478342

Fruchterman, T. M. J., and Reingold, E. M. (1991). Graph drawing by force-directed placement. *Softw. Pract. Exp.* 21, 1129–1164. doi: 10.1002/spe.4380211102

Fu, Q., Lollar, B. S., Horita, J., Lacrampe-Couloume, G., and Seyfried, W. E. Jr. (2007). Abiotic formation of hydrocarbons under hydrothermal conditions: constraints from chemical and isotope data. *Geochim. Cosmochim. Acta* 71, 1982–1998. doi: 10.1016/j.gca.2007.01.022

Garai, J., Haggerty, S. E., Rekhi, S., and Chance, M. (2006). Infrared absorption investigations confirm the extraterrestrial origin of carbonado diamonds. *Astrophys. J. Lett.* 653:L153. doi: 10.1086/510451

Giovannelli, D., Buongiorno, J., Prabhu, A., Eleish, A., Huang, F., Fox, P. A., et al. (2019). Tracking the evolution of our planet using large scale geochemistry and metagenomic data. *AGUFM* 2019:V11C-06.

Glasby, G. P. (2006). Abiogenic origin of hydrocarbons: an historical overview. *Resour. Geol.* 56, 83–96. doi: 10.1111/j.1751-3928.2006.tb00271.x

Glikson, A. Y., and Pirajno, F. (2018). *Asteroids Impacts, Crustal Evolution and Related Mineral Systems with Special Reference to Australia*. Berlin: Springer.

Golden, J. J., McMillan, M., Downs, R. T., Hystad, G., Goldstein, I., Stein, H. J., et al. (2013). Rhenium variations in molybdenite (MoS2): evidence for progressive subsurface oxidation. *Earth Planet. Sci. Lett.* 366, 1–5. doi: 10.1016/j.epsl.2013.01.034

Golden, J. J., Pires, A. J., Hazen, R. M., Downs, R. T., Ralph, J., and Meyer, M. (2016). "Building the Mineral evolution database: implications for future big data analysis," in *Proceedings of the Geological Society of America Annual Meeting Abstracts with Programs, 7*, Denver, CO. doi: 10.1130/abs/2016AM-286024

Grew, E. S., Dymek, R. F., De Hoog, J. C. M., Harley, S. L., Boak, J., Hazen, R. M., et al. (2015). Boron isotopes in tourmaline from the ca. 3.7–3.8 Ga Isua supracrustal belt, Greenland: sources for boron in Eoarchean continental crust and seawater. *Geochim. Cosmochim. Acta* 163, 156–177. doi: 10.1016/j.gca.2015.04.045

Grew, E. S., and Hazen, R. M. (2014). Beryllium mineral evolution. *Am. Mineral.* 99, 999–1021. doi: 10.2138/am.2014.4675

Grew, E. S., Hystad, G., Hazen, R. M., Krivovichev, S. V., and Gorelova, L. A. (2017). How many boron minerals occur in Earth's upper crust? *Am. Mineral.* 102, 1573–1587. doi: 10.2138/am-2017-5897

Grew, E. S., Krivovichev, S. V., Hazen, R. M., and Hystad, G. (2016). Evolution of structural complexity in boron minerals. *Can. Mineral.* 54, 125–143. doi: 10.3749/canmin.1500072

Hand, E. (2018). Mars methane rises and falls with the seasons. *Science* 359, 16–17. doi: 10.1126/science.359.6371.16

Hazen, R. M., Bromberg, Y., Downs, R., Eleish, A., Falkowski, P., Fox, P., et al. (2019a). "Deep carbon through deep time: data-driven insights," in *Deep Carbon: Past to Present*, eds B. Orcutt, R. Dasgupta, and I. Daniel (Cambridge: Cambridge University Press), 620–652. doi: 10.1017/9781108677950.020

Hazen, R. M. (2013). Paleomineralogy of the Hadean eon: a preliminary species list. *Am. J. Sci.* 313, 807–843. doi: 10.2475/09.2013.01

Hazen, R. M. (2018). Titan mineralogy: a window on organic mineral evolution. *Am. Mineral.* 103, 341–342. doi: 10.2138/am-2018-6407

Hazen, R. M. (2019). An evolutionary system of mineralogy: proposal for a classification based on natural kind clustering. *Am. Mineral.* 104, 810–816. doi: 10.2138/am-2019-6709CCBYNCND

Hazen, R. M., Bekker, A., Bish, D. L., Bleeker, W., Downs, R. T., Farquhar, J., et al. (2011). Needs and opportunities in mineral evolution research. *Am. Mineral.* 96, 953–963. doi: 10.2138/am.2011.3725

Hazen, R. M., Downs, R. T., Eleish, A., Fox, P., Gagné, O. C., Golden, J. J., et al. (2019b). Data-driven discovery in mineralogy: recent advances in data resources, analysis, and visualization. *Engineering* 5, 397–405. doi: 10.1016/J.ENG.2019.03.006

Hazen, R. M., Downs, R. T., Jones, A. P., and Kah, L. (2013a). "Carbon mineralogy and crystal chemistry," in *Reviews in Mineralogy and Geochemistry*, eds R. M. Hazen, A. Jones, and J. Baross (Chantilly, VA: Mineralogical Society of America), 7–46. doi: 10.2138/rmg.2013.75.2

Hazen, R. M., Downs, R. T., Kah, L., and Sverjensky, D. (2013b). Carbon mineral evolution. *Rev. Mineral. Geochem.* 75, 79–107. doi: 10.2138/rmg.2013.75.4

Hazen, R. M., and Ferry, J. M. (2010). Mineral evolution: mineralogy in the fourth dimension. *Elements* 6, 9–12. doi: 10.2113/gselements.6.1.9

Hazen, R. M., Grew, E. S., Downs, R. T., Golden, J., and Hystad, G. (2015a). Mineral ecology: chance and necessity in the mineral diversity of terrestrial planets. *Can. Mineral.* 53, 295–324. doi: 10.3749/canmin.1400086

Hazen, R. M., Grew, E. S., Origlieri, M. J., and Downs, R. T. (2017a). On the mineralogy of the "Anthropocene Epoch."*Am. Mineral.* 102, 595–611. doi: 10.2138/am-2017-5875

Hazen, R. M., Hummer, D. R., Hystad, G., Downs, R. T., and Golden, J. J. (2016). Carbon mineral ecology: predicting the undiscovered minerals of carbon. *Am. Mineral.* 101, 889–906. doi: 10.2138/am-2016-5546

Hazen, R. M., Hystad, G., Downs, R. T., Golden, J. J., Pires, A. J., and Grew, E. S. (2015b). Earth's "missing" minerals. *Am. Mineral.* 100, 2344–2347. doi: 10.2138/am-2015-5417

Hazen, R. M., Hystad, G., Golden, J. J., Hummer, D. R., Liu, C., Downs, R. T., et al. (2017b). Cobalt mineral ecology. *Am. Mineral.* 102, 108–116. doi: 10.2138/am-2017-5798

Hazen, R. M., Liu, X.-M., Downs, R. T., Golden, J. J., Pires, A. J., Grew, E. S., et al. (2014). Mineral evolution: episodic metallogenesis, the supercontinent cycle, and the coevolving geosphere and biosphere. *Soc. Econ. Geol. Spec. Publ.* 18, 1–15.

Hazen, R. M., and Morrison, S. M. (2019). An evolutionary system of mineralogy, part I: stellar mineralogy (>13 to 4.6 Ga). *Am. Mineral.* 105, 627–651. doi: 10.2138/am-2020-7173

Hazen, R. M., Papineau, D., Bleeker, W., Downs, R. T., Ferry, J. M., McCoy, T. J., et al. (2008). Mineral evolution. *Am. Mineral.* 93, 1693–1720. doi: 10.2138/am.2008.2955

Hazen, R. M., Sverjensky, D. A., Azzolini, D., Bish, D. L., Elmore, S. C., Hinnov, L., et al. (2013c). Clay mineral evolution. *Am. Mineral.* 98, 2007–2029.

Heaney, P. J., Vicenzi, E. P., and De, S. (2005). Strange diamonds: the mysterious origins of carbonado and framesite. *Elements* 1, 85–89. doi: 10.2113/gselements.1.2.85

Huang, F., Daniel, I., Cardon, H., Montagnac, G., and Sverjensky, D. A. (2017). Immiscible hydrocarbon fluids in the deep carbon cycle. *Nat. Commun.* 8:15798. doi: 10.1038/ncomms15798

Hummer, D. R., Noll, B. C., Hazen, R. M., and Downs, R. T. (2017). Crystal structure of abelsonite, the only known crystalline geoporphyrin. *Am. Mineral.* 102, 1129–1132.

Hunter, D. R. (2007). Curved exponential family models for social networks. *Soc. Netw.* 29, 216–230. doi: 10.1016/J.SOCNET.2006.08.005

Hunter, D. R., and Handcock, M. S. (2006). Inference in curved exponential family models for networks. *J. Comput. Graph. Stat.* 15, 565–583. doi: 10.1198/106186006X133069

Huskić, I., and Friščić, T. (2018). Understanding geology through crystal engineering: coordination complexes, coordination polymers and metal–organic frameworks as minerals. *Acta Crystallogr. Sect. B Struct. Sci. Cryst. Eng. Mater.* 74, 539–559. doi: 10.1107/S2052520618014762

Huskiæ, I., and Frišèiæ, T. (2019). Geomimetic approaches in the design and synthesis of metal-organic frameworks. *Philos. Trans. R. Soc. A Math. Phys. Eng. Sci.* 377:20180221. doi: 10.1098/rsta.2018.0221

Huskić, I., Pekov, I. V., Krivovichev, S. V., and Frišèić, T. (2016). Minerals with metal-organic framework structures. *Sci. Adv.* 2:e1600621. doi: 10.1126/sciadv.1600621

Hystad, G., Downs, R. T., Grew, E. S., and Hazen, R. M. (2015a). Statistical analysis of mineral diversity and distribution: earth's mineralogy is unique. *Earth Planet. Sci. Lett.* 426, 154–157. doi: 10.1016/j.epsl.2015.06.028

Hystad, G., Downs, R. T., and Hazen, R. M. (2015b). Mineral species frequency distribution conforms to a large number of rare events model: prediction of earth's missing minerals. *Math. Geosci.* 47, 647–661. doi: 10.1007/s11004-015-9600-3

Hystad, G., Eleish, A., Hazen, R. M., Morrison, S. M., and Downs, R. T. (2019a). Bayesian estimation of earth's undiscovered mineralogical diversity using noninformative priors. *Math. Geosci.* 51, 401–417. doi: 10.1007/s11004-019-09795-8

Hystad, G., Morrison, S. M., and Hazen, R. M. (2019b). Statistical analysis of mineral evolution and mineral ecology: the current state and a vision for the future. *Appl. Comput. Geosci.* 1:100005. doi: 10.1016/j.acags.2019.100005

Kebukawa, Y., and Cody, G. D. (2015). A kinetic study of the formation of organic solids from formaldehyde: implications for the origin of extraterrestrial organic solids in primitive solar system objects. *Icarus* 248, 412–423. doi: 10.1016/J.ICARUS.2014.11.005

Kimura, J., and Kitadai, N. (2015). Polymerization of building blocks of life on Europa and other icy moons. *Astrobiology* 15, 430–441. doi: 10.1089/ast.2015.1306

Koga, T., and Naraoka, H. (2017). A new family of extraterrestrial amino acids in the Murchison meteorite. *Sci. Rep.* 7:636. doi: 10.1038/s41598-017-00693-9

Kolaczyk, E. D. (2009a). *Sampling and Estimation in Network Graphs*. New York, NY: Springer, doi: 10.1007/978-0-387-88146-1_5

Kolaczyk, E. D. (2009b). *Statistical Analysis of Network Data*. New York, NY: Springer-Verlag.

Kolaczyk, E. D., and Csárdi, G. (2014). *Statistical Analysis of Network Data with R*. New York, NY: Springer New York. doi: 10.1111/insr.12095_10

Kolesnikov, A., Kutcherov, V. G., and Goncharov, A. F. (2009). Methane-derived hydrocarbons produced under upper-mantle conditions. *Nat. Geosci.* 2, 566–570. doi: 10.1038/ngeo591

Krivovichev, S. (2012). Topological complexity of crystal structures: quantitative approach. *Acta Crystallogr. Sect. A Found. Crystallogr.* 68, 393–398. doi: 10.1107/S0108767312012044

Krivovichev, V. G., Charykova, M. V., and Krivovichev, S. V. (2018). The concept of mineral systems and its application to the study of mineral diversity and evolution. *Eur. J. Mineral.* 30, 219–230. doi: 10.1127/ejm/2018/0030-2699

Krivovichev, S. V. (2013). Structural complexity of minerals: information storage and processing in the mineral world. *Mineral. Mag.* 77, 275–326. doi: 10.1180/minmag.2013.077.3.05

Krivovichev, S. V. (2016). Structural complexity and configurational entropy of crystals. *Acta Crystallogr. Sect. B Struct. Sci. Cryst. Eng. Mater.* 72, 274–276. doi: 10.1107/S205252061501906X

Krivovichev, S. V. (2018). Ladders of information: what contributes to the structural complexity of inorganic crystals. *Zeitschrift für Krist. Cryst. Mater.* 233, 155–161. doi: 10.1515/zkri-2017-2117

Krivovichev, S. V., Krivovichev, V. G., and Hazen, R. M. (2017). Structural and chemical complexity of minerals: correlations and time evolution. *Eur. J. Mineral.* 30, 231–236. doi: 10.1127/ejm/2018/0030-2694

Kvenvolden, K. A. (1995). A review of the geochemistry of methane in natural gas hydrate. *Org. Geochem.* 23, 997–1008. doi: 10.1016/0146-6380(96)00002-2

Lafuente, B., Downs, R. T., Yang, H., and Stone, N. (2015). "The power of databases: the RRUFF project," in *Highlights in Mineralogical Crystallography*, eds T. Armbruster and R. M. Danisi (Berlin: De Gruyter).

Lewis, R. S., Ming, T., Wacker, J. F., Anders, E., and Steel, E. (1987). Interstellar diamonds in meteorites. *Nature* 326, 160–162. doi: 10.1038/326160a0

Li, S., Huskić, I., Novendra, N., Titi, H. M., Navrotsky, A., and Frišèić, T. (2019). Mechanochemical synthesis, accelerated aging, and thermodynamic stability of the organic mineral paceite and its cadmium analogue. *ACS Omega* 4, 5486–5495. doi: 10.1021/acsomega.9b00295

Liu, C., Eleish, A., Hystad, G., Golden, J. J., Downs, R. T., Morrison, S. M., et al. (2018a). Analysis and visualization of vanadium mineral diversity and distribution. *Am. Mineral.* 103, 1080–1086. doi: 10.2138/am-2018-6274

Liu, C., Hystad, G., Golden, J. J., Hummer, D. R., Downs, R. T., Morrison, S. M., et al. (2017a). Chromium mineral ecology. *Am. Mineral.* 102, 612–619. doi: 10.2138/am-2017-5900

Liu, C., Knoll, A. H., and Hazen, R. M. (2017b). Geochemical and mineralogical evidence that Rodinian assembly was unique. *Nat. Commun.* 8:1950. doi: 10.1038/s41467-017-02095-x

Liu, C., Runyon, S. E., Knoll, A. H., and Hazen, R. T. (2018b). The same and not the same: ore geology, mineralogy and geochemistry of Rodinia assembly. *Earth Sci. Rev.* 196:102860. doi: 10.1016/j.earscirev.2019.05.004

Lusher, D., Koskinen, J., and Robins, G. (eds). (2012). *Exponential Random Graph Models for Social Networks*. Cambridge: Cambridge University Press. doi: 10.1017/CBO9780511894701

Ma, X., Hummer, D., Golden, J., Fox, P., Hazen, R., Morrison, S., et al. (2017). Using visual exploratory data analysis to facilitate collaboration and hypothesis generation in cross-disciplinary research. *ISPRS Int. J. Geo Information* 6:368. doi: 10.3390/ijgi6110368

Maynard-Casely, H. E., Cable, M. L., Malaska, M. J., Vu, T. H., Choukroun, M., and Hodyss, R. (2018). Prospects for mineralogy on Titan. *Am. Mineral.* 103, 343–349. doi: 10.2138/am-2018-6259

McCollom, T. M. (2013). Laboratory simulations of abiotic hydrocarbon formation in Earth's deep subsurface. *Rev. Mineral. Geochem.* 75, 467–494. doi: 10.1515/9781501508318-017

McCord, T. B., Carlson, R. W., Smythe, W. D., Hansen, G. B., Clark, R. N., Hibbitts, C. A., et al. (1997). Organics and other molecules in the surfaces of Callisto and Ganymede. *Science* 278, 271–275. doi: 10.1126/science.278.5336.271

McMillan, M. M., Downs, R. T., Stein, H. J., Zimmerman, A., Beitscher, B. A., Sverjensky, D. A., et al. (2010). Molybdenite mineral evolution: a study of trace elements through time. *AGU Fall Meet. Abstr.* 1:2293.

Merdith, A. S., Williams, S. E., Müller, R. D., and Collins, A. S. (2017). Kinematic constraints on the Rodinia to Gondwana transition. *Precambrian Res.* 299, 132–150. doi: 10.1016/J.PRECAMRES.2017.07.013

Mills, S. J., Kampf, A. R., Nestola, F., Williams, P. A., Leverett, P., Hejazi, L., et al. (2017). Wampenite, C18 H16, a new organic mineral from the fossil conifer locality at Wampen, Bavaria, Germany. *Eur. J. Mineral.* 29, 511–515. doi: 10.1127/ejm/2017/0029-2621

Morrison, S. M., and Hazen, R. M. (2020). An evolutionary system of mineralogy, part II: Interstellar and solar nebula primary condensation mineralogy (> 4.565 Ga). *Am. Mineral.* doi: 10.2138/am-2020-7447

Morrison, S. M., Prabhu, A., Eleish, A., Narkar, S., Fox, P., Golden, J. J., et al. (2020). "Mineral affinity analysis: predicting unknown mineral occurrences with machine learning," in *Proceedings of the Goldschmidt Annual Meeting*.

Morrison, S. M., Eleish, A., Liu, C., Hummer, D., Giovannelli, D., Meyer, M., et al. (2017a). "Network analysis applications: exploring geosphere and biosphere co-evolution with big data techniques," in *Proceedings of the Goldschmidt Annual Meeting*, Paris.

Morrison, S. M., Liu, C., Eleish, A., Prabhu, A., Li, C., Ralph, J., et al. (2017b). Network analyses of mineralogical systems. *Am. Mineral.* 102, 1588–1596. doi: 10.2138/am-2017-6104

Morrison, S. M., Runyon, S. E., and Hazen, R. M. (2018). The paleomineralogy of the hadean eon revisited. *Life* 8:64. doi: 10.3390/life8040064

Müller, R. D., Cannon, J., Qin, X., Watson, R. J., Gurnis, M., Williams, S., et al. (2018). GPlates: building a virtual earth through deep time. *Geochem. Geophys. Geosyst.* 19, 2243–2261. doi: 10.1029/2018GC007584

Nasdala, L., and Pekov, I. V. (1993). Ravatite, C14HIO, a new organic mineral species from Ravat, Tadzhikistan. *Eur. J. Miner.* 5, 699–705. doi: 10.1127/ejm/5/4/0699

Newman, M. E. J. (2006). Finding community structure in networks using the eigenvectors of matrices.pdf. *Phys. Rev. E* 74:36104. doi: 10.1103/PhysRevE.74.036104

Newman, M. E. J., and Mark, E. J. (2010). *Networks?: an Introduction*. Oxford: Oxford University Press.

Oftedal, I. (1922). "Minerals from the burning coal seam at Mt. Pyramide, Spitsbergen," in *Resultater av de Norske Statsunderstottede Spitsbergenekspeditioner:UTGIT PAA Den Norske Stats Bekostning Ved Spitsbergenkomiteen 1*, eds W. Werenskiold and I. Oftedal (Oslo: Det Norske Videnskaps-Akademi), 9–14.

Ott, U. (2009). Nanodiamonds in meteorites: properties and astrophysical context. *J. Achiev. Mat. Manuf. Eng.* 37, 779–784.

Otte, E., and Rousseau, R. (2002). Social network analysis: a powerful strategy, also for the information sciences. *J. Inf. Sci.* 28, 441–453. doi: 10.1177/016555150202800601

Pattison, P., Kalish, Y., and Lusher, D. (2007). An introduction to exponential random graph (p*) models for social networks. *Soc. Netw.* 29, 173–191. doi: 10.1016/J.SOCNET.2006.08.002

Pekov, I. V., Chukanov, N. V., Belakovskiy, D. I., Lykova, I. S., Yapaskurt, V. O., Zubkova, N. V., et al. (2016). Tinnunculite, IMA 2015-021a. *Mineral. Mag.* 80, 199–205.

Perry, R. S., Mcloughlin, N., Lynne, B. Y., Sephton, M. A., Oliver, J. D., Perry, C. C., et al. (2007). Defining biominerals and organominerals: direct and indirect indicators of life. *Sediment. Geol.* 201, 157–179. doi: 10.1016/j.sedgeo.2007.05.014

Perry, S., Morrison, S., Runyon, S., Prabhu, A., Eleish, A., Zhong, H., et al. (2018). "Big data network analysis of uranium mineral occurrences and formation mechanisms," in *Proceedings of the International Mineralogical Association Conference* (Melbourne).

Piro, O. E., and Baran, E. J. (2018). Crystal chemistry of organic minerals – salts of organic acids: the synthetic approach. *Crystallogr. Rev.* 24, 149–175. doi: 10.1080/0889311X.2018.1445239

Pizzarello, S., Cooper, G. W., and Flynn, G. J. (2006). The nature and distribution of the organic material in carbonaceous chondrites and interplanetary dust particles. *Meteor. Early Sol. Syst. II* 1, 625–651.

Prabhu, A., Morrison, S. M., Eleish, A., Zhong, H., Huang, F., Golden, J. J., et al. (2019a). *Creating, Managing and Evaluating Data Legacies: Updates on the Global Earth Mineral Inventory*. AGU, Abstract U11C-0.

Prabhu, A., Morrison, S. M., Eleish, A., Narkar, S., Fox, P. A., Golden, J. J., et al. (2019b). Predicting unknown mineral localities based on mineral associations. *AGUFM* 2019:EP23D-2286.

Prabhu, A., Morrison, S. M., Eleish, A., Zhong, H., Huang, F., Golden, J., et al. (2020). Global Earth Mineral Inventory: a deep carbon observatory data legacy. Special Issue. *Geosci. Data J.* doi: 10.1002/GDJ3.106

Rost, R. (1942). Supplements to the mineralogy of the burning (coal) heaps in the region of Kladno. Rozpravy II. *Třídy Ces. Akad.* 52, 1–4.

Sephton, M. A., and Hazen, R. M. (2013). On the origins of deep hydrocarbons. *Rev. Mineral. Geochem.* 75, 449–465. doi: 10.2138/rmg.2013.75.14

Sephton, M. A. (2002). Organic compounds in carbonaceous meteorites. *Nat. Prod. Rep.* 19, 292–311. doi: 10.1039/b103775g

Shin, K., Kumar, R., Udachin, K. A., Alavi, S., and Ripmeester, J. A. (2012). Ammonia clathrate hydrates as new solid phases for Titan, Enceladus, and other planetary systems. *Proc. Natl. Acad. Sci. U.S.A.* 109, 14785–14790. doi: 10.1073/pnas.1205820109

Shirey, S. B., Cartigny, P., Frost, D. J., Keshav, S., Nestola, F., Nimis, P., et al. (2013). Diamonds and the geology of mantle carbon. *Rev. Mineral. Geochem.* 75, 355–421.

Skinner, H. C. W. (2005). Biominerals. *Mineral. Mag.* 69, 621–641. doi: 10.1180/0026461056950275

Smith, E. M., Shirey, S. B., Nestola, F., Bullock, E. S., Wang, J., Richardson, S. H., et al. (2016). Large gem diamonds from metallic liquid in Earth's deep mantle. *Science* 354, 1403–1405. doi: 10.1126/science.aal1303

Snijders, T. A. B., Pattison, P. E., Robins, G. L., and Handcock, M. S. (2006). New specifications for exponential random graph models. *Sociol. Methodol.* 36, 99–153. doi: 10.1111/j.1467-9531.2006.00176.x

Snjiders, T. A. B. (2002). Markov chain Monte Carlo estimation of exponential random graph models. *J. Soc. Struct.* 3, 1–5.

Sverjensky, D. A., and Huang, F. (2015). Diamond formation due to a pH drop during fluid–rock interactions. *Nat. Commun.* 6:8702. doi: 10.1038/ncomms9702

Wang, P., Robins, G., Pattison, P., and Lazega, E. (2013). Exponential random graph models for multilevel networks. *Soc. Netw.* 35, 96–115. doi: 10.1016/J.SOCNET.2013.01.004

Webster, C. R., Mahaffy, P. R., Atreya, S. K., Flesch, G. J., Mischna, M. A., Meslin, P.-Y., et al. (2015). mars atmosphere. mars methane detection and variability at Gale crater. *Science* 347, 415–417. doi: 10.1126/science.1261713

Webster, C. R., Mahaffy, P. R., Atreya, S. K., Moores, J. E., Flesch, G. J., Malespin, C., et al. (2018). Background levels of methane in Mars' atmosphere show strong seasonal variations. *Science* 360, 1093–1096. doi: 10.1126/science.aaq0131

Witzke, T., de Wit, F., Kolitsch, U., Blass, G., Stracher, G. B., Prakash, A., et al. (2015). Mineralogy of the burning Anna I coal mine dump, Alsdorf, Germany. *Coal Peat Fires Glob. Perspect.* 3, 203–240. doi: 10.1016/b978-0-444-59509-6.00007-7

Young, A., Flament, N., Maloney, K., Williams, S., Matthews, K., Zahirovic, S., et al. (2019). Global kinematics of tectonic plates and subduction zones since the late Paleozoic Era. *Geosci. Front.* 10, 989–1013. doi: 10.1016/J.GSF.2018.05.011

Zalasiewicz, J., Kryza, R., and Williams, M. (2014). The mineral signature of the Anthropocene in its deep-time context. *Geol. Soc. London Spec. Publ.* 395, 109–117. doi: 10.1144/sp395.2

Zhang, S., Morrison, S. M., Prabhu, A., Ma, C., Huang, F., Gregory, D., et al. (2019). Natural clustering of pyrite with implications for its formational environment. *AGUFM* 2019:EP23D-2284.

Zinner, E., Ming, T., and Anders, E. (1987). Large isotopic anomalies of Si, C, N and noble gases in interstellar silicon carbide from the Murray meteorite. *Nature* 330, 730–732. doi: 10.1038/330730a0

Zolensky, M., Fries, M., Chan, Q. H.-S., Kebukawa, Y., Bodnar, R., Burton, A., et al. (2015). *Survival of Organic Materials in Ancient Cryovolcanically-Produced Halite Crystals*. NASA Technical Reports Server (NTRS) JSC-CN-32901. Moffet Field, CA.

Conflict of Interest: The authors declare that the research was conducted in the absence of any commercial or financial relationships that could be construed as a potential conflict of interest.

Advantages of publishing in Frontiers

OPEN ACCESS
Articles are free to read for greatest visibility and readership

FAST PUBLICATION
Around 90 days from submission to decision

HIGH QUALITY PEER-REVIEW
Rigorous, collaborative, and constructive peer-review

TRANSPARENT PEER-REVIEW
Editors and reviewers acknowledged by name on published articles

Frontiers
Avenue du Tribunal-Fédéral 34
1005 Lausanne | Switzerland

Visit us: www.frontiersin.org
Contact us: info@frontiersin.org | +41 21 510 17 00

REPRODUCIBILITY OF RESEARCH
Support open data and methods to enhance research reproducibility

DIGITAL PUBLISHING
Articles designed for optimal readership across devices

FOLLOW US
@frontiersin

IMPACT METRICS
Advanced article metrics track visibility across digital media

EXTENSIVE PROMOTION
Marketing and promotion of impactful research

LOOP RESEARCH NETWORK
Our network increases your article's readership